206(3), 2026

COMBUSTION ENGINES

PTNSS

OPOLE UNIVERSITY OF TECHNOLOGY

XII INTERNATIONAL
CONGRESS ON COMBUSTION ENGINES

POLISH SCIENTIFIC SOCIETY OF COMBUSTION ENGINES

21th-23rd June 2027

Opole University of Technology
Faculty of Mechanical Engineering
St. Mikołajczyka str. 5, 45-271 Opole, Poland

Due to the dynamic development of machine and vehicle powertrains, the "Combustion Engines" scientific journal, while retaining its historical title, currently publishes works related not only to internal combustion engines, but also other powertrains, including hybrid drives, electric drives and fuel cells.

PTNSS Supporting Members
Członkowie wspierający PTNSS

BOSMAL Automotive Research and Development Institute Ltd
Instytut Badań i Rozwoju Motoryzacji BOSMAL Sp. z o.o

Motor Transport Institute
Instytut Transportu Samochodowego

Institute of Aviation
Sieć Badawcza Łukasiewicz – Instytut Lotnictwa

Automotive Industry Institute
Sieć Badawcza Łukasiewicz – Przemysłowy Instytut Motoryzacji

Sieć Badawcza Łukasiewicz – Poznański Instytut Technologiczny

AVL List GmbH

Air Force Institute of Technology
Instytut Techniczny Wojsk Lotniczych

Military Institute of Armoured & Automotive Technology
Wojskowy Instytut Techniki Pancernej i Samochodowej

Toyota Motor Poland Ltd. Sp. z o.o.

RADWAG Balances and Scales
RADWAG Wagi Elektroniczne

FOGO Sp. z o.o.

Horus Energia Sp. z o.o.

John Deere Polska Sp. z o.o.

COMBUSTION ENGINES

A Scientific Magazine

2026, 206(3)

Year LXV

PL ISSN 2300-9896
PL eISSN 2658-1442

Publisher:
Polish Scientific Society of Combustion Engines
61-131 Poznan, ul. J. Rychlewskiego 1, Poland
tel.: +48 61 6475959
E-mail: sekretariat@ptnss.pl
WebSite: http://www.ptnss.pl
Papers available on-line: http://combustion-engines.eu

Scientific Board:

Krzysztof Wisłocki – chairman, Poland (*Poznan University of Technology*)
Yuzo Aoyagi – Japan (*Okayama University*)
Ewa Bardasz – USA (*National Academy of Engineering*)
Piotr Bielaczyc – Poland (*BOSMAL Automotive Research and Development Institute Ltd.*)
Zdzisław Chłopek – Poland (*Warsaw University of Technology*)
Tadeu Cordeiro de Melo – Brazil (*Petrobras*)
Jan Czerwinski – Switzerland (*CJ Consulting*)
Radostin Dimitrov – Bulgaria (*University of Varna*)
Friedrich Dinkelacker – Germany (*Leibniz Universität Hannover*)
Hubert Friedl – Austria (*AVL*)
Barouch Giechaskiel – Italy (*European Commission, JRC Italy*)
Leslie Hill – UK (*Horiba*)
Timothy Johnson – USA (*Corning Inc.*)
Kazimierz Lejda – Poland (*Rzeszow University of Technology*)
Helmut List – Austria (*AVL*)
Toni Kinnunen – Finland (*Proventia*)
David Kittelson – USA (*University of Minnesota*)
Christopher Kolodziej – USA (*Delphi Automotive Systems*)
Hu Li – UK (*University of Leeds*)
Vaselin Mihaylov – Bulgaria (*University of Varna*)
Federico Millo – Italy (*Politecnico Torino*)
Jeffrey D. Naber – USA (*Michigan Technological University*)
Andrzej Niewczas – Poland (*Motor Transport Institute*)
Marek Orkisz – Poland (*Rzeszow University of Technology*)
Dieter Peitsch – Germany (*TU Berlin*)
Stefan Pischinger – Germany (*FEV Germany*)
Andrzej Sobiesiak – Canada (*University of Windsor*)
Stanisław Szwaja – Poland (*Częstochowa University of Technology*)
Piotr Szymański – Nederlands (*European Commission, JRC*)
Leonid Tartakovsky – Israel (*Technion – Israel Institute of Technology*)
Andrzej Teodorczyk – Poland (*Warsaw University of Technology*)
Xin Wang – China (*Beijing Institute of Technology*)
Thomas Wallner – USA (*Argonne National Laboratory*)
Michael P. Walsh – USA (*International Council on Clean Transportation*)
Mirosław Wendeker – Poland (*Lublin University of Technology*)

Contents

Longwic R, Kuszneruk M, Tatarynow D. Selected parameters of the combustion process in a compression-ignition engine at different angles of the beginning of injection of mixtures of rapeseed oil with n-hexane 3
Kneba Z. Cabin heating of electric buses 9
Skuza A, Szumska E, Jurecki R. The impact of traffic intensity on the performance and efficiency of hybrid electric vehicles 14
Lijewski P, Fuć P, Brydziński A, Zygmanowski M. Analysis of energy consumption of electric two-wheeled vehicles based on road cycle simulation 27
Laskowski P, Wojs M, Wiśniowski P, Zimakowska-Laskowska M, Kozłowski E. Biogas-fuelled internal combustion engines for micro-scale energy generation: a review of technologies and configurations for systems below 50 kW 34
Nieścioruk MJ, Boroiu A-A, Onescu C, Ozuna G, Ávila AB, Kubiak P, Levchenko D, Wozniak M, Siczek K. The use of hydrogen to supply combustion engines – part 2 44
Sitnik L, Andrych-Zalewska M, Mielinska A. Method of assessing the fuel consumption of a car engine in its long-term natural operation 61
Wiśniowski P, Zimakowska-Laskowska M, Taubert S, Kozłowski E, Ślęzak M, Żbik K. Comparison of pollutant concentrations and engine operating parameters during cold start with petrol and LPG 68
Piórkowski P, Andrzejewski M, Nowak M. The analysis of the use of hydrogen in commercial vehicles 79
Nguyen Thin Q, Nguyen Van D. An analytical study on the performance of spark-ignition engines operating with ammonia fuel 87
Żurawski P, Trytek A. Investigation of the effect of engine running time on the material characteristics of a piston 96
Grzelak M, Borucka A, Rykała M. Analysis of the influence of selected powertrain design parameters on fuel consumption in passenger vehicles 105
Niewiadomski P, Adamczyk F, Członka J. Concept and design of the transport cover for the harvesting unit of a self-propelled forage harwester 112
Palkus K. Numerical analysis of front deflector at outer air seal of low pressure turbine 121
Wojciechowski H, Michalak D, Merkisz J. Differences in structural design and safety requirements of urban buses in Europe and North America 130
Marimuthu K, Sundararaj AJ, Nair AG, Muthumari T. Experimental and kinetic analysis of low to intermediate temperature auto-ignition of binary ethylene-acetylene blends 140
Bebkiewicz K, Grzelak P, Chłopek Z, Biernat K. Modeling of stochastic passenger car velocity processes for the purpose of pollutant emissions inventory 151
Kurzydym D. 1D model of a three-way catalyst in MATLAB/Simulink for assessing pollutant reduction in the NEDC emission test 159
Kropisz O, Skobiej K, Zandecki B. Impact of 2026 FIA technical regulations on Formula 1 power units, aerodynamics and energy management 170
Górzyńska M, Pielecha I. Hydrogen combustion in piston engines: challenges and modeling approaches 179
Khrulev A, Dmytriev S. Study of pulse jet engine thermodynamic cycle using workflow mathematical modeling 199
Pham VC, Ngo DN, Hoang VS, Le VV. Comprehensive review of methanol and LNG as alternative fuels for marine diesel engines 210
Nowak M, Flis B. Engines used in modern unmanned aerial vehicles 229
Cebulska W, Hadryś D, Rajca A. Comparison of magnetic induction emissions in electric, hybrid and conventional cars 237

Declaration of the original version
The original version of the Combustion Engines journal is the electronic version.

Cover
I – Volvo EPA 2027 Powertrain | Next-Generation D13 Engine
(www.volvotrucks.us);
background (Francesco Ungaro – pexels.com)
IV – Mercedes-benz-integrated-starter-generator-ISG
(carmagazine.co.uk)

Publisher:
Polish Scientific Society of Combustion Engines
61-131 Poznan, ul. J. Rychlewskiego 1, Poland
tel.: +48 61 6475959
E-mail: sekretariat@ptnss.pl
WebSite: http://www.ptnss.pl

The Publisher of this magazine does not endorse the products or services advertised herein. The published materials do not necessarily reflect the views and opinions of the Publisher.

© Copyright by
Polish Scientific Society of Combustion Engines
All rights reserved.
No part of this publication may be reproduced, stored in a retrieval system or transmitted, photocopied or otherwise without prior consent of the copyright holder.

The journal is under the patronage of the Transport Committee and the Machine Building Committee of the Polish Academy of Sciences

The journal is registered and listed in the Polish and international database

Papers published in the
Combustion Engines
quarterly receive 70 points as stated by the Notification of the Minister of Science dated 5 January 2024.

Editorial:

Institute of Powertrains and Aviation
Poznan University of Technology
61-138 Poznan, Piotrowo 3 Street
tel.: +48 61 2244505, +48 61 2244502
E-mail: papers@ptnss.pl

Prof. Jerzy Merkisz, DSc., DEng. (Editor-in-chief)
Prof. Miłosław Kozak, DSc., DEng.
Prof. Jacek Pielecha, DSc., DEng. (Editorial Secretary for Science)
Prof. Ireneusz Pielecha, DSc., DEng.
Prof. Jacek Hunicz, DSc., DEng.
Prof. Liping Yang, DSc., DEng.
Prof. Pravesh Chandra Shukla, DSc., DEng.
Di Zhu, DEng.
Wojciech Cieślik, DSc., DEng.
Filip Szwajca, DEng. (Technical Editors)
Joseph Woodburn, DEng. (Proofreading Editor)
Wojciech Serdecki, DSc., DEng. (Statistical Editor)

Article citation info:
Longwic R, Kuszneruk M, Tatarynow D. Selected parameters of the combustion process in a compression-ignition engine at different angles of the beginning of injection of mixtures of rapeseed oil with n-hexane. Combustion Engines. 2026;206(3):3-8. https://doi.org/10.19206/CE-211599

Rafał LONGWIC
Michał KUSZNERUK
Dawid TATARYNOW

Combustion Engines
Polish Scientific Society of Combustion Engines

Selected parameters of the combustion process in a compression-ignition engine at different angles of the beginning of injection of mixtures of rapeseed oil with n-hexane

ARTICLE INFO

Received: 21 June 2025
Revised: 1 October 2025
Accepted: 1 October 2025
Available online: 10 December 2025

The article presents the results of experiments in which a compression-ignition engine was fueled with a mixture of rapeseed oil with a 10% addition of n-hexane. The effect of changing the fuel injection start angle on selected indicators of the combustion process was evaluated. The tests were conducted at a fixed vehicle speed of 90 km/h. The addition of n-hexane made it possible to improve the characteristics of the combustion process of rapeseed oil. The maximum combustion pressure increased to 9.5 MPa (DF: 9.66 MPa; RO: 8.71 MPa), and the ignition delay was shortened. Advancing the pilot injection by –6°CA resulted in stabilization of the kinetic combustion phase; in reality, due to map interpolations and auto-adaptation strategies of the controller, the offset was approx. –4°CA, indicating that it must be taken into account in the interpretation of the results. The average indexed pressure reached 0.805 MPa (DF: 0.813 MPa; RO: 0.728 MPa), and the maximum pressure build-up rate (dp/dα) reached 0.375 MPa/°CA, approaching the 0.399 MPa/°CA recorded for DF. The rate of heat release was in the range of 86–93 kJ/m³·°CA, clearly lower than that of RO (130 kJ/m³·°CA). The results confirm that appropriate modification of the fuel composition, together with a properly selected injection angle, allows compression-ignition engines to burn renewable fuels. The results of the measurements were described with regression relationships, which allows their use in further simulation and development work.

Key words: *alternative fuels, injection angle, diesel engine, indication, rapeseed oil*

This is an open access article under the CC BY license (http://creativecommons.org/licenses/by/4.0/)

1. Introduction

In recent decades, alternative fuels for compression-ignition engines have gained importance in both urban public transport and passenger vehicles. Road and chassis-dynamometer studies consistently demonstrate that conditioning of both conventional and alternative fuels can improve combustion quality and reduce particulate and smoke emissions, as confirmed in full-scale tests on passenger cars and buses [4–6]. This trend responds to environmental imperatives, rising fossil-fuel prices, and the pursuit of greater energy independence. To successfully deploy plant-derived fuels such as rapeseed oil, a comprehensive understanding of combustion processes in electronically controlled diesel injection systems is essential.

This paper addresses the practical use of rapeseed oil enriched with n-hexane in compression-ignition engines. Numerous studies [15–17] have shown that the effectiveness of such a solution depends primarily on the proper modification of the injection system – in particular, on the selection of the injection timing. The high viscosity and surface tension of rapeseed oil cause deterioration of atomization, prolonged injection duration, and delayed autoignition [2, 3, 11]. The introduction of a 10% volume share of n-hexane – as proven in studies [8], reduces the viscosity by more than 50%, lowers the density and surface tension of the mixture, bringing its physicochemical properties closer to diesel fuel. Several benefits of this modification have been observed. First, the reduction in flow resistance allows the fuel system to maintain nominal pressures, which prevents overloading the high-pressure pump [12]. Second, the improved atomization and faster evaporation of the n-hexane fraction promote homogeneous formation of the fuel-air mixture, resulting in an 8–12% increase in average indexed pressure in the 2000–3000 rpm speed range [13]. Third, n-hexane dissolves deposits accumulating in the injector needle zone, reducing their build-up and prolonging the nozzle's trouble-free period [14]. Road tests also eliminated the phenomenon of impeded hot start, observed with RO (rapeseed oil) – only fuelling [10].

However, the limitations of the solution in question cannot be overlooked. The lower cetane number of the mixture (a decrease of 3–5 relative to DF) prolongs the ignition delay phase; at nominal injection settings, this results in a shift of the maximum combustion pressure beyond the optimal angular range, which lowers the indexed efficiency and raises the exhaust gas temperature [3]. A prerequisite for using a mixture of canola oil with 10% n-hexane is the adaptation of the injection strategy. A compilation of research results [7, 9] allows us to formulate two key conclusions, i.e., that the addition of 10% n-hexane significantly improves the physicochemical properties of RO, bringing viscosity, density and surface tension closer to levels acceptable for reservoir injection systems. That efficient combustion requires accelerating the onset of injection.

The purpose of the following discussion, therefore, is a preliminary analysis of how to select the injection angle for an engine fueled by rapeseed oil-based fuel blended with 10% n-hexane, and to assess the impact of these changes on the combustion process.

2. Materials and methods

2.1. Tests stand

The object of the study was a compression-ignition engine with a bunker injection system, which was built into in a Fiat Qubo vehicle. The vehicle's engine met the EURO 5

exhaust gas standard. The data and technical parameters of the test engine are given in Table 1.

Table 1. Main characteristics of the Fiat Qubo vehicle used for the tests

Parameter	Unit
Engine displacement	1248 cm³
Cylinder bore	69.6 mm
Piston stroke	82 mm
Compression ratio	16.8:1
Maximum power	55 kW/75 HP
Maximum torque	190 Nm
Idle speed	850 ±20 rpm
Engine speed at maximum torque	1500 rpm
Fuel injection / supply system	Common rail system
Exhaust aftertreatment systems	Exhaust gas recirculation (EGR), particulate filter

The test stand is shown in a block diagram (Fig. 1). The test vehicle could be fueled with diesel fuel from the vehicle's main tank and other liquid fuel mixtures from an installed auxiliary tank, which allowed quick replacement of the test fuel. The entire process was managed by the engine controller (ECU1 – Electronic Control Unit 1). Fuel consumption was measured using a flow meter, which took into account the return overflow from the injectors and high-pressure pump. Fuel was then fed sequentially to the high-pressure pump, the fuel tank and the injectors. The control and measurement track allowed recording the engine's operating parameters under dynamic conditions, measuring fuel consumption and environmental and energy parameters. The AVL IndiMicro 602 measurement system allowed the recording of rapidly varying in-cylinder pressures and the analysis of injection parameters. Other actual values of engine operation were recorded using the Multiecuscan OBD II (On Board Diagnostics) diagnostic interface.

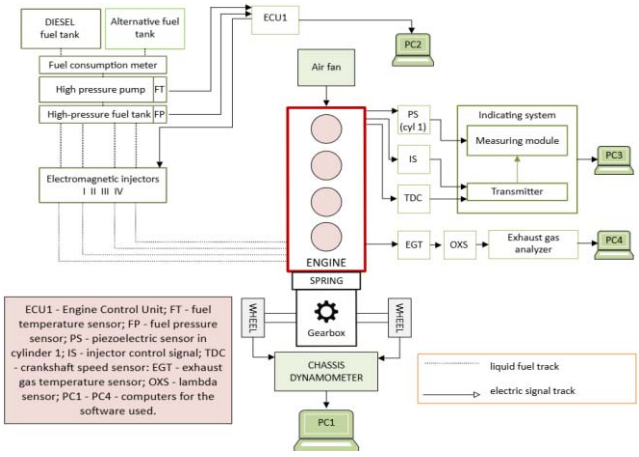

Fig. 1. Block diagram of the test bench

2.2. Course of tests

As part of the preliminary tests, the test vehicle was subjected to simulated tests on a chassis dynamometer according to the Worldwide Harmonized Light Vehicles Test Procedure (WLTP) [1]. Measurement points were selected, i.e., driving at a constant speed of 90 km/h. During the tests performed, the engine was operated with the load resulting from the resistance to motion (rolling resistance, air resistance) mapped on the chassis dynamometer set in "driving simulation" mode. Three fuels were selected to power the engine with nominal software in the controller, which were assigned designations used consistently throughout the rest of the article: "DF" – diesel fuel as a reference (reference) test; "RO 90%Hex10%" – rapeseed oil with the addition of 10% n-hexane; "RO" – rapeseed oil.

2.3 Modification of the start time of the first pre-injection

The different viscosity, density and flash point of the canola oil-n-hexane mixture compared to diesel [14] necessitate the modification of the injection start angle, among other things. As a reference test, power and torque measurements were carried out on a chassis dynamometer, feeding the engine with diesel at nominal engine controller settings. In order to select the angle of first pilot injection for the RO 90%Hex10% mixture, ten tests were carried out in which each time the angle of first pilot injection was delayed by "–1°CA" from the measured nominal value of "–32°CA". It was noted that at the value of delaying the first pilot injection by "–6°CA", the parameters measured on the chassis dynamometer were the closest with respect to the measurement when the engine was fed with diesel fuel with nominal engine controller software. On this basis, the angle of the first pilot injection of "–38°CA" was selected (Fig. 2). It was assigned the following designation used consistently hereafter: "Pilot(–6°)RO 90%Hex10%" – canola oil with the addition of 10% n-hexane, with the first pilot injection adjusted by –6°CA.

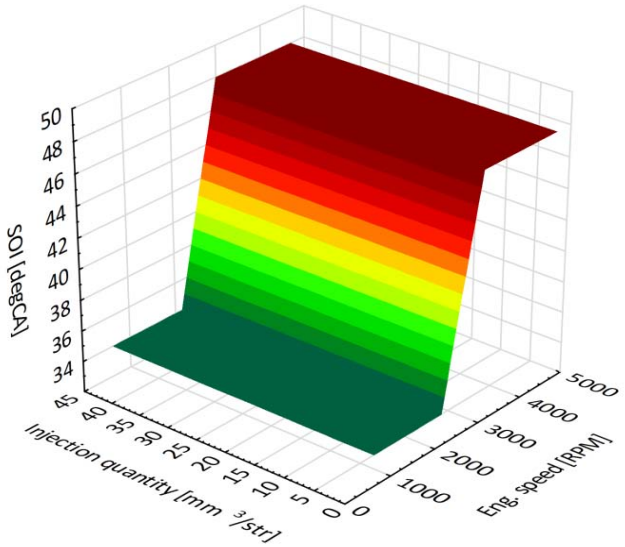

Fig. 2. Modified control map of the angle of the first pilot injection [°CA] depending on the injection rate [mm^3/cycle] and engine crankshaft speed [rpm]

3. Results

Figures 3 to 6 show the course of cylinder pressure, the rate of heat release, and the signal controlling the opening of the injectors as a function of the engine's crankshaft rotation when fed successively with diesel, canola oil, canola oil with 10% n-hexane addition, and canola oil with 10% n-hexane addition with the first pilot injection adjusted by

–6°CA, while running on a chassis dynamometer at 90 km/h.

In Figure 3, at $\alpha_{inj} \approx -12$°CA for diesel fuel, the cylinder pressure rises to about 8.98 MPa, and the maxima of heat release and pressure appear near TDC, indicating a short ignition delay time and a rapid combustion phase. On the other hand, the use of rapeseed oil (Fig. 4) at an injection angle $\alpha_{inj} \approx -2$°CA, affects the pressure maximum, which was 8.71 MPa near $\alpha_{Pc,max} \approx 11$°CA. Adding 10% n-hexane (Fig. 5) allowed to reach $P_{(c,max)} \approx 8.38$ MPa at $\alpha_{Pc,max} \approx 11.7$°CA – lower than with diesel fuel. Analyzing the dQ/dα characteristics, it was noted that this fuel ignites significantly faster than pure rapeseed oil. Figure 6, shows the results obtained for canola oil feed with 10% n-hexane, where shifting the injection angle by "–6°CA" earlier relative to the nominal control, led to a significant increase in maximum pressure (up to 9.47 MPa) and reaching its maximum at an angle $\alpha_{Pc,max} \approx 11.7$°CA. The previously introduced pilot dose shortened the ignition delay time of the main fuel dose, resulting in a more rapid combustion just after TDC. Delaying (or appropriately "phase-shifting") the pilot injection can reduce surges at less stressed operating points. It is noteworthy that although the control system was set to shift the pilot injection angle by –6°CA relative to the nominal map, the recording of measurements at 90 km/h did not achieve exactly this change. This is because the engine controller uses a series of interpolations based on values from neighboring cells of the injection map and additionally applies auto adaptive strategies (e.g., as a function of speed, fuel dose or exhaust gas temperature). In the tests in question, instead of the expected –6°CA, the real value of the pilot injection offset averaged about –4°CA relative to the reference value, as can be seen from the actual angles recorded in the charts. On the one hand, this illustrates the flexibility and adaptability to current operating conditions, on the other hand, it shows that the nominally introduced correction does not always translate linearly into an identical angle change in the actual engine cycle, so the interpretation of the results should always take into account the specifics of the controller and its operation under the dynamic conditions of actual operation.

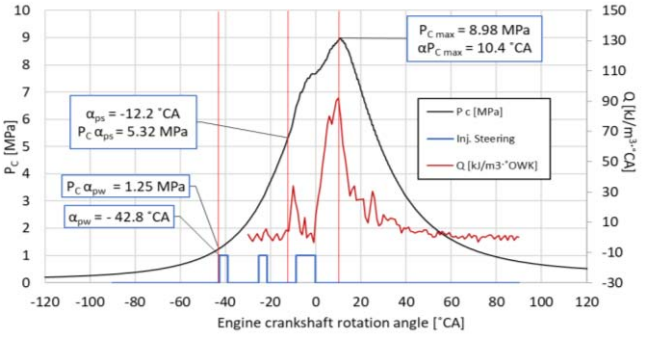

Fig. 3. The course of cylinder pressure, heat release rate, and injector opening control signal as a function of engine crankshaft rotation when fed with diesel fuel while running on a chassis dynamometer at 90 km/h

Figures 7 through 12 show the recorded average index pressure, a box plot of average index pressure from 70 measurement cycles, maximum combustion pressure, maximum rate of combustion pressure build-up, average fuel burn rate, and maximum heat release rate when fed successively with diesel fuel, canola oil, canola oil with 10% n-hexane addition, and canola oil with 10% n-hexane addition with the first pilot injection adjusted by –6°CA, while running on a chassis dynamometer at 90 km/h.

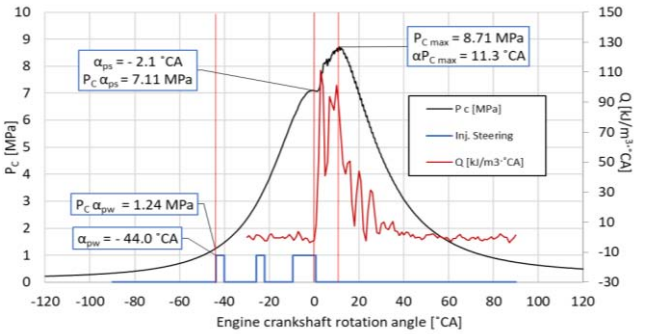

Fig. 4. The course of the cylinder pressure, the rate of heat release, and the signal controlling the opening of the injectors as a function of the engine's crankshaft rotation when fed with rapeseed oil while running on a chassis dynamometer at 90 km/h

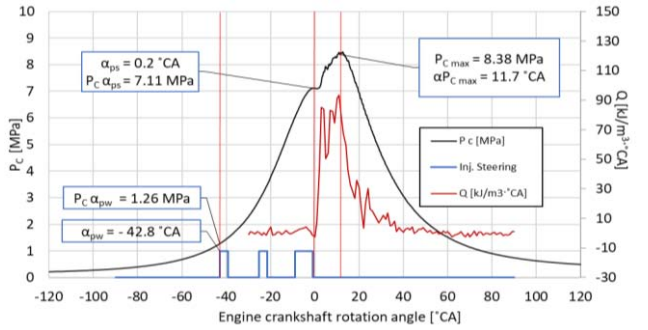

Fig. 5. The course of the cylinder pressure, the rate of heat release, and the signal controlling the opening of the injectors as a function of the engine's crankshaft rotation when fed with canola oil with the addition of 10% n-hexane, while running on a chassis dynamometer at 90 km/h

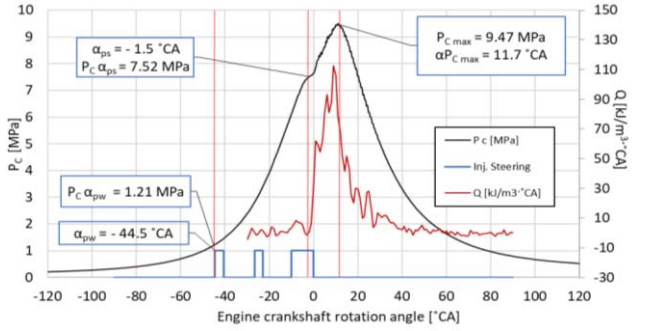

Fig. 6. The course of cylinder pressure, heat release rate, injector opening control signal as a function of engine crankshaft rotation when feeding with canola oil with 10% n-hexane with the first pilot injection adjusted by –6°CA, while driving on a chassis dynamometer at 90 km/h

The value of the average indexed pressure for DF was 0.816 MPa. For the 70 cycles analyzed, it was characterized by a narrow distribution and high consistency of individual measurements, indicating their stability. The value of the maximum combustion pressure, recorded during diesel fuel tests, was 9.58 MPa. The maximum pressure build-up rate

(dp/dα) for DF was 0.399 MPa/°CA. The amount of fuel burned, was 966.9 kJ/m³. The maximum rate of heat release was 90.4 kJ/m³·°CA.

When fed with canola oil, the value of the average indexed pressure reached 0.805 MPa. For 70 engine cycles, this parameter reached the lowest value among all fuels. The maximum combustion pressure was 10.58 MPa. The maximum pressure build-up rate (dp/dα), for canola oil reached 0.540 MPa/°CA. The average burn rate was 1084.3 kJ/m³. The recorded maximum rate of heat release was 130.0 kJ/m³·°CA.

When fed with rapeseed oil with 10% n-hexane addition, the value of the average indexed pressure was 0.728 MPa. The value of the average pressure was the smallest among all the fuels tested for the 70 cycles analyzed and had the least variability. Such a result may be due to the variability of the combustion process in the presence of a small addition of n-hexane. The maximum combustion pressure was 9.00 MPa. The maximum pressure build-up rate (dp/dα) was 0.417 MPa/°CA. The value of the average burn rate for RO 90%Hex10% was 910.9 kJ/m³. As for the maximum rate of heat release – for the RO 90%Hex10% mixture it was 92.6 kJ/m³·°CA.

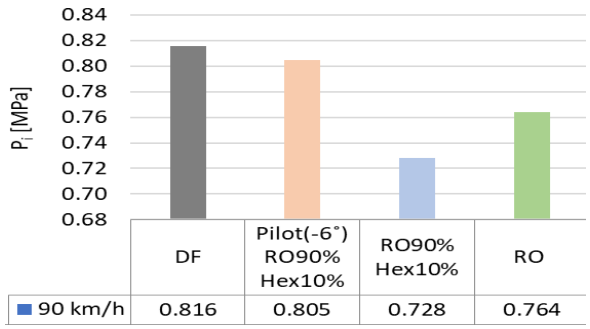

Fig. 7. Average indexed pressure, while running on a chassis dynamometer at 90 km/h, for selected fuels and control variant. The results were averaged from 100 engine cycles

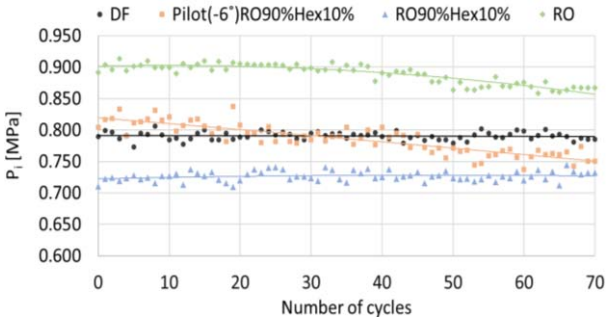

Fig. 8. The course of the average indexed pressure during driving on a chassis dynamometer at 90 km/h, for selected fuels and control variant depending on 70 engine cycles

In the case of feeding the engine with a mixture of rapeseed oil with 10% n-hexane additive and using an adjusted pilot injection start angle of –6°CA (Pilot(–6°)RO 90% Hex10%), the value of the average indexed pressure was 0.786 MPa. For the 70 engine cycles analyzed, it was most similar to diesel The value of maximum combustion pressure for Pilot(–6°)RO 90%Hex10% was 9.66 MPa. For the maximum pressure build-up rate (dp/dα), the measured value was 0.375 MPa/°CA. In terms of energy requirements, the average fuel burnup for this variant was 966.9 kJ/m³. The maximum heat rate (Qmax) reached 96.7 kJ/m³·°CA.

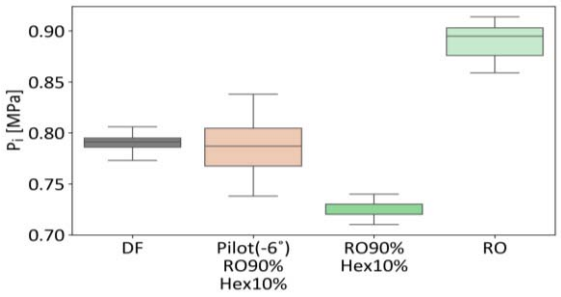

Fig. 9. Box plot showing a comparison of the distributions of mean indicated pressure measurements for the fuels tested for 70 engine cycles

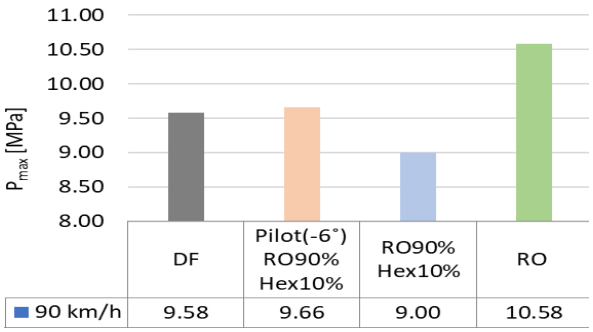

Fig. 10. Maximum combustion pressure during driving on a chassis dynamometer at 90 km/h, for selected fuels and control variant. The results were averaged from 100 engine cycles

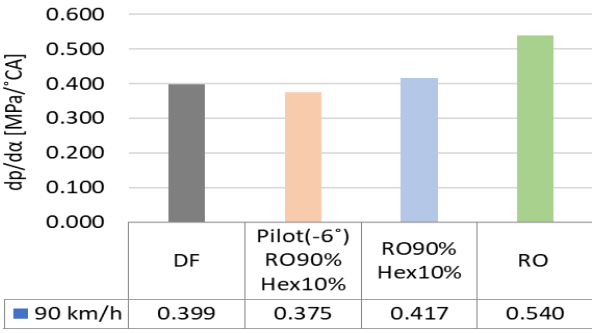

Fig. 11. The maximum speed of combustion pressure build-up, while running on a chassis dynamometer at 90 km/h, for selected fuels and control variant. The results were averaged from 100 engine cycles

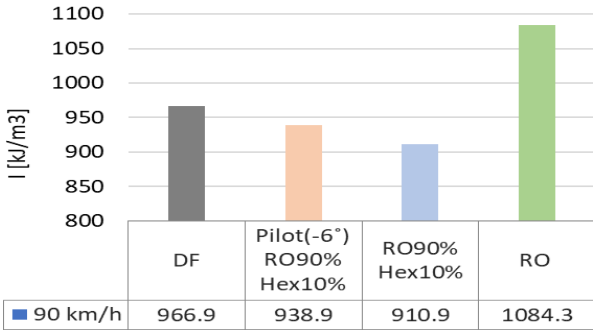

Fig. 12. The average amount of fuel burned, while running on a chassis dynamometer at 90 km/h, for selected fuels and control variant. The results were averaged from 100 engine cycles

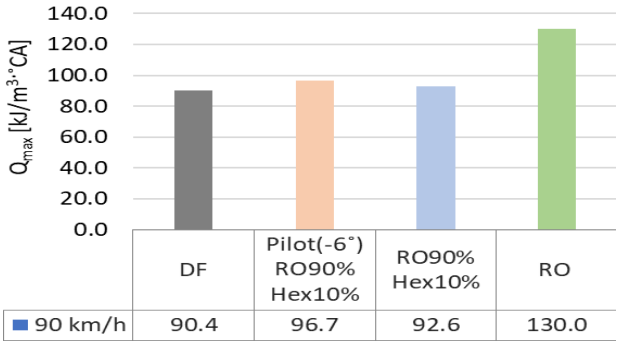

Fig. 13. The maximum rate of heat release, when running on a chassis dynamometer at 90 km/h, for selected fuels and control variant. The results were averaged from 100 engine cycles

4. Conclusions

The study shows that the use of an earlier start of pilot injection, shifted by –6°CA, when feeding the engine with a mixture of rapeseed oil with 10% n-hexane, improved the parameters of the combustion process and brought them closer, to the reference values obtained when burning diesel. It is worth noting that when fed with a mixture of RO 90%Hex10% without changing the injection angle, the average indexed pressure was 0.728 MPa, which is less than for diesel (DF = 0.816 MPa). The maximum combustion pressure, on the other hand, reached 9.00 MPa, which was the lowest of all the tested power variants. The reduced intensity of the combustion process was also confirmed by the course of the pressure build-up rate (dp/dα), which was 0.417 MPa/°CA, noticeably below the level for DF. Introducing a change in the pilot injection start angle by –6°CA brought significant benefits. The average indexed pressure increased to 0.805 MPa, reaching a level similar to DF. The maximum combustion pressure increased to a value of 9.66 MPa, which is virtually identical to DF (9.58 MPa). The course of pressure build-up: dp/dα was 0.375 MPa/°CA, below the level for diesel. The average fuel burn rate increased from 910.9 to 966.9 kJ/m³. Similarly, the maximum heat release rate was 96.7 kJ/m³·°CA, close to the value for diesel (90.4 kJ/m³·°CA). In conclusion, changing the pilot injection onset angle for the RO90%Hex10% mixture was a key procedure that made it possible to improve the ignition limits of the mixture used and achieve engine performance similar to that of diesel combustion. Improvements were achieved not only in combustion parameters but also in cyclic stability and combustion uniformity.

Nomenclature

CA	crank angle
CI	compression ignition
DF	diesel fuel
dp/dα	pressure build-up rate as a function of crankshaft rotation angle
dQ/dα	heat release rate as a function of crankshaft rotation angle
DI	direct injection
EGR	exhaust gas recirculation
NO_x	nitrogen oxides
OBD	on board diagnostics
P_c	cylinder pressure
$P_{c\,max}$	maximum cylinder pressure
Q_{max}	maximum heat release rate
RO	rapeseed oil
SOI	start of injection
TDC	top dead center
WLTP	Worldwide Harmonised Light Vehicles Test Procedure
$\alpha_{(inj)}$	injection angle
$\alpha_{Pc\,max}$	angle of rotation of the crankshaft at which there is maximum pressure in the cylinder

Bibliography

[1] Adamiak B, Andrych-Zalewska M, Merkisz J, Chłopek Z. The uniqueness of pollutant emission and fuel consumption test results for road vehicles tested on a chassis dynamometer. Eksploat Niezawodn. 2025;27(1). https://doi.org/10.17531/ein/195747

[2] Harari PA, Banapurmath NR, Yaliwal VS, Yunus Khan TM, Badruddin IA, Kamangar S et al. Effect of injection timing and injection duration of manifold injected fuels in reactivity-controlled compression ignition engine operated with renewable fuels. Energies. 2021;14(15):4621. https://doi.org/10.3390/en14154621

[3] Jaworski A, Kuszewski H, Longwic R, Sander P. Assessment of self-ignition properties of canola-oil/n-hexane blends in a constant-volume combustion chamber and compression-ignition engine. Appl Sci. 2023;13(19):10558. https://doi.org/10.3390/app131910558

[4] Kozak M. Exhaust emissions from a diesel passenger car fuelled with a diesel fuel-butanol blend, SAE Technical Paper. 2011-28-0017. 2011. https://doi.org/10.4271/2011-28-0017

[5] Kozak M, Merkisz J. Oxygenated diesel fuels and their effect on PM emissions. Appl Sci. 2022;12:7709. https://doi.org/10.3390/app12157709

[6] Kozak M, Lijewski P, Waligórski M. Exhaust emissions from a hybrid city bus fuelled by conventional and oxygenated fuel. Energies. 2022;15:1123. https://doi.org/10.3390/en15031123

[7] Kryshtopa S, Górski K, Longwic R, Smigins R, Krysthopa L. Increasing parameters of diesel engines by their transformation for methanol conversion products. Energies. 2021; 14(6):1-19. https://doi.org/10.3390/en14061710

[8] Longwic R. Diesel engine operations with alternative fuels. Taylor & Francis Group. 2024. https://doi.org/10.1201/9781003466291

[9] Longwic R, Sander P. The course of combustion process under real conditions of work of a traction diesel engine supplied by mixtures of canola oil containing n-hexane. IOP Conf Ser Mater Sci Eng. 2018;421:1-11. https://doi.org/10.1088/1757-899X/421/4/042050

[10] Longwic R, Sander P, Jańczuk B, Zdziennicka A, Szymczyk K. Modification of canola-oil physicochemical properties by hexane and ethanol with regard to its application in diesel engine. Energies. 2021;14(15):4469. https://doi.org/10.3390/en14154469

[11] Longwic R, Sander P, Nieoczym A, Lotko W, Krzysiak Z, Samociuk et al. Effect of some properties of hydrocarbon

fuels on self-ignition delay. Chemical Industry. 2017;96(5): 1123-1127. https://doi.org/10.15199/62.2017.5.30
[12] Nwafor O, Rice G. Performance of rapeseed-oil blends in a diesel engine. Appl Energy. 1996;54:345-354. https://doi.org/10.1016/0306-2619(96)00004-9
[13] Olbert R. The Elsbett engine – a low-pollution vegetable-oil alternative. Der Elsbett-Motor: Saubere Energie aus Pflanzenöl, U.S. DOE OSTI, 1990.
[14] Pasyniuk P, Golimowski W. Wpływ oleju rzepakowego na parametry pracy silnika wysokoprężnego ciągnika rolniczego John Deere 6830 (in Polish). J Research & Applications in Agricultural Engineering. 2011;50(2):118-121. https://bibliotekanauki.pl/articles/336144
[15] Pratap Singh A, Jena A, Agarwal AK. Multiple fuel injection strategy for premixed-charge compression-ignition combustion engine using biodiesel blends. Int J Engine Research. 2023;24(3):123-138. https://doi.org/10.1177/14680874211066743
[16] Simpson T, Depcik C. Multiple fuel injection strategies for compression-ignition engines. Energies. 2022:15(14):5214. https://doi.org/10.3390/en15145214
[17] Strauß L, Weiß L, Rieß S, Wensing M. Injection, mixing and auto-ignition of e-fuels for compression-ignition engines. MTZ Worldwide. 2024;85(12):48-55. https://doi.org/10.1007/s38313-023-1569-6

Prof. Rafał Longwic, DSc., DEng. – Department of Automotive Vehicles, Lublin University of Technology, Poland.
e-mail: *r.longwic@pollub.pl*

Dawid Tatarynow, MEng. – Department of Automotive Vehicles, Lublin University of Technology, Poland.
e-mail: *d.tatarynow@pollub.pl*

Michał Kuszneruk, MEng. – Department of Automotive Vehicles, Lublin University of Technology, Poland.
e-mail: *m.kuszneruk@pollub.pl*

Article citation info:
Kneba Z. Cabin heating of electric buses. Combustion Engines. 2026;206(3):9-13. https://doi.org/10.19206/CE-211730

Zbigniew KNEBA

Combustion Engines
Polish Scientific Society of Combustion Engines

Cabin heating of electric buses

ARTICLE INFO

Received: 16 May 2025
Revised: 25 August 2025
Accepted: 6 October 2025
Available online: 23 January 2026

The thermal balance of vehicle cabins when only an internal combustion engine was used was an insignificant element of the vehicle design. The excess thermal energy on board did not require energy saving. Only the cold start was slightly problematic. However, it could still use a combustion heater that quickly warmed up the cabin. In purely electric cars, each use of electricity stored in the battery shortens the vehicle's range. Three types of heating are used in this case: a) an electric air heater; b) an electric heater for the liquid cooling the drive components; c) a heat pump receiving heat from the drive components, also temporarily supported by an electric air or liquid heater. The use of a heat pump is the most promising and is also used in cheap city cars (e.g. Renault ZOE). The source of thermal energy for a heat pump is: a) vehicle drive engine(s); b) AC/DC converters – charger, DC/DC – charger, DC/AC – motor inverter; c) battery. In cheaper vehicles, air cooling is partially used; currently, a mixture of antifreeze fluids is used. The article presents a calculation example for a city bus cabin.

Key words: *electrical bus, bus cabin heating, bus road test, vehicle heating systems, heat pump*

This is an open access article under the CC BY license (http://creativecommons.org/licenses/by/4.0/)

1. Introduction

People's feelings of thermal comfort are entirely subjective. Firstly, it depends on temperature, humidity, lighting, noise, and air speed. Other influencing factors. Other influencing factors include individual characteristics such as emotional state, health, previous experiences, age, and gender.

The interest in vehicle air conditioning systems stems from the fact that people spend more and more time in vehicles. According to the source [1], this is 9 hours and 35 minutes per week in their cars. Unfortunately, no information on the average time a passenger spends on a city bus was found in the literature.

2. State of the art

There are many mathematical models for calculating thermal comfort in passenger car cabins. There are only a few publications on city buses [3, 11].

Pala and Oz in 2015 developed mathematical models of bus air conditioning by calibrating these models based on experimental data [5]. Velt and Daanen in 2017 dealt with electric buses in relation to their energy efficiency during operation of air conditioning systems. They assumed the maximization of driving range on one battery charge at a cabin temperature of 22.5°C to 20.9°C [8].

Scurtu and Jurco in 2019: modelled air flows in the bus cabin with the possibility of using air guides to improve thermal comfort [8]. More common are scientific articles on energy consumption in passenger cars [4, 6]. Pielecha [6] writes in 2020 that there are two control strategies for regenerative braking: charging priority and heating priority. Mamala [4] has written that limiting the speed in cities to 30 km/h reduces the number of accidents but increases the specific energy consumption. The minimum specific energy consumption is in the speed range from 30 to 45 km/h.

Vehicle structures allow engineers to create conditions that are beneficial for traveling people only to a certain extent. There are the following limitations:

– the vehicle structure must meet safety requirements – resistance to operational loads and crash tests, which limits the use of materials and the size of window openings
– the cabin must be ergonomic
– the vehicle must not exceed the recognized environmental preservation standard.

The interest in vehicle air conditioning systems stems from the fact that people spend more and more time in vehicles. According to the source [1], this is 9 hours and 35 minutes per week in their cars.

In a city bus, the most difficult phenomena to model are the air exchange when opening multiple doors and changing the number of passengers and their position in the cabin. In this work, a very simplified heat exchange model based on basic criteria numbers from thermodynamics was adopted. The object of the research was an electric city bus, the technical data of which are presented in the publication [7].

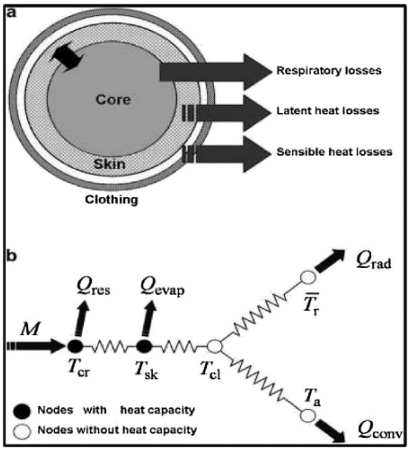

Fig. 1. Model of heat exchange between human body and environment [4]

People sitting in a bus are a source of heat. It is assumed that a sitting person emits a heat flux per unit area

of about 58 W/m^2. A standing person emits 70 W/m^2. The model of heat exchange with the environment is presented in Fig. 1.

In passenger cars designed especially for short city trips, the fuzzy logic cabin heating strategy (FLC) can, according to the author [5], increase the range by up to 14%. FLC regulates the power of the layer heater, which is dependent on the battery state and current, as well as the coolant and cabin temperature. So there is a priority for charging and not heating. In buses, due to the variable number of passengers in the cabin, the thermal inertia changes. The advantage of the bus operation method is almost uninterrupted driving (no cooling cycles while standing for a long time) and the possibility of heating from the electrical network before starting the trip. Due to their utility features, city buses often have an air conditioning system placed on the roof, and numerous cabin ventilation ducts distribute heated or cooled air inside the cabin. Such a construction is shown in Fig. 2.

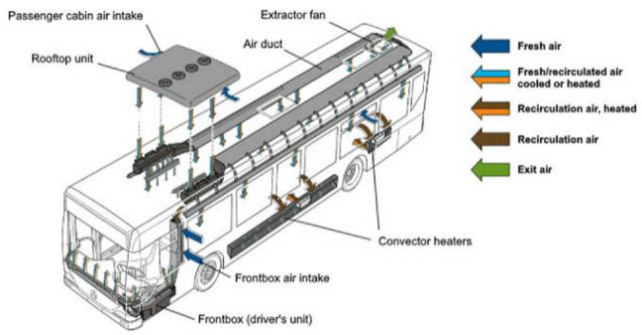

Fig. 2. Air conditioning system of a city bus [11]

This drawing shows traditional electric heaters (electric resistance) placed in the wall halfway along the body and under the rear seats. In the case of electric bus drive, electric heaters are used for limited operating time only at very low ambient temperatures.

2.1. Thermal comfort conditions in the vehicle

People's perception of heat or cold is subjective and include individual characteristics such as: emotional state, health, previous experiences, age, and gender.

For technical calculations, average temperatures around the passenger must be assumed. The air flow in the bus cabin, where there are many obstacles, is uneven. Hence, passengers standing in different places will experience thermal comfort differently.

The cabin is cooled more due to the opening of the doors and greater heat loss through the door windows. The purpose of the calculations is to determine the air inlet temperature to the cabin. A large part of the heating air circulates in recirculation, and a slightly smaller amount is taken from the environment and discharged to the environment. In the work [11], optimization calculations were performed for 7 passengers in different parts of the cabin. The heating air temperature calculated in computer simulations is 31ºC.

2.2. Calculations of the heat balance of the bus cabin

In the publication, the winter operating conditions of a heat pump heating system are discussed. The primary heat source is the waste heat of the bus drive system. The air is heated in the pump evaporator and distributed in the cabin through ventilation ducts. The evaporator draws heat mainly from the cooling systems: battery, inverter, traction motor.

To assess the heat demand, it is necessary to calculate the heat outflow to the environment during driving, the heat loss through air exchange when opening the doors at bus stops and the heat inflow from passengers.

3. Bus thermal balance

3.1. Load of the powertrain and heat sources

Heat flows away from the body to the environment through the walls and insulated roof, often made of composite, windows and chassis. There is practically no heat exchange through the rear wall of the body.

Sources of waste heat that can be used to heat the cabin. While driving, many machines and electrical devices require heat dissipation for their stable operation at proper working temperatures. These components are primarily:

– battery
– electric drive motor
– inverter.

The heat flux dissipated from these devices is a function of the power needed to drive the bus and power its accessories. This power is usually tested in real city driving conditions or simulated tests. Such tests for city transport are SORT (Standardized On Road Test) developed by the "Union Internationale des Transport Publics" [10].

The test speed profiles are shown in Fig. 3a and Fig. 3b.

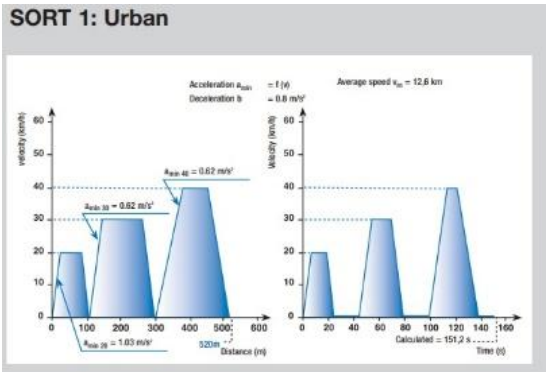

Fig. 3a. SORT urban test speed profile [7]

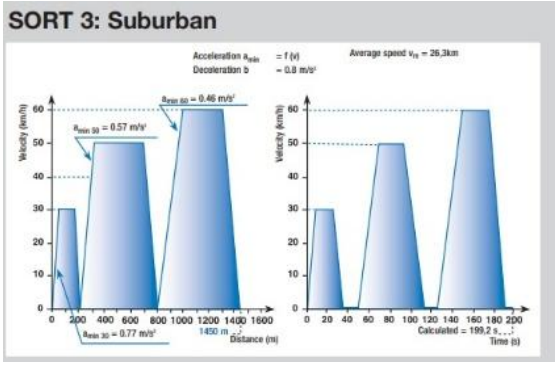

Fig. 3b. SORT suburban test speed profile [7]

However, the actual load of the drive system resulting from city driving usually has greater variability over time. Such actual loads recorded during the driving of a public transport bus in Lublin are shown in Fig. 4.

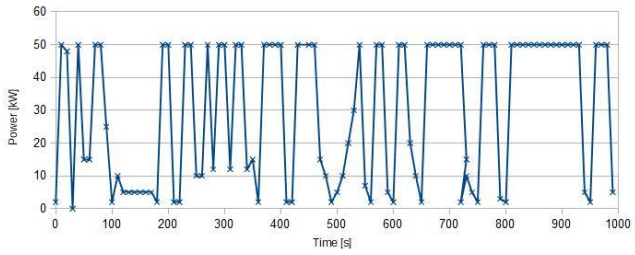

Fig. 4. Instantaneous power values at the battery terminals while driving a city bus

3.2. Battery cooling

The battery thermal balance is shown by equation (1)

$$C_{Li}\frac{dT_c}{dt}=Q_c+Q_s-Q_B \quad (1)$$

where: C_{li} – thermal capacity of the battery, T_c – battery temperature, Q_c – heat flux resulting from current flow, Q_s – entropy change, Q_B – heat exchange of the battery with the environment.

The generation of heat related to current flow depends on the internal resistance of the battery. Joule's law can be used to describe this phenomenon, written as equation (1)

$$Q_c = I^2R \quad (2)$$

where: I – current, R – internal resistance.

Heat generation is related to the change in entropy described by formula (3)

$$Q_s = -T_c\Delta S\frac{I}{F} \quad (3)$$

where: ΔS – entropy change in the battery, F – Faraday's constant.

Heat dissipation to the environment is described by formula (4)

$$Q_B=Ak(T_c - T_{amb}) \quad (4)$$

where: A – heat exchange surface, k – heat transfer coefficient through the battery casing, T_{amb} – battery coolant temperature or ambient temperature.

Due to the large variability of power at the battery terminals over time (Fig. 4), the share of heat accumulated in the battery mass after it has been heated up is negligible. All the heat generated results from the profile of electric power flow is proportional to the current flow at a constant voltage. The presented graphs (Fig. 4) show that the peak power drawn from the battery is 50 kW, but for longer periods, the power is much lower. Therefore, the heat flows discharged from the battery, inverter and traction motor can be used to heat the cabin in the quantities given in Table 1. For estimated calculations, the efficiency of heat sources was assumed.

To calculate the amount of heat generated in the battery more precisely, it is necessary to know the internal resistance of a single cell and the configuration of the cell connection, e.g. 0.6 mΩ/cell with a voltage of 3.7 V. With these data (velocity profile from Fig. 4), the course of the heat flux generated in the battery as a function of time was calculated using formula (2) – Fig. 5.

Table 1. Estimation of heat flows for cabin heating

Device	Average power supplied [kW]	Efficiency of the unit	Heat flow of the device cooling [kW]
battery	37	0.98	0.74
inverter	34	0.90	3.4
drive motor	30	0.85	4.5

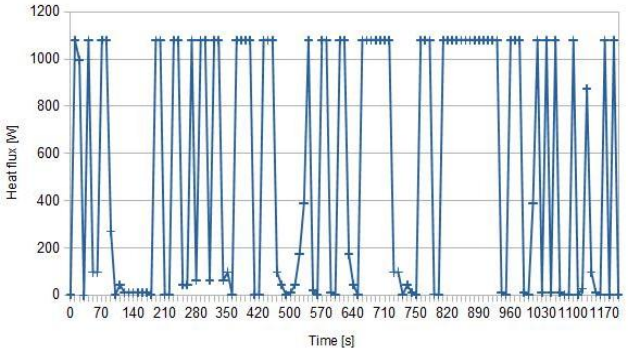

Fig. 5. Heat flux generated in the battery during bus travel according to the speed profile from Fig. 4

This flow flows to the battery cooling liquid in the radiator of the shape shown in Fig. 6.

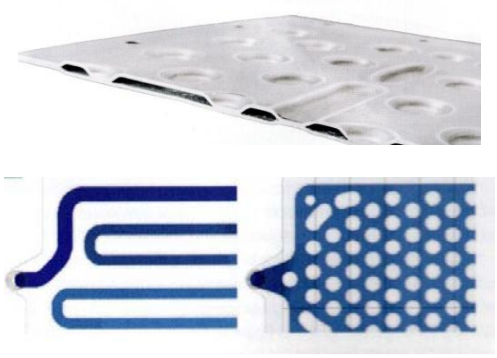

Fig. 6. Shapes of cooling plates and the course of channels made in them [11]

The fact that only one wall of the battery cell is in contact with the cooling plate means that this cooling is not very effective and some of the heat escapes to the environment and not to the cooling liquid. Only part of the heat generated during battery load can be used to heat the cabin.

3.3. Motor cooling

Motors in buses are cooled from the outside by a stream of air from a fan. This method is not effective and leads to high temperatures, especially of the rotor windings, as shown in Fig. 7.

In passenger cars, a liquid cooling circuit of the engine and inverter is used with channels in both the rotor and the stator. This method of heat collection is illustrated in Fig. 8.

A significant amount of heat then passes to the coolant. It can therefore be assumed that all of the heat losses of these components can be used to heat the cabin.

Fig. 7. Temperature inside the bus traction engine without an internal liquid cooling circuit [2]

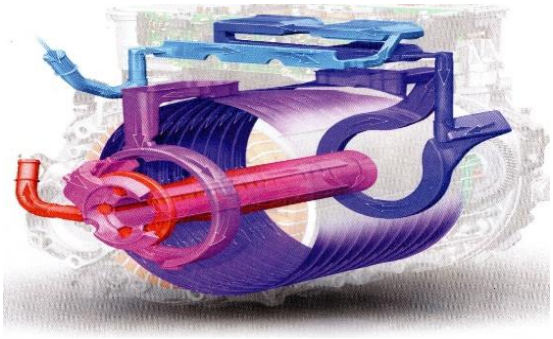

Fig. 8. Channels inside a passenger car traction engine [2]

3.4. Heat removal from the cabin

Heat flows out of the cabin in two ways

- by air exchange during cabin ventilation and opening doors at bus stops
- by heat exchange through the walls of the bus body.

Due to the adopted standards of air supplied to vehicle cabins for passengers in the amount of approximately 30 m^3 for one person during 1 hour, the ventilation air flow is proportional to the number of passengers.

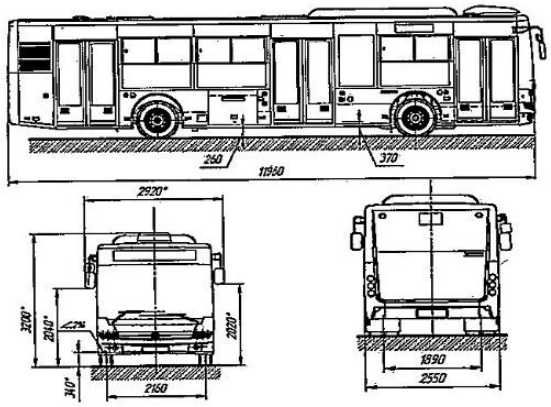

Fig. 9. City bus technical data of the sample bus network voltage 500 V; battery 119 cells of 4.2 V, R = 2.28 Ω; inverter; traction motor 170 kW (continuous power) [7]

Heat flow from the body to the environment takes place primarily through the side walls, front wall and roof. The chassis and rear wall can be omitted due to the low air flow velocity and small heat exchange surface. Heat flow calculations were performed on the example of a city bus (Fig. 9).

The air flows that remove heat from the external walls of the bus, including the side walls, roof and front wall, were taken into account, omitting the rear wall and chassis. The wall insulation is made of a 50 mm layer of polyvinyl chloride. Such insulation results in very low thermal transmittance of the walls, especially when compared to the transmittance of windows and doors (see Table 2). For this reason, manufacturers use multi-layered glass. Between the glass layers, there is a PVB (poly-vinyl-butyral) film with a thickness of 0.76 mm.

Table 2. Results of heat loss calculations through the bus walls under the following conditions: inside temperature 20°C, outside temperature 0°C, different driving speeds

The speed of air flowing over the side walls [km/h]	Insulated side walls and roof area of the body [m^2]	Area of glazed openings on the sides of the body [m^2]	Heat transfer coefficient through walls [W/m^2K]	Heat transfer coefficient through glass panes [W/m^2K]	Heat dissipation flow [W]
10	75.13	21.38	0.057	40.993	20190
20			0.057	41.018	20202
30			0.057	41.022	20204
40			0.057	41.024	20205

The model of heat exchange with the environment uses the Reynolds, Prandtl and Nusselt criteria numbers.

Table 3. Results of heat loss calculations through the bus walls under the following conditions: inside temperature 20°C, variable outside temperature, driving speed 20 km/h

Outside temperature [C]	Heat dissipation flow [W]
–5	25,252
0	20,202
5	15,151
10	10,101

The heat flux needed to heat the cabin at a temperature lower than –5°Cwould be even greater. In the literature [3], the heating power at –10°Cis mentioned as 40 kW.

3.5. Linde cycle

The Linde heating cycle is shown in Fig. 10. An 8°C temperature difference was assumed between the temperature of the fluid used in the evaporator to cool the drive components and the temperature of the refrigerant (R1234YF).

It is implemented by a heat pump operating in the temperature range resulting from the external and internal conditions of the vehicle. In the considered example, the evaporation temperature is –13ºC and condensation 20ºC. The Linde cycle shown in the graph indicates the required compressor compression at the level of 3.35. The heat that can be used is delta s·T = (1830 – 1100)·295 = 730 J/kgK·295 K = 215,350 kJ/kg. To obtain a heat flux of 25,252 W. The flow rate of the refrigerant in the system should be 25,252/215,350 = 0.117 kg/s.

The five main parameters collected from literature papers that are interesting to study their variation effect on the heat pump performance of battery electric bus are: the compressor speed, the mass flow rate of the air entering the condenser, the mass flow rate of the air entering the

evaporator, the recirculation rate, and the flow effective area of the expansion valve.

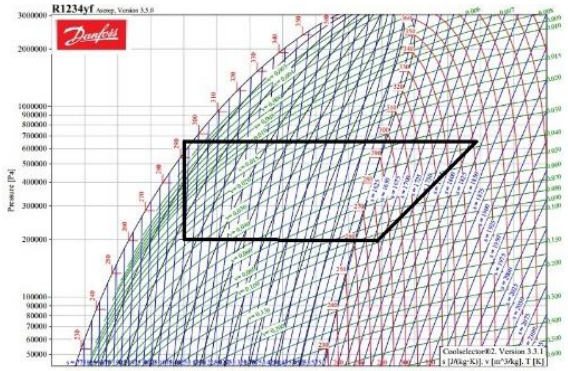

Fig. 10. Linde cycle

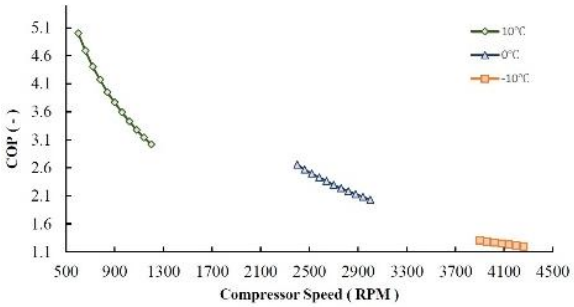

Fig. 11. Change of COP coefficient as a response to the change of external conditions [5]

If the outside temperature decreases, the compressor must increase its performance. Such changes result in a decrease in the COP coefficient, as shown in Fig. 11.

To ensure low energy consumption, an electric bus must be equipped with a complex air conditioning and heating system. Its structure is shown in Fig. 12.

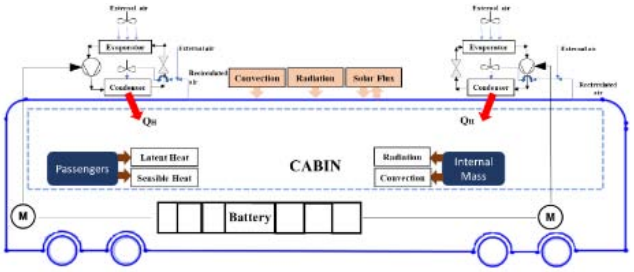

Fig. 12. HVAC – cabin configuration [5]

4. Conclusions

The most important thing is to limit heat conduction through the windows. Waste heat of machines and drive devices is sufficient to heat the cabin when using a heat pump to the temperature –5°C. Increasing the amount of energy for cabin heating is possible by replacing the air cooling of the traction motor with liquid cooling. The heat pump operates with a COP coefficient of 2.1. The compressor in the system should have an adjustable speed. The goal of calculating the heating circuit with a heat pump for the bus cabin in the form of circuit operating parameters was achieved.

Bibliography

[1] ABC Motor: Pasamos 9 horas y 35 minutos de media semanales metidos en el coche. https://www.abc.es/motor/reportajes/abci-pasamos-9-horas-y-35-minutos-media-semanales-metidos-coche-201704271427_noticia.html

[2] Fu P, Zhao L, Wang X, Sun J, Xin Z. A review of cooling technologies in lithium-ion power battery thermal management systems for new energy vehicles. Processes. 2023;11: 3450. https://doi.org/10.3390/pr11123450

[3] Haddad RA, Basma H, Mansour C. Analysis of heat pump performance in battery electric buses. 32nd International Conference on Efficiency, Cost, Optimization, Simulation and Environmental Impact of Energy Systems, Jun 2019, Wroclaw, Poland. https://hal.science/hal-02169864v1/document

[4] Mamala J, Graba M, Mitrovic J, Prażnowski K, Stasiak P. Analysis of speed limit and energy consumption in electric vehicles. Combustion Engines. 2023;195(4):83-89. https://doi.org/10.19206/CE-169370

[5] Pala U, Oz HR. An investigation of thermal comfort inside a bus during heating period within a climatic chamber. Appl Ergon. 2015;48:164-176. https://doi.org/10.1016/j.apergo.2014.11.014

[6] Pielecha I. Control algorithms for a range extender vehicle with an combustion engine. Combustion Engines. 2020; 183(4):3-10. https://doi.org/10.19206/CE-2020-401

[7] Rymarz J. Badania efektywności eksploatacyjnej autobusów komunikacji miejskiej (in Polish). Wydawnictwo Politechniki Lubelskiej 2021.

[8] Scurtu IL, Jurco AN. Airflow and thermal comfort of the bus passengers. J Ind Design Eng Graphics. 2019;14(1): 171-174. http://sorging.ro/jideg/index.php/jideg/article/view/44

[9] Steinstraeter M, Buberger J, Minnerup K, Trifonov D, Horner P, Weiss B et al. Controlling cabin heating to improve range and battery lifetime of electric vehicles, eTransportation. 2022;13:100181, https://doi.org/10.1016/j.etran.2022.100181

[10] UITP. SORT – Standardised On-Road Tests Cycles. https://mohamedmezghani.com/images/stories/site/Brochures/5SORT-2004-ENG.pdf

[11] Vaswani RRH. Optimization of the heating system in a bus cabin: a numerical approach through OpenFOAM. Master's Degree Course in Mechanical Engineering. Politechnico di Torino 2020. https://webthesis.biblio.polito.it/secure/15401/1/tesi.pdf

[12] Velt KB, Daanen HAM. Optimal bus temperature for thermal comfort during a cool day. Appl Ergon. 2017;62:72-76. https://doi.org/10.1016/j.apergo.2017.02.014

Zbigniew Kneba, DSc., DEng. – Faculty of Mechanical Engineering and Ship Technology, Gdansk University of Technology.
e-mail: *zkneba@pg.edu.pl*

Article citation info:
Skuza A, Szumska E, Jurecki R. The impact of traffic intensity on the performance and efficiency of hybrid electric vehicles. Combustion Engines. 2026;206(3):14-26. https://doi.org/10.19206/CE-212529

Adriana SKUZA
Emilia SZUMSKA
Rafał JURECKI

Combustion Engines
Polish Scientific Society of Combustion Engines

The impact of traffic intensity on the performance and efficiency of hybrid electric vehicles

ARTICLE INFO

Received: 3 June 2025
Revised: 12 October 2025
Accepted: 13 October 2025
Available online: 10 February 2026

This paper investigates the impact of traffic congestion on fuel consumption and CO_2 emissions in hybrid electric vehicles (HEVs) operating in urban driving conditions. The analysis encompassed four distinct HEV configurations – PHEV, mixed, MHEV, and split-axle hybrid – and evaluated their performance across five urban routes (T1–T5) exhibiting diverse congestion levels, as well as under the WLTC Low cycle. The data were acquired via simulation using AVL Cruise M, leveraging velocity profiles recorded during peak afternoon traffic. The Monte Carlo method was employed to estimate result variability, yielding 24,000 data points per variable. Findings reveal that PHEVs exhibited the most favorable performance, achieving the lowest fuel consumption (0.00–0.02 l) and CO_2 emissions (0.00–0.05 kg), particularly in stop-and-go urban driving due to their electric operating mode. MHEVs demonstrated the least efficiency, with mixed and split-axle hybrid vehicles performing at an intermediate level. ANOVA and Tukey's post-hoc test statistically validated significant distinctions across HEV types and routes. This research underscores the criticality of real-world testing environments and offers valuable implications for HEV design and the evolution of testing protocols for sustainable urban transportation.

Key words: *hybrid electric vehicle, fuel consumption, CO_2 emission, urban traffic congestion, Monte Carlo simulation*

This is an open access article under the CC BY license (http://creativecommons.org/licenses/by/4.0/)

1. Introduction

Hybrid electric vehicles (HEVs) have emerged as a pivotal component in the global shift towards sustainable transportation, striking a balance between energy efficiency, environmental impact, and economic viability. Compared to purely electric vehicles, HEVs offer significantly extended range and come at a lower cost. When contrasted with conventional internal combustion engine vehicles, they exhibit reduced fuel consumption and substantially lower emissions.

Currently, the market offers various types of hybrid electric vehicles. HEVs integrate an internal combustion engine with an electric powertrain. Plug-in hybrid electric vehicles (PHEVs) incorporate a higher-capacity battery, facilitating external grid charging. A key advantage of PHEVs is their ability to operate solely in electric mode, which significantly reduces fuel consumption. Hybrids demonstrably enhance fuel efficiency and reduce emissions compared to conventional vehicles. This is primarily achieved through the recuperation of kinetic energy during regenerative braking and the optimized operation of the internal combustion engine [5, 8, 10].

In recent years, advancements in battery technology have played a pivotal role in enhancing the energy efficiency of hybrid vehicles. High-performance batteries, characterized by greater energy density and extended lifespans, have enabled hybrid vehicles to achieve superior fuel economy and lower emissions. Moreover, the evolution of lithium-ion batteries has significantly contributed to the overall efficiency of hybrid systems [7, 17].

The efficiency of hybrid vehicles is critically dependent on advanced energy management systems. These systems are designed to optimally distribute power between the internal combustion engine and the electric motor, thereby minimizing energy losses. Strategies such as predictive energy optimization and adaptive control algorithms have been developed to further enhance fuel efficiency and reduce emissions [2, 18].

Hybrid electric vehicles have been the subject of extensive research for years. One of the particularly discussed topics is the issue of harmful exhaust emissions[16, 27]. Studies consistently indicate that vehicles operating under congested traffic conditions can consume up to 30% more fuel compared to those in free-flowing traffic. This increased fuel consumption directly correlates with elevated emissions of carbon dioxide (CO_2), nitrogen oxides (NO_x), and particulate matter (PM) [11, 22, 24]. While studies involving real-world vehicle testing with installed measurement equipment have demonstrated that hybrids can achieve a CO_2 reduction of up to 30% compared to conventional vehicles [14, 19, 21], the environmental benefits of HEV are highly dependent on their specific configuration and driving conditions. For instance, reference [1] investigated the energy consumption of a PHEV under real-world driving conditions over a distance of 12,500 km, analysing the interaction between the internal combustion engine and the electric motor. Instantaneous energy consumption varied from 0.6 to 1.4 MJ/km, with higher values correlating with internal combustion engine operation and consequently, increased CO_2 emissions. Research findings presented in [19] demonstrated that during urban driving, a hybrid vehicle operated solely on its electric motor for 67.70% of the distance travelled and 75.40% of the driving time, leading to a significant reduction in emissions. Furthermore, studies in [3, 4, 6] have indicated that the energy characteristics of both HEVs and PHEVs are highly dependent on various usage conditions, including temperature, trip length, charging frequency, and battery energy capacity. A study [25] analysed vehicle emissions in Toronto and Beijing, demonstrating that hybrid vehicles significantly reduce exhaust

emissions compared to conventional vehicles. In Toronto, reductions were observed at 21.6% for CO_2, 31.3% for CO, and 53.0% for NO_x. Beijing showed even greater reductions: 41.0% for CO_2, 28.9% for CO, and 68.5% for NO_x. The more substantial reduction in CO_2 and NO_x emissions in Beijing was attributed to less dynamic driving conditions. The work [12] investigated the fuel consumption of both hybrid and conventional vehicles under real-world conditions. Hybrids demonstrated a significant reduction in fuel consumption at low and medium speeds. It was observed that as speed increased, the differences in fuel consumption between these vehicle types diminished. Conversely, research [15] investigated fuel consumption reductions achieved by hybrid vehicles relative to conventional vehicles under diverse traffic conditions and driving styles in Bangkok. The most substantial fuel consumption reduction for HEVs was noted in urban traffic with smooth driving (approximately 56%), while smaller reductions were observed in suburban and highway driving. Aggressive driving considerably increased fuel consumption in both vehicle types, with HEVs being more susceptible to this driving style in terms of percentage increase in consumption.

Hybrid vehicles, which integrate an internal combustion engine with an electric motor, appear to be a promising solution for urban transportation challenges, particularly in congested conditions like traffic jams. In large cities, especially during peak hours, traffic is characterized by frequent stops and low speeds. Traffic congestion demonstrably leads to increased fuel consumption and elevated emissions of pollutants, including CO_2, NO_x, PM_x, and HC (hydrocarbons), thereby negatively impacting air quality and public health [13, 20]. As evidenced by the previously cited studies, HEVs exhibit significantly lower fuel consumption and emissions in urban environments.

Despite extensive research on hybrid vehicles, a significant gap persists in comprehensive analyses evaluating the impact of real-world traffic congestion on diverse hybrid configurations. Specifically, there's a deficit of studies employing actual road data to compare various hybrid architectures in terms of fuel consumption and emissions. Previous work has often been limited to general assertions about the necessity of urban-centric analyses, without precisely defining the specific knowledge gaps that could be addressed.

In response to the identified research gap, this study utilizes real-world velocity profiles, derived from actual driving data, to simulate the operation of four distinct hybrid vehicle types under varying urban congestion conditions. This methodology enables a more detailed assessment of their operational parameters and the optimization of powertrain management strategies in the context of contemporary urban challenges. The primary objective of this research is to quantitatively evaluate how different levels of traffic congestion impact key hybrid vehicle parameters, specifically fuel consumption and CO_2 emissions. The findings are expected to provide valuable insights for both powertrain designers and policymakers regarding the improvement of urban transportation efficiency.

This study addresses this gap by providing analyses based on real-world velocity profiles from congested urban environments. This approach will allow for a more precise evaluation of the efficiency of hybrid powertrain vehicles in congested urban conditions and enable better adaptation of powertrain control strategies to the realities of contemporary cities. This research, therefore, not only aligns with the current understanding in the field but also contributes to addressing global challenges concerning transportation, climate change, and urbanization.

2. Experimental methods

2.1. Real-world data acquisition

Real-world urban driving testing aimed to acquire velocity profiles of a representative vehicle, enabling the modeling of typical driving scenarios in highly congested areas. A precise Kistler GPS Data Logger was used to record motion parameters such as instantaneous velocity, longitudinal acceleration, time, and geographical coordinates. This logger offers high measurement accuracy (10 Hz sampling frequency, GPS position accuracy < 2.5 m), ensuring the reliability of the collected data.

The data acquisition process was conducted along five distinct urban routes (T1–T5) situated within an European medium-sized city (Kielce, Poland). These routes were chosen to encompass a variety of driving conditions, including frequent stops at intersections, fluctuating speeds in urban traffic, and segments with smoother flow. Each route was approximately 5 km in length, which allowed for the collection of representative data relevant to typical urban commutes. Measurement data were gathered during the afternoon rush hour (3:00 PM–5:00 PM), a period characterized by the highest traffic intensity and significant congestion, accurately reflecting the real-world challenges of urban transportation. As an example, the velocity (v) and longitudinal acceleration (a) profiles as a function of time for route T2 are presented in the Fig. 1.

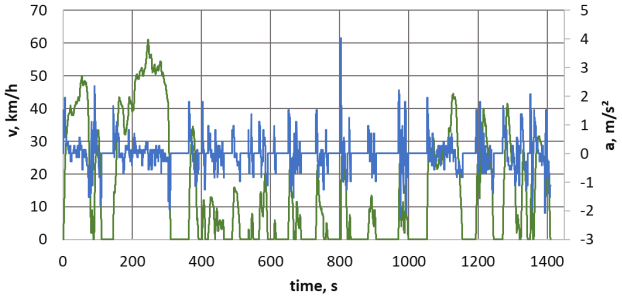

Fig. 1. Velocity (v) and acceleration (a) profiles for route T2

The collected velocity profiles served as input data for simulation studies in AVL Cruise M software. The goal of these simulations was to estimate fuel consumption and CO_2 emissions on the selected urban routes, and to compare them against the standard WLTC Low cycle.

2.2. Modelling and simulation studies in AVL Cruise M

Simulation studies were conducted using AVL Cruise M software, an advanced tool designed for the analysis of vehicle powertrains. This software allows for detailed modeling of vehicle dynamics, energy consumption, and ex-

haust emissions based on specified driving cycles. For the comparative evaluation of four hybrid vehicle types in this study, AVL Cruise M was employed. The following configurations were analyzed: plug-in hybrid electric vehicles (PHEV), mild hybrid electric vehicles (MHEV), series-parallel hybrid (mixed), and split-axle hybrid, where the internal combustion engine powers the front axle and the electric drive powers the rear axle. Selected technical parameters of the analyzed vehicles are presented in Table 1.

Table 1. Technical specifications of selected hybrid vehicle types

Parameter		PHEV	mixed	MHEV	split-axle hybrid
Inernal Combustion Engine	Engine displacement, cm^3	1800	1800	1800	2478
	Number of cylinders	4	4	4	4
	Engine inertia, $kg \cdot m^2$	0.1	0.18	0.18	0.18
	Engine stall speed, rpm	500	500	500	500
	Maximum engine speed, rpm	6500	6500	6500	6000
Battery	Minimum voltage, V	123	240	37	37
	Maximum voltage, V	184	360	54	54
	Maximum charge, Ah	20	20	20	20
	Initial state of charge, %	80	50	50	50
Electric motor	Maximum motor torque, N·m	180	55	63.4	153.6
	Maximum motor power, kW	56.55	15	9.25	24.63
	Speed at maximum motor torque, rpm	0	0	0	0
	Speed at maximum motor power, rpm	3000	4000	2707	3500
	Maximum generator torque, N·m	172.5	55	60.8	152.96
	Maximum generator power, kW	54.64	15	4.62	24.13

The objective of this study is to assess the potential of various hybrid vehicle configurations within the context of sustainable transportation. To achieve this, four HEV types were selected, each characterized by a distinct degree of electric powertrain involvement in delivering power to the wheels and facilitating vehicle movement. This involvement directly influences fuel consumption and CO_2 emissions. Understanding the efficiency and benefits of these configurations under diverse operating conditions is a crucial element of this analysis. The PHEV, equipped with a high-capacity battery and external charging capability, allows a significant portion of the journey to be completed solely in electric mode. This configuration offers the lowest fuel consumption, directly translating to reduced emissions. In contrast, the MHEV features a minimal degree of electrification, where an electric motor (typically an integrated starter-generator, or ISG) primarily assists the internal combustion engine (ICE) during start up and acceleration. It also enables regenerative braking to recover energy into a small-capacity battery. The ICE's contribution remains dominant throughout the vehicle's operation, and pure electric driving is generally not possible or limited to very short distances and low speeds. Figure 2 presents the MHEV vehicle model in AVL Cruise M.

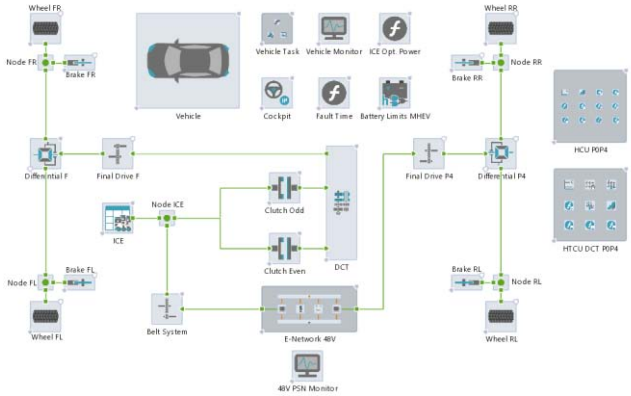

Fig. 2. MHEV vehicle model in AVL Cruise M

The series-parallel (mixed) configuration, also known as a full hybrid, allows for independent or combined operation of both the internal combustion engine and the electric motor in delivering torque to the powertrain. This enables all-electric driving for short distances and at lower speeds. Regardless of traction conditions, the internal combustion engine operates within its optimal range, assisting the electric motor during acceleration while continuously charging the battery. This configuration facilitates a more significant reduction in fuel consumption and emissions through regenerative braking and electric assistance.

The split-axle configuration is characterized by a drivetrain separation where one axle (typically the front) is powered by an internal combustion engine, while the other (the rear) is driven by an electric motor. This setup allows for single-axle or all-wheel drive operation depending on driving conditions and power demand, with the internal combustion engine generally playing a dominant role.

To accurately reflect real-world driving conditions, the simulations incorporated velocity profiles collected from five distinct routes, designated T1–T5. These profiles were derived from actual data gathered in urban and suburban environments, allowing for the inclusion of diverse traffic conditions such as frequent stops, fluctuating speeds, and varying traffic densities. Additionally, to provide a reference point for standardized testing, the Worldwide Harmonized Light Vehicles Test Cycle (WLTC) Low was included as a comparative benchmark.

Within the AVL Cruise M environment, each vehicle type was subjected to simulations across six driving cycles (T1–T5 and WLTC Low). These simulations were configured to record key analytical parameters: fuel consumption and CO_2 emissions. These parameters are crucial for assessing the environmental impact and operational efficiency of the vehicles. The collected data were subsequently ana-

lysed to evaluate how each hybrid vehicle type performed under varying driving conditions. This comprehensive approach allowed for a comparative analysis of the four HEV types, providing quantitative data on their relative operational characteristics and limitations in both real-world conditions and defined test cycles.

2.2. Assessing fuel consumption and CO_2 emission variability using Monte Carlo simulation

To overcome the limitations of single observations for each hybrid powertrain type and route profile combination, a Monte Carlo simulation was employed. This method enabled the generation of synthetic data based on the original measurements. This approach allowed for the assessment of differences in fuel consumption and CO_2 emissions among the four HEV types (PHEV, mixed, MHEV, split-axle hybrid) and the six test routes (T1–T5, WLTC Low).

Fuel consumption and CO_2 emissions for each HEV type and route combination were modeled using a gamma distribution. This choice is justified by the gamma distribution's effectiveness in describing non-negative and skewed data, which is characteristic of fuel consumption and emission measurements. The parameters of the gamma distribution, specifically shape (α) and scale (β), were calculated based on the mean (μ), equal to the observed value, and an assumed standard deviation (σ), according to the following equations:

$$\alpha = \left(\frac{\mu}{\sigma}\right)^2 \tag{1}$$

$$\beta = \frac{\sigma^2}{\mu} \tag{2}$$

In instances where μ=0, a minimum standard deviation of $\sigma = 0.001$ was assumed. This guarantees a positive variance, enabling sample generation. In the baseline scenario, the following assumptions were made:

$$\sigma = 0.1 \cdot \mu \tag{3}$$

This approach reflects the typical variability in this type of data in the absence of empirical repetitions. To verify the impact of this assumption, a sensitivity analysis was conducted for alternative values:

$$\sigma = 0.05 \cdot \mu \tag{4}$$

and

$$\sigma = 0.2 \cdot \mu \tag{5}$$

For each of the 24 combinations (4 HEV types × 6 routes), 1000 simulated observations were generated, resulting in a total of 24,000 data points for each variable (fuel consumption and CO_2 emissions). This number of simulations ensured sufficient data for subsequent statistical analyses.

The Monte Carlo simulation process was conducted using the R programming language and involved the following stages:

1. For each combination of HEV type and route, 1000 values for fuel consumption and CO_2 emissions were generated from a gamma distribution with parameters α and β.
2. Mean values and 95% confidence intervals were computed for the simulated data, enabling the estimation of result variability.
3. A two-way analysis of variance (ANOVA) was performed, including an interaction term between HEV type and route, to assess the statistical significance of differences in fuel consumption and CO_2 emissions.
4. Tukey's post-hoc test was then applied to identify specific differences among HEV types and individual routes.

Additionally, a sensitivity analysis was conducted to assess the impact of the assumed standard deviation on the results. Three values of $\sigma \in \{0.05\ \mu, 0.10\ \mu, 0.20\ \mu\}$ were tested, and the resulting ANOVA outcomes and confidence intervals were compared. This analysis allowed for an evaluation of the stability of the conclusions based on the assumed level of data variability. The findings presented in [9, 22, 25] suggest that the chosen σ values in the Monte Carlo simulations are justified to reflect a realistic range of variability for fuel consumption and CO_2 emissions.

3. Results

3.1. Comparison of real-world route parameters and WLTC Low Test

Data for the analysis were collected from five real-world driving cycles (T1–T5). These cycles were conducted under typical urban conditions, characterized by heavy congestion, frequent stops, and variable traffic. Additionally, the WLTC Low phase was included as a standard reference cycle. The mean and maximum values of velocity and acceleration, along with stop times, were estimated. A summary of the selected route parameters is presented in Table 2.

Table 2. Summary of selected route parameters

Route/ Parameter	T1	T2	T3	T4	T5	WLTC Low
Duration, s	685	1409	780	1135	1022	589
Stop duration, s	99	594	129	339	138	146
Share of idling in total travel time, %	14%	42%	17%	30%	14%	25%
Max. velocity, km/h	56	61	61	51.5	54	56.9
Mean velocity w/o stops, km/h	35.17	25.08	29.7	26.78	24.4	25.7
Mean velocity w/ stops, km/h	30.09	14.51	24.79	18.78	21.11	18.9
Min. acceleration, m/s^2	–3.61	–2.22	–2.92	–3.06	–2.92	–1.47
Max. acceleration, m/s^2	3.61	4.03	2.36	2.64	2.78	1.47

In the T1–T5 cycles, maximum velocity range from 51.5 km/h (T4) to 61 km/h (T2 and T3), whereas the WLTC Low cycle exhibits a maximum velocity of 56.9 km/h. Average velocity, including stops, varies significantly across the urban cycles, from 14.51 km/h (T2) to 30.09 km/h (T1), compared to 18.9 km/h in WLTC Low. Excluding stops, these values increase; for instance, T1 rises to 35.17 km/h and WLTC Low to 25.70 km/h.

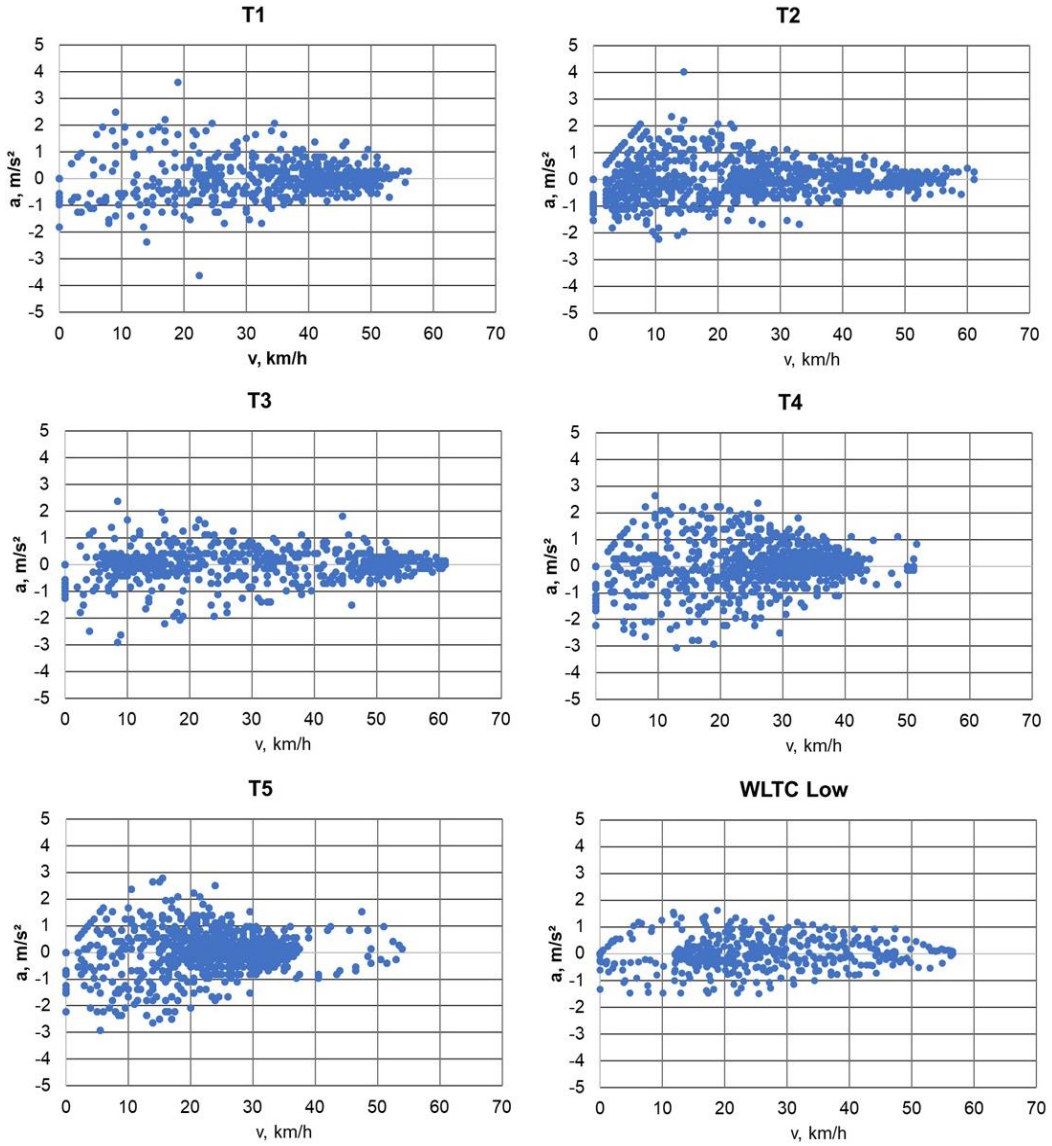

Fig. 3. Distribution of longitudinal accelerations (a) and velocities (v) in analyzed cycles

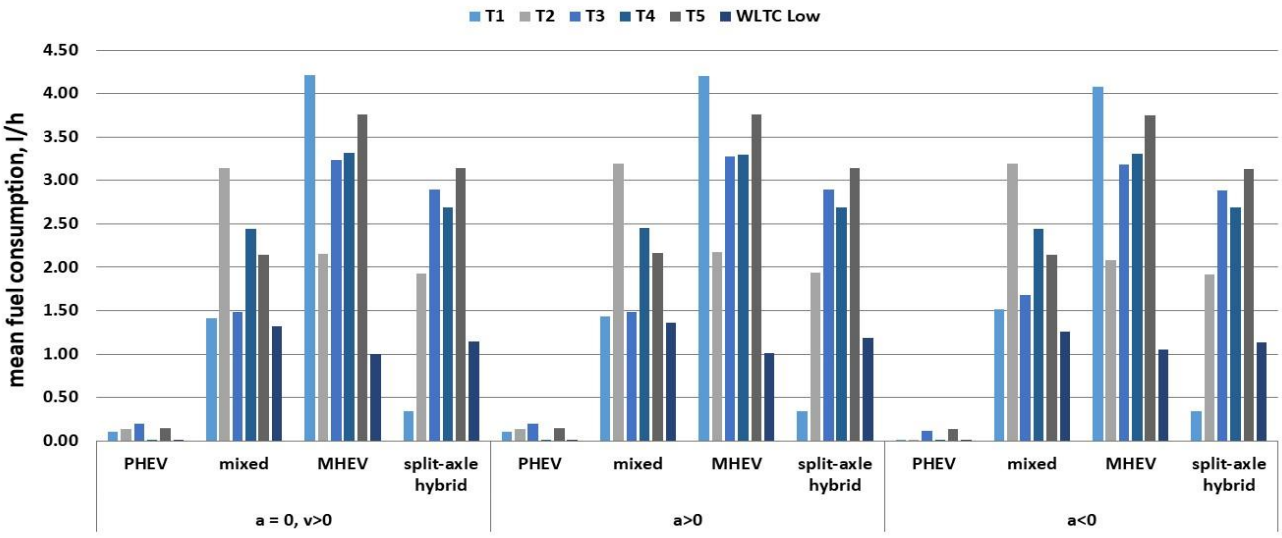

Fig. 4. Mean fuel consumption across selected driving phases

The velocity profiles as a function of time of selected routes show numerous brief accelerations after stops, contrasting with the smoother profile of WLTC Low. Figure 3 illustrates the recorded longitudinal accelerations (a) across the analysed cycles, highlighting the considerable diversity in the results. Notably, the WLTC Low cycle shows the smallest range of longitudinal acceleration values.

The T1–T5 cycles demonstrate greater variability than the WLTC Low: lower average velocity with stops (e.g., 14.51 km/h in T2 vs. 18.9 km/h in WLTC Low), higher maximum accelerations (up to 4.03 m/s² vs. 1.47 m/s²), and a larger proportion of idle time (up to 42% in T2 vs. 25% in WLTC Low). These discrepancies suggest that standard test profiles, such as the WLTC Low, do not fully capture real-world urban driving conditions. Data from T1–T5 can therefore be instrumental in designing vehicles optimized for energy consumption, fuel efficiency, and emissions.

3.2. Analysis of fuel consumption for different HEV types in congested conditions

The initial analysis focused on the fuel consumption values obtained by the selected HEV types across each of the T1–T5 routes and in the WLTC Low test. Table 3 presents the fuel consumption (in liters) for four types of hybrid powertrains over five highly congested urban drives (T1–T5) and in the WLTC Low cycle.

Table 3. Summary of fuel consumption [l] for selected hybrid vehicle types

Route/ HEV type	T1	T2	T3	T4	T5	WLTC Low
PHEV	0.01	0.02	0.02	0.00	0.02	0.00
mixed	0.12	0.52	0.15	0.32	0.25	0.09
MHEV	0.33	0.36	0.30	0.44	0.45	0.08
split-axle hybrid	0.28	0.33	0.28	0.37	0.36	0.07

Plug-in Hybrid Electric Vehicles (PHEV) consistently demonstrated the lowest fuel consumption, ranging from 0 to 0.02 l in urban tests and 0.00 l in the WLTC Low cycle. This highlights the predominant use of electric propulsion, given an initial battery state of charge (SOC) of 80%. The series-parallel (mixed) hybrid consumed between 0.12 l and 0.52 l in urban traffic and 0.09 l in the WLTC Low cycle. Mild Hybrid Electric Vehicles (MHEV), featuring a smaller electric motor assisting the internal combustion engine, exhibited higher fuel consumption (0.30–0.45 l in urban tests). However, they achieved 0.00 l in the WLTC Low cycle due to the significant proportion of idle time within that cycle and the capability for temporary engine shutdown. The split-axle hybrid, with an internal combustion engine on the front axle and an electric motor on the rear, consumed between 0.28 l and 0.37 l on urban routes and 0.07 l in the WLTC Low cycle. This indicates good recuperation efficiency, though its overall fuel efficiency is surpassed by PHEVs. Table 4 shows the fuel consumption in liters per km for four types of hybrid powertrains over five highly congested urban drives (T1–T5) and in the WLTC Low cycle.

Differences in fuel consumption between real-world routes and the WLTC Low cycle emphasize the importance of accounting for high congestion in testing. PHEVs appear to be the most efficient in urban conditions, particularly on routes with frequent stops, such as T2. These results unequivocally demonstrate that the level of hybridization and the drivetrain architecture are pivotal factors influencing fuel consumption in highly congested urban driving conditions.

Table 4. Summary of fuel consumption [l/km] for selected hybrid vehicle types

Route/ HEV type	T1	T2	T3	T4	T5	WLTC Low
PHEV	0.002	0.003	0.004	0.000	0.003	0.000
mixed	0.024	0.104	0.031	0.065	0.051	0.025
MHEV	0.066	0.073	0.060	0.087	0.091	0.053
split-axle hybrid	0.056	0.065	0.057	0.073	0.072	0.021

Based on the data presented in Table 4, significant differences in fuel consumption were observed across the selected hybrid vehicle types. As evidenced by the results, the PHEV consistently demonstrated the lowest fuel consumption, with values approaching zero in the T4 and WLTC Low routes, highlighting its superior efficiency in these specific conditions. In contrast, both MHEV and the split-axle hybrid exhibited higher fuel consumption across all routes, with the mixed hybrid showing the most varied performance, including the highest consumption value of 0.104 l/km in the T2 route. The data clearly indicates that the PHEV's design allows it to achieve substantially lower fuel consumption per kilometer compared to the other hybrid architectures, particularly under specific driving conditions.

To analyse fuel consumption across various traffic phases, instantaneous data were categorized into three groups: acceleration ($a > 0$), constant speed driving ($a \approx 0$), and braking ($a < 0$). Figure 4 presents the mean fuel consumption values (in l/h) during each traffic phase on selected routes.

During the constant speed driving phase ($a = 0$, $v > 0$) on routes T4 and WLTC Low, the PHEV does not utilize its internal combustion engine. On the remaining routes, low mean fuel consumption values, ranging from 0.11 to 0.20 l/h, were recorded. The other HEV types exhibit fuel consumption during the constant speed phase. The mixed hybrid consumes from 0.59 l/h (T1) to as much as 1.31 l/h (T2), the MHEV from 0.86 l/h (T2) to 1.75 L/h (T1), and the split-axle hybrid from 0.80 l/h (T2) to 1.49 l/h (T1). This consumption is attributed to the continuous operation of the internal combustion engine during this driving phase.

During acceleration ($a > 0$), particularly at high acceleration rates, the PHEV necessitated the cooperation of both powertrains. The maximum mean fuel consumption in this phase for PHEV was 0.083 l/h on route T3. The other hybrid types required the internal combustion engine to operate during acceleration on all urban routes. It can be observed that the fuel consumption value is dependent on the level of hybridization. For the series-parallel (mixed) configuration, the range of mean values on real-world speed profiles was from 0.60 l/h (T1) to 1.329 l/h (T2). For MHEV, where the electric drive only assists the internal combustion engine, mean fuel consumption values ranged from 0.91 l/h (T2) to 1.750 l/h (T1). In the case of the split-

axle hybrid, where the internal combustion engine is the primary energy source, this range was from 0.81 l/h to 1.492 l/h (T1).

During the deceleration phase (a < 0), the PHEV recorded low fuel consumption values on cycles T3 and T5, specifically 0.05 l/h and 0.06 l/h, respectively. The other hybrid vehicles exhibited fuel consumption in every analysed driving cycle. The mixed hybrid maintained mean fuel consumption values between 0.63–1.330 l/h, the MHEV between 0.87–1.70 l/h, and the split-axle between 0.80–1.49 l/h.

During the idle phase, fuel consumption in hybrid vehicles is contingent upon their ability to shut down the internal combustion engine. Figure 5 illustrates the mean fuel consumption values recorded by the analysed HEV types while idling.

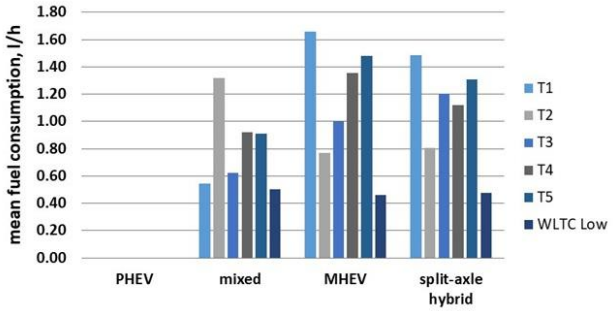

Fig. 5. Mean fuel consumption at idle (v = 0)

In every urban route and the WLTC Low cycle, the PHEV exhibits zero fuel consumption at idle. Its substantial battery capacity and full-electric mode capability make it the most efficient HEV type for conditions with frequent stops, notably in routes like T2 and T4.

Conversely, the MHEV consumes fuel while idling on urban routes. The highest mean idle fuel consumption was observed on route T1, reaching 1.66 l/h, while the lowest was 0.77 l/h on route T2. This can be attributed to the electric drive primarily assisting the internal combustion engine during periods of high power demand. However, when the battery's SOC falls to a predetermined lower limit, the ICE additionally provides power to recharge the battery.

In the WLTC Low cycle, the mean idle fuel consumption was significantly lower than that observed in the real-world speed profile cycles, amounting to 0.46 l/h. The mixed hybrid exhibited fuel consumption at idle across all tests. The lowest mean fuel consumption for the mixed hybrid was recorded in T1 at 0.55 l/h, while the highest was in T2 at 1.32 l/h. Lacking external charging capability, series-parallel hybrids power their electrical system exclusively through regenerative braking or the internal combustion engine. Consequently, if the SOC is low, the internal combustion engine is activated even at idle to recharge the battery. In contrast to series-parallel hybrids, split-axle hybrids do not possess the ability to shut down the internal combustion engine at idle. In split-axle hybrids, the internal combustion engine powers one axle, typically the front, and the electric motor drives the other axle, usually the rear. Crucially, there is no direct mechanical connection between these two drives. The mean fuel consumption for split-axle hybrids across the analysed routes ranged from 0.81–1.49 l/h.

In real-world urban conditions, where idle time ranges from 14% to 42%, PHEVs distinguish themselves as the most fuel-efficient HEV type during idling periods. Their capability for exclusive electric-mode operation eliminates fuel consumption in this phase, which is critical in congested urban areas. MHEVs exhibit variable efficiency, demonstrating lower effectiveness on urban routes but higher efficiency in the WLTC Low cycle. Mixed and split-axle hybrids are less effective in reducing fuel consumption at idle, underscoring the importance of designing hybrid systems specifically optimized for electric mode operation under such conditions.

3.3. Investigation of CO_2 emissions for different HEV types in congested conditions

This section of the study analyzes CO_2 emissions from various hybrid vehicle types across five real-world urban routes with high congestion (T1–T5), as well as in the standardized WLTC Low cycle. Table 4 presents the total CO_2 emissions (in kilograms) for each hybrid type on routes T1–T5 and in the WLTC Low cycle.

Table 5. Summary of CO_2 emissions [kg] for selected hybrid vehicle types

Route/ HEV type	T1	T2	T3	T4	T5	WLTC Low
PHEV	0.02	0.04	0.05	0.00	0.04	0.00
mixed	0.29	1.25	0.37	0.78	0.61	0.21
MHEV	0.79	0.87	0.72	1.05	1.09	0.33
split-axle hybrid	0.67	0.79	0.68	0.88	0.86	0.18

PHEV consistently exhibited the lowest CO_2 emissions across all examined scenarios. On urban routes, emissions ranged from 0 kg (T4) to 0.05 kg (T3), while in the WLTC Low cycle, reaching zero was assumed. These minimal values are attributed to the PHEV's capability for all-electric operation, which is particularly effective for short distances and in conditions with frequent stops. On route T4, characterized by a high proportion of idle time, the electric propulsion entirely eliminated CO_2 emissions, confirming the high efficiency of PHEV in congested urban environments.

The mixed hybrid recorded CO_2 emissions ranging from 0.29 kg (T1) to 1.25 kg (T2) on urban routes, with a value of 0.21 kg in the WLTC Low cycle. The highest emission on route T2 can be attributed to the longer duration of the drive and a significant proportion of idle time, necessitating more frequent operation of the internal combustion engine. In the WLTC Low cycle, the smoother driving profile resulted in significantly lower emissions, indicating greater efficiency for this powertrain type under controlled conditions compared to real-world urban traffic.

MHEVs exhibited the highest CO_2 emissions on urban routes, ranging from 0.72 kg (T3) to 1.09 kg (T5), yet demonstrated zero emissions (0.00 kg) in the WLTC Low cycle. The elevated values in urban conditions stem from their limited electric-mode capability and smaller battery capacity, leading to more frequent internal combustion engine engagement, particularly during dynamic accelerations. The zero emissions in the WLTC Low cycle suggest

the effectiveness of the engine stop-start function under stable test conditions, a benefit that does not fully translate to real-world urban traffic.

The split-axle hybrid demonstrated CO_2 emissions ranging from 0.67 kg (T1) to 0.88 kg (T4) on urban routes, and 0.18 kg in the WLTC Low cycle. This powertrain architecture allows for a degree of flexibility in energy management, positioning it between the mixed hybrid and PHEV in terms of CO_2 emission levels. The lower emissions observed in the WLTC Low cycle, as compared to urban routes, suggest better adaptation to smooth traffic flow rather than congested conditions.

This study revealed that PHEVs are the most environmentally friendly HEV type in urban conditions, generating minimal or zero CO_2 emissions due to their electric propulsion. Mixed and split-axle hybrids demonstrated moderate results, whereas MHEVs, owing to their limited energy flexibility, generated the highest CO_2 emissions in urban traffic. The discrepancies between the results on urban routes and the WLTC Low cycle underscore the significant impact of real-world driving conditions on CO_2 emissions. This suggests the necessity of developing more realistic testing standards for evaluating the environmental performance of hybrid vehicles. Table 6 shows the total CO_2 emissions per km for each hybrid type on routes T1–T5 and in the WLTC Low cycle.

Table 6. Summary of CO_2 emissions [kg/km] for selected hybrid vehicle types

Route/ HEV type	T1	T2	T3	T4	T5	WLTC Low
PHEV	0.005	0.008	0.009	0.000	0.008	0.000
mixed	0.058	0.250	0.074	0.155	0.122	0.059
MHEV	0.158	0.175	0.145	0.210	0.218	0.125
split-axle hybrid	0.134	0.157	0.137	0.176	0.173	0.050

Based on the data presented in Table 6, significant differences in CO_2 emissions were observed across the selected hybrid vehicle types. Consistent with its fuel consumption, the PHEV demonstrated the lowest CO_2 emissions, with values approaching zero in the T4 and WLTC Low routes, highlighting its superior environmental performance in these specific conditions. In contrast, both the MHEV and the mixed hybrid consistently exhibited the highest emission rates, with the MHEV reaching a peak of 0.218 kg/km on route T5. The data clearly indicate that the PHEV's operational mode allows it to achieve substantially lower CO_2 emissions per kilometer compared to the other hybrid configurations.

Subsequently, the mean CO_2 emissions in kg/h were analysed. These measurements were taken across five real-world urban routes (T1–T5) and in the standardized WLTC Low cycle, considering three distinct driving phases: constant speed ($a = 0$, $v > 0$), acceleration ($a > 0$), and braking ($a < 0$). The average CO_2 emission values for the vehicles analysed are presented in Fig. 6.

During constant speed driving, PHEVs exhibit the lowest CO_2 emissions, ranging from 0.00–0.20 kg/h, primarily due to their electric mode capability. The mixed hybrid shows higher emissions, from 1.32–3.15 kg/h, indicating more frequent use of the internal combustion engine. MHEVs generate the highest emissions, at 1.00–4.22 kg/h, attributed to their limited electric support. The split-axle hybrid achieves intermediate values, from 0.34–3.14 kg/h, reflecting the moderate efficiency of its split powertrain.

During acceleration, CO_2 emissions generally increase. PHEVs continue to emit the least, ranging from 0.00–0.20 kg/h, which confirms the efficiency of their electric powertrain. The mixed hybrid shows higher values, from 1.36–3.19 kg/h, due to increased load on the internal combustion engine during intense acceleration. MHEVs generate the highest mean emissions, at 1.01–4.20 kg/h, indicating limited electric drive support. The split-axle hybrid exhibits intermediate values, from 0.34–3.14 kg/h, with emissions tending to rise under more demanding conditions.

During the deceleration phase, thanks to braking regeneration, CO_2 emissions are generally lower than during acceleration. PHEV again achieves minimal values, ranging from 0.00–0.13 kg/h, which indicates a significant contribution from the electric mode during driving in each cycle. The mixed hybrid shows higher emissions, from 1.26–3.19 kg/h, with a maximum on T2. MHEVs are characterized by the highest values, from 1.05–4.08 kg/h, indicating limited emission reduction capabilities in this phase. The split-axle hybrid falls in between, at 0.35–3.14 kg/h, offering moderate efficiency.

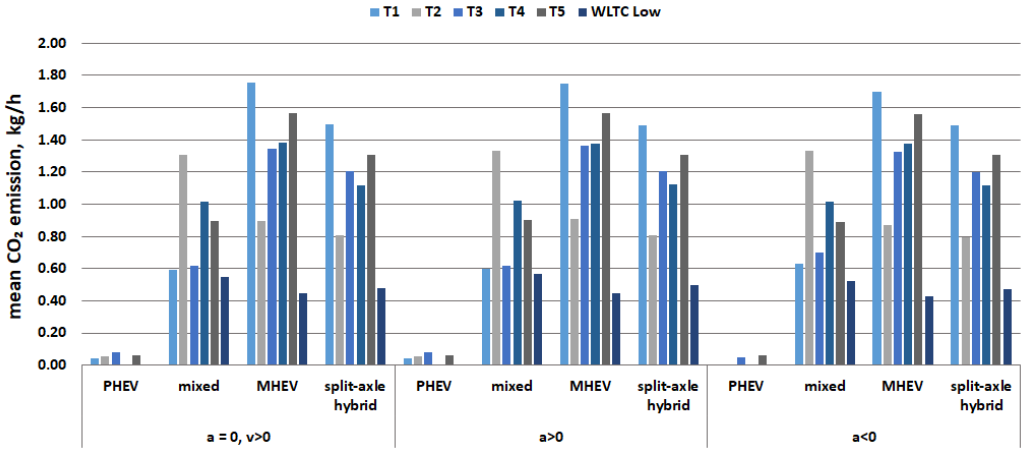

Fig. 6. Mean CO_2 emissions across selected driving phases

Idling, a significant aspect of urban traffic, is a crucial parameter in assessing the ecological performance of HEVs, as different hybrid technologies demonstrate varying capacities for emission reduction during this phase. The Fig. 7 presents the average CO_2 emission values across five cycles with velocity profiles gathered during real-world urban driving conditions and in the WLTC Low cycle.

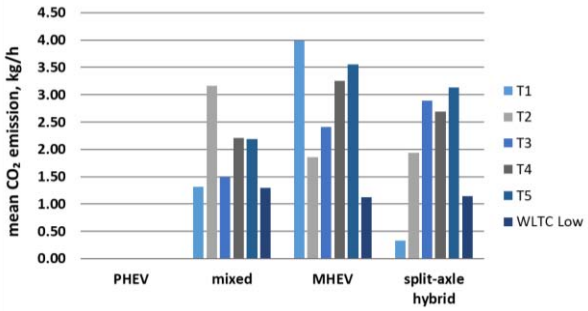

Fig. 7. Mean CO_2 emissions at idle (v = 0)

Analysis of CO_2 emissions during idle periods revealed significant differences among hybrid types. The PHEV consistently emitted 0.00 kg/h across all routes (T1–T5) and in the WLTC Low cycle, underscoring the efficiency of its electric powertrain and its capacity for complete internal combustion engine switch off, which is particularly advantageous in urban driving conditions. The mixed hybrid exhibited varied emissions, ranging from 1.31–3.16 kg/h on T1–T2, yet 0.00 kg/h in the WLTC Low cycle. This variation indicates the internal combustion engine's activity in real-world urban conditions during idling, likely for battery recharging purposes. The MHEV generated the highest emissions, from 1.85–3.98 kg/h on T2-T1, and 1.12 kg/h in the WLTC Low cycle. This is attributed to its limited ability to switch off the ICE.

3.4. Estimating variability in hybrid vehicle fuel consumption and CO_2 emissions using Monte Carlo simulation

This subsection presents the results of a study on the variability of fuel consumption and CO_2 emissions across the 4 analyzed hybrid vehicle types. The analysis was conducted using the Monte Carlo simulation method, which allowed for the estimation of these parameters under various test routes (T1–T5 and WLTC Low) despite a limited number of empirical data points. The results encompass mean values, confidence intervals, and statistical analysis, enabling the evaluation of differences between vehicle types and routes. For each combination of hybrid powertrain and route, 1000 observations were generated, yielding a total of 24,000 data points for each variable (fuel consumption and CO_2 emissions). ANOVA results demonstrated statistically significant effects for both fuel consumption and CO_2 emissions across all analyzed scenarios.

The simulated fuel consumption results, including mean values and 95% confidence intervals for selected vehicle type and route combinations, are presented in Fig. 8.

Analysis of variance revealed statistically significant differences in fuel consumption between vehicle types and routes. For $\sigma = 0.05$, the main effect of HEV type was highly significant, as confirmed by an F-value of 613193 ($p < 0.001$). This indicates substantial variations in fuel consumption among the different hybrid vehicle types. The route effect was also statistically significant, with an F-value of 211648 ($p < 0.001$), underscoring the considerable impact of driving conditions on fuel consumption.

The interaction between HEV type and route was also statistically significant ($F = 48{,}779$, $p < 0.001$), suggesting that the effectiveness of individual HEV types is dependent on the specific characteristics of the route. As σ increased to 0.1, the F-statistics decreased, but the effects remained significant: for HEV type, $F = 151{,}279$ ($p < 0.001$); for route, $F = 52{,}342$ ($p < 0.001$); and for the interaction between hybrid type and route, $F = 12076$ ($p < 0.001$). For $\sigma = 0.2$, the F-values were $F = 37{,}950$ ($p < 0.001$) for HEV type, $F = 13{,}084$ ($p < 0.001$) for route, and $F = 3073$ ($p < 0.001$) for the interaction between route and hybrid type, respectively. These consistent values confirm the stability of the obtained results.

Table 5 presents the results of Tukey's post-hoc test, comparing the mean differences in CO_2 emissions among hybrid powertrain types. It includes the mean difference, the lower and upper bounds of the 95% confidence interval (CI), and the adjusted p-value, where $p < 0.05$ indicates a significant difference.

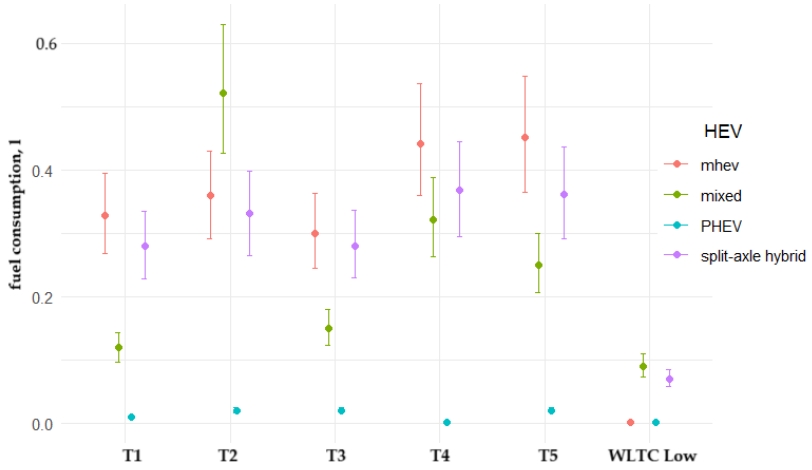

Fig. 8. Distributions of fuel consumption [l] with 95% confidence intervals for $\sigma = 0.1$

Table 5. Tukey's post-hoc test results for fuel consumption differences [l] among hybrid vehicle types

Parameter	Mean difference	Lower CI	Upper CI	p-value
mixed – MHEV	–0.071	–0.074	–0.069	< 0.001
PHEV – MHEV	–0.302	–0.304	–0.299	< 0.001
split-axle hybrid – MHEV	–0.031	–0.034	–0.029	< 0.001
PHEV – mixed	–0.230	–0.233	–0.228	< 0.001
split-axle hybrid – mixed	0.040	0.037	0.042	< 0.001
split-axle hybrid – PHEV	0.270	0.268	0.273	< 0.001

Tukey's post-hoc test revealed statistically significant differences in fuel consumption between all pairs of HEV types (p = 0). The most substantial difference was observed between PHEV and MHEV (mean difference: –0.3015 l, 95% CI: [–0.3041, –0.2990]), indicating that PHEV consumes significantly less fuel than MHEV. PHEV also differed significantly from mixed hybrid (mean difference: -0.2304 l, 95% CI: [–0.2329, –0.2278]) and split-axle hybrid (mean difference: 0.2701 l, 95% CI: [0.2676, 0.2727]), demonstrating the lowest fuel consumption among all types. The mixed hybrid consumed less fuel than the MHEV (mean difference: –0.0712 l, 95% CI: [–0.0737, –0.0686]), but more than the split-axle hybrid (mean difference: 0.0398 l, 95% CI: [0.0372, 0.0423]). The split-axle hybrid positioned itself between the MHEV (mean difference: –0.0314 l, 95% CI: [–0.0340, –0.0289]) and the mixed hybrid, indicating intermediate fuel efficiency. These results confirm that PHEV are the most fuel-efficient HEV type.

Figure 9 displays the Monte Carlo simulation results for CO_2 emissions, showing their distributions, mean values, and 95% confidence intervals across various vehicle types and route combinations.

Analysis of CO_2 emissions revealed a significant impact of both hybrid vehicle type and route, as well as their interaction, on emission levels ($p < 0.001$ for all effects and assumed significance levels of σ). At a significance level of $\sigma = 0.05$, the ANOVA test showed a highly significant effect of HEV type ($F = 629{,}708$), route effect ($F = 212{,}121$), and a significant interaction between these factors ($F = 49{,}068$). Similar, highly significant effects ($p < 0.001$ for all) were also observed at significance levels of $\sigma = 0.1$ (F for HEV type = 155,357, F for route = 52,430, F for interaction = 12,137) and $\sigma = 0.2$ (F for HEV type = 38,784, F for route = 13,056, F for interaction = 3029).

In summary, the ANOVA results consistently indicate a statistically significant influence of hybrid vehicle type, route characteristics, and their interaction on CO_2 emission levels, regardless of the assumed significance level ($\alpha = 0.05, 0.1, 0.2$). The results of Tukey's post-hoc test for differences in CO_2 emission values (kg) between hybrid vehicle types are presented in Table 6.

Table 6. Tukey's post-hoc test results for CO_2 emissions differences [kg] among hybrid vehicle types

Parameter	Mean difference	Lower CI	Upper CI	p-value
mixed – MHEV	–0.166	–0.172	–0.160	< 0.001
PHEV – MHEV	–0.725	–0.731	–0.719	< 0.001
split-axle hybrid – MHEV	–0.073	–0.079	–0.067	< 0.001
PHEV – mixed	–0.559	–0.565	–0.553	< 0.001
split-axle hybrid – mixed	0.093	0.087	0.099	< 0.001
split-axle hybrid – PHEV	0.652	0.646	0.658	< 0.001

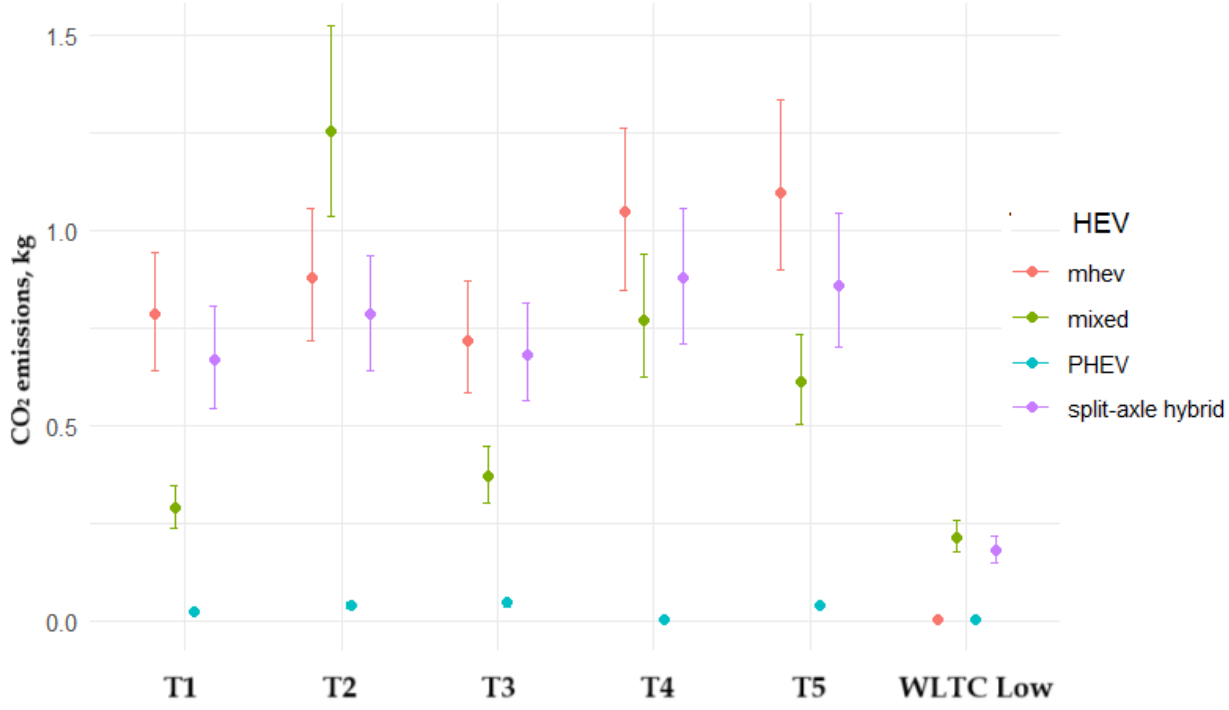

Fig. 9. Distributions of CO_2 emissions [kg] with 95% confidence intervals for $\sigma = 0.1$

Tukey's post-hoc test for CO_2 emissions (kg) revealed statistically significant differences between all pairs of HEV types ($p = 0$). The largest difference was observed between PHEV and MHEV (mean difference: –0.7252 kg, 95% CI: [–0.7313, –0.7191]), indicating that PHEV emits significantly less CO_2 than MHEV. PHEV also demonstrated lower emissions compared to mixed hybrid (mean difference: –0.5591 kg, 95% CI: [–0.5652, –0.5530]) and split-axle hybrid (mean difference: 0.6520 kg, 95% CI: [0.6459, 0.6581]), achieving the lowest emission values among all types. The mixed hybrid emitted less CO_2 than the MHEV (mean difference: –0.1661 kg, 95% CI: [–0.1722, –0.1600]), but more than the split-axle hybrid (mean difference: 0.0929 kg, 95% CI: [0.0868, 0.0990]). The split-axle hybrid was positioned between the MHEV (mean difference: –0.0732 kg, 95% CI: [–0.0793, –0.0671]) and the mixed hybrid, indicating an intermediate emission level. These results underscore the superior environmental efficiency of PHEVs compared to other HEV types.

The results indicate that both the hybrid vehicle type and the test route exert a crucial influence on fuel consumption and CO_2 emissions. Furthermore, the interaction between these factors suggests that the efficiency of specific HEV types can be optimized depending on driving conditions.

4. Discussion

The findings presented in this study significantly contribute to understanding the impact of traffic congestion on fuel consumption and CO_2 emissions in hybrid electric vehicles operating in urban environments. The simulation analysis, performed using AVL Cruise M software with real-world speed profiles from five urban routes (T1–T5) and the standardized WLTC Low cycle, provided detailed data on the efficiency of four HEV types: plug-in hybrid electric vehicle (PHEV), series-parallel (mixed) configuration, mild hybrid electric vehicle (MHEV), and split-axle hybrid. The application of the Monte Carlo method enabled the estimation of result variability, enhancing the reliability of the analysis despite limited empirical data.

This study distinguishes itself from previous work by its comprehensive approach, analysing four distinct hybrid powertrain configurations under conditions of high traffic congestion. Earlier studies often focused on a single hybrid type or standardized test cycles, leaving a gap in understanding HEV efficiency in diverse, real-world urban conditions. This research fills that gap by offering a thorough comparison, making its findings more representative of actual transportation challenges.

The study revealed that fuel consumption and emission levels are dependent on the hybrid powertrain configuration. Analysis of the driving and idle phases uncovered critical areas for optimizing hybrid powertrain control strategies, particularly during heavy traffic. For example, on route T2, where idle time accounted for 42% of the duration, the mixed hybrid consumed 0.52 l of fuel, whereas the PHEV consumed only 0.02 l. Consequently, under conditions of frequent stops and starts, series-parallel (mixed) and split-axle hybrids are characterized by continuous internal combustion engine operation, leading to increased fuel consumption and higher CO_2 emissions. The data indicate that MHEVs may exhibit lower efficiency in high-density traffic areas, as evidenced by the higher fuel consumption and emissions observed during acceleration cycles and idle phases.

A comparison of fuel consumption and CO_2 emission values from urban routes and the WLTC Low cycle highlights the limitations of current testing standards in reflecting real-world driving conditions. In the WLTC Low cycle, the PHEV exhibited zero fuel consumption, a result of its capability for all-electric operation, facilitated by a large battery energy capacity and an initial battery SOC of 80%. However, on routes T2 and T4, fuel consumption and emissions were significantly higher for all HEV types except the PHEV. It can therefore be concluded that current test cycles do not fully capture the challenges associated with congestion, potentially leading to underestimated fuel consumption and emission values in official vehicle specifications.

Despite certain limitations, such as the absence of empirical tests and the omission of environmental and operational variables (e.g., driving style or temperature) in the AVL Cruise M simulations, as well as the non-inclusion of temperature effects on battery efficiency and fuel consumption, this study possesses significant strengths.

The use of real-world velocity profiles considerably enhances the representativeness of the results for urban conditions, thereby increasing their practical value. Additionally, the application of the advanced Monte Carlo method to estimate result variability constitutes a rigorous approach that effectively compensates for the lack of empirical data, providing a solid foundation for the conclusions. Consequently, despite the mentioned limitations, this study makes a valuable contribution to understanding the impact of congestion on hybrid vehicle efficiency and establishes a robust basis for further research.

5. Conclusions

This research provides crucial insights into the impact of varying urban traffic congestion on fuel consumption and CO_2 emissions in hybrid electric vehicles. It leveraged simulations within the AVL Cruise M environment, utilizing real-world speed profiles (T1–T5) and the standardized WLTC Low cycle. The application of the Monte Carlo method enabled a reliable assessment of result variability across four distinct HEV types.

The analysis revealed that PHEV exhibited minimal fuel consumption and CO_2 emissions, especially in scenarios with frequent stops. This is directly linked to their ability to operate extensively in electric mode, made possible by its high-capacity batteries. Conversely, MHEV demonstrated the lowest efficiency in high-traffic conditions, primarily because its electric drive serves only a supporting role. The split-axle configuration showed better efficiency in smooth traffic flow, underscoring the influence of the hybrid powertrain type on fuel consumption and CO_2 emissions depending on operational conditions. Therefore, the degree of electrification/hybridization is a crucial determinant of the energy and environmental efficiency of hybrid vehicles in urban environments, particularly concerning traffic congestion. A higher degree of electrification, as seen in PHEVs, enables a significant reduction in fuel consumption and CO_2 emissions, making such vehicles most suitable for

high-traffic conditions where frequent stops and dynamic driving phases are dominant.

The results also highlighted the imperfections of current testing standards (e.g., WLTC Low) in reflecting real-world urban traffic conditions, potentially leading to an underestimation of actual fuel consumption and emissions. This suggests a need for optimizing hybrid powertrain control strategies, especially in areas characterized by high traffic congestion. It is also worth noting the importance of promoting advanced hybrid technologies, such as PHEVs, within transportation policies.

In summary, the study provides crucial quantitative data that can support the design of more efficient hybrid vehicles and the shaping of urban transportation policies. It emphasizes the pivotal role of real-world road conditions in HEV assessment and indicates the necessity of adapting testing standards to the specifics of urban traffic.

Nomenclature

ANOVA	analysis of variance
CI	confidence interval
CO_2	carbon dioxide
GPS	global positioning system
HC	hydrocarbons
HEV	hybrid electric vehicle
ICE	internal combustion engine
MHEV	mild hybrid electric vehicle
NO_x	nitrogen oxide
PHEV	plug-in hybrid electric vehicle
PM	particulate matter
SOC	state of charge
WLTC	Worldwide Harmonized Light Vehicles Test Cycle

Bibliography

[1] Bieniek A, Graba M, Mamala J, Prażnowski K, Hennek K. Energy consumption of a passenger car with a hybrid powertrain in real traffic conditions. Combustion Engines. 2022;191(4):15-22. https://doi.org/10.19206/CE-142555

[2] Cao Y, Yao M, Sun X. An overview of modelling and energy management strategies for hybrid electric vehicles. Appl Sci. 2023;13(10):5947. https://doi.org/10.3390/app13105947

[3] Choi M, Cha J, Song J. Analysis of fuel economy reduction factors of hybrid electric vehicles in winter using on-road driving data. Energy. 2024;289:129977. https://doi.org/10.1016/j.energy.2023.129977

[4] Dauphin R, Prevost V, Degeilh P, Melgar J, Fittavolini C, Smith A et al. Evaluation of plug-in hybrid vehicles in real-world conditions by simulation. Transp Res D Trans Environ. 2023;119:103721. https://doi.org/10.1016/j.trd.2023.103721

[5] Delso-Vicente A-T, Camperos M-C, Almonacid-Durán M. The evolution of electric and hybrid vehicles and their influence on sustainable transport: a review and future research lines. Sust Tech Ent. 2025;4(2):100100. https://doi.org/10.1016/j.stae.2025.100100

[6] Fernandes P, Macedo E, Tomas R, Coelho MC. Hybrid electric vehicle data-driven insights on hot-stabilized exhaust emissions and driving volatility. Int J Sustain Transp. 2024;18(1):84-102. https://doi.org/10.1080/15568318.2023.2219629

[7] Keegan G, Nelendran P, Oluwafemi O. Modeling and simulation of hybrid electric vehicles for sustainable transportation: insights into fuel savings and emissions reduction. Energies. 2024;17(20):5225. https://doi.org/10.3390/en17205225

[8] León R, Montaleza C, Maldonado JL, Tostado-Véliz M, Jurado F. Hybrid electric vehicles: a review of existing configurations and thermodynamic cycles. Thermo. 2021; 1(2):134-150. https://doi.org/10.3390/thermo1020010

[9] Ma Y, Wang J. Personalized drivng behaviors and fuel economy over realistic commute traffic: modelling, correlation and prediction. IEEE Trans Veh Technol. 2022; 71(7):7084-7094. https://doi.org/10.1109/TVT.2022.3171165.

[10] Muhammad A, Haruna IS. Hybrid electric vehicles: a mini overview. JMMST. 2021;5(1):27-36. https://doi.org/10.15282/jmmst.v5i1.6055.

[11] O'Driscoll R, Stettler MEJ, Molden N, Oxlet T, ApSimon HM. Real world CO_2 and NO_x emissions from 149 Euro 5 and 6 diesel, gasoline and hybrid passenger cars. Sci Total Environ. 2018;621:282-290. https://doi.org/10.1016/j.scitotenv.2017.11.271

[12] Orecchini F, Santiangeli A, Zuccari F, Ortenzi F, Genovese A et al. Energy consumption of a last generation full hybrid vehicle compared with a conventional vehicle in real drive conditions. Energy Procedia. 2018;148:289-296. https://doi.org/10.1016/j.egypro.2018.08.080

[13] Pečman J, Šarkan B, Ližbetinová L, Ľupták V, Loman M, Bartuška L. Impact of acceleration style on vehicle emissions and perspectives for improvement through transportation engineering solutions. The Archives of Automotive Engineering – Archiwum Motoryzacji. 2024; 104(2):48-62. https://doi.org/10.14669/AM/189665

[14] Pielecha J, Skobiej K, Kurtyka K. Exhaust emissions and energy consumption analysis of conventional, hybrid, and electric vehicles in real driving cycles. Energies. 2020; 13(23):6423. https://doi.org/10.3390/en13236423

[15] Pitanuwat S, Sripakagorn A. An investigation of fuel economy potential of hybrid vehicles under real-world driving conditions in Bangkok. Energy Procedia. 205;79: 1046-1053. https://doi.org/10.1016/j.egypro.2015.11.607

[16] Pryciński P. Selected emissivity assessment issues for electric and hybrid vehicles. Combustion Engines. 2025; 202(3):27-35. https://doi.org/10.19206/CE-205274

[17] Rashid S, Pagone E. Cradle-to-grave lifecycle environmental assessment of hybrid electric vehicles. Sustainability. 2023;15(14):11027. https://doi.org/10.3390/su151411027

[18] Rențea C, Bataus M, Maican S, Oprean M, Fratila G. The influence of the hybridization factor on vehicle energetic consumption for different e-gearbox configurations. IOP Conf Ser: Mater Sci Eng. 2021;1037:012050. https://doi.org/10.1088/1757-899X/1037/1/012050

[19] Šarkan B, Gnap J, Kiktová M. The importance of hybrid vehicles in urban traffic in terms of environmental impact. The Archives of Automotive Engineering – Archiwum Motoryzacji. 2019;85(3):115-122. https://doi.org/10.14669/AM.VOL85.ART8

[20] Šarkan B, Loman M, Harantová V. Identification of places with deteriorated air quality in city of Žilina in relation to

road transport. The Archives of Automotive Engineering – Archiwum Motoryzacji. 2023;102(4):68-90. https://doi.org/10.14669/AM/176958

[21] Skuza A, Szumska E, Jurecki R. Fuel consumption and CO_2 emission analysis of hybrid and conventional vehicles in urban conditions. Combustion Engines. 2023;195(4):48-55. https://doi.org/10.19206/CE-169569

[22] Szumska E, Jurecki R, Pawełczyk M. Evaluation of the use of hybrid electric powertrain system in urban traffic conditions. Eksploat Niezawodn. 2020;22(1):154-160. https://doi.org/10.17531/ein.2020.1.18

[23] Thomas J, Huff S, West B, Chambon P. Fuel consumption sensitivity of conventional and hybrid electric light-duty gasoline vehicles to driving style. SAE Int J Fuels Lubr. 2017;10(3):9379 https://doi.org/10.4271/2017-01-9379

[24] Veza I, Asy'ari MZ, Idris M, Epin V, Fattah IMR, Spraggon M. Electric vehicle (EV) and driving towards sustainability: comparison between EV, HEV, PHEV and ICE vehicles to achieve net zero emissions by 2050 from EV. Alexandria Engineering Journal. 2023;82:459-467. https://doi.org/10.1016/j.aej.2023.10.020

[25] Wang A, Xu J, Zhang M, Zhai Z, Song G, Hatzopoulou Z. Emissions and fuel consumption of a hybrid electric vehicle in real-world metropolitan traffic conditions. Appl Energy. 2022;306:118077. https://doi.org/10.1016/j.apenergy.2021.118077

[26] Zachiotis AT, Giakoumis EG. Monte Carlo simulation methodology to assess the impact of ambient wind on emissions from a light-commercial vehicle running on the Worldwide-Harmonized Light-Duty Vehicles Test Cycle (WLTC). Energies. 2021;14(3):661. https://doi.org/10.3390/en14030661

[27] Zimakowska-Laskowska M, Laskowski P. Comparison of pollutant emissions from various types of vehicles. Combustion Engines. 2024;197(2):139-145. https://doi.org/10.19206/CE-181193

Adriana Skuza, MEng. – Faculty of Mechatronics and Mechanical Engineering, Kielce University of Technology, Poland.
e-mail: *askuza@tu.kielce.pl*

Prof. Rafał Jurecki, DSc., DEng. – Department of Automotive Engineering and Transport, Kielce University of Technology, Poland.
e-mail: *rjurecki@tu.kielce.pl*

Emilia Szumska, DSc., DEng. – Faculty of Mechatronics and Mechanical Engineering, Kielce University of Technology, Poland.
e-mail: *eszumska@tu.kielce.pl*

Article citation info:
Lijewski P, Fuć P, Brydziński A, Zygmanowski M. Analysis of energy consumption of electric two-wheeled vehicles based on road cycle simulation. Combustion Engines. 2026;206(3):27-33. https://doi.org/10.19206/CE-215450

Piotr LIJEWSKI
Paweł FUĆ
Artur BRYDZIŃSKI
Marcin ZYGMANOWSKI

Combustion Engines
Polish Scientific Society of Combustion Engines

Analysis of the energy consumption of electric two-wheeled vehicles based on the road cycle simulation

ARTICLE INFO

Received: 15 June 2025
Revised: 25 November 2025
Accepted: 10 December 2025
Available online: 26 January 2026

The paper focuses on the development and validation of a simulation model that allows the assessment of the influence of the design and operating parameters on the maximum range of an urban electric two-wheeler. The performed research included real-world tests under urban conditions, covering a distance of 5.2 km, while monitoring the electrical parameters of an electric scooter. The sampling resolution was 0.1 seconds. The results of the measurements allowed for estimating the range of the vehicle under real-world conditions to be 60.053 km, corresponding to an energy consumption of 2.15 kWh/100 km. Based on the experimental data, the authors developed an advanced simulation model in the MATLAB environment. The model included dynamic acceleration/deceleration cycles, aerodynamic drag, rolling resistance and battery characteristics. The simulation of the driving cycle has shown the vehicle range of 60.778 km with the energy consumption of 2.12 kWh/100 km. The simulation results are characterized by a very high convergence with the results obtained in the road cycles. The simulation model enables the analysis of vehicle range variability in relation to various design and operating parameters, including gross vehicle weight, aerodynamic drag, drivetrain efficiency, and battery characteristics. The investigations described in the paper support the advancement of electromobility, thus, adding to the improvement of urban transport.

Key words: *electric vehicle, electric scooter, energy-consumption rate*

This is an open access article under the CC BY license (http://creativecommons.org/licenses/by/4.0/)

1. Introduction

Currently manufactured electric urban two-wheelers can be divided into three categories: traditional scooters, bicycles and ekick-scooters. Table 1 presents the technical data of different electric scooter models fitted with Li-ion batteries and compares their parameters and functionalities. Vehicles fitted with Li-ion batteries are characterized by higher energy capacity, which directly translates into improved range and better ride dynamics. Models such as the Iamelectric IML NCE-S or the Iamelectric T-REX, fitted with high-capacity batteries (4896 Wh and 5040 Wh, respectively), have a greater range and higher maximum speeds. It can be assumed that the electric vehicle market will develop, this applies not only to two-wheelers, but also to other categories of vehicles [4, 5].

Table 1. Technical data of selected electric scooters

Model	Battery capacity [V, Ah]	Battery energy [Wh]	Motor power [W]	Maximum speed [km/h]	Declared maximum range [km]
Iamelectric Eagle Lithium	60, 20	1200	1200	45	50
Iamelectric Hawk Lithium	72, 20	1440	1800	45	65
Iamelectric IML NCF-S	2 × 60, 34	4080	4310	80	80
Iamelectric IML NCE-S	2 × 72, 34	4896	6600	90	130
Iamelectric T-REX	72, 70	5040	6000	110	100

Energy consumption is a crucial parameter that significantly influences the performance and functionality of electric vehicles (EVs). The energy consumption parameter describes the amount of energy (expressed in kilowatt-hours – kWh) required to cover a certain distance, typically 100 kilometers (kWh/100 km). Siemionek [13] defines the energy consumption of a vehicle in motion, allowing for energy loss throughout the entire drivetrain, the vehicle's technical condition, and the weight of the passengers. Similar studies were presented in [7], where the investigation objective was to examine the dynamic and energy consumption of an electric scooter by varying key input parameters, including rider mass, electric scooter mass, wind speed, wheel radius, and slope grade. A simulation model of an electric scooter was developed in MATLAB-Simulink to simulate the scooter's velocity, required power, battery voltage, and powertrain torque. In [3], the authors presented the role of battery condition in electric vehicles as a main parameter affecting vehicle distance. Boumediene et al. [2] developed a control algorithm for energy management to maintain the scooter battery and supercapacitor at their optimal states of charge. An electric scooter's powertrain performance under varying loads is simulated in MATLAB and Simulink to verify the effectiveness of the EMS. The simulation results validate the effectiveness of the proposed approach and demonstrate the novel EMS as a suitable solution for energy management.

Yuan et al. [15] emphasize the significance of energy consumption. “In order to assure standardization, the ECR indicator (ECR – Energy-Consumption Rate) is determined under certain test conditions – a standard cycle that is deemed to be the most representative driving profile.” The ECR is the fundamental parameter that allows for an accurate analysis of the energy performance of electric vehicles

under standard test conditions, ensuring consistency and comparability of the results.

To sum up, the energy consumption of electric vehicles is defined as the amount of energy consumed per unit of covered distance. The value of this parameter is influenced by the vehicle's design (weight, drivetrain efficiency, and aerodynamics) and the operating parameters, which include the driving style and route profile. Standardized measurement methods, such as driving cycles, allow for comparable results and parameter analysis under different scenarios.

Two-wheeled electric vehicle energy consumption modeling is not widely discussed in the literature. In [12], the authors focused on modeling the energy performance and energy consumption of an e-scooter using the AUTONOMIE simulation tool [1]. Literature also describes a methodology based on assessing energy consumption derived from the scooter motor's power output and road data [9]. In [8], the authors propose a model that utilizes the MATLAB environment; however, its application requires very detailed engine and drivetrain data. A similar solution was proposed in [10], where the developed model uses MATLAB/Simulink. In [14], a dynamic simulation model was proposed that was experimentally validated on a chassis dynamometer. In [16], the authors presented a method for developing an electric scooter model to simulate its performance, especially its range estimation. The modeling method was the use of an electric scooter model developed in MATLAB/Simulink. Based on the dimensions and targeted performance, the authors simulated the device to determine its power and energy requirements. The research results of the simulation were validated in an experimental test on a dynamometer and in on-road conditions.

Selecting the correct battery technology is of vital importance. The technical parameters, such as capacity, weight, number of charging cycles, and performance under varying operating conditions, have a direct influence on the vehicle's range, performance, and useful life. Based on the analysis of different types of vehicles (Table 2), we can infer that Li-ion (lithium-ion) and Li-Po (lithium polymer) batteries are characterized by the highest specific energy and energy density, making them the best choice for electric scooters.

Table 2. Comparison of the battery parameters

Parameter	NiCd	NiZn	NiMH	Li-ion/Li-Po
Specific energy [Wh/kg]	40–60	100	60–120	100–265
Energy density [Wh/l]	50–150	280	140–300	250–730
Specific power [W/kg]	150	> 900	250–1000	250–340
Charge/discharge efficiency [%]	70–90	80	66	80–90
Self-discharge indicator [%]	10	13	30	8–5
Cycle durability [cycle]	2000	400–1000	500–1000	400–1200
Cell voltage [V]	1.2	1.65	1.2	NMC 3.6/3.7; LiFePo4 3.2

2. Research methodology

The research object has been presented in Fig. 1. It is an electric scooter. It is an urban two-wheeled electric vehicle, known as the Eagle Lithium, made by Iamelectric. The basic parameters of the object have been shown in Table 3. The vehicle is driven by a 1200 W electric motor that allows a maximum speed of 45 km/h. The unit is powered by a 70 V 20 Ah lithium-ion battery.

Fig. 1. Iamelectric Eagle Lithium scooter used for test [11]

Table 3. Basic parameters of the tested object [11]

Parameter	Data
Homologation	Yes
Equivalent of petrol scooter	50cc
Battery	Lithium-ion
Battery capacity	70V 20Ah
Battery charging time	4–6 hours
Battery weight	10 kg
Battery lifespan	1000 cycles
Electric motor power	1200 W
Maximum range	Up to 45 km (1 person, 70 kg)
Maximum speed	45 km/h
Tire size (front/rear)	3.50–10"
Curb weight	63 kg
Max. Permissible payload	188 kg
Gross vehicle weight	263 kg
Dimensions	1810 × 710 × 1100 mm

The planned experiment aimed to determine the energy characteristics of the tested object's operation under real-world operating conditions. The tests were carried out on a route of 5.2 km in length (Fig. 2), which the object covered in 10 minutes. The tests included recording the variations in voltage (V) and current (mA) in the power supply circuit of the electric motor. The tests were conducted using real-time measurement equipment. The recorded data were also transmitted in real-time to the computing unit located at Poznan University of Technology. The data transmission was completed through a computer installed in the scooter rear trunk (wireless communication, Internet access).

The Fluke i30s, utilizing the Hall effect, was used to measure the current and voltage at the input to the electric motor. Using the Advantech Elmatica UNO 137, the data

were processed in real-time. The Advantech CR 1601W recorded and forwarded data to the Internet. Prior to commencing the tests, the sensors were calibrated to ensure measurement accuracy. The measurement equipment recorded the voltage and current values continuously at a sampling frequency of 10 Hz. The data collected during the tests enabled a detailed analysis of the voltage (V) and current (mA) variations as a function of time. The data were used to develop a detailed mathematical model, which constitutes the basis for the simulation.

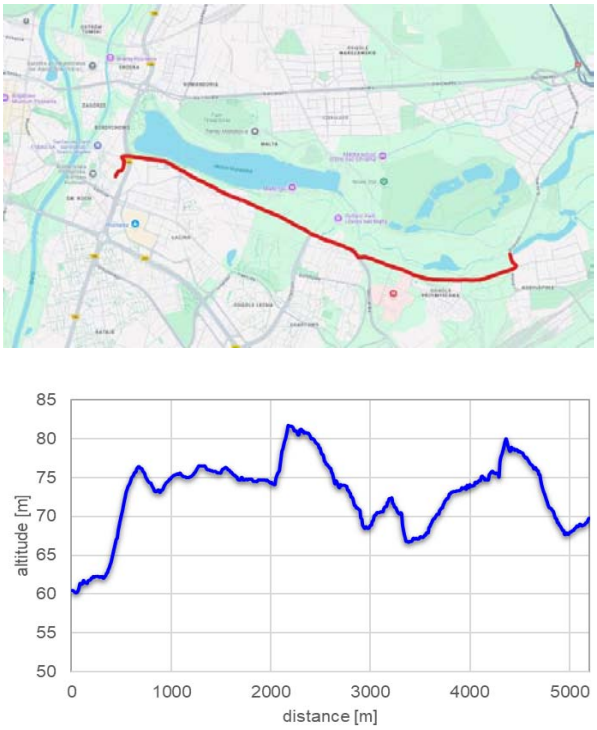

Fig. 2. Test route [google.com/maps]

3. Results

Based on the recorded data, the authors calculated the instantaneous energy consumption (P) as per the relation:

$$P = \frac{U \cdot I}{1000} [kW] \quad (1)$$

The results of the calculations showing the instantaneous energy consumption were used to generate a graph, as shown in Fig. 3. From the analysis of the graph, it is evident that the instantaneous energy consumption is characterized by visible fluctuations that reflect the driving dynamics. The maximum values of energy consumption, reaching 1.4 kW, occur during vehicle acceleration. The total energy consumption by the motor of the tested object was calculated as the sum of the instantaneous energy for all recorded samples. The calculations were made according to the equation as shown below:

$$E = \frac{(P \cdot \Delta t)}{3600} [kWh] \quad (2)$$

The results of the calculations show that the accumulated amount of energy used during the test was the value calculated from equation (2):

$$E \approx 0.112 \text{ kWh}$$

The obtained results also show that the energy consumption was clearly dependent on the driving dynamics. The highest energy consumption occurred in the acceleration phase.

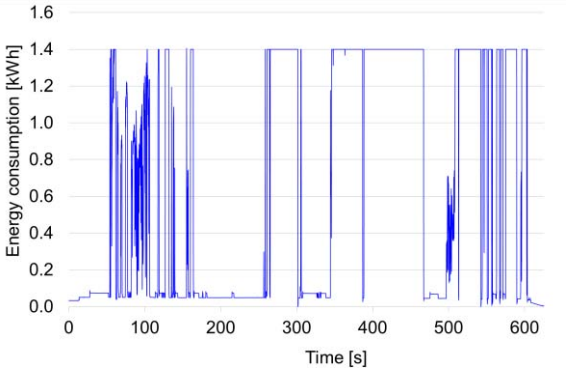

Fig. 3. Instantaneous energy consumption as a function of time

The voltage values during the test varied in the range from approx. 62 V to the nominal value of 70 V (Fig. 4). Instantaneous voltage drops to approx. 60 V occurred during heavy battery load, particularly during acceleration. This phenomenon is characteristic of the operation of lithium-ion battery cells, where the voltage drops in response to high energy demand.

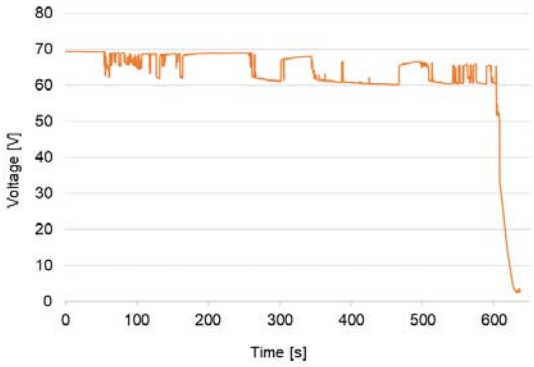

Fig. 4. Voltage changes as a function of time

During the tests, the current reached its maximum value of 25 A during heavy acceleration (Fig. 5). Low current values, close to 0 A, were recorded when the vehicle was stationary or when coasting and the electric motor was not engaged.

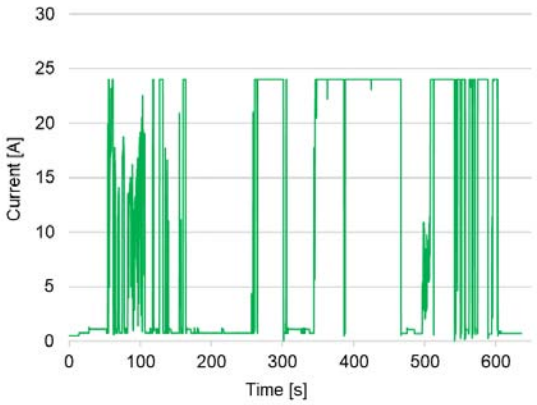

Fig. 5. Change in the current as a function of time

Figure 6 presents the cumulative value of energy consumption, reflecting the total amount of energy drawn from the battery during the tests. The greatest increase in energy consumption was observed during the acceleration phase, indicating a significant load on the battery resulting from high power demand.

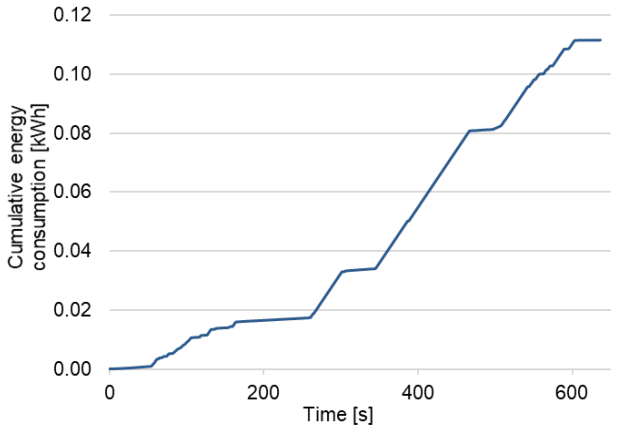

Fig. 6. Cumulative energy consumption as a function of time

Based on the collected data related to energy consumption and battery parameters, the authors performed an analysis aimed at assessing the projected range of the tested object. The results of the calculations have been presented in Table 4.

Table 4. Assessment of the projected range of the tested object

Description	Value
Total energy consumed [kWh] = (Samples · delta t)/3600	0.112
Remaining energy [Wh]	1288.472
Remaining charge percentage [%]	92.034
Used charge percentage [%]	7.966
Estimated range at 100% battery efficiency [km]	65.275
Estimated range at 92% battery efficiency [km]	60.053

4. Simulation of the scooter range

The simulation of the driving cycle, based on real-world data collected during tests, aimed to reproduce the actual driving profile of the test object and estimate its range, allowing for dynamic speed changes, accelerations, and decelerations. Based on the analysis of the real-time data collected during the tests, the authors observed that within a 10-minute experiment, 40 acceleration cycles were identified.

The simulation served as a tool to validate the compliance of the calculated results with those obtained under real-world conditions. Gołębiewski and Prajwowski have presented the mathematical formulas used as the basis for the simulation in [11]. The input data necessary to carry out the simulation were those modeled from the data obtained under real-world driving conditions. The input data necessary to carry out the simulation are shown in Table 5.

In the first step of the simulation, the authors entered the most fundamental parameters of the vehicle (Fig. 7). The input data may vary, as it is possible to use factory data related to specific models of electric scooters.

Table 5. Simulation input data

Parameter	Value
Maximum motor power output (Pmax)	1200 W (1.2 kW)
Maximum speed (Vmax)	45 km/h (12.5 m/s)
Vehicle weight (m)	160 kg
Air density (rho)	1.225 kg/m^3
Aerodynamic drag coefficient (Cd)	0.6
Frontal area of the vehicle (A)	0.6 m^2
Rolling resistance coefficient (f_r)	0.015
Gravitational acceleration (g)	9.81 m/s^2
Battery capacity (capacity Ah)	20 Ah
Battery voltage (V_battery)	70 V
Nominal battery energy (E_battery)	1400 Wh (5.040.000 J)
Battery efficiency (eta_battery)	92% (0.92)
Drivetrain efficiency (eta_drive)	95% (0.95)
Acceleration/deceleration cycles (n_cycles)	40 cycles
Acceleration (a_acc)	1.5 m/s^2
Deceleration (a_dec)	–1.5 m/s^2
Total test time (t_test)	600 s (10 min)

```
% Scooter range Iamelectric Eagle Lithium

% Vehicle data
P_max = 1.2 * 1000; % Max engine power W (1.2 kW)
V_max = 45 / 3.6;  % Max velocity m/s (45 km/h)
m = 160;           % Vehicle duty (kg)
rho = 1.225;       % Air density (kg/m^3)
C_d = 0.6;         % Aerodynamic drag coefficient
A = 0.6;           % Frontal area (m^2)
f_r = 0.015;       % Rolling resistance coefficient
g = 9.81;          % Gravitational acceleration (m/s^2)
```

Fig. 7. Parameters of the vehicle

where:
P_max – maximum motor power output; P_max = 1200 W
V_max – maximum speed of the vehicle; V_max = 45/3.6 m/s
m – vehicle weight including the driver, the vehicle equipment and measurement devices m = 160 kg
rho – air density under standard conditions, used to calculate aerodynamic drag rho = 1.225 kg/m^3
C_d – drag coefficient, determining the aerodynamic performance of the vehicle C_d = 0.6
A – frontal area influencing the aerodynamic drag; A = 0.6 m^2
f_r – rolling resistance coefficient, allowing for loss resulting from the contact of the tires with the road; f_r = 0.015
(g) – gravitational acceleration, used for calculating the mass forces g = 9.81 m/s^2.

The input data presented in Fig. 8 describe the parameters of the battery that were vital for the correct performance of the vehicle range simulation.

```
% Battery data
capacity_Ah = 20;  % Capacity (Ah)
voltage_V = 70;    % Battery voltage (V)
E_battery_Wh = 1400; % Battery energy (Wh)
E_battery_J = E_battery_Wh * 3600; % Battery energy (J)
battery_efficiency = 0.92; % Battery efficiency (92%)
E_battery_J = E_battery_J * battery_efficiency; % Battery effective energy
```

Fig. 8. Parameters of the battery

where:
capacity_Ah – battery capacity capacity_Ah = 20 Ah
voltage_V – rated battery voltage voltage_V = 70 V
E_battery_Wh – nominal energy of the battery expressed in watt-hours E_battery_Wh = 1400 Wh

E_battery_J – nominal energy of the battery converted into joules E_battery_J = 1400 × 3600 = 5040000 J
battery_efficiency – battery efficiency; battery_efficiency = 92% = 0.92
E_battery_Jr – effective energy available at the battery terminals, calculated as the product of nominal energy and battery efficiency; E_battery_Jr = 5040000 × 0.92 = 4636800 J.

The formulas presented in Fig. 9 describe the efficiency of the drivetrain and calculations of the motion resistance.

```
% Powertrain efficiency
drive_train_efficiency = 0.95; % Powertrain efficiency (95%)

% Motion resistance efficiency calculation
% Air drag: F_drag = 0.5 * rho * C_d * A * V^2
% Rolling resistance: F_roll = m * g * f_r
```

Fig. 9. Efficiency of the drivetrain and calculations of the motion resistance

where:
drivetrain_efficiency – drive_train_efficiency = 95% = 0.95
F_drag – aerodynamic drag, described as F_drag = 0.5 × rho × C_d × A × V^2 [N]
rho – air density [kg/m^3], (C_d) – drag coefficient [-]
A – vehicle frontal area [m^2]
V – vehicle speed squared [m/s]
F_roll – rolling resistance force described with the formula F_roll = m × g × f_r [N]
m –vehicle weight including the weight of the driver and the equipment [kg], (g) – gravitational constant [m/s^2]
f_r – rolling resistance coefficient [-].

The parameters presented in Fig. 10 define the acceleration/deceleration cycles.

```
% Acceleration and deceleration parameters
n_cycles = 40;        % Number of acceleration mode in 10 minute
a_acc = 1.5;          % Acceleration (m/s^2)
a_dec = -1.5;         % Deceleration (m/s^2)
time_acc = V_max / a_acc; % Acceleration time to max velocity (s)
time_dec = V_max / abs(a_dec); % Deceleration time to stop (s)
time_test = 10 * 60;   % Total cycle time (s)
```

Fig. 10. Parameters of the acceleration/deceleration cycles

where:
n_cycles – number of full cycles of acceleration and deceleration per each 10 minutes of test n_cycles = 40
a_acc – vehicle acceleration a_acc = 1.5 m/s²
a_dec – vehicle deceleration a_dec = –1.5 m/s²
time_acc – acceleration time, calculated as the quotient of the maximum speed and acceleration; time_acc = V_max / a_acc [s]
time_dec – deceleration time calculated as the quotient of the maximum speed and the absolute value of deceleration time_dec = V_max / abs(a_dec) [s]
t_test – total time of the simulation covering all driving cycles, t_test = 600 [s].

The fragment of code presented in Fig. 11 pertains to the analysis of vehicle operating conditions at a constant maximum speed.

```
% Motion and idle time calculation
active_time = time_test; % active motion time (s)

% Assumation constant vehicle velocity
V = V_max;
F_drag = 0.5 * rho * C_d * A * V^2;
F_roll = m * g * f_r;
F_total = F_drag + F_roll; % Drag force

% Required power constant velocity
P_required = F_total * V / drive_train_efficiency; % Power (W) (with powertrain efficiency)

% Verification max vehicle velocity
if P_required > P_max
    disp('Vehicle is not able to going with constant velocity.');
    return;
end
```

Fig. 11. Calculating the active time of the vehicle and when stationary

where:
active_time – active time equal to the total time of the test active_time = 600 s
V – vehicle speed assumed as constant and equal to the maximum vehicle speed V = V_max [m/s]
F_drag – aerodynamic drag calculated as F_drag = 0.5 × rho × C_d × A × V² [N]
F_roll – rolling resistance determined from the formula F_roll = m × g × f_r [N]
F_total – total resistance force being the sum of aerodynamic drag and rolling resistance; F_total = F_drag + F_roll [N]
P_required – power required to overcome the total resistance at a constant speed, calculated as P_required = F_total × V/drive_train_efficiency [W]
P_max – maximum power output of the motor used to verify the possibility of the vehicle to maintain the maximum speed [W].

The fragment of a code presented in Fig. 12 pertains to the simulation of 40 cycles of acceleration and deceleration that were recorded during a 10-minute test under real-world conditions.

```
% Simulation 40 cycle acceleration and deceleration in 10 minute
E_total_J = 0; % Total Energy consumption (J)
for i = 1:n_cycles
    % Acceleration mode
    F_acc = m * a_acc + F_total; % Acceleration force
    P_acc = min(P_max, F_acc * V_max / drive_train_efficiency); % Acceleration power
    E_acc = P_acc * time_acc; % Energy consumption during acceleration (J)

    % Deceleration mode
    F_dec = m * abs(a_dec); % Deceleration force (only deceleration, without drag)
    P_dec = F_dec * (V_max / 2) / drive_train_efficiency; % Approximately power (deceleration)
    E_dec = P_dec * time_dec; % Deceleration energy consumption (J)

    %
    E_total_J = E_total_J + E_acc + E_dec;
end
```

Fig. 12. Simulation of 40 cycles of acceleration/deceleration per each 10-minute portion of the test

where:
E_total_J – total energy used by the vehicle during the simulation, initially 0 and updated after each cycle [J]
i – index of an iterative loop, in which subsequent acceleration/deceleration cycles are carried out i=: n_cycles [-]
F_acc – acceleration force F_acc = m × a_acc + F_total [N]
P_acc – power used during acceleration P_acc = min(F_acc × V_max, P_max) [W]
E_acc – energy used during acceleration E_acc = P_acc × time_acc [J]
F_dec – deceleration force F_dec = m · abs(a_dec) [N],
P_dec – power used during deceleration P_dec = F_dec × (V_max / 2)/drive_train_efficiency [W],
E_dec – energy used during deceleration E_dec = P_dec × time_dec [J].

The fragment of code presented in Fig. 13 pertains to the analysis of the energy remaining in the battery, taking

into account the energy used during the 40 acceleration/deceleration cycles.

```
% Summing cycle energy with constant velocity
E_battery_remaining_J = E_battery_J - E_total_J;

% Verification energy level
if E_battery_remaining_J <= 0
    disp('Discharged battery after acceleration mode and deceleration mode.');
    return;
end
```

Fig. 13. Summing up the energy used during the cycles

where:

E_battery_remaining_J – remaining battery energy after completion of the cycles E_battery_remaining_J = E_battery_J – E_total_J [J]

E_total_J – total energy used during vehicle operation in cycles [J]

if E_battery_remaining_J <= 0 – logical condition validating if the battery is discharged, which would result in ending of the simulation,

return – a command to stop the software operation if the battery is discharged

E_battery_remaining_J > 0 – condition indicating that the vehicle still has energy resources and the simulation can be continued.

The fragment of code presented in Fig. 14 pertains to calculations of the battery operation time and the projected vehicle range, making allowances for energy use during acceleration and deceleration cycles.

The results of the simulations related to the vehicle's maximum range and battery energy consumption indicate compliance with the results obtained during tests performed under real-world conditions. The obtained results confirm the correctness of the simulation model and its compatibility with real-world operating conditions.

Under actual operating conditions, with the assumed battery efficiency of 92%, the projected vehicle range (as declared by the manufacturer) reaches 60.053 km. In the MATLAB simulation, the vehicle's range is estimated to be 60.778 km. The difference between these results is merely 0.725 km, which corresponds to a relative error of 1.2%. It should be acknowledged that such a difference is miniscule and the simulation model successfully reproduces the real-world operating conditions of the vehicle.

```
% Calculation battery operation time  with constant velocity
% Required energy for time unit (W) P_required (W)
% Battery operation time: t = E_battery_remaining / P_required

t_max_sec = E_battery_remaining_J / P_required; % Operation time (s)
t_max_h = t_max_sec / 3600; % Operation time (h)

% calculation vehicle range after acceleration mode and deceleration mode
range_km = (V * t_max_sec) / 1000; % Range km (for activity time)
```

Fig. 14. Calculation of the battery operating time

where:

t_max_sec – battery operating time after finishing the acceleration and deceleration cycles t_max_sec = E_battery_remaining_J / P_required [s]

t_max_h – battery operating time expressed in hours t_max_h = t_max_sec / 3600 [h]

range_km – vehicle range after the cycles range_km = (V × t_max_sec) / 1000 [km].

5. Conclusions

The results of the investigations indicate that the developed simulation tool can be used to estimate energy consumption by two-wheeled electric vehicles. The accuracy of the tool is fully satisfactory, as confirmed by experimental investigations conducted under real-world operating conditions in urban traffic. The proposed model can be used to assess the influence of design parameters, such as vehicle weight, rolling resistance coefficient, and aerodynamic drag, on the vehicle's energy performance and range. Another potential application of the model is assessing energy consumption based on traffic conditions. In further stages of the research, the authors plan to expand the simulation tool to other applications, such as two-wheeled vehicles with higher power output, operated in conditions other than urban. Additionally, the authors consider adapting the tool to simulate the energy consumption of other road vehicles, particularly passenger cars (PCs).

Bibliography

[1] Argonne National Laboratory. (2017). AUTONOMIE. http://www.autonomie.net/index.html

[2] Boumediene S, Nasri A, Hamza T, Hicham C, Kayisli K, Garg H. Fuzzy logic-based Energy Management System (EMS) of hybrid power sources: battery/super capacitor for electric scooter supply. J Eng Res. 2024;12(1):148-159. https://doi.org/10.1016/j.jer.2023.07.008

[3] Caban, J, Małek A, Kroczyński D. A method for assessing the technical condition of traction batteries using the metalog family of probability distributions. Energies. 2024;17: 3096. https://doi.org/10.3390/en17133096

[4] Dižo J, Blatnický M, Lovska A, Molnár D, Šuvada R. An engineering design of a scooter. In: Rackov M, Miltenović A, Banić M. (eds) Machine and industrial design in mechanical engineering. Mech Mach Sci. 2025;174. Springer, Cham. https://doi.org/10.1007/978-3-031-80512-7_62

[5] Dudziak A, Droździel P, Stoma M, Caban J. Market electrification for BEV and PHEV in relation to the level of vehicle autonomy. Energies. 2022;15:3120. https://doi.org/10.3390/en15093120

[6] Gogola M. Are the e-bikes more dangerous than traditional bicycles? XI International Science-Technical Conference Automotive Safety, Žastá, Slovakia. 2018:1-4. https://doi.org/10.1109/AUTOSAFE.2018.8373344

[7] Hieu LT, Lim OT. Effects of the structure and operating parameters on the performance of an electric scooter. Sustainability. 2023;15:8976. https://doi.org/10.3390/su15118976

[8] Larminie L, Lowry J, Electric vehicle technology explained: Second Ed. John Wiley & Sons Ltd 2012.

[9] Mendes M, Duarte G, Baptista P. Introducing specific power to bicycles and motorcycles: application to electric mobility. Transp Res Part C Emerg Technol. 2015;51:120-135. https://doi.org/10.1016/j.trc.2014.11.005

[10] Naresh K, Bharat Kumar P, Anjaneyulu K. Simulation of energy recycling technique for an electric scooter using MATLAB/SIMULINK environment. International Research Journal of Engineering and Technology. 2015;2(6):542-547. https://www.irjet.net/archives/V2/i6/IRJET-V2I687.pdf

[11] Prajwowski K, Golebiewski W, Lisowski M, Abramek KF, Galdynski D. Modeling of working machines synergy in the process of the hybrid electric vehicle acceleration. Energies. 2020;13(21):5818. https://doi.org/10.3390/en13215818
[12] Saxena S, Gopal A, Phadke A. Electrical consumption of two-, three- and four-wheel light-duty electric vehicles in India. Appl Energy. 2014;115:582-590. https://doi.org/10.1016/j.apenergy.2013.10.043
[13] Siemionek E. Energochłonność pojazdów z napędem elektrycznym. Wydawnictwo Politechniki Lubelskiej. Lublin 2021.
[14] Tseng CY, Lue YF, Lin YT, Siao JC, Tsai CH, Fu LM. Dynamic simulation model for hybrid electric scooters. IEEE International Symposium on Industrial Electronics. 2009:1464-1469. https://doi.org/10.1109/ISIE.2009.5222809
[15] Yuan X, He J, Li Y, Liu Y, Ma Y, Bao B et al. Data-driven evaluation of electric vehicle energy consumption for generalizing standard testing to real-world driving. Patterns. 2024; 5(4). https://doi.org/10.1016/j.patter.2025.101173
[16] Yuniarto MN, Wiratno SE, Nugraha YU, Sidharta I, Nasruddin A. Modeling, simulation and validation of an electric scooter energy consumption model: a case study of Indonesian electric scooter. IEEE Access. 2022;10:48510-48522. https://doi.org/10.1109/ACCESS.2022.3171860

Prof. Piotr Lijewski, DSc., DEng. – Faculty of Civil and Transport Engineering, Poznan University of Technology, Poland.
e-mail: *piotr.lijewski@put.poznan.pl*

Artur Brydziński, Eng. – Faculty of Civil and Transport Engineering, Poznan University of Technology, Poland.
e-mail: *artur.brydzinski@student.put.poznan.pl*

Prof. Paweł Fuć, DSc., DEng. – Faculty of Civil and Transport Engineering, Poznan University of Technology, Poland.
e-mail: *pawel.fuc@put.poznan.pl*

Marcin Zygmanowski, Eng. – Faculty of Civil and Transport Engineering, Poznan University of Technology, Poland.
e-mail: *marcin.zygmanowski@student.put.poznan.pl*

Article citation info:
Laskowski P, Wojs M, Wiśniowski P, Zimakowska-Laskowska M, Kozłowski E. Biogas-fuelled internal combustion engines for micro-scale energy generation: a review of technologies and configurations for systems below 50 kW. Combustion engines. 2026;206(3):34-43. https://doi.org/10.19206/CE-208913

Piotr LASKOWSKI
Marcin WOJS
Piotr WIŚNIOWSKI
Magdalena ZIMAKOWSKA-LASKOWSKA
Edward KOZŁOWSKI

Combustion Engines
Polish Scientific Society of Combustion Engines

Biogas-fuelled internal combustion engines for micro-scale energy generation: a review of technologies and configurations for systems below 50 kW

ARTICLE INFORMATION

Received: 2 June 2025
Revised: 31 July 2025
Accepted: 2 August 2025
Available online: 25 September 2025

The growing demand for sustainable and decentralised energy solutions drives the development of micro-scale biogas power generation systems using internal combustion engines (ICEs) as prime movers. This paper reviews the technological advances and structural configurations of ICEs designed to burn biogas in generator systems with power outputs of up to 50 kW. The study investigates the adaptation of spark-ignition and dual-fuel engines, optimisation of compression ratios, fuel delivery systems, and ignition strategies to increase efficiency and reliability. Furthermore, the impact of biogas composition on engine performance and emissions is investigated, addressing the challenges of changes in methane and pollutant content. The review provides information on recent innovations, including engine modifications to run lean and integration of advanced control systems to increase efficiency and durability. By synthesising current research and practical applications, this paper aims to guide the selection and development of optimised ICE solutions for distributed microgas power generation.

Key words: *biogas, micro-generation, internal combustion engines, dual-fuel*

This is an open access article, distributed under the CC BY license (http://creativecommons.org/licenses/by/4.0/)

1. Introduction

The growing power of decarbonisation, securing access to energy in rural areas, and strengthening the energy supply, through decentralised systems of renewable energy sources. One of the main leads is micro biogas installations (< 50 kW), used in cogeneration and island systems [7, 67].

Biogas, produced by anaerobic digestion of organic waste, produces net GHG emissions and waste from production and storage, which uses electricity [25, 57]. The drive of these installations consists of internal combustion engines (ICE) – scalable systems and economic units.

Operational challenges result from the heterogeneous composition of biogas, corresponding to CH_4 (40–70%), which is responsible for the calorific value, while CO_2, H_2S, and water vapour reduce the occurrence and acceleration of material degradation [12, 70, 71]. This requires, among others, CR modification, ignition calibration, modernisation of the intake/exhaust applications, and the use of pilot fuel dosing in DF engines [16].

With the advancement of gas cleaning and control technologies (e.g., ECU), it is possible to achieve unavailability levels of 35–46% and control above 80% [33, 42]. Lean-burn variants and H_2 enrichment further reduce NO_x, CO, and CH_4 emissions [51, 53].

Biogas-fuelled ICE systems are increasingly vulnerable to combustion and off-grid impacts, increasing their importance in low-emission and waste management strategies [35, 55].

The article presents an overview of biogas micro-installations' technology, properties, and operating parameters ≤ 50 kW. Component types (SI, DF), design adaptations, the impact of fuel composition on performance and emissions, and key challenges and research perspectives are analysed for the benefit of the engineering community and decision-makers in implementing biogas energy systems.

The scientific literature was searched in Scopus, Web of Science, ScienceDirect, and Google Scholar databases to conduct the study. Publications from 2010–2024, reviewed peer-reviewed articles, conference papers, and thematic reviews on biogas engines with a power of ≤ 50 kW were reported. Extreme emphasis on complexity in works on:

- adaptation of SI and DF to biogas
- the impact of biogas composition on operating and emission parameters
- micro-CHP efficiency systems
- micro-installation implementation studies.

There are over 120 literature items, resulting in the final version including over 100 publications that meet the criteria for additional and up-to-date information. Legal acts and technical standards (e.g., EU MCPD, Stage V, Tier 4) were also checked, as well as data from manufacturers of utility and prototype devices.

2. Characteristics of biogas and its impact on engine operation

2.1. Characteristics of engine fuels

Biogas is a renewable fuel of growing importance in the context of energy sources. Produced in the process of anaerobic fermentation of organic waste, it consists mainly of methane (CH_4) and supplied carbon (CO_2), usually automatically in 50–70% and 30–50% [46, 47, 72, 73]. The additive may contain hydrogen sulphide (H_2S), water vapour, nitrogen, oxygen, and trace amounts of silicon, e.g., siloxanes [18, 44]. The composition of biogas is essential for its calorific value and directly affects the emissions and durability of the propulsion system. To illustrate the electrical disconnect between biogas and other gaseous fuels, Table 1 provides the source calorific value of selected energy sources in small-scale engine installations.

Table 1. Comparison of the calorific value of selected gas fuels [2, 9, 22, 42]

Fuel	Main composition	Calorific value [MJ/m³]	Comments
Biogas (raw)	CH_4 (50–70%), CO_2	18–25	Variable value depending on composition
Biomethane	CH_4 > 96%	35–39	After purification, it is comparable to natural gas
Natural gas (CNG)	CH_4 ~95–98%	35–39	Stable properties, high-pressure
LPG (propane-butane)	C_3H_8/C_4H_{10} (mixture)	46–50	Liquefied, very high energy density
Hydrogen (H_2)	100% H_2	10–13	Low calorific value but high gravimetric energy density

As can be seen from the table, raw biogas has a higher calorific value than other natural gases, LPG, or purified biomethane, which directly impacts lower engine power, the need for additional use, or the use of dual fuel. Additionally, biogas composition indicates that the calorific value can be activated over time, making it difficult to operate the drive units stably without advanced control systems.

2.2. The influence of biogas composition on the engine operation

The calorific value of biogas, typically in the range of 18–25 MJ/m^3 (Table 1), depends on the leading share of methane, which determines the power contained in the fuel. The share of CH_4 promotes efficient and fuel-efficient combustion [31], while CO_2 acts as a dissolved agent, reducing combustion temperature, flame propagation velocity, and cylinder pressure [2, 43]. The results of the research by Kovacs et al. [45] show that higher CO_2 content in biogas leads to lower combustion temperature and longer ignition time, which can affect combustion knock and engine starting, but at the cost of reducing usable power

Table 2. The influence of selected biogas components on engine operation and emissions [10, 11, 16, 19, 22, 29, 30, 35, 41, 49, 58, 61]

Component	Impact on engine operation	Impact on emissions
CH_4 enrichment	Increased power, ignition triggering. Higher reliability and power	Loss of CO and HC
High CO_2 content	Lower combustion pressure and temperature. Lower power, larger ignition sizes	NO_x reduction, CO, and HC coefficient
Water enrichment	Improved failure stability, increased efficiency. Better performance, ignition result	Decrease in CO, HC, (sometimes NO_x increase)
H_2S	Corrosion, oil degradation	SO_2 emission
Siloxane	SiO_2 deposits, abrasive wear	No agreement
For water	Intake system erosion	No data
Lowering the intake temperature	Better fuel efficiency with available CH_4	Lower CO, more stable mileage
Injection optimisation	Reduced knock, more power	Lower NO_x, more stable combustion

H_2S and siloxanes are as follows: H_2S causes engine oil corrosion and degradation [11], and siloxanes lead to the formation of SiO_2 deposits on engine mechanical components [44]. Water vapour can be erosive to the intake system [34]. The detailed impact of CH_4 enrichment, CO_2 dilution, H_2S content, siloxanes, and water vapour on both combustion dynamics and emissions is summarised in Table 2.

Table 2 summarises the effects of key biogas components – such as methane, carbon dioxide, hydrogen sulphide, and siloxanes – on engine performance and exhaust emissions. These properties influence combustion quality, ignition behaviour, engine wear, and the emission profile of biogas-fuelled systems.

2.3. Impact on secondary emissions

Biogas as a fuel, discharged to NO_x emissions and used (PM), and its use in cogeneration systems allows for achieving thermal efficiency (Brake Thermal Efficiency, BTE – defined as (1) at the level of 17–30% [10]. However, the CO_2 content can increase CO and HC emissions [32, 66].

$$\mathrm{BTE} = \frac{\mathrm{P}\cdot 10^3}{\mathrm{m_f}\cdot \mathrm{LHV_f}\cdot 10^3} \tag{1}$$

where: P – brake output power [W], LHV_f – Fuel calorific value [MJ/kg], m_f – fuel mass flow (kg/s).

Adding H_2 improves combustion efficiency, ignition acceleration, and CO, HC, and NO_x emissions [16, 17, 22, 23]. However, too much H_2 can increase NO_x [41].

Table 3 shows the emission intensity of biogas compared to other fuels.

Table 3. Functional and emission intensity energy of biogas from other fuels [6, 16, 21, 21, 36, 43, 76]

Fuel	BTE [%]	NO_x	CO	slip CH_4	Comments
Biogas (raw)	17–22	↓ 30–90%	↑	1.5–3%	High CO with lean mixtures
Biomethane	22–28	~ natural gas	~ natural gas	<1%	Comparable to natural gas
Biogas + H_2	25–30	↑ (at >20% H_2)	↓	↓	NO_x boosted but improves performance and load
Diesel oil	27–33	Tall	Short	Lack	High NO_x and PM emissions
Liquefied petroleum gas	25–30	Moderate	Short	Lack	Lower emissions than diesel oil, higher than biomethane
Legend: ↓ – lower than diesel oil; ↑ – higher than reference; ~ – comparable value					

The emission value in Table 3 is qualitative and is marked with symbols: ↓ – use than the reference value (e.g., diesel oil), ↑ – higher, ~ – comparable. The data comes from many literary sources and is adapted. The individual numerical values are presented in Table 7.

Requirements (e.g., EU Stage V, MCPD) often do not consider the specification of units < 50 kW and fuel or variable composition. In practice, this means difficulties meeting the NO_x standard (e.g., < 100 mg/Nm^3 in MCPD)

and CH_4 emission limits, especially without using catalytic technologies or fuel refilling systems.

2.4. Biogas purification and standardisation

Efficient removal of H_2S (e.g., by adsorption on carbon monoxide or activated carbon), siloxanes (zeolites, phase-related), and moisture (condensation) is essential for engine protection [18, 68].

Dynamic gas composition [69] and biogas enrichment with hydrogen (up to 20%) support stable engine operation even with variable fuel composition [53]. Increasing attention should also be paid to optimising energy consumption in fermentation processes, including control algorithms and time series analysis [65], which can control the electricity of the entire biogas system.

Effective application methods and fuel quality control are essential to achieve long-term efficiency and performance fuelled by biogas. Raw biogas contains content, primarily hydrogen sulphide (H_2S), water vapour, and siloxanes, which occur due to engine operation, catalytic converters, and exhaust gas start-up systems.

2.5. Technical modifications and operating parameters

Effective use of biogas in combustion engines requires design adaptations and optimisation of operating parameters. Precise compression ratio application, high-energy ignition application, biogas, and pilot fuel dosage (in dual-fuel mode), and control of ignition occurrence and composition of the assembly [10]. Bieniek et al. [13] conducted an experimental adaptation of a high-load Diesel engine to biogas fuelling, determining efficiency and extreme CO and NO_x emissions reductions – the first with a pilot ignition switch.

Electrical time control, necessary for data from the drives and solutions such as ECU, ANN, or fuzzy logic, allows the unit operations to be adjusted to fluctuations in fuel composition and environmental conditions. A comprehensive overview of how selected technical interventions influence both operational and environmental performance is provided in Table 4.

Table 4. The influence of selected technical parameters on operating and emission parameters [2, 15, 20, 26, 37, 60, 69, 77]

Modification	Technical effect	Emission effect
CR optimisation (12–18)	Increased peak pressure and temperature, risk of knock	Decrease in CO/HC, possible increase in NO_x
High energy ignition	Stability of the debris	The fall of HC
Injection optimisation (DF)	Increase in power, decrease in knocking noise	NO_x reduction
Monitoring the composition of biogas	Real-time parameter adjustments	Stability, fuel residue

Table 4 provides a summary of how selected technical modifications, such as compression ratio adjustment, high-energy ignition systems, and biogas composition monitoring, affect engine performance and emissions. These interventions play a key role in maintaining combustion stability and minimising pollutants in variable-fuel micro-biogas engines.

3. Types and configurations that include micro-installations

3.1. Spark ignition (SI) engines

In biogas micro-installations (< 50 kW), the most commonly used are spark-ignition (SI) piston engines, dual-fuel systems of compression-ignition engines, and micro-gas turbines. The choice of technology depends on the expected efficiency, quality of available biogas, and availability.

SI engines are the most commonly used energy sources in micro biogas plants due to their effects and good performance when working with a fuel source. They operate on the principle of releasing a biogas solution from the air initiated by spark ignition.

Thermal efficiency is 22–28%, with modern designs using two-spark ignition and an output frequency prechamber [38, 64]. The disadvantage is their sensitivity to changes in biogas composition, including the first CH_4 content.

3.2. Dual-fuel compression ignition engines

In a dual-fuel compression ignition engine, diesel (pilot fuel) and biogas are used simultaneously. There is a higher thermal efficiency (25–32%) and the possibility of operating with biogas quality [6]. This system works well in rural and industrial environments where substrate availability may change.

The disadvantage is the highest NO_x emissions and its use for ignition and fuel proportioning control [28].

3.3. Micro gas turbines

Microturbines are compact, emitting, and quiet, making them ideal for municipal devices and installations with environmental requirements. They are characterised by 25–30% thermal efficiency and reveal NO_x [50].

Their main disadvantage is the high investment cost and limited availability of services, especially in developing countries.

The drive unit selection in biogas micro-installations should include operation, emissions, fuel quality, substrate, service, and integration possibilities.

Spark ignition (SI) engines and dual fuel (DF) systems are used due to their simplicity, availability, and opening up of the biogas packaging. However, low-emission and compact microturbines are characterised by high costs and limited availability.

The engine selection should be correlated with the system operation profile and its connection to cogeneration and energy storage.

4. Performance, emissions, and adaptation challenges of biogas-powered engines

Using biogas as a fuel in high-power combustion engines requires several construction units and supporting technologies. The results are side effects of calorific value, occurrence (H_2S, CO_2, siloxanes), and the presence of composition over time. Effective adaptation of the engine to start biogas allows its operation and emission, and extends the durability of the drive unit and the entire system.

Biogas is an alternative to diesel oil, LPG, and natural gas in micro-scale applications. Once appropriately adapted through dedicated engine configurations, it can offer func-

tional performance (expressed by brake thermal efficiency, BTE) and reduced emissions of pollutants such as NO_x, CO, CH_4, and PM.

Compared to traditional fuels, biogas-powered engines operate under different thermodynamic conditions due to their lower calorific value and the presence of non-combustible CO_2. These factors generally result in lower engine power and BTE values. However, the addition of hydrogen, syngas, or water injection has increased BTE by 2–4%, depending on the combustion strategy and engine type [22, 23, 59].

Regarding biogas emissions, the following are decreasing: lower NO_x and PM levels compared to diesel oil, but CO and CH_4 emissions, especially in spark-ignition engines (Table 5).

Table 5. Thermal efficiency and emissions of selected service functions

Configurable	BTE [%]	NO_x [g/kWh]	CO_2 [g/kWh]	CH_4 [g/kWh]	Comments
Diesel oil (on)	30–40	6–10	0.5–1.0	< 0.1	High efficiency, high NO_x emissions
Dual fuel (biogas)	25–32	3–6	2–5	1.5–3.5	High DF substitution, but CH_4 emissions
~~SI~~ on biogas	22–28	1–3	3–6	4–10	Low NO_x, high methane loss
SI + H_2 (20%)	24–30	2–4	1-3	2-6	Higher efficiency requires ignition control
Liquefied petroleum gas	28–35	2–5	0.3–0.6	<0.1	Low emissions, good combustion parameters
Natural gas	32–38	2–4	0.5–1.0	0.5–2.0	Better emission control than biogas

Emission values (in g/kWh) refer to steady-state engine operation, as reported in the cited literature. Specific test conditions (engine load, speed, and fuel quality) may vary between sources.

While biogas engines offer environmental benefits in terms of lower particulate emissions and potential CO_2 neutrality, their performance must still comply with national and international emission standards, which are often designed for larger or continuously operating systems.

In the micro-generation (< 50 kW) context, meeting the requirements of EU Stage V, MCPD, or EPA Tier 4 regulations is particularly challenging. These standards rarely account for small-scale, intermittently operating units with variable fuel quality. As a result, biogas micro-installations often face difficulties in meeting stringent limits on CH_4 and NO_x emissions. Table 5 summarises reported emission levels for biogas-fuelled engines and highlights the variability between system configurations.

Table 6. Example emission limits for engines <50 kW (EU/MCPD) Sources: EU Regulation 2016/1628; EU Directive 2015/2193 (MCPD); US Environmental Protection Agency (EPA) Tier 4; WHO Guidelines (2021)

Standard	Engine power	NO_x [mg/Nm³]	CO_2 [mg/Nm³]	CH_4 [mg/Nm³]	Comments
EU Stage V (NRMM)	19–37 kW	400	500	–	No CH_4 limit applies to mobile app
EU MCPD	1–50 MW (for gas)	100	100	20–50	Applies to stationary, biogas is subject to exceptions
Level 4 Final (USA)	< 56 kW	400–600	500–600	–	Brake adjustment CH_4; only NO_x and CO
UNDP/WHO (recommendations)	–	< 200	< 500	< 30	For off-grid installations in developing countries

As Table 6 shows, setting emission limits for biogas-fired micro-installations can be problematic, especially for methane (CH_4), which is not always regulated but has a high greenhouse gas potential (GWP = 28–34). Additional problems arise with intermittent operation and variable biogas composition, which affects combustion and uncontrolled emissions.

In the application, compensatory measures are used:

- local emission compensation through cogeneration
- units with cleaning agents (oxidation catalysts, SCR)
- adaptive control systems depending on the biogas composition.

The emission-related limitations in micro-biogas systems highlight the need for targeted technological strategies and regulatory adjustments. In most cases, achieving compliance requires a combination of combustion control techniques, fuel quality optimisation, and selective aftertreatment methods – all of which increase system complexity and cost.

Furthermore, current emission regulations often lack dedicated testing procedures for systems operating under variable loads or hybrid fuel conditions (e.g., dual-fuel with pilot ignition). This creates uncertainty in design and certification, making it difficult for small-scale producers to introduce innovative systems into the market without costly homologation procedures.

To ensure the successful deployment of biogas micro-installations, especially in off-grid and rural areas, it is necessary to promote standardised protocols for low-power systems and offer regulatory flexibility for modular and hybridised units. Support mechanisms, both technical and legal, should reflect the unique operating conditions and environmental benefits of decentralised biogas utilisation.

Numerous technological adaptations have been proposed and tested in micro-biogas systems in response to these challenges. These include advanced ignition control (e.g., high-energy ignition systems, variable ignition timing), hydrogen or water enrichment, and real-time gas composition monitoring. Some setups employ dual-fuel strategies with diesel pilot injection to improve cold-start performance and combustion stability.

Table 7 presents selected examples of such modifications and their effects on thermal efficiency, pollutant emissions, and engine stability. Although most of these solutions improve operational parameters, they also increase system complexity and cost, which must be considered in small-scale applications.

Table 7. Overview of technical biogas adaptations [1, 15, 27, 37, 48, 54, 60, 62, 77]

Adaptation area	Solution description	Technical effects
Compression ratio	CR = 12–13 (SI), CR = 16–18 (DF)	Enhanced regulation, CO/HC reduction, NO_x emission increase
Ignition systems	Twin spark plug, digital, high-energy ignition	Improved ignition performance
Injection system (DF)	Optimisation of injection angle and pressure (250 bar, 26–30° BTDC)	Greater efficiency and cleaner combustion
Biogas purification	Membranes (MMMs), ILs, biomethanation with H_2	Higher purity CH_4, elimination of corrosion
Cogeneration and integration	Micro-CHP, PV hybrid, H_2 production	Overall efficiency > 75%; large-scale system

Design and electrical adaptations are key to the efficient use of biogas in microgeneration. Limited importance: appropriate compression ratio, injection and ignition optimisation, and application of biogas regulation. Integration with cogeneration systems and production of AC for waste, decarbonised, and flexible electricity. An overview of the procedure is in Table 7.

5. Supply and emissions of residues

The use of biogas in micro-scale combustion engines is an alternative to fossil fuels due to its renewable nature, the possibility of starting production, and its relatively low carbon footprint. However, the effectiveness of such an operation is strongly dependent on several factors, including the quality of the biogas, the type of leakage from the engines, and fuel economy and emission control systems. The high content of methane (CH_4) affects the engine's efficiency. It is then supplied from coal (CO_2) as a component to reduce the pressure and flame propagation rate, affecting efficiency [43, 72]. Typical thermal functionality (BTE) in such systems ranges from 17% to 24% [8, 14]. However, in the case of dual fuel, a BTE of 25–28% is possible with diesel oil substitution of up to 90% [6]. Additional biogas supplementation with hydrogen enables further efficiency increases to about 30% while reducing fossil fuel consumption by more than 70% [16, 40, 41]. To fully exploit the potential of biogas as a low-emission fuel, it is necessary to implement alternative adaptive technologies such as control systems, advanced technologies, and advanced gas composition strategies.

Performance values and emissions reported in the literature (Table 5) may vary depending on fuel quality, system type, and operational failures.

All emission values in units of [g/kWh], as a typical range for everyday use. In case of divergence of literature data, average or representative values are used. Available tables (e.g., Table 3) may include qualitative notations (↑/↓) to illustrate trends in terms of the reference design (e.g. Diesel oil).

The presented list allows for determining the available practical applications, thermal, emitted, and fuel type, which is a key element in selecting the optimal configuration of a biogas micro-installation, both under the condition of use and when used.

6. Examples of applications in studies

6.1. Introduction

Biogas micro-installations are important as decentralised energy sources on farms and municipal installations. They come in many forms – from simplified power reactors of spark-ignition engines to connected CHP systems cooperating with PV and energy storage.

Another interesting development direction is the use of biogas in hybrid drive systems. Kovacs et al. [45] (2023) discussed the reasons for the use of a combustion engine powered by biogas in a series set: the power supply was started, and the operational appearance occurred, which caused it to be connected to microgrids and off-grid applications.

The study identified occurrence, key importance, and implementation barriers, including substrate, power sources from other energy sources, and operational and economic system power supply.

Biogas micro-installations are becoming increasingly common as independent energy sources in farms, homes, and municipal installations. Their operation depends on the substrate's quality, the system's scale, the connection with other energy sources, and storage possibilities. Selected practical implementations from various countries and contexts are presented in Table 9, illustrating the diversity of scale, substrates, and integration strategies.

Table 9. Examples of micro-scale biogas installations in various utility contexts [24, 27, 52, 75]

Location/Context	System Type	Effects/Observations
Slovenia – life	CHP, ICE	Profitability depends on scale and substrate additives
Poland – farm	8.1 kW combustion engine	Self-sufficiency, surplus commercial energy to the grid
Vietnam – home life	Bioreactor < 2 m³	Stable, gas quality, spare parts demand
India – Local Installation	DF + substrate zoo	Good performance, problems with substrate quality, and service
Argentina – Micro-CHP with PV	CHP + PV + energy	Highly available energy, low net CO_2 emissions

Based on the analysed case studies presented in Table 9, several patterns can be identified:

First, both the scale and substrate quality have a direct impact on the profitability of micro-scale biogas systems. Installations using high-quality feedstocks in appropriately scaled configurations demonstrate better energy and economic performance.

Second, while integration with PV panels or storage units may increase system autonomy, it also introduces complexity and a higher risk of operational failures, particularly in low-resource settings.

Moreover, simple systems, such as domestic bioreactors, are commonly employed where electricity demand is modest and grid access is limited.

Finally, key operational challenges such as automation, component wear, and maintenance remain manageable, provided that appropriate control mechanisms and user training are in place.

6.2. Commercial unit and research prototypes

To illustrate the differences between commercially implemented units and research-prototype solutions, selected examples of biogas micro-installations are presented in characteristic tables. Available systems on the market and experimental systems are studied through research studies—comparison of additional types of systems, their costs, and technological status.

Table 10. Examples of commercial and experimental micro-scale biogas systems [3, 27, 52]

Producer/Design	Type/Scale	Status	Comments
Sistema.bio (Mexico)	Bioreactor < 10 m³	Commercial	Solution for the household
HomepageBiogas (Israel)	Installation 1–2 m³	Commercial	Easy to use, low heat output
ECN (Netherlands)	Cogeneration 1–10 kW	Prototype	Integrated with PV and battery
IIT Delhi (India)	DF, 5–7 kW	Prototype	Configured on an animal substrate
PV-BIOGEN (Argentina)	Cogeneration + PV + H_2	Prototype	Hybrid, low net emissions

Table 10 presents an overview of selected micro-scale biogas systems, classifying them as commercial or prototype. Commercial systems (e.g., Sistema.bio, HomeBiogas) are characterised by simplicity of operation and investment costs but generally provide limited power and functionality. In contrast, prototype solutions often integrate advanced technologies (CHP, PV, H_2), increasing their efficiency and reliability but also increasing implementation costs and complexity.

Table 11 summarises the technical and economic parameters for three typical configurations of biogas micro-installations. Home systems have the shortest payback time but no electricity supply. CHP units achieve higher efficiency but require biogas and automation – hybrid systems (CHP+PV) discharge energy at the cost of capital and output costs.

These data indicate that electrical decisions in biogas micro-installations require technical parameters, local economic conditions, access to batteries, and the potential for connection to other energy sources. The future of this service lies in solutions that can be applied to specific end-user needs.

The presented data shows that the system selection should be available each time for applications, energy purposes, resources, and institutional support. There is no universal solution – micro-installation success depends on considering the technological and economic configuration.

Research prototypes with higher scope and accessibility, but often at the cost of investment and technical expenses. Commercial solutions with the frequency of risk, but at the cost of efficiency and scalability.

Table 11. Efficiency and profitability of selected micro-installations

System Type	BTE [%]	Investment cost [EUR/kW]	Insurance period [years]	Comments
Homemade bioreactor	–	300–800	1.5–3	No generation
Cogeneration 3–10 kW	25–32	1200–2000	4–7	Automation requirement and burden
CHP+PV hybrid	28–35	1800–3000	6–10	High remaining independence

Analysis of case studies from different regions of the world confirms that biogas micro-installations are a real, technological solution and a solution for decentralised renewable energy. Their key advantages:

- providing power in rural and off-grid conditions
- possibility of use with renewable energy sources (e.g., PV, storage)
- waste utilisation and exhaust gas disposal
- competitive investment profitability, especially in public services.

However, the success of these systems depends on the conscious operation of technology, scale, and parameters defined by the user. Key measures determining and maintaining installations in:

- appropriate selection of technology (SI, DF engines, microturbines)
- optimisation of the substrate and use of the user profile
- possibility of integration with the power grid or energy storage facilities
- access to technical and financial support (e.g., subsidies, green savings).

Conclusions from the general analysis are as follows: biogas micro-installations – general in the case of CHP and DF applications – are technologically developed, are a solution, and are economically feasible. Alternative solution – there is no one universal model of success.

7. Prospects and directions of development

Micro-scale biogas technologies are the result of experiments to be applied. Their nearest future is:

- Standardisation and simplification of installation – through prefabricated CHP modules, plug-and-play turnkey systems, and gas-integrated units. This solution creates cost risk and eases implementation, especially in rural regions [4, 5, 39].
- Integration with RES microgrids – biogas acts as a dispatchable source, unstable PV-wind + storage systems. The effects of such applications have been confirmed, among others, in Bolivia, India, and Cameroon [74, 78].
- AI and predictive systems – machine learning (ANN, LSTM, fuzzy logic) allow for predicting biogas quality, automating combustion, and reducing emissions [56, 69].
- Link to the circular economy – digestate as fertiliser, heat recovery for heating, use of residues as algal substrates, and biogas as a precursor for H_2 production [27, 63].

Micro-scale biogas installations have the potential to become decentralised energy links. Their development depends on eliminating technological and financial barriers, providing support, and using automation and prediction tools. This is not the future – it is already a built foundation for the energy of the 21st century.

In the years, however, the synergy of biogas use with hydrogen technology, photovoltaics, and artificial intelligence may cause the risk of a classic breakthrough. Such hybrid, intelligent micro-installations will become electricity and an active, adaptive participant in micro-networks – algorithmically controlled, functional in terms of losses, and related to variable operating conditions.

8. Conclusions

Biogas, a renewable and locally available energy source, is a real alternative to fossil fuels in micro-energy installations using devices with a capacity of up to 50 kW. The conducted review of literature and studies allows for the following conclusions:

1. Spark ignition (SI) engines and dual-fuel systems are most commonly used in biogas applications. Controlled modifications (compression ratio, ignition system, dosing) can achieve 22–30% thermal efficiencies with limited NO_x and CO emissions.
2. The composition of biogas, which contains methane and CO_2, significantly impacts the combustion process, emission residues, and engine operation residues: poor control and ignition control.
3. Pollutants such as H_2S and siloxanes are used in the engine; therefore, effective methods are used, e.g., adsorption on activated carbon or membrane techniques.
4. Modern control strategies, available on AI and adaptive (ANN, fuzzy logic), enable adjustment of engine operating parameters to the variable biogas composition required and reduce CH_4 and CO emissions.
5. Research shows that micro biogas installations can be available and economically viable, especially in CHP systems and when integrated with energy storage systems and fertiliser management, in the open with other biofuels, labels such as biodiesel, bioethanol or pellets, biogas distinguished by electrical waste production from waste, characteristic for applications (heat, electricity, motor fuel) and net carbon footprint. Its calorific value is lower, and in terms of environmental and functional balance, biogas presents itself as one of the most universal and sustainable energy sources.
6. The challenge includes high operating costs, the need for durability, and the lack of fuel standardisation. Responsibilities may include developing materials resistant to, taking on the role of prosumers, and complying with energy policy.

From an application perspective, the most likely applications for the development directions include:

– the miniaturisation of the CHP switch, biogas switch,
– enrichment of biogas with water.

Moreover, integrating large-scale generators with broadband-connected microgrids and the Internet of Things (IoT) supports energy optimisation.

Nomenclature

ANN	artificial neural network
BTE	brake thermal efficiency
CH_4	methane
CHP	combined heat and power
CI	compression ignition
CNG	compressed natural gas
CO	carbon monoxide
CO_2	carbon dioxide
CR	compression ratio
DF	dual fuel
ECU	electronic control unit
GHG	greenhouse gases
H_2	hydrogen
H_2S	hydrogen sulphide
ICE	internal combustion engine
IL	ionic liquid
LPG	liquefied petroleum gas
LSTM	long short-term memory
MCPD	Medium Combustion Plant Directive
MMMs	mixed matrix membranes
NO_x	nitrogen oxides
PCA	principal component analysis
PM	particulate matter
RES	renewable energy sources
SCR	selective catalytic reduction
SI	spark ignition

Bibliography

[1] Ahmad A, Singh A. Predictive modeling and optimization of engine characteristics with biogas–biodiesel-powered dual-fuel mode: a neural network-coupled box–Behnken design. Arab J Sci Eng. 2024;49(2):2661-2680. https://doi.org/10.1007/s13369-023-08375-7

[2] Ahmed SA, Zhou S, Zhu Y, Tsegay AS, Feng Y, Ahmad N et al. Effects of pig manure and corn straw generated biogas and methane enriched biogas on performance and emission characteristics of dual fuel diesel engines. Energies. 2020; 13(4):889. https://doi.org/10.3390/en13040889

[3] Akkouche N, Loubar K, Nepveu F, Kadi MEA, Tazerout M. Micro-combined heat and power using dual fuel engine and biogas from discontinuous anaerobic digestion. Energ Convers Manage. 2020;205:112407. https://doi.org/10.1016/j.enconman.2019.112407

[4] Ali S, Yan Q, Irfan M, Chen Z. Evaluating barriers on biogas technology adoption in China: the moderating role of awareness and technology understanding. Front Environ Sci. 2022;10:887084. https://doi.org/10.3389/fenvs.2022.887084

[5] Ali S, Yan Q, Razzaq A, Khan I, Irfan M. Modeling factors of biogas technology adoption: a roadmap towards environmental sustainability and green revolution. Environ Sci Pollut Res. 2022;30(5):11838-11860. https://doi.org/10.1007/s11356-022-22894-0

[6] Alrbai M, Ahmad AD, Al-Dahidi S, Abubaker AM, Al-Ghussain L, Alahmer A et al. Performance and sensitivity analysis of raw biogas combustion under homogenous charge compression ignition conditions. Energy. 2023;283: 128486. https://doi.org/10.1016/j.energy.2023.128486
[7] Alstone P, Gershenson D, Kammen DM. Decentralized energy systems for clean electricity access. Nature Clim Change. 2015;5(4):305-314. https://doi.org/10.1038/nclimate2512
[8] Ambarita H. Performance and emission characteristics of a small diesel engine run in dual-fuel (diesel-biogas) mode. Case Studies in Thermal Engineering. 2017;10:179-191. https://doi.org/10.1016/j.csite.2017.06.003
[9] Angelidaki I, Treu L, Tsapekos P, Luo G, Campanaro S, Wenzel H et al. Biogas upgrading and utilization: current status and perspectives. Biotechnol Adv. 2018;36(2):452-466. https://doi.org/10.1016/j.biotechadv.2018.01.011
[10] Barik D, Murugan S. Investigation on combustion performance and emission characteristics of a DI (direct injection) diesel engine fueled with biogas–diesel in dual fuel mode. Energy. 2014;72:760-771. https://doi.org/10.1016/j.energy.2014.05.106
[11] Bertinatto R, Friedrich L, Bariccatti RA, Souza SNMD, Gurgacz F, Pazuch FA. Analysis of lubricant oil contamination and degradation and wear of a biogas-fed Otto cycle engine. Acta Sci Technol. 2017;39(4):409. https://doi.org/10.4025/actascitechnol.v39i4.29458
[12] Bezerra FEC. Biogas as an energy source for internal combustion engines: a review. Holos. 2020;7:1-14. https://doi.org/10.15628/holos.2020.10129
[13] Bieniek A, Mamala J, Graba M, Prażnowski K, Śmieja M, Wereszczyński D. Application of biogas to supply the high compression ratio engine. Combustion Engines. 2019; 179(4):40-46. https://doi.org/10.19206/CE-2019-406
[14] Bora BJ, Saha UK. Optimisation of injection timing and compression ratio of a raw biogas powered dual fuel diesel engine. Appl Therm Eng. 2016;92:111-121. https://doi.org/10.1016/j.applthermaleng.2015.08.111
[15] Bora BJ, Saha UK, Chatterjee S, Veer V. Effect of compression ratio on performance, combustion and emission characteristics of a dual fuel diesel engine run on raw biogas. Energ Convers Manage. 2014;87:1000-1009. https://doi.org/10.1016/j.enconman.2014.07.080
[16] Bouguessa R, Tarabet L, Loubar K, Belmrabet T, Tazerout M. Experimental investigation on biogas enrichment with hydrogen for improving the combustion in diesel engine operating under dual fuel mode. Int J Hydrogen Energ. 2020; 45(15):9052-9063. https://doi.org/10.1016/j.ijhydene.2020.01.003
[17] Boussetla S, Mameri A, Hadef A. NO emission from non-premixed MILD combustion of biogas-syngas mixtures in opposed jet configuration. Int J Hydrogen Energ. 2021; 46(75):37641-37655. https://doi.org/10.1016/j.ijhydene.2021.01.074
[18] Bragança I, Sánchez-Soberón F, Pantuzza GF, Alves A, Ratola N. Impurities in biogas: analytical strategies, occurrence, effects and removal technologies. Biomass Bioenerg. 2020;143:105878. https://doi.org/10.1016/j.biombioe.2020.105878
[19] Bui VG, Bui TMT, Tran VN, Huang Z, Hoang AT, Tarelko W et al. Flexible syngas-biogas-hydrogen fueling spark-ignition engine behaviors with optimized fuel compositions and control parameters. Int J Hydrogen Energ. 2023;48(18): 6722-6737. https://doi.org/10.1016/j.ijhydene.2022.09.133
[20] Bui VG, Tu Bui TM, Ong HC, Nižetić S, Bui VH, Xuan Nguyen TT et al. Optimizing operation parameters of a spark-ignition engine fueled with biogas-hydrogen blend integrated into biomass-solar hybrid renewable energy system. Energy. 2022;252:124052. https://doi.org/10.1016/j.energy.2022.124052
[21] Buivydas E, Navickas K, Venslauskas K. A life cycle assessment of methane slip in biogas upgrading based on permeable membrane technology with variable methane concentration in raw biogas. Sustainability. 2024;16(8):3323. https://doi.org/10.3390/su16083323
[22] Bundele H, Kurien C, Varma PS, Mittal M. Experimental and computational study on the enhancement of engine characteristics by hydrogen enrichment in a biogas fuelled spark ignition engine. Int J Hydrogen Energ. 2022;47(71): 30671-30686. https://doi.org/10.1016/j.ijhydene.2022.07.029
[23] Bundele H, Varma PS, Kurien C, Mittal M. Enhancement of low operating load limit and engine characteristics by hydrogen addition in a biogas-fueled spark-ignition engine. J Eng Gas Turb Power. 2023;145(2):021006. https://doi.org/10.1115/1.4056101
[24] Czekała W, Gawrych K, Smurzyńska A, Mazurkiewicz J, Pawlisiak A, Chełkowski D et al. The possibility of functioning micro-scale biogas plant in selected farm. Journal of Water and Land Development. 2017;35(1):19-25. https://doi.org/10.1515/jwld-2017-0064
[25] Czubaszek R, Wysocka-Czubaszek A, Banaszuk P. Importance of feedstock in a small-scale agricultural biogas plant. Energies. 2022;15(20):7749. https://doi.org/10.3390/en15207749
[26] Das AK, Padhi MR, Behera DD, Das SS. Evaluation of a diesel engine performance and emission using biogas in dual fuel mode. Mech Eng for Soc and Ind. 2024;4(2):167-176. https://doi.org/10.31603/mesi.11407
[27] Del Pópolo Grzona MV, Izurieta EM, Adrover ME, Borio DO, López E, Pedernera MN. Design studies of a pure hydrogen production plant from biogas. Int J Hydrogen Energ. 2024;52:1-10. https://doi.org/10.1016/j.ijhydene.2023.07.202
[28] Dev S, Stevenson D, Yousefi A, Guo H, Butler J. An experimental study on a dual-fuel generator fueled with diesel and simulated biogas. ASME 2021 Internal Combustion Engine Division Fall Technical Conference. American Society of Mechanical Engineers 2021. V001T04A004 https://doi.org/10.1115/ICEF2021-67429
[29] Feroskhan M, Ismail S. A review on the purification and use of biogas in compression ignition engines. Int J Automot Mech Eng. 2022;14(3):4383-4400. https://doi.org/10.15282/ijame.14.3.2017.1.0348
[30] Feroskhan M, Ismail S, Natarajan G, Manavalla S, Khan TMY, Khadar SDA et al. A comprehensive study of the effects of various operating parameters on a biogas-diesel dual fuel engine. Sustainability. 2023;15(2):1232. https://doi.org/10.3390/su15021232
[31] Feroskhan M, Ismail S, Panchal SH. Study of methane enrichment in a biogas fuelled HCCI engine. Int J Hydrogen Energ. 2022;47(5):3504-3514. https://doi.org/10.1016/j.ijhydene.2021.02.216
[32] Feroskhan M, Thangavel V, Subramanian B, Sankaralingam RK, Ismail S, Chaudhary A. Effects of operating parameters on the performance, emission and combustion indices of a biogas fuelled HCCI engine. Fuel. 2021;298:120799. https://doi.org/10.1016/j.fuel.2021.120799
[33] Gholamian E, Mehr AS, Yari M, Carton JG. Dynamic simulation and techno-economic assessment of hydrogen utilization in dual fuel (hydrogen/biogas) micro gas turbine systems for a wastewater treatment plant. Process Saf Environ. 2023;169:220-237. https://doi.org/10.1016/j.psep.2022.10.045

[34] Gupta P, Kurien C, Mittal M. Biogas (a promising bioenergy source): a critical review on the potential of biogas as a sustainable energy source for gaseous fuelled spark ignition engines. Int J Hydrogen Energ. 2023;48(21):7747-7769. https://doi.org/10.1016/j.ijhydene.2022.11.195

[35] Ha Y-H, Kumar SS. Investigating decentralized renewable energy systems under different governance approaches in Nepal and Indonesia: how does governance fail? Energy Research & Social Science. 2021;80:102214. https://doi.org/10.1016/j.erss.2021.102214

[36] Hoda A, Rahman TMR, Asrar W, Khan SA. A comparative study of natural gas and biogas combustion in a swirling flow gas turbine combustor. Combust Sci Technol. 2022; 194(13):2613-2640. https://doi.org/10.1080/00102202.2021.1882441

[37] Hotta SK, Sahoo N, Mohanty K, Kulkarni V. Ignition timing and compression ratio as effective means for the improvement in the operating characteristics of a biogas fueled spark ignition engine. Renew Energ. 2020;150:854-867. https://doi.org/10.1016/j.renene.2019.12.145

[38] Jatana GS, Himabindu M, Thakur HS, Ravikrishna RV. Strategies for high efficiency and stability in biogas-fuelled small engines. Exp Therm Fluid Sci. 2014;54:189-195. https://doi.org/10.1016/j.expthermflusci.2013.12.008

[39] Kapoor R, Ghosh P, Kumar M, Vijay VK. Evaluation of biogas upgrading technologies and future perspectives: a review. Environ Sci Pollut Res. 2019;26(12):11631-11661. https://doi.org/10.1007/s11356-019-04767-1

[40] Khan O, Alsaduni I, Equbal A, Parvez M, Yadav AK. Performance and emission analysis of biodiesel blends enriched with biohydrogen and biogas in internal combustion engines. Process Saf Environ. 2024;183:1013-1037. https://doi.org/10.1016/j.psep.2024.01.049

[41] Khatri N, Khatri KK. Hydrogen enrichment on diesel engine with biogas in dual fuel mode. Int J Hydrogen Energ. 2020; 45(11):7128-7140. https://doi.org/10.1016/j.ijhydene.2019.12.167

[42] Kim S, Sung T, Kim K. Thermodynamic performance analysis of a biogas-fuelled micro-gas turbine with a bottoming organic rankine cycle for sewage sludge and food waste treatment plants. Energies. 2017;10(3):275. https://doi.org/10.3390/en10030275

[43] Kim Y, Kawahara N, Tsuboi K, Tomita E. Combustion characteristics and NOx emissions of biogas fuels with various CO_2 contents in a micro co-generation spark-ignition engine. Appl Energ. 2016;182:539-547. https://doi.org/10.1016/j.apenergy.2016.08.152

[44] Konkol I, Cebula J, Bohdziewicz J, Piotrowski K, Sakiewicz P, Piechaczek-Wereszczyńska M et al. Mineral deposit formation in gas engines during combustion of biogas from landfills and municipal WWTP. Ecol Chem Eng S. 2020; 27(3):347-356. https://doi.org/10.2478/eces-2020-0022

[45] Kovacs VB, Torok A, Bereczky A, Szwaja S. Biogas utilization in an internal combustion engine working in a serial hybrid propulsion system. Combustion Engines. 2012;148(1): 17-24. https://doi.org/10.19206/CE-117047

[46] Kriaučiūnas D, Pukalskas S, Rimkus A, Barta D. Analysis of the influence of CO_2 concentration on a spark ignition engine fueled with biogas. Appl Sci. 2021;11(14):6379. https://doi.org/10.3390/app11146379

[47] Kriaučiūnas D, Žvirblis T, Kilikevičienė K, Kilikevičius A, Matijošius J, Rimkus A et al. Impact of simulated biogas compositions (CH_4 and CO_2) on vibration, sound pressure and performance of a spark ignition engine. Energies. 2021; 14(21):7037. https://doi.org/10.3390/en14217037

[48] Legrottaglie F, Mattarelli E, Rinaldini CA, Scrignoli F. Application to micro-cogeneration of an innovative dual fuel compression ignition engine running on biogas. International Journal of Thermofluids. 2021;10:100093. https://doi.org/10.1016/j.ijft.2021.100093

[49] Leonov E, Trubaev P. The effect of biogas composition on the characteristics of the combustion process. DJES. 2022;1-9. https://doi.org/10.24237/djes.2022.15201

[50] Liu A, Fan R, Liu Q, Xi L, Zeng W. Numerical and experimental study on combustion characteristics of micro-gas turbine biogas combustor. Energies. 2022;15(21):8302. https://doi.org/10.3390/en15218302

[51] Mahmoodi R, Yari M, Ghafouri J, Poorghasemi K. Effect of reformed biogas as a low reactivity fuel on performance and emissions of a RCCI engine with reformed biogas/diesel dual-fuel combustion. Int J Hydrogen Energ. 2021;46(30): 16494-16512. https://doi.org/10.1016/j.ijhydene.2020.09.183

[52] Mandal A, Cho H, Chauhan BS. ANN Prediction of performance and emissions of CI engine using biogas flow variation. Energies. 2021;14(10):2910. https://doi.org/10.3390/en14102910

[53] Mariani A, Minale M, Unich A. Use of biogas containing CH_4, H_2 and CO_2 in controlled auto-ignition engines to reduce NO_x emissions. Fuel. 2021;301:120925. https://doi.org/10.1016/j.fuel.2021.120925

[54] Moya C, Santiago R, Hospital-Benito D, Lemus J, Palomar J. Design of biogas upgrading processes based on ionic liquids. Chem Eng J. 2022;428:132103. https://doi.org/10.1016/j.cej.2021.132103

[55] Mperejekumana P, Shen L, Zhong S, Gaballah MS, Muhirwa F. Exploring the potential of decentralized renewable energy conversion systems on water, energy, and food security in Africa. Energ Convers Manage. 2024;315:118757. https://doi.org/10.1016/j.enconman.2024.118757

[56] Mukasine A, Sibomana L, Jayavel K, Nkurikiyeyezu K, Hitimana E. Maximizing biogas yield using an optimized stacking ensemble machine learning approach. Energies. 2024;17(2):364. https://doi.org/10.3390/en17020364

[57] Nindhia TGT, McDonald M, Styles D. Greenhouse gas mitigation and rural electricity generation by a novel two-stroke biogas engine. J Clean Prod. 2021;280:124473. https://doi.org/10.1016/j.jclepro.2020.124473

[58] Nyamukamba P, Mukumba P, Chikukwa ES, Makaka G. Biogas upgrading approaches with special focus on siloxane removal – a review. Energies. 2020;13(22):6088. https://doi.org/10.3390/en13226088

[59] Porpatham E, Ramesh A, Nagalingam B. Effect of hydrogen addition on the performance of a biogas fuelled spark ignition engine. Int J Hydrogen Energ. 2007;32(12):2057-2065. https://doi.org/10.1016/j.ijhydene.2006.09.001

[60] Porpatham E, Ramesh A, Nagalingam B. Effect of compression ratio on the performance and combustion of a biogas fuelled spark ignition engine. Fuel. 2012;95:247-256. https://doi.org/10.1016/j.fuel.2011.10.059

[61] Rahman KA, Ramesh A. Studies on the effects of methane fraction and injection strategies in a biogas diesel common rail dual fuel engine. Fuel. 2019;236:147-165. https://doi.org/10.1016/j.fuel.2018.08.091

[62] Rodero MDR, Muñoz R, González-Sánchez A, Ruiz HA, Quijano G. Membrane materials for biogas purification and upgrading: fundamentals, recent advances and challenges. Journal of Environmental Chemical Engineering. 2024; 12(5):114106. https://doi.org/10.1016/j.jece.2024.114106

[63] Romagnoli F, Spaccini F, Boggia A, Paoli R, Feofilovs M, Ieviņa B et al. Microalgae cultivation in a biogas plant: environmental and economic assessment through a life cycle approach. Biomass a Bioenerg. 2024;182:107116. https://doi.org/10.1016/j.biombioe.2024.107116

[64] Roubaud A, Favrat D. Improving performances of a lean burn cogeneration biogas engine equipped with combustion prechambers. Fuel. 2005;84(16):2001-2007. https://doi.org/10.1016/j.fuel.2004.02.023
[65] Rybak G, Kozłowski E, Król K, Rymarczyk T, Sulimierska A, Dmowski A et al. Algorithms for optimizing energy consumption for fermentation processes in biogas production. Energies. 2023;16(24):7972. https://doi.org/10.3390/en16247972
[66] Salhi M, Berrich E, Romdhane M, Aloui F. Experimental investigation of performance and exhaust emissions of pyrolytic olive pomaces biofuels blends without and with additives fueled internal combustion engine. Handbook of Thermal Management Systems. Elsevier 2023:785-800. https://doi.org/10.1016/B978-0-443-19017-9.00031-3
[67] Schnidrig J, Chuat A, Terrier C, Maréchal F, Margni M. Power to the people: on the role of districts in decentralized energy systems. Energies. 2024;17(7):1718. https://doi.org/10.3390/en17071718
[68] Secco C, Fuziki MEK, Tusset AM, Lenzi GG. Reactive processes for H_2S removal. Energies. 2023;16(4):1759. https://doi.org/10.3390/en16041759
[69] Soehartanto T, Fitriyanah DN, Aisyah PY. Design of ECU (electronic control unit) as biogas pressure control to micro genset. IJOE. 2021;6(3):73. https://doi.org/10.12962/j23378557.v6i3.a7264
[70] Valipour Berenjestanaki A, Kawahara N, Tsuboi K, Tomita E. Performance, emissions and end-gas autoignition characteristics of PREMIER combustion in a pilot fuel-ignited dual-fuel biogas engine with various CO_2 ratios. Fuel. 2021; 286:119330. https://doi.org/10.1016/j.fuel.2020.119330
[71] Vasan V, Sridharan NV, Feroskhan M, Vaithiyanathan S, Subramanian B, Tsai P-C et al. Biogas production and its utilization in internal combustion engines – a review. Process Saf Environ. 2024;186:518-539. https://doi.org/10.1016/j.psep.2024.04.014
[72] Verma S, Das LM, Kaushik SC. Effects of varying composition of biogas on performance and emission characteristics of compression ignition engine using exergy analysis. Energ Convers Manage. 2017;138:346-359. https://doi.org/10.1016/j.enconman.2017.01.066
[73] Verma S, Das LM, Kaushik SC, Tyagi SK. An experimental investigation of exergetic performance and emission characteristics of hydrogen supplemented biogas-diesel dual fuel engine. Int J Hydrogen Energ. 2018;43(4):2452-2468. https://doi.org/10.1016/j.ijhydene.2017.12.032
[74] Villarroel-Schneider J, Mainali B, Martí-Herrero J, Malmquist A, Martin A, Alejo L. Biogas based polygeneration plant options utilizing dairy farms waste: a Bolivian case. Sustainable Energy Technologies and Assessments. 2020;37:100571. https://doi.org/10.1016/j.seta.2019.100571
[75] Vindiš P, Pažek K, Prišenk J, Rozman Č. The economic efficiency of micro biogas plants: a sustainable energy solution in Slovenia – case study. Energies. 2024;17(20):5066. https://doi.org/10.3390/en17205066
[76] Xue J, Li Y, Peppers J, Wan C, Kado NY, Green PG et al. Ultrafine particle emissions from natural gas, biogas, and biomethane combustion. Environ Sci Technol. 2018;52(22): 13619-13628. https://doi.org/10.1021/acs.est.8b04170
[77] Yamasaki Y, Kanno M, Suzuki Y, Kaneko S. Development of an engine control system using city gas and biogas fuel mixture. Appl Energ. 2013;101:465-474. https://doi.org/10.1016/j.apenergy.2012.06.013
[78] Yimen N, Hamandjoda O, Meva'a L, Ndzana B, Nganhou J. Analyzing of a photovoltaic/wind/biogas/pumped-hydro off-grid hybrid system for rural electrification in Sub-Saharan Africa – case study of Djoundé in Northern Cameroon. Energies. 2018;11(10):2644. https://doi.org/10.3390/en11102644

Piotr Laskowski, DEng. – Faculty of Automotive and Construction Machinery Engineering, Warsaw University of Technology, Poland.
e-mail: *piotr.laskowski@pw.edu.pl*

Piotr Wiśniowski, DEng. – Environment Protection Centre, Motor Transport Institute, Warsaw, Poland.
e-mail: *piotr.wisniowski@its.waw.pl*

Marcin Wojs, DEng. – Faculty of Automotive and Construction Machinery Engineering, Warsaw University of Technology, Poland.
e-mail: *marcin.wojs@pw.edu.pl*

Magdalena Zimakowska-Laskowska, DEng. – Environment Protection Centre, Motor Transport Institute, Poland.
e-mail:
magdalena.zimakowska-laskowska@its.waw.pl

Edward Kozłowski, DSc., prof. LUT – Faculty of Management, Lublin University of Technology, Poland.
e-mail: *e.kozlovski@pollub.pl*

Article citation info:
Nieścioruk MJ, Boroiu A-A, Onescu C, Ozuna G, Ávila AB, Kubiak P et al. The use of hydrogen to supply combustion engines – part 2. Combustion Engines. 2026;206(3):44-60. https://doi.org/10.19206/CE-214622

Mariusz J. NIEŚCIORUK
Andrei-Alexandru BOROIU
Constantin ONESCU
Gustavo OZUNA
Agustín Brau ÁVILA
Przemyslaw KUBIAK
Dmytro LEVCHENKO
Marek WOZNIAK
Krzysztof SICZEK

Combustion Engines
Polish Scientific Society of Combustion Engines

The use of hydrogen to supply combustion engines – part 2

ARTICLE INFO

Received: 28 April 2025
Revised: 6 October 2025
Accepted: 23 November 2025
Available online: 14 January 2026

The present study reviews the state-of-art regarding the application of H_2 in the automotive industry. This part focuses on dual-fuel (DF) internal combustion engines (ICEs) supplied with fuel and H_2. This is a continuation of the earlier part, which focused on out-of-engine studies on the effect of H_2 combustion processes, ICEs supplied with H_2, and vehicles powered by fuel cells (FCs). Using H_2 in diesel engines via the DF strategy enables a decrease in diesel fuel consumption and a reduction in harmful exhaust emissions. Using H_2 in diesel engines powered by diesel/biodiesel mixtures also allows for reducing reliance on fossil fuels. Also, incorporating nanomaterials or oxygen-containing compounds into diesel fuel formulations may enhance the combustion efficiency of H_2-powered diesel engines, thereby increasing thermal efficiency and reducing fuel consumption. However, additional studies are required on this subject.

Key words: *hydrogen, dual-fuel engine, combustion engine, emission*

This is an open access article under the CC BY license (http://creativecommons.org/licenses/by/4.0/)

1. Introduction

Nowadays, hydrogen (H_2) is increasingly used to power internal combustion engines (ICEs) in both mobile and stationary applications. Developments in the transport and energy sectors have heightened interest in using fuels derived from renewable sources rather than fossil ones.

The present study reviews the state-of-art in the application of H_2 in the automotive industry. This part focuses on dual-fuel (DF) ICEs supplied with conventional fuel and H_2 and continues the earlier part that examined out-of-engine H_2 combustion studies, ICEs operating solely on H_2, and vehicles powered by fuel cells (FCs).

2. Dual-fuel combustion engines supplied with conventional fuel and hydrogen

According to [8], in case of a gas shortage, DF ICEs can operate on gaseous fuel with a diesel pilot or solely on diesel. Converting an existing diesel ICE to dual-fuel operation is relatively straightforward and requires only minor modifications. Because of the excellent anti-knock properties of H_2, the original cylinder geometry can be retained and the compression ratio (CR) preserved.

According to [17], DF ICEs are recommended when using H_2-enriched compressed natural gas (HCNG) with an H_2 mass fraction of 0–50%; when NH_3 or pure H_2 is used, compression-ignition (CI) ICEs are preferable for environmental reasons.

Several studies have confirmed the positive role of exhaust-gas recirculation (EGR) in DF ICEs fueled with conventional fuel and H_2.

Purayil et al. [70] observed that H_2–gasoline DF ICEs use H_2 as the main fuel and gasoline as the auxiliary fuel. Such engines exhibit high thermal efficiency at low and partial loads, but their power output declines at high loads. The optimal configuration combines H_2 direct injection with gasoline port-fuel injection (PFI), which mitigates abnormal combustion but increases emissions. Using EGR reduced emissions by up to 77.8% at an EGR rate of 18%; higher rates, however, induced combustion instability.

Alrazen et al. [3] reported that the air–fuel (A/F) ratio, engine speed and load significantly influence the performance and emissions of diesel ICEs enriched with H_2. Brake thermal efficiency (BTE), brake power (BP), brake mean effective pressure (BMEP), and specific energy consumption (SEC) all depend on operating conditions when H_2 is introduced. Increasing the H_2 fraction decreases unburned hydrocarbons (UHCs), CO, CO_2, particulate matter (PM), and smoke, whereas NO_x rises; this increase can be controlled through injection strategies, EGR, water injection, or exhaust after-treatment.

Banerjee et al. [9] reported that initiating H_2 dual-fuel combustion with a diesel pilot improves conventional diesel performance while reducing regulated emissions, even though H_2 enrichment tends to raise NO_x. Because H_2 has a wide flammability range, high diffusivity, and low ignition energy, DF combustion tolerates higher EGR rates than conventional diesel. Extensive EGR alleviates NO_x–PM trade-offs without compromising performance and can obviate complex NO_x after-treatment.

Dimitriou and Tsujimura [27] demonstrated that the use of H_2 in compression ignition (CI) engines markedly reduces HC, CO, CO_2, and smoke – often by more than 50% under optimal conditions. Higher H_2 fractions raise the heat-release rate and BTE but also elevate in-cylinder temperature, sharply increasing NO_x, especially at high loads. EGR reduces NO_x in proportion to the EGR rate but may raise smoke, CO, and HC owing to lower O_2. Combining H_2 with optimized EGR simultaneously cuts all emissions relative to pure diesel operation, yet NO_x remains the principal challenge.

Rosha et al. [74] reviewed many studies on H_2 addition to diesel or biodiesel (BD) pilots in DF CI ICEs and concluded that:

- H_2's higher laminar flame speed, shorter ignition delay, and lower minimum ignition energy accelerate flame propagation and kernel development
- BTE and BP generally improve with greater H_2 energy share owing to shorter combustion duration, higher heat-release rate, and higher peak pressure; however, knocking increases, BMEP falls in fuel-rich mode, and rises modestly under lean burn
- Because H_2 is carbon-free, CO, CO_2, and HC emissions fall at all loads, whereas NO_x increases due to higher temperature.

Arjun et al. [7] reported that the addition of Brown (HHO) gas, a mixture of H_2 and O_2 produced by electrolysis, to ICEs raised BP by 2–5.7% and BTE by 10.3–34.9%, reduced brake-specific fuel consumption (BSFC) by 20–30%, and cut CO and HC by 18% and 14%, respectively. NO_x responses varied among studies.

Thiyagarajan et al. [96] investigated H_2 addition to various BD/vegetable oils on CI ICE performance. BTE, BSFC, in-cylinder pressure and heat release rate, as well as UHCs, CO, NO_x, and smoke emissions, were thoroughly assessed. H_2 inclusion generally enhances ICE performance compared to BD/vegetable oil, though it remains comparable to or lower than diesel. H_2 addition improved BTE and fuel efficiency in CI ICEs, regardless of the fuel type utilized. This results from the higher heating value and faster combustion characteristics of H_2. H_2 combustion enhances burning efficiency, leading to higher heat release rates and maximum pressures. The high auto-ignition temperature of H_2 limits its exclusive use in CI ICEs. H_2 can serve as fuel in CI ICEs alongside pilot fuel, with the knock limitation for H_2 being approximately 20%. All emissions, except NO_x, exhibited a downward trend with H_2 inclusion. H_2 significantly reduces CO_2 emissions based on the carbon content in the molecular structure of BD or vegetable oil. Since H_2 is carbon-free, emissions of HC, CO, and smoke are consequently reduced. However, the decrease depends solely on the quantity of H_2 introduced and the type of fuel used. H_2 combustion increases NO_x emissions regardless of the fuel type used. To mitigate this effect, various after-treatment systems, such as selective catalytic reduction (SCR), exhaust gas recirculation (EGR), selective non-catalytic reduction (SNCR), and non-selective catalytic reduction (NSCR), have been suggested.

Following an extensive analysis of HHO production through various generators and its application in heating and power contexts, Paparao and Murugan [68] found that HHO can serve as an alternative fuel in SI ICEs either independently or in combination with gasoline or similar fuels. Thermal efficiency increased while BSFC decreased with HHO use in SI ICEs. CO, HC, and CO_2 emissions decreased in SI ICEs powered by HHO fuel throughout the entire operating range. Furthermore, gaseous HHO can be utilized in CI ICEs operating in dual-fuel (DF) configuration. When HHO was employed in CI ICEs in DF mode, BTE improved and BSFC decreased. CO, HC, and smoke emissions decreased, while NO_x increased throughout the entire ICE operating range.

When examining various efficiency reports and emission characteristics of CI ICEs powered by HHO, Ridhuan et al. [4] discovered that HHO gas enhanced brake power (BP) and torque. In all cases, an improvement in brake thermal efficiency was observed. This was because HHO gas contains H_2, which has a higher calorific value than fossil fuels. Simultaneously, BSFC was reduced, and the combined effects of H_2 and oxygen facilitated complete combustion, enhancing combustion efficiency when HHO gas was introduced. HHO gas inclusion improved BP, brake torque (BT), and BTE while reducing BSFC and lowering CO and HC emissions. The increase in CO_2 emissions indicated complete combustion. Consequently, utilizing HHO gas in CI ICEs improved ICE efficiency and reduced exhaust emissions.

Hosseini et al. [38] reported that HHO enrichment serves as a practical solution to enhance diesel ICE performance while minimizing exhaust emissions. HHO also addresses storage and safety concerns associated with H_2 use in diesel ICEs. HHO can boost BTE of diesel ICEs and reduce BSFC by increasing the calorific value of air-fuel (A/F) mixtures and improving combustion efficiency. HHO addition can enhance heat release rates and in-cylinder pressure of diesel ICEs due to increased flame speed and diffusivity of monoatomic H_2. HHO inclusion in diesel fuel may reduce ignition delays by creating a uniform air-fuel mixture. HHO incorporation may lead to notable decreases in CO, CO_2, UHC, smoke, and particulate matter (PM) emissions from diesel ICEs. This effect may be attributed to the presence of H_2 and oxygen in carbon-free HHO, which accelerates fuel oxidation processes and ensures complete combustion. HHO gas may successfully address the negative impacts of adding gaseous fuel to diesel fuel, such as reduced efficiency metrics and increased CO and UHC emissions.

Akal et al. [2] evaluated H_2 application as a fuel for vehicles and as an additional fuel source. They discovered that due to the elevated self-ignition temperature of H_2 fuel, it is better suited for use in gasoline ICEs. Incorporating H_2 into gasoline in specific ratios can further increase compression ratios (CRs), enhancing ICE efficiency and performance. In numerous studies, depending on the quantity of H_2 incorporated into fuel, ICEs have demonstrated improvements in both performance and fuel efficiency. Moreover, due to the structural characteristics of ICEs, gasoline ICEs are better positioned to utilize H_2 enrichment in terms of emissions and BSFC levels. When H_2 fuel was added to the LPG ICEs, there was a slight decrease in torque and power. When the quantity of H_2 supplied to the LPG system was increased, the BSFC and harmful emissions from these ICEs decreased. However, gaseous fuels and H_2 fuel reduce volumetric efficiency since they occupy more space in the ICE cylinder compared to gasoline. This can be addressed by designing various combustion chambers, increasing the cylinder capacities of ICEs that will utilize H_2 fuel, and incorporating variable valve timing and different valve designs. In diesel ICEs, different outcomes were noted based on the quantity of H_2 added to the fuel and the ICE speed. Although the torque and power outputs of certain ICEs increased with H_2 utilization, other ICEs experienced

a decline in torque and power values as speeds increased. Due to H_2's elevated ignition temperature, it is unsuitable for direct application in diesel ICEs. Consequently, in numerous studies, various techniques were employed to inject H_2 into the cylinder. In various studies where H_2 fuel was added to diesel ICEs, a reduction in CO_2 emissions and soot production in exhaust emissions was noted, although an enhancement in NO_x emissions was also recorded. Many ICEs utilizing H_2 achieved reduced BSFC and harmful exhaust emissions.

Wang et al. [104] noted that H_2 fuel is beneficial as a fuel for automotive ICEs due to its advantages of wide flammability limits and high flame speed. Its introduction can significantly enhance the combustion and emission properties of ICEs. Regardless of ICE type, efficiency can be enhanced through targeted H_2 doping methods and specific H_2 doping ratios. Nevertheless, the optimal mode and proportion vary based on operating conditions. The performance of H_2 ICEs and H_2 blended ICEs is highly influenced by H_2 injector positions and H_2 injection control strategies.

Deheri et al. [22] noted that H_2, as a fuel with higher flame speed and lower ignition energy, enhances peak cylinder pressure and heat release rate. H_2 use as a fuel cause knocking in CI ICEs and increases NO_x emissions due to its rapid flame propagation. Combustion parameters like maximum in-cylinder pressure and heat release rate can be enhanced by up to 30%, while combustion duration and ignition delay can be reduced by 4 to 5%, by introducing biogas (BG) and H_2 into the cylinder alongside advanced injection timing and increased CRs. Diethyl Ether (DEE) serves as a beneficial additive alongside these alternative fuels to enhance combustion properties. DF mode reduced NO_x and smoke emissions by up to 60%, while HC and CO emissions may increase by up to 30%. However, these emissions can be controlled by employing control techniques and adding additional components with the pilot fuel.

Das et al. [19] also reported that H_2 in producer gas (PG) is the key element affecting ICE performance. A higher percentage of H_2 in producer gas enhances combustion efficiency and peak cylinder pressure (PCP). Nevertheless, a higher amount of inert gases, such as CO_2 and N_2, in PG inhibits pre-flame development that leads to knocking. Incomplete combustion during DF mode led to increased emissions of HC and CO compared to diesel mode. Utilizing BD as a pilot fuel enhances combustion efficiency of both gaseous and liquid fuels by supplying adequate O_2, leading to decreased levels of HC and CO. Moreover, H_2 incorporation in PG decreases the amount of carbon particles in the fuel and increases the average gas temperature, thereby reducing CO. Regarding producer gas use, a higher quantity of H_2 increases NO_x emissions.

H_2 use in diesel ICEs does not necessarily require significant modifications to the internal combustion engine (ICE). In their comprehensive review, Hosseini et al. [38] explained that H_2 can be utilized in existing CI diesel ICEs in DF configurations with minor adjustments. The specific physicochemical traits of H_2, including its higher calorific value, flame speed, and diffusivity, can significantly enhance the efficiency and combustion properties of diesel ICEs. Being a carbon-free fuel, H_2 can also reduce harmful emissions from diesel ICEs, such as CO, UHC, PM, soot, and smoke. Nevertheless, diesel ICEs running on H_2 experience knocking combustion and elevated NO_x emissions. This review thoroughly examines the impact of H_2 or gaseous fuels containing H_2 (such as syngas (SG) and HHO gas) on the performance of DF diesel ICEs. H_2 can effectively decrease all carbonaceous emissions from diesel ICEs. Real-time H_2 injection control can eliminate its disadvantages in diesel ICEs. H_2 cannot enhance all performance metrics and exhaust emissions of diesel ICEs simultaneously. Nevertheless, modifying pilot fuel through additives, mixing H_2 with other gaseous fuels, changing ICE settings, improving operational conditions, adapting ICE design, utilizing HHO gas, and implementing exhaust gas catalysts may facilitate the development of safe, efficient, and cost-effective H_2-powered diesel ICEs.

H_2 inclusion in diesel fuel may enhance the BTE of diesel ICEs and reduce the BSFC rates. This may result from the increased heating value and faster burning of gaseous H_2. H_2 might also offset the reduced calorific value of BD while addressing its primary limitations, such as decreased BTE and increased BSFC. Increased H_2 addition levels may enable more uniform charge combustion, resulting in improved combustion characteristics. However, introducing H_2 above a specific threshold, especially under high ICE loads, could lead to knocking issues. The H_2 inclusion rate that results in knocking varies among ICEs, fuels, and operating conditions. Thus, a definitive guideline for the optimal H_2 inclusion rate cannot be established [38].

Selected characteristics of DF ICEs powered by diesel fuel, reviewed by Hosseini et al. [38], are shown in Fig. 1. The studied ICEs operated at speeds with a mean value of 1724 rpm and a standard deviation (SD) of 528. The displacement of such ICEs had a mean value of 1674 cm^3 and a high SD of 2325 cm^3. ICE minimum loads reached the mean value of 27.3% and SD of 34%, while maximum loads reached the mean value of 82% and SD of 32%. ICE load can vary between 0 and 100%. The ICE's minimum CR reached a mean value of 16.41 and SD of 4.72, while the maximum CR reached a mean value of 16.49 and SD of 4.78.

The effect of load, EGR and H_2 supply on BTE and BSFC for DF ICEs ignited by diesel fuel is shown in Fig. 2. For the data presented in Fig. 2a, 16% and approximately 65% of the analyzed cases exhibited missing data for BTE and BSFC, respectively. 13.5% showed reductions, approximately 3% and none showed no effect, and about 68% and 21.6%, respectively, showed increases. For the data presented in Fig. 2b, 28.5% and 71.4% of the analyzed cases exhibited missing data for BTE and BSFC, respectively. No cases showed reductions or no effects, and approximately 71.5% and 58.6%, respectively, showed increases. For data in Fig. 2c, 25% and 87.5% of analyzed cases exhibited missing data for BTE and BSFC, respectively; 12.5% and none showed reductions, no cases showed no effect; and about 62.5% and 12.5%, respectively, showed increases.

Integrating H_2 into pure diesel fuel may enhance the BTE of diesel ICEs [37, 46, 71, 72]. Incorporating H_2 into pure diesel fuel can result in a more complete combustion process due to its higher flame temperature and faster flame speed compared to conventional diesel [35, 47, 62, 112].

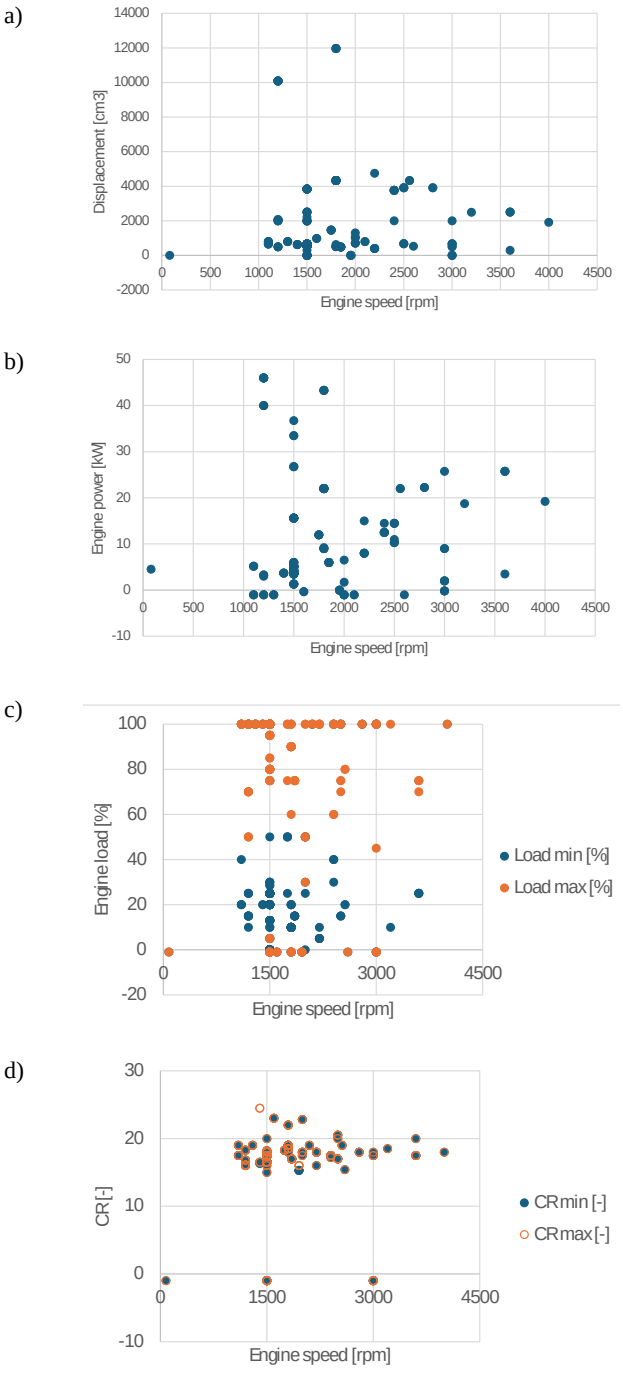

Fig. 1. Selected characteristics of DF ICEs ignited by diesel fuel speed (negative values correspond to missing data); a) displacement versus ICE speed, b) ICE power from 1-cylinder versus ICE, c) ICE load versus ICE speed, d) ICE CR versus ICE speed based on data from [38]

H_2 can improve the combustion of diesel fuel because its premixed flames possess wider flammability limits than hydrocarbon fuels, thereby enhancing the BTE of diesel ICEs [78]. H_2 can also shift the peak heat release closer to the injection (TDC) point, resulting in improved cycle efficiency of diesel ICEs [78]. Nonetheless, utilizing H_2 in a diesel ICE does not always guarantee an improvement in BTE. Although H_2 has higher energy content per unit mass compared to diesel fuel, factors such as the air-fuel (A/F) ratio and ICE design can significantly affect BTE. A factor

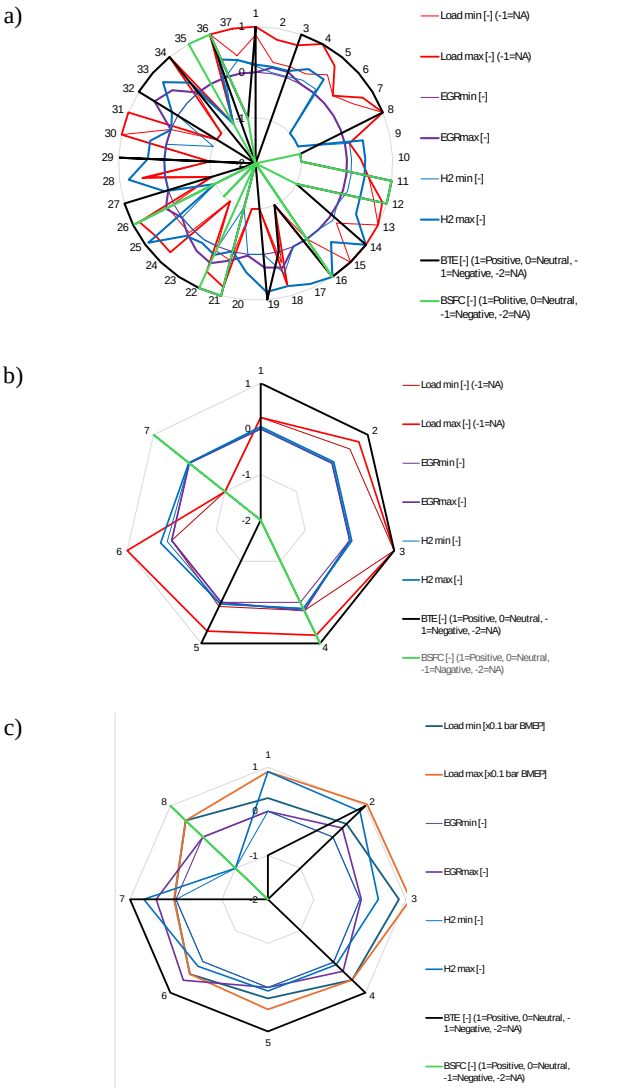

Fig. 2. The effect of load, EGR and H2 supply on BTE and BSFC for DF ICEs ignited by diesel fuel; a) for ICE load [%], EGR [%], and H_2 supply [%], b) for ICE load [%], EGR [%], and H_2 supply [lpm] approximately converted to [%], c) for ICE load [×0.1 bar BMEP], EGR [%], and H_2 supply [%], based on data from [38]. There are shown minimal and maximal limits for load (Load min and Load max, respectively), EGR (EGRmin and EGRmax, respectively) and H_2 supply (H_2 min and H_2 max, respectively) in the Figure

that can enhance the BTE of diesel ICEs is the high energy content of H_2. This effect arises from H_2's elevated calorific value, which drives the H_2-diesel combustion process toward completion, resulting in better ICE efficiency [47, 112]. Although higher calorific fuels generate more heat during combustion, this does not necessarily ensure complete combustion.

The completeness of the combustion process depends on the A/F ratio and the mixing of fuel and air within the combustion chamber. Moreover, incorporating H_2 into diesel fuel can improve A/F mixture homogeneity due to its gaseous state [23, 47], resulting in rapid energy release and enhanced combustion [79].

Incorporating H_2 into diesel fuel can enhance diesel ICE BTE through various mechanisms. One approach is to achieve a leaner equivalence ratio and reduce combustion

duration [55]. However, the effect of H_2 addition on the equivalence ratio may vary depending on specific ICE operating conditions and the amount of H_2 introduced. Although injecting H_2 via the inlet port may slightly reduce airflow, leading to a leaner mixture equivalence ratio, increasing H_2 percentage can also result in a richer mixture. Nevertheless, with increased H_2 addition rates, the overall A/F ratio can be maintained at or near stoichiometric to avoid efficiency reduction caused by higher H_2 levels. Also, the heat capacity ratio (adiabatic index) of H_2 exceeds that of hydrocarbon fuels, potentially enhancing diesel ICE BTE. Additionally, the rapid combustion rate of H_2 may reduce heat loss to the surroundings, further improving BTE [108]. However, increasing H_2 beyond a certain threshold may cause knocking [80]. The short quenching distance of the H_2 flame increases the likelihood of flame contact with combustion chamber walls, resulting in increased convective heat transfer and reduced BTE at high H_2 content [112]. Therefore, the precise influence of H_2 addition on BTE depends on specific ICE configuration and operating conditions.

While some studies indicate that H_2 addition to diesel fuel improves combustion efficiency, others suggest the opposite [28, 87], Varde and Frame [100] proposed that incorrect piston positioning relative to peak in-cylinder pressure due to H_2-diesel mixing may reduce diesel ICE BTE. This issue may be resolved by adjusting diesel fuel injection timing, either advancing or retarding it, to optimize combustion timing and mitigate negative impacts on ICE performance. Although H_2 addition into the intake air increases heat absorption by H_2 molecules, it does not necessarily reduce flame temperature. H_2 addition may lower oxygen availability for combustion, potentially reducing combustion efficiency [67]. It is essential to note that H_2 has a higher molar heat capacity than nitrogen, which can increase the overall heat capacity of the mixture. Nonetheless, H_2 addition often leads to an increased overall equivalence ratio, raising combustion temperature. Conversely, low BTE in H_2-diesel dual-fuel operation can be attributed to heat losses resulting from the short flame quenching distance and the high thermal conductivity of H_2, which increases convective heat losses and reduces overall efficiency [26]. Heat loss rates also rise when H_2 is mixed with diesel due to increased wall heat flux, lowering BTE [65].

H_2 addition to diesel under varying ICE loads may result in differing efficiency trends [21, 102].

H_2 addition can reduce BTE under low loads because diesel injection rates decrease, possibly resulting in insufficient pilot fuel to fully combust added H_2. At higher ICE loads, BTE improvements are observed due to increased pilot diesel injection, providing adequate ignition energy for gaseous fuel combustion [57]. H_2 may enhance diesel combustion at higher loads due to the broader flammability limits of its premixed flames, resulting in improved A/F mixture combustion. Additionally, increasing H_2 supplementation at higher loads can increase in-cylinder pressure thanks to its rapid combustion and wide flammability limits [25]. These factors, when combined, can improve BTE in H_2-diesel dual-fuel operation at high loads. In dual-fuel ICEs, H_2 and diesel fuel are injected separately.

The H_2 inclusion rate is typically independent of ICE load and speed, regardless of the injection method, allowing the adjustment of the H_2-to-diesel ratio to ensure consistent combustion and improved efficiency.

The comparative BSFC metric represents fuel consumption per unit brake power (BP) output [109]. Two approaches determine BSFC in diesel ICEs running on H_2 fuel. The first divides the combined mass flow rates of H_2 and diesel by generated power [21, 45, 66]. The second converts the H_2 mass flow into an equivalent diesel amount based on lower heating values, then sums the diesel and converted H_2 mass flows before dividing by the power output [42, 43]. Both express BSFC in g/kWh or kg/kWh. The second method is considered more practical and reliable, as the first may be misleading for fuels with different densities and energy contents [75].

Many studies [14, 46] demonstrated that H_2 addition to intake air reduces BSFC due to its high diffusivity and flame speed, facilitating uniform mixing and improved combustion, increasing BP while reducing BSFC [23, 45,–47, 90]. However, excessive H_2 introduction may increase BSFC due to oxygen limitation, causing incomplete combustion [45].

Although some studies show H_2 improves diesel ICE efficiency, others dispute this [42, 87], This can occur because H_2 addition reduces available oxygen in the combustion chamber, impairing combustion [45]. Mismatches between diesel injection timing and H_2 addition can cause suboptimal combustion timing and insufficient combustion duration, lowering BP and raising BSFC. Brake Specific Energy Consumption (BSEC) is a more reliable efficiency metric, as it is unaffected by fuel characteristics [33]. H_2 addition may improve BSEC by accelerating combustion reactions and enhancing mixture homogeneity [20, 23, 46, 95]. However, excessive H_2 can reduce local oxidant concentration and combustion efficiency [29]. Some studies report BSEC increase due to the mismatch between diesel ICE combustion and gaseous H_2 [48], and increased H_2 mass flow may exacerbate this [108].

The elevated flame temperature of H_2 can increase peak in-cylinder pressure and heat release rates in diesel ICEs. H_2 addition can shorten combustion duration owing to rapid flame speed and faster A/F mixing. However, H_2 inclusion may lengthen ignition delay due to low cetane number and higher auto-ignition temperature. Due to its carbon-free nature and enhanced mixture uniformity, H_2 can significantly reduce emissions of CO, CO_2, HC, PM, smoke, and soot. Nonetheless, H_2 may increase NO_x emissions due to higher in-cylinder peak pressure and temperature [38].

The effect of load, EGR, and H_2 supply on particulate matter (PM), hydrocarbons (HC), NO_x, CO, and CO_2 emissions for DF ICEs excited by diesel fuel is shown in Figure 3. For data in Fig. 3a, 10.1%, 5.4%, 2.7%, 1.1%, and 30% of analyzed cases exhibited missing data for PM, HC, NO_x, CO, and CO_2 emissions, respectively; 8.1%, 21.6%, 43.2%, 8.1%, and 2.7%, respectively, showed reductions; 2.7%, 1.1%, 8.1%, none, and none, respectively, showed no effect; and 78.3%, 62.1%, 45.9%, 81%, and 67.5%, respectively, showed increases. For Fig. 3b, 14.2% of cases had missing data for PM, HC, NO_x, CO, and 28.5% for CO_2 emissions; 14.2% showed reductions for PM, HC, NO_x, and

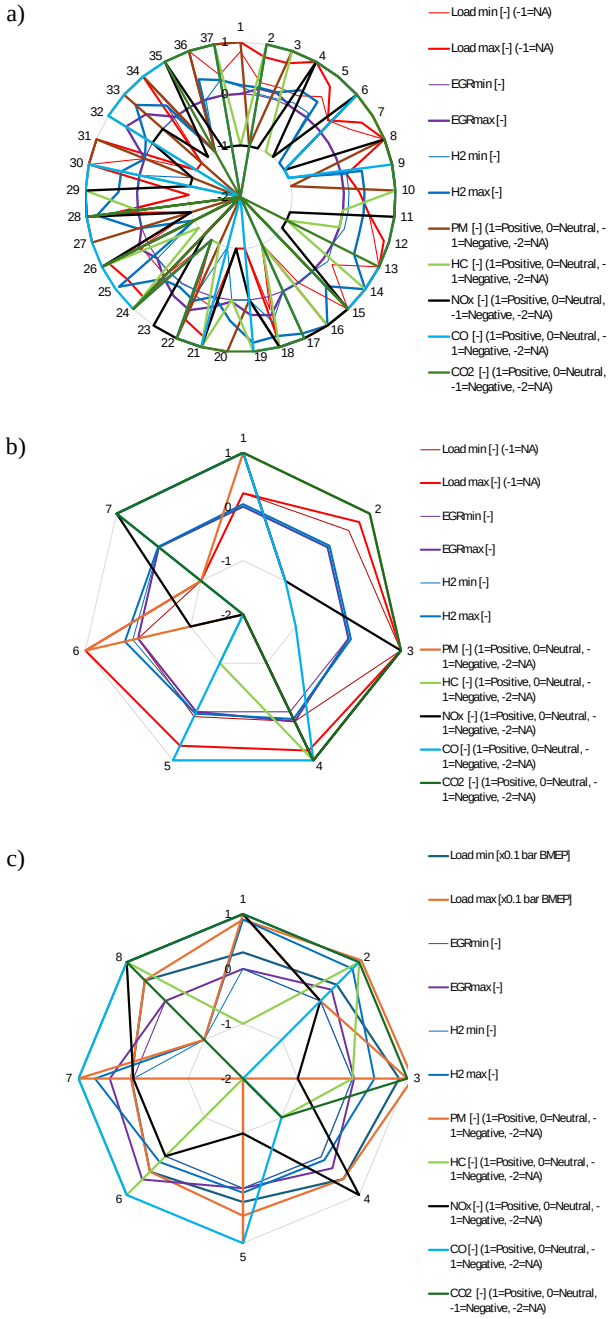

Fig. 3. The effect of load, EGR and H_2 supply on PM, HC, NO_x, CO and CO_2 emissions for DF ICEs ignited by diesel fuel; a) for ICE load [%], EGR [%], and H_2 supply [%], b) for ICE load [%], EGR [%], and H_2 supply [lpm] converted approximately to [%], c) for ICE load [×0.1 bar BMEP], EGR [%], and H_2 supply [%], based on data from [38]. There are shown minimal and maximal limits for load (Load min and Load max, respectively), EGR (EGRmin and EGRmax, respectively) and H_2 supply (H_2 min and H_2 max, respectively) in Figure

CO, none for CO_2; none showed no effects; and 71.4%, 71.4%, 57.1%, 57.1%, and 71.4% showed increases. For Figure 3c, 25%, 12.5%, none, 12.5%, and 37.5% had missing data for PM, HC, NO_x, CO, and CO_2; 12.5%, 25%, 25%, 12.5%, and 12.5% showed reductions; 12.5%, 12.5%, 37.5%, none, and none showed no effect; and 50%, 50%, 37.5%, 75%, and 50% showed increases.

The amount of soot released from the diesel ICE depends on the equilibrium between soot production and ~~its~~ oxidation [105]. H_2 addition to diesel fuel may reduce soot emissions [1, 5]. H_2 can effectively unify the A/F mixture, enhancing combustion efficiency and reducing soot emissions [46]. Incorporating H_2 into diesel fuel may lower carbon levels or increase the H/C ratio of the fuel, thereby reducing soot emissions [61]. By decreasing the proportion of diesel fuel in the mixture, soot oxidation may be enhanced while initial soot formation is reduced [94]. Smoke is an apparent byproduct of incomplete combustion. H_2 addition to diesel fuel may reduce smoke emissions due to the carbon-free nature of gaseous H_2 or an increased H/C ratio in the A/F mixture [81, 83]. The combustion of H_2 generates water and does not produce smoke emissions [80]. The high diffusivity of H_2 may improve A/F mixture uniformity and increase O_2 availability, further reducing smoke emissions [66]. The intense flame produced during H_2 combustion can oxidize carbon particles arising from diesel combustion [82]. The formation of a premixed H_2-air charge during DF operation may eliminate the source of smoke emissions from diesel ICEs [101]. However, excessive H_2 induction may increase smoke emissions by creating an overly rich A/F mixture [78].

PM consists of carbon-based substances resulting from the incomplete combustion of hydrocarbon fuels [80]. PM is a complex pollutant that includes both soluble and insoluble fractions, as well as dry components [98, 106]. Soot, classified as an insoluble fraction, constitutes a significant portion of PM (slightly over 50%) [98]. The remainder of PM (~50%) comprises unburned hydrocarbons (UHCs), partially oxidized hydrocarbons, unburned or partially burned lubricating oil, wear particles, and sulfates (SO_4^{2-}) derived from the fuel [60, 98]. The majority of soot consists of elemental carbon, which adsorbs organic compounds such as polycyclic aromatic hydrocarbons and their derivatives, sulfates, nitrates (NO_3^-), metals, and various trace elements [13]. PM particles exist in both liquid and agglomerated solid forms. Primary particles in the liquid phase are typically volatile organic compounds and sulfates, ranging in size from 5 to 50 nm. Agglomerated particles mainly consist of soot, volatile and nonvolatile organic fractions, metallic residues, and sulfates, with sizes ranging from 50 to 500 nm [36]. Soot aggregates primarily from inside the combustion chamber, while PM is generated outside it [36]. PM may decrease with H_2 enrichment due to the absence of carbon in H_2 and a reduced diesel fuel injection rate [57]. Adding H_2 to diesel fuel may increase flame temperature and improve hydrocarbon combustion, reducing PM generation [67]. Replacing diesel fuel with H_2 can create a more uniform A/F mixture, reducing fuel-rich zones and lowering PM emissions. Incomplete combustion in fuel-rich zones near injector sprays can result in PM formation [58]. Adding H_2 may decrease both particle size and concentration due to its inhibitory effect on hydrogen abstraction and acetylene (C_2H_2) addition processes [114].

Furthermore, it appears that the agglomeration of additional particles into larger clusters can be reduced by incorporating H_2 into ultra-low-sulfur diesel [115]. H_2 addition may also alter the nanostructure of primary particles emitted from the diesel ICE. A shift from a “turbostratic interlayer” to an “onion-like” structure was observed with H_2

addition at 1200 and 1800 rpm under 30% load. Moreover, the "shell-core" structure can transition to a "shell-amorphous" structure with H_2 addition at 1200 and 1800 rpm under 70% load. Compression ignition (CI) diesel ICEs generate PM mainly due to non-uniform combustion resulting from localized fuel-rich zones within the combustion chamber [15]. H_2 can promote a more uniform A/F mixture, reducing PM emissions. H_2 addition may also lower PM emissions from ICEs running on biodiesel (BD) due to a reduced proportion of carbon-containing BD in the A/F mixture [12, 63, 113]. The product of H_2 combustion is water, not PM [15]. The main factors influencing PM oxidation in CI ICEs are the O_2 concentration and temperature inside the cylinder.

UHC compounds are typically found in low-temperature regions of the combustion chamber, such as near cylinder walls, where the temperature is insufficient for complete combustion of the A/F mixture [22]. Incorporating H_2 may reduce UHC emissions from diesel ICEs due to the absence of carbon in H_2 fuel [10]. Introducing H_2 into the intake air may extend the ignition delay, allowing for better A/F mixing prior to ignition [58]. Gaseous H_2 can fully homogenize the A/F mixture due to its high diffusivity [46], improving combustion efficiency and reducing UHC emissions. The wide flammability range and short quenching distance of H_2 may also improve the combustion of A/F mixtures [108]. The rapid burning rate of H_2 can enhance diesel combustion, leading to lower UHC emissions [82]. H_2 addition may increase in-cylinder temperature, enhancing UHC oxidation after combustion [47].

However, H_2 incorporation into diesel fuel may also increase UHC emissions [20, 42]. This may occur if the pilot fuel supply is insufficient to fully ignite the gaseous fuel [26], or if H_2 reduces the O_2 concentration in the A/F mixture, resulting in incomplete diesel fuel combustion [66]. Rapid H_2 combustion may consume most of the available O_2, leading to incomplete oxidation of diesel injected late in the cycle [100]. The high burning speed of H_2 may also increase UHC emissions due to flame quenching [81]. Extending the ignition delay under fuel-lean conditions with H_2 addition may also result in incomplete combustion [114].

The formation rate of NO_x in diesel ICEs largely depends on O_2 concentration, A/F mixture residence time, and in-cylinder temperature. Atmospheric N_2 and O_2 can undergo various chemical reactions, forming NO_x in high-temperature regions [39]. Conventional diesel combustion produces high levels of NO_x and soot due to diffusive flame characteristics [48]. Low-temperature combustion can reduce both NO_x and soot emissions from diesel ICEs [51], [76]. Various low-temperature combustion strategies, such as homogeneous charge compression ignition (HCCI), premixed charge compression ignition (PCCI), and reactivity-controlled compression ignition (RCCI), have been developed and studied [51]. RCCI can operate over a wide load range, achieving near-zero NO_x and soot emissions by adjusting fuel blends and injection strategies [49, 50, 111]. RCCI ICEs control in-cylinder reactivity to manage the combustion phase [51]. In this dual-fuel process, at least two fuels with different reactivities are used [30, 49]. A/F homogeneity is achieved by introducing low-reactivity fuels (e.g., methanol, natural gas, gasoline, ethanol) through the intake port, while ignition is initiated by direct injection of a high-reactivity fuel (e.g., diesel, biodiesel, dimethyl ether) [11, 34].

In RCCI diesel combustion, combustion chamber regions are cooler compared to conventional diesel, significantly reducing heat transfer from the piston bowl and improving BTE [44]. While RCCI offers attractive features, its CO and UHC emissions are typically higher than in standard diesel combustion [34]. When H_2 is added to low-reactivity fuels, RCCI ICEs produce much lower CO and UHC emissions, as shown by Kakoee and Gharehghani [41]. However, H_2 addition beyond a certain threshold may increase NO_x and soot emissions by raising in-cylinder temperature.

H_2 addition to diesel fuel may increase NO_x emissions [20], [107]. The high calorific value of H_2 can elevate peak in-cylinder pressure and temperature, leading to higher NO_x emissions [77]. The rapid flame speed of H_2 can promote complete combustion, further increasing pressure and temperature [85]. H_2 addition may also raise local temperatures earlier in the expansion phase, accelerating NO_x formation [100]. The increased ignition delay due to H_2 addition can create a more homogeneous A/F mixture before ignition, raising in-cylinder temperature and contributing to higher NO_x emissions [58]. NO_x emissions from H_2 port injection can exceed those from H_2 induction [101]. Port injection can improve combustion and volumetric efficiency while increasing combustion temperature [101].

However, H_2 incorporation into diesel fuel may also reduce NO_x emissions if the engine operates with a leaner mixture [83]. A very lean equivalence ratio can lower peak combustion temperature, reducing NO_x emissions [81]. H_2 can promote a more uniform A/F mixture, eliminating fuel-rich zones and allowing temperature to rise more gradually, thus reducing NO_x production [1]. NO_x reduction may also occur at high H_2 supplementation rates if combustion duration increases, lowering the heat release rate [28]. Water vapor (H_2O) generated from H_2 oxidation may lower in-cylinder temperature and further reduce NO_x emissions [108]. H_2 addition may reduce the amount of diesel fuel consumed during the diffusive combustion phase, which is a major source of NO_x [108].

H_2 introduction into the intake air can reduce CO emissions [20, 112] due to a lower C/H ratio in the fuel mixture [32]. The high diffusivity of H_2 promotes a homogeneous combustible mixture, enhancing combustion and reducing CO emissions [42, 77]. The rapid flame speed of H_2 enhances combustion and increases in-cylinder temperature, thereby further reducing CO emissions [66, 77]. This reduction may also be linked to the ability of H_2 to operate at lean equivalence ratios [84], [112]. However, H_2 addition to diesel fuel under certain conditions may increase CO emissions. This can occur if H_2 reduces O_2 availability, leading to incomplete oxidation [26]. Elevated in-cylinder temperature from H_2 addition may promote CO_2 dissociation into CO and O [56]. The rapid H_2 reaction rate may deplete O_2 in the combustion chamber, leaving less for CO oxidation. O_2 may be consumed in H_2 oxidation and radical formation [10]. H_2O from H_2 oxidation may also participate in the steam reforming of diesel hydrocarbons, increasing CO

emissions [10]. H_2 addition may increase CO production under high engine loads due to reduced O_2 and shorter reaction times [82]. However, CO emissions may decrease when H_2 is blended with diesel under low loads, due to ample O_2 in leaner A/F mixtures [82].

H_2 incorporation into diesel fuel may lower CO_2 emissions [52, 112], due to the carbon-free nature of H_2 [66]. Furthermore, increasing the overall H/C ratio of the fuel blend by adding H_2 can shorten combustion duration and improve combustion efficiency [61, 77]. The high diffusivity of H_2 may also create a more uniform premixed combustible mixture [20], driving combustion toward completion [77]. The rapid flame speed of H_2 can improve fuel blend combustion efficiency, potentially reducing CO_2 emissions [20]. However, under high engine loads, H_2 addition may reduce CO_2 emissions due to combustion instability and O_2 deficiency [80].

Sutkowski and Mareczek [93] examined the MUZG and WUZG systems designed for managing the combustion of H_2-based fuels. These systems enable operation even with pure H_2 while effectively controlling combustion parameters, such as preventing knock, regulating combustion temperature, and controlling flame speed, among others. This is achieved by early detection of knock or misfire signals, monitoring exhaust temperature, and implementing corrective actions in the next engine cycle if deviations are detected. The WUZG system also enables independent monitoring of each cylinder with its individual mixture composition, or temporary deactivation of a cylinder if combustion becomes unstable, thereby potentially preventing cylinder failure. The system logs engine operation and can detect even minor deviations from target performance, enabling preventive measures to be taken before damage occurs. This prevents scenarios where engine power is limited or the engine must be shut down due to operational faults. The integrated MUZG/WUZG system offers enhanced operational flexibility, allowing transitions between different fuel supply systems. MUZG is prioritized for fuels with low pressure and low H_2 content, while WUZG is preferred for higher-pressure or higher-H_2 fuels. The system can be expanded to accommodate additional hydrocarbon gases blended with H_2. MUZG is applicable to bi-fuel engines operating on both liquid and gaseous fuels (e.g., biodiesel and biomethane), whereas WUZG can be used in dual-fuel engines that combine biodiesel with H_2 or alcohols.

Longwic et al. [54] examined the acceleration of a diesel ICE fueled by both diesel and H_2 on a test bench equipped with a 1.3 Multijet diesel, H_2 storage, and measurement instruments (Table 1). Empirical tests included ICE assessment at idle and at specific speeds using a chassis dynamometer, as well as vehicle acceleration in selected gears from predefined engine speeds. They found that supplying both diesel and H_2 to the intake manifold increased the mean indicated pressure at idle by approximately 144% compared to diesel-only operation. The amount of heat release, peak combustion pressure, and maximum rate of pressure rise also increased. However, for engine operating conditions other than idle, there was a decrease in heat output, heat release rate, combustion chamber pressure, and mean indicated pressure. In these tests, the H_2 flow was controlled to ensure no gas accumulation and prevent possible explosions in the intake manifold under any operating condition. Stock diesel fuel injection timing maps were not modified. Currently, it appears that H_2 supplied to the intake manifold can improve engine performance at idle. However, to achieve safe and noticeable improvements under other conditions, both the H_2 amount and diesel fuel quantity must be adjusted according to the engine's operating parameters.

Longwic et al. [53] tested a diesel engine powered by various fuels using a specialized H_2 injection system with dedicated control software. Control parameters included H_2 injection pressures of 1.5, 1.8, and 2.0 MPa and injector opening durations of 2.5, 3.0, and 3.5 ms.

Analysis of the engine operating in diesel-H_2 dual-fuel mode demonstrates that rapidly changing in-cylinder combustion parameters can be effectively monitored. As H_2 injection duration and pressure increase, the amount of air required for proper combustion also rises. The control system responded by reducing the amount of diesel fuel injected per cycle as additional H_2 was provided. However, the range of H_2 pressure and injection duration was limited, so the reduction in diesel fuel quantity was nearly the same across the tested range. Proper regulation of the diesel-H_2 ratio is essential for stable engine operation under load.

Research on a diesel engine operated with H_2 enabled the identification of control parameters for integrating renewable fuel to reduce fossil fuel consumption, specifically diesel. Operating the test vehicle on a dynamometer in 4th gear at 2600 rpm, optimal fast-variable cylinder parameters were achieved with an injector activation time of 3.5 ms at 0.20 MPa. Modified control strategies resulted in an average 21.5% reduction in diesel consumption.

Noga and Moskal [64] examined the suitability of a pressure-sensing glow plug (PSG) for monitoring combustion in an H_2-powered engine (Table 1). The combustion characteristics of H_2 in spark-ignition (SI) engines differ significantly from those of conventional fuels, making cylinder pressure monitoring essential for optimizing power, efficiency, and minimizing NO_x emissions, which are the primary pollutants in H_2 engines. A PSG was selected for its cost-effectiveness, availability, and durability. Initial tests were conducted on a small single-cylinder SI engine coupled to a 48 V generator. Tests were run at various speeds and generator loads using gasoline with a research octane number (RON) of 95. To simulate H_2 combustion and achieve faster pressure rise, tests were also performed with unaltered light gasoline (lower RON). Comparing the PSG signal with that of a reference pressure transducer installed in the cylinder allowed characterization of PSG behavior under different conditions. Pressure waveforms from both sensors varied according to engine speed and load. The developed transfer functions from the PSG signal to actual in-cylinder pressure may be applied to other engines, allowing cost-effective combustion monitoring in H_2 SI engines after appropriate calibration.

Cupiał and Szwaja [18] studied producer gas combustion in SI and DF CI engines using a diesel pilot (15% of nominal amount), with compression ratios (CR) of 8, 12 (SI engine), and 17 (CI engine) (Table 1). The study focused on

combustion instabilities, including cycle-to-cycle variability and knock phenomena. H_2 combustion was also investigated for comparison. The authors found that producer gas is knock-resistant, even with 16% H_2 content. However, significant cycle-to-cycle variability was observed when producer gas was burned in the SI engine. The DF CI engine could operate more efficiently and stably with producer gas, with no misfires or knock. On the other hand, H_2 combustion in the DF engine resulted in heavy knock, making it unsuitable as a primary fuel. Conversely, gases with high H_2 content are generally not prone to knock, especially when CO_2 is present in quantities similar to H_2, as this greatly increases resistance to knocking.

Tira et al. [97] examined the performance of diesel ICEs fueled with biogas (BG) and H_2 (Table 1). In these experiments, simulated BG (60% CH_4 and 40% CO_2 by volume) and H_2 (2% by volume) were introduced into the intake manifold, while diesel fuel was injected into the cylinder as a pilot ignition source. The results showed that BG and H_2 reduced PM levels compared to pure diesel combustion. Specifically, total PM decreased by up to 39% and smoke by 33%. A slight increase in particle count was observed, with particle size distribution shifting toward the nucleation mode, which is advantageous for after-treatment systems. However, BTE decreased with the addition of gaseous fuel.

Siadkowska and Barański [89] investigated (direct H_2 injection) in a four-cylinder, four-stroke DF ADCR ICE (Table 1). Analyzed parameters included mean effective pressure, peak pressure, crank angle at peak pressure, and heat release. Both early and late direct H_2 injection timing strategies were tested. The authors found that:

- Significant statistical differences were observed in burning process parameters between early and late injection, based on the Student's t-test ($\alpha = 0.05$): for IMEP (56%), peak pressure (88%), heat released (56%), and crank angle at peak pressure (56%)
- In 94% of measurement points, the coefficient of variation for IMEP remained below 5%, indicating stable combustion progression
- Changing direct H_2 injection timing from early to late affects only the combustion process; the degree of this influence depends on H_2 dosage and initial torque. At the highest H_2 dosages, the maximum load threshold of the test setup was nearly reached, resulting in engine knocking, which may account for the observed instabilities.

Depczyński et al. [24] examined the effects of H_2 as an additive to gasoline in ICEs within a hybrid powertrain, focusing on efficiency and environmental sustainability (Table 1). Their study centered on evaluating fuel consumption and CO_2 emissions during the NEDC driving cycle. A mathematical model was developed incorporating H_2 addition and hybrid powertrain operation during the NEDC cycle. They found that a 2% increase in H_2 content in gasoline reduced BSFC by 2.8–3.5%, depending on engine speed. The hybrid system enabled effective energy recovery during braking, enhancing overall system efficiency.

Shadidi et al. [86] investigated the effects of using H_2 as an auxiliary fuel in both SI and CI ICEs on engine efficiency and emissions. Utilizing H_2 as a fuel reduces torque, power, and brake thermal efficiency (BTE), while simultaneously increasing brake specific fuel consumption (BSFC). H_2 use significantly lowers CO, UHC, CO_2, and soot emissions; however, NO_x emissions increase.

Stępień [92] reviewed the unique physical, chemical, and operational properties of H_2 used as an ICE fuel, focusing on H_2 port fuel injection (PFI) and direct injection (DI) technologies. The author compared various fuel injection and ignition strategies, highlighting the benefits of combining selected solutions. Potential risks of improper H_2 combustion – such as pre-ignition, delayed ignition, knocking, and backfiring – were analyzed. Special attention was given to optimizing the air-fuel ratio for combustion quality, NO_x emissions, and engine efficiency, as well as exhaust gas treatment. Required modifications to adapt conventional ICEs for H_2 operation were also discussed. It was found that H_2 represents a promising alternative fuel for SI ICEs, significantly improving efficiency and reducing emissions to a fraction of the levels of conventional fuels. However, its use has notable drawbacks, including elevated NO_x emissions, reduced durability, and reliability concerns.

Fabiś et al. [29] studied the relationship between combustion noise and operational parameters of an ICE powered by LPG, CNG, and CNG-H_2 mixtures in comparison to a gasoline-fueled ICE. Indicators of various resonances within the combustion chamber and related vibration signals from the engine's cylinder block were examined for a single combustion cycle. A four-cylinder, 1.6 dm^3 SI ICE modified to operate on LPG, CNG, and CNG-H_2 mixtures with H_2 volumetric fractions of 5, 10, 15, 20% to 30% was evaluated. For comparison, gasoline was used as the reference fuel. The authors found that fluctuations in in-cylinder pressure significantly affect the vibration signal from the engine block. For CNG-H_2 mixtures of 20% and 30% H_2, a distinct reduction in combustion noise was observed compared to the other fuels studied.

Sharma and Dhar [88] investigated how different compression ratios (CRs) influence the maximum possible H_2 energy share in a DF ICE. A numerical model was used to examine combustion and emission characteristics with H_2 introduced via port fuel injection (PFI). They found a trade-off between maximum H_2 energy share and CR. The knock-limited maximum H_2 energy share increased from 20% to 45% as the CR was reduced from 19.5 to 14.5. With increasing H_2 energy share, emissions – except for NO_x – typically decreased across all tested CRs.

Jamrozik et al. [40] reported that investigating DF combustion with diesel and H_2 (0–30%) showed that adding up to 30% H_2 increased peak combustion pressure by 13%, increased heat release rate by 46%, and raised the maximum rate of pressure rise by 35% under full load conditions. Although efficiency improved with H_2 concentrations up to 25%, engine stability decreased at higher H_2 levels, and NO_x and HC emissions increased. Therefore, careful optimization of H_2-diesel mixtures is essential to enhance efficiency while managing emissions [91].

Pham et al. [69] examined the efficiency, combustion, and emission characteristics of ICEs using alternative fuels (H_2, NG, BD) in DF CI ICEs. Due to differing fuel properties, DF operation typically improved brake specific energy consumption (BSEC) compared to standard diesel operation.

Table 1. The characteristics of selected dual-fuel internal combustion engines powered by H_2

Refs	Model ICE type	Combustion system	H_2 supply method	Bore × stroke [mm]	Displacement [dm^3]	CR [-]	Max power [kW]/ Speed [rpm]	Max torque [Nm]/ speed [rpm]
[54]	Fiat Qubo 1.3 MultiJet 4-cylinders, vertical 4-stroke forced air cooled diesel	Multipoint injection system	H_2 is supplied from the cylinder to the inlet channel via tubing. Pressure controlled by a valve and measured with a manometer. Flow rate measured by a Vogtlin mass flow meter in the line supplying H_2 to the system	69.6 × 82	1.248	16.8:1	55/4000	190/1500
[18]	Deutz F2L511 2-cylinders, 4-stroke, air cooled, diesel	6-hole injector for adjustable diesel fuel dosing. One cylinder modified to operate in SI mode	H_2 or producer gas supplied via ~~an~~ injection system mounted on the inlet manifold or via a mixer	100 × 105	1.650 (unmodified), 0.825 (modified)	8:1; 12:1 (1 cylinder modified to operate at SI mode); 17:1 (diesel)		
[97]	Lister-Petter TR1 1-cylinder, Bowl-in-piston, air cooled diesel	3-hole direct injection. Pilot liquid fuel injected near the end of the compression phase	Bottled H_2 supplied via the intake manifold (~2% of air intake). H_2 premixed before entering the combustion chamber	98.4 × 101.6	0.773	15.45:1	8.6/2500	39.2/1800
[89]	Andoria-Mot ADCR ICE 4-cylinder, 4-stroke DF diesel ICE		The glow plugs replaced by injectors for ~~of~~ compressed H_2		2.636	17.5:1		
[64]	WEIMA 168FA 4-stroke, SI, 1-cylinder, air cooled		Unmodified light gasoline as a solvent to simulate H_2 supply		0.163		3.8/3600	
[24]	VAZ-21081 ICE, 4-stroke, 4-cylinder, gasoline	distributed FI system	H_2 supplied as a part of hybrid system	76 × 60.6	1.1	9:1	39.7/5600	77.9/3600
[8]	1-cylinder, air-cooled, (DI), 4-stroke HATZ D-series DI diesel ICE		H_2 fed into the mixer in the intake manifold. Diesel fuel flow rate controlled by a modified original diesel FI system					

However, the overall efficiency of DF ICEs – measured by BTE and volumetric efficiency – remained considerably lower. DF operation significantly increased in-cylinder pressure and heat release rate while prolonging the ignition delay. Emission characteristics revealed a trade-off between NO_x and HC emissions: NO_x, PM, and smoke decreased, depending on engine load, blend ratio, and injection timing. However, HC and CO emissions in DF ICEs were several times higher than in conventional diesel engines.

Tutak et al. [99] studied a DF ICE running on diesel and NG, with H_2 enrichment to improve the NG component. They found that increasing H_2 levels improved combustion efficiency, reducing combustion duration by 30% and halving the time to 50% mass fraction burned. The maximum H_2 energy share was determined to be 19%; beyond this, engine stability declined due to increased cycle-to-cycle variability and knocking.

Rorimpandey et al. [73] emphasized the role of injection sequence, timing, and ambient temperature on combustion. Injecting the pilot diesel before H_2 cooled and delayed H_2 ignition. In contrast, injecting H_2 first improved air–gas mixing, but lean combustion occurred if H_2 was injected later, especially at low ambient temperatures.

Bakar et al. [8] explored the effects of varying H_2 flow rates on combustion, efficiency, and emissions in a DF diesel ICE. Tests conducted at various engine speeds and H_2 flow rates revealed that specific flow rates had a significant impact on engine efficiency and emissions. In particular, BTE increased at lower flow rates due to shorter combustion duration and improved phasing, while higher flow rates increased CO, CO_2, and smoke emissions.

Numerous studies indicate that increasing the H_2 proportion in DF ICEs improves combustion efficiency and reduces emissions, but requires careful management to prevent engine instability and increased NO_x emissions.

These studies highlight the influence of CR, injection timing, and H_2 flow rate on efficiency, demonstrating that while H_2 enhances fuel efficiency and reduces emissions, careful integration is essential to ensure engine stability and prevent combustion-related issues.

Wagemakers and Leermakers [103] reported that using H_2 or SG in DF combustion generally increases NO_x emissions, likely due to higher fire temperatures and burning speeds. HC and CO emissions also tend to increase in DF combustion, primarily due to incomplete combustion of mixtures trapped in crevices. Efficiencies of various gaseous fuels are similar, with minor gains observed for H_2 and LPG, and slight reductions for NG and SG.

Hosseini et al. [38] explained that although SG is low in carbon, its use in diesel ICEs may reduce thermal efficiency and increase BSFC, mainly due to the low volumetric calorific value and high CO_2 content of SG. Nanoparticles and oxygenated additives may help compensate for this by promoting complete combustion, though further research is needed. Adding less energetic SG reduces peak heat release rate and in-cylinder pressure in diesel ICEs. The high specific heat capacity and CO_2 content of SG may also extend ignition delay. Reduced burning rates and adiabatic flame temperature may result in longer combustion duration.

Adding SG to diesel/BD fuel may increase CO, CO_2, and UHC emissions from diesel ICEs. CO in SG and high charge dilution can lead to incomplete combustion. Oxygenated additives to diesel/BD may raise CO_2 emissions due to enhanced oxidation. These additives may also increase UHC emissions, as higher heat of vaporization can lower in-cylinder temperature. Adding nanoparticles to diesel/BD could reduce UHC emissions by promoting oxidation, but further research is required [38].

Integrating SG into diesel/BD fuel may reduce NO_x emissions from diesel ICEs. SG may lower concentrations of N_2 and O_2 in the intake air, decreasing the likelihood of thermal NO_x formation. SG may reduce PM emissions by decreasing the liquid fuel injection rate, which is more prone to sooting. However, adding SG may also increase soot/smoke emissions by lowering in-cylinder O_2 concentration and causing incomplete combustion. Conversely, some studies suggest that SG can lead to more homogeneous fuel mixtures and lower local air-fuel equivalence ratios, thus reducing soot/smoke emissions [38].

Ando et al. [6] evaluated the performance of low-heating-value gases from gasification and two-stage pyrolysis/reforming in a naturally aspirated single-cylinder SI ICE with CRs of 9.4 and 11.9. The gas from gasification was rich in H_2 (lower heating value of 3.83 MJ/Nm³), while the two-stage pyrolysis gas was rich in CH_4 (lower heating value of 4.2 MJ/Nm³). A gas mixer replaced the carburetor to control the air–fuel ratio. Both fuels achieved similar BTE to CNG. The H_2-rich gas enabled stable engine operation at λ up to 2.00. Compared to both CNG and CH_4-rich pyrolysis gas, NO_x and HC emissions were significantly lower for the H_2-rich gas. The CH_4-rich gas also exhibited very low NO_x levels.

Chintala and Subramanian [16] reported that PM emissions can be notably reduced while improving thermal efficiency by using H_2 in DF ICEs (diesel-H_2). In H_2 DF ICEs, HC, CO, and smoke emissions approach zero, while CO_2 and CH_4 emissions from CI ICEs are substantially reduced. However, the maximum H_2 energy share in DF ICEs at rated load is limited to 6–25% due to elevated peak cylinder pressures and pressure rise rates, which can cause knocking and autoignition of the H_2-air mixture. In addition, NO_x emissions in DF mode are 29–58% higher than in conventional diesel mode due to high localized in-cylinder temperatures. Appropriate optimization strategies can increase the maximum H_2 energy share to 79% while reducing NO_x emissions to levels comparable to those of conventional diesel operation.

Mehra et al. [59] observed that incorporating H_2 into CNG (HCNG) ICEs enhances BTE and significantly reduces cycle-to-cycle variations (CCV) and BSFC due to H_2's combustion characteristics. HCNG is safer than pure H_2 due to its lower energy content. Under certain conditions, the thermal efficiency of HCNG ICEs is notably higher than that of CNG ICEs, without increasing harmful emissions. However, adding H_2 to natural gas increases NO_x emissions due to higher combustion temperatures. This can be mitigated by lean combustion or three-way catalyst (TWC) systems. Using EGR with TWC reduces combustion temperature, directly lowering NO_x emissions. THC, CO, CO_2, and CH_4 emissions decrease notably with H_2 addition. However, H_2 also increases the engine's tendency to knock due to peak cylinder temperatures and high ignitability. H_2 enables higher CRs without combustion instability compared to CNG, further enhancing BTE. For SI ICEs, optimal performance is achieved with 20–30% H_2 enrichment. HCNG ICEs offer better fuel efficiency than conventional CNG ICEs, and direct fuel injection (DFI) systems further reduce BSFC compared to PFI.

According to [110], blending H_2 with natural gas in SI ICEs shifts the lean limit toward a leaner mixture, increasing combustion speed and temperature. Even a small addition of H_2 by volume catalytically improves hydrocarbon ignition, and in pure CNG, the required spark advance can be reduced due to H_2's high flame speed. HCNG mixtures improve engine efficiency, especially at low loads, but with increasing H_2 content from 10% to 30%, NO_x emissions rise by 4–20% due to higher in-cylinder temperatures. Implementing about 10% EGR for HCNG blends can significantly reduce NO_x emissions and BSFC compared to natural gas. Maximum brake torque can be achieved under leaner combustion conditions by increasing H_2 content.

Hosseini et al. [38] explained that H_2 can address issues associated with using gaseous fuels (e.g., biogas, methane, CNG, NG, LPG) in diesel ICEs, including extended ignition delay, reduced engine efficiency, slower burning rates, and increased CO and UHC emissions. H_2 can improve efficiency metrics of diesel ICEs running on biogas by offsetting the low calorific value of CO_2-rich biogas and optimizing its combustion. Similarly, increasing H_2 levels can enhance efficiency in diesel ICEs running on CH_4 by accelerating combustion. Notably, CH_4 can compensate for some limitations of H_2 combustion (e.g., short quenching distance). H_2 can offset the low flame speed of CNG and NG, enhancing their combustion in diesel ICEs. H_2 can improve the BTE of LPG-fueled diesel ICEs by stabilizing the LPG flame in lean mixtures. H_2 enrichment can raise the heat release rate and in-cylinder pressure in ICEs with biogas, methane, CNG, and NG by increasing mixture calorific value and laminar flame speed. Adding H_2 may extend the combustion duration of diesel ICEs powered by

natural gas and methane by widening flammability limits. Enriching CNG and LPG with H_2 shortens combustion duration by accelerating the burning rate.

Significantly, methane (CH_4) can mitigate certain limitations of hydrogen (H_2) combustion, such as its minimal quenching distance. H_2 can effectively offset the low flame speed of compressed natural gas (CNG) and natural gas (NG), thereby enhancing their combustion in diesel internal combustion engines (ICEs). H_2 has the potential to improve the brake thermal efficiency (BTE) of diesel ICEs fueled by liquefied petroleum gas (LPG) by stabilizing the LPG flame in lean gaseous air-fuel (A/F) mixtures. H_2 enrichment can increase the heat release rate and in-cylinder pressure of diesel ICEs fueled by biogas (BG), methane, CNG, and NG by raising the calorific value and laminar flame speed of the A/F mixture. Adding H_2 may extend the combustion duration of diesel ICEs powered by natural gas and methane by broadening the flammable limits of the A/F mixture. Enriching CNG and LPG with H_2 shortens the combustion duration of diesel ICEs by accelerating the burning rate of the A/F blend [38].

The use of H_2 can reduce combustion duration in diesel ICEs by increasing the burning rate of the A/F mixture [38].

The inclusion of H_2 in BG extends the ignition delay in diesel ICEs due to a decrease in the oxygen content of the intake mixture. Conversely, the addition of H_2 to CH_4, CNG, and LPG may reduce the ignition delay in diesel ICEs due to enhanced combustion kinetics [38].

Emissions of CO and unburned hydrocarbons (UHC) from diesel ICEs can be significantly reduced by enriching BG, CH_4, CNG, NG, and LPG with H_2. This reduction is largely attributed to the partial substitution of carbon-rich fuels with H_2, which accelerates the combustion rate of the gaseous fuel. Incorporating H_2 into BG, CH_4, CNG, and NG may lower CO_2 emissions from diesel ICEs by reducing the carbon-to-hydrogen (C/H) ratio of the gas mixtures. However, H_2 may increase NO_x emissions from ICEs using BG, CH_4, CNG, or NG-diesel blends due to a rise in peak in-cylinder pressure and temperature. Introducing H_2 to LPG may positively reduce NO_x emissions from diesel ICEs by decreasing the extent of high-temperature zones around the diesel flame. Incorporating carbon-free H_2 into BG, CH_4, and CNG can reduce smoke and soot emissions from diesel ICEs. The high diffusivity of H_2 promotes thorough homogenization of the combustible mixture, improving combustion efficiency and reducing smoke emissions [38].

Emerging Indirect Regenerative Evaporative Technology (IRET), also known as the Maisotsenko cycle (M-cycle), may offer complementary benefits for H_2- and diesel-powered combustion engines [116]. When applied to the engine inlet system, this technology can significantly lower inlet air temperature and enhance charge cooling, potentially mitigating knocking, improving power density, and further reducing NO_x emissions [31] – even at high H_2 enrichment rates. The IRET's unique ability for both sensible and latent cooling with minimal water usage is particularly promising for high-efficiency, low-emission engine applications, especially under demanding or transient operating conditions. Recent R&D on Maisotsenko-powered cycles [116] suggests that when integrated with advanced engine management systems, these cooling techniques could enable more aggressive optimization of H_2 supply, EGR rates, and injection strategies, while maintaining combustion stability and minimizing particulate formation. Their adaptability to variable engine loads and ambient conditions makes them a viable candidate for next-generation engine architectures aiming to maximize renewable fuel utilization (e.g., H_2, biodiesel) and minimize environmental impact. Further experimental and numerical research is encouraged to evaluate the real-world performance and durability of such integrated systems, especially in scenarios with high combustion temperatures and aggressive emission control demands.

3. Summary

The present review enabled the current state-of-the-art to be obtained relative to dual-fuel (DF) internal combustion engines (ICEs) supplied with fuel and hydrogen (H_2). The benefits and challenges of using such engines were discussed.

The reviewed ICEs operated within a relatively narrow speed range, 1724 ±528 rpm. The displacement of such ICEs was in a wide range of 1674 ±2325 cm^3. Additionally, ICE minimal loads spanned a wide range of values, from 27.3% ±34%, and similarly, maximum loads reached values in the range of 50–100%. Of course, the ICE load could vary between 0 and 100%. The ICE's CR did not vary too much. The minimum CR reached values varied in the range of 16.41 ±4.72, while the maximum CR values varied in the range of 16.49 ±4.78; thus, variations in CR values are significant.

It should be noted in particular that for many of the analyzed engine cases, there is a lack of data regarding the effect (especially the combined one) of load, EGR, and H_2 supply on BTE and BSFC. For a slightly smaller number of such engine cases, there was a lack of data regarding the effect (especially the combined one) of load, EGR, and H_2 supply on PM, HC, NO_x, CO, and CO_2. Furthermore, comparing data for these engines was difficult because engine load was reported in either percent or bars, and H_2 supply in percent or L/min, necessitating categorization of the data into three different groups. This necessitates the development of a standard for collecting and presenting data from the tested DF ICEs.

For analyzed cases of common effect of varying load, EGR and H_2 supply on BTE and on BSFC, respectively it was found that up to 13.5% of the cases related to their lowering, almost no cases related to no effect on them, as well about 62.5–71.5% and 12.5–58.6% of the cases, respectively, related to their enhancing.

For analyzed cases of common effect of varying load, EGR and H_2 supply on PM, HC, NO_x, CO and CO_2 emissions, respectively it was found that below: 14.2%, 25%, 43.2%, 28.5% and 12.5% of the cases, respectively related to their lowering, while below 12.5%, 12.5%, 37.5%, none and none of the cases, respectively related to no effect on them, and similarly related to their enhancing. Especially positive is the role of EGR in DF ICEs.

The application of H_2 in diesel engines via the dual-fuel (DF) strategy represents a promising pathway to reduce diesel consumption, lower carbonaceous emissions, and decrease dependence on fossil fuels. The review highlights that H_2-DF combustion can significantly reduce CO, CO_2,

HC, and PM emissions, while maintaining or improving brake thermal efficiency (BTE) under optimized conditions. However, the technology faces two major technical challenges: elevated NO_x emissions and increased susceptibility to knocking, both of which are strongly influenced by H_2 concentration, engine load, and pilot fuel properties.

To address NO_x emissions, a range of strategies – including exhaust gas recirculation (EGR), selective catalytic reduction (SCR), water injection, urea dosing, external cylinder cooling, and Lean-NO_x traps – have proven effective, with EGR offering a particularly attractive solution due to H_2's tolerance for high dilution rates. Combustion stability and knock resistance can be managed by carefully adjusting the maximum H_2 inclusion rate for each engine configuration and operating scenario, though further research is needed to establish universal guidelines.

The use of H_2 in combination with biodiesel (BD) further reduces reliance on fossil fuels, but the optimal BD/H_2 blend ratio and injection strategy remain to be systematically defined. While H_2 drastically reduces total particulate matter (PM), it may increase the number of ultrafine particles, posing potential health and environmental risks that warrant further investigation.

Incorporating nanomaterials and oxygenated compounds into diesel fuel formulations has the potential to further enhance combustion efficiency and reduce emissions. However, the long-term impacts of these additives on engine durability, emissions, and aftertreatment systems require a comprehensive study. Lifecycle assessments (LCA) are also necessary to evaluate the full environmental benefits and trade-offs of H_2-DF engines, including resource use and end-of-life considerations for advanced materials.

Ultimately, integrating H_2-DF engines with hybrid electric systems may provide additional efficiency gains and enhanced transient performance. Future research should focus on system optimization, health impacts of ultrafine particles, durability of novel materials, evaluation of the viability of advanced evaporative technologies (IRET) [116] and the development of robust, adaptive control strategies for a wide range of applications.

Nomenclature

A/F	air-fuel
BD	biodiesel
BG	biogas
BSFC	brake specific fuel consumption
BP	brake power
BT	brake torque
BTE	brake thermal efficiency
CI	compression ignition
CNG	compressed natural gas
CR	compression ratio
DF	dual fuel
DI	direct injection
EGR	exhaust gas recirculation
FI	fuel injection
ICE	internal combustion engine
LPG	liquefied petroleum gas
PFI	port fuel injection
SG	syngas
SI	spark ignition
UHC	unburned hydrocarbons

Bibliography

[1] Ahmadi R, Hosseini SM. Numerical investigation on adding/substituting hydrogen in the CDC and RCCI combustion in a heavy duty engine. Appl Energy. 2018;213:450-468. https://doi.org/10.1016/j.apenergy.2018.01.048

[2] Akal D, Öztuna S, Büyükakın MK. A review of hydrogen usage in internal combustion engines (gasoline-Lpg-diesel) from combustion performance aspect. Int J Hydrog Energy. 2020;45:35257-35268. https://doi.org/10.1016/j.ijhydene.2020.02.001

[3] Alrazen HA, Abu Talib AR, Adnan R, Ahmad KA. A review of the effect of hydrogen addition on the performance and emissions of the compression – Ignition engine. Renew Sustain Energy Rev. 2016;54:785-796. https://doi.org/10.1016/j.rser.2015.10.088

[4] Amir Ridhuan, Shahrul Azmir Osman, Mas Fawzi, Ahmad Jais Alimin, Saliza Azlina Osman. A review of comparative study on the effect of hydroxyl gas in internal combustion engine (ICE) on engine performance and exhaust emission. J Adv Res Fluid Mech Therm Sci. 2021;87:1-16. https://doi.org/10.37934/arfmts.87.2.116

[5] An H, Yang WM, Maghbouli A, Li J, Chou SK, Chua KJ. A numerical study on a hydrogen assisted diesel engine. Int J Hydrog Energy. 2013;38:2919-2928. https://doi.org/10.1016/j.ijhydene.2012.12.062

[6] Ando Y, Yoshikawa K, Beck M, Endo H. Research and development of a low-BTU gas-driven engine for waste gasification and power generation. Energy. 2005;30:2206-2218. https://doi.org/10.1016/j.energy.2004.08.024

[7] Arjun TB, Atul KP, Muraleedharan AP, Walton PA, Bijinraj PB, Raj AA. A review on analysis of HHO gas in IC engines. Mater Today Proc. 2019;11:1117-1129. https://doi.org/10.1016/j.matpr.2018.12.046

[8] Bakar RA, Widudo K, Ramasamy D, Yusaf T, Kamarulzaman MK et al. Experimental analysis on the performance, combustion/emission characteristics of a DI diesel engine using hydrogen in dual fuel mode. Int J Hydrog Energy. 2024; 52:843-860. https://doi.org/10.1016/j.ijhydene.2022.04.129

[9] Banerjee R, Roy S, Bose PK. Hydrogen-EGR synergy as a promising pathway to meet the PM–NOx–BSFC trade-off contingencies of the diesel engine: A comprehensive review. Int J Hydrog Energy. 2015;40:12824-12847. https://doi.org/10.1016/j.ijhydene.2015.07.098

[10] Barrios CC, Domínguez-Sáez A, Hormigo D. Influence of hydrogen addition on combustion characteristics and particle number and size distribution emissions of a TDI diesel engine. Fuel. 2017;199:162-168. https://doi.org/10.1016/j.fuel.2017.02.089

[11] Bazrafshan J, Jazayeri SA, Salarian H, Ebrahimi M, Khaleghinia J. The effect of hydrogen addition on a RCCI engine performance fueled with natural gas\diesel fuel at low load range. J Engine Res. 2022;65:60-74. https://doi.org/10.22034/er.2022.697906

[12] Bika AS, Franklin LM, Kittelson DB. Emissions effects of hydrogen as a supplemental fuel with diesel and biodiesel. SAE Int J Fuels Lubr. 2008;1:283-292. https://doi.org/10.4271/2008-01-0648

[13] Burtscher H. Physical characterization of particulate emissions from diesel engines: a review. J Aerosol Sci. 2005;36: 896-932. https://doi.org/10.1016/j.jaerosci.2004.12.001
[14] Castro N, Toledo M, Amador G. An experimental investigation of the performance and emissions of a hydrogen-diesel dual fuel compression ignition internal combustion engine. Appl Therm Eng. 2019;156:660-667. https://doi.org/10.1016/j.applthermaleng.2019.04.078
[15] Chaichan MT. Performance and emission characteristics of CIE using hydrogen, biodiesel, and massive EGR. Int J Hydrog Energy. 2018;43:5415-5435. https://doi.org/10.1016/j.ijhydene.2017.09.072
[16] Chintala V, Subramanian KA. A comprehensive review on utilization of hydrogen in a compression ignition engine under dual fuel mode. Renew Sustain Energy Rev. 2017;70: 472-491. https://doi.org/10.1016/j.rser.2016.11.247
[17] Chojnowski J, Karczewski M, Szamrej GA. Dual-fuel engines using hydrogen-enriched fuels as an ecological source of energy for transport, industry and power engineering. Combustion Engines. 2024;198:3-12. https://doi.org/10.19206/CE-176800
[18] Cupiał K, Szwaja S. Producer gas combustion in the internal combustion engine. Combustion Engines. 2010;141:27-32. https://doi.org/10.19206/CE-117143
[19] Das S, Kashyap D, Kalita P, Kulkarni V, Itaya Y. Clean gaseous fuel application in diesel engine: a sustainable option for rural electrification in India. Renew Sustain Energy Rev. 2020;117:109485. https://doi.org/10.1016/j.rser.2019.109485
[20] Deb M, Sastry GRK, Bose PK, Banerjee R. An experimental study on combustion, performance and emission analysis of a single cylinder, 4-stroke DI-diesel engine using hydrogen in dual fuel mode of operation. Int J Hydrog Energy. 2015; 40:8586-8598. https://doi.org/10.1016/j.ijhydene.2015.04.125
[21] Debnath BK, Saha UK, Sahoo N. Effect of hydrogen-diesel quantity variation on brake thermal efficiency of a dual fuelled diesel engine. J Power Technol. 2012;92:55-67.
[22] Deheri C, Acharya SK, Thatoi DN, Mohanty AP. A review on performance of biogas and hydrogen on diesel engine in dual fuel mode. Fuel. 2020;260:116337. https://doi.org/10.1016/j.fuel.2019.116337
[23] Demirci A, Koten H, Gumus M. The effects of small amount of hydrogen addition on performance and emissions of a direct injection compression ignition engine. Therm Sci. 2018;22:1395-1404. https://doi.org/10.2298/TSCI170802004D
[24] Depczyński WP, Marchenko A, Mishchenko S, Mishchenko M. The effect of hydrogen addition to traditional petrol engine fuel in a hybrid power plant on its environmental performance and fuel efficiency. Combustion Engines. 2025; 200(1):87-94. https://doi.org/10.19206/CE-199735
[25] Dhole AE, Yarasu RB, Lata DB, Baraskar SS. Mathematical modeling for the performance and emission parameters of dual fuel diesel engine using hydrogen as secondary fuel. Int J Hydrog Energy. 2014;39:12991-13001. https://doi.org/10.1016/j.ijhydene.2014.06.084
[26] Dhole AE, Yarasu RB, Lata DB, Priyam A. Effect on performance and emissions of a dual fuel diesel engine using hydrogen and producer gas as secondary fuels. Int J Hydrog Energy. 2014;39:8087-8097. https://doi.org/10.1016/j.ijhydene.2014.03.085
[27] Dimitriou P, Tsujimura T. A review of hydrogen as a compression ignition engine fuel. Int J Hydrog Energy. 2017;42: 24470-24486. https://doi.org/10.1016/j.ijhydene.2017.07.232
[28] Dimitriou P, Tsujimura T, Suzuki Y. Low-load hydrogen-diesel dual-fuel engine operation – a combustion efficiency improvement approach. Int J Hydrog Energy. 2019;44: 17048-17060. https://doi.org/10.1016/j.ijhydene.2019.04.203
[29] Fabiś P, Flekiewicz B, Flekiewicz M. On board recognition of different fuels in SI engines with the use of dimensional and non-dimensional vibration signal parameters. Combustion Engines. 2009;136:69-75. https://doi.org/10.19206/CE-117222
[30] Firmansyah, Aziz ARA, Heikal MR, Abidin EZZ, Panchatcharam N. Reactivity controlled compression ignition (RCCI) of gasoline-CNG mixtures. Ceper BA, Yldz M, ed. Improv. Trends Intern. Combust. Engines, InTech; 2018. https://doi.org/10.5772/intechopen.72880
[31] Foss K, Brunet M, Todd J, Ramirez C, Karakra M, Beyer C. Diesel NOx reduction using the Maisotsenko cycle. College of Engineering Department of Mechanical & Aerospace Engineering: California State University, Long Beach; 2013.
[32] Ghazal OH. Performance and combustion characteristic of CI engine fueled with hydrogen enriched diesel. Int J Hydrog Energy. 2013;38:15469-15476. https://doi.org/10.1016/j.ijhydene.2013.09.037
[33] Godiganur S, Suryanarayana Murthy CH, Reddy RP. 6BTA 5.9 G2-1 Cummins engine performance and emission tests using methyl ester mahua (Madhuca indica) oil/diesel blends. Renew Energy. 2009;34:2172-2177. https://doi.org/10.1016/j.renene.2008.12.035
[34] Gürbüz H, Sandalcı T. Numerical analysis of diesel injection strategies on emissions and performance in CH4/diesel powered RCCI diesel engine with high ratio EGR. Alex Eng J. 2023;64:517-526. https://doi.org/10.1016/j.aej.2022.09.012
[35] Hamdan MO, Selim MYE, Al-Omari S-AB, Elnajjar E. Hydrogen supplement co-combustion with diesel in compression ignition engine. Renew Energy. 2015;82:54-60. https://doi.org/10.1016/j.renene.2014.08.019
[36] Han W, Lu Y, Jin C, Tian X, Peng Y, Pan S et al. Study on influencing factors of particle emissions from a RCCI engine with variation of premixing ratio and total cycle energy. Energy. 2020;202:117707. https://doi.org/10.1016/j.energy.2020.117707
[37] Hoang AT, Pham VV. A study on a solution to reduce emissions by using hydrogen as an alternative fuel for a diesel engine integrated exhaust gas recirculation, Namakkal, India: 2020:020035. https://doi.org/10.1063/5.0007492
[38] Hosseini SH, Tsolakis A, Alagumalai A, Mahian O, Lam SS, Pan J et al. Use of hydrogen in dual-fuel diesel engines. Prog Energy Combust Sci. 2023;98:101100. https://doi.org/10.1016/j.pecs.2023.101100
[39] Hosseinzadeh-Bandbafha H, Khalife E, Tabatabaei M, Aghbashlo M, Khanali M, Mohammadi P et al. Effects of aqueous carbon nanoparticles as a novel nanoadditive in water-emulsified diesel/biodiesel blends on performance and emissions parameters of a diesel engine. Energy Convers Manag. 2019;196:1153-1166. https://doi.org/10.1016/j.enconman.2019.06.077
[40] Jamrozik A, Grab-Rogaliński K, Tutak W. Hydrogen effects on combustion stability, performance and emission of diesel engine. Int J Hydrog Energy. 2020;45:19936-19947. https://doi.org/10.1016/j.ijhydene.2020.05.049
[41] Kakoee A, Gharehghani A. Comparative study of hydrogen addition effects on the natural-gas/diesel and natural-gas/dimethyl-ether reactivity controlled compression ignition mode of operation. Energy Convers Manag. 2019;196: 92-104. https://doi.org/10.1016/j.enconman.2019.05.113

[42] Karagöz Y, Güler İ, Sandalcı T, Yüksek L, Dalkılıç AS. Effect of hydrogen enrichment on combustion characteristics, emissions and performance of a diesel engine. Int J Hydrog Energy. 2016;41:656-665. https://doi.org/10.1016/j.ijhydene.2015.09.064

[43] Karagöz Y, Sandalcı T, Yüksek L, Dalkılıç AS. Engine performance and emission effects of diesel burns enriched by hydrogen on different engine loads. Int J Hydrog Energy. 2015;40:6702-6713. https://doi.org/10.1016/j.ijhydene.2015.03.141

[44] Kokjohn SL, Hanson RM, Splitter DA, Reitz RD. Fuel reactivity controlled compression ignition (RCCI): a pathway to controlled high-efficiency clean combustion. Int J Engine Res. 2011;12:209-226. https://doi.org/10.1177/1468087411401548

[45] Köse H, Ciniviz M. An experimental investigation of effect on diesel engine performance and exhaust emissions of addition at dual fuel mode of hydrogen. Fuel Process Technol. 2013;114:26-34. https://doi.org/10.1016/j.fuproc.2013.03.023

[46] Koten H. Hydrogen effects on the diesel engine performance and emissions. Int J Hydrog Energy. 2018;43:10511-10519. https://doi.org/10.1016/j.ijhydene.2018.04.146

[47] Kumar RS, Loganathan M, Gunasekaran EJ. Performance, emission and combustion characteristics of CI engine fuelled with diesel and hydrogen. Front Energy. 2015;9:486-494. https://doi.org/10.1007/s11708-015-0368-4

[48] Li J, Ling X, Liu D, Yang W, Zhou D. Numerical study on double injection techniques in a gasoline and biodiesel fueled RCCI (reactivity controlled compression ignition) engine. Appl Energy. 2018;211:382-392. https://doi.org/10.1016/j.apenergy.2017.11.062

[49] Li J, Yang W, Zhou D. Review on the management of RCCI engines. Renew Sustain Energy Rev. 2017;69:65-79. https://doi.org/10.1016/j.rser.2016.11.159

[50] Li J, Yang WM, An H, Zhao D. Effects of fuel ratio and injection timing on gasoline/biodiesel fueled RCCI engine: a modeling study. Appl Energy. 2015;155:59-67. https://doi.org/10.1016/j.apenergy.2015.05.114

[51] Li J, Yang WM, Goh TN, An H, Maghbouli A. Study on RCCI (reactivity controlled compression ignition) engine by means of statistical experimental design. Energy. 2014;78: 777-787. https://doi.org/10.1016/j.energy.2014.10.071

[52] Lilik GK, Zhang H, Herreros JM, Haworth DC, Boehman AL. Hydrogen assisted diesel combustion. Int J Hydrog Energy. 2010;35:4382-4398. https://doi.org/10.1016/j.ijhydene.2010.01.105

[53] Longwic R, Tatarynow D, Kuszneruk M, Wozniak-Borawska G. Preliminary tests of a Diesel engine powered by diesel and hydrogen. Combustion Engines. 2023;195(4): 35-39. https://doi.org/10.19206/CE-169485

[54] Longwic R, Woźniak G, Sander P. Compression-ignition engine fuelled with diesel and hydrogen engine acceleration process. Combustion Engines. 2020;180:47-51. https://doi.org/10.19206/CE-2020-108

[55] Luo Q, Hu J-B, Sun B, Liu F, Wang X, Li C et al. Experimental investigation of combustion characteristics and NOx emission of a turbocharged hydrogen internal combustion engine. Int J Hydrog Energy. 2019;44:5573-5584. https://doi.org/10.1016/j.ijhydene.2018.08.184

[56] Masood M, Ishrat MM. Computer simulation of hydrogen–diesel dual fuel exhaust gas emissions with experimental verification. Fuel. 2008;87:1372-1378. https://doi.org/10.1016/j.fuel.2007.07.001

[57] Masood M, Mehdi SN, Ram Reddy P. Experimental investigations on a hydrogen-diesel dual fuel engine at different compression ratios. J Eng Gas Turbines Power. 2007;129: 572-578. https://doi.org/10.1115/1.2227418

[58] McWilliam L, Megaritis A. Experimental investigation of the effect of combined hydrogen and diesel combustion on the particulate size distribution from a high speed direct injection diesel engine. Int J Veh Des. 2009;50:107. https://doi.org/10.1504/IJVD.2009.024970

[59] Mehra RK, Duan H, Juknelevičius R, Ma F, Li J. Progress in hydrogen enriched compressed natural gas (HCNG) internal combustion engines – a comprehensive review. Renew Sustain Energy Rev. 2017;80:1458-1498. https://doi.org/10.1016/j.rser.2017.05.061

[60] Mohankumar S, Senthilkumar P. Particulate matter formation and its control methodologies for diesel engine: A comprehensive review. Renew Sustain Energy Rev. 2017; 80:1227-1238. https://doi.org/10.1016/j.rser.2017.05.133

[61] Monemian E, Cairns A, Gilmore M, Newman D, Scott K. Evaluation of intake charge hydrogen enrichment in a heavy-duty diesel engine. Proc Inst Mech Eng Part J Automob Eng. 2018;232:139-147. https://doi.org/10.1177/0954407017738375

[62] Naber J. Hydrogen combustion under diesel engine conditions. Int J Hydrog Energy. 1998;23:363-371. https://doi.org/10.1016/S0360-3199(97)00083-9

[63] Nag S, Sharma P, Gupta A, Dhar A. Experimental study of engine performance and emissions for hydrogen diesel dual fuel engine with exhaust gas recirculation. Int J Hydrog Energy. 2019;44:12163-12175. https://doi.org/10.1016/j.ijhydene.2019.03.120

[64] Noga M, Moskal T. Evaluation of a pressure sensing glow plug in terms of its application possibility to control the combustion process of a hydrogen-powered spark-ignition engine. Combustion Engines. 2024;196:140-145. https://doi.org/10.19206/CE-172820

[65] Owston R, Magi V, Abraham J. Wall interactions of hydrogen flames compared with hydrocarbon flames. SAE Technical Paper 2007-01-1466. 2007. https://doi.org/10.4271/2007-01-1466

[66] Ozgur T, Tosun E, Ozgur C, Tuccar G, Aydın K. Numerical studies of engine performance, emission and combustion characteristics of a diesel engine fuelled with hydrogen blends. Adv Mater Res. 2014;1016:582-586. https://doi.org/10.4028/www.scientific.net/AMR.1016.582

[67] Pan H, Pournazeri S, Princevac M, Miller JW, Mahalingam S, Khan MY, et al. Effect of hydrogen addition on criteria and greenhouse gas emissions for a marine diesel engine. Int J Hydrog Energy. 2014;39:11336-11345. https://doi.org/10.1016/j.ijhydene.2014.05.010

[68] Paparao J, Murugan S. Oxy-hydrogen gas as an alternative fuel for heat and power generation applications – a review. Int J Hydrog Energy. 2021;46:37705-37735. https://doi.org/10.1016/j.ijhydene.2021.09.069

[69] Pham Q, Park S, Agarwal AK, Park S. Review of dual-fuel combustion in the compression-ignition engine: Spray, combustion, and emission. Energy. 2022;250:123778. https://doi.org/10.1016/j.energy.2022.123778

[70] Purayil STP, Hamdan MO, Al-Omari SAB, Selim MYE, Elnajjar E. Review of hydrogen–gasoline SI dual fuel engines: engine performance and emission. Energy Rep. 2023; 9:4547-4573. https://doi.org/10.1016/j.egyr.2023.03.054

[71] Putrasari Y, Praptijanto A, Nur A, Santoso WB, Pratama M, Dimyani A et al. Thermal efficiency and emission characteristics of a diesel-hydrogen dual fuel CI engine at various loads condition. J Mechatron Electr Power Veh Technol. 2018;9:49-56. https://doi.org/10.14203/j.mev.2018.v9.49-56

[72] Qin Z, Yang Z, Jia C, Duan J, Wang L. Experimental study on combustion characteristics of diesel–hydrogen dual-fuel engine. J Therm Anal Calorim. 2020;142:1483-1491. https://doi.org/10.1007/s10973-019-09147-y
[73] Rorimpandey P, Yip HL, Srna A, Zhai G, Wehrfritz A, Kook S et al. Hydrogen-diesel dual-fuel direct-injection (H2DDI) combustion under compression-ignition engine conditions. Int J Hydrog Energy. 2023;48:766-783. https://doi.org/10.1016/j.ijhydene.2022.09.241
[74] Rosha P, Dhir A, Mohapatra SK. Influence of gaseous fuel induction on the various engine characteristics of a dual fuel compression ignition engine: A review. Renew Sustain Energy Rev. 2018;82:3333-3349. https://doi.org/10.1016/j.rser.2017.10.055
[75] Sahoo PK, Das LM, Babu MKG, Naik SN. Biodiesel development from high acid value polanga seed oil and performance evaluation in a CI engine. Fuel. 2007;86:448-454. https://doi.org/10.1016/j.fuel.2006.07.025
[76] Salahi MM, Esfahanian V, Gharehghani A, Mirsalim M. Investigating the reactivity controlled compression ignition (RCCI) combustion strategy in a natural gas/diesel fueled engine with a pre-chamber. Energy Convers Manag. 2017; 132:40-53. https://doi.org/10.1016/j.enconman.2016.11.019
[77] Sandalcı T, Karagöz Y. Experimental investigation of the combustion characteristics, emissions and performance of hydrogen port fuel injection in a diesel engine. Int J Hydrog Energy. 2014;39:18480-18489. https://doi.org/10.1016/j.ijhydene.2014.09.044
[78] Saravanan N, Nagarajan G. Performance and emission studies on port injection of hydrogen with varied flow rates with Diesel as an ignition source. Appl Energy. 2010;87: 2218-2229. https://doi.org/10.1016/j.apenergy.2010.01.014
[79] Saravanan N, Nagarajan G. Hydrogen-diesel dual fuel combustion in a direct injection diesel engine. Int J Renew Energy Technol. 2011;2:259. https://doi.org/10.1504/IJRET.2011.040863
[80] Saravanan N, Nagarajan G. An experimental investigation of hydrogen-enriched air induction in a diesel engine system. Int J Hydrog Energy. 2008;33:1769-1775. https://doi.org/10.1016/j.ijhydene.2007.12.065
[81] Saravanan N, Nagarajan G. An experimental investigation on optimized manifold injection in a direct-injection diesel engine with various hydrogen flowrates. Proc Inst Mech Eng Part J Automob Eng. 2007;221:1575-1584. https://doi.org/10.1243/09544070JAUTO609
[82] Saravanan N, Nagarajan G. Performance and emission study in manifold hydrogen injection with diesel as an ignition source for different start of injection. Renew Energy. 2009;34:328-334. https://doi.org/10.1016/j.renene.2008.04.023
[83] Saravanan N, Nagarajan G, Dhanasekaran C, Kalaiselvan KM. Experimental investigation of hydrogen fuel injection in DI dual fuel diesel engine. SAE Technical Paper 2007-01-1465. 2007. https://doi.org/10.4271/2007-01-1465
[84] Saravanan N, Nagarajan G, Kalaiselvan KM, Dhanasekaran C. An experimental investigation on hydrogen as a dual fuel for diesel engine system with exhaust gas recirculation technique. Renew Energy. 2008;33:422-427. https://doi.org/10.1016/j.renene.2007.03.015
[85] Saravanan N, Nagarajan G, Sanjay G, Dhanasekaran C, Kalaiselvan KM. Combustion analysis on a DI diesel engine with hydrogen in dual fuel mode. Fuel. 2008;87:3591-3599. https://doi.org/10.1016/j.fuel.2008.07.011
[86] Shadidi B, Najafi G, Yusaf T. A Review of hydrogen as a fuel in internal combustion engines. Energies. 2021;14: 6209. https://doi.org/10.3390/en14196209
[87] Sharma P, Dhar A. Effect of hydrogen supplementation on engine performance and emissions. Int J Hydrog Energy. 2018;43:7570-7580. https://doi.org/10.1016/j.ijhydene.2018.02.181
[88] Sharma P, Dhar A. Compression ratio influence on combustion and emissions characteristic of hydrogen diesel dual fuel CI engine: Numerical Study. Fuel. 2018;222:852-858. https://doi.org/10.1016/j.fuel.2018.02.108
[89] Siadkowska K, Barański G. Combustion stability for early and late direct hydrogen injection in a dual fuel diesel engine. Combustion Engines. 2024;196:89-98. https://doi.org/10.19206/CE-171390
[90] SinghYadav V, Soni SL, Sharma D. Performance and emission studies of direct injection C.I. engine in duel fuel mode (hydrogen-diesel) with EGR. Int J Hydrog Energy. 2012;37: 3807-3817. https://doi.org/10.1016/j.ijhydene.2011.04.163
[91] Skobiej K. A review of hydrogen combustion and its impact on engine performance and emissions. Combustion Engines. 2025;200(1):64-70. https://doi.org/10.19206/CE-195470
[92] Stępień Z. Analysis of the prospects for hydrogen-fuelled internal combustion engines. Combustion Engines. 2024; 197(2):32-41. https://doi.org/10.19206/CE-174794
[93] Sutkowski M, Mareczek M. Operational experience and new developments for industrial gas engines fuelled with hydrogen fuels. Combustion Engines. 2024;197(2):146-151. https://doi.org/10.19206/CE-183185
[94] Talibi M, Hellier P, Balachandran R, Ladommatos N. Effect of hydrogen-diesel fuel co-combustion on exhaust emissions with verification using an in–cylinder gas sampling technique. Int J Hydrog Energy. 2014;39:15088-15102. https://doi.org/10.1016/j.ijhydene.2014.07.039
[95] Thiyagarajan S, Sonthalia A, Edwin Geo V, Chokkalingam B. Effect of waste exhaust heat on hydrogen production and its utilization in CI engine. Int J Hydrog Energy. 2020;45: 5987-5996. https://doi.org/10.1016/j.ijhydene.2019.06.032
[96] Thiyagarajan S, Varuvel E, Karthickeyan V, Sonthalia A, Kumar G, Saravanan CG et al. Effect of hydrogen on compression-ignition (CI) engine fueled with vegetable oil/biodiesel from various feedstocks: A review. Int J Hydrog Energy. 2022;47:37648-37667. https://doi.org/10.1016/j.ijhydene.2021.12.147
[97] Tira HS, Gill SS, Theinnoi K, Shenker J, Lau CS, Tsolakis A et al. The study of simulated biogas on combustion and emission characteristics in compression ignition engines. Combustion Engines. 2010;141:47-55. https://doi.org/10.19206/CE-117146
[98] Tripathi G, Dhar A, Sadiki A. Recent advancements in aftertreatment technology for internal combustion engines – an overview. Srivastava DK, Agarwal AK, Datta A, Maurya RK, ed. Adv. Intern. Combust. Engine Res., Singapore: Springer Singapore; 2018:159-179. https://doi.org/10.1007/978-981-10-7575-9_8
[99] Tutak W, Jamrozik A, Grab-Rogaliński K. Effect of natural gas enrichment with hydrogen on combustion process and emission characteristic of a dual fuel diesel engine. Int J Hydrog Energy. 2020;45:9088-9097. https://doi.org/10.1016/j.ijhydene.2020.01.080
[100] Varde K, Frame G. Hydrogen aspiration in a direct injection type diesel engine-its effects on smoke and other engine performance parameters. Int J Hydrog Energy. 1983;8:549-555. https://doi.org/10.1016/0360-3199(83)90007-1
[101] Verma S, Kumar K, Das LM, Kaushik SC, Tyagi SK. Experimental analysis on the effect of hydrogen supply systems in a diesel dual fuel engine. J Energy Env Sustain. 2019;7:59-62.
[102] Verma S, Suman A, Das LM, Kaushik SC, Tyagi SK. A renewable pathway towards increased utilization of hydro-

gen in diesel engines. Int J Hydrog Energy. 2020;45:5577-5587. https://doi.org/10.1016/j.ijhydene.2019.05.213
[103] Wagemakers AMLM, Leermakers CAJ. Review on the effects of dual-fuel operation, using diesel and gaseous fuels, on emissions and performance. SAE Technical Paper 2012-01-0869. 2012. https://doi.org/10.4271/2012-01-0869
[104] Wang L, Hong C, Li X, Yang Z, Guo S, Li Q. Review on blended hydrogen-fuel internal combustion engines: A case study for China. Energy Rep. 2022;8:6480-6498. https://doi.org/10.1016/j.egyr.2022.04.079
[105] Wang Z, Li L, Wang J, Reitz RD. Effect of biodiesel saturation on soot formation in diesel engines. Fuel. 2016;175:240-248. https://doi.org/10.1016/j.fuel.2016.02.048
[106] Wei Y, Wang K, Wang W, Liu S, Chen X, Yang Y et al. Comparison study on the emission characteristics of diesel- and dimethyl ether-originated particulate matters. Appl Energy. 2014;130:357-369. https://doi.org/10.1016/j.apenergy.2014.05.058
[107] Yang Z, Chu C, Wang L, Huang Y. Effects of H2 addition on combustion and exhaust emissions in a diesel engine. Fuel. 2015;139:190-197. https://doi.org/10.1016/j.fuel.2014.08.057
[108] Yilmaz IT, Gumus M. Effects of hydrogen addition to the intake air on performance and emissions of common rail diesel engine. Energy. 2018;142:1104-1113. https://doi.org/10.1016/j.energy.2017.10.018
[109] Zare A, Nabi MN, Bodisco TA, Hossain FM, Rahman MM, Ristovski ZD et al. The effect of triacetin as a fuel additive to waste cooking biodiesel on engine performance and exhaust emissions. Fuel. 2016;182:640-649. https://doi.org/10.1016/j.fuel.2016.06.039
[110] Zareei J. A Review on numerical and experimental results of hydrogen addition to natural gas in internal combustion engines. Int J Renew Sustain Energy. 2014;3:6. https://doi.org/10.11648/j.ijrse.20140301.12
[111] Zhou DZ, Yang WM, An H, Li J. Application of CFD-chemical kinetics approach in detecting RCCI engine knocking fuelled with biodiesel/methanol. Appl Energy. 2015;145:255-264. https://doi.org/10.1016/j.apenergy.2015.02.058
[112] Zhou JH, Cheung CS, Leung CW. Combustion, performance, regulated and unregulated emissions of a diesel engine with hydrogen addition. Appl Energy. 2014;126:1-12. https://doi.org/10.1016/j.apenergy.2014.03.089
[113] Zhou JH, Cheung CS, Leung CW. Combustion, performance and emissions of ULSD, PME and B50 fueled multi-cylinder diesel engine with naturally aspirated hydrogen. Int J Hydrog Energy. 2013;38:14837-14848. https://doi.org/10.1016/j.ijhydene.2013.08.128
[114] Zhou JH, Cheung CS, Zhao WZ, Leung CW. Diesel–hydrogen dual-fuel combustion and its impact on unregulated gaseous emissions and particulate emissions under different engine loads and engine speeds. Energy. 2016;94:110-123. https://doi.org/10.1016/j.energy.2015.10.105
[115] Zhou JH, Cheung CS, Zhao WZ, Ning Z, Leung CW. Impact of intake hydrogen enrichment on morphology, structure and oxidation reactivity of diesel particulate. Appl Energy. 2015;160:442-455. https://doi.org/10.1016/j.apenergy.2015.09.036
[116] Zhu G, Chow T-T, Maisotsenko VS, Wen T. Maisotsenko power cycle technologies: Research, development and future needs. Appl Therm Eng. 2023;223:120023. https://doi.org/10.1016/j.applthermaleng.2023.120023

Mariusz J. Nieścioruk, MEng. – mjniescioruk AEI, Poland.
e-mail: *mariusz.j@niescioruk.eu*

Prof. Gustavo Ozuna – Department of Industrial Engineering and Systems, Hermosillo 83000, University of Sonora, Mexico.
e-mail: *gozuna@industrial.uson.mx*

Prof. Andrei-Alexandru Boroiu, DSc., DEng. – Faculty of Mechanics and Technology, National University of Science and Technology, Politehnica Bucharest, Romania.
e-mail: *andrei.boroiu@upb.ro*

Prof. Agustín Brau Ávila, DSc., DEng. – Department of Industrial Engineering and Systems, Hermosillo 83000, University of Sonora, Mexico.
e-mail: *agustin.brau@unison.mx*

Przemyslaw Kubiak, DSc., DEng. – Institute of Vehicles and Construction Machinery Engineering, Warsaw University of Technology, Poland.
e-mail: *przemyslaw.kubiak@pw.edu.pl*

Marek Wozniak, DSc., DEng. – Department of Vehicles and Fundamentals of Machine Design, Lodz University of Technology, Poland.
e-mail: *marek.wozniak.1@p.lodz.pl*

Dmytro Levchenko, DEng. – Division of Ecotechnics, Lodz University of Technology, Poland.
e-mail: *dmytro.levchenko@p.lodz.pl*

Krzysztof Siczek, DSc., DEng. – Department of Vehicles and Fundamentals of Machine Design, Lodz University of Technology, Poland.
e-mail: *ks670907@p.lodz.pl*

Constantin Onescu, DEng. – Department of Manufacturing and Industrial Management, University of Pitesti, Romania.
e-mail: *constantin.onescu@gmail.com*

Article citation info:
Sitnik L, Andrych-Zalewska M, Mielinska A. Method of assessing the fuel consumption of a car engine in its long-term natural operation. Combustion Engines. 2026;206(3):61-67. https://doi.org/10.19206/CE-216340

Lech SITNIK
Monika ANDRYCH-ZALEWSKA
Anna MIELINSKA

Combustion Engines
Polish Scientific Society of Combustion Engines

Method of assessing the fuel consumption of a car engine in its long-term natural operation

ARTICLE INFO

Received: 10 May 2025
Revised: 10 October 2025
Accepted: 2 January 2025
Available online: 9 February 2026

The article presents a method based on the theory of cumulative fuel consumption. The outline of the method is presented using data from long-term (many years), natural operation of a middle-class passenger car covering a mileage of over 320,000 km and 647 refuelings. The results of the research and analyses turned out to be extremely adequate for the operational data. The correlation coefficient of the mathematical model describing CFC (cumulative fuel consumption) as a function of mileage (km) was $R^2 > 0.9999$. Such an analysis result can be the basis for determining the ICFC (intensity of cumulative fuel consumption) and SCFC (specifically cumulative fuel consumption) courses as a function of mileage curves (irrespective of other parameters, such as ambient temperature). The three models mentioned collectively constitute the vehicle's energy footprint. It has been shown that the assessment of vehicle fuel consumption created solely on the basis of known indicators, such as FE (average fuel consumption between cycles or its average value (AFE) may not be adequate for assessing the fuel consumption of the car engine, and that is a new finding in the literature on this topic.

Key words: *natural operation, long-term, car engine. fuel consumption, assessing method*

This is an open access article under the CC BY license (http://creativecommons.org/licenses/by/4.0/)

1. Introduction

The fuel consumption is a critical parameter for assessing the performance of combustion engine vehicles (ICEVs) in real-world conditions. Fuel consumption depends on many factors, including driver behavior, traffic conditions, vehicle load, vehicle technical condition, as well as terrain and climate.

The multitude of these factors influencing fuel consumption is not reflected in laboratory tests conducted under standardized driving cycles such as the "old" NEDC (New European Driving Cycle) or the "new" WLTP (Worldwide Harmonized Light Vehicles Test Procedure).

The discrepancies between fuel consumption values determined in laboratory tests and real-world fuel consumption are widely documented, often showing that real-world fuel consumption is significantly higher than the official values.

The problem, however, is how the fuel consumption is determined in real-world driving conditions. The issues related to this are addressed in this article, which presents an original method for assessing fuel consumption in the long-term natural operation of vehicles.

The accurate assessment of long-term fuel consumption in natural operation (i.e., real-life vehicle use over an extended period) is essential for multiple stakeholders, including:

1) Vehicle manufacturers, who must design more fuel-efficient vehicles while complying with emissions regulations

For vehicle manufacturers, real-world fuel consumption is a crucial design parameter that influences consumer choices and compliance with regulations. The growing emphasis on corporate average fuel economy (CAFE) standards [5] and CO_2 emission targets compels manufacturers to:

- develop lighter, more aerodynamic vehicle structures
- improve engine efficiency and integrate hybridization technologies
- optimize powertrain management systems for better fuel economy in variable driving conditions.

Failure to meet regulatory requirements can result in heavy fines and loss of market competitiveness.

2) Individual consumers, who seek fuel-efficient vehicles to reduce operating costs

For individual (private) vehicle users, fuel costs constitute a significant portion of total vehicle ownership expenses. Real-world fuel consumption data allow consumers to:

- make informed decisions when purchasing vehicles
- adapt eco-driving techniques to minimize fuel use
- optimize vehicle maintenance to prevent excessive fuel consumption.

A discrepancy between laboratory and real-world fuel consumption [2] can lead to dissatisfaction, as many consumers base their purchase decisions on official fuel efficiency ratings.

3) Fleet operators, who rely on precise fuel data for cost-effective transportation management

For businesses operating large vehicle fleets, fuel expenses have a direct impact on operational costs and profitability. Logistics and transportation companies use fuel consumption data for:

- fleet optimization, including route planning and load management
- driver training programs to enhance fuel efficiency through better driving practices
- monitoring and reducing carbon footprints to meet sustainability targets.

Studies indicate that fuel-efficient fleet management can reduce fuel costs by up to 20% through data-driven decision-making [8].

4) Policy makers, who need realistic data to shape regulations, taxation policies, and environmental strategies at local, national, and global levels.

At local, national, and global levels, policymakers rely on real-world fuel consumption data to:

– implement realistic fuel economy and emissions standards
– design policies that promote alternative fuels and electric mobility
– develop urban planning solutions that optimize public transportation and traffic flow.

As cities and governments strive for the decarbonization of transportation, accurately assessing fuel consumption is crucial to ensure effective environmental policies and sustainable transportation planning [1, 16].

Given the rising fuel costs and stringent environmental policies aimed at reducing carbon emissions and urban air pollution, assessing real-world fuel consumption is crucial for improving economic efficiency and environmental sustainability in the transportation sector.

The multifaceted relationship between fuel consumption and human health [4] is also important, as the combustion of fossil fuels in transportation causes the emission of harmful pollutants that have a significant impact on public health and contribute to external costs borne not directly by vehicle users, but by society as a whole.

We know that the primary pollutants generated from fuel combustion in ICEV-s include particulate matter ($PM_{2.5}$ and PM_{10}), nitrogen oxides (NO_x), carbon monoxide (CO), volatile organic compounds (VOCs), sulphur dioxide (SO_x), and greenhouse gases (GHGs) such as carbon dioxide (CO_2). These emissions contribute to climate change and associated health risks. Studies by the World Health Organization (WHO) and the European Environment Agency (EEA) indicate that air pollution from vehicle emissions is responsible for millions of premature deaths annually, with urban areas being particularly affected due to high traffic density.

The external costs [6] of these health impacts are substantial. The OECD estimates that the economic burden of air pollution-related diseases, encompassing healthcare expenditures, lost productivity, and reduced life expectancy, amounts to over 5% of global GDP.

In conclusion, the adverse health effects of fuel consumption extend far beyond individual vehicle users, imposing significant social, economic, and environmental burdens. Urgent action is needed to reduce transport-related fuel consumption and emissions [9], improve air quality, and mitigate climate-related health risks through technological advancements, behavioural changes, and regulatory measures. However, this cannot be achieved without adequate methods to assess the actual fuel consumption of vehicles in their long-term (over many years) natural operation.

2. Objectives of this study

This article aims to present a method tool that will be helpful in further studies on the assessment of fuel consumption (and more broadly, energy carriers) in:

– review existing methodologies for measuring fuel consumption in real-world conditions
– analyze the discrepancies between laboratory and real-world fuel efficiency results
– discuss best practices for improving fuel economy in vehicle design, fleet management, and driving behavior
– evaluate the policy implications of real-world fuel consumption data.

By addressing these topics, this study provides a comprehensive framework for assessing long-term fuel consumption in natural vehicle operation, offering insights for manufacturers, consumers, fleet operators, and policymakers.

The main methods used so far to evaluate fuel consumption [7], in real-world conditions [3], are:

• Full Tank Method ("Tank-to-Tank")

This is a simple and fairly accurate method used by drivers and fleet operators. Pros: Simple, reliable for long-distance (great mileage) assessments. Cons: Does not provide real-time consumption changes.

• On-Board Computer Readings

Most modern vehicles have an onboard computer that displays both average and real-time fuel consumption.

Pros: Instant results, useful for adjusting driving habits. Provides both average and instantaneous fuel consumption. Cons: There can be a 5–10% error margin. Older vehicles may lack this feature.

• OBD-II Diagnostics + Mobile Apps

If the vehicle has an OBD-II (On-Board Diagnostics) port, you can use a Bluetooth scanner (such as the ELM327) with apps like Torque or Car Scanner to monitor fuel consumption in real-time.

Pros: Provides precise real-time fuel data from the engine control unit. Allows tracking additional metrics (e.g., engine load, temperature, throttle position). Cons: Requires additional hardware and setup. Accuracy depends on sensor calibration.

• Long-Term Statistical Analysis (Fleet Management)

For commercial fleets, fuel consumption is analyzed over long periods using: Fuel purchase records (e.g., receipts, invoices). Odometer readings (from GPS or tachograph). Driving conditions (urban, highway, cargo load). Pros: Best for fleet management, helps detect inefficiencies. Cons: Requires consistent data collection.

• Real Driving Emissions (RDE) Testing with Portable Emission Measurement Systems (PEMS)

Used in regulatory and scientific studies, this method involves: Installing a portable emissions analyzer (PEMS) on the vehicle. Measuring real-time fuel consumption under real-world driving conditions. Pros: Most accurate real-world method. Cons: Expensive, used mainly in professional research.

Among the above-mentioned methods for assessing the fuel consumption of engines in long-term, natural vehicle use, the most frequently used method is the "full tank" method, also known as "Tank to Tank". However, there are two basic varieties of this method: in one of them, fuel consumption is given in units of the volume of fuel used related to the distance covered (usually in dm^3 per 100 km), in the other, the distance covered on a specific amount of fuel is given (usually in miles per gallon of fuel).

In the EU, the most commonly used factor for assessing the fuel consumption of car engines is fuel economy (FE) expressed in $dm^3/100$ km. This method is also presented in this publication. It is illustrated with the results of long-term studies of ICEV operation in natural use, conducted at the PROEKO Foundation.

A mid-range passenger car with a six-cylinder naturally aspirated V spark-ignition engine with a displacement of 3.5 dm^3 was tested.

By the assumptions that F_i – i-th refueling, t_{di} – mileage to F_i, then the fuel economy (FE) can be expressed as:

$$FE_i = 100F_i/(t_{di} - t_{di-1}) \quad (1)$$

After 647 refuelings (during the operational car investigations), it was achieving the results of fuel economy (FE) illustrated in Fig. 1.

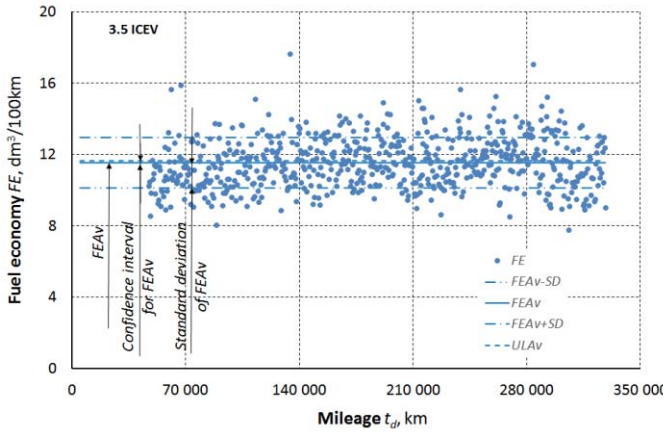

Fig. 1. Fuel economy after 647 refuelings of the investigated car

As can be seen, it is possible to conduct a comprehensive statistical analysis of the obtained results. Such an analysis was conducted, and the selected results are presented in Table 1.

Table 1. Fuel economy

Mean	11.54041
Standard error	0.05568
Median	Nov.81
Mode	Oct.99
Standard deviation	1.416291
Sample variance	2.005879
Kurtosis	0.380084
Skewness	0.423088
Range	9.879941
Minimum	7.76880
Maximum	17.64874
Sum	7466.642
Number	647
Largest (1)	17.64874
Least (1)	Jul.88
Confidence level (95.0%)	0.109336

The presented data yield interesting observations. The average of 11.5 $dm^3/100$ km does not differ from the values obtained in the operation of mid-range cars. It is interesting that the confidence interval for the average is relatively narrow.

However, the relatively large dispersion of the FE_i value from the AFE is worth noting. This is confirmed by the data concerning the hypothetical distribution of FE_i values. The kurtosis of this distribution (0.38 – Table 1) indicates that it is relatively "flat", while the skewness value (0.42 – Table 1) indicates that there are relatively many values significantly smaller than the AFE achieved in presented calculations.

The i value changed from 1 to n. By n refueling the average fuel economy (AFE_n) is as

$$AFE_n = \frac{1}{n}\sum_{i=1}^{n} FE_i \quad (2)$$

Figure 1 shows the values for i = n = 647. It is possible to calculate AFE_i for each i (from 1 to 647). After each refueling, there is AFE_i, and these values do not have to be constant – which is observed in reality. An example of the FE_i and AFE_i values calculated in the presented studies, is given in Fig. 2.

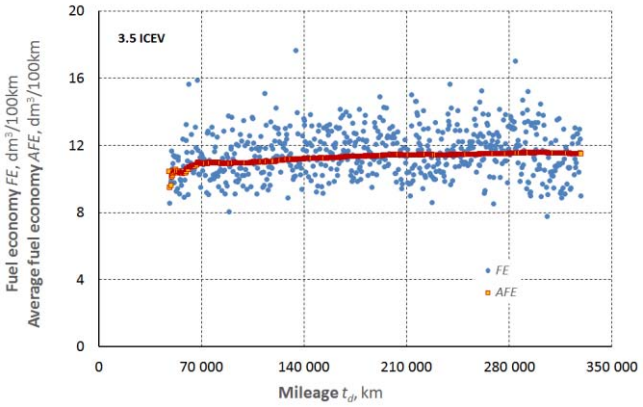

Fig. 2. FE and AFE by 647 refuelings (i = 1 to n = 647)

There are clearly visible large changes in AFE as the vehicle mileage increases. It is characteristic that in the initial period of operation, the changes in AFE are relatively large. After a longer period of operation, the AFE values stabilize. This happens despite the fact that the FE values are still characterized by relatively large value dispersions. Of course, in the existing situation, the assessment of operational fuel consumption in long-term, natural operation may not be adequate to reality. See the value of mode equate 10.98 $dm^3/100$ km – Table 1. Hence, another fuel consumption assessment method was introduced based on the theory of cumulative fuel consumption.

The assessment of the fuel (energy carrier) consumption and energy efficiency of vehicles during their natural operation is crucial for understanding the impact on people and the environment and is essential for the development and implementation of sustainable transport policies. One significant contribution to this field can be the cumulative fuel consumption theory [11], which offers a comprehensive framework for assessing fuel consumption under long-term, real-world conditions.

Furthermore, the resulting concept of the energy footprint of a vehicle provides insight into the total energy consumed over its entire life cycle, from production to disposal.

3. Theory of cumulative fuel consumption

Cumulative fuel consumption theory focuses on quantifying the total fuel consumed by a vehicle over its entire operational life, considering various real-world factors that influence fuel efficiency. This approach contrasts with standardized laboratory tests, which may not accurately reflect actual driving conditions.

The theory introduces several critical components:

- Cumulative Fuel Consumption (CFC): This metric represents the total amount of fuel (energy carrier) consumed by a vehicle over a specific period or distance. It encompasses all operational phases, offering a comprehensive view of fuel usage.
- Intensity of Cumulative Fuel Consumption (ICFC): This parameter measures the rate of fuel consumption over time, reflecting how efficiently a vehicle uses fuel during its operation.
- Specific cumulative fuel consumption (SCFC) – value similar to the AFE.

The cumulative fuel consumption over time t_d (practically mileage) after many transformations, described in detail in [11–13, 15] can be expressed as:

$$\mathrm{CFC}(t_d) = c t_d^{a+1} \tag{3}$$

where: CFC – cumulative fuel consumption, c, a – constants, t_d – the mileage.

Derivative of the (3) is the intensity of the cumulative fuel consumption.

$$\mathrm{ICFC}(t_d) = \frac{d\mathrm{CFC}(t_d)}{dt_d} = c(a+1)t_d^a \tag{4}$$

where: ICFC – intensity of the cumulative fuel consumption; by $t_d = 0$ the ICFC not exist.

Specific cumulative fuel consumption (SCFC)

$$\mathrm{SCFC}(t_d) = \frac{\mathrm{CFC}(t_d)}{t_d} = c t_d^a \tag{5}$$

SCFC is similar to the AFE but the SCFC(t_d) is expressed in dm^3/km.

The usefulness of the cumulative fuel consumption theory will be demonstrated here using data from the long-term operation of 3.5 ICEV test, mentioned earlier.

After each i-th refueling of the car, two main parameters can be noted, i.e. the t_{di} mileage and the amount of fuel filled into the car tank F_i.

After k-refuelings ($i \le k \le n$) existing two parameters

$$t_{dk}, \quad F_{is} = \sum_1^i F_i \quad \text{for} \quad 1 \le i \le n \tag{6}$$

Selected values from the initial and final period of operational testing are presented in Table 2. Full operational data are the responsibility of the authors of this publication.

Table 2. Selected results from 3.5 ICEV long-term natural operational tests

	Datum	Distance	Refueling	Sum of refueling	CFCm [dm^3]	CFC [dm^3]	DCFC [%]
		t_{dk} [km]	F_i [dm^3]	Fis [dm^3]			
1	30.04.2010	47 198.41	36.660	36.66	4 837.84	4 803.47	–0.72
2	02.05.2010	47 658.58	48.149	84.81	4 885.99	4 852.85	–0.68
3	03.05.2010	48 192.77	45.740	130.55	4 931.73	4 910.21	–0.44
4	09.05.2010	48 754.31	55.360	185.91	4 987.09	4 970.53	–0.33
5	14.05.2010	49 233.79	55.950	241.86	5 043.04	5 022.08	–0.42
6	18.05.2010	49 730.97	52.830	294.69	5 095.87	5 075.55	–0.40
7	24.05.2010	50 242.63	55.930	350.62	5 151.80	5 130.61	–0.41
8	28.05.2010	50 706.03	52.860	403.48	5 204.66	5 180.50	–0.47
9	30.05.2010	51 277.22	55.970	459.45	5 260.63	5 242.03	–0.35
10	09.06.2010	51 737.40	52.100	511.55	5 312.73	5 291.63	–0.40
11	12.06.2010	52 200.79	52.640	564.19	5 365.37	5 341.60	–0.44
12	13.06.2010	52 694.75	45.770	609.96	5 411.14	5 394.90	–0.30
13	15.06.2010	53 253.07	52.770	662.73	5 463.91	5 455.17	–0.16
14	20.06.2010	53 692.33	49.820	712.55	5 513.73	5 502.61	–0.20
15	21.06.2010	54 052.75	40.120	752.67	5 553.85	5 541.55	–0.22
16	25.06.2010	54 601.42	49.970	802.64	5 603.82	5 600.86	–0.05
17	28.06.2010	55 021.36	42.000	844.64	5 645.82	5 646.28	0.01
18	29.06.2010	55 590.95	56.490	901.13	5 702.31	5 707.91	0.10
19	01.07.2010	56 123.53	51.420	952.55	5 753.73	5 765.56	0.21
20	05.07.2010	56 652.89	55.800	1 008.35	5 809.53	5 822.90	0.23
21	14.07.2010	57 013.31	44.700	1 053.05	5 854.23	5 861.95	0.13
22	16.07.2010	57 405.90	42.330	1 095.38	5 896.56	5 904.51	0.13
23	18.07.2010	57 724.48	28.440	1 123.82	5 925.00	5 939.06	0.24
71	07.02.2011	79 679.29	67.440	3 557.22	7 920.32	7 906.93	–0.17
644	16.01.2025	327 227.16	53.340	31 919.78	36 333.66	36 581.42	0.68
645	02.02.2025	327 577.92	45.510	31 965.29	36 386.75	36 637.74	0.69
646	17.02.2025	328 020.39	54.800	32 020.09	36 431.88	36 678.93	0.67
647	22.02.2025	328 395.29	33.830	32 053.92	36 481.46	36 734.11	0.69

An illustration of the operating data from all 647 refuellings is shown in Fig. 3.

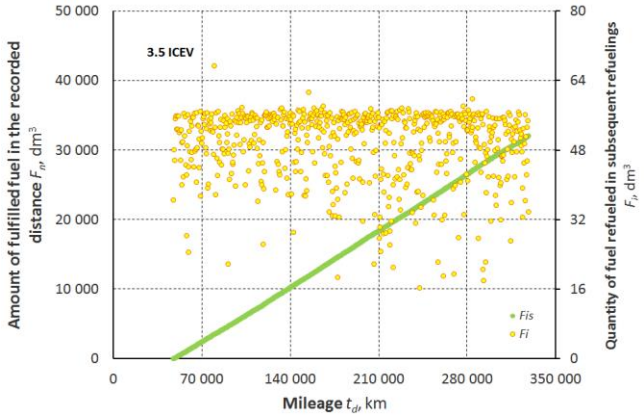

Fig. 3. A typical picture of data after any refueling (647 in this case) the car

The tests were conducted using the full tank ("Tank to Tank") method. The fuel tank capacity of a 3.5 ICEV is 65 dm^3. However, Fig. 3 shows that there are refuellings with a volume exceeding this capacity – see row 71 in Table 2. This is not an error. This is the result of multiple refuellings, of which only the last (of this mini cycle) is a refuelling to a full tank.

The analysis of the volume of refueled fuel reveals that the vast majority of the volume falls within the range of 50–55 dm³.

The F_{is} course is quasi-linear. F_{is} is an element of the cumulative fuel consumption CFC, because CFC is calculated from the moment the vehicle is put into service (by $t_d = 0$).

The situation presented in Fig. 3, where there is no data from the beginning of the vehicle's operation, occurs frequently, in fact, most often. The "missing" fuel consumption from the mileage "zero" to the beginning of the operating data recording (here, 47,198.41 km – Table 2) can be determined using advanced mathematical methods. This was also done in relation to the tested 3.5 ICEV vehicle.

By assuming that:

$$CFC_m = F_{0s} + F_{is} \tag{7}$$

this where: F_{is} –measurement amount of fuel consumed to the t_{dn} in the investigated period of car operation, F_{0s} – estimated amount fuel consumed from the $t_{dn} = 0$ (beginning of the car operation) to the t_{di} (mileage of the first registered refueling by the investigated car operation i = 1), CFCm – estimated plus measurement consumed fuel to the t_{di}, CFC – cumulative fuel consumption from beginning the vehicle operation – equation (3), DCFC – deviation of the CFCm data from CFC data.

The relevant data are given in Table 2 and illustrated here in Fig. 4.

It is worth noting the good prediction of CFC values determined based on CFCm. The percentage deviation of both values (DCFC), throughout the entire study period, does not exceed 1.00% – Fig. 4.

The statistics of model (3) are given in Table 3.

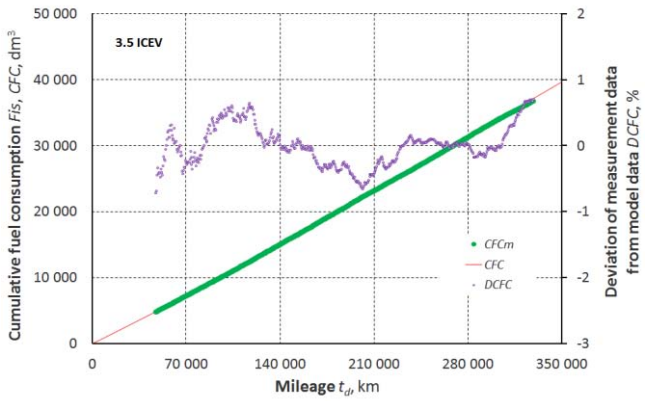

Fig. 4. Cumulative fuel consumption: CFCm – determined based on operational test data, CFC – determined based on the model (3), DCFC deviation of measured values from those determined from the model (3)

Table 3. Statistics of model (3)

Regression statistics	
Multiple R	0.999984
R squared	0.999968
Fitted R-squared	0.999968
Standard error	0.003000
Observation	647
Coefficients	
"c"	0.056862
"a"	0.054089

Having constants "c" and "a" relative to the performance of a specific vehicle, we can present the energy footprint of the vehicle [10, 14]. The energy footprint of the vehicle in the whole operating period in driving status is represented by three quantities, i.e. CFC(t_d), ICFC(t_d) and SCFC(t_d).

These quantities were calculated (for 3.5 ICEV), and their curves are shown in Fig. 5.

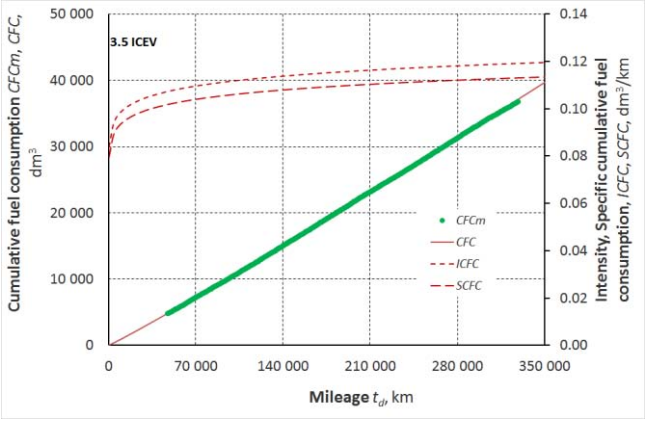

Fig. 5. The energy footprint of a car during its long natural life cycle regarding the use phase

The course of the curves is interesting. The intensity of the cumulative fuel consumption increases from the moment the car is put into service. The specific cumulative fuel consumption behaves similarly. The reasons for this state of affairs can, of course, be manifold. One of the main reasons may be, for example, a change in the operating environment. It is also interesting that the SCFC values,

when multiplied by 100, seem to yield similar results to those of AFE. The result of calculations and comparisons is shown in Fig. 6.

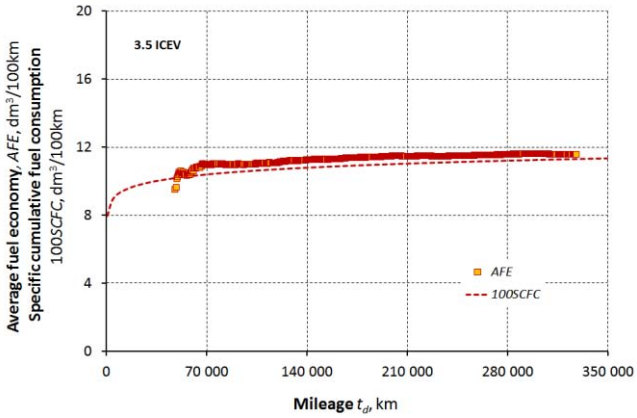

Fig. 6. The result of calculations for comparison of 100SCFC and AFE

The value of 100SCFC over the full mileage range is slightly lower than that of AFE. But 100SCFC may be closer to reality than AFE. In Table 1, we present the skewness value as 0.42, noting that the maximum of the FE statistical distribution falls within the range of fuel consumption smaller than the final AFE value after 647 refuelings, corresponding to a 100SCFC. For this reason, the parameters of the statistical distribution are likely a more effective tool for assessing fuel consumption as AFE. Obviously, it seems best to make fuel consumption assessments using SCFC.

4. Conclusions

Cumulative fuel consumption theory provides a valuable framework for understanding and quantifying fuel consumption in real-world, long-term vehicle operations, offering insights that standardized tests may miss.

The concept of a vehicle's energy footprint is introduced, based on cumulative fuel consumption theory, to more accurately assess a vehicle's energy consumption over its entire operational life.

By analyzing real-world operating data such as fuel consumption records and distances traveled, this methodology provides a comprehensive understanding of a vehicle's energy requirements under natural, long-term operating conditions. The vehicle's energy footprint is visualized using cumulative fuel consumption, cumulative fuel consumption intensity, and specific cumulative fuel consumption curves, offering insight into how fuel efficiency evolves over the vehicle's life.

The presented method of energy carrier consumption assessment has practical implications for:

– Vehicle performance assessment: By analyzing CFCs, ICFCs, and SCFCs, manufacturers and researchers can assess how vehicles perform under a variety of real-world conditions as a function of vehicle mileage (regardless of specific conditions that vary randomly over long periods of operation), leading to improvements in design and fuel efficiency.
– Policy development: Understanding cumulative fuel economy helps policymakers develop policies that promote energy efficiency and reduce environmental impact, as well as forecast energy demand, such as for e-mobility.
– Consumer awareness: Providing consumers with information about a vehicle's cumulative fuel economy can influence purchasing decisions toward more fuel-efficient options.

Combined with vehicle energy footprint analysis, these concepts are crucial for promoting sustainable transportation, informing policy decisions, and guiding consumer choices toward minimizing costs, including external transport costs and environmentally friendly options.

A separate issue is the possibility of using cumulative fuel consumption theory, and more broadly, energy footprint, as a method for multi-aspect comparisons of different vehicle powertrains, including comparisons of vehicle fleets with conventional (ICEV), hybrid (HEV and PHEV), hydrogen (H2EV), and electric (BEV) powertrains.

Based on the assumption that the presented method can be beneficial for producers, decision-makers, and consumers seeking to improve fuel efficiency and reduce environmental impact, further work utilizing it is planned. It seems important to explain the phenomenon of large dispersion in the CFC curves recorded in vehicle fleets. Since model (3) will then become a multidimensional model, artificial neural networks are planned to be used in this context.

Nomenclature

AFE	average fuel economy
CAFÉ	corporate average fuel economy
CFC	cumulative fuel consumption
FE	fuel economy
ICFC	intensity of cumulative fuel consumption
ICEV	combustion engine vehicle
NEDC	New European Driving Cycle
PEMS	portable emission measurement systems
RDE	real driving emission
SCFC	specifically cumulative fuel consumption
WLTP	Worldwide Harmonized Light Vehicles Test Procedure

Bibliography

[1] Dobranskyte-Niskota, A, Perujo A, Pregl M. Indicators to assess sustainability of transport activities. 2007.
[2] Fan P, Yin H, Lu H, Wu Y, Zhai Z, Yu L et al. Which factor contributes more to the fuel consumption gap between in-laboratory vs. real-world driving conditions? An independent component analysis. Energy Policy. 2023;182:113739. https://doi.org/10.1016/j.enpol.2023.113739
[3] Heni H, Diop SA, Coelho LC, Renaud J. Measuring fuel consumption in vehicle routing: new estimation models us-

ing supervised learning measuring fuel consumption in vehicle routing: new estimation models using supervised learning. 2019. https://www.cirrelt.ca/documentstravail/cirrelt-2019-08.pdf
[4] Huang Y, Unger N, Harper K, Heyes C. Global climate and human health effects of the gasoline and diesel vehicle fleets. GeoHealth. 2020;4:1-13. https://doi.org/10.1029/2019GH000240
[5] Kolb RW. Corporate Average Fuel Economy (CAFE) Standards. Encycl Bus Ethics Soc. 2008;5:456. https://doi.org/10.4135/9781412956260.n193
[6] Lemp JD, Kockelman KM. Quantifying the external costs of vehicle use: evidence from America's top-selling light-duty models. Transp Res Part D Transp Environ. 2008;13:491-504. https://doi.org/10.1016/j.trd.2008.09.005
[7] Mahlia TMI, Tohno S, Tezuka T. A review on fuel economy test procedure for automobiles: implementation possibilities in Malaysia and lessons for other countries. Renew Sustain Energy Rev. 2012;16:4029-4046. https://doi.org/10.1016/j.rser.2012.03.032
[8] Reduce Fuel Costs with Fleet Management Software Strategies_MoldStud. https://moldstud.com/articles/p-how-fleet-management-software-can-help-reduce-fuel-costs
[9] Romero CA, Correa P, Ariza Echeverri EA, Vergara D. Strategies for reducing automobile fuel consumption. Appl Sci. 2024;14:1-27. https://doi.org/10.3390/app14020910
[10] Sitnik L. Operational energy footprint of vehicle. Combustion Engines. 2021;186(3):37-40. https://doi.org/10.19206/ce-140245
[11] Sitnik L. Theory of cumulative fuel consumption and example for its application. Proceedings of the XXII International Scientific-Technical Conference TRANS&MOTAUTO '14. Scientific-technical Union of Mechanical Engineering. Varna. 2014:17-20.
[12] Sitnik L. Energy demand assessment for long term operation of vehicles. SAE Technical Paper 2020-01-2165. 2020. https://doi.org/10.4271/2020-01-2165
[13] Sitnik L. Theory of cumulative fuel consumption by LPG powered cars. J Kones Powertrain Transp. 2015;22:275-280. https://doi.org/10.5604/12314005.1168489
[14] Sitnik L, Andrych-Zalewska M, Dimitrov R, Mihaylov V, Mielińska A. Assessment of energy footprint of pure hydrogen-supplied vehicles in real conditions of long-term operation. Energies. 2024;17. https://doi.org/10.3390/en17143532
[15] Sitnik L, Ivanov ZD, Sroka ZJ. Energy demand assessment for long term operation of hybrid electric vehicles. 2020 IOP Conf Ser: Mater Sci Eng. 2020;1002:012026. https://doi.org/10.1088/1757-899X/1002/1/012026
[16] Zhou M, Jin H, Wang W. A review of vehicle fuel consumption models to evaluate eco-driving and eco-routing. Transp Res Part D Transp Environ. 2016;49:203-218. https://doi.org/10.1016/j.trd.2016.09.008

Prof. Lech Sitnik, DSc., DEng. – Faculty of Mechanical Engineering, Wroclaw University of Science and Technology, Poland.
e-mail: *lech.sitnik@pwr.edu.pl*

Prof. Monika Andrych-Zalewska, DSc., DEng. – Faculty of Mechanical Engineering, Wroclaw University of Science and Technology, Poland.
e-mail: *monika.andrych@pwr.edu.pl*

Anna Mielińska – PROEKO Foundation, Poland.
e-mail: *anna.mielinska@pwr.edu.pl*

Article citation info:
Wiśniowski P, Zimakowska-Laskowska M, Taubert S, Kozłowski E, Ślęzak M, Żbik K. Comparison of pollutant concentrations and engine operating parameters during cold start with petrol and LPG. Combustion Engines. 2026;206(3):68-78. https://doi.org/10.19206/CE-216339

Piotr WIŚNIOWSKI
Magdalena ZIMAKOWSKA-LASKOWSKA
Sławomir TAUBERT
Edward KOZŁOWSKI
Marcin ŚLĘZAK
Ksawery ŻBIK

Combustion Engines
Polish Scientific Society of Combustion Engines

Comparison of pollutant concentrations and engine operating parameters during cold start with petrol and LPG

ARTICLE INFO

Received: 16 May 2025
Revised: 3 October 2025
Accepted: 2 January 2026
Available online: 5 March 2026

The cold start of an ICE generates conditions conducive to intensive pollutant emission and reduced thermal efficiency. This study compared the concentrations of selected exhaust components and engine operating parameters during the cold start phase of a dual-fuel vehicle powered by petrol and LPG. The tests were conducted on a chassis dynamometer under identical ambient and load conditions, utilizing a repeatable homologation test. The analysis included HC, CH_4, and NO_x concentrations, which were recorded simultaneously with the internal combustion engine's operating parameters: rotational speed, coolant temperature, throttle position, and load. The collected data enabled the development of mathematical models representing the relationships between the dynamics of the start process and pollutant concentrations. The results indicate significant differences in the start characteristics for individual fuels; in particular, LPG exhibits a distinct emission profile during the early phase of engine operation. Conclusions can serve as the basis for designing start control strategies in dual-fuel vehicles, considering environmental requirements and the further development of emission control systems.

Key words: *emission, petrol, cold start, LPG, engine operating parameters*

This is an open access article under the CC BY license (http://creativecommons.org/licenses/by/4.0/)

1. Introduction

The cold start of the combustion engine remains one of the key challenges for engineers seeking to reduce emissions of pollutants. In the initial phase of engine operation, the catalytic converter is not yet sufficiently heated, and the combustion process takes place in conditions that are not optimal, which results in a rapid increase in the emission of harmful exhaust components – including hydrocarbons (HC), methane (CH_4), carbon monoxide (CO) and nitrogen oxides (NO_x) [14, 15, 48].

The literature indicates that alternative fuels, such as LPG, may exhibit a more favorable emission profile during the cold start phase compared to gasoline – especially in terms of lower HC and CO emissions [4, 14, 43]. The combustion efficiency of LPG, along with its physicochemical properties, favors faster catalyst heating and stabilization of the combustion process [21, 33].

At the same time, an increasing number of studies indicate a significant influence of ambient and engine temperatures on emission levels during this phase of the driving cycle [2, 28, 45]. Low temperatures worsen fuel evaporation, delay reaching the ignition temperature, and catalyst activation, resulting in a significantly higher emission level than during steady-state engine operation [6, 51].

In light of the above, the aim of this work is to conduct a quantitative analysis of the effect of fuel type (petrol vs LPG) and engine operating temperature on the emission of selected pollutants during the cold start phase. The tests were conducted on a chassis dynamometer using the repeatable WLTC test in fixed environmental conditions. The dependence of pollutant concentrations on key operating parameters, such as engine load, coolant temperature and crankshaft rotational speed, was also assessed. The conducted analyses enable the identification of differences in exhaust emission characteristics depending on the fuel type, which may have significant implications for the further development of start-up control strategies and emission control systems in dual-fuel vehicles.

2. Literature review

The cold start of an internal combustion engine refers to starting the drive unit, whose temperature–including that of the coolant and exhaust system components – is significantly lower than the operating temperature. This phenomenon occurs most frequently after a prolonged standstill of the vehicle, especially in low ambient temperature conditions, and is associated with several unfavorable effects, including deterioration of the ignition process, incomplete fuel combustion, and delayed activation of exhaust gas aftertreatment systems [28, 51]. During the cold start phase, a sharp increase in HC and CO emissions is observed, resulting from insufficient catalyst heating and instability in the combustion process. According to [28], the definition of cold start should refer not only to the moment of starting the engine, but also to the time needed to achieve full efficiency of the emission reduction system. Specific limit values are provided in the technical and regulatory literature for recognizing that the engine has completed the cold start phase. According to research and engineering practices, the end of the cold start phase is considered to be the moment when the coolant temperature reaches 70–80°C, and the catalyst temperature exceeds the so-called light-off threshold, usually in the range of 250–300°C. In urban driving conditions, these values are reached on average after 180–500 seconds [29, 52]. In the WLTC procedure, the duration of the cold start phase is estimated at about

140–300 s, while in the FTP-75 procedure, it is assumed that the cold start lasts until the catalyst temperature reaches 250°C. However, the length of this phase can be significantly extended at negative ambient temperatures.

Studies show that in this phase of the driving cycle, the vehicle can emit up to 60% of the total HC and CO emissions [3, 48]. This phenomenon concerns not only older vehicles, but also those meeting Euro 6 standards [15]. The increase in emissions during cold start conditions is strongly correlated with engine operating parameters, such as coolant temperature and catalyst activation time [8, 16, 32, 54]. Emissions also depend on the injection and ignition control strategy [11, 19], as well as the fuel atomization properties at low temperatures [30]. Furthermore, particulate matter (PM) emissions from gas direct injection (GDI) engines are significantly higher than those from port fuel injection (PFI) engines [40].

LPG, as an alternative fuel, exhibits a more favorable emission profile during the cold start phase. Comparative studies have shown that LPG-fueled engines emit less HC, CO, and PM compared to gasoline units [21, 26, 36, 44]. These effects are also supported by recent studies involving innovative LPG hardware/software configurations in low-emission vehicle prototypes [35]. The effects result from improved LPG combustion properties and a more homogeneous fuel-air mixture [42]. The reduction of particulate matter emissions in LPG vehicles can reach up to 99% compared to gasoline, especially in urban conditions and at low ambient temperatures [22, 24, 37]. The literature also highlights the lower sensitivity of LPG to temperature changes, which improves its operational predictability [2, 20, 33].

Ambient temperature plays a key role in shaping the level of pollutant emissions. At temperatures below 0°C, HC and CO emissions can increase by as much as tenfold [3, 5, 16, 34]. Low temperatures extend the catalyst warm-up time and reduce the efficiency of exhaust gas treatment systems [48, 53]. This phenomenon also applies to fugitive emissions and organic gases [53]. LPG maintains a more stable emission profile at low temperatures, which is related to its physicochemical properties and injection strategy [31]. Modern combustion management strategies can effectively reduce the negative impact of temperature on emissions, especially through precise control of ignition and mixture composition [30, 45]. Modeling studies and meta-analyses suggest a complex, nonlinear relationship between temperature and emissions [27–29].

Several technical and operational approaches have been described in the literature to reduce cold start emissions. [9, 10]suggested the use of phase change materials (PCM) for heating the evaporator and pressure regulator in LPG systems, which allows for shortening the transition time to gaseous fuel and reducing CO and HC emissions. Kwak [26] and Gong [8] demonstrated that ignition delay and lean mixtures improve combustion stability and reduce catalyst activation time. Gong et al. [8] suggest that changing the injection strategy and fuel ratio in dual-fuel (methanol/LPG) systems can significantly improve cold start emissions. Modern approaches include the use of split-injection strategies and first-cycle ignition control [11, 19]. The use of electric catalyst heaters, as demonstrated by Gao et al. [7], enables faster attainment of the "light-off" temperature, which significantly reduces pollutant emissions. Hao et al. [12] described a start-up strategy for dual-fuel engines (gasoline/hydrogen), indicating the possibility of reducing HC and CO emissions using special ignition maps. In turn, Teymoori et al. [46] proposed trapping HC emissions using selective sorbents. An alternative direction is the development of filter materials and catalytic coatings dedicated to the cold start phase [6, 53] provided evidence that appropriate fiscal policies, such as carbon pricing, can effectively reduce the number of cold starts in urban environments.

Unburned hydrocarbons (HC) and methane (CH_4) are key pollutant components emitted during the cold start phase. Their presence is mainly due to the low temperature of the combustion chamber and insufficient catalyst activity in the initial seconds of engine operation [14, 40]. CH_4, as a persistent greenhouse gas, has high global warming and tropospheric ozone potential, which makes it particularly problematic in the context of modern emission standards [1, 54]. Studies have shown that gasoline direct injection (GDI) engines emit significantly higher concentrations of CH_4 and HC compared to indirect injection engines, especially in low ambient temperature conditions [31, 40, 53]. In the case of LPG fuelling, methane emissions are usually lower, but still significant – especially in converted engines, where the optimization of combustion parameters is not adapted to the fuel characteristics [20, 41]. Various methods for reducing HC and CH_4 emissions have been suggested in the literature, including the use of adsorption coatings in catalysts [54], trapping HC molecules in porous materials [41, 46] and the adaptation of a multiphase injection strategy that improves mixture homogeneity [8].

2. Methodology

2.1. Vehicle specification and test procedure

The tests were performed using a Ford Focus vehicle with a spark-ignition engine, displacing 1798 cm³ in the Flexifuel version. The vehicle was fitted with an LPG injection system designed for vehicles with indirect fuel injection. A chassis dynamometer was used during the tests to simulate the resistance to motion of the vehicle that covered the WLTC cycle route (Fig. 1). The course of the full WLTC cycle and the engine temperature during the test are shown in the figures below (Fig. 2).

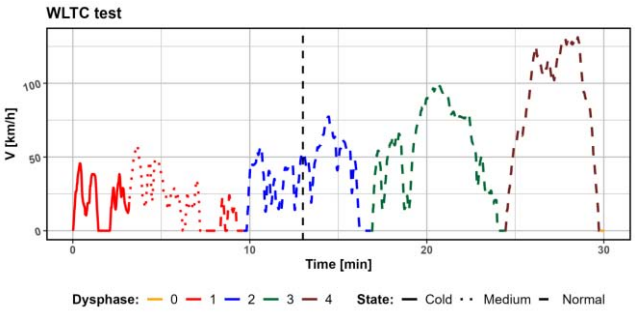

Fig. 1. The complete WLTC cycle on the chassis dynamometer

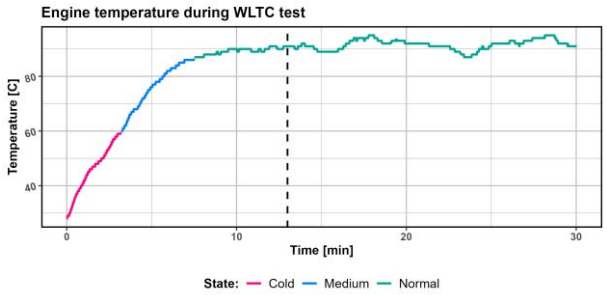

Fig. 2. Engine temperature changes during the WLTC cycle throughout the emissions test

The corresponding distance covered by the vehicle during the WLTC cycle is illustrated in Fig. 3. This plot also shows the division of the test into Cold, Medium, and Normal states, depending on the engine coolant temperature.

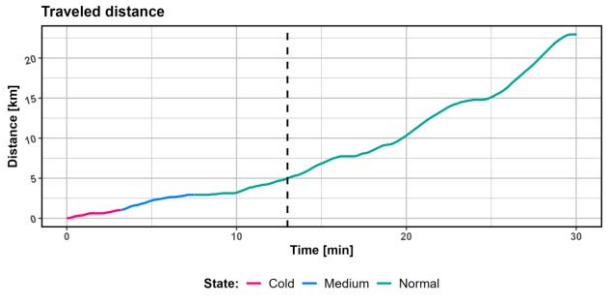

Fig. 3. Distance covered by the vehicle during the WLTC cycle according to the testing procedure on the chassis dynamometer

Engine start at 25°C. The following states were assumed with respect to the engine temperature (T):

– $T < 60°C$ – Cold
– $60°C \leq T < 87°C$ – Medium
– $T \geq 87°C$ – Normal.

In order to compare the results (similar number of concentration readings), the initial 13 min of the test was used for analysis.

2.2. Research tools

The nonparametric Kruskal-Wallis test was used to compare pollution by condition, while the Kolmogorov-Smirnov test was used to compare pollution by fuel type for each condition of the combustion engine. To verify the effect of temperature on the amount of pollution, an analysis of the structural parameters of the nonlinear model describing the effect of engine load, temperature and engine speed on the amount of pollution was performed A similar methodology, combining chassis dynamometer testing with computational modelling, was proposed by Zimakowska-Laskowska et al. [55], confirming the validity of hybrid approaches in vehicle emission research.

2.2.1. Kruskal-Wallis rank sum test

The Kruskal-Wallis test [13, 18] was used to analyze the existence of differences due to the engine operating state depending on the temperature. The Kruskal-Wallis test is used to detect differences between groups when the assumption of normality of distribution in groups is not met. In the considered case, the engine operating state with respect to temperature was selected as the differentiating variable. Let $\{y_i^k\}_{1\leq i\leq n_k}$ denote a sequence representing the concentrations of pollutant readings, where $k \in \{\text{Cold, Medium, Normal}\}$ denotes the belonging to the state according to engine temperature.

To verify the effect of engine condition on pollutant concentrations, $\alpha \in (0,1)$ we create a null hypothesis at the significance level:

H_0: $F_{Cold}(x) = F_{Medium}(x) = F_{Normal}(x)$ for $x > 0$ (distributions of pollutant concentrations are equal and independent of engine operating temperature)

and the alternative hypothesis

H_1: $\exists i, j \in \{\text{Cold,Medium,Normal}\}\ F_i(x) \neq F_j(x)$(engine operating temperature/condition has a significant influence on distribution of pollutant concentration).

Ranking was performed for the entire sample $\{y_i^k\}_{1\leq i\leq n_k}$, $k \in \{\text{Cold,Medium,Normal}\}$. Let R_{ki} denote the rank in the sample of ithe -th element from kthe -th group.

The test statistic is given by:

$$T = \frac{12}{n(n+1)} \sum_{k\in\{\text{Cold,Medium,Normal}\}} \left(\overline{R}_k - \frac{n+1}{2}\right)^2 n_k \qquad (1)$$

where $n = n_{Cold} + n_{Medium} + n_{Normal}$ and $\overline{R}_k = \frac{1}{n_k}\sum_{i=1}^{n_k} R_{ki}$

The test statistic (1) is a measure of the departure of the sample rank means from the mean value of all ranks, which is $(n+1)/2$. The statistic T has a distribution $\chi^2$with 2 degrees of freedom.

2.2.2. Kolmogorov-Smirnov test

For each engine operating state, the pollutants generated by the type of fuel supplied were also compared. The Kolmogorov-Smirnov test was used to compare (verify the differences) the distributions of two features Xand Y(pollutant distributions by fuel type). For each feature (group), based on the observation of the realization $\{x_1, x_2, \ldots, x_{n_1}\}$, $\{y_1, y_2, \ldots, y_{n_2}\}$ we create empirical distributions

$$F_X(t) = \frac{\#\{x_i : x_i \leq t, \quad 1 \leq i \leq n_1\}}{n},$$
$$F_Y(t) = \frac{\#\{y_i : y_i \leq t, \quad 1 \leq i \leq n_2\}}{n}$$

where #denotes the power of the set. For the Kolmogorov-Smirnov test at the significance level $\alpha \in (0,1)$ we create the null hypothesis:

H_0:$\forall t \in (-\infty, \infty)$ $F_X(t) = F_Y(t)$ (the distribution functions are identical),

and the alternative hypothesis:

H_1: $\exists t \in (-\infty, \infty)$, that $F_X(t) \neq F_Y(t)$(the distribution functions of the distributions are significantly different).

The test statistic is given by the formula

$$D^{KS} = \sup_{t\geq 0} |F_X(t) - F_Y(t)| \qquad (2)$$

The statistic D has a Kolmogorov distribution. At the significance level α from the Kolmogorov distribution tables,

we determine the critical value K_α. If $\sqrt{\frac{n_1+n_2}{n_1 n_2}} D^{KS} > K_\alpha$, where n_1 and n_2 denote the sample numbers, then we reject the null hypothesis H_0 in favor of the alternative hypothesis H_1.

2.2.3. Dependence of pollutant concentration on load, temperature and speed

Let $\{(P_t^k, L_t^k, T_t^k, RPM_t^k)\}_{1\le t\le n_k}$ denote a data frame, where P_t^k denotes the concentration of pollutants within 1 s during measurements (ppm), L_t^k – engine load (% of maximum power output of the engine), T_t^k – current engine temperature C, RPM_t^k – engine speed during fuel supply $k \in \{Gasoline,LPG\}$. During engine operation, the concentration of pollutants $P_t^k > 0$ for each $t, 1 \le t \le n_k$. For the analyzed data set, delays (lags) in AVL readings were taken into account due to the time of exhaust gas flow from the engine exhaust manifold to the measuring device. The average delay time of readings is about 6 s. The relationship

$$\log(P_t^k) = \theta_0^k + \theta_1^k L_t^k + \theta_2^k T_t^k + \theta_3^k RPM_t^k + \varepsilon_t \tag{3}$$

was considered, for $k \in \{Gasoline,LPG\}$, while the influence of external factors is described using a random variable with a normal distribution $N(0, \sigma^2)$.

Let

$$X = \begin{bmatrix} 1 & L_1^k & T_1^k & RPM_1^k \\ 1 & L_2^k & T_2^k & RPM_2^k \\ \vdots & \vdots & \vdots & \vdots \\ 1 & L_{n_k}^k & T_{n_k}^k & RPM_{n_k}^k \end{bmatrix}, \quad Y = \begin{bmatrix} \log(P_1^k) \\ \log(P_2^k) \\ \vdots \\ \log(P_{n_k}^k) \end{bmatrix},$$

$$\varepsilon = \begin{bmatrix} \varepsilon_1 \\ \varepsilon_2 \\ \vdots \\ \varepsilon_{n_k} \end{bmatrix}, \quad \Theta = \begin{bmatrix} \theta_0^k \\ \theta_1^k \\ \theta_2^k \\ \theta_3^k \end{bmatrix}$$

Based on the observations, the relationship (3) can be presented in the form

$$Y = X\Theta^k + \varepsilon \tag{4}$$

Using the least squares method, we estimate the unknown parameters of the model (3). If $(X^T X) \neq 0$ then the best linear estimator of unknown parameters is given as follows

$$\hat{\Theta}^k = (X^T X)^{-1} X^T Y \tag{5}$$

The variance estimator of residuals is equal

$$\hat{\sigma}^2 = \frac{1}{n_k - 3 - 1} \sum_{j=1}^{n} \varepsilon_j^2$$

where residual $\varepsilon = Y - X\hat{\Theta} \in \mathbb{R}^n$. The values of the variance of the structural parameters are determined as $(S_0^k, S_1^k, S_2^k, S_3^k) = \mathrm{diag}(\hat{\sigma}^2 (X^T X)^{-1})$. Therefore, each of the structural parameters θ_j^k has a normal distribution $N(\hat{\theta}_j^k, S_j^2)$ for $0 \le j \le 3$.

For equation (3) we examine the significance of the parameter θ_j^k, $j = 0,1,2,3$ namely the influence of the respective factor on the pollutant concentration. In order to assess the influence of individual predictors [14, 18, 37] at the significance level $0 < \alpha < 1$ for each structural parameter we create a null hypothesis

$$H_0: \theta_j^k = 0$$

and the alternative hypothesis

$$H_0: \theta_j^k \neq 0$$

Test statistic

$$t_j = \frac{\hat{\theta}_j^k}{\sqrt{S_j^k}} \tag{6}$$

has t – distribution with $n - 3 - 1$ degrees of freedom. The test probability is equal

$$p_j = 2 \cdot P(T > |t_j|) \tag{7}$$

where T is a random variable with a t-Student distribution with $n - 3 - 1$ degrees of freedom. If $p_j < \alpha$, then for the parameter θ_j^k we reject the working hypothesis H_0 in favor of the alternative hypothesis H_1, therefore the appropriate component significantly affects the concentration of pollutants defined by means of (3). If $p_j \ge \alpha$ then at the significance level αthere are no grounds to reject the hypothesis H_0, then the structural parameter is not significantly different from zero and the predictor has a non-significant effect on explaining the variability of the pollutant concentration during the operation of the engine fueled with fuel $k \in$ {Gasoline, LPG}.

A prediction value of the logarithm of the pollutant concentration is equal

$$\log(\hat{P}_t^k) = \hat{\theta}_0^k + \hat{\theta}_1^k L_t^k + \hat{\theta}_2^k T_t^k + \hat{\theta}_3^k RPM_t^k$$

For the analysis of the model fit [14, 18, 24] the coefficient of determination was estimated

$$R^2 = 1 - \frac{\sum_{j=1}^{n} \varepsilon_j^2}{\sum_{j=1}^{n} \left(\log(P_j^k) - \bar{P}^k\right)^2} \tag{8}$$

where $\bar{P}^k = \frac{1}{n} \sum_{j=1}^{n_k} \log(P_j^k)$. The coefficient of determination R^2shows what part of the variability of the dependent variable is explained by the model. The significance test of the multiple correlation coefficient [13, 23] was used to verify the fit of the model to the empirical data. At the significance level $0 < \alpha < 1$ we create a null hypothesis

H_0: $R = 0$ (multiple correlation coefficient is equal to zero or not significantly different from zero)

and the alternative hypothesis

H_0: $R \neq 0$ (the multiple correlation coefficient is significantly different from zero).

For the model (3) for fuel, $k \in$ {Gasoline,LPG} the test statistic

$$f = \frac{R^2}{1 - R^2} \frac{n_k - 3 - 1}{3} \tag{9}$$

has a Fischer-Snedecor distribution with $(3,\ n_k - 3 - 1)$ degrees of freedom. The test probability is

$$p_k = P(F > f) \tag{10}$$

where Fis a random variable with a Fischer-Snedecor distribution $(3,\ n_k - 3 - 1)$ degrees of freedom. If $p_k \geq \alpha$ then at the significance level α there is no basis for rejecting the hypothesis H_0, therefore the multiple correlation coefficient is not significantly different from zero and the fitfing of the model describing the concentration of pollutants generated by the fuel-fueled engine $k \in \{\text{Gasoline}, \text{LPG}\}$ to the data is too weak. If the test probability $p_k < \alpha$ then the null hypothesis H_0 should be rejected in favor of H_1, then the fitfing of the model to the data is sufficiently high.

2.2.4. Analysis of differences in the impact of load, engine operating temperature, rpm, on pollutant concentration for different fuels

Based on the data $\{(P_t^k, L_t^k, T_t^k, rpm_t^k)\}_{1\leq t\leq n_k}$ for the established pollutant type, we estimate the parameters of the model (3) using the OLS for each of the fuels $k \in \{\text{Gasoline}, \text{LPG}\}$. In order to verify the differences and similarities in the effects of engine load, temperature and rpm on the emission of pollutant concentrations due to the use of different fuel types at the significance level $0 < \alpha < 1$for each of the structural parameters $\theta_j^{\text{Gasoline}}$and $\theta_j^{\text{LPG}}$for $j \in \{1,2,3\}$, we create a null hypothesis

H_0: $\theta_j^{\text{Gasoline}} = \theta_j^{\text{LPG}}$(no significant differences in the effect of the j-th factor when fueled with petrol and LPG)

and the alternative hypothesis

H_1: $\theta_j^{\text{Gasoline}} \neq \theta_j^{\text{LPG}}$(significant difference in the impact of the j-th factor when fueled with petrol and LPG)

Test statistic

$$T_j = \frac{\theta_j^{\text{Gasoline}} - \theta_j^{\text{LPG}}}{\sqrt{\frac{s_j^{\text{Gasoline}}}{n_{\text{Gasoline}}-4} + \frac{s_j^{\text{LPG}}}{n_{\text{LPG}}-4}}} \tag{11}$$

has a normal distribution $N(0,1)$. The test probability is equal

$$p_j = 2 \cdot P(U > |T_j|)$$

where U is a random variable with a distribution $N(0,1)$. If $p_j < \alpha$, then we reject the null hypothesis H_0in favor of H_1, then the influence of j-th factor on the pollution significantly depends on the type of fuel.

3. Results

Basic statistics for the logarithm of pollutant concentrations for various conditions with respect to the engine operating temperature range and for various types of fuel used to power the combustion engine are presented below (Table 1 and Table 2).

Tables 1 and 2 present basic statistics for pollutant concentrations (CH_4, HC, NO_x) generated by the petrol- and LPG-fuelled engine in different engine operating states (cold, medium, and operational). Comparison of the results reveals clear differences in emission profiles between the fuels, with LPG exhibiting more stable pollutant concentrations, particularly during the cold start phase.

To compare the effects of engine operating temperature and fuel type on pollutant emissions, the following graphs present logarithmic concentrations of gases: methane (CH_4), hydrocarbons (HC), and nitrogen oxides (NO_x), varying with engine operating temperature and fuel type (gasoline and LPG). The results indicate significant differences in the emission profiles of these gases under different temperature conditions, with particular emphasis on the

Table 1. Basic statistics of pollution generated by combustion engine powered by gasoline

State	Pollution	minutes	$q_{0.25}$	Mean	Median	$q_{0.75}$	max	Std.dev	Skewnes	Kurtosis
Cold	log(CH_4)	2.13	2.84	3.57	3.32	4.43	6.01	0.94	0.42	–0.83
Cold	log(HC)	4.57	5.18	6.10	5.66	7.25	8.59	1.20	0.75	–0.84
Cold	log(NO_x)	1.19	2.48	4.15	3.94	5.49	7.49	1.72	0.33	–1.10
Medium	log(CH_4)	–0.20	1.52	2.01	2.23	2.58	4.42	0.85	–0.54	0.34
Medium	log(HC)	3.24	3.77	4.13	4.08	4.43	5.47	0.51	0.41	–0.35
Medium	log(NO_x)	0.35	2.11	3.18	2.75	4.28	7.49	1.46	0.60	–0.33
Normal	log(CH_4)	–1.10	0.86	1.60	1.86	2.49	4.16	1.26	-0.53	–0.55
Normal	log(HC)	2.79	3.18	3.69	3.57	4.13	5.61	0.59	0.70	–0.19
Normal	log(NO_x)	–0.10	1.13	2.56	2.44	3.77	7.02	1.75	0.42	–0.65

Table 2. Basic statistics of pollution generated by combustion engine powered by LPG

State	Pollution	minutes	$q_{0.25}$	Mean	Median	$q_{0.75}$	max	Std.dev	Skewnes	Kurtosis
Cold	log(CH_4)	2.66	3.74	4.15	3.96	4.64	5.83	0.70	0.19	–0.21
Cold	log(HC)	5.11	6.02	6.71	6.54	7.62	8.77	1.01	0.19	–1.08
Cold	log(NO_x)	0.59	2.65	4.16	4.18	5.33	7.53	1.68	0.20	–0.93
Medium	log(CH_4)	0.06	2.01	2.60	2.76	3.17	4.66	0.83	–0.34	0.31
Medium	log(HC)	3.24	4.11	4.61	4.56	5.08	6.97	0.72	0.39	–0.14
Medium	log(NO_x)	0.33	2.30	3.38	2.96	4.36	7.27	1.58	0.52	–0.40
Normal	log(CH_4)	–0.75	1.73	2.20	2.39	2.90	4.52	1.06	-0.84	0.54
Normal	log(HC)	2.75	3.50	4.23	4.11	4.96	6.18	0.90	0.23	–0.95
Normal	log(NO_x)	0.08	1.74	3.30	2.97	4.93	7.65	2.02	0.32	–0.90

differences between fuels during the cold start phase. Figures 4–6 illustrate how the concentrations of individual pollutants vary with temperature and fuel type, confirming earlier observations reported in the literature.

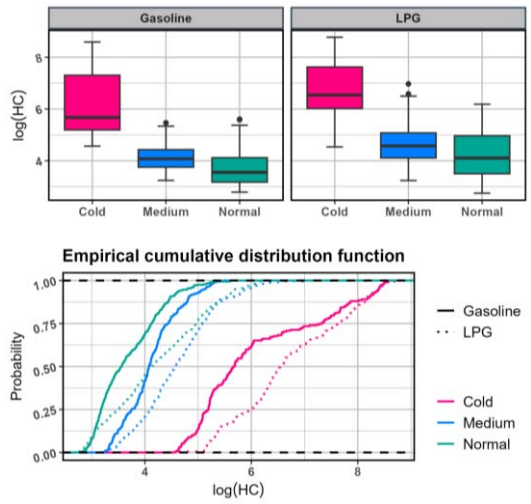

Fig. 4. Comparison of HC concentrations in logarithmic scale depending on engine operating temperature and fuel type

Figure 4 shows a comparison of hydrocarbon (HC) concentrations on a logarithmic scale, plotted against engine operating temperature and fuel type. There is a clear difference in the emission profiles between petrol and LPG, especially during the cold start phase. The dots in the boxplots represent statistical outliers, defined as values lying more than 1.5 times the interquartile range from the nearest quartile.

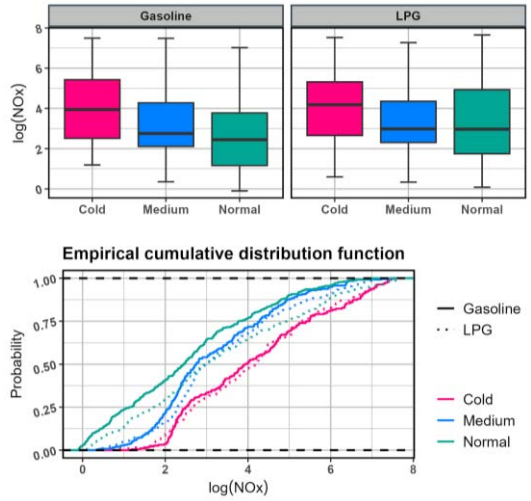

Fig. 5. Comparison of NO_x concentrations in logarithmic scale depending on engine operating temperature and fuel type

Figure 5 shows a comparison of nitrogen oxides concentrations on a logarithmic scale for different engine operating temperatures and fuels. We observe that the differences in NO_x emissions are more pronounced at lower temperatures, where LPG shows a more stable emission profile than gasoline.

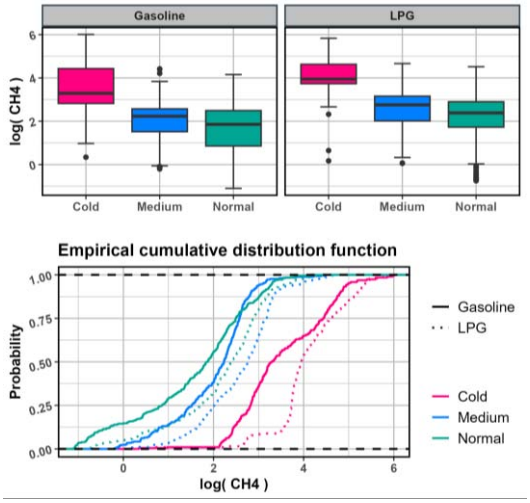

Fig. 6. Comparison of CH_4 concentrations in logarithmic scale depending on engine operating temperature and fuel type

Figure 6 shows methane (CH_4) concentrations on a logarithmic scale, varying with temperature and fuel type. Methane emissions are clearly lower for LPG, especially at higher engine operating temperatures, confirming the more favorable emission profile of this fuel.

Tables 1 and 2, and Fig. 4–6, demonstrate that the Kruskal-Wallis test was employed to investigate the presence of differences in the distribution of pollutant concentrations on a logarithmic scale across engine operating states. The table below presents the values of the test statistics T and the corresponding test probabilities Table 3 shows that for each fuel and for each type of pollutant, the test probability is below the level $\alpha = 0.05$. Therefore, for both Gasoline fuel and LPG, the engine operating temperature significantly affects the value of pollutant concentrations NO_x, CH_4, HC.

Table 3. The result of the Kruskal-Wallis test regarding the differences in the distribution of pollutant concentrations due to the operating temperature range of the combustion engine

Fuel	Pollution	T	p.value
Gasoline	NO_x	78.96	7.144×10^{-18}
Gasoline	HC	511.41	8.901×10^{-112}
Gasoline	CH_4	297.36	2.685×10^{-65}
LPG	NO_x	19.10	7.104×10^{-5}
LPG	HC	604.57	5.239×10^{-132}
LPG	CH_4	484.45	6.3659×10^{-106}

The Kolmogorov-Smirnov test was used to compare the distributions of pollutant concentration differences on a logarithmic scale by fuel type. Empirical distribution functions are presented in Fig. 4–6. Table 4 presents the values of the test statistics D and the test probability values. For the 'Cold' state and NO_x pollution, for the 'Medium' state and NO_x pollution, the test probability is above 0.05, so for these cases , there is no basis for rejecting the working hypothesis; the pollutant concentration distributions are equal or differ insignificantly. For the remaining states and pollutants, the test probability is below the value 0.05, so the pollutant distributions differ significantly.

Table 4. The result of the Kolmogorov-Smirnov test regarding the differences in the distribution of pollutant concentrations due to fuel type

State	Pollution	D	p.value
Cold	NO_x	0.062	0.8475
Cold	HC	0.391	3.781×10^{-13}
Cold	CH_4	0.469	9.533×10^{-19}
Medium	NO_x	0.112	0.07777
Medium	HC	0.344	1.045×10^{-13}
Medium	CH_4	0.382	7.355×10^{-17}
Normal	NO_x	0.153	4.381×10^{-4}
Normal	HC	0.304	8.476×10^{-15}
Normal	CH_4	0.240	2.259×10^{-9}

According to formula (3), the effects of engine load, engine operating temperature, and rpm on the concentration of pollutants were identified. The values of structural parameters, standard deviation of these parameters, test statistic values (6) and test probability (7) for both Gasoline and LPG fueled engines are presented in Tables 5–9.

Table 5. Structural parameter values, standard deviations, test statistic values and test probabilities for contamination HC

	Value	Std.Error	t	p.value
$\theta_0^{Gasoline}$	7.54	0.12	61.46	7.76×10^{-305}
$\theta_1^{Gasoline}$	0.01	0.001	9.66	5.82×10^{-21}
$\theta_2^{Gasoline}$	–0.05	0.001	–49.77	6.7×10^{-247}
$\theta_3^{Gasoline}$	0.0002	0.0001	6.49	1.51×10^{-10}
θ_0^{LPG}	7.99	0.17	46.69	1.99×10^{-230}
θ_1^{LPG}	0.01	0.002	5.87	6.36×10^{-9}
θ_2^{LPG}	–0.05	0.002	–35.26	6.25×10^{-165}
θ_3^{LPG}	0.0004	0.0001	5.95	4.09×10^{-9}

From Table 5 we can see that for both Gasoline and LPG at the significance level 0.05 for each of the structural parameters should be rejected in favor of the alternative hypothesis, each of the factors (engine load, engine temperature, rpm) significantly affects the value of concentration HC. The values of structural parameters $\theta_2^{Gasoline}$ and θ_2^{LPG} are negative, which assumes that with the increase of engine temperature, the concentration decreases HC. It should be noted that the extremely small p-values reported in Table 5 do not carry a physical meaning in themselves but only confirm that the corresponding parameters are highly statistically significant.

Table 6. Structural parameter values, standard deviations, test statistic values and test probabilities for contamination CH_4

	Value	Std.Error	t	p.value
$\theta_0^{Gasoline}$	4.13	0.22	19.18	1.02×10^{-67}
$\theta_1^{Gasoline}$	0.01	0.002	3.81	0.0002
$\theta_2^{Gasoline}$	–0.04	0.002	–21.61	6.77×10^{-82}
$\theta_3^{Gasoline}$	0.001	0.00008	7.16	1.85×10^{-12}
θ_0^{LPG}	4.99	0.19	25.95	4.12×10^{-108}
θ_1^{LPG}	0.002	0.002	1.16	0.25
θ_2^{LPG}	–0.04	0.002	–23.38	1.61×10^{-92}
θ_3^{LPG}	0.0005	0.00007	6.71	3.66×10^{-11}

From Table 6 we can see that for LPG at the significance level 0.05 there is no basis for rejecting the null hypothesis for the parameter θ_1^{LPG}(engine load), while for the remaining parameters, both for Gasoline and LPG, the working hypothesis should be rejected in favor of the alternative hypothesis, therefore each of the factors (engine load, engine temperature, rpm) significantly affects the concentration value CH_4. The values of the structural parameters $\theta_2^{Gasoline}$ and θ_2^{LPG} are negative, which means that with the increase in engine temperature, the concentration decreases CH_4.

Table 7. Structural parameter values, standard deviations, test statistic values and test probabilities for contamination NO_x

	Value	Std.Error	t	p.value
$\theta_0^{Gasoline}$	2.028	0.308	6.589	8.007×10^{-11}
$\theta_1^{Gasoline}$	0.03169	0.003	9.606	9.505×10^{-21}
$\theta_2^{Gasoline}$	–0.029	0.0033	–10.769	2.4104×10^{-25}
$\theta_3^{Gasoline}$	0.00156	0.0001	13.169	5.533×10^{-36}
θ_0^{LPG}	0.596	0.324	1.839	0.0663
θ_1^{LPG}	0.037	0.003	10.725	3.652×10^{-25}
θ_2^{LPG}	–0.014	0.003	–4.973	8.0813×10^{-7}
θ_3^{LPG}	0.0018	0.0001	15.334	1.0557×10^{-46}

Table 7 shows that for LPG, at the 0.05 significance level, there is no basis to reject the working hypothesis for the parameter θ_0^{LPG}, while for the remaining parameters, both gasoline and LPG, the working hypothesis should be rejected in favor of the alternative hypothesis, therefore each of the factors (engine load, engine temperature, rpm) significantly affects the NO_x concentration.

Table 8 presents the values of the standard deviations of the residuals in the model (3), the values of the coefficient of determination R^2, the values of the test statistic (9) and the test probability (10) regarding the significance of the multiple correlation coefficient for each pollutant and each fuel type.

Table 8. Values of the standard deviation σ, coefficient of determination R^2, test statistic F and test probability values

Fuel	Pollution	σ	R^2	F	p.val
Gasoline	NO_x	1.39	0.38	162.83	2.45×10^{-82}
Gasoline	HC	0.56	0.78	966.86	3.56×10^{-265}
Gasoline	CH_4	0.98	0.44	207.42	1.89×10^{-99}
LPG	NO_x	1.47	0.37	152.98	2.57×10^{-78}
LPG	HC	0.78	0.65	488.41	4.19×10^{-180}
LPG	CH_4	0.87	0.46	223.40	3.43×10^{-105}

Table 9 presents the results regarding the significance of differences in structural parameters for model (3) for each of the different fuels.

For pollution, HC there is no basis to reject the null hypothesis for the coefficients with the variables engine load, engine temperature and rpm (differences between parameters in equation (3) for Gasoline and LPG are not significant), whereas for the intercept the null hypothesis is rejected in favor of the alternative hypothesis (significant difference in the effect of fuel type on the concentration value HC).

Table 9. Statistics values of structural parameters and test probability values

Pollution	j	T_j	p_j
NO_x	0	50.89	0.00
NO_x	1	–1.94	0.026
NO_x	2	–5.69	0.00
NO_x	3	–0.62	0.27
HC	0	–23.82	0.00
HC	1	0.96	0.17
HC	2	–0.30	0.38
HC	3	–0.22	0.41
CH_4	0	–37.99	0.00
CH_4	1	2.72	0.003
CH_4	2	–0.64	0.26
CH_4	3	0.21	0.42

For pollution CH_4 there is no basis to reject the null hypothesis for the coefficients with the variables engine temperature and rpm, whereas for the intercept and engine load, the null hypothesis is rejected in favor of the alternative hypothesis (significant difference in the effect of fuel type and engine load for various fuels on the concentration value CH_4).

For NO_x pollution, there is no basis to reject the null hypothesis for the coefficient at rpm (rpm has a similar effect on the NO_x concentration values for different fuels), whereas for the intercept, engine load and engine temperature, the null hypothesis is rejected in favour of the alternative hypothesis (significant difference in the effect of fuel type and engine load and temperature when fuelled with different fuels on the NO_x concentration value).

4. Conclusions and discussion of results

The laboratory measurements carried out and the statistical analysis of the obtained results allowed the formulation of the following conclusions:

1. The increase in engine load has a significant impact on the increase in the level of hydrocarbon, methane and nitrogen oxide emissions, both when fuelled with gasoline and LPG (the exception is the lack of a significant increase in methane emissions for gas fuelling). Although the increase in engine load and crankshaft speed in LPG engines has a smaller impact on emissions compared to gasoline engines, this is due to the unique combustion characteristics of LPG. Thanks to a more homogeneous fuel-air mixture and higher combustion efficiency, the LPG engine is able to maintain a more stable combustion process, even at higher loads and rotational speeds, which limits the increase in emissions.
2. The increase in engine coolant temperature, representing the increase in catalytic converter temperature, has a significant impact on reducing hydrocarbon, methane and nitrogen oxides emissions when fueled with gasoline and LPG. Although both LPG and gasoline have a significant impact on pollutant emissions during the cold start phase, the differences in their emission profiles result from different combustion dynamics. LPG, due to its superior physicochemical properties, promotes faster catalyst heating, which in turn leads to a more rapid reduction in HC and CO emissions compared to gasoline. At the same time, its lower sensitivity to ambient temperature changes makes LPG emissions more stable in winter conditions, which is confirmed by the results of literature studies [21, 44].
3. The increase in the engine crankshaft speed is associated with a significant increase in the emission of hydrocarbons, methane and nitrogen oxides. There were no significant differences between the fuels considered.
4. In the WLTC cycle, the highest emission level occurs at the beginning of the test, when the catalytic converter has not yet reached its starting temperature.
5. Frequent cold starts and short distances covered by the vehicle contribute to increased emissions of harmful exhaust gas components.

The laboratory tests and analysis of the results indicate a relationship between selected engine operating parameters (load, temperature and rotational speed) and the emission of hydrocarbons, methane and nitrogen oxides for gasoline and LPG fuelling. The issue of the relationship between engine load and emission of harmful substances was raised, among others, in the article by Hashem et al. The authors performed an experimental and numerical analysis using simulation software and showed that with increasing load (and constant engine speed) the emission of selected exhaust components increases, including nitrogen oxides. According to the authors, the increase is greater during operation on LPG, which may be due to the faster combustion process when fueled with gas. The data presented in our article also show that increasing load leads to an increase in NO_x for both test fuels. The same authors also examined the issue of the effect of increasing the rotational speed of the engine shaft at constant load. They measured the concentration of nitrogen oxides, among others, which increased with the increase in the shaft rotational speed. They emphasized that this is related to the increase in temperature in the combustion chamber, and this effect was noticeable for gasoline and, to a greater extent, for LPG. These observations are consistent with those presented in the paper.

The results of this study indicate the need for further development of catalyst temperature management strategies, particularly under low ambient temperature conditions, which can significantly enhance the efficiency of pollutant emission reduction in dual-fuel engines. Another area that requires in-depth research is the optimization of ignition and injection strategies in LPG engines, especially in the context of different temperature conditions.

The research presented in the study revealed a significant impact of engine coolant temperature on the emission of hydrocarbons, nitrogen oxides, and methane from the engine. The coolant temperature represents the engine operating conditions, but also the catalytic converter heating process. This effect may be further enhanced by interactions between injected fuel and residual exhaust gases, as demonstrated in HCCI engine studies [17]. This is confirmed by the research conducted by Worsztynowicz and Uhryński [50], who measured, among other things, the temperatures of the coolant and the reactor during their study. The topic of increased emission of harmful substances in exhaust gases right after a cold start is discussed from different perspectives. Woo Jeong et al. [49] investigated

the relationship between the content of ammonia and nitrogen oxides in exhaust gases, varying the temperature. One of their observations was a significantly increased NO_x emission after a cold start, which gradually decreased as the catalytic converter temperature increased. The simulations conducted by Reiter et al. [39] are another confirmation of the problem of methane and nitrogen oxides emissions by LDVs during a cold start. Te authors, among others, drew attention to the variability of emissions depending on the season, additionally emphasizing the effect of temperature on emissions. In winter, the catalytic converter needs even more time to reach the light-off temperature. Usman et al. [47], During their studies on emissions depending on the fuel used, they presented, among others, a graph showing the emissions of hydrocarbons and nitrogen oxides as a function of the crankshaft's rotational speed. With the increase in rotational speed, the emission of nitrogen oxides increased, and that of hydrocarbons decreased. The reduction of hydrocarbon emissions did not occur in our studies.

Nomenclature

CI	compression ignition
CNG	compressed natural gas
DI	direct injection
LPG	liquefied petroleum gas
SI	spark ignition

Bibliography

[1] Adam TW, Astorga C, Clairotte M, Duane M, Elsasser M, Krasenbrink A et al. Chemical analysis and ozone formation potential of exhaust from dual-fuel (liquefied petroleum gas/gasoline) light duty vehicles. Atmos Environ. 2011;45: 2842-2848. https://doi.org/10.1016/j.atmosenv.2011.03.002

[2] Appel D, Hagen FP, Wagner U, Koch T, Bockhorn H, Trimis D. Influence of low ambient temperatures on the exhaust gas and deposit composition of gasoline engines. ASME 2020 Internal Combustion Engine Division Fall Technical Conference, Virtual, Online: American Society of Mechanical Engineers. 2020:V001T04A003. https://doi.org/10.1115/ICEF2020-2932

[3] Bielaczyc P, Szczotka A, Woodburn J. The effect of a low ambient temperature on the cold-start emissions and fuel consumption of passenger cars. Proc Inst Mech Eng Part D-J Automob Eng. 2011;225:1253-1264. https://doi.org/10.1177/0954407011406613

[4] Çinar C, Şahin F, Can Ö, Uyumaz A. A comparison of performance and exhaust emissions with different valve lift profiles between gasoline and LPG fuels in a SI engine. Appl Therm Eng. 2016;107:1261-1268. https://doi.org/10.1016/j.applthermaleng.2016.07.031

[5] Faria MV, Varella RA, Duarte GO, Farias TL, Baptista PC. Engine cold start analysis using naturalistic driving data: City level impacts on local pollutants emissions and energy consumption. Sci Total Environ. 2018;630:544-559. https://doi.org/10.1016/j.scitotenv.2018.02.232

[6] Frondel M, Marggraf C, Sommer S, Vance C. Reducing vehicle cold start emissions through carbon pricing: evidence from Germany. Environ Res Lett. 2021;16:034041. https://doi.org/10.1088/1748-9326/abde06

[7] Gao J, Tian G, Sorniotti A, Karci AE, Di Palo R. Review of thermal management of catalytic converters to decrease engine emissions during cold start and warm up. Appl Therm Eng. 2019;147:177-187. https://doi.org/10.1016/j.applthermaleng.2018.10.037

[8] Gong C, Yan S, Su Y, Wang Z. Effects of fuel injection timing on combustion and emissions of a spark-ignition methanol and methanol/liquefied petroleum gas (LPG) engine during cold start. Energy Fuels. 2009;23:3536-3542. https://doi.org/10.1021/ef900190q

[9] Gumus M. Reducing cold-start emission from internal combustion engines by means of thermal energy storage system. Appl Therm Eng. 2009;29:652-660. https://doi.org/10.1016/j.applthermaleng.2008.03.044

[10] Gumus M, Ugurlu A. Application of phase change materials to pre-heating of evaporator and pressure regulator of a gaseous sequential injection system. Appl Energ. 2011;88: 4803-4810. https://doi.org/10.1016/j.apenergy.2011.06.053

[11] Gutierrez LG, Wooldridge MS, Petersen BR, Wooldridge ST. In-cylinder imaging and emissions measurements of cold-start split injection strategies. J Eng Gas Turbines Power. 2025;147:081014. https://doi.org/10.1115/1.4067602

[12] Hao L, Xu X, Guo X, Ji C, Wang X, Tan J et al. Investigation of cold-start emission control strategy for a bi-fuel hydrogen/gasoline engine. Int J Hydrogen Energ. 2016;41: 18273-18281. https://doi.org/10.1016/j.ijhydene.2016.08.038

[13] Hastie T, Tibshirani R, Friedman J. The elements of statistical learning. Springer New York 2009. https://doi.org/10.1007/978-0-387-84858-7

[14] Henein NA, Tagomori MK. Cold-start hydrocarbon emissions in port-injected gasoline engines. Prog Energy Combust Sci. 1999;25:563-593. https://doi.org/10.1016/S0360-1285(99)00003-9

[15] Hu J, Frey HC, Boroujeni BY. Contribution of cold starts to real-world trip emissions for light-duty gasoline vehicles. Atmosphere. 2022;14:35. https://doi.org/10.3390/atmos14010035

[16] Hu J, Li D, Hall M, Matthews R, Moilanen P, Wooldridge S et al. A parametric study to improve first firing cycle emissions of a gasoline direct injection engine during cold start. Int J Eng Res. 2023;24:3428-3444. https://doi.org/10.1177/14680874231153302

[17] Hunicz J. An experimental study into the chemical effects of direct gasoline injection into retained residuals in a homogeneous charge compression ignition engine. Int J Eng Res. 2016;17:1031-1044. https://doi.org/10.1177/1468087416636492

[18] James G, Witten D, Hastie T, Tibshirani R. An introduction to statistical learning: with applications in R. Springer 2021. https://doi.org/10.1007/978-1-0716-1418-1

[19] Jatana GS, Dal Forno Chuahy F, Szybist J. Effect of split-injection strategies on engine performance and emissions under cold-start operation. SAE Technical Paper 2023-01-0236. 2023. https://doi.org/10.4271/2023-01-0236

[20] Joshua Ikiaye D, Moore Ojapah M. Performance, emission and cost analysis of LPG and gasoline in a single cylinder engine. IJERSTE 2023;12:212-219. https://doi.org/10.55948/IJERSTE.2023.0424

[21] Kim J, Choi K, Myung C-L, Park S. Experimental evaluation of engine control strategy on the time resolved THC and nano-particle emission characteristics of liquid phase LPG direct injection (LPG-DI) engine during the cold start. Fuel Process Technol. 2013;106:166-173. https://doi.org/10.1016/j.fuproc.2012.07.020

[22] Kim K, Kim J, Oh S, Kim C, Lee Y. Lower particulate matter emissions with a stoichiometric LPG direct injection engine. Fuel. 2017;187:197-210. https://doi.org/10.1016/j.fuel.2016.09.058

[23] Kłosowski G, Rymarczyk T, Niderla K, Kulisz M, Skowron Ł, Soleimani M. Using an LSTM network to monitor industrial reactors using electrical capacitance and impedance tomography – a hybrid approach. Eksploat Niezawodn. 2023; 25(1):11. https://doi.org/10.17531/ein.2023.1.11

[24] Kontses A, Triantafyllopoulos G, Ntziachristos L, Samaras Z. Particle number (PN) emissions from gasoline, diesel, LPG, CNG and hybrid-electric light-duty vehicles under real-world driving conditions. Atmos Env. 2020;222:117126. https://doi.org/10.1016/j.atmosenv.2019.117126

[25] Kozłowski E, Borucka A, Oleszczuk P, Leszczyński N. Evaluation of readiness of the technical system using the semi-Markov model with selected sojourn time distributions. Eksploat Niezawodn. 2024;26. https://doi.org/10.17531/ein/191545

[26] Kwak H, Myung C-L, Park S. Experimental investigation on the time resolved THC emission characteristics of liquid phase LPG injection (LPLi) engine during cold start. Fuel. 2007;86:1475-1482. https://doi.org/10.1016/j.fuel.2006.11.023

[27] Laskowski P, Zasina D, Zimakowska-Laskowska M, Orliński P. Modelling hydrocarbons cold-start emission from passenger cars. Adv Sci Technol Res J. 2021;15:117-125. https://doi.org/10.12913/22998624/138764

[28] Laskowski P, Zimakowska-Laskowska M, Matej J, Wiśniowski P. The problem of cold start emissions from vehicles. Combustion Engines. 2024;199(4):43-51. https://doi.org/10.19206/CE-186471

[29] Laskowski P, Zimakowska-Laskowska M, Zasina D. Modelling of the air pollutants' cold-start emissions depending on average vehicles' speed. Combustion Engines. 2022;188:96-103. https://doi.org/10.19206/CE-142171

[30] Lee K, Pintor DL, Assanis D, Cho S, Hwang J. Fuel temperature and injection pressure influence on the cold start GDI sprays. Appl Energy Combust Sci. 2023;16:100206. https://doi.org/10.1016/j.jaecs.2023.100206

[31] Liu F, Shafique M, Luo X. Literature review on life cycle assessment of transportation alternative fuels. Environ Technol Innov. 2023;32:103343. https://doi.org/10.1016/j.eti.2023.103343

[32] Liu H, Liu Q, Wang C. A novel valve strategy for particulate matter reduction in a gasoline direct injection engine operated at cold conditions. Int J Engine Res. 2025;26:325-338. https://doi.org/10.1177/14680874241276263

[33] Liu Z, Li L, Deng B. Cold start characteristics at low temperatures based on the first firing cycle in an LPG engine. Energy Convers Manag. 2007;48:395-404. https://doi.org/10.1016/j.enconman.2006.07.011.

[34] Ludykar D, Westerholm R, Almén J. Cold start emissions at +22, −7 and −20°C ambient temperatures from a three-way catalyst (TWC) car: regulated and unregulated exhaust components. Sci Total Environ. 1999;235:65-69. https://doi.org/10.1016/S0048-9697(99)00190-4

[35] Małek A, Caban J, Sarkan B. Research on low-emission vehicle powered by LPG using innovative hardware and software. The Archives of Automotive Engineering – Archiwum Motoryzacji. 2020;89:19-36. https://doi.org/10.14669/AM.VOL89.ART2

[36] Myung C-L, Kim J, Choi K, Hwang IG, Park S. Comparative study of engine control strategies for particulate emissions from direct injection light-duty vehicle fueled with gasoline and liquid phase liquefied petroleum gas (LPG). Fuel. 2012;94:348-355. https://doi.org/10.1016/j.fuel.2011.10.041

[37] Napolitano P, Alfè M, Guido C, Gargiulo V, Fraioli V, Beatrice C. Particle emissions from a HD SI gas engine fueled with LPG and CNG. Fuel. 2020;269:117439. https://doi.org/10.1016/j.fuel.2020.117439

[38] Pawlik P, Kania K, Przysucha B. Fault diagnosis of machines operating in variable conditions using artificial neural network not requiring training data from a faulty machine. Eksploat Niezawodn. 2023;25. https://doi.org/10.17531/ein/168109

[39] Reiter MS, Kockelman KM. The problem of cold starts: A closer look at mobile source emissions levels. Transp Res Part D Transp Environ. 2016;43:123-132. https://doi.org/10.1016/j.trd.2015.12.012

[40] Saliba G, Saleh R, Zhao Y, Presto AA, Lambe AT, Frodin B et al. Comparison of gasoline direct-injection (GDI) and port fuel injection (PFI) vehicle emissions: emission certification standards, cold-start, secondary organic aerosol formation potential, and potential climate impacts. Environ Sci Technol. 2017;51:6542-6552. https://doi.org/10.1021/acs.est.6b06509

[41] Šarkan B, Jaśkiewicz M, Kubiak P, Tarnapowicz D, Loman M. Exhaust emissions measurement of a vehicle with retrofitted LPG system. Energies. 2022;15:1184. https://doi.org/10.3390/en15031184

[42] Sharma NK. Comparison of spark ignition engine performance and emission analysis using gasoline, LPG and mixture fuels. IJMTST. 2020;6:33-36. https://doi.org/10.46501/IJMTST060608

[43] Talib Hashem G, Al-Dawody MF, Sarris IE. The characteristics of gasoline engines with the use of LPG: an experimental and numerical study. Int J Thermofluids. 2023a;18: 100316. https://doi.org/10.1016/j.ijft.2023.100316

[44] Talib Hashem G, Al-Dawody MF. Use of LPG in SI engine – a review study. Al-Qadisiyah J Eng. 2021;14(1):52-59, https://doi.org/10.30772/qjes.v14i1.751

[45] Tan D, Wang Y, Tan J, Li J, Wang C, Ge Y. Influence of ambient temperature on the CO_2 emitted of light-duty vehicle. J Environ Sci. 2024;140:59-68. https://doi.org/10.1016/j.jes.2023.04.018.

[46] Teymoori MM, Chitsaz I, Kashani NA, Davazdah Emami M. Cold-start emission reduction of the gasoline-powered vehicle utilizing a novel method. Int J Engine Res. 2023;24: 1840-1859. https://doi.org/10.1177/14680874221100816

[47] Usman M, Farooq M, Naqvi M, Saleem MW, Hussain J, Naqvi SR et al. Use of gasoline, LPG and LPG-HHO blend in SI engine: a comparative performance for emission control and sustainable environment. Processes. 2020;8:74. https://doi.org/10.3390/pr8010074

[48] Weilenmann M, Favez J-Y, Alvarez R. Cold-start emissions of modern passenger cars at different low ambient temperatures and their evolution over vehicle legislation categories. Atmos Environ. 2009;43:2419-2429. https://doi.org/10.1016/j.atmosenv.2009.02.005

[49] Woo Jeong J, Baek S, Park S, Lee S, Lim Y, Lee K. Trends in NO_x and NH_3 emissions caused by three-way catalysts. Fuel. 2024;366:131282. https://doi.org/10.1016/j.fuel.2024.131282

[50] Worsztynowicz B, Uhryński A. The analysis of heating process of catalytic converter using thermo-vision. Combustion Engines. 2015;162:41-51.

https://doi.org/10.19206/CE-116864
[51] Yusuf AA, Inambao FL. Effect of cold start emissions from gasoline-fueled engines of light-duty vehicles at low and high ambient temperatures: recent trends. Case Stud Therm Eng. 2019;14:100417. https://doi.org/10.1016/j.csite.2019.100417
[52] Zhang B, Li X, Wan Q, Liu B, Jia G, Yin Z. Hydrocarbon emission control of an adsorptive catalytic gasoline particulate filter during cold-start period of the gasoline engine. Energy. 2023;262:125445. https://doi.org/10.1016/j.energy.2022.125445
[53] Zhang Z, Man H, Zhao J, Jiang Y, Zeng M, Cai Z et al. Primary organic gas emissions in vehicle cold start events: Rates, compositions and temperature effects. J Hazard Mater. 2022;435:128979. https://doi.org/10.1016/j.jhazmat.2022.128979
[54] Zhang Z, Zhong W, Tan D, Cui S, Pan M, Zhao Z et al. Hydrocarbon adsorption mechanism of modern automobile engines and methods of reducing hydrocarbon emissions during cold start process: a review. J Environ Manage. 2024; 353:120188. https://doi.org/10.1016/j.jenvman.2024.120188
[55] Zimakowska-Laskowska M, Kozłowski E, Laskowski P, Wiśniowski P, Świderski A, Orynycz O. Vehicle exhaust emissions in the light of modern research tools: synergy of chassis dynamometers and computational models. Combustion Engines. 2025;200:145-154. https://doi.org/10.19206/CE-201224

Piotr Wiśniowski, DEng. – Motor Transport Institute, Poland.
e-mail: *piotr.wisniowski@its.waw.pl*

Edward Kozłowski, DSc, Prof. LUT – Faculty of Management, Lublin University of Technology, Poland.
e-mail: *e.kozlovski@pollub.pl*

Magdalena Zimakowska-Laskowska, DEng. – Environment Protection Centre, Motor Transport Institute, Poland.
e-mail: *magdalena.zimakowska-laskowska@its.waw.pl*

Prof. Marcin Ślęzak, DSc., DEng. – Motor Transport Institute, Poland.
e-mail: *marcin.slezak@its.waw.pl*

Sławomir Taubert, DEng. – Environment Protection Centre, Motor Transport Institute, Poland.
e-mail: *slawomir.taubert@its.waw.pl*

Ksawery Żbik, MEng. – Environment Protection Centre, Motor Transport Institute, Poland.
e-mail: *ksawery.zbik@its.waw.pl*

Article citation info:
Piórkowski P, Andrzejewski M, Nowak M. The analysis of the use of hydrogen in commercial vehicles. Combustion Engines. 2026;206(3):79-86. https://doi.org/10.19206/CE-216496

Piotr PIÓRKOWSKI
Maciej ANDRZEJEWSKI
Mateusz NOWAK

Combustion Engines
Polish Scientific Society of Combustion Engines

The analysis of the use of hydrogen in commercial vehicles

ARTICLE INFO

Received: 21 June 2025
Revised: 13 November 2025
Accepted: 7 January 2026
Available online: 24 January 2026

The article first presents current trends in power sources for selected heavy-duty vehicles (HDVs) and non-road mobile machinery (NRMM). The next part of the paper focuses on selected examples from the city bus and rail vehicle sectors. The article attempts to capture solutions in the research/design phase as well as post-production and implementation (operation). In the context of the obtained vehicle/rolling stock availability indicators, maintenance facilities and activities (current assessment of technical condition and restoration of serviceability) are important. Therefore, in addition to the use, aspects related to vehicle maintenance areas are also outlined. In addition, the paper analyzes methods to increase the volume of compressed hydrogen gas in tanks. The main idea is hydrogen in transportation applications. The paper addresses several of the more important issues mentioned above.

Key words: *railway, vehicles, buses, hydrogen, exploitation*

This is an open access article under the CC BY license (http://creativecommons.org/licenses/by/4.0/)

1. Introduction

The growing need to reduce fuel consumption and the resulting CO_2 emissions in transport means that alternative solutions are sought to achieve this goal. The requirements for reducing energy intensity result from, among others:

– the levels and stability of prices of fuels and raw materials necessary for the production of vehicles and their components
– the access to fuels and raw materials, which is an element of energy independence and security
– the state of the infrastructure for fuel and energy production, its storage, transmission and distribution and the need to maintain its stability.

The solution may be alternative drives, which not only reduce fuel consumption but also offer diversification and reduce the risk of becoming dependent on one technology. The market offers combustion engines powered by alternative fuels (CNG – Compressed Natural Gas, LNG – Liquified Natural Gas, biogas, ethanol, HVO – Hydrotreated Vegetable Oil, etc.), hybrid drives in various versions (MHEV – Mild Hybrid Electric Vehicle, HEV – Hybrid Electric Vehicle, PHEV – Plug-in Hybrid Electric Vehicle), battery-powered electric drive systems (BEV – Battery Electric Vehicle), and recently also hydrogen-powered vehicles. The latter can use hydrogen as a fuel for combustion engines (H2ICE – Hydrogen Internal Combustion Engine) or for direct electricity generation in fuel cells (FCEV – Fuel Cell Electric Vehicle) [7, 17]. In the future, we can expect further development of synthetic fuel production technology, based on the chemical binding of hydrogen and carbon captured from the atmosphere and biomass [11].

With such a wide range of possibilities, choosing one specific solution can be difficult, especially since most of these technologies are still in development and it is often difficult to estimate target functionalities, parameters, or costs of use [20].

Basically, the choice for each case should be made individually and be preceded by a detailed analysis of the needs, where the main selection criterion, apart from price, should be the level of access to infrastructure and ease of use, related to the available driving range, time and frequency of refuelling/charging.

The task of selecting the right technology for a given user will become even more difficult when hybrid energy storage technologies appear on a large scale, e.g. BEV charging stations supported by battery energy storage units and hydrogen-powered energy generators. From the perspective of heavy transport, a sufficiently large driving range, short refueling/charging times and access to infrastructure are key criteria for selecting technologies, apart from price [23].

One of the previously mentioned technologies that meets or may meet the above requirements in the future is hydrogen fuel cell electric vehicle (FCEV) technology. This is basically a hybrid drive in which a hydrogen-powered PEM fuel cell acts as the primary energy source responsible for the driving range. The secondary energy source that drives dynamics is electrochemical batteries. Their role is to stabilize the operation of the hydrogen fuel cell, which increases its efficiency and allows for energy storage, e.g. during regenerative braking [3]. Electrochemical batteries also power the drive during low-load operation, allowing periodic shutdown of the fuel cell.

Among the various types of fuel cells, PEM (Proton Exchange Membrane) fuel cells are mainly used in means of transport due to their ability to operate at ambient temperatures, short start-up and shut-down times, resistance to shocks and vibrations, and the ability to be powered by oxygen taken from the air [5]. In addition to oxygen, fuel cells require fuel – hydrogen, which has a very high gravimetric energy density of 120 MJ/kg (LHV – Lower Heating Value). Unfortunately, high gravimetric density does not go hand in hand with volumetric density, which is very low in ambient conditions (approx. 10.8 MJ/m^3). This requires transporting hydrogen in high-pressure tanks, stored as a gas at 35–70 MPa [4]. Such high pressures require special

refueling infrastructure and affect the time and energy costs of refueling.

The problems and energy costs result from the laws of thermodynamics, which cause hydrogen to be compressed during filling and thus heated, which further increases its pressure. As a result, after the gas temperature has equalized with the ambient temperature, the pressure in the tanks is lower than it was in the final phase of filling. This can result in incomplete use of the tanks and a limited range [24]. An alternative is to extend the refueling time and/or cool the supplied hydrogen, which requires additional energy [12].

2. The analysis of the city buses market

The share of the hydrogen buses is still not big and in 2020, there were 5648 fuel cell buses all over the world (93.7% in China) [26]. In Europe on 1st January 2023, there were 370 fuel cell buses in operation. Registrations of these kinds of buses in Europe remain marginal, with numbers such as 207 in 2023 and 378 in 2024 [30]. In 2023, the fuel cell buses had only a 4.6% share in the zero-emission bus market in Europe, where the rest of the market belongs to battery electric buses [30]. Despite many manufacturers of fuel cell buses, actually, the fuel cells are used, manufactured mainly by Ballard Power Systems or Toyota [2, 26, 30].

The hydrogen city bus demonstrators were developed in the 1990s. The first fuel cell buses were rather the smaller versions (approx. 9–10 m long), which probably resulted from the low power output of the initial fuel cells and problems with hydrogen storage (limited range) [25]. Toyota and Hino cooperated from 2000 onward in the field of hydrogen city bus development. This cooperation resulted in Toyota FCHV-BUS, which was equipped with two 90 kW PEFC fuel cells and two 80 kW traction motors (Fig. 1) [25].

Nowadays, despite over 30 years of fuel cell bus development, this propulsion system still has an economic disadvantage compared to battery-electric and diesel buses [14, 21, 30]. A study from September 2023 by Eurac Research, which compared the operating costs of battery electric buses with those of fuel cell electric buses, revealed that battery electric buses are 2.3 times cheaper to run per kilometer than fuel cell electric buses (0.55 Euro vs 1.27 Euro) [8, 30].

According to manufacturers, the fuel cell electric buses should combine the advantages of diesel and electric buses. Because the charging time for an electric bus is about 4–5 hours, it is not possible to replace a diesel bus with an electric bus [14, 30]. Hydrogen tanks refueling takes less time than electric battery charging (approx. 15 minutes), which is very similar to diesel refueling [14], and the fuel cell bus does not emit any toxic compounds into the air. Additionally, thanks to a smaller traction battery, the fuel cell bus can be up to 5000 kg lighter than a battery electric bus [25, 26, 31].

The main component of the fuel cell bus drive system is the fuel cell, which produces the electric energy for the electric motors to drive the wheels or charge the batteries. The fuel cell buses are also equipped with an electric battery with much less capacity than in electric buses. In Solaris Urbino Hydrogen, the battery capacity is 29 kWh [30], whereas in Solaris Urbino Electric, it can exceed 520 kWh. In the fuel cell buses, the battery is used only for acceleration and energy recuperation during braking. Very important in fuel cell buses are the hydrogen tanks, which in the past were mainly made of metal (steel and aluminum alloys). The metal technology tanks were cheap, but also heavy. The maximum pressure was about 20 MPa. Currently, the tanks are made of composites. Modern technology enables pressure up to 35 MPa (in some cases, up to 50–70 MPa), increasing vehicle range at a lower mass [19].

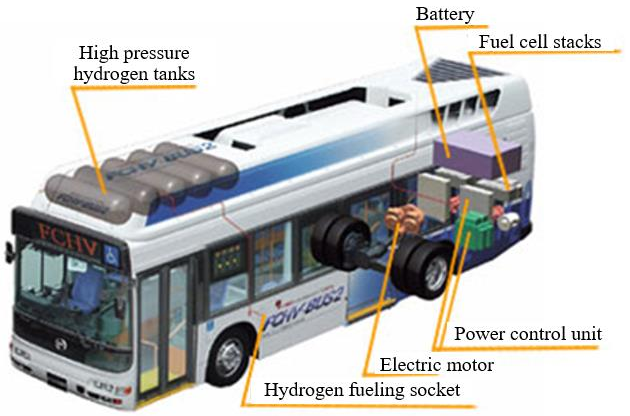

Fig. 1. The propulsion system components of Toyota FCHV-BUS [25]

Table 1. Technical data of Solaris buses with different drive [26, 30]

	Solaris Urbino 12 Electric	Solaris Urbino 12 Hydrogen
Fuel cell power [kW]	–	70
Traction motors power [kW]	200 (option: 2×125)	2×125 (option: 220)
Traction battery capacity [kWh]	200–600	Lithium-ion 29.2

Most solutions use a small traction battery (approx. 30 kW in Solaris Urbino 12 Hydrogen) and a large fuel cell (70 kW in Urbino 12 Hydrogen) – Table 1. It should be mentioned that there are also concepts that use a small fuel cell and a large traction battery. One example is Safra, with a 132 kWh traction battery and a 30 kW fuel cell [30]. According to measurements taken in real driving conditions across three routes, a Solaris Urbino 12 Hydrogen consumes 8.78–9.11 kg of H_2 per 100 km [16].

Another concept presented by Mercedes-Benz is the eCitaro REX, where the battery electric bus (392 kWh batteries) uses a 60 kW fuel cell as a range extender. This vehicle is equipped with hydrogen tanks that store 30 kg of hydrogen. According to the manufacturer, the range exceeds 300 km [26, 30, 31].

3. The railway market analysis

The chapter presents the status quo of selected commercial or R&D projects undertaken by leading entities in the rail vehicle manufacturing industry. It should be noted that among them, well-known Polish companies – rolling stock manufacturers – have experience with hydrogen drives.

The most advanced work on the use of hydrogen in rail transport in Poland (passenger and freight) can be proud of PESA Bydgoszcz S.A. For years, PESA's Hydrogen Ready strategy has been communicated, primarily regarding passenger vehicles (hydrogen multiple units based on the Regio 160 platform). Nevertheless, the first solution with

a hydrogen drive was the design of the SM42-6Dn Hydrogen shunting locomotive. It was created as a result of a thorough modernization and redesign of the SM42 locomotive, commonly used in Poland. There are numerous press reports and publications related to this vehicle [10]. Currently, PESA Bydgoszcz, after a long period of attempts to acquire a partner for longer tests of the vehicle (talks were held with, among others, Orlen) and a hydrogen drive solution (fuel cells), has concluded a cooperation agreement with the operator/carrier Pol-Miedź Trans from the KGHM Polska Miedź S.A. Group.

The field tests at Pol-Miedź Trans are certainly an important stage in the commercialization of hydrogen technology in the Polish railway industry, moving it from the research and development phase to practical operation under difficult industrial conditions.

At H. Cegielski FPS, recent months have culminated in the completion of a multi-year R&D project at the Poznań factory, which operates in the field of modernization and the production of new rail vehicles, mainly passenger cars. In the summer of 2024, the PLUS 227M vehicle (a 2-unit dual-drive multiple unit) obtained homologation, while at the beginning of 2025, the PLUS 228M vehicle (a 3-unit dual-drive multiple unit) was approved for operation on Polish railway lines. Importantly, the H. Cegielski FPS company recently signed a contract to deliver 6 electric multiple units based on the PLUS platform for the Lubuskie province (where the 227M and 228M vehicles were also delivered). This is proof that the family of vehicles from the PLUS platform will be developed.

In 2022, a letter of intent was signed with Łukasiewicz – Poznań Institute of Technology (design work) and Impact Clean Power Technology (supplier of the drive, including the hydrogen component) regarding work on the development of the PLUS vehicle for a hydrogen version (fuel cells or hydrogen combustion in a conventional piston engine). So far, a feasibility study for the project has been conducted in cooperation with the leading design office in the country.

An important platform for the exchange of knowledge and operational experience in the country is the cyclical conference Hydrogen4rail – Future of Transport, initiated by the then Łukasiewicz – Rail Vehicles Institute "TABOR", organized in cooperation with the Polish Chamber of Railways. The main substantive content of the past 5th edition on 16–17.06.2025 was as follows: Hydrogen as an energy carrier in transport - science and practice, Prospects and conditions for the development of hydrogen transport, Strategic planning: hydrogen, diesel or electrification, The process of admitting systems and parts of compressed hydrogen storage systems for hydrogen-powered vehicles in Poland, Introduction of hydrogen technology on the railway in Poland – safety aspects at a railway hydrogen refueling station.

By the way, this event is an example of an evolution towards the potential dissemination of hydrogen fuel in the rail sector and of practitioners' approach to vehicle maintenance (for example, P1–P5 reviews in Poland). After quite optimistic voices in 2021–2022, statements took on a subdued tone in the face of market realities, even from precursors in the implementation of the first homologated vehicles in Europe (Alstom Coradia iLint). This is primarily the result of the market debuts of more vehicles in Germany. After a period of several months of operation (mainly 2023–2024), the efficiency of operation and maintenance of hydrogen-powered EMUs (Electric Multiple Units). The main barriers to development include the high cost of hydrogen fuel, problems with its current supply, and ensuring the absolutely required high quality of the fuel (there are known cases of contaminated hydrogen being supplied to power mass transport vehicles) [13, 22]. In addition, there were technical problems with the traction unit drive systems (high failure rate). Currently, unexpectedly, transport organizers in German states that purchased hydrogen vehicles have to put vehicles with Compressed Ignition engines (Diesel) into operation as a substitute transport, often as a result of long-term rental from rolling stock pools, i.e. companies such as ROSCO (Rolling Stock Company).

Siemens Mobility is also one of the manufacturers that has placed its hydrogen vehicles on the global market. Its Mireo Plus H has undergone tests, among others, on German rail routes in regional traffic. Siemens recently won a contract to supply its solutions. By the end of 2026, three Siemens Mireo Plus H (Fig. 2) trainsets will start operating on the Südostbayernbahn network in Bavaria [28, 29].

Fig. 2. Mireo Plus H by Siemens in two drive versions [29]

The RS ZERO is Stadler's latest regional train offering, designed to replace the popular Regio-Shuttle RS1, which has been the backbone of German and Czech regional rail transport for almost three decades [27]. The RS ZERO's main feature is its low emissions, achieved through modern drive technologies. The RS ZERO is available with two eco-friendly drive systems (Fig. 3):

Hydrogen (Hydrogen-hybrid Electric Multiple Unit – HEMU): uses fuel cells that convert hydrogen into electricity to power the engines. This is a good solution for non-electrified or partially electrified lines, where traditional electric trains cannot be used, and investments in full electrification are unprofitable.

Battery (Battery Electric Multiple Unit – BEMU): operates entirely on batteries, making it suitable for shorter, partially electrified routes and for charging at stations or under the catenary.

The market debut of the RS ZERO prototype with hydrogen drive took place at the InnoTrans 2024 trade fair in Berlin. Stadler also signed an agreement with the Thuringian authorities and the operator Erfurter Bahn to launch a pilot project using the RS ZERO with a hydrogen engine, with passenger test runs planned for mid-2026.

Fig. 3. RS ZERO vehicle produced by Stadler

4. Hydrogen in the light of vehicle maintenance

According to the Office of Rail Transport (UTK) and other National Security Authorities (NSA): the Maintenance Management System (MMS) includes a set of procedures and instructions aimed at minimizing the risk associated with maintaining a railway vehicle and, as a result, ensuring that the maintained vehicles are able to move safely on the railway network [32].

In order to improve the efficiency of the processes of maintaining rail vehicles in a state of fitness for use, specialist software (based on database systems) has been used. There are tailor-made solutions (depending on the specifics of the fleet of vehicles) and so-called boxed solutions (with no possibility of modifying the software or its functionality).

Systematizing detailed issues concerning maintenance management systems is included in Regulation 2019/779. It specifies the requirements that a maintenance management system must meet. It also indicates the criteria used in the certification process to assess it (due to the security of sensitive data). The main feature of a maintenance management system is its division into 4 component functions [32]:

– a management function, which enables supervision over the three so-called maintenance functions (defined below) and their coordination; it also enables ensuring the safe condition of a railway vehicle in the railway system
– a maintenance development function; its task is to shape the vehicle maintenance documentation (DSU – maintenance system documentation) based on the vehicle design documentation and experience from its operation
– a rolling stock maintenance management function; its task is to manage the withdrawal of a vehicle from operation and its subsequent reintroduction into it
– a maintenance performance function; enables the required maintenance of a vehicle or its parts to be carried out.

In summary, the system should ensure that vehicles are maintained in accordance with the vehicle's maintenance documentation and the applicable regulations, including TSIs, and the guidelines and provisions resulting from those regulations. All entities responsible for maintenance are required to develop and implement a maintenance management system.

Digital maintenance management systems will also be needed for hydrogen-powered vehicles. The operation of hydrogen-powered rail vehicles requires special attention due to the unique properties of hydrogen and the technologies used. The key aspects to look out for are listed below [22].

Leak detection: Advanced hydrogen detection systems that can quickly detect even small leaks should be used. Hydrogen is odourless and colourless, making it difficult to detect without specialist sensors.

Ventilation: Vehicles must be equipped with effective ventilation systems to prevent hydrogen accumulation in enclosed spaces, especially in the event of a leak.

Location of tanks and fuel cells: Hydrogen is lighter than air and rises quickly. For this reason, hydrogen tanks and fuel cells are often mounted on the roof of the train so that in the event of a leak, the hydrogen is released into the atmosphere, minimizing the risk of fire or explosion.

Impact resistance: Hydrogen tanks must be designed to withstand extreme loads in the event of a collision or accident, minimizing the risk of hydrogen release. Composite tanks reinforced with carbon fiber are often used.

Emergency procedures: Detailed procedures for handling hydrogen leaks, fires or other incidents must be developed and regularly trained. Emergency services (fire brigades) must also be trained in the specifics of interventions on hydrogen vehicles.

Grounding and protection against electrostatic discharge: Hydrogen is flammable, so proper grounding and measures to prevent electrostatic sparks must be provided, especially during refuelling.

Specialized training: Service personnel must be properly trained in the operation and maintenance of hydrogen systems (fuel cells, tanks, gas systems), as well as traction batteries (if they are part of a hybrid system).

Fuel cell monitoring: Fuel cells have a finite lifespan and require regular monitoring of their performance and condition.

Hydrogen tank condition: The integrity of hydrogen tanks must be regularly checked for mechanical damage, corrosion or leaks.

Cooling systems: Fuel cells generate heat, so cooling systems must be efficient and effective.

System integration: Hydrogen vehicles are often complex hybrid systems (fuel cell + battery). Care must be taken to ensure that all components are properly integrated and interact.

5. Potential to increase driving range

The vehicle's driving range depends almost proportionally on the amount of fuel that can be stored in the tanks. In the case of hydrogen, in addition to tank volume, its amount is also affected by pressure, temperature, and state of matter.

Currently, three hydrogen storage technologies are being considered for use in transport. These are hydrogen storage technologies in the form of:

– gas compressed to a pressure of 35–70 MPa, stored at ambient temperatures in type IV composite tanks, with a density of 20–40 kg/m^3
– liquid, stored at temperatures below –253°C, at a pressure of 0.1–0.4 MPa, in type I cryogenic steel tanks, with a density of 62–65 kg/m^3
– gas compressed to pressures of 50–100 MPa and simultaneously cooled to temperatures from –200 to –240°C,

so-called cryogenic gas, stored in type III steel tanks, reinforced with carbon fiber, with a gas density of 72–90 kg/m^3.

The first of the mentioned technologies (storing hydrogen as a gas compressed to 35–70 MPa at ambient temperature) is already widely used commercially. For passenger cars, the standard of 70 MPa is used, and for trucks, 35 MPa, although work is already underway to introduce the 70 MPa standard in heavy transport, which will extend driving ranges by up to around 67% (by increasing the density from approx. 24 kg/m³ to approx. 40 kg/m³ in standard temperature). This will require adapting the tanks' design and modifying the communication protocols between the refuelling station and the vehicle. Communication between the hydrogen refuelling station and the vehicle is the responsibility of standards developed by SAE International, in particular:

– SAE J2601 – a standard that specifies hydrogen refueling protocols for fuel cell vehicles. It defines parameters such as pressure, temperature and refueling time to ensure safe and efficient filling of hydrogen tanks
– SAE J2799 – a standard that describes the communication interface between a vehicle and a hydrogen refueling station. It enables the exchange of information such as vehicle identification, tank status, and refueling preferences, allowing the optimization of the refueling process.

The technology for storing hydrogen in liquid form is still in development, although the first public liquid hydrogen refuelling station using sLH₂ (subcooled Liquid Hydrogen) technology, developed jointly by Daimler Truck and Linde Engineering, has been launched in Wörth am Rhein, Germany. This station enables trucks to be refuelled quickly and safely in 10 to 15 minutes, providing a range of over 1000 km for vehicles such as the Mercedes-Benz GenH₂ Truck [15].

The technology of storing hydrogen in the form of a compressed and simultaneously cooled gas, the so-called cryogenic gas, is the most complicated, which is why it is also at the earliest stage of development. However, it offers the greatest possibilities, which is why its progress should be monitored. It is being developed, among others, by the German company Cryomotive as part of the CryoTRUCK project [6].

Looking further ahead, rail transport could explore the use of alternative hydrogen-bearing chemical compounds that would enable direct utilization in fuel cells – particularly MCFC units – thus eliminating the need for upstream reforming processes. In all of the above cases, the operation of fuel cells in transport applications must be supported by batteries or supercapacitors [18].

In the context of the above technologies, the simplest way to increase range is to optimize the compressed gas refueling process.

When refueling a pressure tank, the first law of thermodynamics applies in the form [24]:

$$\Delta U = \Delta Q + \Delta H_{in} \tag{1}$$

where: ΔU – change in internal energy of the gas in the tank, ΔQ – heat supplied (+ sign) or given off to the environment (–sign), ΔH_{in} – enthalpy of the gas supplied to the tank.

In the above equation, ΔQ defines the heat delivered or released to the environment. Since the temperature of the gas in the tank increases during refueling and is usually much higher than the ambient temperature, it can be assumed that this is heat released to the environment by convection and described by the relationship:

$$\Delta Q = \int \dot{Q} dt = \int \alpha \cdot A \cdot (T - T_{amb}) \cdot dt \tag{2}$$

where: α – heat convection coefficient [W/(m^2·K)], A – heat exchange surface (tank) [m^2], $T - T_{amb}$– temperature difference of gas in tank T and environment T_{amb} [K].

The enthalpy of the gas supplied to the tank $\Delta H_{in}(P_{in}, T_{in})$ depends on its thermodynamic parameters, i.e. pressure P_{in}, but most of all temperature T_{in}. In order to limit the temperature increase of the gas collected in the tank, i.e. $\Delta U(T)$, it is possible to minimize the enthalpy of the gas supplied to the tank $\Delta H_{in}(P_{in}, T_{in})$ on the one hand by cooling the supplied hydrogen (low values of T_{in}) and/or by effectively releasing heat ΔQ to the environment through convection.

In the case of convection, the parameter that determines its effectiveness is, among other things, time, which is why slow, long-term filling of tanks is preferred. Unfortunately, this often contradicts the requirements of users who expect the shortest possible refueling times, which is why in such cases a more expensive solution is used, consisting in cooling the refueled gas (low T_{in}values). Cooling the supplied hydrogen to a specific temperature T_{in}before refueling requires appropriate energy.

The amount of energy required to cool hydrogen is increased by the Joule–Thomson effect, which for hydrogen in refueling conditions takes on negative values. The Joule–Thomson coefficient η_{JT} is defined by the relationship:

$$\eta_{JT} = \partial T / \partial P \tag{3}$$

and determines how the temperature ∂T changes when the pressure ∂P changes, occurring at constant enthalpy.

Negative values of the Joule–Thomson coefficient η_{JT} indicate that hydrogen heats up by a certain amount after expansion. During refuelling, hydrogen flows from the buffer tank of the refuelling station (higher pressure) to the vehicle tank (lower pressure) – these results from the fact that after the pressure reducer of the buffer tank, hydrogen has a reduced pressure (adapted to the pressure in the vehicle tank), but a higher temperature than in the buffer tank. In extreme cases, temperature increases can reach 50 degrees and significantly affect the energy balance of the refuelling process [24].

Figure 4 shows a comparison of hydrogen tank refueling processes, initiated at an ambient temperature of 273 K, from a mass of 0.2 kg (point 1) to 5 kg (black continuous line).

For refuelling in adiabatic conditions (i.e., without heat exchange with the environment), the process occurs along the red curve from point 1 to point 2. The lack of heat exchange with the environment, in simplified terms, corresponds to the conditions of very fast refuelling, when the refuelling time tends to zero. Such rapid refuelling, even

when the supplied gas is cooled, can raise the tank temperature by several dozen degrees. The increase in temperature, in turn, causes an additional rise in gas pressure in the tank and creates additional stresses in the tank structure. Leaving the tank refuelled in this way for a longer period allows it to cool to ambient conditions through convective heat transfer. During heat exchange with the environment, the gas pressure decreases by several to several dozen MPa, moving from point 2 to point 3, along the black continuous line of constant mass.

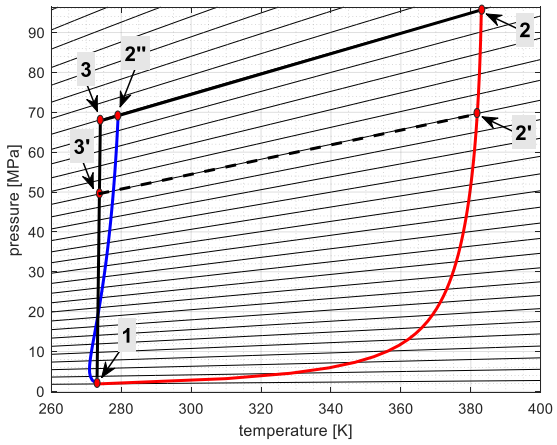

Fig. 4. The comparison of hydrogen tank refueling processes: adiabatic (red curve 1–2), adiabatic with strong cooling (blue curve 1–2") and isothermal (black line 1–3)

Therefore, during quick refuelling, a decision should be made whether to refuel "to the full", but with excess pressure at the end of filling (point 2), or whether it is better to end the refuelling at point 2' not exceeding the nominal gas pressure at the end of refuelling (approx. 70 MPa), but at the cost of a smaller fill after the tank cools down (point 3' at the end of the black dashed line of constant mass).

The adiabatic refueling situation shown in Fig. 4 (along the red curve) is extreme and theoretical, because in reality, even a short 3–5 minute refueling allows some heat to be dissipated to the environment. In reality, the increases in temperature and pressure will be slightly lower, but the problem will still be significant.

An alternative solution presented in Fig. 4 is isothermal refueling, i.e., maximizing heat exchange with the environment, e.g., by extending the refueling process as far as possible (vertical black line from point 1 to point 3). With such refueling, the tank will be filled to full capacity (point 3) without any excess, unnecessary increases in temperature and pressure, but at the cost of a very long filling time.

The next, most efficient, but most complicated and unfortunately the most expensive method is the option of fast refueling in adiabatic conditions, to full and without significant excess temperature and pressure increases (blue curve from point 1 to point 2'' in Fig. 4). Such refueling is theoretically possible, but requires cooling the supplied gas to very low temperatures of even from –100°C to –120°C. In this case, all the benefits are achieved, i.e. short refueling time, to full and without unnecessary temperature and pressure increases, but at a very high price of energy invested in strong cooling of the supplied gas.

Mixed variants are also possible, combining the above-mentioned solutions, e.g. refueling extended in time to a dozen or so or several dozen minutes, allowing for the release of more heat to the environment, while cooling the supplied hydrogen to a temperature of around –40°C (a standard commonly used in refueling passenger cars). In such a case, a compromise will be reached among refueling time, excess temperature and pressure, and hydrogen-cooling costs. The exact parameters of the refueling process can be selected for a specific case using simulation research methods.

6. Summary

Hydrogen technologies in heavy-duty transport – including city buses, rail vehicles and trucks – are shaped by a set of common requirements. These types of vehicles must achieve long driving ranges, maintain high operational availability, and allow refuelling times similar to diesel solutions, all while keeping the associated energy and economic costs at acceptable levels. As the article shows, these factors strongly influence the choice of hydrogen storage and refuelling strategies in each transport segment, even though the specific vehicle architectures differ. Despite this diversity, the fundamental challenges remain shared across the sector.

Meeting these requirements is not straightforward. Achieving long ranges depends not only on tank capacity but also on hydrogen density, system pressure, refuelling temperature and the thermodynamic behaviour of the gas during filling. Transport operators demand rapid refuelling, while designers face the laws of thermodynamics, which result in significant increases in temperature and pressure during rapid hydrogen transfer. These effects directly influence tank durability, safety margins and the amount of fuel that can be stored after cooling. Therefore, selecting an appropriate refuelling strategy involves a compromise between refuelling time, system pressure, cooling of the supplied hydrogen, and the economic and energy costs associated with each option.

The theoretical considerations presented in the article, including the formulation based on the first law of thermodynamics and the influence of the Joule–Thomson effect, provide important tools for evaluating these trade-offs. They demonstrate how the shape of the refuelling process – adiabatic, isothermal, or mixed – affects the final mass of hydrogen in the tank, the required infrastructure, and operational costs. Such modelling can support the selection of optimal strategies for different categories of heavy-duty transport, where the balance between time, cost and achievable range is essential.

In addition to compressed hydrogen storage (35–70 MPa), which currently dominates vehicle applications, the article also highlights emerging technologies with significantly higher volumetric energy density. Liquid hydrogen (LH_2) and cryogenic compressed hydrogen (CcH_2) offer the potential for even greater driving ranges and may play a key role in long-haul heavy transport in the future. Their development could substantially reshape the technical and economic landscape of hydrogen refuelling systems.

Many facts, as well as strategies and plans (including the EU and individual vehicle manufacturers), indicate that

efforts to improve the efficiency of hydrogen fuel use will not cease [3, 7]. The time horizon will depend on the pace of development of individual technologies in the so-called entire value chain. Starting with fuel production, components used to build vehicles, and finally, the technology used to manufacture end products.

Local environmental effects or ecological benefits in areas where people live, resulting from the use of hydrogen-fueled vehicles, should be considered alongside all issues related to the construction and operation of rolling stock. As shown by the first experiences of carriers and the commercial use of vehicles, mostly on regional lines, engineers still have a lot of work to do to improve the efficiency of H_2-powered mass transport vehicles. The rolling stock availability indicators required by contracts are also important. The reliability of the solutions is expected to be at the highest possible level. Despite the challenges in improving the properties of fuel cell vehicles, H_2 as a fuel is, in many respects, a better choice for energy storage, for example, in electrochemical energy storage systems [1].

Without a doubt, it is necessary to remember the education and training of specialists who will be able to provide the appropriate scope of vehicle maintenance. The homologation requirements (TSI) and maintenance requirements (MMS/ECM – Entity in Charge of Maintenance) for hydrogen vehicles are greater. For safety reasons, great attention must also be paid to procedures, especially in emergency or crisis situations.

Overall, the article demonstrates that while hydrogen-powered buses, rail vehicles and trucks operate in different environments and serve different transport roles, they share remarkably similar technological challenges. Their effectiveness ultimately depends on the same set of factors: hydrogen storage density, safe and fast refuelling, energy efficiency of the process, infrastructure readiness and long-term operating costs. This shared foundation enables the development of common engineering principles and analytical tools – as presented in the paper – that support informed decision-making and guide the future development of hydrogen technologies for heavy-duty transport.

Nomenclature

BEV	battery electric vehicle
CNG	compressed natural gas
DSU	maintenance system documentation
ECM	entity in charge of maintenance
EMU	electric multiple units
FCEV	fuel cell electric vehicles
HDV	heavy-duty vehicles
HEV	hybrid electric vehicles
HVO	hydrotreated vegetable oil
LHV	lower heating value
LNG	liquefied natural gas
MMS	maintenance management system
NRMM	non-road mobile machinery
NSA	National Security Authority
PEM	proton exchange membrane
ROSCO	rolling stock company
TSI	technical specifications of interoperability
UTK	Office of Rail Transport

Bibliography

[1] Andrzejewski M, Pielecha I, Merkisz J, Swiechowicz R, Nowak M. Modern drive systems of rail vehicles. Combustion Engines. 2019;178(3):76-81. https://doi.org/10.19206/CE-2019-314

[2] Ballard, FCmove products. Available online: https://www.ballard.com/wp-content/uploads/2024/11/Ballard-Data-Sheet-FCmove-XDv2_20250305_landscape-2.pdf (accessed on 15.06.2025).

[3] Baroutaji A, Wilberforce T, Ramadan M, Olabi AG. Comprehensive investigation on hydrogen and fuel cell technology in the aviation and automotive sectors. Renew Sustain Energy Rev. 2019;106:31-40. https://doi.org/10.1016/j.rser.2019.02.022

[4] Bossel U. Does hydrogen have a future? European Fuel Cell Forum. 2006.

[5] Carrette L, Friedrich KA, Stimming U. Fuel cells – fundamentals and applications. Fuel Cells. 2001;1(1):5-39. https://doi.org/10.1002/1615-6854(200105)1:1<5::AID-FUCE5>3.0.CO;2-G

[6] Cryomotive GmbH. CryoTRUCK – Cryogenic compressed hydrogen storage for heavy-duty transport. Technical Report 2023.

[7] Danielak A, Kozak M, Cierniewski M. Prospects for the development of fuel cells in railway applications. Combustion Engines. 2025;203(4):16-22. https://doi.org/10.19206/CE-208507

[8] Estrada Poggio A, Balest J, Zubaryeva A, Sparber W. Monitored data and social perceptions analysis of battery electric and hydrogen fuelled buses in urban and suburban areas. J Energy Storage. 2023;72;108411. https://doi.org/10.1016/j.est.2023.108411

[9] European Commission, A hydrogen strategy for a climate-neutral Europe. 8.6.2020. https://ec.europa.eu/energy/sites/ener/files/hydrogen_strategy.pdf (accessed on 15.06.2025).

[10] Gallas D, Stobnicki P, Bolzhelarskyi Y. Types and applications of hydrogen fuel cells in transport. Rail Vehicles/ Pojazdy Szynowe. 2022;(3-4):31-36. https://doi.org/10.53502/RAIL-157018

[11] Glenk G, Reichelstein S. Economics of converting renewable power to hydrogen. Nature Energy. 2019;4:216-222. https://doi.org/10.1038/s41560-019-0326-1

[12] Hwang JJ. Energy and exergy analyses of hydrogen liquefaction. Int J Hydrogen Energy. 2010;35(9):3709-3716. https://doi.org/10.1016/j.ijhydene.2010.01.082

[13] Kapetanović M, Núñez A, van Oort N, Goverde RMP. Energy model of a fuel cell hybridelectric regional train in passenger transport service and vehicle-to-grid applications. J Rail Transp Plan Manag, 2023;28:100415. https://doi.org/10.1016/j.jrtpm.2023.100415

[14] Kołodziejski M, Matuszak Z, Żabińska I. Possibilities of using hydrogen buses in urban transport. Silesian University of Technology – Organization and Management. Series No. 161, 2022.

[15] Linde Engineering & Daimler Truck. World's first public sLH₂ refuelling station – Technical Overview. 2024.

[16] Matla J, Kaźmierczak A, Grzebyk M, Hardy T. The study of hydrogen consumption in 12-meter fuel cell electric urban buses. Combustion Engines. Online first. https://doi.org/10.19206/CE-211731
[17] National Energy Technology Laboratory – Solid Oxide Fuel Cell Program. Fuel Cell fact sheet. US Department of Energy. Program 133, 2021. https://www.netl.doe.gov/sites/default/files/2021-10/Program-133.pdf
[18] Pielecha I, Cieślik W, Szałek A. The use of electric drive in urban driving conditions using a hydrogen powered vehicle – Toyota Mirai. Combustion Engines. 2018;172(1):51-58. https://doi.org/10.19206/CE-2018-106
[19] Qian C, Ruiqiang Z, Zhusheng S, Jianguo L. Review of common hydrogen storage tanks and current manufacturing methods for aluminum alloy tank liners. Int J Lightweight Mater Manuf. 2024;7:269e284. https://doi.org/10.1016/j.ijlmm.2023.08.002
[20] Raza W, Ali F, Raza N, Luo Y, Kim KH, Yang J et al. Recent advancements in supercapacitor technology. Nano Energy. 2018;52:441-473. https://doi.org/10.1016/j.nanoen.2018.08.013
[21] Rosen MA, Koohi-Fayegh S. The prospects for hydrogen as an energy carrier: an overview of hydrogen energy and hydrogen energy systems. Energy Ecol Environ. 2016;1:10-29. https://doi.org/10.1007/s40974-016-0005-z
[22] Ruf Y, Zorn T, Akcayoz De Neve P, Andrae P, Erofeeva S, Garrison F. Study on the use of fuel cells & hydrogen in the railway environment. Report 3. Shift2Rail Joint Undertaking and Fuel Cells and Hydrogen Joint Undertaking, 2019.
[23] Staffell I, Scamman D, Abad AV, Balcombe P, Dodda PE, Ekins P et al. The role of hydrogen in future energy systems. Energy Environ Sci. 2019;12:463-491. https://doi.org/10.1039/C8EE01157E
[24] Yang JC. A thermodynamic analysis of gaseous hydrogen refuelling. Int J Hydrogen Energy. 2009;34(16):6712-6721. https://doi.org/10.1016/j.ijhydene.2009.06.015
[25] https://en.wikipedia.org/wiki/Toyota_FCHV#FCHV-BUS (accessed on 18.06.2025)
[26] https://en.wikipedia.org/wiki/Fuel_cell_bus (accessed on 18.06.2025).
[27] https://kolejowyportal.pl/rs-zero-bezemisyjny-nastepca-kultowego-regio-shuttle-rs1/#google_vignette (accessed on 18.06.2025).
[28] https://raportkolejowy.pl/pierwsze-wodorowe-pociagi-mireo-plus-h-od-siemens-mobility-w-ruchu-pasazerskim-w-dwoch-landach/ (accessed on 18.06.2025).
[29] https://www.mobility.siemens.com/pl/pl/produkty/pojazdy-szynowe/pociagi-podmiejskie-i-regionalne/mireo/mireo-plus-h.html (accessed on 18.06.2025).
[30] https://www.sustainable-bus.com/fuel-cell-bus/fuel-cell-bus-hydrogen/ (accessed on 18.06.2025).
[31] https://www.sustainable-bus.com/fuel-cell-bus/rnv-mannheim-ecitaro-fuel-cell-range-extender/ (accessed on 18.06.2025).
[32] https://utk.gov.pl/pl/bezpieczenstwo-systemy/zarzadzanie-utrzymaniem/19218,System-zarzadzania-utrzymaniem.html (accessed on 18.06.2025).

Prof. Piotr Piórkowski, DSc., DEng. – Faculty of Automotive and Construction Machinery Engineering, Warsaw University of Technology, Poland.
e-mail: *piotr.piorkowski@pw.edu.pl*

Mateusz Nowak, DEng. – Faculty of Civil and Transport Engineering. Poznan University of Technology, Poland.
e-mail: *mateusz.s.nowak@put.poznan.pl*

Maciej Andrzejewski, DEng. – Experts, The Association of Rail Transport Experts and Managers, Poland.
e-mail: *m.andrzejewski@seim-tsz.pl*

Article citation info:
Nguyen Thin Q, Nguyen Van D. An analytical study on the performance of spark-ignition engines operating with ammonia fuel. Combustion Engines. 2026;206(3):87-95. https://doi.org/10.19206/CE-216441

Quynh NGUYEN THIN
Dung NGUYEN VAN

Combustion Engines
Polish Scientific Society of Combustion Engines

An analytical study on the performance of spark-ignition engines operating with ammonia fuel

ARTICLE INFO

Received: 10 July 2025
Revised: 17 December 2025
Accepted: 6 January 2026
Available online: 24 January 2026

Ammonia is a promising fuel due to its low cost, carbon-free energy carrier, renewable hydrogen carrier, scalability and flexibility, global availability, and long-term energy storage. It can be synthesized from renewable energy sources and used as a carbon-free fuel in internal combustion engines. When ammonia is completely burned, due to the relatively low combustion temperature of the ammonia-air mixture and the absence of carbon in the molecule, the only toxic emissions are nitrogen oxides. These nitrogen oxide emissions can be effectively reduced by the selective catalytic reduction technology, in which ammonia acts as a reductant in the selective catalytic reduction system. This study presents the characteristics of a spark-ignition internal combustion engine 4CH 7.6/7 powered by ammonia fuel. The results show that the maximum brake torque on the wide-open throttle operating characteristics increases by 6.1%, while the maximum brake power decreases by 30%, and the brake-specific ammonia fuel consumption is almost 2 times higher than that of gasoline at the same engine power. Moreover, with a research octane number of ammonia up to 110, it will help improve anti-knock properties. Along with that, increasing the compression ratio and using turbochargers can be considered to improve engine performance.

Key words: *SI engine, gasoline fuel, ammonia fuel, knock probability determination.*

This is an open access article under the CC BY license (http://creativecommons.org/licenses/by/4.0/)

1. Introduction

Climate change resulting from greenhouse gas emissions has become an increasingly pressing global issue. A substantial portion of these emissions – including greenhouse gases and other harmful pollutants – originates from human activities, particularly from internal combustion engine vehicles. As most automobiles still operate on fossil fuels, the transportation sector is a major contributor to global greenhouse gas emissions and environmental pollution. In response to international and national commitments to achieving net-zero emissions, researchers and automotive manufacturers are actively seeking solutions to reduce both greenhouse gas emissions and toxic pollutants released into the environment. The solutions being studied and applied are improving the mixing quality of the fuel-air mixture, utilizing high-pressure turbocharging, employing exhaust gas recirculation, and utilizing exhaust gas treatment units [5, 9, 13]. Among the solutions that have been researched and implemented to address emissions are the adoption of alternative fuels and the utilization of renewable energy sources. Environmentally friendly alternative fuels derived from biomass – renewable within the carbon cycle – have garnered significant attention. However, recent research has increasingly focused on fuels that do not emit greenhouse gases during combustion and can serve as substitutes for gasoline in spark-ignition engines. Notably, hydrogen and ammonia have emerged as promising candidates for use in future vehicle applications.

Ammonia is a naturally occurring inorganic chemical compound that is lighter than air and liquefies easily. The boiling point of ammonia is –33.43°C at 1.013 atm and solidifies into colorless crystals at –77.7°C [3]. It is widely used in agriculture and is typically produced from hydrogen derived from fossil fuels, which means it is not considered a "green" product. However, green ammonia can be produced if the hydrogen is generated by alternative methods such as water electrolysis using wind or solar energy. Green ammonia could become a cheaper fuel for the shipping industry compared to hydrogen produced from renewable energy, as it is easier to store and can be combusted in standard internal combustion engines. Ammonia's low viscosity promotes better spray and mixing with air compared to gasoline. Green ammonia is also being researched as a fuel for aircraft, by exposing ammonia to a catalyst to split it into nitrogen and hydrogen, which is then burned in an aircraft engine [14].

The properties of different fuels are compared, as shown in Table 1. It can be observed that the lower heating value of gasoline is twice as high as that of ammonia, and the flame speed of gasoline is up to 39 times greater than that of ammonia. Additionally, the energy density of gasoline is nearly three times higher than that of ammonia [2, 10, 11].

The adoption of alternative fuels such as NH_3 and H_2 plays a pivotal role in efforts to reduce carbon dioxide emissions in the transportation sector, while also driving the transition toward a sustainable energy ecosystem. Some countries have actively incorporated NH_3 into their energy strategies as a low-carbon fuel. Notably, in January 2020, the U.S. House of Representatives introduced a draft bill recognizing NH_3 as a “low-carbon fuel”. At the same time, the Royal Society in the United Kingdom released a policy report titled “Ammonia: zero-carbon fertiliser, fuel and energy store”, providing scientific foundations and policy analysis to support the integration of NH_3 into clean energy technologies [4]. However, research has shown that compared to other fuels, ammonia fuel has certain drawbacks, including a high auto-ignition temperature and a slow flame speed, which are among the most significant challenges faced by ammonia-fueled engines [2, 3, 8, 14].

Table 1. Compare the properties of gasoline with hydrogen and ammonia [2, 3, 10–12].

Property	Gasoline	Gaseous H_2	Liquid H_2	Ammonia
Molecular	C_8H_8	H_2	H_2	NH_3
Fuel density [kg/m^3]	698.3	17.5	71.1	602.8
Lower heating value [MJ/kg]	44.5	120.1	120.1	18.8
Energy density [MJ/m^3]	31,074	2101	8539	11,333
Volumetric energy density at 0.1 MPa and 293 K [MJ/L]	34	0.010–0.011	–	11.5
Laminar burn velocity [m/s]	0.58	3.51	3.51	0.15
Auto-ignition temperature [K]	573	844	844	930
Research octane number (RON)	90–98	> 130	> 130	110
Mass carbon content [%]	85.5	–	–	–
Flammability limits [vol%]	1.4–7.6	4–75	4–75	16–25
Absolute minimum ignition energy [mJ]	0.14	0.018	–	8.0
Latent heat of vaporazation [kJ/kg]	305	–	445.6	1370
Quench distance [mm]		0.64	–	7

Ammonia (NH_3) can be used as an alternative fuel for internal combustion engines (ICEs). With the explosion of fuel cell research, ammonia has also been studied as a fuel source for proton exchange membrane fuel cells (PEMFCs), alkaline fuel cells (AFCs), and solid oxide fuel cells (SOFCs). SOFCs are the most efficient when compared to ammonia fuel cells and ICEs. However, their disadvantages are power density, load adaptability, and relatively high battery manufacturing costs. When operating at near maximum power, the efficiency of internal combustion engines has been shown to be higher than both ICEs and AFCs. In addition, internal combustion engines have great advantages in terms of manufacturing costs, maintenance costs, global repair teams, long durability, acceptable power density, and operating characteristics [1, 6].

ICEs using NH_3 as an alternative fuel have performance parameters quite comparable to conventional ICEs at both full load and partial load modes. However, conventional ICEs typically produce significantly higher levels of toxic emissions, including hydrocarbons (HC), nitrogen oxides (NO_x) and particulate matter (PM). Most importantly, CO_2 emissions from fossil fuel combustion in ICEs are one of the main contributors to greenhouse gas emissions, thereby aggravating climate change [3, 14]. Therefore, research on carbon-free fuels such as hydrogen and ammonia has received widespread attention both in the automotive industry and in research institutes.

Although H_2 is emerging as a key element in the transition to a carbon-neutral economy, widespread adoption still faces challenges related to safety, vehicle placement to ensure mileage comparable to conventional fuel engines, storage capacity, and distribution infrastructure for hydrogen. Finally, a very important factor to consider is its relatively low volumetric energy density (2.9 MJ/L at 70 MPa), rapid combustion rate, and high exhaust gas temperature [14]. In contrast, NH_3 offers a higher volumetric energy density (7.1 MJ/L) along with an existing transportation infrastructure, providing clear advantages in terms of flexibility and efficiency. These characteristics position NH_3 as a practical choice for future energy systems involving storage, transportation, and power generation. These characteristics position NH_3 as a practical option for future energy systems involving storage, transport. With easier storage than hydrogen, it can take advantage of existing liquefied petroleum gas or compressed natural gas infrastructures for use in converted internal combustion engines [3]. This is a factor that helps reduce fuel costs and makes it more accessible to the market. NH_3 helps create many realizable solutions to address the sustainability challenge in the energy sector.

The use of ammonia as an alternative fuel also faces several obstacles, such as:

– The rate of chemical reaction occurring in the combustion chamber is lower than with traditional fuels due to the high ignition temperature and low flame propagation speed when burning ammonia. This slow chemical reaction rate results in some unburned ammonia being released with the exhaust gases. As a result, ammonia combustion mainly produces NO emissions, with small amounts of NO_2 and nitrogen oxides N_2O, but also unburned ammonia emissions [12]. In this case, a solution for handling unburned NH_3 in the exhaust treatment needs to be considered and studied.
– Ammonia has a high latent heat of vaporization of 1370 kJ/kg. For example, ethanol, liquid hydrogen, and gasoline have latent heats of vaporization of 840, 445.6, and 305 kJ/kg, respectively. This means that if ammonia is injected into the engine combustion chambers, the combustion temperature can drop dramatically, causing incomplete combustion and reducing engine efficiency. The flame extinction distance for a stoichiometric mixture of air and ammonia is 7 mm (Table 1), which is about 10 times more than in the case of hydrogen. This means that heat loss through the walls of the combustion chamber will be lower in the case of ammonia.
– The use of ammonia in SI engines is limited by narrow flammability limits and low flame speed, causing incomplete combustion.
– The effects of ammonia on lubricating oil and engine lifespan have not been fully studied [12].

It can be observed that ammonia is a promising fuel with scalability, flexibility, global availability, and long-term energy storage capability. This study presents the simulation results of a gasoline engine operating on ammonia under the Miller cycle. The findings serve as a foundation for converting conventional engines to operate on green ammonia fuel [7].

2. Research subject and research model

The engine used for this study is a four-cylinder, four-stroke 4CH 7.6/7 engine. Gasoline is injected into the intake manifold, the engine is naturally aspirated and ignited by spark plugs. The main specifications of the 4CH 7.6/7 engine are presented in Table 2.

Table 2. The main specifications of the 4CH 7.6/7 engine

Parameters [unit]	Value
Piston stroke/cylinder diameter [mm/mm]	71/76
Number of cylinders [–]	4
Stroke number [–]	4
Compression ratio [–]	10.5
Engine displacement [cm^3]	1289
Maximum power [kW]	60
Speed at maximum power [min^{-1}]	5000
Maximum torque [Nm]	100
Speed at maximum torque [min^{-1}]	2000
Environmental standards	Euro 4
Inlet valve:	
Diameter [mm]	36
Valve lift [mm]	8.8
Open [deg. CA bTDC]	33
Duration opening [deg. CA]	292
Exhaust valve:	
Diameter [mm]	31
Valve lift [mm]	8.65
Open [deg. CA bTDC]	47
Duration opening [deg. CA]	244

To establish the simulation model of the above-mentioned engine, the following assumptions and considerations are made:

1. The intake gases inside the cylinder are considered ideal and are assumed to remain nearly in thermodynamic equilibrium. During the gas exchange process, the cylinder space is an open thermodynamic system with a changing volume. When this process is completed, the cylinder becomes a closed system.

2. The in-cylinder processes are described using the differential form of the law of conservation of energy, states. The mass of the gases exchanged during the intake process is conserved. In addition, the law of conservation of energy is applied to the flow of the medium through the intake ports. To describe the state of the gas mixture in the combustion chamber, the Clapeyron equation is used.

3. The temperature and composition of the gas mixture determine its internal energy. The heat transfer equations and the quasi-static flow model represent the boundary conditions, heat exchange and mass exchange between the system and the surrounding environment. Heat transfer to the cylinder wall is calculated using Newton's law of cooling.

4. The heat transfer coefficients are determined by the Woschni model. These coefficients are determined separately for the intake, compression and expansion processes. The heat transfer through the wall and the heat exchange of the system are calculated taking into account the temperature distribution along the cylinder and the change in contact area when the volume changes due to the piston movement.

5. The gas dynamic boundary conditions are analyzed in the region adjacent to the cylinder. During gas exchange, the pressure in the intake and exhaust manifolds is assumed to be constant. The gas flow through the valve orifice, which has a time-varying area, is calculated using a one-dimensional, quasi-steady flow model. Additionally, the processes of exhaust gas expulsion and fresh charge intake are also considered.

6. The software supports the simulation of the supercharging system's operation through two main modules: one for simulating the working cycle of a spark-ignition (SI) engine, and another for simulating the integration of the SI engine with a turbocharging system. The schematic diagram of the SI engine model integrated with a turbocharger, following the sequence of the two modules, is shown in Fig. 1.

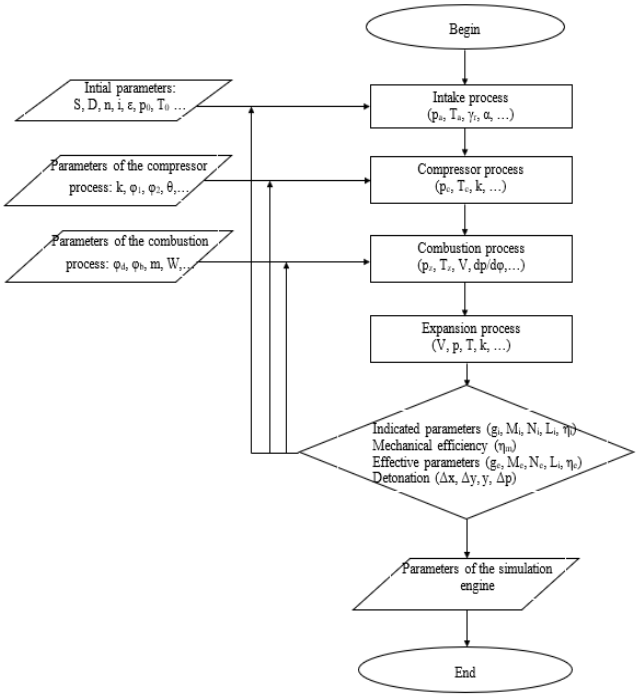

Fig. 1. Mathematical model of 4CH 7.6/7 engine using turbocharger

The boundary condition parameters used for the simulation model are presented in Table 3.

Table 3. Boundary condition parameters

Inlet temperature	298 K
Inlet pressure	0.1 MPa
Exhaust pressure	0.102 MPa
Exhaust temperature	843 K
Piston surface temperature	548 K
Piston tail temperature	573 K
Cylinder wall temperature	518 K

In this study, Wiebe's calculation method is used to calculate the heat release in the combustion chamber of the engine. The Wiebe formula is written as (1).

$$x(\varphi) = 1 - e^{-W\left(\frac{\varphi-\varphi_b}{\varphi_d}\right)^{(m+1)}} \quad (1)$$

where: m, W – coefficient of determination of the heat dissipation curve, φ – current time of the combustion process, φ_b is the crankshaft angle position where the combustion process begins, φ_d – is the combustion duration which is determined by the crankshaft angle.

Depending on the type of fuel used and the operating conditions of the engine, the values of m, W and φ_d need to be determined appropriately to obtain accurate model results.

With the value of the coefficient m, a series of calculations are performed and compared with the experimental values for different model internal combustion engines. The value of m for the model is chosen so that the simulation results obtained (maximum pressure in the combustion chamber and maximum pressure increase rate of the engine) are close to the experimental values.

The thermal efficiency of the SI engine can be improved by achieving an optimal combustion phase and a higher compression ratio. However, this can lead to engine knocking. The phenomenon of engine knocking in an SI engine is one of the main causes of typical damage to the engine's cylinder-piston system. Figure 2 illustrates the knock combustion process of fuel in an SI engine when running on gasoline.

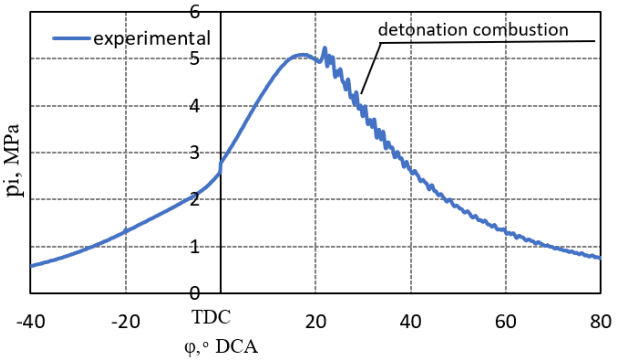

Fig. 2. Knock combustion process in the SI engine 4CH 7.6/7 when using gasoline (n = 4000 rpm; α = 1; IT = 20° bTDC)

For the numerical solution to this problem, a specific index (y) has been chosen, and the calculation is performed using the formula of Daud and Eise [4], which is essentially the Livengood-Wu integral:

$$y = \frac{1}{19.75}\left(\frac{ON}{100}\right)^{-3.4107}\int_0^{\tau}(10.2p)^{1.7}e^{\frac{-3800}{T}}d\tau \qquad (2)$$

where ON is the octane rating of the fuel; τ is the current time since the beginning of compression (seconds); p and T are the corresponding pressure (MPa) and temperature (K) in the engine cylinder; e is the base of the natural logarithm (e = 2.7183).

3. Model accuracy evaluation

To assess the accuracy of the established model, it is necessary to compare the pressure results obtained from the model with the experimental results.

The simulation results are compared with the test results of the 4CH 7.6/7 engine running on gasoline at a crankshaft speed of n = 3000 rpm, with an air-fuel ratio α = 1 and an ignition timing (IT) angle of 15° before top dead center (bTDC). The heat release duration is φ_z = 70°. The results are shown in Fig. 3. It can be seen that the pressure variation in the combustion chamber during simulation closely follows the results measured on the actual engine. The pressure value of the model is broken at the TDC and is larger in the expansion stage.

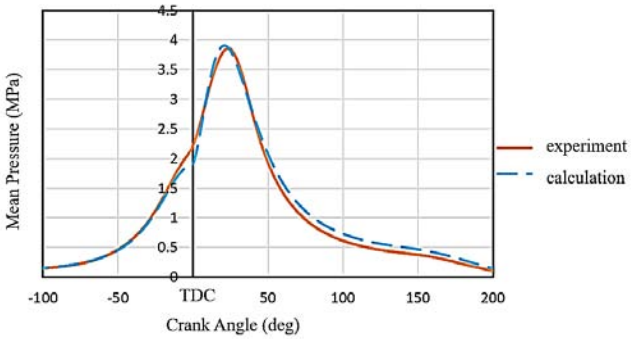

Fig. 3. Simulation and experimental results of SI 4CH 7.6/7 gasoline engine (n = 3000 min^{-1}; α = 1; IT = 15° bTDC; m = 1.7; φ_z = 70°)

Continuing with another engine, the study also evaluated the simulation results performed with an SI 4CH 11.5/7.7 engine using ammonia, with the parameters presented in Table 4. The test engine was placed in the laboratory and converted to operate using ammonia. Figure 4 shows the comparison between the model calculations and experimental data at the engine speed operating mode n = 1000 rpm; excess air coefficient of α = 1, IT = 15° bTDC, φ_z = 52°. In this case, it can be seen that the peak pressure value of the model result and the experimental result coincide at 15 degrees after TDC. However, the pressure value in the combustion chamber of the model is smaller than the experimental value but the deviation is still within the acceptable range.

Table 4. Parameters of the 4CH 11.5/7.7 converter engine using ammonia

Parameter	Meaning
Number of cylinders [–]	4
Stroke number [–]	4
Cylinder diameter [mm]	115
Piston stroke [mm]	77
Connecting rod length [mm]	177
Compression ratio [–]	11.75
Number of valves per cylinder [–]	4
Power [HP]	120
Torque [Nm]	160
Environmental standards	Euro 4
Number of valves [–]	16

It can be observed that, in both test cases, the model yields results that are relatively close to the experimental data. The deviation in value is clearly observed at the TDC, the point where the pressure reaches its maximum, and a part of the expansion phase. However, the error value is within an acceptable range. Therefore, the model can be used for the subsequent stages of research.

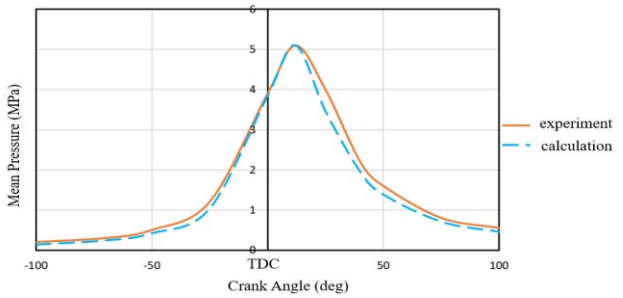

Fig. 4. Comparison of experimental and calculated indicator diagrams of SI engine 4CH 11.5/7.7 when operating on ammonia (n = 1000 min^{-1}; α = 1; IT = 15° bTDC; m = 1.2; φ_z = 52°)

4. Results and discussion

4.1. Engine external characteristics

The external characteristics of the engine are the first focus when converting the engine to run on ammonia. Figures 5a and 5b show the external characteristic results of the engine before and after the conversion. The characteristics are determined when the engine operates at the maximum throttle opening, and the ignition timing is adjusted to achieve the maximum power output.

From the results, it can be seen that when the engine switches from gasoline to ammonia as fuel, the maximum brake torque (M_{emax}) increases by 6.1%, while the maximum brake power (N_{emax}) decreases by 30% when measured under external characteristic conditions. Due to ammonia's lower volumetric energy density and calorific value compared to gasoline, the specific fuel consumption when using ammonia is nearly twice as high as gasoline for the same engine power output. This issue needs to be addressed in maintaining engine power during the transition, as the amount of fuel required per cycle must be recalculated. Additionally, the fuel tank volume may need to be larger to ensure that the vehicle's range remains unchanged.

In addition, another issue that needs to be recalculated is the air/fuel ratio when converting the engine to use ammonia. The theoretical air/fuel ratio when using ammonia is determined through the reaction of ammonia with oxygen in the air through reaction equation 3:

$$4NH_3 + 3O_2 = 2N_2 + 6H_2O + \text{heat} \quad (3)$$

The air/fuel ratio when using NH_3 can be calculated as follows:

$$\alpha_{NH_3} = \frac{m_a}{m_f} \quad (4)$$

where: m_a is mass of air. If air is considered to consist of two components, nitrogen $m_{N_2}$and oxygen m_{O_2}, then m_a can be calculated as follows:

$$m_a = m_{O_2} + m_{N_2} = 32 \times 3 + 3 \times 79/21 \times 28 = 415.72 \text{ g}$$

It should be noted that nitrogen makes up approximately 79% and oxygen makes up 21% by mass of air.
m_f is the mass of fuel.

$$m_f = 4 \times 17 = 68 \text{ g}$$

$$\alpha_{NH_3} = \frac{m_a}{m_f} = \frac{415.72}{68} = 6.11$$

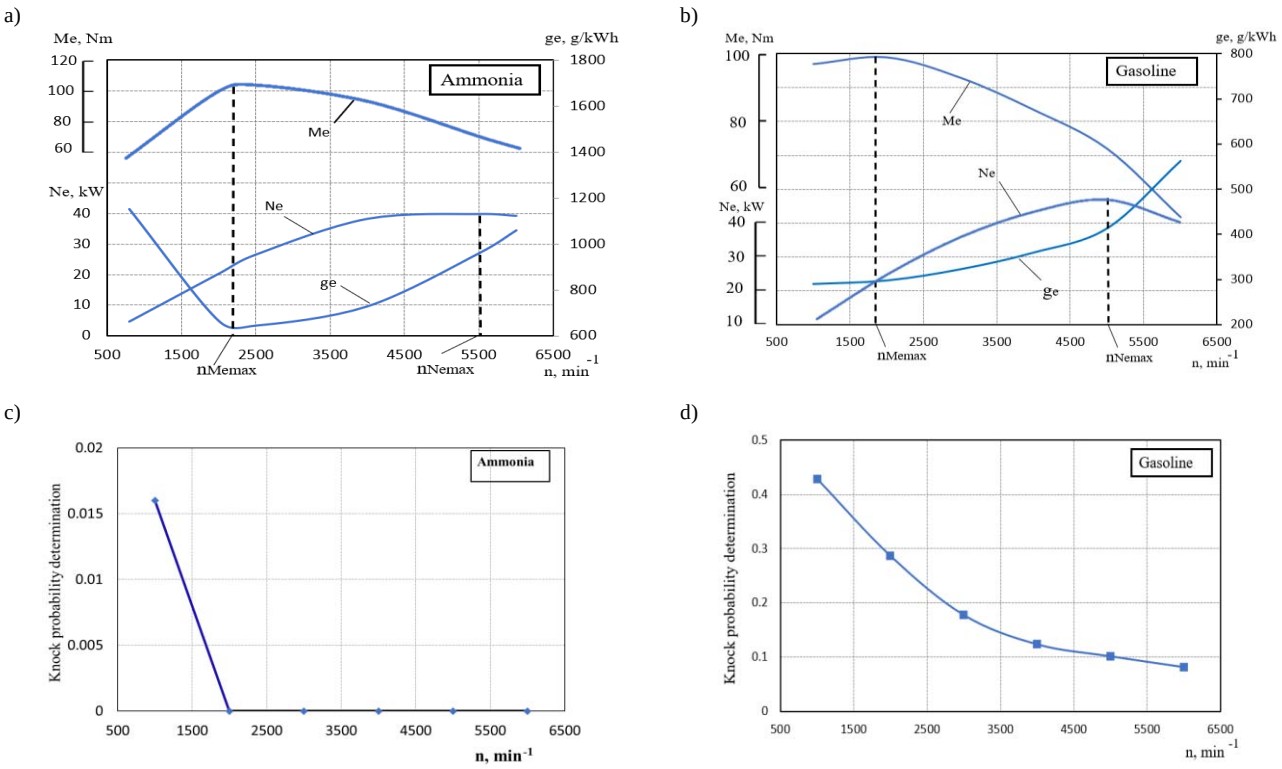

Fig. 5. External speed characteristics and knocking probability of the SI engine 4CH 7.6/7: a, c) engine using ammonia; b, d) engine using gasoline

If we calculate the A/F ratio by volume, we can determine as follows:

$$\alpha^{V}{}_{NH_3} = \frac{V_a}{V_f} = \frac{n_a}{n_f} \quad (5)$$

where V_a, n_a respectively the volume or moles of air, V_f, n_f respectively the volume or moles of fuel.

$$\alpha^{V}{}_{NH_3} = \frac{3 + 3\,x\,79/21}{4} = 3.57$$

Percentage of ammonia occupying in the combustion chamber:

$$\%NH_3 = \frac{V_{NH_3}}{V_{total}} \quad (6)$$

where V_{NH_3} is volume of NH_3 in the mixture and V_{total} is mixture volume.

$$V_{total} = V_{NH_3} + V_a$$

Therefore, we get the following result:

$$\%NH_3 = \frac{4}{3 + \frac{3 \times 79}{21} + 4} = 0.22$$

Thus, the A/F ratio of the engine using ammonia has a big change from 14.7 to 6.11. The injection process needs to ensure the amount of air/fuel according to the calculation results.

For SI engines, another critical factor is evaluating the stability of the engine's operation. This factor is the octane rating, used to assess the engine's knocking resistance. Since ammonia has a higher octane rating than gasoline, the probability of knocking in the forced ignition engine when using ammonia decreases. The results are shown in Figures 5c and 5d. It can be observed that for the same engine speed, the probability of knocking occurrence when using ammonia decreases by a factor of 100 to 150 times.

4.2. Effect of compression ratio

The compression ratio is defined as the ratio of the volume of the combustion chamber when the piston is at bottom dead center to the volume when it is at top dead center. The compression ratio significantly affects the efficiency of the engine. The effect of the compression ratio on the engine efficiency of the ideal cycle is shown in the following expression as follows:

$$\eta_t = 1 - \frac{1}{\varepsilon^{k-1}} \quad (7)$$

where: ε is compression ratio; k is the ratio of specific heats and it is defined as follows:

$$k = c_p/c_v \quad (8)$$

where: c_p is the specific heat at constant pressure ($J \cdot kg^{-1} \cdot K^{-1}$), c_v is the specific heat at constant volume ($J \cdot kg^{-1} \cdot K^{-1}$).

Thus, as the compression ratio increases, the efficiency of the cycle also increases.

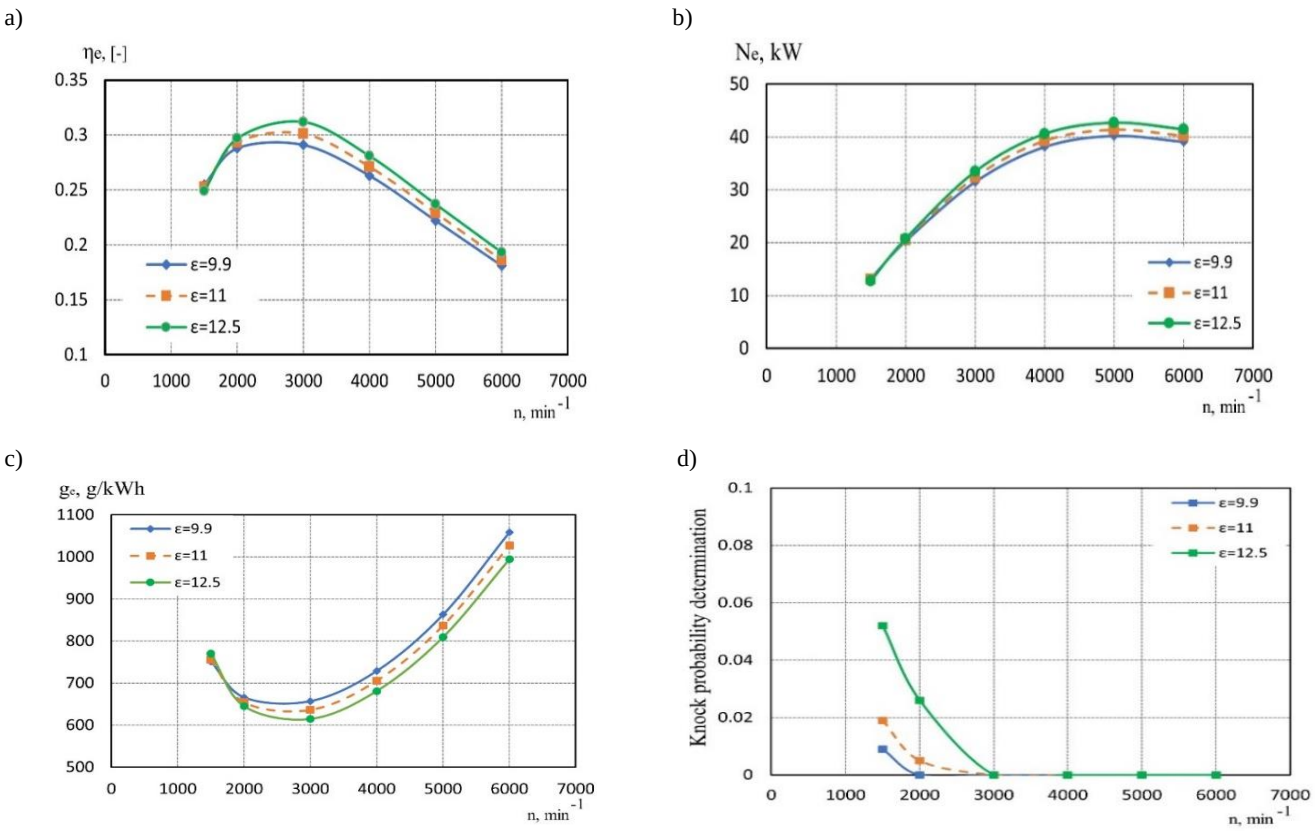

Fig. 6. Variation of engine parameters when using ammonia fuel with different compression ratios: a) brake efficiency; b) brake power; c) brake specific fuel consumption; d) probability of knocking occurrence

Due to the higher octane rating, engines using ammonia can achieve a higher compression ratio. With a high octane number, engines using ammonia can increase the compression ratio. In the calculation model, the engine using ammonia was simulated with compression ratios ranging from 9.9 to 12.5 under full load. The ignition timing was optimized for each speed mode and compression ratio, and the fuel-air mixture was adjusted according to the prescribed ratio for ammonia. The results of the engine are shown in Fig. 6.

It can be seen that, when operating at speeds ranging from 1500 to 6000 rpm, with the throttle fully open and without turbocharging, the probability of knocking combustion when using ammonia fuel decreases as the engine speed increases, and this value increases as the compression ratio of the engine increases (Fig. 6d).

The engine's efficiency and brake power increase as the compression ratio increases. The brake efficiency reaches its maximum at n = 3000 rpm (Fig. 6a), while the brake power reaches its maximum at n = 5000 rpm (Fig. 6b). After reaching the maximum, these values decrease as the engine speed increases. In addition, the minimum BSFC was found in the speed range from 2000 to 3000 rpm (Fig. 6c). The results obtained are a solution to improve the performance of gasoline engines when converting fuel. We can increase the compression ratio for gasoline engines or a further solution is to convert diesel engines to be able to use ammonia.

4.3. Effect of boost pressure

When considering forced ignition engines, an improved cycle of interest is the Miller cycle. The Miller cycle is a variation of the Otto cycle developed to improve thermal efficiency and reduce emissions in internal combustion engines. This cycle was invented by Ralph Miller in 1947 and is often applied to turbocharged gasoline or diesel engines.

The Miller cycle changes the intake valve closing timing to control the compression process, thereby reducing the work consumed during compression and increasing overall efficiency. There are two methods for adjusting the intake valve closing timing: early intake valve closing and late intake valve closing. Gasoline engines using the Miller cycle help reduce the work consumed during compression, increase thermal efficiency, reduce the risk of knocking, and reduce NO_x emissions due to the lower combustion temperature.

In the model, the intake valve closing timing is adjusted to enable the engine to operate according to the Miller cycle. The effect of boost pressure on the forced ignition engine operating under the Miller cycle is considered at an engine speed of 2000 rpm, with the throttle fully open, and the ignition timing optimized for the corresponding boost values. The variation of the cycle parameters is shown in Fig. 7.

The probability of knocking increases as the intake manifold pressure increases and decreases as the intake valve closing angle increases, since it depends on the amount of new fuel-air mixture supplied to the engine. The conversion to ammonia helps the engine have better knock resistance compared to gasoline engines (Fig. 7a, b). The maximum brake torque and brake power are achieved at maximum boost pressure and minimum intake valve closing angle, and these values are higher when the engine runs on ammonia compared to gasoline. As the intake valve closing angle increases, brake specific torque increases (Fig. 7c, d).

The brake efficiency of the engine improves by increasing the intake manifold pressure and intake valve closing angle. In this case, there is no significant difference in brake efficiency when comparing ammonia fuel with gasoline fuel (Fig. 7g, h).

BSFC decreases as the boost pressure increases in both modelling cases (with ammonia and gasoline). This is consistent with the conclusions reached when applying turbochargers to internal combustion engines. Under naturally aspirated engine conditions, the BSFC of an ammonia engine (746 g/kWh) is more than twice that of a gasoline engine (325 g/kWh) at 120 °CA bTDC (Fig. 7e, f). The main reason for the increase in fuel consumption is the large difference in the lower calorific value between the two types of fuel and the same intake valve closing angle.

5. Conclusion

It can be seen that ammonia is an environmentally friendly fuel and also has a renewable nature. Because NH_3 has no carbon in its molecular composition, the combustion products do not contain greenhouse gases. In addition, the advantages of storage, transportation and supply to vehicles make ammonia a fuel with great potential.

When switching from gasoline to ammonia at the engine's external characteristics, the maximum brake torque on the external characteristics increases by 6.1%, while the maximum brake power decreases by 30%. Along with that, with the calorific value and volumetric energy density of NH_3 being lower than that of gasoline, the brake specific fuel consumption of the engine when using NH_3 increases by almost two times. This is the problem that needs to be solved for the engine's fuel system when converting.

Moreover, with a higher octane value than gasoline, it allows for an increase in the compression ratio of the converted engine. This helps to improve the performance of the NH_3 engine operating on the Miller cycle.

Finally, the research results also show that it is possible to apply the solution of increasing the boost pressure to improve the engine's working parameters. When increasing the initial pressure, the engine's performance and torque increase while the engine's brake-specific fuel consumption decreases. When the boost pressure increases up to 3 bar, the engine's detonation ability is equivalent to that of a gasoline engine without turbocharging.

Based on the results obtained, corresponding solutions will be proposed to improve the engine's working process when converting.

Acknowledgements

This research is funded by the University of Transport and Communications (UTC) under grant number T2026-CK-006.

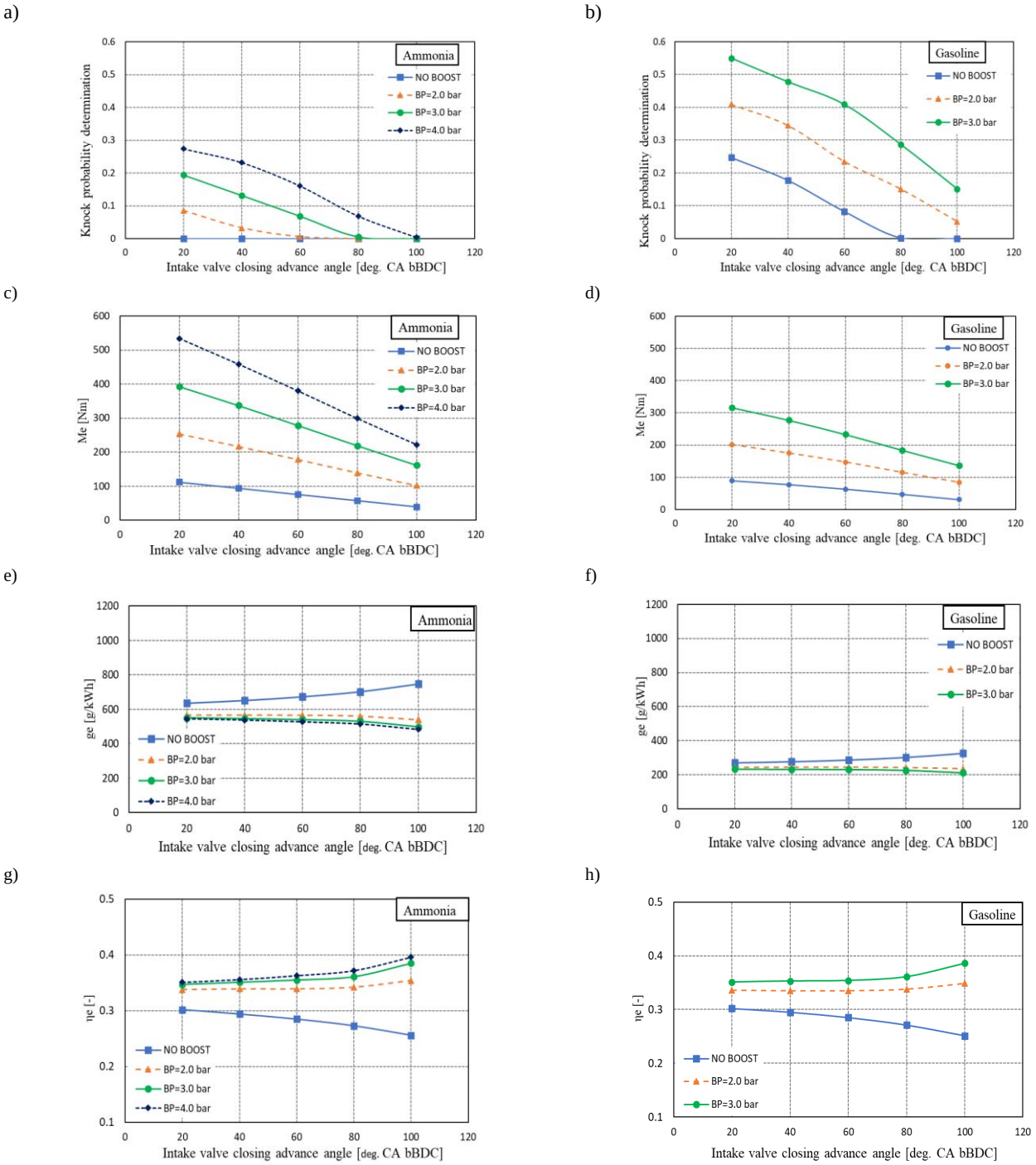

Fig. 7. The operating parameters of the SI 4CH 7.6/7 engine working in the Miller cycle with a variable intake valve closing angle. a, b) probability of knocking occurrence; c,d) brake torque ; e,f) brake specific fuel consumption; g,h) brake efficiency

Nomenclature

AFCs	alkaline fuel cells
bBDC	before bottom dead center
BP	boost pressure
BSFC	brake specific fuel consumption
bTDC	before top dead center
H_2	hydrogen
HC	hydrocarbons
ICEs	internal combustion engines
IT	ignition timing
NH_3	ammonia
NO_x	nitrogen oxides
PM	particulate matter
PEMFCs	proton exchange membrane fuel cells
SI	spark ignition
SOFCs	solid oxide fuel cells

Bibliography

[1] Briceno-Mena LA, Venugopalan G, Romagnoli JA, Arges CG. Machine learning for guiding high-temperature PEM fuel cells with greater power density. Patterns. 2021;2(2). https://doi.org/10.1016/j.patter.2020.100187

[2] Cardoso JS, Silva V, Rocha RC, Hall MJ, Costa M, Eusébio D. Ammonia as an energy vector: current and future prospects for low-carbon fuel applications in internal combustion engines. J Clean Prod. 2021;296:1256562. https://doi.org/10.1016/j.jclepro.2021.126562

[3] Cheng Q, Muhammad A, Kaario O, Ahmad Z, Martti L. Ammonia as a sustainable fuel: review and novel strategies. Renew Sustain Energy Rev. 2025;207:114995. https://doi.org/10.1016/j.rser.2024.114995

[4] Douaud AM, Eyzat P. Four-octane-number method for predicting the anti-knock behavior of fuels and engines. SAE Technical Paper 780080. 1978. https://doi.org/10.4271/780080

[5] Dunin AY, Nguyen Thin Quynh, Golubkov LN, Computational study of the effect of increasing the fuel injection pressure up to 3000 bar on the performance of the diesel engine and its gaseous emissions. International Conference on Engineering Management of Communication and Technology (EMCTECH). 2020:65-70. https://doi.org/10.1109/EMCTECH49634.2020.9261516

[6] Giddey S, Badwal SPS, Munnings C, Dolan M. Ammonia as a renewable energy transportation media. ACS Sustainable Chem Eng. 2017;5(11):10231-10239. https://doi.org/10.1021/acssuschemeng.7b02219

[7] Hong C, Ji C, Wang S, Xin G, Wang Z, Meng H et al. An experimental study of various load control strategies for an ammonia/hydrogen dual-fuel engine with the Miller cycle. Fuel Proc Technol. 2023;247:107780. https://doi.org/10.1016/j.fuproc.2023.107780

[8] Huang Z. Fuel blend combustion for decarbonization. Proc Combust Inst. 2024;40(1-4). https://doi.org/10.1016/j.proci.2024.105776

[9] Kuta K, Nadimi E, Przybyła G, Żmudka Z, Adamczyk W. Ammonia CI engine aftertreatment systems design and flow simulation. Combustion Engines. 2022;190(3):3-10. https://doi.org/10.19206/CE-143158

[10] Kim K, Roh G, Kim W, Chun K. A preliminary study on an alternative ship propulsion system fueled by ammonia: environmental and economic assessments. J Mar Sci Eng. 2020; 8(3). https://doi.org/10.3390/jmse8030183

[11] MacFarlane DR, Cherepanov PV, Choi J, Suryanto BHR, Hodgetts RY, Bakker JM et al. A roadmap to the ammonia economy. Joule. 2020;4(6):1186-1205. https://doi.org/10.1016/j.joule.2020.04.004

[12] Stępień Z. Ammonia as an alternative fuel to internal combustion engines. Combustion Engines. 2025;200(1):117-127. https://doi.org/10.19206/CE-200289

[13] Thin Quynh N, Duc Le H, Dunin, A. Influences of injector geometry parameters on fuel injection characteristics and parameters of a diesel engine. Transport and Communications Science Journal. 2023;74(4):530-543. https://doi.org/10.47869/tcsj.74.4.12

[14] Valera-Medina A, Xiao H, Owen-Jones M, David WIF, Bowen PJ. Ammonia for power. Prog Energy Combust Sci. 2018;69:63-102. https://doi.org/10.1016/j.pecs.2018.07.001

Quynh Nguyen Thin, DEng. – Department of Engine Machinery, University of Transport and Communications, Ha Noi, Vietnam.
e-mail: *thinquynh@utc.edu.vn*

Dung Nguyen Van, DEng. – Department of Internal Combustion Engine, Le Quy Don Technical University, Ha Noi, Vietnam.
e-mail: *Nguyenvandung1996kchy@gmail.com*

Article citation info:
Żurawski P, Trytek A. Investigation of the effect of engine running time on the material characteristics of a piston. Combustion Engines. 2026;206(3):96-104. https://doi.org/10.19206/CE-216443

Paweł ŻURAWSKI
Andrzej TRYTEK

Combustion Engines
Polish Scientific Society of Combustion Engines

Investigation of the effect of engine running time on the material characteristics of a piston

ARTICLE INFO

Received: 20 July 2025
Revised: 16 December 2025
Accepted: 6 January 2026
Available online: 25 February 2026

Regardless of the class of passenger car, manufacturer, or type of internal combustion engine, vehicle owners strive to ensure the longest possible period of reliable engine operation. The reliability and performance of an internal combustion engine are key indicators of its quality and prestige. Numerous research and development studies have focused on optimizing piston design and identifying the causes of piston failure. However, to better understand degradation mechanisms and trends in modern piston design, it is necessary to investigate the phenomena affecting the piston during typical engine service life. Thermomechanical stresses, friction, elevated and fluctuating temperatures, and contaminants all contribute to piston wear and reduce its service life. In this study, a new aluminum piston was compared with a piston extracted from an engine after approximately 200,000 kilometers of operation. The influence of engine operating time on piston surface condition, hardness, microstructure, and surface quality was analyzed. These parameters provide insight into the impact of friction and thermal loads on piston wear. Based on the investigations, the influence of piston operating time on surface degradation and changes in the mechanical properties of the piston material was determined. Furthermore, areas most susceptible to long-term loads and exhibiting the highest wear were identified. The results enable identification of piston regions requiring reinforcement or design optimization to minimize the risk of damage from prolonged engine operation.

Key words: *pistons, microstructure, wear, tribological analysis*

This is an open access article under the CC BY license (http://creativecommons.org/licenses/by/4.0/)

1. Introduction

In internal combustion engines and compressors, the piston's movement with sealing rings in the cylinder liner plays a key role in energy consumption, primarily due to elevated friction and component wear. The effect of friction is not limited to energy losses; it also poses a risk of component failure and engine power reduction [2, 14]. The wear intensity of the piston assembly depends on numerous factors, including operating pressure and temperature, engine rotational speed, surface roughness, engine load, material quality, the performance of the cooling system, the type of lubricating oil used, and potential manufacturing defects [4, 7, 14, 25–27].

A significant mismatch in thermal expansion between the aluminum piston and the cast iron cylinder liner can reduce the working clearance and impair the formation of the lubricating oil film. Inadequate lubrication of the piston–liner contact surfaces increases friction-generated heat, further intensifying thermal expansion and potentially leading to seizure of the interacting components [26]. Several strategies exist to mitigate these risks, such as surface roughness optimization, application of protective coatings, chemical composition modifications, and the use of composite materials [3, 6]. Equally important is the proper selection of engine oil and ensuring effective delivery to all critical contact zones [23]. The highest frictional forces in the piston assembly occur during cold start-up. According to the literature, the system initially operates under boundary or mixed lubrication conditions and gradually transitions to hydrodynamic lubrication. Poor oil selection or improper maintenance may initiate accelerated wear processes or even lead to piston failure [15].

During its operating cycle, the piston undergoes deformation due to gas pressure and contact forces acting along its working plane. The lateral and angular movement of the piston causes impacts between the piston skirt and the cylinder liner, leading to dynamic fluctuations in hydrodynamic forces. The maximum impact force occurs in diesel engines during the compression stroke and is concentrated at the upper ends of the piston skirt. An increase in clearance between the piston skirt and the cylinder liner results in greater lateral displacement and a larger tilt angle, which, in turn, increases the piston's lateral acceleration and intensifies impact forces [9]. An example of engine block damage caused by this phenomenon is shown in Fig. 1.

Fig. 1. Photograph of a four-cylinder passenger car engine block [16]

The wide variety of piston damage types and their underlying causes compels engine designers to consider the effects of design changes on piston durability from the earliest development stages. Therefore, numerous studies are conducted to analyze piston wear mechanisms, such as the one presented in this article, as well as attempts to develop algorithms capable of predicting the influence of design modifications on service life – e.g., through thermal exchange modeling [8, 12].

2. Literature review

Accurate identification of piston damage requires knowledge not only of metallurgy and piston design but also of the operational principles of internal combustion engines. The diagnostic process is challenging, as the root cause is often not immediately visible [20]. When analyzing piston failures, they can be classified according to the location of the damage [21]:

- damage to the piston crown
- damage to the piston pin boss or skirt
- damage to the piston rings
- damage to the cylinder liner.

However, a more functional and diagnostically useful classification is based on the underlying cause of the failure. One of the most common and severe types is piston seizure due to overheating, as illustrated in Fig. 2. There are four primary causes of such failures: delayed combustion-induced overheating, incorrect piston installation (wrong piston type), blocked oil injection, and cooling system malfunction [21].

Fig. 2. Photograph of a piston damaged by seizure [21]

Another common type of piston failure in internal combustion engines is damage to the piston crown. This type of failure may have multiple causes, including: incorrect valve recess depth, excessive piston protrusion above the cylinder deck, carbon deposits on the piston crown, excessive machining of the cylinder head sealing surfaces, improper cylinder head sealing, insufficient valve clearance, and incorrect valve timing [21]. An example of piston crown damage is shown in Fig. 3.

Fig. 3. Photograph of a piston with a damaged crown [21]

A more dramatic form of piston failure in internal combustion engines is piston material melting. An example of a piston exhibiting material melting is shown in Fig. 4. According to the literature, there are six primary causes of piston melting:

- incorrect fuel injection quantity
- improper injection timing
- faulty or damaged injector nozzles
- delayed ignition
- insufficient compression
- oscillations in the fuel injection lines.

Fig. 4. Photograph of a piston damaged by crown melting [21]

Another common type of piston failure is cracking of the piston crown and combustion chamber area [19, 21]. This type of damage is particularly frequent in older-generation diesel engines. An example of such failure is shown in Fig. 5. The most common causes include:

- incorrect fuel injection timing
- damaged or unsuitable injector nozzle
- improper fuel injection quantity
- lack of piston cooling
- chip tuning (increasing engine power without accounting for thermal limits)

– installation of pistons with improper combustion bowl geometry
– insufficient compression.

Fig. 5. Photograph of a piston damaged by cracking in the combustion chamber [21]

Axial wear caused by contamination is shown in Figure 6. Dirt and other impurities that enter the engine oil form an abrasive mixture that acts like sandpaper, leading to wear of the piston skirt. Infrequent oil and filter changes can significantly accelerate piston degradation and may ultimately result in critical engine failure.

Fig. 6. Photograph of a piston damaged by dirt intrusion [21]

Numerous scientific publications have investigated the causes of piston damage and methods for its prevention. One particularly noteworthy study is [19] by Siadkowska, which provides a detailed analysis of steel and aluminum piston designs. A comprehensive source of technical knowledge is also provided by Kolbenschmidt [20] and Motorservice [21], which offer in-depth classifications of piston damage types, supported by extensive illustrations. The mechanisms of friction-related piston failure in internal combustion engines are thoroughly discussed in publications [17–19, 22]. One of the more interesting articles discussing the proper preparation of piston surfaces and coatings that extend piston service life is by Wróblewski and Nakashima, whose studies have a significant impact on current knowledge of the relationship between the surface condition of an internal combustion engine piston and its durability [28].

2. Analysis of the effect of piston operating time on its mechanical properties

2.1. Comparative visual analysis of pistons

To investigate the influence of engine operating time on the mechanical and tribological properties of a piston, a comparative analysis was conducted between a new diesel engine piston and a piston from an engine with approximately 200,000 kilometers of mileage. The analyzed pistons are shown in Fig. 7. Both pistons share an identical design and components. The diameters of both pistons are identical, and they are manufactured from the same material. The operating conditions of the engines from which the examined pistons were taken are comparable. The only structural difference is the presence of valves in one piston. However, it should be emphasized that the present analysis focuses on the influence of engine operation on the properties and microstructure of the piston material, rather than on design differences. The first piston ring groove contains a reinforcing cast iron insert, designed to increase the mechanical strength of the piston. This insert is made of spheroidal graphite iron, subjected to alfin treatment, and subsequently cast with molten aluminum to form a durable metallurgical bond. Additionally, both pistons are equipped with an internal cooling channel to protect the piston crown and combustion chamber from overheating caused by the high thermal loads generated during combustion.

The piston pin bores are fitted with cold-pressed brass bushings to extend the piston's service life.

Fig. 7. Analyzed pistons from diesel engines

Figure 8 presents a comparison of the piston crown and combustion chamber area between a new and a used internal combustion engine piston. On the surface of the used piston crown, residual soot is visible in the form of a black deposit. Minor scratches were also observed, likely caused during disassembly or handling. No cracks, melting, or material loss were identified. The crown edges remain smooth, with no visible deformation. The piston crown and combustion chamber surfaces show no wear beyond what

would be expected from the normal combustion process of the air-fuel mixture during engine operation.

a) b)

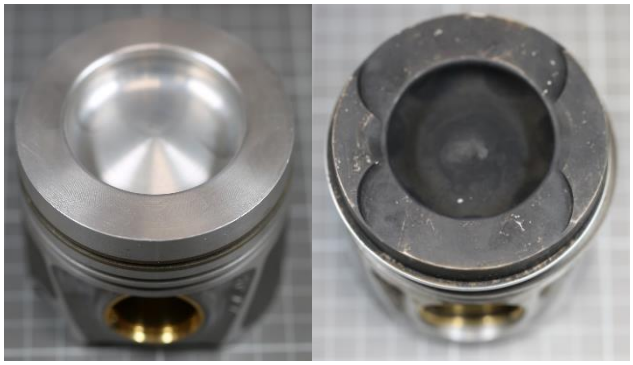

Fig. 8. Piston crown with combustion chamber: a) new diesel engine piston, b) piston after approximately 200,000 kilometers of operation

Figure 9 presents a comparison of the skirt and ring land areas of a new piston and a used piston from an internal combustion engine with approximately 200,000 kilometers of service. The comparison reveals noticeable wear on the piston's lateral surface. The graphite-based coating on the load-bearing surface has worn off, with no longitudinal scratches observed. The wear pattern corresponds to the contact zone between the piston and the cylinder wall. A significant accumulation of carbon deposits is visible on the fire land, forming a thick layer. Discoloration is also apparent on the ring land surfaces.

a) b)

Fig. 9. View of the piston skirts from internal combustion engines: a) unused piston, b) used piston

The final area showing visible changes compared to the new piston is the underside of the piston crown in the combustion chamber region, as shown in Fig. 10. Despite the presence of an internal cooling channel, this surface was exposed to significant thermal stress. No surface damage or cracking was observed on the inner side of the piston. However, the area exhibits signs of overheating, likely due to localized exceedance of thermal limits.

The presence of significant thermal influence, visible wear, and surface scratches prompted the authors of this study to perform a hardness analysis across the piston cross-section, examine its microstructure, and observe the lateral surfaces under magnification. The results of these investigations are presented in the following sections of the article.

Fig. 10. View of the overheated internal area of a used internal combustion engine piston

2.2. Chemical composition analysis of piston material

The most commonly used material in the production of internal combustion engine pistons is silumin – an Al-Si-based alloy valued for its unique technological and physicochemical properties [1, 5, 6, 10, 11, 13, 24]. The most frequently used silumins are hypoeutectic alloys containing approximately 11–13% silicon and hypereutectic alloys with 17–24% silicon. A significant drawback of these alloys is the rapid decrease in tensile strength and hardness with increasing temperature. For hypoeutectic silumins, tensile strength decreases by approximately 40–50% at 250°C, and by up to 65% at 300°C. In the case of hypereutectic silumins, the decrease is about 5% lower [4].

Piston-grade silumins are among the most chemically complex aluminum alloys. Their composition typically includes elements from the Al–Si–Cu–Mg system, with additions of Ni, Mn, Fe, Zn, and occasionally Mo, Cr, V, Co, and W. They are also modified with elements such as K, Na, and Sr (silicon eutectic modifiers), Ti, Sc, V, Zr, B (grain refiners), as well as P and S (modifiers of primary silicon crystals) [4].

To determine the chemical composition, the analyzed pistons were sectioned along their axis, perpendicular to the piston pin bore. The measurements were carried out using a spectrometer. Measurement points are marked in Fig. 11 for the new piston and in Fig. 12 for the used piston. Three measurements were taken on the new piston and four on the used piston.

The results of the chemical composition measurements are presented in Table 1. The analysis indicates that the examined pistons are made of silumin containing approximately 12.3% silicon and around 4% copper. The main alloying elements include magnesium (Mg), nickel (Ni), iron (Fe), manganese (Mn), zinc (Zn), and titanium (Ti). Both materials exhibit nearly identical chemical compositions, and the minor differences observed may be attributed to variations between production batches at the piston manufacturing facility.

Fig. 11. Chemical composition measurement points on a new internal combustion engine piston

Fig. 12. Chemical composition measurement points on a used internal combustion engine piston

Table 1. Chemical composition analysis of used and new pistons

Element [%]	Used piston	New piston
Si	12,35	12,34
Cu	3,91	3,98
Mg	0,708	0,6
Ni	2,97	2,85
Fe	0,479	0,389
Mn	0,0724	0,113
Zn	0,083	0,062
Ti	0,029	0,033
Pb	0,004	0,003
Zr	0,05	0,05
V	0,037	0,044
Sn	0,0025	0,0023
P ppm	30,16	29,72
Cr	0,0099	0,016
Na	<0,3	<0,3
Ca ppm	1,07	2,2
Sb ppm	12,1	16,77
Li ppm	<0,05	<0,05
Sr ppm	<0,1	<0,1

The piston-grade silumin used in the analyzed pistons exhibits the following physical-mechanical properties:

- thermal conductivity at 200°C: approximately 128 W/(m·K)
- coefficient of linear thermal expansion: 21×10^{-6} 1/K
- tensile strength (Rm): approximately 240 MPa
- hardness: ranging between 110 and 150 HB.

2.2. Hardness profile analysis

The operating cycle of a piston in an internal combustion engine involves repeated heating and cooling. The temperature dependence of material strength presents a significant limitation for both increasing engine efficiency and extending service life. To evaluate the effect of the engine's thermal cycles on mechanical properties, both a new piston and a used piston (with approximately 200,000 kilometers of service) were sectioned longitudinally along the axis, in a plane perpendicular to the piston pin bore. Hardness measurements were performed using the Brinell hardness scale (HB). The measurement points for the new piston are shown in Fig. 13. The hardness values ranged from 118 to 131 HB, with an average value of 124.6 HB and a measurement spread of 13 HB.

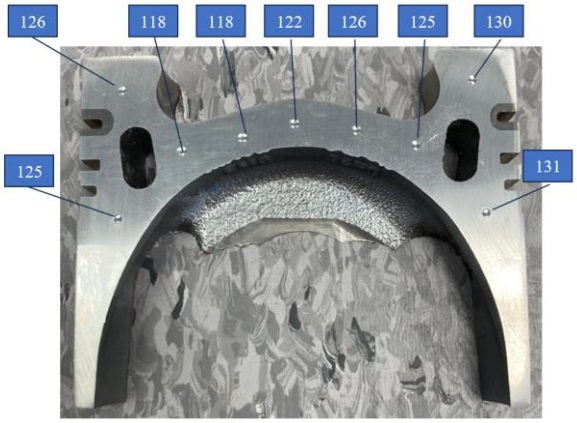

Fig. 13. Unused diesel engine piston with marked hardness measurement points and HB values

The hardness measurement points for the used piston are shown in Fig. 14. Measurements were taken at seven locations. The highest recorded hardness was 94 HB, while the lowest was 84 HB. The average hardness of the used piston was 90 HB, with a spread of 11 HB. The lowest hardness values were observed near the piston crown, whereas the highest values occurred near the oil gallery on the combustion chamber side.

Figure 15 compares the hardness profiles of a new diesel engine piston and a piston with 200,000 kilometers of service. The new piston exhibits consistently higher hardness across the entire cross-section, on average approximately 28% greater than that of the used piston. The most significant reduction in hardness was observed near the piston crown, amounting to approximately 34%.

To verify the significant hardness reduction observed near the piston crown, additional hardness measurements were performed directly on the crown surface. Four measurements were taken for both the new and the used piston: two along the axis of the piston pin bore and two in a plane perpendicular to that axis. The locations of the measurement points are shown in Fig. 16.

Fig. 14. Used diesel engine piston with marked hardness measurement points and HB values

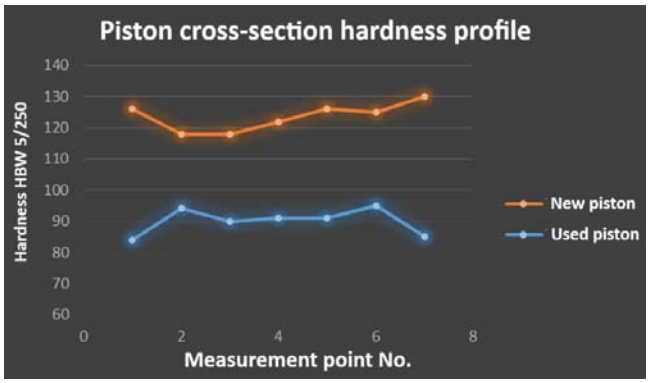

Fig. 15. Comparison of hardness profiles of new and used pistons in cross-section

The measured hardness values on the crown of the new piston were: 124, 127, 117, and 127 HBW. For the used piston, the corresponding values were: 80, 79, 82, and 79 HBW. The hardness reduction along the piston pin bore axis was approximately 33%, while along the skirt axis it was about 38%. This significant decrease in hardness on the piston crown is likely due to prolonged exposure to elevated temperatures during engine operation. Such a substantial loss of hardness adversely affects the fatigue strength and overall durability of the piston, increasing the risk of premature wear or mechanical failure.

a) b)

Fig. 16. Hardness measurement of the piston crown: a) new piston, b) used piston

According to the literature, the local temperature on the piston surface in the combustion chamber region may reach approximately 250–350°C. For the AlSi12Cu4Ni2Mg alloy used in the analyzed pistons, the temperature range of 250–300°C corresponds to the onset of the material's slow softening process. Prolonged exposure to such elevated temperatures during engine operation can lead to a gradual reduction in hardness. This provides clear evidence that further research and development on new piston alloys or technologies to enhance the durability of aluminum pistons is fully justified.

2.3. Microstructural analysis

High temperatures, along with cyclic heating and cooling, affect the material's hardness and mechanical properties. To determine whether these factors influenced the surface condition and microstructure, metallographic cross-sections were prepared for both the new and used pistons, as shown in Fig. 17a and 17b, respectively.

a) b)

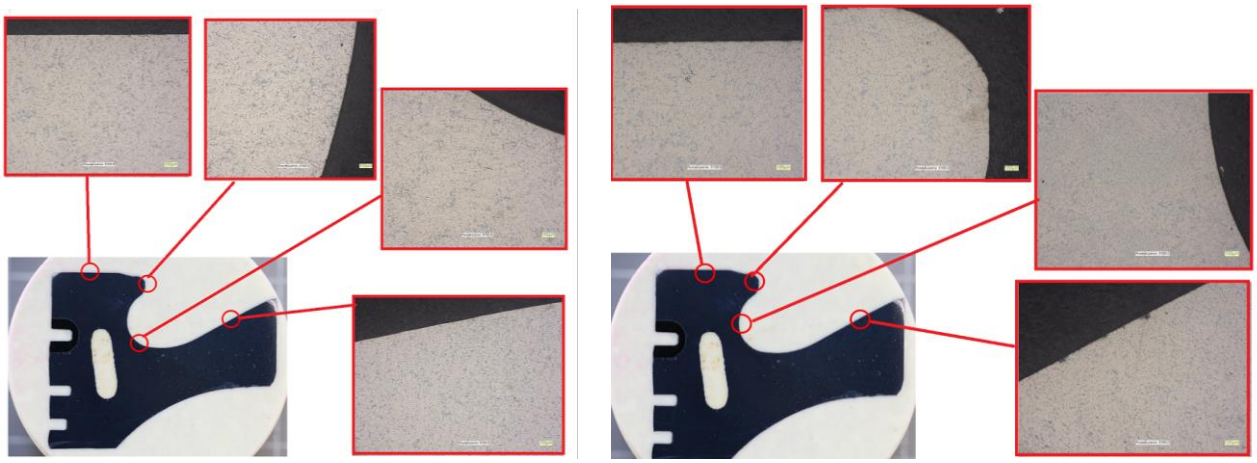

Fig. 17. Microstructure analysis locations: a) new piston, b) used piston

The metallographic specimen included the ring land area, piston crown, and combustion chamber region. Figure 17a shows the new piston with the selected areas marked for analysis. Four zones were examined: the piston crown, the combustion chamber edge, and two locations within the combustion chamber. All examined edges in the new diesel engine piston were continuous, uniform, and free of any irregularities. The microstructure in these areas was fine-grained and consistent across all analyzed zones. Figure 18a shows the edge of the combustion chamber in the new piston, while Fig. 18b presents the same area in the used piston. In the used piston, burn marks and localized edge degradation up to 0.04 mm deep were observed. These thermal erosions are numerous and distributed across the entire surface of the combustion chamber.

a)

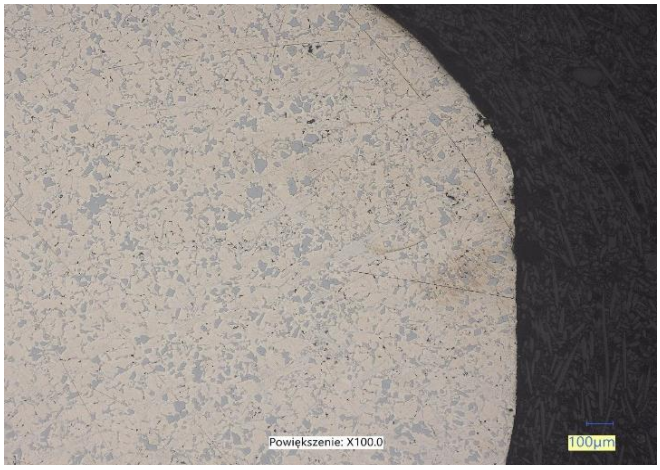

b)

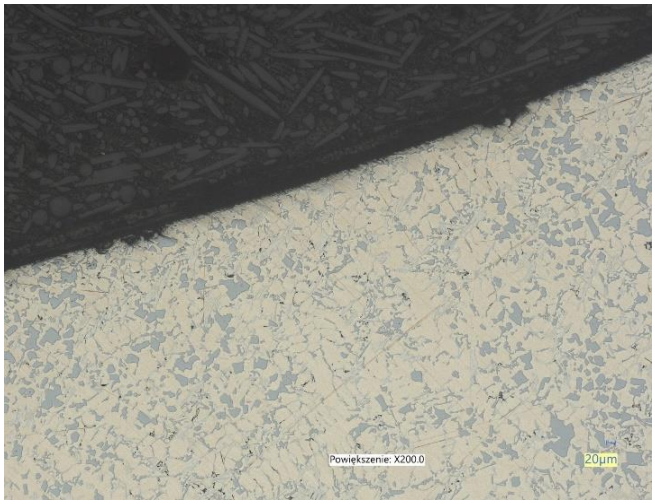

Fig. 18. View of typical burn marks on the surface of a used piston: a) combustion chamber edge, b) combustion chamber

Analysis of the microstructure of the used internal combustion engine piston in various regions revealed grain refinement in the combustion chamber area adjacent to the piston's internal cooling channel, as shown in Fig. 19a. When compared to the microstructure near the piston crown (Fig. 19b), the difference in grain size is clearly noticeable. This effect was not observed in the new piston. The analyzed region is subjected to both high temperatures and pressures generated during combustion, as well as thermal gradients caused by the cooling channel extracting heat from the combustion chamber. The presence of the cooling channel may have contributed to the observed local microstructural refinement in this area.

a)

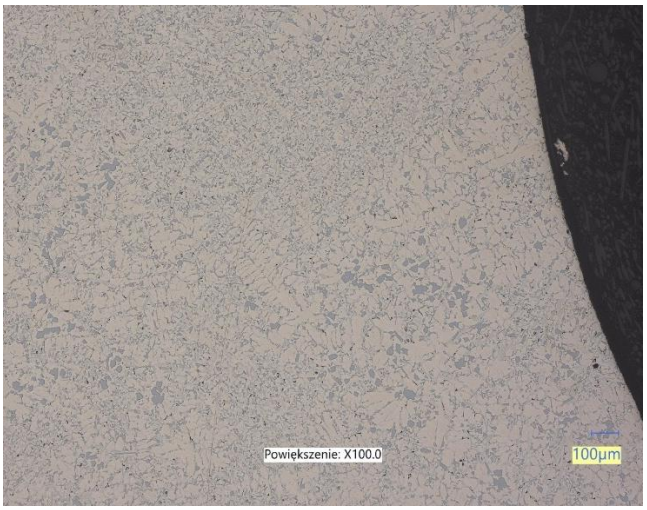

b)

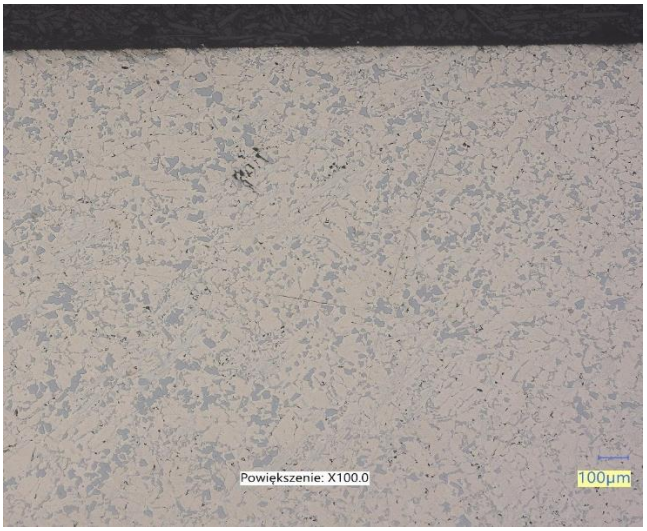

Fig. 19. Metallographic cross-section of the upper part of the piston pin bore in the used piston

For comparison, Fig. 20 presents the microstructure of the new piston in the combustion chamber region. The structure is homogeneous, with clearly visible solidification lines typical of the silumin casting process. A distinct difference can be observed between the microstructures of the new and used pistons. The edge in this area is smooth, uniform, and free of any discontinuities.

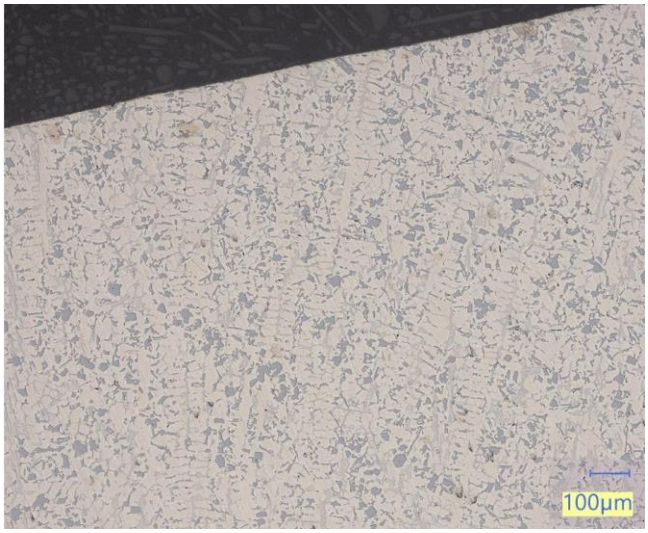

Fig. 20. Metallographic cross-section of the combustion chamber of a new internal combustion engine piston

3. Conclusions

Pistons in internal combustion engines undergo gradual wear throughout their service life due to friction, elevated temperatures, and the high pressures generated during engine operation. Understanding these degradation mechanisms enables the design of more durable and reliable pistons, which directly impacts both vehicle performance and operational costs.

The analysis clearly demonstrated that, during engine operation, significant alterations occur on the piston surface, particularly in the combustion chamber area and on the piston crown; both the material hardness and its microstructure undergo measurable changes. Based on the comparative analysis of a new piston and a piston extracted after approximately 200,000 kilometers of engine operation, the following conclusions can be drawn:

- Traces of graphite layer wear were observed on the skirt surface of the used piston
- Signs of thermal degradation were visible on the inner, central region of the piston
- The average hardness across the cross-section of the used piston was 34 HB lower than that of the new piston
- The piston crown of the used piston exhibited a hardness reduction of 44 HB compared to the new one
- At 100× magnification, thermal damage and crater formation were observed on the surface of the combustion chamber area
- In the region near the cooling channel, microstructural grain refinement was evident in the used piston.

These findings suggest that destructive processes may already have initiated in the analyzed piston, potentially leading to failure if continued operation is pursued.

If the manufacturer aims to extend the service life of pistons in this engine type, the following improvements are recommended:

- Reinforcement of the combustion chamber, e.g., by applying Durablow® technology or protective coatings on the piston crown
- Enhancement of heat dissipation efficiency through optimization of the cooling channel geometry
- Reduction of frictional wear on the piston skirt by applying advanced graphite-based coatings.

Although many approaches exist to improve piston durability, lifecycle analyses, such as the one presented in this study, provide valuable insights into the specific areas of piston design that require refinement.

Bibliography

[1] Adil H, Gerguri S, Durodola J, Audebert F, Bonatesta F, Saporiti F. Evolution of materials for internal combustion engines pistons. Int J Res. 2023;10(8):203-214. https://doi.org/10.52403/ijrr.20230827

[2] Amara M, Abbes MT, Dokkiche A, Benbrike M. Enhancement of tribological behavior for diesel engine piston of solid skirt by an optimal choice of interface material. World Academy of Science, Engineering and Technology International Journal of Mechanical and Mechatronics Engineering. 2016;10(7). https://scholar.waset.org/1307-6892/10005042

[3] Boopathi D, Palanivendhan M, Philip J, Dhulipalla HV. Tribological properties of coated and uncoated materials for piston ring applications. IOP Conf Ser: Mater Sci Eng. 2021;1059:012022. https://doi.org/10.1088/1757-899X/1059/1/012022

[4] Czekaj E. Nickel-free piston silumins with improved dimensional stability. Foundry Institute Krakow; 2011. https://doi.org/10.13140/2.1.3012.4809

[5] Czerepak M, Piątkowski J. Casting of combustion engine pistons before and now on the example of FM Gorzyce. Arch Foundry Eng. 2023;23(2):58-65. https://doi.org/10.24425/afe.2023.144296

[6] Dolata AJ, Wieczorek J, Dyzia M, Starczewski M. Assessment of the tribological properties of aluminum matrix composites intended for cooperation with piston rings in combustion engines. Materials. 2022; 15(11):3806. https://doi.org/10.3390/ma15113806

[7] Elagouz A, Ali KA, Xianjun H, Abdelkareem MAA. Techniques used to improve the tribological performance of the piston ring–cylinder liner contact. IOP Conf Ser: Mater Sci Eng. 2019;563:022024. https://doi.org/10.1088/1757-899X/563/2/022024

[8] Fei C, Lei T, Qian Z, Shu Z. Piston thermal analysis of heavy commercial vehicle diesel engine using anthanum zirconate thermal-barrier coating. Energies. 2022;15(12):4225. https://doi.org/10.3390/en15124225

[9] Forero JD, Valencia Ochoa G, Palacios Alvarado W. Study of the piston secondary movement on the tribological performance of a single-cylinder low-displacement diesel engine. Lubricants. 2020;8(11): 97. https://doi.org/10.3390/lubricants8110097

[10] Jankowski A. Researches of novel composite pistons for combustion engines. Journal of KONES Powertrain and Transport. 2013;20(4). https://doi.org/10.5604/12314005.1137609

[11] Kałużny J, Merkisz J, Stepanenko A, Wróblewski E, Gapiński B, Piasecki A et al. Piston assembly in the most powerful 2.0 L diesel engine – case study of the current tribological system and innovative concepts for the future. Combustion Engines. 2017;171(4):127-133. https://doi.org/10.19206/CE2017-421

[12] Liu Y, Lei J, Chen J, Wen J, Jiang X, Peng H. Research on lightweight design method of diesel engine steel piston based on heat transfer characteristics. Appl Therm Eng. 2024;248(B):123344. https://doi.org/10.1016/j.applthermaleng.2024.123344

[13] Manasijevic S, Markovic S, Acimovic-Pavlovic Z, Raic K, Radisa R. Effect of heat treatment on the microstructure and mechanical properties of piston alloys. Mater Technol. 2013;47:585-591.

[14] Milojevic S, Dzunic D, Marić D, Skrucany T, Mitrovic S, Pesic. Tribological assessment of a luminum cylinder material for piston compressors in trucks and buses brake systems. Technical Gazette. 2021;28(4): 1268-1276. https://doi.org/10.17559/TV-20200915110030

[15] Mistry HR, Bhatt DV. Multi-scale morphological metrology of piston-ring-textured cylinder liner assembly in relation to their tribological properties. Proceedings of the 10th International Symposium on Measurement and Quality Control. 2010.

[16] Ninove FP, Mathia TG, Mazuyer D, Pawlus P, Carras S, Gruszka J. Study of tribological parameters on SI engine – a case study. Int J Adv Eng Technol. 2011; 1(3):111-117.

[17] Obert P, Müller T, Füßer HJ, Bartel D. The influence of oil supply and cylinder liner temperature on friction, wear and scuffing behavior of piston ring–cylinder liner contacts – a new model test. Tribol Int. 2016;94:306-314. https://doi.org/10.1016/j.triboint.2015.08.026

[18] Olander P, Jacobson S. Scuffing resistance testing of piston ring materials for marine two-stroke diesel engines and mapping of the operating mechanisms. Wear. 2015;330-331:42-48. https://doi.org/10.1016/j.wear.2015.01.074

[19] Pusterhofer M, Summer F, Wuketich D, Grün F. Development of a model test system for a piston ring/cylinder liner contact with focus on near-to-application seizure behaviour. Lubricants. 2019;7(12): 104. https://doi.org/10.3390/lubricants7120104

[20] Rampolla B, Siegman K, Spaulding J. Root cause analysis of failed diesel engine aluminum pistons. J Fail Anal Prev. 2013;13:128-135. https://doi.org/10.1007/s11668-012-9649-y

[21] Rheinmetall Catalogue. Piston damage and its causes. Motorservice (accessed on 2024 Aug 29). https://www.ms-motorservice.com

[22] Schiffer J, Krampl H, Godor I, Grün F, Betz M, Laiminger S. Optimization of the piston ring–cylinder liner system in gas engines for power generation. Proceedings of the 27th CIMAC World Congress on Combustion Engine Technology; 2013 May 13-16; Shanghai.

[23] Shahabuddin M, Mofijur M, Fattah IMR, Kalam MA, Masjuki HH, Chowdhury MA et al. Study on the Tribological characteristics of plant-oil-based biolubricant with automotive liner–piston ring materials. Curr Res Green Sustain Chem. 2022;5:100262. https://doi.org/10.1016/j.crgsc.2022.100262

[24] Siadkowska K, Majczak A, Barański G. Studying a construction of piston for the aircraft CI engine. Combustion Engines. 2017;168(1):161-167. https://doi.org/10.19206/CE-2017-126

[25] Siemieńska-Janowska B, Piertowski S. The effects of temperature on strength of the new piston aluminium materials. Journal of KONES Internal Combustion Engines. 2003;10(3-4). https://ilot.lukasiewicz.gov.pl/KONES/2003/1-2/30.pdf

[26] Skulić A, Bukvic M. Tribological properties of piston–cylinder set in internal combustion engines. Appl Eng Lett. 2016;1(1):29-33. https://www.researchgate.net/publication/316630257

[27] Štefániková M, Moravčík R, Kocúrová K. The analysis of causes of lorry piston combustion engine damage: a review. Materials Engineering – Materiálové inžinierstvo. 2012;19:47-51.

[28] Wróblewski P, Bratkowski P. Effect of using a combination of coatings on reducing structural defects in the working area of the combustion chamber and on the energy efficiency of a reciprocating internal combustion engine. Combustion Engines, 2025;202(3): 118-130. https://doi.org/10.19206/CE-207651

Paweł Żurawski, MEng. – Doctoral School of the Rzeszow University of Technology, Poland.
e-mail: *zurawskipawel15@gmail.com*

Prof. Andrzej Trytek, DSc., DEng. – Faculty of Mechanics and Technology, Rzeszów University of Technology, Poland.
e-mail: *trytek@prz.edu.pl*

Article citation info:
Grzelak M, Borucka A, Rykała M. Analysis of the influence of selected powertrain design parameters on fuel consumption in passenger vehicles. Combustion Engines. 2026;206(3):105-111. https://doi.org/10.19206/CE-217140

Małgorzata GRZELAK
Anna BORUCKA
Magdalena RYKAŁA

Combustion Engines
Polish Scientific Society of Combustion Engines

Analysis of the influence of selected powertrain design parameters on fuel consumption in passenger vehicles

ARTICLE INFO

Received: 18 June 2025
Revised: 18 December 2025
Accepted: 19 January 2026
Available online: 4 February 2026

In view of increasingly stringent environmental requirements and global efforts to reduce greenhouse gas emissions, it is becoming increasingly important to identify the design factors of powertrains that directly affect fuel efficiency and carbon dioxide (CO_2) emissions. This study analyses the impact of selected technical parameters of passenger vehicles powertrains – in particular, engine displacement, number of cylinders, type of transmission and type of fuel – on fuel consumption in urban, highway and combined conditions, as well as on CO_2 emissions. The study used operational data covering the design parameters of selected passenger vehicle models on the market. The statistical analysis identified significant relationships between the drive system's design and its environmental impact. The results of the study can make a significant contribution to the development of forecasting tools to support the design of new-generation engines, as well as to decision-making and to the formulation of strategies for the sustainable development of low-emission transport technologies.

Key words: *fuel consumption, multivariate regression, CO_2 emission, powertrain parameters*

This is an open access article under the CC BY license (http://creativecommons.org/licenses/by/4.0/)

1. Introduction

Reducing harmful emissions into the environment is one of the main objectives of climate policy. The regulations introduced by the European Union aim to reduce greenhouse gas emissions from the transport sector. The above results in stricter emission standards for newly designed and manufactured vehicles. Therefore, conducting research in the field of vehicle operation, especially powertrain systems, is an important element in meeting European standards, such as Regulation (EU) 2021/1119 of the European Parliament and of the Council of 30 June 2021, as well as United Nations SDGs (especially goal 13).

The clear need to optimize transportation energy efficiency is undoubtedly one of the main goals not only of climate policy but also of manufacturers' actions, as it simultaneously improves economic indicators. Identifying design solutions that will significantly reduce fuel consumption and, consequently, emissions is therefore a priority. At the same time, the result can be guidelines and recommendations for practice use by both manufacturers and end users, leading to the development of modern technological solutions to minimize operating costs, increase the competitiveness of automotive companies, and advance innovative zero-emission propulsion technologies.

The above elements made the analysis of selected design parameters of passenger vehicle powertrains in terms of their impact on fuel consumption in different modes of vehicle driving the purpose of the article. As the main research problem, the question was adopted: to what extent do individual factors shape the energy efficiency of motor vehicle powertrains? For the purpose of the study, a detailed analysis of a database consisting of 7,384 observations was carried out, which included measurements of engine displacement, number of cylinders, number of gears in the transmission and its type, fuel type and fuel consumption values in the urban cycle, highway driving and mixed cycle. The article uses a multivariate regression model, which enables selection of design parameters that significantly affect fuel consumption levels, as well as quantification of the interdependence between them and emission factors. Consequently, this type of analysis is an important contribution to the pursuit of sustainable development in the automotive sector and the reduction of the negative environmental impact of transportation.

2. Literature review

The impact of individual engine and transmission design parameters on fuel consumption has been widely studied in the literature, particularly amid increasing demands for energy efficiency and CO_2 reduction in the transportation sector. A review has shown that both engine and transmission parameters have a key impact on fuel consumption [4]. Among the design factors of passenger vehicle internal combustion engines, engine displacement, compression ratio, turbocharging, and the weight of the engine and the entire vehicle are listed as those that significantly affect fuel consumption and vehicle emissions [26].

Engine displacement is one of its key parameters, which determines the total volume of all cylinders [1]. It directly affects the performance characteristics of the power unit [35], including mainly torque, power and fuel consumption. Available in the literature, studies indicate that as engine displacement increases, more fuel is consumed, mainly because a larger amount of fuel-air mixture can be burned. Research results indicate that engines with smaller displacement (1.0 to 1.6 L) have fuel consumption up to 15–20% lower than those with 2.0 to 3.0 L [8, 24].

Other parameters mentioned in the literature that affect fuel consumption are compression ratio and turbocharging [6]. Zhu et al. indicate that increasing the compression ratio improves the engine's thermal efficiency, thereby reducing specific fuel consumption by 5–8% [33]. Turbocharging, on the other hand, is a technology that increases the amount of air supplied to the cylinders using a turbocharger [11]. This

solution enables reducing the engine's capacity while maintaining its power, a process known as downsizing [28]. This makes it possible to reduce fuel consumption from 5% in gasoline engines [19] to 12% in compression-ignition engines [13], thereby reducing CO_2 emissions by 7% to 15% [3]. In contrast, combining a turbocharger with a properly adjusted compression ratio can improve fuel economy by up to 20% [18].

The last-mentioned parameter related to engine characteristics is its weight. It is estimated that each 100 kg increase in vehicle weight results in a 0.3 to 0.6 liter increase in fuel consumption per 100 km [17]. For modern aluminum engines, which can reduce weight by 20–30 kg, fuel consumption decreases by 2–4% [34].

Other parameters that affect CO_2 emissions and fuel consumption are transmission parameters. A review of available research has shown that, in this area, the following should be specified [16]: the number of ratios (gears) and their span, the type of gearbox and its mechanical efficiency, as well as the driver's shifting strategy. Available research indicates that increasing the number of gear ratios results in a better match between engine speed and driving conditions, thereby allowing the engine to operate within its optimal range [30]. It is estimated that using a gearbox with 6 ratios (compared to a 4-speed) results in a fuel savings of about 3% (without affecting vehicle performance) [19]. The gear ratio value is also an important parameter. Lisowski points out that a higher ratio at the highest gear will lower engine rpm at constant speed, thus minimizing energy loss [15].

Studies also show that fuel consumption is affected by the type of transmission and its mechanical efficiency. Wang et al. indicate that manual transmissions have higher mechanical efficiency (up to 98%) than automatic transmissions (86% to 87%), which directly translates into lower fuel consumption [31]. Manual transmissions are also lighter than classic automatic transmissions. On the other hand, Al.-Saedi et al. note that modern solutions – such as direct-shift gearbox (DSG) transmissions, which are based on advanced electronics and precise shift control – can match or even surpass manual transmissions in terms of fuel economy, especially in urban conditions [19].

A variety of research methods are used in the literature to analyze the impact of specific vehicle design parameters on fuel consumption and CO_2 emissions [25]. These include experimental laboratory tests (dynamometers) [9] and real-world measurements during driving cycles [27]. Also popular are computer simulations, the use of artificial intelligence methods, including artificial neural networks, as well as mathematical modeling methods [12], including Markov processes [21] or multi-criteria algorithms [32].

In this study, the multivariate regression method was used to analyze the influence of selected design parameters of the vehicle's powertrain. Its application enabled answering the question of which recorded parameter values significantly affect fuel consumption and the extent of this influence. As part of the study, three models were built: for driving in an urban cycle, on the highway, and in a mixed cycle, which were further evaluated and compared.

3. Research method and results

3.1. Multivariate regression model

A multivariate regression model was used to analyze the impact of selected design parameters of passenger vehicle powertrains on fuel consumption and CO_2 emissions. This is a statistical method for modeling the relationship among multiple variables, enabling the testing of significance and the evaluation of the influence of selected factors on the phenomenon under study [10]. The multivariate regression model usually takes the form of an equation, which can be represented as the following relationship (1):

$$Y = b_0 + b_1 x_1 + b_2 x_2 + \cdots + b_k x_k + \varepsilon, \qquad (1)$$

where: Y – dependent variable, $X_1, X_2, \ldots, X_k$ – independent variables, b_i – parameters of the regression model (where $i = 0 \ldots k$), ε – random component.

The model parameters are estimated using least squares, which involves selecting the model coefficients to minimize the sum of squared residuals between the observed and predicted values [23].

Each time, the estimated model must be verified. The significance of the estimated parameters is evaluated to confirm their impact on the phenomenon under study, and the distribution of the model's residuals is analyzed to confirm that the model has been correctly built. The quality of the model, i.e., its fit to the empirical data, is determined by the coefficient of determination (R2).

A Student's t-test was used to test the significance of the model parameters, which tested the following hypotheses:
H_0: $\beta_i = 0$, no statistically significant effect of the explanatory variable X_i on the variable Y,
H_1: $\beta_i \neq 0$. There is a statistically significant effect of the explanatory variable X_i on the variable Y,
which were verified for the adopted significance level $\alpha = 0.05$.

Diagnosis of the model's residuals was carried out by testing the consistency of their distribution with the normal distribution using the chi-square test, for which the following hypotheses were formulated [14]:
H_0: $P(X = S_i) = p_i$ for $i = 1,2, \ldots, k$ – the studied characteristic X has a discrete distribution $(p_1, p_2, \ldots, p_k)$,
H_1: there is such a class j for which $P(X = S_i) \neq p_i$.

And autocorrelation, based on the Durbin-Watson test, based on the accepted hypotheses [14]:
H_0: $\rho = 0$ – the autocorrelation coefficient of the model residuals is statistically equal to zero,
H_1: $\rho \neq 0$ – the autocorrelation coefficient of the elements of the series is statistically different from zero.

The quality of the model fit was evaluated using the coefficient of determination R^2, which is estimated according to relation (2) [10]:

$$R^2 = \frac{\sum_{i=1}^{n}(\hat{y}_i - \bar{y})^2}{\sum_{i=1}^{n}(y_i - \bar{y})^2} \qquad (2)$$

where: n – the number of observations, y_i – empirical value of the variable Y, $\hat{y}_i$ – the theoretical value of the Y variable determined from the model, $\bar{y}$ – the arithmetic mean of the values of the Y variable.

This article analyzes the effects of selected design parameters of passenger vehicle powertrains on fuel consumption and CO_2 emissions. A database of 7,384 observations of selected parameters of passenger vehicle internal combustion engines was used for the study. The recorded data concerns passenger vehicles circulating in Canada, which were manufactured mainly in 2016 and 2017. Only passenger cars of different brands with similar total weight were analyzed. The values of the parameters of fuel consumption in the urban cycle, highway cycle and in the combined cycle were recorded, as well as engine displacement, type of transmission (automatic, manual), number of gears, type of fuel (diesel, premium gasoline, gasoline, ethanol 85%) and number of cylinders.

The study began with a detailed analysis of the selected explanatory variables, i.e. fuel consumption in urban mode, while driving on the highway and in combined mode (values measured both while moving in the city and on the highway). In the first step, basic values of descriptive statistics were calculated, including the mean and median (Table 1).

Table 1. Values of basic descriptive statistics

Dependent variable	Mean	Median	Standard deviation	Skewness	Kurtosis
Fuel consumption in the urban cycle	12.55	12.10	3.48	0.79	1.14
Fuel consumption on highway	9.03	8.70	2.21	1.07	2.00
Fuel consumption in mixed cycle	10.97	10.60	2.88	0.88	1.35

The results indicate that the highest mean of fuel consumption was recorded during urban driving, while the lowest was recorded during highway driving. Since the conformity of the tested distribution to the normal distribution was not confirmed (the obtained p-value in each group was 0.00), a nonparametric Friedman test (performed for the three groups simultaneously) was used to compare the significance of differences between mean values, followed by a Wilcoxon test performed individually between pairs. Figure 1 shows a box plot of the mean values in each group of observations.

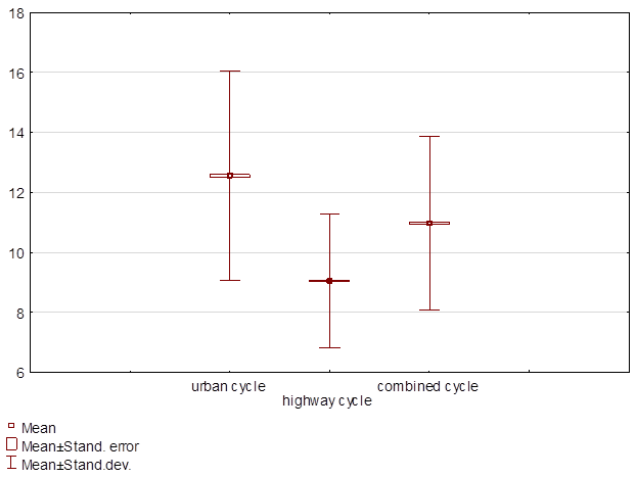

Fig. 1. Box plot of the mean values in each group of observation

Friedman's test tested the statistical hypotheses of equality of the sum of ranks for successive measurements:
$H_o: \theta_1 = \theta_2 = \ldots = \theta_k$,
H_1: not all θ_j are equal to each other for $(j = 1, 2 \ldots k)$.
where:
$\theta_1, \theta_2 \ldots \theta_k$ – medians of the studied feature in subsequent measurements in the studied population.

The Friedman T statistic calculated by the test was 13,847.04, with a corresponding p = 0.00, which allows us to conclude that there are statistically significant differences in the medians between the listed three groups. In the next step, the groups were compared individually in pairs using the Wilcoxon test (Table 2). The test tested the following hypotheses [2]:
$H_o: F_1 = F_2$ (there is no significant difference in the distributions of the variables),
$H_1: F_1 \neq F_2$.

Table 2. Wilcoxon test results

	Highway cycle		Mixed cycle	
	T	p	T	p
Urban cycle	11,529.5	0.00	10,014.0	0.00
Highway cycle			10,171.5	0.00

The obtained test statistic and its p-value confirmed the presence of differences in fuel consumption across all groups. On this basis, in the next step, an analysis of the impact of selected design parameters of the vehicle's powertrain on fuel consumption within the selected groups was carried out.

3.2. Analysis of the effect of selected powertrain design parameters on fuel consumption in the urban cycle

In the first step, a multivariate regression model was built from observations recorded during the urban cycle. Due to the collinearity of the parameters number of cylinders and engine displacement (correlation coefficient 0.97), it was decided to exclude the parameter number of cylinders from the model. The estimated values of the model parameters and the corresponding p-values are shown in Table 3.

Table 3. Estimated values of regression model parameters in urban cycle

Independent variable	Level	The value of parameter	p
Intercept		5.63	0.00
Engine displacement		1.91	0.00
Transmission	A	0.12	0.00
Number of gears		–0.08	0.00
Fuel type	premium gasoline	1.45	0.00
Fuel type	gasoline	0.94	0.00
Fuel type	ethanol85	6.28	0.00

At the adopted level of significance ($\alpha = 0.05$), all selected variables have a significant impact on fuel consumption. Due to the inclusion of qualitative variables in the study, it was necessary to select a single reference level (class) for each variable. For the transmission type, manual transmission was used as the reference level, and for the fuel type, diesel. Based on the calculations, the following regression equation was formulated:

$$y = 5.63 + 1.91 \cdot E_d + 0.12 \cdot T_A - 0.08 \cdot G + 1.45 \cdot F_{pg} + 0.94 \cdot F_g + 6.28 \cdot F_e$$

where: E_d – engine displacement, C_n – number of cylinders, T_A – transmission type, G – number of gears, F_{pg} – fuel type, premium gasoline (98-octane and more), F_g – fuel type – gasoline (95-octane), F_e – fuel type – ethanol 85.

The next step was to verify the validity of the constructed model using residual analysis and assess the quality of the fit. It began by checking the distribution of residuals for conformity to the normal distribution. In the chi-square test, the calculated test statistic T = 218.04 and the corresponding p-value of 0.25 confirm normality of the random component (Fig. 2).

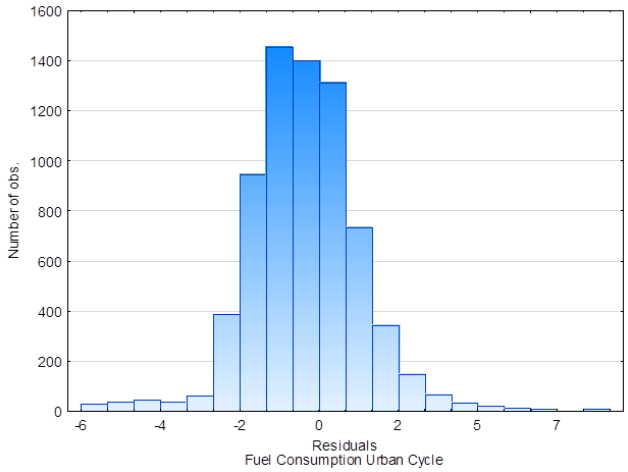

Fig. 2. Histogram of the residuals of the regression model for the urban cycle

In the next step, the Durbin-Watson test statistic for autocorrelation of residuals was calculated: DW = 1.96. It is assumed that in the absence of autocorrelation, the value of the statistic should be close to 2. In addition, the relationship between the test statistic and the threshold values dl and du from the Durbin-Watson table for k = 5 and n = 7000 was verified. The control values were dl = 1.95 and du = 2.04, respectively. The calculated value of the test statistic falls within the range <1.95;2.04>, which allows us to accept the null hypothesis and assume that there is no autocorrelation in the model residuals. The above conclusions indicate that the constructed model should be considered correct.

A coefficient of determination was calculated for the estimated model, which is $R^2 = 0.81$, meaning that as much as 81% of the variation in the observed values of the dependent variable is explained by it, which should be considered a satisfactory result.

Based on the results obtained, it can be concluded that both an increase in engine displacement by 1 L results in an increase in fuel consumption by 1.91 L/100. It should also be noted that, in the sample analyzed, an increase of 0.12 L/100 km in consumption was observed for vehicles with automatic transmissions compared to those with manual transmissions. In contrast, vehicles with more gears had lower fuel consumption. An increase of 1 in the number of available gear ratios resulted in a 0.08 L/100 km decrease in fuel consumption, due to the engine's ability to better adapt its operation to driving conditions. The last factor analyzed was the type of fuel. In relation to diesel-powered engines, the use of premium gasoline resulted in a 1.45 L/100 km increase in consumption, while regular gasoline resulted in a 0.94 L/100 km increase. For engines powered by ethanol fuel (85%) the sharp increase in fuel consumption of 6.28 L/100 km was observed.

3.3. Analysis of the effect of selected powertrain design parameters on fuel consumption in the highway cycle

As another, a multivariate regression model was built for the highway cycle. The estimated values of the model parameters and their corresponding p-values are shown in Table 4.

Table 4. Estimated values of regression model parameters in highway cycle

Independent variable	Level	The value of parameter	p
Intercept		4.92	0.00
Engine displacement		1.11	0.00
Transmission	A	0.34	0.00
Number of gears		–0.10	0.00
Fuel type	premium gasoline	0.95	0.00
Fuel type	gasoline	0.83	0.00
Fuel type	ethanol85	4.53	0.00

For all estimated parameters, the p-values are 0.00, indicating they are statistically significant and affect fuel consumption. Based on the calculations, the following regression equation was formulated:

$$y = 4.92 + 1.11 \cdot E_d + 0.34 \cdot T_A - 0.10 \cdot G + 0.95 \cdot F_{pg} + 0.83 \cdot F_g + 4.53 \cdot F_e$$

In the next step, the model residuals and the fit quality were again verified. In the chi-square test, the calculated test statistic was T = 201.55, with p = 0.10, confirming the normal distribution of the random component (Fig. 3).

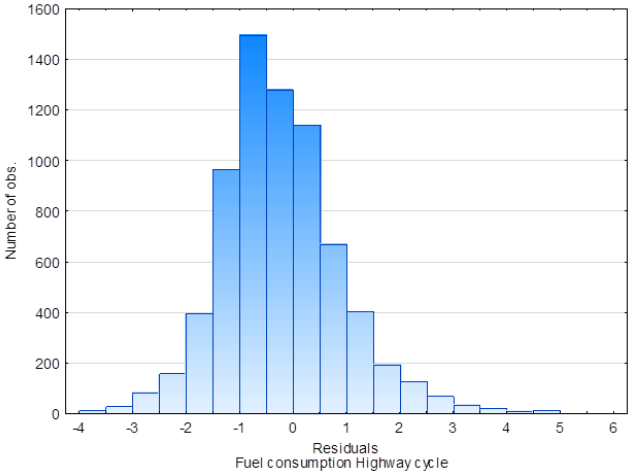

Fig. 3. Histogram of the residuals of the regression model for the highway cycle

In the next step, the value of the Durbin-Watson test statistic was calculated, which was DW = 1.97. The calculated value of the test statistic falls within the range <1.95;2.04>, which indicates that there is no autocorrelation in the model residuals. On this basis, again, the constructed model should be considered correct.

A coefficient of determination was also calculated for the estimated model, which is R^2 = 0.72, meaning that as much as 72% of the variation in the observed values of the dependent variable is explained by it, which should be considered a sufficient result.

Based on the results obtained, the following conclusions were drawn. In highway driving, increasing engine displacement by 1 liter results in a 1.11 L/100 km increase in fuel consumption. It should also be noted that in the sample analyzed, an increase of 0.17 L/100 km in consumption was observed for vehicles with automatic transmissions compared to those with manual transmissions. In contrast, vehicles with more gears had lower fuel consumption. An increase of 1 in the number of available gear ratios resulted in a 0.11 L/100 km decrease in fuel consumption. In the case of the variable fuel type, it can be concluded that In relation to diesel-powered engines, the use of engines powered by premium gasoline, gasoline and ethanol fuel (85%) resulted in an increase in consumption of 0.95 L/100 km, 0.83 L/100 km and 4.53 L/100 km, respectively.

3.4. Analysis of the effect of selected powertrain design parameters on fuel consumption in the combined cycle

Lastly, a mixed-mode multivariate regression model was built. Again, the model's parameter values were estimated, and the corresponding p-values are shown in Table 5.

Table 5. Estimated values of the regression model parameters in the combined cycle

Independent variable	Level	The value of the parameter	p
Intercept		5.31	0.00
Engine displacement		1.55	0.00
Transmission	A	0.22	0.00
Number of gears		–0.09	0.00
Fuel type	premium gasoline	1.22	0.00
Fuel type	gasoline	0.88	0.00
Fuel type	ethanol85	5.49	0.00

For all estimated parameters, the p-values are 0.00, indicating they are statistically significant and affect fuel consumption. The regression equation has the following form:

$$y = 5.31 + 1.55 \cdot C_c + 0.22 \cdot T_A - 0.09 \cdot G + 1.22 \cdot F_{pg} + 0.88 \cdot F_g + 5.49 \cdot F_e$$

In the next step, the model residuals and the fit quality were again verified. In the chi-square test conducted, the calculated value of the test statistic was T = 211.32 and the corresponding p = 0.45, confirming the fit to the normal distribution of the random component (Fig. 4).

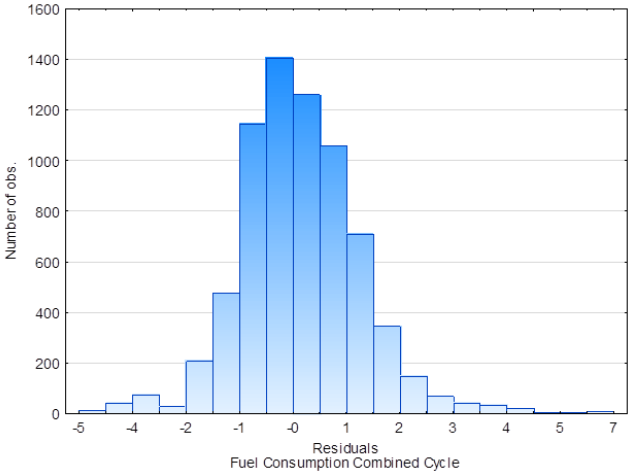

Fig. 4. Histogram of the residuals of the regression model for the combined cycle

In the next step, the Durbin-Watson test statistic was calculated, yielding DW = 1.96. The calculated value of the test statistic falls within the range <1.95;2.04>, which indicates that there is no autocorrelation in the model residuals. On this basis, again, the constructed model should be considered correct.

A coefficient of determination was also calculated for the estimated model: R^2 = 0.79, indicating that 79% of the variation in the observed values of the dependent variable is explained by the model, which should be considered a satisfactory result.

Based on the results obtained, the following conclusions were drawn. In highway driving, increasing engine displacement by 1 L results in a 1.55 L/100 km increase in fuel consumption. It should also be noted that, in the sample analyzed, an increase of 0.22 L/100 km in consumption was observed for vehicles with automatic transmissions compared to those with manual transmissions. In contrast, vehicles with more gears had lower fuel consumption. Increasing the number of available gear ratios by 1 resulted in a 0.09 L/100 km decrease in fuel consumption. For variable fuel types, it can be concluded that, compared with diesel-powered engines, engines powered by premium gasoline, gasoline, and ethanol (85%) resulted in increases of 1.22 L/100 km, 0.88 L/100 km, and 5.49 L/100 km, respectively.

4. Conclusions

Understanding which design parameters affect passenger vehicle fuel consumption is crucial for both individual users and the transportation sector as a whole. Knowledge of these relationships enables better management of operating costs by increasing vehicle fuel efficiency and optimizing the driver's driving style. On the other hand, the relevance of this issue stems from the ongoing efforts to achieve a sustainable transformation of transportation. Lower fuel consumption means lower CO_2 emissions into the environment. It should be noted that there is a linear relationship between CO_2 emissions and fuel consumption. Per 1 liter of fuel consumed, the approximate CO_2 emissions are 2.3 kg for gasoline, 2.66 kg for diesel, and 1.5 kg for ethanol [7, 29]. Therefore, in the above study, a multivariate regression model was used to analyze the signifi-

cance and strength of the effect of vehicle powertrain parameters, such as engine displacement, number of cylinders, type of transmission, number of gears and type of fuel on fuel consumption recorded during urban, highway and mixed cycle driving.

Based on the results, it can be concluded that the studied phenomenon is influenced by all selected design parameters. In each recorded mode, increasing engine displacement increases fuel consumption. It should also be noted that, based on the sample studied, this increase is evident in vehicles with automatic transmissions. It should also be noted that as the number of gear ratios increases, consumption decreases, mainly because the engine performs more optimally under given driving conditions. In addition, for compression-ignition engines, an increase in fuel consumption is observed for spark-ignition engines (regular and premium gasoline) and for vehicles fueled with 85% ethanol.

The above studies can be used in practice by individual users to reduce vehicle operating costs, provide support in vehicle selection, and increase their awareness of environmental protection. They can also serve as a support for automotive concerns during vehicle design, providing information on optimal configurations of the studied design parameters (for example, combining a smaller displacement with a higher number of gears).

From the perspective of individual users, the results clearly show which configuration choices can help reduce operating costs. Choosing vehicles with smaller engine displacement, more gear ratios, and appropriately selected transmission types can contribute to measurable reductions in fuel consumption and, consequently, CO_2 emissions. At the same time, awareness that certain fuel types (e.g. high-ethanol fuel) may require higher volumetric consumption encourages a more informed assessment of real operating costs and environmental effects rather than relying solely on nominal fuel price.

For automotive manufacturers, the study provides quantitative evidence supporting the design direction of combining downsized engines with advanced multi-gear transmissions. Such configurations enable acceptable performance while reducing fuel consumption in real driving conditions.

The environmental context is also important. Given the linear relationship between fuel consumption and CO_2 emissions, every reduction in fuel demand translates directly into lower greenhouse gas emissions over the vehicle's life cycle. This is particularly relevant in the context of sustainable transport policies and tightening emission standards, where improving the efficiency of conventional powertrains remains an important complement to the development of electromobility.

The study thus fits into the broader research and regulatory trend to decarbonize road transport. By confirming and specifying relationships described in the literature, it strengthens the empirical basis for guidelines on vehicle design and for recommendations addressed to drivers (e.g. choice of vehicle specification adapted to usage profile). Ultimately, the results obtained are consistent with and confirm those of available studies in the literature.

Bibliography

[1] Adamiak B, Andrych-Zalewska M, Merkisz J, Chłopek Z. The uniqueness of pollutant emission and fuel consumption test results for road vehicles tested on a chassis dynamometer. Eksploat Niezawodn. 2025;27(1). https://doi.org/10.17531/ein/195747

[2] Adegbaye AL, Adeoti OA. Neutrosophic wilcoxon signed-rank test with application to diabetes data. J Med Dent Sci Res. 2024;11(2):17-23. www.questjournals.org/jmdsr/papers/vol11-issue2/11021723.pdf

[3] Andrych-Zalewska M, Chłopek Z, Merkisz J, Pielecha J. Research on the results of the WLTP procedure for a passenger vehicle. Eksploat Niezawodn. 2024;26(1). https://doi.org/10.17531/ein/176112

[4] Andrych-Zalewska M, Chlopek Z, Pielecha J, Merkisz J. Investigation of exhaust emissions from the gasoline engine of a light duty vehicle in the Real Driving Emissions test. Eksploat Niezawodn. 2023;25(2). https://doi.org/10.17531/ein/165880

[5] Araveeporn A. Modified Liu parameters for scaling options of the multiple regression model with multicollinearity problem. Mathematics. 2024;12(19):3139. https://doi.org/10.3390/math12193139

[6] Cebulska W, Hadrys D. Comparison of vibration emissions in electric and conventional cars. Combustion Engines. 2025;202(3), 74-80. https://doi.org/10.19206/CE-204690

[7] Dias De Oliveira ME, Vaughan BE, Rykiel EJ. Ethanol as fuel: energy, carbon dioxide balances, and ecological footprint. BioScience. 2005;55(7):593-602. https://doi.org/10.1641/0006-3568(2005)055[0593:EAFECD]2.0.CO;2

[8] Folęga P, Burchart D, Kubik A, Turoń K. Application of the life cycle assessment method in public bus transport. Eksploat Niezawodn. 2025;27(3):204539. https://doi.org/10.17531/ein/204539

[9] Gonera J, Janulin M, Vrublevskyi O. Effect of vehicle operating parameters on fuel consumption and the overall energy efficiency of the drive system. Arch Transp. 2024;72(4): 109-128. https://doi.org/10.61089/aot2024.gb7qdr81

[10] Grzelak M, Borucka A, Świderski A. Assessment of the influence of selected factors on the punctuality of an urban transport fleet. Transport Problems. 2020;15. https://doi.org/10.21307/tp-2020-069

[11] Hassan QH, Al-Abboodi H. Experimental investigation of the impact of methanol-diesel blends on diesel engine emissions and performance. Combustion Engines. 2025;201(2): 150-157. https://doi.org/10.19206/CE-204494

[12] Kozłowski E, Borucka A, Oleszczuk P, Leszczyński N. Evaluation of readiness of the technical system using the semi-Markov model with selected sojourn time distributions. Eksploat Niezawodn. 2024;26(4). https://doi.org/10.17531/ein/191545

[13] Laskowski P, Zimakowska-Laskowska M. Simulation study of the effect of ethanol content in fuel on petrol engine performance and exhaust emissions. Combustion Engines. 2025;201(2):129-135. https://doi.org/10.19206/CE-204049

[14] Lin CW, Lin YT, Lian SL, Lee SS, Zen PJ, Hsu WH. Applying a multivariate simultaneous linear regression model to analyze the mediating effect of English leisure activities on English learning motivation and learning effectiveness. Eng Proc. 2023;38(1):48. https://doi.org/10.3390/engproc2023038048

[15] Lisowski M. Symulacyjna ocena wpływu wartości przełożenia na właściwości trakcyjne samochodu i zużycie paliwa. Autobusy: Technika, Eksploatacja, Systemy Transportowe. 2007;(6):274-278.
[16] Liu H, Han L, Cao Y. Improving transmission efficiency and reducing energy consumption with automotive continuously variable transmission: a model prediction comprehensive optimization approach. Appl Energy. 2020;274:115303. https://doi.org/10.1016/j.apenergy.2020.115303
[17] Milojević S, Savić S, Marić D, Stopka O, Krstić B, Stojanović B. Correlation between emission and combustion characteristics with the compression ratio and fuel injection timing in tribologically optimized diesel engine. Tehnički vjesnik. 2022;29(4):1210-1219.
[18] Murawski J, Pryciński P, Sierpiński G, Jachimowski R. Prospects for the development of zero- and low-emission vehicles in urban distribution systems in terms of the situation on the fuel market. Military Logistics Systems. 2022; 57(2):41-62. https://doi.org/10.37055/slw/163229
[19] Namar MM, Jahanian O, Shafaghat R, Nikzadfar K. Engine downsizing; global approach to reduce emissions: a worldwide review. HighTech Innov J. 2021;2(4):384-399. https://doi.org/10.28991/HIJ-2021-02-04-010
[20] Oglieve CJ, Mohammadpour M, Rahnejat H. Optimisation of the vehicle transmission and the gear-shifting strategy for the minimum fuel consumption and the minimum nitrogen oxide emissions. Proc Inst Mech Eng Part D: J Automob Eng. 2017;231(7):883-899. https://doi.org/10.1177/0954407017702985
[21] Oszczypała M, Ziółkowski J, Małachowski J. Semi-Markov approach for reliability modelling of light utility vehicles. Eksploat Niezawodn. 2023;25(2):161859. https://doi.org/10.17531/ein/161859
[22] Qarouach A, Matulaitis K, Butautas R, Conte D. Impact of playing middle and side pick-and-roll actions with aggressive and containing defensive strategies on workload during small-sided games in male basketball players. Int J Sports Physiol Perform. 2025;1(aop):1-7. https://doi.org/10.1234/ijspp.2025.1234567890.
[23] Rejman M, Szkudlarek P. The least squares method as a tool for assessment of the stroke parameters and velocity in monofin swimming. Methods Protoc. 2025;8(1):19. https://doi.org/10.3390/mps8010019
[24] Romero CA, Correa P, Ariza Echeverri EA, Vergara D. Strategies for reducing automobile fuel consumption. Appl Sci. 2024;14(2):910. https://doi.org/10.3390/app14020910
[25] Rykała M, Grzelak M, Rykała Ł, Voicu D, Stoica RM. Modeling vehicle fuel consumption using a low-cost OBD-II interface. Energies. 2023;16(21):7266. https://doi.org/10.3390/en16217266
[26] Rymaniak Ł, Merkisz J, Szymlet N, Kamińska M, Weymann S. Use of emission indicators related to CO_2 emissions in the ecological assessment of an agricultural tractor. Eksploat Niezawodn. 2021;23(4):605-11. https://doi.org/10.17531/ein.2021.4.2
[27] Sileghem L, Bosteels D, May J, Favre C, Verhelst S. Analysis of vehicle emission measurements on the new WLTC, the NEDC and the CADC. Transp Res Part D Transp Environ. 2014;32:70-85. https://doi.org/10.1016/j.trd.2014.07.008
[28] Skobiej K. A review of hydrogen combustion and its impact on engine performance and emissions. Combustion Engines. 2025;200(1):64-70. https://doi.org/10.19206/CE-195470
[29] Sullivan JL, Baker RE, Boyer BA, Hammerle RH, Kenney TE, Muniz L et al. CO_2 emission benefit of diesel (versus gasoline) powered vehicles. Environ Sci Technol. 2004; 38(12):3217-3223. https://doi.org/10.1021/es034928d
[30] Voicu D, Stoica RM, Vilău R, Marinescu M, Digulescu A, Despina-Stoian C et al. Frequency analysis of vibrations in terms of human exposure while driving military armoured personnel carriers and logistic transportation vehicles. Electronics. 2023;12(14):3152. https://doi.org/10.3390/electronics12143152
[31] Wang H, Ge S, Guo D, Jiang Y. Fuel consumption of a wheel loader with power reflux hydraulic transmission system. J Vibroeng. 2023;25(7):1327-1341. https://doi.org/10.21595/jve.2023.22980
[32] Zhang Y, Wang L. Real-time fault monitoring method for logistics vehicles based on chaotic ant colony algorithm. Eksploat Niezawodn. 2025;27(4):203395. https://doi.org/10.17531/ein/203395
[33] Zhu T, Yan X, Gao Z, Qiu Y, Zhu L, Huang Z. Combustion and emission characteristics of ammonia-hydrogen fueled SI engine with high compression ratio. Int J Hydrogen Energy. 2024;62:579-590. https://doi.org/10.1016/j.ijhydene.2024.03.035
[34] Ziółkowski J, Oszczypała M, Małachowski J, Szkutnik-Rogoż J. Use of artificial neural networks to predict fuel consumption on the basis of technical parameters of vehicles. Energies. 2021;14(9):2639. https://doi.org/10.3390/en14092639
[35] Žvirblis T, Hunicz J, Matijošius J, Rimkus A, Kilikevičius A, Gęca M. Improving diesel engine reliability using an optimal prognostic model to predict diesel engine emissions and performance using pure diesel and hydrogenated vegetable oil. Eksploat Niezawodn. 2023;25(4):174358. https://doi.org/10.17531/ein/174358

Małgorzata Grzelak, DEng. – Faculty of Security, Logistics and Management, Military University of Technology, Poland.
e-mail: *malgorzata.grzelak@wat.edu.pl*

Prof. Anna Borucka, DSc., DEng. – Faculty of Security, Logistics and Management, Military University of Technology, Poland.
e-mail: *anna.borucka@wat.edu.pl*

Magdalena Rykała, DEng. – Faculty of Security, Logistics and Management, Military University of Technology, Poland.
e-mail: *magdalena.rykala@wat.edu.pl*

Article citation info:
Niewiadomski P, Adamczyk F, Członka J. Concept and design of the transport cover for the harvesting unit of a self-propelled forage harvester. Combustion Engines. 2026;206(3):112-120. https://doi.org/10.19206/CE-217407

Przemysław NIEWIADOMSKI
Florian ADAMCZYK
Jakub CZŁONKA

Combustion Engines
Polish Scientific Society of Combustion Engines

Concept and design of the transport cover for the harvesting unit of a self-propelled forage harvester

ARTICLE INFO

Received: 6 November 2025
Revised: 2 January 2026
Accepted: 26 January 2026
Available online: 19 February 2026

This paper presents a conceptual model of a transport cover for a grain maize harvesting attachment. To develop a model of the cover structure, a dimensional base in the form of a harvesting unit was required, to which the designed transport cover was referred. The existing Dominoni SL 978 harvest unit was used as a dimensional base, and a model of the design base was created, accounting for the most important dimensions. The conceptual model was adapted to the design base, taking into account the design assumptions, resulting in a model of a transport cover. To mount the cover to the attachment, a dedicated hooking system has been designed.

Key words: *transport cover, harvesting unit, self-propelled forage harvester, design*

1. Introduction

Agriculture and the food industry are among the fundamental sectors of the economy. This results in a large volume of agricultural goods, as well as work performed with appropriate machinery and equipment [18]. Although the equipment of farms with agricultural machinery depends on the type of agricultural production [16], the basic self-propelled vehicle is the combine harvester [13, 23, 30]. This is an agricultural machine used for harvesting grains [4], such as wheat [24], corn, barley, or rice [1, 7, 8, 15].

Combine harvesters with an axial threshing and separating device, after improvements to the axial drum design, are increasingly used for harvesting other cereals [31]. It is characterized by specially designed components that enable efficient and rapid harvesting [12, 26], separation of grain from chaff [22], and transport and storage of harvested grain. Combine harvesters are equipped with various types of centrifuges, sieves, sifters, and other mechanisms for precise separation of grains and removal of plant residues. They can also be equipped with systems for cutting and chopping straw and attachments for harvesting corn intended for grain [34]. The primary power source for combine harvesters is combustion engines (NRMM (Non-Road Mobile Machinery) engines). Among all off-road engines, these vehicles' engines operate under specific conditions [2, 3]. Despite intensive work on the development of alternative drive systems [28, 33], combustion engines will likely remain the main power source for self-propelled vehicles, tractors, and agricultural machinery for many years to come [19], including combine harvesters, also as units cooperating with generators in hybrid drive systems [20].

Due to their large dimensions and weight, combine harvesters may require special transport on public roads. Depending on the additional equipment, transporting such a machine may require the use of additional safety devices, such as safety guards. In this context, transporting a combine harvester with a corn header requires compliance with applicable road regulations.

Research on the safety of agricultural machinery in road traffic is therefore crucial to protecting both road users and agricultural machinery operators [32]. Numerous reports and scientific studies on this topic analyze the risks posed by the movement of agricultural machinery on roads and propose countermeasures and recommendations to improve safety. The results of these studies often emphasize the need to increase passenger car drivers' awareness of the presence of agricultural machinery on roads, improve the visibility of agricultural machinery through the use of appropriate markings, lighting, and guards, and introduce regulations governing the safe behavior of both machinery operators and drivers of other vehicles.

Conducting research in this area is crucial for continuously improving the safety of agricultural machinery in road traffic and for reducing accidents involving it. Transport safety is crucial to protecting people, property, and the environment. Therefore, implementing appropriate mechanical engineering solutions is key to improving road transport safety. Thanks to modern technologies and engineering solutions, it is possible to provide more resilient and safer means of transport and transport infrastructure, including through the use of appropriate safeguards.

This article presents research focused on improving the safety of agricultural equipment transport (corn harvester attachments). Collaboration among engineers, manufacturers, transport and forwarding operators, and regulatory institutions led to the development of a safety guard solution that increased safety and efficiency in agricultural transport. The article was written within the framework of engineering and technical sciences and addresses issues related to the design, research, production, operation, and safety of transport means and methods, which align with the journal's thematic scope.

Agricultural tractors, slow-moving vehicles (e.g. combine harvesters) and vehicle combinations consisting of an agricultural tractor or a slow-moving vehicle and a special trailer (e.g. a combine harvester with a trolley attached to the transport of a harvesting unit) are strictly subject to the provisions of the Road Traffic Act and the Act "Technical conditions of vehicles and the scope of their necessary equipment". This means that these vehicles must not be wider than 3 meters when moving on public roads [36]. If the vehicle or combination of vehicles exceeds 3 meters in

width but does not exceed 3.5 meters, the driver may be able to apply for a category I permit, which authorizes the driver to drive on public roads as a non-standard vehicle [37].

Therefore, the aforementioned legal regulations exclude the vast majority of combine harvesters with a harvesting unit from driving on public roads. The width of these complexes usually exceeds 4 meters (only a few older structures have units 2 to 3.5 meters wide) [36, 37].

The situation is slightly different for foldable harvesting units, whose transport width does not exceed 3.5 meters. Hence, especially for maize harvesting for silage and grain, folded harvesting units have been developed in recent years [5, 17].

For self-propelled forage harvesters and maize silage harvesters, solutions exist to increase road safety; for manufacturers of folding harvesting units, however, it is difficult to find transport guards that increase safety.

In the context of the above, the concept of a special transport cover for the attachment (header) for combine harvesters intended for harvesting grain maize was undertaken, which is presented in this publication. A lightweight, simple structure, ease of installation, and ease of use characterize the developed solution. The designed cover meets all the requirements of the traffic regulations for vehicle protection systems on public roads.

2. Transport security – an overview of dedicated solutions

2.1. Transport protection of shearing units of self-propelled forage harvesters

Transport guards, called transport protections by some manufacturers. are most often automatic opening and closing, and their task is to shield the outside complex shear units, which contain sharp working elements that primarily pose a threat to pedestrians, cyclists, and other road users not protected by the vehicle body [5, 11, 25, 29].

Table 1 provides a brief overview of the existing protection solutions used by leading manufacturers of forage harvesters.

To sum up, it can be said that transport guards are standard on manufacturers' self-propelled forage harvesters and maize silage harvesters. Technological advancement means that the machine operator does not have to leave the cab to fold or disassemble the cover. Manufacturers use two solutions for connecting the cover to the machine's structure or its harvesting unit: transport covers, which are developed as an integral part of the device [38, 39], or structures dismantled during work (harvesting plants) [40]. The advantage of the latter solution is that when working in the field, the forage harvester is not burdened with additional cover weight. Among the removable guards, some solutions do not require the operator to lower the cab to the forage harvester's working position for the time of its disassembly.

Table 1. Transport protection of the shear units of mobile forage harvesters [39–40]

Model	Description
Claas	As part of its Claas Orbis series of headers, the company offers solutions for transport on public roads. For the Orbis 600, 600 SD and 750 models, the manufacturer offers transport protection in the form of manually folded elements mounted on the front and sides of the device. On the front element, there are red and white markings, position lights and turn signals. Fabric covers with red and white markings are installed on the sides of the working unit. It takes 25 seconds to unfold the Orbis 900 without transport protection, and 30 seconds with it. The transport protection structure consists of a central main part made of a material with red and white warning markings and position lights, as well as two side sections with red and white warning markings. The side guards fold in parallel with the unfolding of the working tool, then, with the help of a hydraulic system and a special hinge, the main front curtain is folded, which rests on the intake channel during the operation of the machine forage harvester [38].
Krone EasyCollect	It is a two-part device, both parts of which are positioned vertically in the transport position, significantly simplifying the design of the unfolding system. In this model, the transport protection is a structure that attaches directly to the device's frame. The safety structure is equipped with a centrally positioned front support wheel, designed to take some of the weight of the accessory. This arrangement significantly relieves the front axle of the forage harvester. The transport protection in this solution is detached during the machine's operation [39].
Krone XCollect	It is a three-piece device available in working widths of 6 m, 7.50 m, and 9 m. However, because the working device's design and folding into the transport position differ, it has a different structure. Krone used a two-piece frame in the XCollect model. The side panels have additional elements that, when unfolded, overlap the header's front. Similar to the EasyCollect or the competing Class Orbis, the Krone XCollect is equipped with a foldable, integrated transport chassis that relieves the front axle of the forage harvester when driving on public roads [39].
Kemper	Kemper shearing units with designations 345pro and 360pro are equipped with transport guards as standard, along with position lights and turn signals. The company's flagship product for moving machines on the road is the Komfort chassis, which can be used with Kemper harvesting units. The manufacturer has designed a separate transport guard that remains completely detached from the shearing tool during work. The chassis is fully automated, and the light connector has been specially designed so that the operator does not have to leave the cab to connect to the forage harvester installation [40].

2.2. Solutions dedicated to grain maize harvesting attachments

The grain corn harvester is a work unit attached to the combine harvester, whose purpose is to pick corn cobs from the plant and deliver them to the threshing and cleaning unit for further processing (grain extraction). It has special units that pull in the plant stem, tear off the cob, direct it to the combine harvester's threshing system, and shred the remaining stem, facilitating the plant's decomposition. The attachment (header) is built as a row device, so the number of connected collecting units determines the number of harvested rows of plants and, thus, the working width of the entire attachment for harvesting maize for grain [9].

Claas implemented a dedicated solution, developing a grain maize harvester called Rovio 4 to replace the older Corio design. As in the previous solution, the Rovio 4 has a transport protection (transport cover) in the form of a front strip with red and white warning markings, position lights and turn signals (Fig. 1).

Fig. 1. Claas Corio with transport protection fitted [38]

On the right and left side of the header there are two tarpaulins to cover the working elements. The entire structure is dismantled by hand. For this solution, the front separation teeth of the header must be folded into the transport position

3. Research methodology

3.1. Aim of the study

The main objective of the work was to develop a concept and design for a transport cover for a grain corn harvesting attachment, which will directly affect the safety of the self-propelled machine's movement on public roads. When starting the design work, several guidelines were adopted. The most important of them are written below:

- the developed solution should be characterized by a light and simple structure
- should be easy to install
- simplicity of operation is required, limiting the combine operator's involvement to the minimum necessary.

The proposed cover must also meet the requirements of the traffic regulations for vehicle protection systems on public roads.

3.2. Scope of research and development work

In the work, a four-stage research procedure was used, as illustrated in Table 2.

Table 2. Scheme of the study procedure

No. (Z)	Research activities – catalogue of works
Z1	Development of a transport security concept for a grain corn harvesting attachment
Z2	Obtaining a dimensional base for the designed cover by dimensioning the existing corn harvesting attachment
Z3	Creating a model of a dimensional base (snap-in) in CAD
Z4	Development of a model of transport security in a CAD computer program, taking into account key elements for designed transport cover
Z5	Analysis of parameters and selection of materials and elements envisaged for the production of the cover
Z6	Development of the structural design of the transport cover for the grain corn harvesting attachment, for the combine harvester
Z7	Development of an electrical harness diagram for road lighting mounted on cover elements
Z8	Preparation of construction documentation of a designed transport cover for a grain corn harvesting attachment for a combine harvester grain

3.3. Research tools and resources

Each stage of the project will be based on a corresponding method. The models of the corn attachment and the transport cover will be created using 3D modeling in the CAD program Autodesk AutoCAD. To design the structure, perform stress analyses and create technical drawings, the INVENTOR PROFESSIONAL software, also part of CAD programs, was used. In addition, the DFMA (Design for Manufacture and Assembly) method will be used in the design of the transport cover, through the use of standardized steel elements that facilitate their acquisition and thus reduce the time required to build the structure. The analysis of warning elements (red and white markings, lights) will be performed using the Delphic method, a heuristic method [6, 14].

4. Implementation of research work

4.1. Transport cover concept for grain maize harvesting attachment – starting point

Taking into account the adopted design assumptions and the developed review of the design of similar devices, when developing the concept of the transport cover for the grain corn harvesting attachment mounted to combine harvesters, it was decided to follow the solutions of Kemper and Krone. In the analysed solutions, the covers are a separate structure, removable during the machine's operation. Such a solution does not require significant interference in the structure of the harvesting unit and does not force the use of complicated mechanisms for folding and unfolding the cover. As a result, removing the cover for the duration of the main machine also prevents the combine from being burdened with additional weight during field operation.

4.2. Conceptual model of transport cover for grain corn harvesting attachment

The conceptual model of the transport cover (Fig. 2) accounts for the adopted design assumptions and the requirements set out in the road traffic law and the relevant act [36].

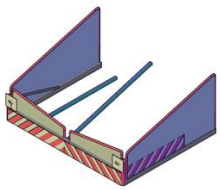

Fig. 2. Conceptual model of transport cover for grain corn harvesting attachment (folded)

The design under development is intended to cover the elements located at the front and sides of the harvesting unit. The front part of the cover is also designed to protect other road users from large, protruding crop dividers, which could, for example, cause punctures to the vehicle body during a collision. To meet the conditions for appropriate marking of elements protruding beyond the vehicle outline, alternating white and red stripes have been applied to the transport cover. They are intended to warn other road users of potential danger and the need to be extra careful. The main task of the side panels is to cover sharp elements and prevent unauthorized contact by outsiders. To facilitate daily operation of the grain maize harvesting attachment, a simple mechanism for unfolding the side panels is used (Fig. 3). As a result, the operator can carry out checks and maintenance on the harvesting unit without detaching the guard.

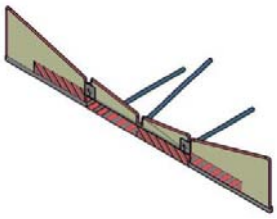

Fig. 3. Conceptual model of transport cover for grain corn harvesting attachment (unfolded)

The foldable structure of the harvesting unit covers the position lights and turn signals of the combine, so it was necessary to fix the lighting elements (lights, combination lamp) in a visible position, in accordance with the provisions of the road law, on the transport cover. It is expected that the cover will protrude more than 1 m beyond the front outline of the vehicle (combine), therefore, in accordance with the provisions of the Act [36], a white light visible from the front of the machine should be used on the front of the guard. The developed cover provides for the use of front combination lamps that meet this legal requirement.

4.3. Grain maize harvesting attachment model

To make models of the grain corn harvesting attachment, a device from the Italian manufacturer Dominoni, model SL 978 [41], was used as a base for construction (Fig. 4).

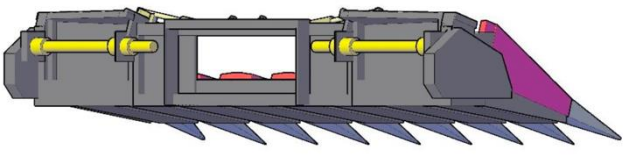

Fig. 4. Model of grain corn harvester attachment (unfolded)

It is an eight-row working unit, which, when folded into the transport position, is 3.25 m wide and weighs 3000 kg (Fig. 5).

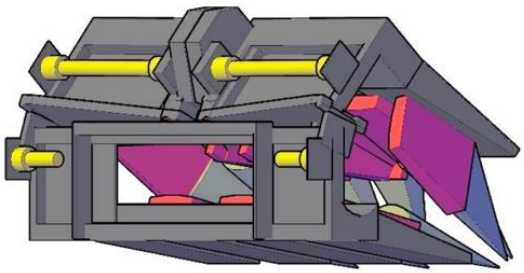

Fig. 5. Model of grain corn harvesting attachment (transport position)

These parameters indicate that, according to the Polish road law, in order for a combine harvester to be able to move with a hitched (aggregated) attachment on public roads, it is necessary to have a permit for vehicles belonging to category I.

The model of the attachment does not fully reflect the real, complete harvesting unit. It was created as a design basis for the transport shield, so it contains only the most important parameters modeled: transport width, length, height, and equipment elements that could interfere with the shield's design. In particular, elements from selected mounting locations of the supporting elements of the cover for the attachment were modeled, for which the aforementioned adjustments to the attachment structure will be necessary.

Dominoni manufactures harvesting units for grain harvesters and field forage harvesters compatible with machines from various manufacturers [41]. For this purpose, it uses specially developed adapters (Fig. 6) so that the design of the harvesting units remains unchanged.

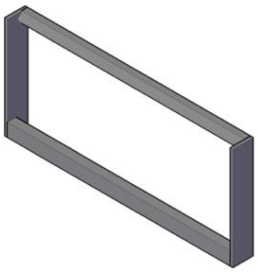

Fig. 6. Adapter Model

During the design of the transport cover, the header adapter was modified to allow the cover to be hooked to the header at the aforementioned three attachment points. The modifications introduced do not interfere with the main structure of the corn harvesting attachment and do not prevent or hinder the aggregation of the harvesting unit with the combine harvester.

4.4. Transport cover model

The transport cover model for the grain corn harvester was based on a conceptual model, matching its components to the Dominoni harvesting unit model (Fig. 7).

Fig. 7. Model of transport cover hooked on the header (unfolded position)

The width of the cover at its widest point in the transport position is 3.46 meters, allowing it to move on public roads with the guard installed after obtaining a category I permit (Fig. 8).

This requirement for this model of attachment stems from its design, with a transport width of more than 3 metres. In accordance with the assumptions also contained in the concept model description, it is envisaged that the side guards are unfolded to the sides. This is a necessary action to hook and detach the cover from the harvesting unit.

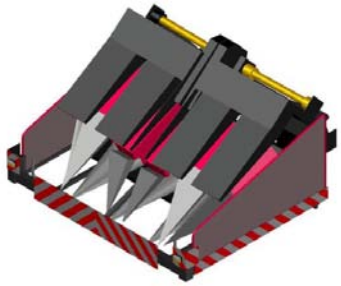

Fig. 8. Model of transport cover hooked on the header (transport position)

In this shield arrangement, the operator gains adequate visibility, allowing him to drive precisely to the guard to attach it. If the side guards are folded and the harvesting unit is folded into the transport position, the operator will not have adequate visibility to drive up to the cover precisely. An additional benefit resulting from such a well-developed design and the rules for its use is the possibility of servicing the corn harvesting attachment (e.g., lubrication, checking the technical condition of components) without the need to detach the cover.

During transport, the side panels are secured to the main frame of the cover with fasteners, preventing them from moving freely.

Subsequently, a dedicated cover mounting system with three connection points was designed, necessitating a slight modification to the header adapter (Fig. 9).

Fig. 9. Adapter model – modified version

The main weight of the cover will rest on the centrally located hook-shaped hook. The lower attachment points of the cover mainly serve a protective and stabilizing function. They have been routed to avoid collisions with the working elements of the harvesting unit, such as the shredder knives. After unfastening it, the cover will be detached by lowering the harvesting unit to the ground and driving the combine backwards.

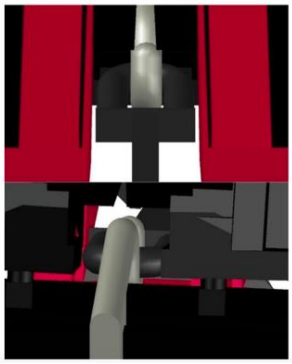

Fig. 10. Top transport cover mount

The modifications to the adapter do not affect the main structure of the harvesting unit. Figure 10 shows that the top attachment of the transport cover does not interfere with the components of the grain corn harvester attachment in the transport position.

4.5. Transport cover design

4.5.1. Input data

Inventor Professional CAD software was used to design the transport cover structure, which allows access to standardized parts and components and is also compliant with Polish Standards. This program also allows you to perform stress analyses of the elements of the structure used for simulations in a static system.

As a result of these analyses, the correctness of the selection of appropriate structural elements and material (grade of structural steel) was verified. During the design, square and round pipes with dimensions in accordance with PN-EN 10219-2 [35] were used. For this standard, unalloyed steels with designations S235JRH, S275J0H, S275J2H, S355J0H, S355J2H and fine-grained steels S275NH, S275NLH, S355NH, S355NLH, S460NH, S460NLH are provided.

The process of selecting the structure's color by comparing visualizations of different colors and their shades was also carried out. To make the warning strips alternately white and red, a self-adhesive prismatic foil was used, which provides additional visibility in adverse conditions and after dusk. The lighting will be provided by an LED combination lamp that includes a turn signal light and a white position light.

4.5.2. Static stress analyses of the cover frame structure

The finite element method (FEM) is a popular technique for solving engineering problems, including structural load analysis, particularly at key structural nodes of the structures under analysis. For this reason, it was used in this research. The basic assumption was to analyze the maxi-

mum allowable loads at key connecting nodes of the developed frame. The following assumptions were taken into account when analyzing the loads on the guard frame:

- Load Type: Loads derived from the weight of the guard material, which is the canvas, and the strength parameters of the structural materials used (steel elements).
- Load Distribution: A load distribution consistent with the structure and operation of the guard components was assumed. The highest loads were assumed on the main crossbeam, the connections between the side frame elements and the crossbeams, and the guard suspension elements on the machine frame.
- Boundary Conditions: The boundary conditions of the structure resulting from the adopted materials and design solutions were determined.
- Materials and Material Properties: The materials and their technical parameters are discussed in section 1 – 4.5.2.

During the design of the shield frame, simulation analyses were performed to assess the structure's von Mises stresses, based on the Huber-Mises-Hencky hypothesis [10]. They are calculated based on the values of the three main stresses, the components' displacements, and the material-specific safety factor. The final design was made of unalloyed steel S235JRH. The dimensions of the profiles used and the dedicated elements are shown in the attached drawings. The first simulation reflects the effect of the Earth's acceleration on the structure. Figure 11 shows the Von Mises stress distribution on the structural elements of the cover frame.

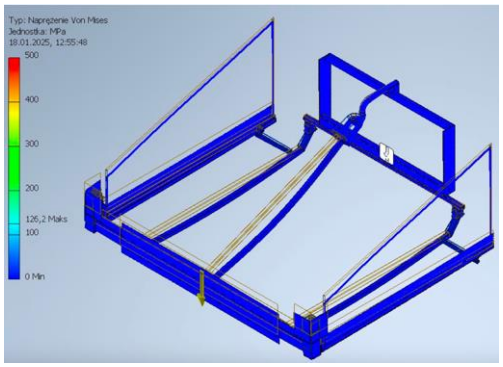

Fig. 11. Von Mises stresses – gravity

During the simulation analyses, welds were also considered, so the maximum stresses, resulting from welding and shear stresses, reached 126.2 MPa. They occur at the junction of two elements. The calculated stress in the structure is in the range of 0 to 50 MPa, with the yield strength at 235 MPa.

Figure 12 shows the factor of safety, which is directly correlated with Von Mises stresses.

The minimum safety factor in deterministic methods is assumed subjectively, based on similar constructions and their applications. Its use is necessary because the mechanical and geometrical features of the structure, the loads acting on the structure, the calculation accuracy and their compliance with the actual operation of the structure may differ from the assumptions of the constructor [7]. It is assumed that the ratio of critical stress to design working stress should be at least 3.3. On the other hand, Rabotonov [27] proposed reducing this value to 2 [10]. During the design, a minimum coefficient value of 2. This condition has been met. If the stresses resulting from welded joints were excluded, the value of this indicator would be much higher. This effect is suggested by the color corresponding to the safety factor of 5 in the legend.

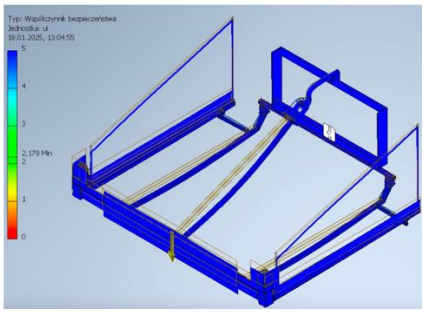

Fig. 12. Safety factor – gravity

Figure 13, on the other hand, shows the way in which the elements of the frame structure move under the influence of the Earth's acceleration.

The transparent skeleton shows the original positions of the elements, while the coloured structure shows their displacements under the influence of the loads acting on them due to gravity. The program, in order to illustrate how elements move, tends to visually exaggerate the displacements. On the other hand, the maximum value on the indicator indicates that the movement of the elements is no more than 0.25 mm.

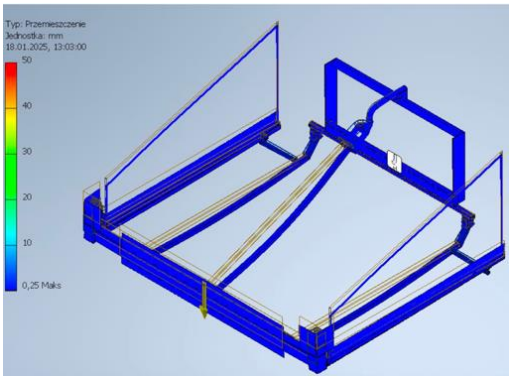

Fig. 13. Displacement of elements – gravity

The results of simulation analyses of the impact of acceleration on the shield structure showed that it is possible to reduce the dimensions of some structural elements to reduce the weight of the transport shield. The high safety index evidences this. However, during a road collision, the transport cover is the first point of contact between the combine harvester and the vehicle, so it was decided not to reduce the dimensions of the selected components.

4.5.3. Physical parameters of the transport shield structure

The transport cover for the grain corn harvester is 3.5 meters wide at its widest point, and the side panels are 2.8

meters long, covering all the working elements of the harvesting unit. The weight of the complete cover structure is 255 kg, which is 8.5% of the grain corn harvesting attachment's weight. Modifications to the adapter that allow the cover to be attached to the attachment elements weigh 36.1 kg. For the research, technical documentation and a list of materials needed for the construction and installation of the cover were prepared.

The assembly diagram of the entire developed transport cover for the grain maize harvesting attachment is shown in Fig. 14.

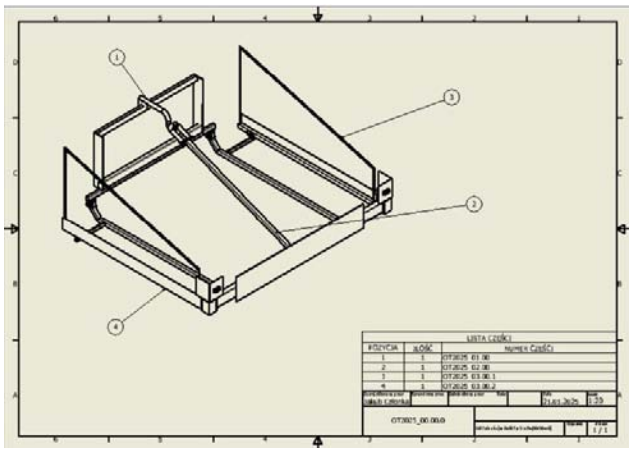

Fig. 14. Assembly diagram of the cover structure

4.5.4. Electrical installation of the cover lighting

The electrical system for the canopy lighting will be based on a standard solution used in agricultural vehicles and machinery. In this case, the combine harvester has an electrical system for an external, specialized trolley to transport the harvesting units, with a socket at the rear. To connect the lighting to the canopy, run an electrical cable with a socket to the front of the combine and mount it in a safe location that does not interfere with the operation of the harvesting units or the processes of disconnecting and connecting the harvesting unit to the combine. The electrical system uses a seven-pin connector, with the following pins corresponding to the following lights (Fig. 15): fog light, left parking light, right parking light, brake light, left turn signal, right turn signal, and ground wire.

Fig. 15. 7 PIN plug [42]

Road traffic regulations require full visibility in front of the vehicle when traveling on public roads, especially in low-visibility conditions. To meet these requirements, the guard elements, in addition to the red and white reflective warning markings, feature two combination lamps on the right and left sides. These lamps are divided into two zones: high beam and turn signal, and are connected detachably via a cable and plug to the electrical socket on the base machine.

5. Discussion and conclusions

Journeys on public roads of combine harvesters and forage harvesters are currently often carried out at speeds of 40 km·h^{-1}. To increase the vehicle's safety during such journeys on public roads, manufacturers of these machines introduce various additional elements into their designs.

Among them, we can distinguish transport covers, called transport protection by some manufacturers. Slightly older models are not equipped with this type of protective elements, so the work involved developing and constructing a transport cover for attachment to a combine harvester for row-harvested maize [21, 38–41].

By starting the research, the solutions used by transport guards among manufacturers of self-propelled forage harvesters and attachments for grain maize harvesting were analyzed. The methods for marking non-standard vehicles and the legal regulations to be followed for a vehicle with such a cover to move on public roads were verified [36, 37].

Based on the analyses, a conceptual model of a transport cover dedicated to the grain corn harvesting attachment was developed. To develop a model of the cover structure, a dimensional base in the form of a harvesting unit was required, to which the designed cover would be referenced. The existing Dominoni SL 978 harvesting unit [41] was used as a dimensional basis, and a design model was developed that accounts for the most important dimensions.

The conceptual model was adapted to the design base, taking into account the design assumptions, resulting in a model of a transport cover. To mount the cover to the attachment, a dedicated hooking system has been designed. The next step was to make a structure based on the cover model Transport. For this purpose, the Inventor Professional program was used, with which appropriate elements compliant with Polish standards were selected. The material of components (steel grade) was selected based on simulation analyses. Their results showed the potential to reduce the dimensions of the adopted structural elements. Given the importance of the harvester's harvesting unit cover for the road safety of other road users, it was decided to retain the originally selected elements.

Due to the dimensions of the grain maize harvesting attachment and the designed cover, lighting had to be placed on its structure. For this purpose, a diagram of the electrical installation was created. The last stage was the development of the construction documentation of the transport cover for the grain corn harvesting attachment.

Thus, it must be stated that the adopted goal of the work has been fully achieved. In accordance with the adopted assumptions, a simple, lightweight, and easy-to-use cover for the combine harvester unit was developed, more precisely, an attachment for row-harvesting corn for grain by the combine harvester. The designed design meets the requirements for moving on public roads of the main machine (combine). Thus, it increases the safety of the movement of this type of vehicle with harvesting units attached to the front, folded for transport across crossings. The developed cover is designed to combine harvesters that were not factory-equipped with this element, thereby increasing safety

when driving on public roads. Some models of combine harvesters and forage harvesters of large corporations in the industry have dedicated safety solutions of this type. In these cases, transport covers have been included in the structures already at the design stage of the harvesting unit itself, e.g. folding distributors in Claas Rovio 4, automatic folding/detaching of the cover from the level of the operator's cab (Claas, Krone, Kemper), and a dedicated connector for lights in the Kemper Komfort chassis.

While the design of the corn header's transport guard presented in this paper is an important issue, aimed at ensuring efficient and safe harvesting, there are several significant limitations and potential directions for further research:

– Impact of vibrations during transport: During transport, corn headers can experience intense vibrations, which can degrade the guard's durability. Therefore, it is crucial to assess the impact of vibrations on the guard's design and develop technical solutions to reduce vibrations and ensure the guard's stability during transport.
– Guard durability: Another important aspect is the durability of the header's transport guard. It is necessary to test the materials' resistance to weather conditions, mechanical damage, and the intense loads associated with field work. Possible directions for further research include the use of modern composite materials and structural reinforcement techniques to increase the guard's durability.
– Compatibility with headers of different working widths: Depending on the model and manufacturer of the corn harvesting machine, the headers' working widths may vary. Therefore, it is important to develop a cover design that is universal and compatible with various header widths. Research directions may include developing systems to adjust the cover width and testing their compatibility with various header types.
– Issues related to ergonomic aspects and examining the time required for assembly and disassembly, which are essential for practical usability.

Therefore, further research on the design of the corn header transport cover should focus on reducing vibration-related impacts, increasing durability, and ensuring universality and compatibility across various header widths. The potential for further research in this area is significant, and always aims to improve efficiency and safety. Therefore, these will be the subject of further research by the authors of this study.

Bibliography

[1] Afify MK, Nada AA, Mechail WM. Selection the proper system of planting and harvesting for rice crop. Misr J Ag Eng. 2000;17(2):388-400.

[2] Andrych-Zalewska M, Chłopek Z, Merkisz J, Pielecha J. Exhaust emission from a vehicle engine operating in dynamic states and conditions corresponding to real driving. Combustion Engines. 2019;178(3):99-105. https://doi.org/10.19206/CE-2019-317

[3] Andrych-Zalewska M, Chłopek Z, Merkisz J, Pielecha J. Research on exhaust emissions in dynamic operating states of a combustion engine in a Real Driving Emissions test. Energies. 2021;14(18):5684. https://doi.org/10.3390/en1418

[4] Arnaout MA, Abdel-Wahab MK, El-Sharabasy MM. Selecting the proper system for mechanizing grain crops harvesting in thesmall holdings. Misr J Ag Eng. 1998;15(1):133-144.

[5] Białczyk W, Cudzik A, Czarnecki J. Ciągniki i pojazdy rolnicze (in Polish). Oficyna Wydawnicza Atut – Wrocławskie Towarzystwo Oświatowe. Wrocław 2012.

[6] Cempel C. Teoria i inżynieria systemów (in Polish). Wydawnictwo Instytutu Technologii Eksploatacji. Radom 2006.

[7] Chinsuwa W, Chuan-Udom S, Phayom W. Rice harvest losses assessment. TSAE Journal. 2002;9(1):14-19.

[8] Chinsuwa W, Pongjan N, Chuan-Udom S, Phayom W. Effects of threshing bar inclination and clearance between concave rods on performance of axial flow rice thresher. TSAE Journal. 2003;10(1):25-30.

[9] Członka J. Transport cover design for grain corn harvesting attachment. Engineering work carried out under the supervision of F. Adamczyk at the Department of Biosystems Engineering at the Poznan University of Life Sciences, Poznan 2025.

[10] Dietrich M, Kocańda S, Korytkowski B, Ozimowski W, Stupnicki J, Szopa T. Podstawy konstrukcji maszyn (in Polish). WNT. Warsaw 1995.

[11] Dreszer K, Pawłowski T, Szczepaniak J, Szymanek M, Tanaś W. Maszyny rolnicze (in Polish). Wydawnictwo PIMR. Poznań 2015.

[12] Ghonimy MI, Rostom MN. Tech-economical approach tocombine harvesters evaluation. Misr J Ag Eng. 2002;19(1):83-99.

[13] Hossain M, Hoque M, Wohab M, Miah, MM, Hassan M. Technical and economic performance of combine harvester in farmers field. Bangladesh Journal of Agricultural Research. 2015;40:291-304.

[14] Jaros M, Pabis S. Inżynieria systemów (in Polish). Wydawnictwo SGGW. Warsaw 2007.

[15] Kamaruzaman J, Roy SK, Ismail WIW, Ahmad D. Performance evaluation of a combine harvester in malaysian paddy field. Institute of Bioscience, Faculty of Engineering, Universiti Putra, Malaysia 2001.

[16] Kuboń M. Possession and utilization of transport facili-ties in farms engaged in various agricultural production types. Inżynieria Rolnicza. 2007;8(96):141-148.

[17] Łubiński M, Filipowicz A, Żółtowski W. Konstrukcje metalowe. Cz. 1. Podstawy projektowania (in Polish). Wydawnictwo „Arkady". Warsaw 2000.

[18] Mahrouf ARM, Rafeek MIM. Mechanization of paddy harvesting: an economic perspective. Socio Economic and planning center. Peradeniya. Sri Lanka 2010.

[19] Merkisz J, Pielecha J, Jasiński R. Analiza parametrów operacyjnych silnika i emisji spalin ciągnika rolniczego podczas pracy na hamowni (in Polish). WUT J Trans. Eng. 2017;115:145-159.
[20] Merkisz J. Tendencje rozwojowe silników spalinowych maszyn i agregatów rolniczych (in Polish). Technika Rolna Ogrodnicza Leśna.2010;2:4-9.
[21] Mieszkalski L. Metodyka projektowania narzędzi i maszyn rolniczych w zarysie (in Polish). Wydawnictwo ART. Olsztyn 1995.
[22] Mirzazade A, Shamsollah A, Asghar M. Intelligent modeling of material separation and combine harvester's thresher by ANN. Intl J Agri Crop Sci. 2012; 4(23):1767-1777.
[23] Miu P. Combine harvesters theory, modeling, and design. CRC Press Taylor & Francis Group. New York 2016.
[24] Omran MS. A comparative study of the most widely harvesting system for wheat crop in Egiypt. Misr J Ag Eng. 2007;25(3):804-823.
[25] Owsiak Z, Lejman K. Maszyny rolnicze (in Polish). Wydawnictwo ATUT. Wrocław 2012.
[26] Pishgar-Komleh SH, Keyhani A, Sarkari MRM, Jafari A. Assessment and determination of seed corn combine harvesting losses and energy consumption. Elixir Agriculture. 2013;54:12631-12637.
[27] Rabotnov YN, Leckie FA, Prager W. Creep problems in structural members. J Appl Mech. 1970;37(1). https://doi.org/10.1115/1.3408479
[28] Sikora M, Orliński P. Hydrotreated vegetable oil fuel within the Fit for 55 package. Combustion Engines. 2024;197(2):3-8. https://doi.org/10.19206/CE-174554
[29] Skrobacki A, Ekielski A. Pojazdy i ciągniki rolnicze (in Polish). Wydawnictwo „Wieś Jutra". Warsaw 2012.
[30] Špokas L, Adamčuk V, Bulgakov V. Nozdrovický L. Te experimental research of combine harvesters. Res Agr Eng. 2016;62:106-112.
[31] Špokas L, Steponavičius D, Wacker P. Besonderheiten der Dinkelernte und des Ausdruschprozesses bei Dinkel. Tagungsband VDI–MEG–Kolloquium Landtechnik. Mähdrescher H. 2005;38:95-102.
[32] Špokas L. Infuence of technological parameters of combine harvester "NEW HOLLAND" to grain macro damage. IAg Eng LUA&LU of Ag. 2006;38:27-41.
[33] Stępień Z. Ammonia as an alternative fuel to internal combustion engines. Combustion Engines. 2025; 200(1):117-127. https://doi.org/10.19206/CE-200289
[34] Ye Y, Liu X, Lin J, Chang J, Chen Y. Design of hydrostatic drive system for corn combine harwester, Agricultural Machinery Usage & Maintenance, 2016; 7:13-14.
[35] PN-EN 10219-2:2019-07. Cold Welded Seam Sections from Structural Steels – Part 2: Tolerances, Dimensions and Static Quantities.
[36] Regulation of the Minister of Infrastructure of 31 December 2002 on the technical conditions of vehicles and the scope of their necessary equipment (Journal of Laws 2024.502 par.45 sec. 3 point 1).
[37] Road Traffic Law (Journal of Laws 2024.1251 art. 64b), (Journal of Laws of 1997 No. 98 item 602 Appendix 1).
[38] www.claas.com.pl (Claas company website).
[39] www.krone-agriculture.com (Krone company website).
[40] www.kemper-stadtlohn.de (Kemper company website).
[41] www.dominoni.com (Dominoni company website).
[42] www.agrorami.pl

Przemysław Niewiadomski, DSc, DEng., Prof. UPP – Faculty of Environmental Engineering and Mechanical Engineering, Poznan University of Life Sciences, Poland.
e-mail: *przemyslaw.niewiadomski@up.poznan.pl*

Florian Adamczyk, DSc., DEng., Prof. UPP – Faculty of Environmental Engineering and Mechanical Engineering, Poznan University of Life Sciences, Poland.
e-mail: *florian.adamczyk@up.poznan.pl*

Jakub Członka, Eng. – Faculty of Environmental Engineering and Mechanical Engineering, Poznan University of Life Sciences, Poland.
e-mail: *86330@student.up.poznan.pl*

Article citation info:
Palkus K. Numerical analysis of front deflector at outer air seal of low pressure turbine. Combustion Engines. 2026;206(3):121-129. https://doi.org/10.19206/CE-217829

Kacper PALKUS

Combustion Engines
Polish Scientific Society of Combustion Engines

Numerical analysis of the front deflector at the outer air seal of low-pressure turbine

ARTICLE INFO

Received: 15 November 2025
Revised: 28 January 2026
Accepted: 5 February 2026
Available online: 12 February 2026

A new design solution – the front deflector – intended to improve the performance of the outer air seals of the low-pressure turbine is analyzed in this paper using steady Reynolds-Averaged Navier-Stokes (RANS) simulations of a three-stage, state-of-the-art LPT model, including inner and outer cavities. The regions near the casing in the LPT still show potential for improvement, mainly due to flow interactions associated with the outer air seals. One recent concept for improving these areas is the front deflector. The solution is to modify the front part of the cavity. Its operating principle is to introduce an additional labyrinth for the leakage while simultaneously minimizing the front cavity volume. In the paper, several scenarios for implementing this feature are analyzed, including reducing the front-cavity volume without a static fin and adding a static fin to create an auxiliary labyrinth. Furthermore, the effects on the flow and the potential improvements in LPT efficiency associated with the solution are discussed. The former reduces front-cavity recirculation and its interaction with the mainstream; the latter reduces seal leakage when the fin length is sufficient. Across three stages, the predicted changes in LPT isentropic efficiency are on the order of 0.03–0.06%, depending on the scenario.

Key words: *front deflector, outer air seal, low-pressure turbine, efficiency, new design, CFD*

This is an open access article under the CC BY license (http://creativecommons.org/licenses/by/4.0/)

1. Introduction

There is considerable interest in improving the turbomachine sealing system because it directly affects the performance of the entire engine. Enhancement in performance can be achieved by either boosting or altering the thermodynamic cycle or increasing the efficiencies of particular components [4].

Efficient operation of the low-pressure turbine is of high importance at the component level. activities aimed at improving the efficiency of this module are meaningful for the environment, airlines, and engine producers.

On the other hand, modern CFD-assisted designs of turbomachinery are already considerably loaded and optimized. The application of high-tech solutions, such as low-loss airfoils via controlled laminar-turbulent boundary-layer transition, ultra-thin trailing edges, optimized work distribution, endwall contouring, and other technologies, has enabled the edges of maximal efficiency in today's low-pressure turbine (LPT).

As a result, the overall isentropic efficiency of the best designs is already very high for the currently optimized designs, and gains of the order of 0.1% in isentropic efficiency are difficult to achieve; however, they are still highly required [19].

Nonetheless, there are a few areas requiring further development. The potential still exists in regions at the sides of the main gas path [19], where inner and outer air seals can be differentiated. Sealing systems in low-pressure turbines are indispensable because they ensure proper engine operation. Nevertheless, as reported by different researchers, they inevitably decrease efficiency by as much as a few percentage points [9, 22].

In this paper, the main focus is on the outer air seals (OAS) of LPT. A representative state-of-the-art outer air seal is shown in Fig. 1. It comprises a labyrinth seal created between the blade fins and an abradable structure e.g. honeycomb. Labyrinth seals are effective and reliable. They are already very well-grounded solutions, robust and proven – perfect for aircraft engines as highlighted in [17]. This type of sealing can withstand high demands and harsh conditions in outer cavities.

As indicated by Hendricks et al. [10], sealing requirements vary significantly between shroud regions at blade tips and near the shaft for sealing of platform and cavity interfaces. IAS are located near the disk regions, OAS in the vicinity of the casing. As a result, the outer seals operate at twice the radius of the inner cavities at very high circumferential speeds. Typically, the outer air seals configurations consist of two or, at most, three fins. It is because additional mass at such a radius is unfavorable for the durability of the rotating blade. Between the two locations, there are also meaningful differences in pressure gradients, thermal and structural requirements. Another challenge posed by materials capabilities – not only due to the temperature level but also with respect to contact at the interface between rotating and nonrotating parts, as pointed out by Chupp et al. [3]. Furthermore, there are significant relative radial and axial movements of the parts. As a result, it is extremely difficult to maintain relatively small clearances between rotating and nonrotating parts in these regions. Another notable distinction between the inner and outer sealing regions is the amount of cooling flow. OAS experiences much less purging and, as a result, operates at higher temperatures, which is limiting for many solutions.

Despite the ongoing need for enhancements to the sealing system, various solutions cannot be implemented for OAS due to the range of abovementioned multidisciplinary limitations. For instance, a promising advance in sealing is brush seals, which can be configured in different ways [2, 3, 12]. The sealing performance of brush seals is superior to that of conventional labyrinth seals. At a certain clearance, they can reduce leakage by up to 80% compared to the straight labyrinth [3]. While brush seals are suitable for compressors and some turbine internal locations, they are

not applicable to OAS for several reasons, including substantial variations in clearances, reliability at high temperatures, and deterioration and oxidation of wires [3, 6].

Different researchers have applied modifications to the OAS cavities to improve inflow to the mainstream and reduce leakage. In a typical arrangement, fins point upwards from the blade shroud. Mahle and Schmierer [16] proposed applying an inverse fin configuration, typical of steam turbines, to an aircraft LPT. Klingels [14] proposes a combined configuration of conventional and inverse fin designs. Besides two conventional fins at the LPT blade shroud, in the rear part of the cavity, his design includes another static fin that points down. Features in the rear part of OAS are also researched by Rosic et al. [23]. The authors investigate three different concepts: shaping of the rear part of the exit cavity, an axial deflector, and a radial deflector in several geometrical variations. Most designs demonstrate the positive impact of the devices in the rear cavity. Nevertheless, the application of such devices to OAS of LPT is problematic due to the considerable axial rotor movement, which limits most such solutions. A recent idea by Nishii and Hamabe [18] proposes a secondary-flow suppression structure in the rear part of a cavity. It is an additional radial opening of the rear cavity. In this way, the leakage flow is expected to decrease slightly. In this configuration, the blade's movements are not restricted. Fanelli et al. [5] propose another solution, suggesting the incorporation of small airfoil-shaped structures in specific locations along the blade shroud. A good example of a well-performing advance with respect to outer seals is the application of a separate active clearance control system to the low-pressure turbine. It has become state-of-the-art for today's turbines. It provides an increase in LPT performance on the same basis as for high-pressure turbines, by maintaining radial clearances at a consistently low level throughout the mission.

Sealing systems for turbomachinery are constantly evolving, with ongoing development of available solutions and recent advances. However, due to various limitations in novel low-pressure turbines, many of these concepts are not applicable.

The objective of this paper is to analyze the front deflector (FD) as a new concept for outer air seals. The developed solution is intended to be simple and straightforward for implementation. The research primarily focuses on the aerodynamic operation and key sensitivities of the solution, providing directions for its further development. Furthermore, the research contributes to a deeper understanding of OAS operations, particularly in relation to the effects associated with the proposed designs. Front deflector concept and its initial multidisciplinary evaluation.

1.1. Baseline case – state-of-the-art LPT OAS

The solution discussed in this paper is intended for improving LPT operation in the area of outer air seals. Figure 1 presents a typical OAS design for LPT, which is chosen as the baseline. It is a labyrinth seal with two fins and an abradable honeycomb structure.

The functional principle of this sealing system is based on creating a labyrinth of fins and a honeycomb, effectively reducing the leakage mass flow rate over the blade and, consequently, overall losses and increasing machine performance. The leakage goes through the fins and further inflows into the mainstream before the subsequent vane.

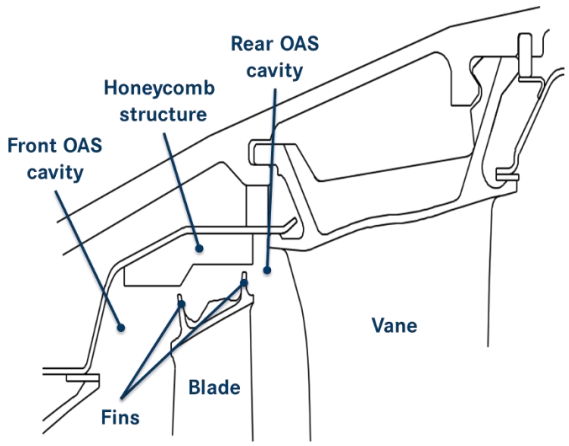

Fig. 1. Schematic representation of a state-of-the-art Outer Air Seal of LPT EP3324002B1 [14]

It is important to note that the blade moves relative to the non-rotating parts during the mission of an engine, due to thermal and structural displacements. Thus, it is not possible to design anything in the area of the blade movements. Interaction between the blade and the honeycomb is allowed. In regular operation, the fins rub into the honeycomb. In addition, it should be noted that the LPT may be equipped with the ACC system, providing tight running clearances over the mission.

The discussed design is a well-established configuration of the outer air seal, proven to be robust and reliable throughout the LPT's life cycle.

1.2. New solution - Front Deflector

The concept developed to improve the OAS is the front deflector. It is schematically pictured in Fig. 2, which follows patent application [20], confirming the novelty of the solution. It is a modification of the front part of the OAS cavity. The underlying principle of the concept is to introduce an additional labyrinth to reduce leakage and to minimize the front volume.

The labyrinth is intended to reduce leakage through the seal. By decreasing the cavity volume, the gas path contour approaches the ideal flow path, reducing interactions between the large vortices in the OAS cavity and the mainstream. It is expected that the solution will further improve performance in off-design operation when the blade moves close to the deflector. Additionally, the front fin of the blade can be inclined towards the static fin to improve the overlapping labyrinth.

The assessment indicates that it is a relatively simple solution that enhances the front part of OAS.

The length of the static fin depends on the blade's keep-out zones, which vary by machine. There are various ways to realize the front deflector concept; however, the aerodynamic benefits of the front deflector depend on the primary geometrical features that influence the cavity volume.

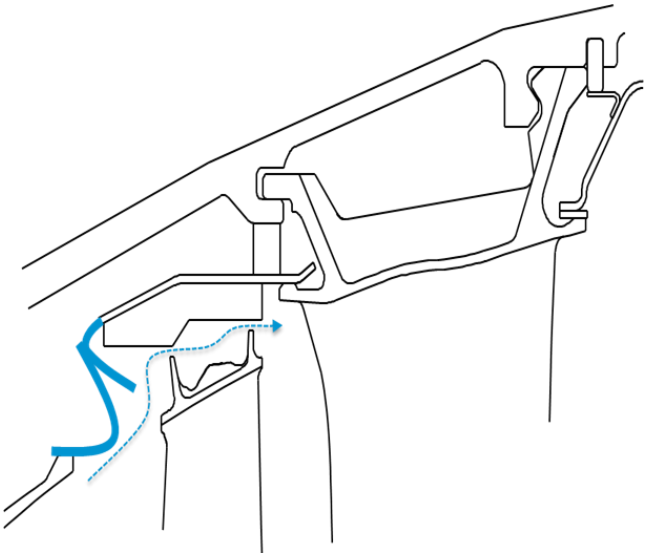

Fig. 2. Schematic representation of the front deflector concept. Reference patent EP19209602A1 [20]

The deflector is expected to provide aerodynamic advantages at the LPT design point and during off-design operation, as the blade moves closer to the deflector due to the rotor's axial movement relative to the casing. In these operating conditions, the feature will provide additional sealing improvement.

2. Numerical CFD modeling

2.1. Geometry and mesh

To evaluate the aerodynamic benefits of the Front Deflector, the feature is designed for all stages of the researched LPT. It is analyzed in several configurations, using CFD to assess the aerodynamic efficiency benefit. The CFD model of the turbine reflects an aerodynamic 3-stage rig of a modern LPT. Figure 3 provides a visual representation of the machine.

Accurately reflected geometry is of primary importance for numerical prediction. Therefore, airfoils, including all meaningful details, are thoroughly modeled. In addition, the model incorporates cavities at the inner and outer endwalls. As demonstrated by Gier et al. 0, the inclusion of cavities is of significant importance for the reliable prediction of the LPT flow field and its characteristics, particularly for efficiency. Similar conclusions were drawn by Giboni et al. [8] and Henke et al. [11].

The machine-discretization approach corresponds to the procedure used by Mahle [15]. It assumes separate meshing of the mainstream and the cavities, which enables high-quality grids. Structured, hexahedral meshes are generated for both the main gas path and the cavities. The complete mesh consists of around 24 million cells, including 6 million representing cavities. The grids are refined at walls and in regions of high gradients, e.g., at the fins of the labyrinth seals. The averaged dimensionless wall distance y+ is around 1 at the airfoils and at the endwalls in the mainstream. This contributes to the proper resolution of boundary layers. Resolution at the cavity walls is intentionally coarser. It is also considered that resolving the boundary layers in the cavities would significantly increase the model size. Thus, Wall Functions are applied in these regions. The justification of this approach for outer air seals is broadly described in [19].

The quality of the meshes is considered very good and meets best practices for the applied CFD solver. Exemplary grids for a cavity are shown in Fig. 5.

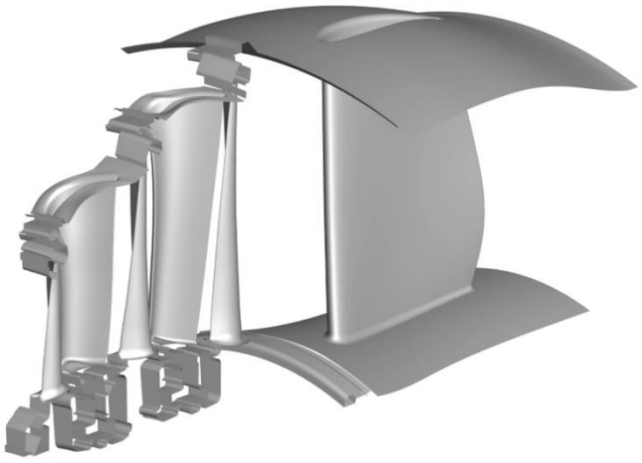

Fig. 3. CFD model of the analyzed LPT

2.2. CFD setup

For the efficiency assessment, numerical steady-state Reynolds-Averaged Navier-Stokes simulations were conducted. Wein et al. [25, 26] performed high-quality measurements of a straight outer air seal and compared them with RANS and Large Eddy Simulations. They demonstrate the potential application of properly configured RANS for OAS analyses. Their findings indicate that, despite local deviations in flow behavior, RANS delivers robust and valid predictions of the primary flow features that drive phenomena in the outer cavities. RANS also remains the industrial standard and is deemed sufficient for many turbine research as pointed by Vanhaelst et al. [24].

For the analyses, the TRACE solver, specialized for turbomachinery applications, has been employed. It is a density-based code, developed by the German Aerospace Center (DLR) and MTU Aero Engines. TRACE uses a predictor-corrector solution strategy. It allows fully implicit discretization of the equations at a given time step. Higher resolution spatial discretization schemes are used. For TRACE, it is the second-order accurate Fromm scheme [7], together with a special van Albada limiter [1] to stabilize the solving process. For time integration, implicit procedures are used until a steady state is reached.

The two-equation Wilcox k-ω model [27] is used for turbulence modeling. As verified by Gier et al. [9] and Henke et al. [11], it provides reliable prediction with respect to low-pressure turbines, including cavities, for a range of Reynolds numbers typical for aircraft engines. The setup also includes other extensions; in particular, the turbulence model is corrected by the Kato-Launder [13] formulation to account for turbulent kinetic energy production at stagnation points.

2.3. Boundary conditions

The low-pressure turbine under investigation is simulated at its design point. At the inlet of the CFD model of the turbine, boundary conditions measured in the test rig are specified. This includes radial distributions of total pressure, total temperature, turbulence quantities, and velocity angles. At the outlet, static pressure is set, assuming radial equilibrium. Both the inlet and the outlet are non-reflecting. The boundary conditions imposed at the walls are shown in Fig. 4. All walls are assumed to be adiabatic.

In steady simulations, the rows in the mainstream are connected via mixing planes, following the typical approach used in turbomachinery simulations. This way enables the connection of vanes and blades with different speeds and pitches defined in the flow domains.

Also, in the cavities and at necessary locations, mixing planes between stationary and rotating domains are specified. Additionally, special interfaces, described by Yang [28], are used to connect the cavities and the mainstream. The approach is illustrated in Fig. 4. The interfaces facilitate the transfer of numerical information between the two sides, modeling inflow or outflow. To ensure proper connection between the two, the grids at the interfaces are adjusted to provide a similar resolution on both sides.

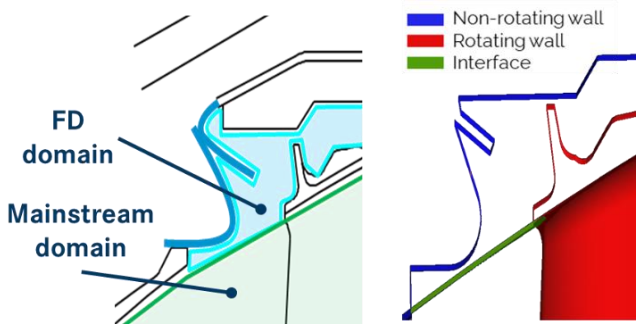

Fig. 4. CFD modeling of the front deflector

2.4. Convergence behavior

The simulations are considered converged after revising several conditions. Parameters of the machine, such as mass flow, pressure ratio, and efficiency, are monitored for the entire system and for individual rows at specified intervals. Additionally, the behavior of averaged flow quantities at interfaces is monitored to ensure solution stability. The global and maximal residuals are also monitored. For all simulations in this article, the global RMS residuals are fairly below $1 \cdot 10^{-5}$. The simulations are stopped manually once a prolonged steady state is reached, provided that the above criteria are met. For all researched cases, the efficiency fluctuations were an order of magnitude smaller than reported changes.

2.5. Introduction of the front deflector to the baseline CFD model

As previously mentioned, the modification reflecting the front deflector is applied to the outer air seals for all stages of the reference LPT. Figure 5 indicates the crucial geometrical parameters of the front deflector. Those are the protrusions of the deflector covering the front cavity volume and the length of the static fin. In the researched configurations at different stages those parameters vary $a_x = 0.4 - 0.5\ b_x$ and $L = 0.7 - 1.2\ H$.

The modeling approach is depicted in Fig. 4. The fluid control domain of the cavity, including the surrounding area of the feature, is modeled and appended to the main gas path with interfaces. The setup applied to the modified cases corresponds to that used in the reference turbine.

Figure 5 also presents meshes for different configurations of the front deflector. The cases represent: baseline outer air seal; cavity with reduced front volume without a static fin; and front deflector with a static fin.

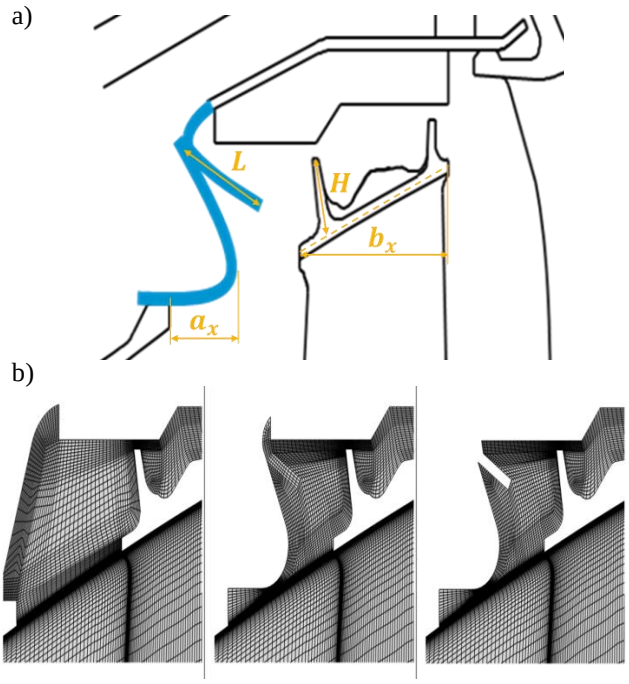

Fig. 5. Primary geometrical parameters of front deflector (a), comparison of the meshes for different configurations. From the left: reference cavity, front deflector without static fin and front deflector with static fin

The changes to the mesh are kept to a minimum level – only the front part of the cavity is modified. In particular, the number of cells at the interface is the same for all configurations. The region near the fin of the blade is already unchanged. A small refinement is necessary in the vicinity of the additional static fin, which is deemed acceptable. Mesh criteria for the modifications are also considered acceptable.

The validity of the applied CFD models is comprehensively discussed in [19]. The findings confirm high accuracy of the prediction for the outer air seals using the employed numerical method. It is concluded that modifications to the OAS, which affect the mainstream flow, can be quantified in terms of changes in turbine efficiency. The overall LPT isentropic efficiency is calculated between LPT inlet and outlet as:

$$\eta_{LPT} = \frac{h_{t,out} - h_{t,in}}{h_{t,out,is} - h_{t,in}} \quad (1)$$

3. Results and discussion

3.1. Evaluation of the performance of the front deflector without the static fin

At first, the aerodynamic performance and benefits resulting from reducing the front OAS cavity with the front deflector without a static fin are assessed. Two configurations, as shown in Fig. 6, are analyzed and compared to the baseline case.

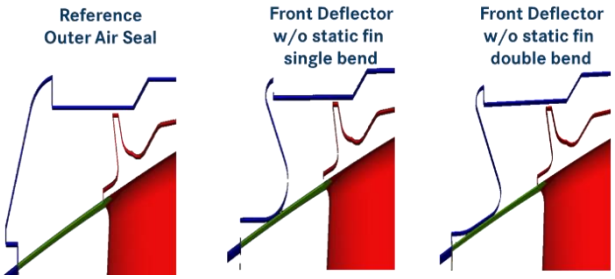

Fig. 6. Investigated cases of front cavity reduction with front deflector without static fin

The first modification represents the feature geometry with a single bend, while the second uses a double bend. The solution with two bends allows for reducing the step and achieving a very close reproduction of the ideal flow path. In this way, it is assumed that step losses can be further reduced. According to Gier et al. [9], the significance of step losses increases for smaller leakages through the seal, which is often the case in today's turbines due to advanced systems for running clearance reduction. Thus, looking for fractions of efficiency, it is also worth checking this direction for improvements.

Detailed CFD simulations of all cases, presented in Fig. 7, indicate that both solutions are beneficial but perform nearly equally.

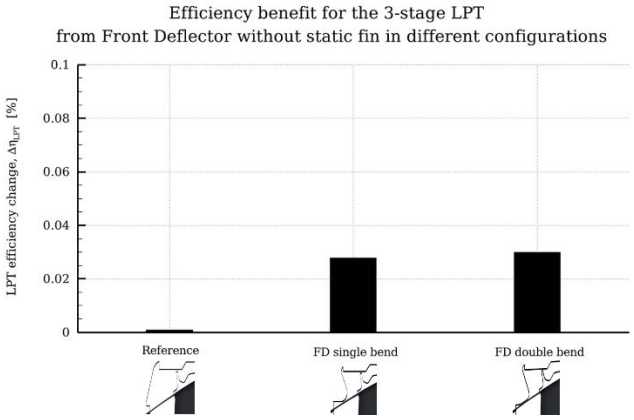

Fig. 7. LPT efficiency benefits from front cavity reduction with front deflector without the static fin

The overall benefit is considered comparable between the two configurations. This indicates that such a small additional step in the flow path, which adds an additional perturbation to the fluid, has a relatively small impact on the overall improvement. Figures 8 and 9 present the flow field of the investigated cases.

As evident from these figures, the large vortices in the front cavity are considerably reduced when the cavity volume is decreased. The primary benefit is indeed the reduction in interactions.

As shown in Fig. 8, the front cavity recirculation zones interact with the mainstream, generating shear losses due to the difference in circumferential velocity between the two flows.

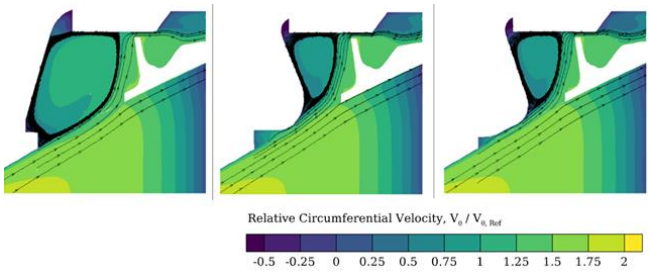

Fig. 8. Relative circumferential velocity and streamlines for investigated cases of front deflector without static fin in different configurations

Moreover, the figure reveals that, in addition to contributing to the reduction of the vortex, the FD simultaneously reduces the circumferential velocity in the front part of the cavity, which is closer to the mainstream velocity. Consequently, the mixing losses are smaller, as also indicated by Fig. 9.

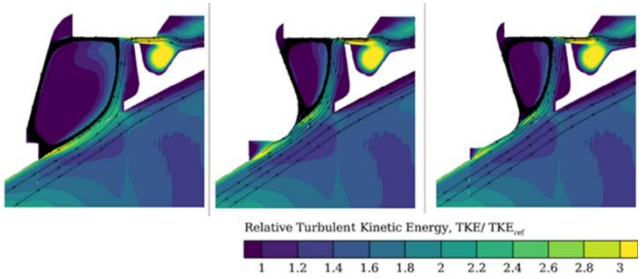

Fig. 9. Relative turbulent kinetic energy and streamlines for investigated cases of front deflector without static fin in different configurations

Table 1. Comparison of the characteristic numbers for OAS with front deflector without static fin for different configurations for one stage

	Reference	FD single bend	FD double bend
Axial Reynolds number, Re_{ax}	1760	1760	1760
Outlet Swirl ratio, K_{out}	0.68	0.66	0.66
Windage heating, σ	0.19	0.19	0.19

As shown in Fig. 8 and Fig. 9, the primary leakage path is not affected by the presence of the front deflector without the static fin. This observation is further supported by the dimensionless numbers for OAS [21], provided for one seal across different FD variants in Table 1. These quantities

are: axial Reynolds number, swirl ratio and windage heating according to the equations below:

$$\mathrm{Re}_{ax} = \frac{\dot{m}}{2\pi R\mu} \tag{2}$$

$$K = \frac{V_\theta}{NR} \tag{3}$$

$$\sigma = \frac{2c_p(T_{t,out} - T_{t,in})}{U^2} \tag{4}$$

For all variants, the characteristic numbers are nearly the same. It indicates that the seal's general operation remains unchanged across the investigated designs of the concept without a static fin. In particular, the axial Reynolds number [21], which provides insights into leakage behavior, is comparable. Thus, it is concluded that reducing the front cavity volume does not affect leakage through the seal, suggesting it is not the reason for the observed benefit in the cases without the static fin.

Reducing the front cavity volume with the front deflector (without the static fin) consistently weakens the large vortices in the front cavity and lowers their interaction with the mainstream, leading to a small but repeatable LPT efficiency benefit around 0.03% for the solution implemented in all stages. Leakage behavior remains unchanged, indicating that the improvement results solely from reduced cavity–mainstream interaction rather than from any modification of the seal leakage.

3.2. Evaluation of the performance of the front deflector with the static fin

The static fin creates an additional labyrinth for leakage and, in this way, reduces it. To assess the sensitivity of the FD concept to the length of the fin, two cases are considered: a short fin and a long fin. These variants are compared with the reference OAS design and with the case without a static fin. The investigated configurations are presented in Fig. 10.

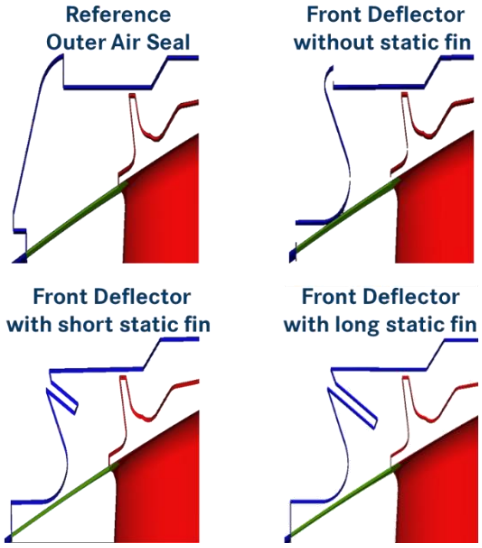

Fig. 10. Investigated design cases of the front deflector with a static fin

Analyzing the flow field shown in Fig. 11, it is apparent that the vortex present in the front cavity is further reduced with the application of the static fin. Nevertheless, revising the benefit in LPT efficiency presented in Fig. 13, it is evident that the short static fin does not provide any further improvement compared to the front deflector without the static fin. It can be concluded that a decrease in the vortices in the front cavity has a meaningful impact only if it reduces their interaction with the mainstream.

This is reflected in Fig. 11, which compares the two cases by the relative TKE level and the lack of influence on the streamlines due to the leakage. Thus, the short fin does not function as intended, as its primary purpose is to create an additional labyrinth to reduce leakage. It is additionally confirmed in Table 2 by comparing the axial Reynolds number [21].

It points to a conclusion that the length of the fin is crucial for the overall benefit from the solution. It is evident that as the clearance between the blade and the static fin decreases, the leakage encounters more blockage, resulting in its reduction. Nevertheless, it is important to ensure the blade does not come into contact with the fin to avoid damage. Taking this into account, further investigation of the case with the longer fin is conducted.

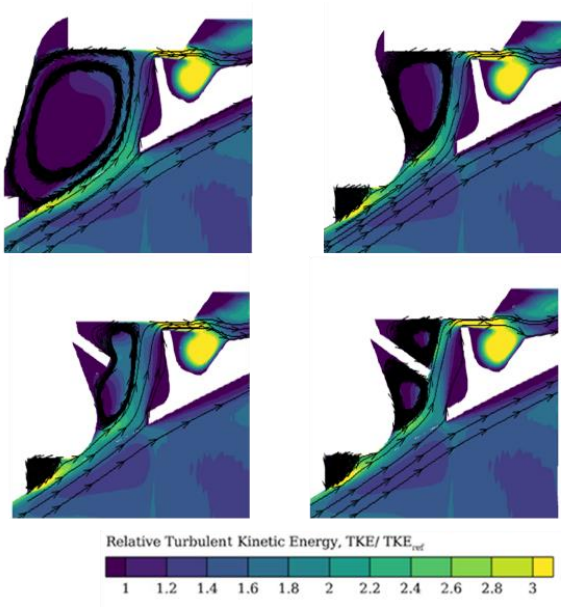

Fig. 11. Relative turbulent kinetic energy and streamlines for investigated cases of front deflector with static fin in different configurations

As noticeable in Table 2, the analyses show that the front deflector with the longer static fin reduces the axial Reynolds number [21] of the investigated OAS. The figure shows that the longer fin reduces leakage by around 6% compared to the reference case. This reflects positively on the efficiency gain, as depicted in Fig. 13.

Moreover, Table 2 shows that applying the front deflector does not visibly affect the outlet swirl ratio or windage heating [21]. Only in the configuration with the long static fin is a small change in the outlet swirl observed. Thus, it is concluded that in the rear part of the cavity and behind it, the mixing as well as internal losses are not noticeably changed with the application of the front deflector. This is also confirmed by revising plots in Fig. 11, because already

in the vicinity of the first fin, there are no significant differences between the configurations.

Table 2. Comparison of characteristic numbers for OAS with a front deflector and with static fin for different configurations

	Reference	FD without static fin	FD with short static fin	FD with long static fin
Axial Reynolds number, Re_{ax}	1760	1760	1750	1650
Outlet swirl ratio, K_{out}	0.68	0.66	0.65	0.64
Windage heating, σ	0.19	0.19	0.19	0.19

Further insight into the flow above the first fin is shown in Fig. 12 below. It provides profiles of relative velocity above the first fin of the seal. This comparison clearly shows that the front deflector concept has no significant influence on the velocity. Upon analysis, only a small decrease of up to 6% can be observed. This decrease is visible for both axial and circumferential components.

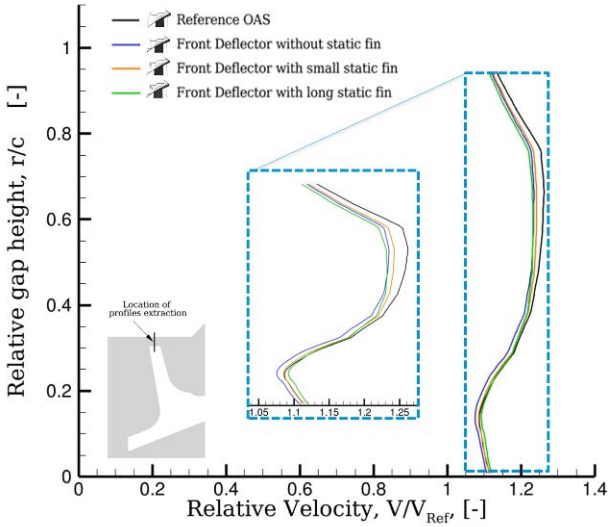

Fig. 12. Profile of relative velocity above the first fin of the outer air seal for different configurations of the front deflector

Based on Fig. 13, the overall efficiency potential of the front deflector concept is estimated to lie between 0.03% and 0.06%, depending on the length of the static fin. As pointed out earlier, the configuration with the short static fin is close to the variant without a static fin. Thus, for turbines where the length of the fin is significantly limited due to keep-out zones of the blade, it is applicable to omit the static fin. Additionally, it is anticipated that the concept can yield further benefits when combined with inclined fins to enhance the efficiency gains.

The addition of a static fin improves performance only when the fin is long enough to act as an effective additional labyrinth. While the short fin does not reduce leakage, the long fin reduces OAS leakage and yields a higher LPT efficiency gain of up to 0.06% for the solution implemented across all stages. Other flow characteristics remain largely unchanged, highlighting fin length as the key parameter influencing the benefit.

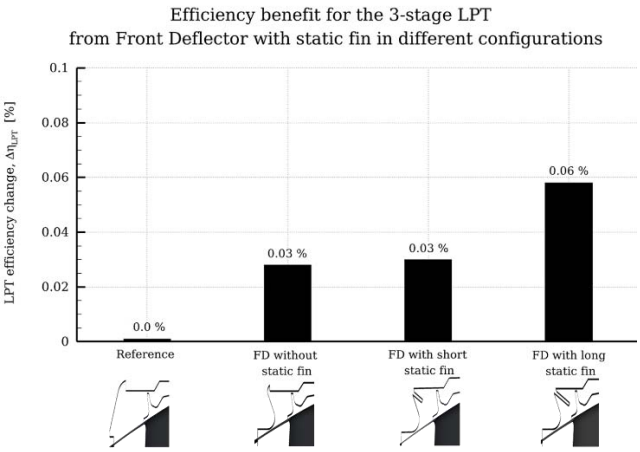

Fig. 13. LPT efficiency benefit from front deflector in different configurations

4. Future work

Analyses of cases with the longer fin indicate the feature could have potential in off-design operation when the blade moves forward. Verifying this requires future work.

Furthermore, successful implementation in an engine requires a detailed assessment of durability, mechanical robustness, and manufacturability of the proposed geometry.

Experimental validation of the specific designs also remains outstanding and is essential to confirm the numerical findings presented herein.

5. Conclusions

This work investigated a new front deflector concept for outer air seals in a low-pressure turbine, aiming to improve near-casing aerodynamic performance at minimal integration cost, while simultaneously providing a small overall efficiency benefit.

The assessment was carried out on a three-stage, state-of-the-art LPT configuration with detailed inner and outer cavities using steady RANS simulations.

The concept has been investigated in two main configurations – with and without the static fin. The feature improves OAS performance in two ways. Firstly, it reduces interactions between the mainstream and the front cavities for all investigated configurations.

Secondly, it provides an additional labyrinth for the leakage reduction in the configuration with the long static fin.

The efficiency gain in the case without the static fin results from reduced interactions in the front cavity. The reduction in the front cavity volume does not influence the leakage through the seal, yielding a small but repeatable efficiency benefit.

It is observed that the inclusion of a static fin reduces leakage only if it is long enough, and this depends strongly on the turbine's design.

The overall improvement in LPT efficiency from the front deflector implemented across all three stages is between 0.03% and 0.06%, depending on the application. The

final benefit must be weighed against implementation costs to justify its adoption in engines.

Acknowledgements

The author would like to express sincere gratitude to MTU Aero Engines for the permission to publish the research.

Nomenclature

a_x	[m]	axial protruding of FD
b_x	[m]	axial shroud length
c	[m]	radial clearance
c_p	[J/(kg·K)]	specific heat capacity
h	[J/kg]	specific enthalpy
H	[m]	first fin height
L	[m]	FD static fin length
$\dot{m}$	[kg/s]	mass flow rate
K	[–]	swirl ratio
N	[rpm]	rotational speed
R	[m]	average radius of fins
Re_{ax}	[–]	axial Reynolds number
Ref		any reference quantity
T	[K]	temperature
$U = \frac{\pi N}{30} R$	[m/s]	rotor fins circumferential velocity
V_x	[m/s]	axial velocity component
V_r	[m/s]	radial velocity component
V_θ	[m/s]	circumferential velocity component
η	[–]	isentropic efficiency
μ	[Pa·s]	dynamic viscosity
σ	[–]	windage heating
Δ		change in any quantity
FD		front deflector
IAS/OAS		inner / outer air seal
LPT		low pressure turbine
TKE		turbulent kinetic energy

Bibliography

[1] Albada van GD, Leer van B, Roberts W. A comparative study of computational methods in cosmic gas dynamics. Astron Astrophys. 1982;108(1):76-84. https://ui.adsabs.harvard.edu/abs/1982A%26A...108...76V/abstract

[2] Brush seals: World-class sealing technology. MTU Aero Engines. 2014. Report No. EN10/20/MUC/00500/AD/RI/D.

[3] Chupp RE, Hendricks RC, Lattime SB, Steinetz BM. Sealing in turbomachinery. NASA, Glenn Research Center, Cleveland, USA, NASA Technical Memo. NASA/TM-2006-214341. 2006.

[4] Dewanji D, Rao AG, van Buijtenen JP. Conceptual study of future aero-engine concepts. Int J Turbo Jet Engines. 2010;26(4):263-276. https://doi.org/10.1515/TJJ.2009.26.4.263

[5] Fanelli JJA, Bassery JJA, Dupeyre RJP, Francois EL. Aube mobile pour une roue d'une turbomachine. Applicant: Safran Aircraft Engines. Patent No. FR3092864A1. 2020.

[6] Flitney RK. Seals and sealing handbook. Ed 6th. Butterworth-Heinemann. 2007. https://doi.org/10.1016/B978-0-08-099416-1.00002-4

[7] Franke M, Kugeler E, Nurnberger D. Das DLR-Verfahren TRACE: Moderne Simulationstechniken für Turbomaschinenströmungen. In: DGLR-Jahrbuch. Deutscher Luft- und Raumfahrtkongre; 2005 Sep 26-29.

[8] Giboni A, Wolter K, Menter JR, Pfost H. Experimental and numerical investigation into the unsteady interaction of labyrinth seal leakage flow and main flow in a 1.5-stage axial turbine. Proceedings of ASME Turbo Expo 2004; 2004 Jun 14–17; Vienna. https://doi.org/10.1115/GT2004-53024

[9] Gier J, Stubert B, Brouillet B, de Vito L. Interaction of shroud leakage flow and main flow in a three-stage LPT. J Turbomach. 2005;127(4):649-658. https://doi.org/10.1115/1.2006667

[10] Hendricks RC, Chupp RE, Lattime SB, Steinetz BM. Turbomachine interface sealing. NASA Technical Memorandum NASA/TM – 2005-213633. 2005.

[11] Henke M, Wein L, Kluge T, Guendogdu Y, Biester MH, Seume JR. Experimental and numerical verification of the core-flow in a new low-pressure turbine. Proceedings of ASME Turbo Expo 2016; 2016 Jun 13-17; Seoul. ASME. https://doi.org/10.1115/GT2016-57101

[12] Justak JF. Hydrodynamic brush seal. Patent US6428009B2. 2001.

[13] Kato M, Launder BE. The modeling of turbulent flow around stationary and vibrating square cylinders. 9th Symposium on Turbulent Shear Flows. Kyoto 1993. https://api.semanticscholar.org/CorpusID:117728958

[14] Klingels H. Sealing system for a turbomachine and axial flow turbomachine. Patent EP3324002B1. 2021.

[15] Mahle I. Improving the interaction between leakage flows and main flow in a low pressure turbine. ASME. 2010;GT2010-22448:1177-1186. https://doi.org/10.1115/GT2010-22448

[16] Mahle I, Schmierer R. Inverse fin arrangement in a low pressure turbine to improve the interaction between shroud leakage flows and main flow. ASME. 2010;GT2010-22448:1177-1186. https://doi.org/10.1115/GT2011-45250

[17] NASA Conference, Seal/Secondary Air System Workshop. NASA/CP-2009-215677. 2008:131-193.

[18] Nishii D, Hamabe M. Secondary flow suppression structure. Patent WO2021199718A1. 2004.

[19] Pałkus K. Low pressure turbine efficiency increase by developing new concept of outer air seal. Doctoral Thesis 2024.
[20] Pałkus K, Lauer C, Schmierer R. Axial turbomachine sealing system. Patent EP3822461A1. 2021.
[21] Pałkus K, Strzelczyk PM. Dimensionless numbers relationships for outer air seal of low pressure turbine. Int J Turbomach Propuls Power. 2021;6(3):33. https://doi.org/10.3390/ijtpp6030033
[22] Pfau A, Schlienger J, Rusch D, Kalfas AI, Abhari RS. Unsteady flow interactions within the inlet cavity of a turbine rotor tip labyrinth seal. J Turbomach. 2005; 127(4):679-688. https://doi.org/10.1115/1.2008973
[23] Rosic B, Denton JD, Curtis EM, Peterson AT. The influence of shroud and cavity geometry on turbine performance: an experimental and computational study – part I and II. J Turbomach. 2008;130(4): 041002. https://doi.org/10.1115/1.2777202
[24] Vanhaelst R, Bannack C, Klose M. Comparison of two measurement methods for the determination of extended turbine maps at the eATL test bench of the Ostfalia UAS. Combustion Engines. 2017;169(2): 43-48. https://doi.org/10.19206/CE-2017-208
[25] Wein L. Large-Eddy-Simulation von Deckband labyrinthdichtungen [dissertation]. Hannover: Leibniz University Hannover 2020. https://doi.org/ 10.15488/10202
[26] Wein L, Kluge T, Seume JR, Hain R, Fuchs T, Kahler C et al. Validation of RANS turbulence models for labyrinth seal flows by means of particle image velocimetry. Proceedings of ASME Turbo Expo 2020; 2020 Sep 21–25. https://doi.org/10.1115/GT2020-14885
[27] Wilcox DC. Turbulence modeling for CFD. 2nd ed. DCW Industries 1998.
[28] Yang H, Nuernberger D, Kersken H. Toward excellence in turbomachinery computational fluid dynamics: a hybrid structured-unstructured Reynolds-Averaged Navier–Stokes solver. J Turbomach. 2006;128(2): 390-402. https://doi.org/10.1115/1.2162182

Kacper Palkus, DEng. – Faculty of Mechanical Engineering and Aeronautics, Rzeszow University of Technology, Poland.
MTU Aero Engines Polska, Jasionka, Poland.
e-mail: *kacp.palkus@gmail.com*

Article citation info:
Wojciechowski H, Michalak D, Merkisz J. Differences in structural design and safety requirements of urban buses in Europe and North America. Combustion Engines. 2026;206(3):130-139. https://doi.org/10.19206/CE-222660

Hubert WOJCIECHOWSKI
Dariusz MICHALAK
Jerzy MERKISZ

Combustion Engines
Polish Scientific Society of Combustion Engines

Differences in structural design and safety requirements of urban buses in Europe and North America

ARTICLE INFO

Received: 28 January 2026
Revised: 28 May 2026
Accepted: 29 May 2026
Available online: 29 June 2026

This article conducts a comparative analysis of the design and safety requirements for urban buses in Europe and North America. European and American regulations are assessed for their impact on vehicle body design, structural strength, evacuation solutions, flammability of materials, accessibility, and vehicle equipment configuration. The analysis demonstrates that differing regulatory approaches across both regions result in significant differences in the structural architecture, safety systems, and functional organization of city buses. These differences are found to limit the ability to configure fully universal designs for both markets.

Key words: *city buses, technical norms, safety*

This is an open access article under the CC BY license (http://creativecommons.org/licenses/by/4.0/)

1. Introduction

Bus transport remains a key element of urban mobility systems in both Europe and North America, accounting for a significant portion of public transport journeys and acting as a link between rail transport and local commuting [46]. In the last decade, growing environmental and vehicle quality requirements (electrification, improved accessibility, raised passenger information standards) have imposed new constraints and innovative incentives on transport manufacturers and organizers [11, 58]. At the same time, the regulatory frameworks on both sides of the Atlantic shape these processes differently, leading to design and operational differences that are noticeable even in the most typical market segments – city buses with a length of approximately 12 m (≈ 40 ft) and 18 m (≈ 60 ft). In Europe, bus design and approval are based primarily on the regulations of the United Nations Economic Commission for Europe (UNECE) and the General Safety Regulation (GSR) (including those concerning body structure, doors and emergency exits, and flammability of materials) as well as on Euro VI and subsequent emission standards [12, 49]. In the United States and Canada, a similar role is played by sets of federal standards and guidelines, including the Federal Motor Vehicle Safety Standards (FMVSS) (including emergency exits, flammability of materials), Americans with Disabilities Act (ADA) regulations regarding accessibility, and U.S. Environmental Protection Agency (EPA) regulations for heavy vehicles [30, 57, 58]. The clash of these two orders results in a number of design differences, from body dimensions and geometry (e.g., permissible width), through door layout and width, and passenger transfer logic, to accessibility solutions (ramp type, wheelchair space orientation), lighting, signage, and integration of Heating, Ventilation, and Air Conditioning (HVAC) systems and electronics [49, 57].

Despite the abundance of normative sources and industry reports, the literature lacks a single, synthetic approach that systematically compares the design and operation of city buses in the EU and North America. Existing literature on urban buses primarily focuses on selected, narrowly defined problem areas. Operational studies analyze passenger exchange strategies and the impact of solutions such as all-door boarding on dwell time and perceived service quality [9, 22]. Research in ergonomics and accessibility investigates the interior layout of low-floor buses and the accommodation conditions for wheelchair users and other passengers requiring mobility assistance [8]. Meanwhile, studies addressing structural safety usually compare individual homologation procedures, such as ECE R66 and FMVSS 220, limiting their scope to structural resistance in rollover scenarios [18].

At the same time, a rapidly developing body of research is devoted to the electrification of bus transport, concentrating mainly on vehicle scheduling, charging strategies, and operational cost optimization [6]. More recent comparative studies between Europe and North America primarily address the functional and legal requirements for automated bus systems rather than the comprehensive architecture of urban buses [21]. As a result, there is still no integrated study that simultaneously compares European and North American regulatory frameworks and their implications for structural design, interior layout, accessibility solutions, operational assumptions, and the overall safety of urban buses.

This gap hinders the drawing of design and purchasing conclusions in tender procedures, as well as comparisons of operational efficiency across different urban contexts. The novelty of this study lies in combining these perspectives into a single, coherent comparative analysis of the European Union and North American approaches to urban bus design and regulation. The present work was conducted using a comparative analysis of international regulations, type-approval standards, tender specifications, and technical documentation for city buses in operation in Europe and North America.

2. Regulatory framework

2.1. Europe (EU/UNECE) – construction, fire safety

The basis for European type approval of M2/M3 buses is UN Regulation No. 107, which specifies, among other

things, vehicle classes, requirements for doors and emergency exits, passenger compartment, markings, and equipment [49]. For dimensions, the 2.55 m width limit is important. For flammability of materials and resistance to fuels/lubricants, UN Regulation No. 118 applies, including test methods and assessment criteria [50]. For exhaust emissions from heavy-duty vehicles (including city buses), the framework is Regulation (EC) No. 595/2009 (Euro VI) and its implementing acts [12]. Together, this creates a set of requirements that, on the EU side, directly affects the geometry, interior layout, material selection, and system integration in buses.

2.2. United States and Canada – safety, availability, dimensions

In the USA, key safety requirements are defined by the federal FMVSS standards: FMVSS 217 (emergency exits, window retention and release, operating forces, dimensions, markings) [30] and FMVSS 302 (ignition resistance and flame spread rate of interior materials) [31]. Bus accessibility is defined by 49 CFR Part 38 (ADA) – including parameters for ramps, wheelchair spaces and attachments, voice/light information systems, and the location of control devices [57]. For gauge dimensions, the federal width limit of 102 inches (≈2.59 m) on the National Network, resulting from 23 CFR §658.15 [13], is important. For exhaust emissions, the final EPA Heavy-Duty Phase 3 requirements apply, covering, among others, transit and school buses [58]. This regulatory package sets different design priorities in North America than in the EU (e.g., emergency exit architecture, flammability criteria, consequences of a wider gauge, and specific ADA requirements).

Differences and their design implications:

- Emergency exits and windows: R107/EU vs. FMVSS 217/USA – differences in the location and dimensions of evacuation portals and window release requirements [30, 49]
- Flammability of materials: UNECE R118 vs. FMVSS 302 – impact on the selection of upholstery, linings, and insulation [31, 50]
- Accessibility: UNECE vs. precise ADA Part 38 requirements (ramps, wheelchair space and orientation, information interfaces) – implications for door location and interior layout [57]
- Clearance dimensions: The EU uses a practical 2.55 m, while the US uses 102″ (≈2.59 m) – differences translate into seating arrangements, aisle widths, and turning circles [13, 49]
- Emissions: Euro VI (EU) vs. EPA HD Phase 3 (USA) – different compliance and propulsion planning paths (e.g., limit compliance strategies, electrification) [11, 12, 58].

3. Dimensions, geometry and running gear

3.1. Normative assumptions and constraints

Bus dimensions result from a compromise between capacity and accessibility requirements and the spatial constraints of the street network. On the EU side, UN R107 design regulations (vehicle classes M2/M3, minimum circulation spaces, doors, emergency exits) are key, indirectly determining overhang length, floor height, and aisle width [49]. In North America, vehicle width limits on the national network are set by the federal limit of 102″ (≈2.59 m), which translates into a slightly wider gauge than is typical in the EU (practically 2.55 m) [13, 14]. Street design guidelines for bus traffic emphasize that the choice of vehicle design has direct consequences for curves, platform edges, and lane widths [25, 27, 46].

- The length (≈ 12 m / 40 ft) allows for a full low floor in the door area and a rear service section. R107 does not mandate a specific length, but requirements regarding the number and location of doors and aisles determine the minimum usable space [49]
- Width: The difference of 2.55 m (EU) vs. 2.59 m = 102″ (US) changes the potential seating arrangement (number of seats side-by-side and aisle width) and turning kinematics; a wider body typically requires larger curves while maintaining the same tires/wheelbase [27, 28, 46]
- Height depends on the drive/HVAC architecture R107 requirements for exits and roof equipment, which indirectly affect the available space under the roof [49].

4. Design and operational consequences

4.1. Door layout, passenger flow and passenger space

In European buses, the standard is a full low floor in the door zone and a system of at least 2–3 pairs of doors (Fig. 1), designed for parallel flows of boarding and alighting and a short dwell time during rush hours [38, 49].

Fig. 1. Door layout of a European bus

In North America (40 ft), the 2-door model (Fig. 2) and front-door boarding (entrance at the front, exit at the rear) are predominant, which is related to the location of fare boxes at the front doors [2, 17]. More and more agencies are testing or implementing boarding with all doors open on high-demand lines, which, in research and evaluations, results in a significant reduction in dwell time and lower stop-to-stop variability [26]. In North American vehicles, despite a slightly wider gauge (102″ ≈ 2.59 m) favoring a wider aisle, the geometry itself, without changing the boarding policy, is worse than in Europe [13, 26].

Differences in floor architecture translate into space management and passenger flows. In the EU, a full low floor across all doors promotes rearward vehicle movement and more standing space in the door areas. In the USA/Canada, 40-foot low-floors are common, with a raised

platform above the drive axle (a step in the rear) that limits the natural rearward movement of passengers in a 2-door configuration [44]. In European practice, thanks to 2–3 pairs of doors and a wide corridor between them, capacity (number of passenger exchanges per stop) is higher [26, 35, 38]. In the EU, a greater variety of seat orientations is permitted, including space above the wheel arches and seats longitudinally or rearward positioned locally (Fig. 3).

Fig. 2. Door layout of an American bus

Fig. 3. Seat arrangement in an EU bus

In practice, NA seats are usually positioned forward-facing or longitudinally to the aisle (Fig. 4), and rear-facing seating arrangements in the passenger area are rare; regulations and guidelines focus, among other things, on providing forward-facing seats in the priority area [17, 26].

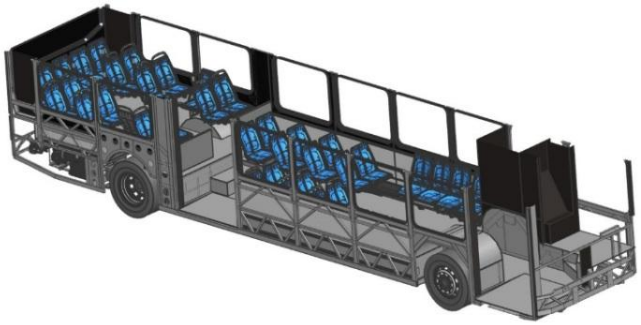

Fig. 4. Seat arrangement in an NA bus

Accessibility and wheelchair access are managed differently. In the EU (e.g., in city specifications), the ramp is usually located at the middle door (Fig. 5), and the wheelchair position is usually rearward-facing (Fig. 6) with an appropriate backrest. This facilitates the dispersion of flows at entrances and minimizes collisions with traffic near the driver's cabin [11, 40, 45].

Fig. 5. EU wheelchair ramp

Fig. 6. EU wheelchair space

In NA, in accordance with ADA Part 38 and Access Board guidelines [55], at least one position must allow forward-facing immobilization, and many operators combine ramp operation at the front door with driver assistance. A typical solution is a folding (flip-out) ramp in the first door (Fig. 7) [35, 56, 57].

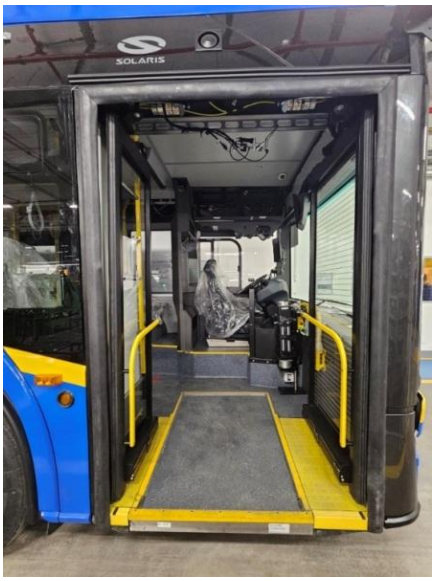

Fig. 7. NA wheelchair ramp

Interior ergonomics also differ in many respects. In the EU, multi-door systems strive for wide standing areas and as many free aisles as possible at the doors (fewer fare barriers in the entry area), which facilitates fast turnover. In NA, many systems, especially outside Bus Rapid Transit (BRT), still concentrate validation at door 1. They use more longitudinal seats in the front to increase standing area during peak hours [2, 17, 26].

5. Safety

5.1. Glazing and evacuation through windows.

In terms of passenger safety, both Europe and North America have clearly defined regulatory requirements for body design and evacuation systems. These include emergency exit doors, side and rear emergency windows, and requirements for their signage and accessibility. Despite the common goal of ensuring rapid and safe evacuation, the detailed technical solutions and regulatory philosophies differ on both sides of the Atlantic.

In Europe, UN ECE R107 requires an appropriate number of emergency exits and, at the same time, equips these areas with glass-breaking devices (hammers) at specified locations and with specified markings. In practice, this favors the use of bonded glass with safety hammers (Fig. 8) [49].

Fig. 8. EU emergency exit windows

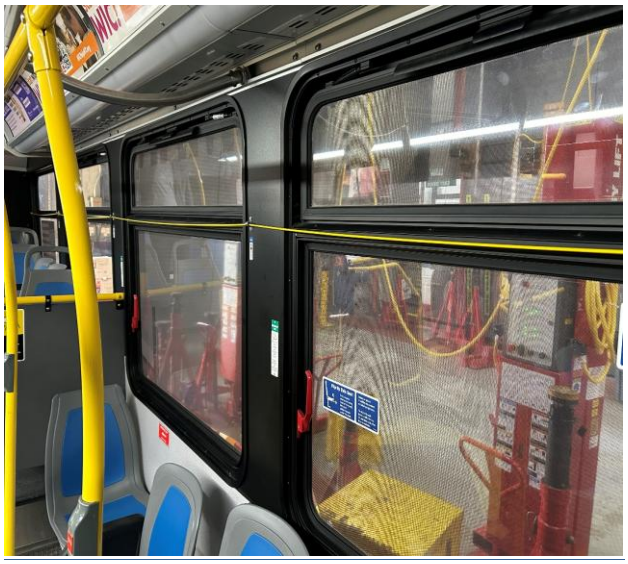

Fig. 9. Emergency windows NA

In North America, the FMVSS 217 standard precisely defines the number and types of emergency exits (doors, emergency windows, roof exits) as well as requirements for operating forces, opening dimensions, and signage. As a result, NA transit buses commonly feature tilt-and-slide windows with levers and instructions at the window. These are not glued but bolted to the bus frame (Fig. 9).

5.2. Bumpers

For city buses in the US, the federal bumper standard 49 CFR Part 581 does not apply to buses (it applies to passenger cars), which is confirmed by both the text of the regulation and interpretations by the National Highway Traffic Safety Administration (NHTSA) [5]. In practice, however, public transportation agencies (transit agencies) require the use of energy-absorbing bumpers at the front and rear (Fig. 10) and low-speed tests (e.g., 5 mph). These requirements stem not from federal regulations, but from purchasing standards developed by the American Public Transportation Association (APTA). The APTA Bus Procurement Guidelines document is a set of technical recommendations used in preparing tender specifications. An RFP (Request for Proposals), in turn, is a formal request for proposals published by the contracting authority (transportation agency) specifying detailed technical requirements for the vehicle. Numerous RFPs (e.g., SRTA, Tuscaloosa) explicitly require front and rear bumpers with specific resistance parameters and the ability to return to their original shape after impact [5, 39, 47]. Reinforced rear bumpers in North America also have practical operational significance. In depot conditions, they enable buses to be maneuvered using special pushers mounted on service vehicles. In emergency situations, they also allow a disabled bus to be safely pushed out of the lane using a properly prepared service vehicle. This solution requires appropriate reinforcement of the bumper zone structure and its integration with the vehicle frame.

Fig. 10. Front and rear bumpers NA

In North America, front-mounted bicycle racks are a common solution on buses; recommendations and implementation examples appear in APTA materials and city/agency operational guides. As a standard, 2–3-position racks are used, mounted at the front (Fig. 11), which allows the driver to observe loading/unloading [3, 33]. At the same time, the American regulator clarifies the legal framework: the NHTSA interpretation of FMVSS 108 indicates that bicycles in a rack are "temporary cargo," and the rack itself cannot obscure required lights/reflectors. If the installation does not render the mandatory devices inoperable, it is

permissible; this also applies to installation by transit agencies themselves [33]. In several jurisdictions (e.g., California), length- and front-reach regulations have been clarified to explicitly allow extensions of up to ~40″ forward of the front of the bus. At the operational level, National Association of City Transportation Officials (NACTO)/city guidelines remind that the stand changes the turning geometry/front overhang and requires additional clearance at platforms and in the bay (e.g., typical clearance of 4 ft in front of the front at the stop) [3, 41].

Fig. 11. NA bicycle racks

In Europe, front racks are not permitted and do not pass approval procedures due to requirements regarding pedestrian safety/external protruding elements, field of vision, and light markings. In the UK, technical authorities have assessed front racks as unacceptable on city buses [29, 37]. Furthermore, Transport for London (TfL) explicitly states that installing front racks does not meet the Bus Safety Standard requirements and negatively affects parking times/capacity; bicycle parking and interchange integration are preferred [24]. These generalizations also appear in EU projects, which indicate that front racks are not permitted in the EU due to the risk of pedestrian injury from protruding elements [23, 38].

5.3. Signage and pictograms

In the EU, R107 regulates the marking of safety devices, but in practice, ISO-compliant pictograms and legible photoluminescent markings predominate, with a smaller proportion of long texts (Fig. 12) [49].

Fig. 12. EU safety markings and pictograms

In North America, ADA regulations (49 CFR Part 38), in conjunction with FMVSS 217, result in a large number of labels and text stickers concerning, among others, priority seats, wheelchair positions and instructions, emergency exits and audio-visual information (Fig. 13–15) [30, 57].

Fig. 13. Safety markings and pictograms NA

Fig. 14. Signage and pictograms – informational NA

Fig. 15. Signage and pictograms – prohibiting certain behaviors NA

5.4. Stop-request: buttons and pull-cords

In Europe, STOP buttons predominate (Fig. 16), arranged according to operator specifications, while meeting the R107 requirements regarding accessibility and legibility of control elements [49].

Fig. 16. STOP buttons in the EU

In the US and Canada, the stop-request system must be accessible from the wheelchair attachment points and provide both an audible and visual signal. Regulations §38.37 allow operators to choose the activation mechanism – either a pull cord (Fig. 17) or a button. In practice, this translates into the widespread use of pull cords that operate in parallel with buttons. Their presence is acknowledged in many operators' operating procedures – for example, in standard operating instructions. Pull cords are particularly valued for their ease of use, reliability, and ease of integration with

existing signaling systems, as well as passenger and operator habits. Additionally, their physical form can be more intuitive for passengers with limited dexterity, supporting ADA-compliant accessibility. In older vehicles, pull cords may be the primary mechanism for requesting a stop, while in newer models, they are used as a supplement to buttons, increasing the flexibility of the system [1, 20, 57].

Fig. 17. Pull cord

5.5. Standards for the installation and color of lights and rear windows

On the EU side, the basis is UN/ECE R48 (installation) together with specific regulations (e.g. R6 – turn signals), which rigidly define the colors: at the front, turn signals must be yellow (amber), at the rear also amber, and position and brake lights are signaled in red [52, 53]. In the EU, a horizontal arrangement of lights is predominant (Fig. 18).

In North America, FMVSS 108 permits red or yellow turn signals at the rear, with yellow at the front; this has led to different lighting semantics and design practices for rear lamp assemblies for years [29, 32]. Additionally, three red identification lamps are required at the upper edge of the rear, which influences the arrangement of lighting elements and the composition of the rear wall [15]. In NA design practice, vertical "towers" of lamps at the corners (stop/tail, turn signal, reversing) in a column arrangement are often used (Fig. 18), which facilitates meeting visibility requirements and integration with bumpers and service panels. In NA, purchasing specifications often do not require a rear window [4]. Similarly, a number of RFPs state that if a bus has a rear window, the manufacturer must meet additional specification requirements [41]. In Europe, the dominant practice for 12-meter city buses is to retain the rear window. Exceptions occur when the HVAC/drive installation occupies the window area and the customer accepts a closed rear end [41, 52].

Fig. 18. EU and NA lights layout

5.6. Flammability of internal materials

In the EU, UN/ECE R118 is used, which covers the behavior of materials when exposed to fire (flammability, burning rate, melting/dripping) and, in newer editions, the ability to repel fuel or oil (Annex 9 test). R118 defines three basic reactions to fire tests: horizontal flame spread (Annex 6), melting and dripping (Annex 7), and vertical flame spread (Annex 8); the limiting criteria are, for example, ≤ 100 mm/min for horizontal and vertical tests, and in the melting test, no ignition of cotton wool by drops. The scope of the regulation applies (depending on the version) to materials in the passenger compartment and additional components (e.g., insulation in the engine/heating compartment – Annex 9 oil immersion test; electrical cables – Annex 10 resistance to flame propagation). A material that passes Annex 8 (vertical) generally also meets Annex 6 (horizontal) [10, 50].

In the US/Canada, FMVSS 302 is the basis for a single horizontal test that measures the flame spread rate of materials inside the passenger compartment (including panels, carpets, linings, headliners, seat belts, and curtains; each layer within 13 mm of the cabin airspace is considered). The passing criterion is ≤ 102 mm/min or extinguishment before 60 s and < 51 mm of burnt length. The procedure describes sample preparation (102 × 356 mm), conditioning, and Bunsen burner flame conditions [31, 43].

Key practical differences include:

- Test philosophy and completeness. R118 is a set of tests (horizontal/vertical/melting + special tests for fuels and cables) that more broadly reflects real-world fire scenarios in buses; FMVSS 302 is limited to horizontal combustion of cabin materials. Consequently, the same material may meet FMVSS 302 requirements but not R118 Annex 7/8 requirements (e.g., due to vertical spread or dripping) [19, 50].
- Thresholds and criteria. FMVSS 302: ≤ 102 mm/min (horizontal); R118: ≤ 100 mm/min (horizontal and vertical). Minor numerical differences are less significant than the test orientation (vertical vs. horizontal) and the melting/dripping condition in R118.
- Scope of components. FMVSS 302 explicitly lists a long list of interior components and states that any layer within 13 mm of the cabin is subject to the requirements. R118 separates responsibilities between interior components, hot cell insulation (Annex 9), and ductwork (Annex 10) [31, 50].
- Design implications: for buses, this means that it's easier to avoid meeting EU requirements for vertical elements (walls, curtains, and covers) and overhead materials (Annex 7), and for insulation in hot zones, fuel/oil resistance must be confirmed. Therefore, materials that are acceptable overseas may require a different selection in EU tenders.

5.7. Electronic cabinet and equipment layout

In Europe, city bus manufacturers prefer service bays in the rear corners, hidden behind large flaps and logically separating the HV/LV and drivetrain. Manufacturers' materials emphasize modular component packaging in the rear and roof areas, which minimizes the need for cassettes above the wheel arches in the interior and allows for

ground-level servicing of entire corner sections after opening the flaps.

In North American buses, key HV/LV points (battery disconnects, HV system access, fuse and control panels) are most often located in the rear curbside so that service and emergency procedures can be performed from sidewalk level. Driver/crew instructions explicitly instruct drivers/crews to approach the rear curbside and open the Battery Disconnect access door in an emergency, clearly locating the main power disconnect point at the rear of the vehicle [42]. In parallel, product materials describe an easily accessible compartment housing the traction power electronics and on-board systems—a typical modular service cabinet. In North American practice, there is also a variant of the electrical cabinet, accessible from the inside on the left wheel well (Fig. 19), for mounting on-board electronics, which perpetuates the practice of using the front left wheel well as a location for selected modules.

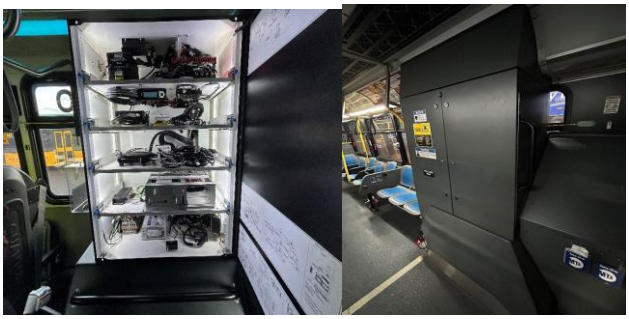

Fig. 19. Electrical cabinet on the wheel arch NA

5.8. Frame strength and structural safety

Design differences between buses in Europe and North America stem not only from regulations regarding doors, lighting, and accessibility, but also from differing approaches to frame strength, passive safety, and methods for assessing the superstructure. In Europe, the core regulations include UNECE regulations, particularly R66.02, R29, and R100, while in the US, this role is primarily fulfilled by the Altoona test program, supplemented by guidelines on static roof loads. It's worth noting that, unlike passenger cars, neither the EU nor the North American states has a separate, mandatory side impact test for city buses.

5.9. Rollover test

In the EU, the primary regulation for the structural resistance of M2/M3 buses is UN/ECE R66.02 [54]. The regulation defines criteria for maintaining a survival space, which must remain intact after a vehicle rolls over. During the physical test, the bus body is placed on a platform tilted around a predetermined pivot point. Once the critical angle is exceeded, the structure freely falls onto the impact surface (Fig. 20).

The regulations specify:

- the pivot point and rollover axis
- vehicle preparation method (weight, configuration, fluid status)
- the precise boundaries of the survival space
- criteria for permissible structural deformation.

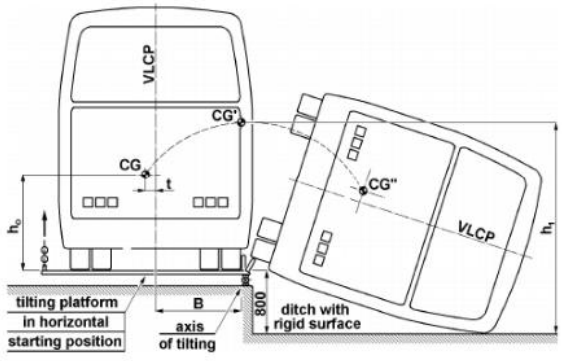

Fig. 20. Rollover test in the EU [59]

The test is considered as passed if, after the rollover, no structural, skin, or equipment element enters the survival space, which defines the geometric shape within which passengers must fit after the structure deforms. Deformations of the pillars, body, and roof do not violate the protective zone. Doors and emergency exits remain operable in accordance with R107 requirements (after deformation corrections specified in the procedure).

Other methods for confirming compliance with R66.02 are also available:

- Physical rollover of the complete vehicle. This is the most reliable method, but also the most expensive. It is primarily performed at manufacturer research centers
- Section rollover (module test). A section of the structure is tested (usually the side section and roof). This method is less expensive and widely used in homologation
- FEM simulation (Finite Element Method). The regulations allow for full confirmation of compliance through numerical analysis—provided that the model has been previously calibrated using the results of a physical section test [36, 54].

5.10. Lateral roll test

EU countries also use a static stability test in which the bus is tilted until a critical angle is reached, typically around 28–35° (Fig. 21). This test assesses the center of gravity and vehicle stability, supplementing the requirements of R66.02 [54].

Fig. 21. View of the bus during the lateral tilt test [7]

5.11. Frontal impact – driver's compartment protection (UN/ECE R29)

Protection of the driver's cab against deformation in a collision is defined by UN/ECE R29 [51]. Although the regulation originally applies to trucks, many urban bus manufacturers use its requirements as a design reference:

- cab resistance to frontal impact
- maintaining the driver's protective space
- reinforcing the upper and lower elements of the front structure.

In low-floor vehicles, these requirements are met by additional reinforcements on the floor and A-pillars.

5.12. R100 – Electric Bus Safety (HV)

UN/ECE R100 regulation specifies the safety of high-voltage systems in electric vehicles [48], including:

- impact resistance of the battery housing
- protection against puncture and short circuit after a collision
- insulation requirements
- protection against water ingress.

5.13. Altoona Program (FTA Bus Testing Program)

In the US, there is no regulation directly equivalent to the European R66. The structural strength and durability of buses are assessed primarily by the Altoona program – an accelerated durability test on a special test track (49 CFR Part 665) [16]. Altoona focuses on operational durability.

These tests include:

- structural fatigue testing (12-year simulation cycle)
- frame strength and deformation assessment
- structural torsion and deflection tests
- dynamic loading of roof components (HVAC, batteries)
- suspension system and body stiffness tests.

5.14. Roof Load Test – static roof load

In accordance with NHTSA guidelines and the bidding standards of many transportation agencies, transit buses in North America are subjected to a static roof load test [34]. The load is quasi-static and is applied to the roof structure in a controlled manner, typically through a beam that distributes the force over a defined area. Depending on the customer's specifications, the load value is typically several thousand pounds or a specified percentage of the gross vehicle weight. The test verifies that:

- the roof structure can support the specified load without loss of load-bearing capacity
- there is no permanent deformation of the supporting structure
- the roof equipment mountings (HVAC, traction batteries, converters) remain intact.

Unlike the European R66, this test does not simulate a vehicle rollover but rather tests the strength of the local roof structure.

5. Conclusions

The conducted comparative review demonstrated that the differences between urban buses operating in Europe and North America are systemic and stem primarily from differing regulatory frameworks and vehicle design philosophies. In Europe, bus design is directly subordinated to detailed UNECE regulations, which precisely define requirements for body strength, rollover protection of the passenger compartment, high-voltage system safety, evacuation, and fire behavior of materials. This approach leads to a high degree of superstructure standardization and a clear emphasis on passive safety and structural integrity. In North America, the regulatory system is based on a combination of FMVSS regulations, ADA accessibility requirements, and procurement and operational practices shaped by transportation agencies. The emphasis is shifted to service life, operational functionality, and vehicle configuration flexibility. The Altoona program and static roof load tests verify the durability of the structure under operational conditions. These differences directly impact the frame architecture, passenger compartment organization, evacuation solutions, interior material selection, exterior lighting configuration, service component layout, and vehicle accessories. As a result, designs intended for the European and North American markets can rarely be considered fully universal. The same bus model typically requires distinct approval and design variants, tailored to the specifics of a given legal and operational system. Differences in regulatory approaches mean that urban bus design is not only a technical issue but also the result of integrating the legal, infrastructural, and operational requirements specific to a given market. Understanding these conditions is crucial for manufacturers planning transatlantic operations, for transport organizers formulating tender requirements, and for further research on design optimization in the context of the globalization of the urban bus market.

Nomenclature

ADA	Americans with Disabilities Act
APTA	American Public Transportation Association
BRT	bus rapid transit
CFR	Code of Federal Regulations
DOT	Department of Transportation
EPA	Environmental Protection Agency
EU/UE	European Union
eCFR	Electronic Code of Federal Regulations
FMCSA	Federal Motor Carrier Safety Administration
FMVSS	Federal Motor Vehicle Safety Standards
FTA	Federal Transit Administration
HVAC	heating, ventilation and air conditioning
LCC/TCO	life cycle cost/total cost of ownership
NA	North America
NACTO	National Association of City Transportation Officials
NHTSA	National Highway Traffic Safety Administration
RFP	request for proposal
SFMTA	San Francisco Municipal Transportation Agency
TfL	Transport for London
TRB	Transportation Research Board
TRL	Transport Research Laboratory

Bibliography

[1] Amalgamated Transit Union Local 587. Transit operators standard operating procedures. Seattle (WA): ATU Local 587; 2012.

[2] American Public Transportation Association. Automatic fare collection system planning and deployment. Washington (DC): APTA; 2010.

[3] American Public Transportation Association. Bicycle and transit integration. Washington (DC): APTA; 2018.

[4] American Public Transportation Association. Bus procurement guidelines. Washington (DC): APTA.

[5] American Public Transportation Association. Standard bus procurement guidelines. Washington (DC): APTA; 2013–2024.

[6] Behnia F, Schuelke-Leech BA, Mirhassani M. Optimizing sustainable urban mobility: a comprehensive review of electric bus scheduling strategies and future directions. Sustain Cities Soc. 2024;108:105497. https://doi.org/10.1016/j.scs.2024.105497

[7] Cogent Seating Ltd. Tilt Testing Swansea (UK).

[8] D'Souza C, Paquet V, Lenker JA, Steinfeld E. Effects of transit bus interior configuration on performance of wheeled mobility users during simulated boarding and disembarking. Appl Ergon. 2017;62:94-106. https://doi.org/10.1016/j.apergo.2017.02.008

[9] El-Geneidy A, van Lierop D, Grisé E, Boisjoly G, Swallow D, Fordham L et al. Get on board: assessing an all-door boarding pilot project in Montreal, Canada. Transp Res A Policy Pract. 2017;99:114-124. https://doi.org/10.1016/j.tra.2017.03.005

[10] El Houssami M, Försth M, Fredriksson H, Drean V, Guillaume E, Hofmann-Böllinghaus A et al. Fire safety of interior materials of buses. Fire and Materials. 2023;47(7):910-924. https://doi.org/10.1002/fam.3134

[11] European Commission. Emissions from heavy-duty vehicles (Euro VI): certification rules. Brussels: European Commission; 2022.

[12] European Parliament and Council. Regulation (EC) No 595/2009. Brussels: Official Journal of the European Union; 2009.

[13] Federal Highway Administration. 23 CFR § 658.15 – Width on the National Network. Washington (DC): FHWA; 2015.

[14] Federal Highway Administration. A policy on geometric design of highways and streets. Washington (DC): FHWA; 2017.

[15] Federal Motor Carrier Safety Administration. 49 CFR § 393.11. Washington (DC): FMCSA.

[16] Federal Transit Administration. Bus testing program (Altoona). Washington (DC): FTA; 2020.

[17] Federal Transit Administration. Fare collection. Washington (DC): FTA; 2015.

[18] Gepner B, Bojanowski C, Kwasniewski L, Wekezer J. Effectiveness of ECE R66 and FMVSS 220 standards in rollover crashworthiness assessment of paratransit buses. Int J Automot Technol. 2014;15(4):581-591. https://doi.org/10.1007/s12239-014-0061-3

[19] Klippel A, Hofmann A, Gnutzmann T, Piechnik K. Reaction-to-fire testing of bus interior materials: assessing burning behaviour and smoke gas toxicity. Fire and Materials. 2023;47:665-680. https://doi.org/10.1002/fam.3108

[20] Legal Information Institute. 49 CFR § 38.37. Ithaca (NY): Cornell Law School.

[21] Lindner J, Margreiter M, Bogenberger K. Functional requirements for automated bus transit systems based on human driver tasks. J Public Transp. 2026;28:100162. https://doi.org/10.1016/j.jpubtr.2026.100162

[22] Los Angeles Metro. All-door boarding pilot evaluation. Los Angeles (CA): LA Metro; 2016.

[23] London Bus Services Ltd. Bus vehicle specification. London: LBS; 2024–2025.

[24] Mercedes-Benz Buses. eCitaro. Stuttgart: Daimler Buses; 2025.

[25] National Academies of Sciences, Engineering, and Medicine. Highway and street design vehicles: an update. Washington (DC): National Academies Press; 2023.

[26] National Association of City Transportation Officials. Better boarding, better buses. New York (NY): NACTO; 2017.

[27] National Association of City Transportation Officials. Transit street design guide. Washington (DC): Island Press; 2016.

[28] National Association of City Transportation Officials. Urban street design guide. New York (NY): NACTO; 2013.

[29] National Highway Traffic Safety Administration. 49 CFR § 571.108 – FMVSS No. 108. Washington (DC): NHTSA.

[30] National Highway Traffic Safety Administration. 49 CFR § 571.217 – FMVSS No. 217. Washington (DC): NHTSA.

[31] National Highway Traffic Safety Administration. 49 CFR § 571.302 – FMVSS No. 302. Washington (DC): NHTSA.

[32] National Highway Traffic Safety Administration. Effectiveness of amber rear turn signals. Washington (DC): Federal Register.

[33] National Highway Traffic Safety Administration. Interpretation of FMVSS No. 108. Washington (DC): NHTSA; 2008.

[34] National Highway Traffic Safety Administration. Roof load tests for heavy vehicles. Washington (DC): NHTSA; 2008–2017.

[35] New Flyer Industries. Xcelsior (40 ft). Winnipeg: New Flyer; 2021–2023.

[36] Pravilonis T, Eidukynas V, Sokolovskij E. An analysis of the reliability of a bus safety structure on carrying out the numerical and experimental tests. Sensors. 2020;20(24):7092. https://doi.org/10.3390/s20247092

[37] San Francisco Municipal Transportation Agency. All-door boarding evaluation. San Francisco (CA): SFMTA; 2014.

[38] Solaris Bus & Coach. Urbino 12 electric. Bolechowo: Solaris; 2023.

[39] Southeastern Regional Transit Authority. Bus technical specifications. New Bedford (MA): SRTA; 2014.

[40] Transport for London. Accessible bus stop design guidance. London: TfL; 2010.

[41] Transport for London. Bus vehicle specification. London: TfL; 2025.

[42] Transport for London, Transport Research Laboratory. GSR review of the bus safety standard. London: TfL; 2021–2024.

[43] Transport Research Laboratory. Bus safety standard – future roadmap. Wokingham: TRL; 2019–2021.

[44] Transportation Research Board. TCRP Synthesis 2: Low-floor transit buses. Washington (DC): National Academies Press; 1994.

[45] Transportation Research Board. TCRP Synthesis 50. Washington (DC): National Academies Press; 2003.

[46] Transportation Research Board. Transit capacity and quality of service manual. Washington (DC): National Academies Press; 2013.

[47] Tuscaloosa Transit Authority. Request for proposals. Tuscaloosa (AL): TTA; 2016.

[48] United Nations Economic Commission for Europe. Regulation No. 100. Geneva: UNECE; 2013–2022.

[49] United Nations Economic Commission for Europe. Regulation No. 107. Geneva: UNECE; 2015.

[50] United Nations Economic Commission for Europe. Regulation No. 118. Geneva: UNECE; 2019.
[51] United Nations Economic Commission for Europe. Regulation No. 29. Geneva: UNECE; 2002–2020.
[52] United Nations Economic Commission for Europe. Regulation No. 48. Geneva: UNECE.
[53] United Nations Economic Commission for Europe. Regulation No. 6 and Regulation No. 148. Geneva: UNECE.
[54] United Nations Economic Commission for Europe. Regulation No. 66/66.02. Geneva: UNECE; 2010–2021.
[55] U.S. Access Board. ADA accessibility guidelines for transportation vehicles. Washington (DC): Federal Register; 2013.
[56] U.S. Access Board. ADA vehicle guidelines. Washington (DC): U.S. Access Board.
[57] U.S. Department of Transportation. 49 CFR Part 38 – ADA accessibility specifications. Washington (DC): DOT.
[58] U.S. Environmental Protection Agency. Regulations for greenhouse gas emissions from commercial trucks (Heavy-Duty Phase 3). Washington (DC): EPA; 2024.
[59] Wekezer JW, Li F, Kwasniewski P, Rahman S. Laboratory testing program for FE crash analyses of paratransit buses. 2014.

Hubert Wojciechowski, Eng. – Faculty of Civil and Transport Engineering, Poznan University of Technology, Poland.
e-mail:
hubert.wojciechowski.1@student.put.poznan.pl

Dariusz Michalak, DEng. – Member of the Management Board of Solaris Bus & Coach Sp. z o. o., Poland.
e-mail: *dariusz.michalak@solarisbus.com*

Prof. Jerzy Merkisz, DSc., DEng. – Faculty of Civil and Transport Engineering, Poznan University of Technology, Poland.
e-mail: *jerzy.merkisz@put.poznan.pl*

Article citation info:
Marimuthu K, Sundararaj AJ, Nair AG, Muthumari T. Experimental and kinetic analysis of low to intermediate temperature auto-ignition of binary ethylene-acetylene blends. Combustion Engines. 2026;206(3):140-150. https://doi.org/10.19206/CE-217944

Kesavan MARIMUTHU
Aldin Justin SUNDARARAJ
Abhijith Girish NAIR
Thangapandi MUTHUMARI

Combustion Engines
Polish Scientific Society of Combustion Engines

Experimental and kinetic analysis of low to intermediate temperature auto-ignition of binary ethylene-acetylene blends

ARTICLE INFO

Received: 25 January 2026
Revised: 6 February 2026
Accepted: 9 February 2026
Available online: 13 February 2026

Understanding the ignition characteristics of binary hydrocarbon blends is essential for designing high-speed propulsion systems such as scramjets, where ignition under short residence time is a critical challenge. In this work, the ignition delay behaviour of ethylene-acetylene/air mixtures was examined through shock tube experiments and kinetic simulations under engine-relevant conditions. Ethylene was used as the primary fuel and blended with acetylene at 5%, 10%, and 20% by volume to form binary mixtures, at an equivalence ratio of 1.0, temperatures between 560–1030 K, and pressures of 2.5–9 bar. The ignition delay time was determined from peak pressure rise and CH chemiluminescence behind the reflected shock. Unlike previous blended fuel studies dominated by saturated hydrocarbons, this work presents a comprehensive dataset for ethylene-acetylene blends at low to intermediate temperatures and increasing the acetylene fraction from 5% to 20% reduces the ignition delay time by up to 50–60% in the 700–850 K and 2–5 bar regime. Numerical simulations were performed using ANSYS Chemkin in a closed, homogeneous, constant-volume reactor with the NUIG, ARAMCO, LLNL, and San Diego mechanisms. The sensitivity and rate-of-production analyses reveal that ignition is governed by HO_2–H_2O_2 radical chemistry, with the thermal decomposition of H_2O_2 triggering rapid OH formation. Acetylene enhances ignition by promoting the regeneration of HCCO radicals and accelerating the transition to chain-branching chemistry.*

Key words: *auto ignition, chemical kinetics, fuel blends, sensitivity and rate-of-production analysis*

This is an open access article under the CC BY license (http://creativecommons.org/licenses/by/4.0/)

1. Introduction

The development of combustion models for high-speed propulsion systems requires a comprehensive understanding of the ignition characteristics of unsaturated hydrocarbons, alongside a detailed knowledge of the fundamental chemical kinetics governing the oxidation pathways of small hydrocarbon intermediates. Ethylene (C_2H_4) and acetylene (C_2H_2) are within the lower hydrocarbon combustion chemistry. These compounds are widespread products originating from the pyrolysis and oxidation of nearly all larger alkanes and alkenes, and their subsequent consumption significantly alters global reaction kinetics, characteristics of flame propagation, and the formation pathways of pollutants, including the elaborate chemistry that leads to soot precursors. Ethylene acts as a critical transitional entity in the degradation of higher hydrocarbons, facilitating the reactivity transition between saturated and unsaturated compounds. In contrast, acetylene, distinguished by its strong triple bond and heightened chemical reactivity, functions as both a catalyst for chain branching and an essential precursor for soot and polycyclic aromatic hydrocarbons. The chemical interaction between these two species profoundly affects ignition characteristics, flame dynamics, and emissions within hydrocarbon combustion systems. Experimental data on the ignition behaviour of binary ethylene-acetylene mixtures are limited, restricting the validation of detailed kinetic mechanisms. Ignition delay time, defined as the interval between the arrival of the reflected shock and ignition onset, provides a direct measure of fuel reactivity. Recent studies have shown that ignition delay measurements strongly depend on the start of combustion, particularly at low and intermediate temperatures where pressure rise is weak. Boruc et al. [3] established that optical diagnostics, such as radical chemiluminescence, provide more reliable and repeatable ignition delay measurements than pressure-based methods alone, especially for fuels with long induction periods. Shock tube experiments enable reliable IDT measurements under well-controlled, near-constant-volume conditions across wide temperature and pressure ranges. These measurements provide the foundation for validating detailed chemical kinetic mechanisms that support computational modelling frameworks such as CHEMKIN. Such validation is particularly essential within the low-to-intermediate temperature range, where the majority of kinetic models continue to demonstrate substantial uncertainties in accurately capturing the oxidation behaviour of C_2–C_3 unsaturated hydrocarbons [11]. Several shock-tube and rapid-compression-machine investigations have measured ignition delay times for individual C_2–C_3 hydrocarbons across wide pressure and temperature ranges, forming the core validation datasets for kinetic mechanisms such as NUIG and Aramco Mechanism. The current study aims to address the lack of IDT data for binary C_2H_4/C_2H_2 blends, quantify the effect of acetylene addition, and identify dominant radical pathways over a wide range of low-intermediate temperatures.

Earlier studies on pure ethylene, ethane, and propane have consistently highlighted the fundamental kinetic features governing their oxidation behaviour. Across a broad range of pressures (1–40 bar) and temperatures (700–2600 K), extensive experimental datasets have mapped ignition delay characteristics, chain-branching pathways, and temperature-regime transitions for these C_2–C_3 hydrocarbons [8, 17, 24, 32]. Foundational shock tube investigations by Burcat & Lifshitz [4], de Vries [8], and Kopp [16] established the high-temperature ignition delay behaviour of

ethylene and ethane, including the sensitivity to equivalence ratio, dilution, and pressure. Propane oxidation has similarly been characterised through both shock tube and rapid compression machine (RCM) measurements, with Gallagher et al. [10] providing key high-pressure ignition data. Dagaut and co-workers [6, 7] performed detailed speciation studies in JSRs for ethylene, ethane, and propane at pressures up to 10 bar (800–1250 K) and validated the hierarchical development of chemical mechanisms, which build C_1–C_2 core sub-mechanisms upward to larger fuels. High-pressure, intermediate-temperature datasets continue to reveal important kinetic gaps. Herzler [11] reported propane-air ignition delays at 10–30 bar and 900–1300 K, identifying a pronounced drop in apparent activation energy below 1050 K and demonstrating that multiple detailed mechanisms systematically overpredict ignition delays in this region, demonstrating strong low-temperature chain-branching driven by propyl-peroxy isomerisation pathways. Complementary shock-tube work by Walker [31] on CH_4/C_2H_6 mixtures (1180–2248 K, 1 atm) confirmed that modest ethane additions strongly shorten ignition delays, with the largest incremental effect at low ethane fractions, while revealing increasing model experiment divergence as ethane concentration rises. Shock-tube investigations by De Vries & Petersen [9] performed a systematic shock-tube study of methane-based binary and ternary blends (L21 design) at gas-turbine-relevant conditions (20 atm, 800 K, ϕ = 0.5) and they report a mean ignition time near 7.9 ms ($\sigma \approx$ 1.9 ms) for the tested blends and document a pronounced low-temperature (NTC-like) reduction in apparent activation energy that causes ignition to be much faster than extrapolation from high-temperature data would predict, where existing mechanisms fail to capture. Engine-based studies have further confirmed that modifying fuel composition directly affects autoignition delay and combustion phasing, strengthening the broader relevance of ignition delay studies for practical propulsion and energy systems [23]. Early work by Holton et al. [12] measured autoignition delay times in an atmospheric flow reactor for methane, ethane, propane and representative binary/ternary methane-based blends across 930–1140 K and equivalence ratios 0.5–1.25, and measured delays for premixing using a chemical-reactor-network model and found that 5–10 mol% additions of ethane or propane strongly promote methane ignition reducing delays by roughly 30–50%. Comparative studies on blended fuels, however, remain limited. While extensive data exist for pure fuels, fewer systematic studies consider binary blends under engine-relevant conditions. Lowry et al. [18] demonstrated synergistic effects in laminar flame speeds of methane/ethane/propane blends, emphasizing that blending can yield reactivity deviations that cannot be predicted by simple linear interpolation. Jach et al. [14] presented that fuel blending can influence ignition delay through changes in low-temperature radical and peroxide chemistry, for glycerol-doped gasoline and diesel surrogates over wide temperature and pressure ranges. Mixed reactors have also been used to study low-temperature oxidation and PAH production. Wang et al. [33] performed jet-stirred reactor experiments (600–1100 K, ϕ = 0.5–3.0) on acetylene, identifying aromatic intermediates including benzene, toluene, styrene and ethylbenzene, and establishing $C_2 + C_4 \rightarrow$ fulvene $\rightarrow$ benzene as the dominant low-temperature ring-formation route. Their accompanying mechanism (295 species) provided improved agreement for small hydrocarbons and early aromatics, though challenges remain for predicting larger PAHs. Similarly, Shao et al. [25] report high-pressure shock-tube ignition delay data for methane, ethylene, propene, and their binary blends using OH*, pressure, and IR absorption diagnostics, establish temperature-dependent scaling laws, and show strong synergistic effects, with certain CH_4/C_2H_4 mixtures igniting substantially faster than the pure fuels. At the mechanism-development level, multiple NUIG studies have compiled extensive databases of C_1–C_2 ignition delays. More recently, Baigmohammadi et al. [2] consolidated shock-tube and RCM IDTs for pure CH_4, C_2H_4 and C_2H_6 (800–2000 K, 1–80 bar), validating NUIGMech and mapping temperature-dependent sensitivities of RO_2, QOOH and H_2O_2 pathways. A follow-up study, Baigmohammadi et al. [1] extended the analysis to binary C_1-C_2 blends (CH_4/C_2H_6, CH_4/C_2H_4, C_2H_4/C_2H_6), providing improved NUIGMech1.0 validation, detailed sensitivity maps, and empirical ignition-delay correlations for engineering use within specified regimes. Martinez et al. [21] provide a comprehensive experimental and modelling dataset for C_2–C_3 binary blends across a broad range of temperatures (750–2000 K), pressures (1–135 bar), equivalence ratios and dilutions, and demonstrated that updated detailed kinetics in NUIGMech1.1 reveal strong synergistic effects of small propane additions at low temperatures. Cheng et al. [26] performed detailed shock-tube and rapid-compression-machine experiments on gasoline surrogates and ethanol blends, observing pronounced ethanol-induced suppression of low-temperature (NTC) reactivity and the disappearance of first-stage ignition at high ethanol levels, with modest promotion of reactivity at the highest temperatures. Additional mechanistic insight into additive effects comes from numerical reactor studies. The impact of C_2 additions on n-decane ignition was investigated by Huang et al. [13], who reported significant temperature-dependent effects: acetylene consistently increases ignition, ethylene promotes above 1000 K, and ethane inhibits below 1150 K but promotes at higher temperatures. Sensitivity analysis showed how tiny C_2 species may significantly change large-fuel ignition by identifying transitions between H_2O_2-dominated chain branching at low T and HO_2/OH/H-atom chemistry at higher T.

2. Experimental approach

The ignition delay studies were performed using the shock tube available at the Propulsion and High Enthalpy Lab, Karunya Institute of Technology and Sciences. Helium was used as the primary driver gas. To improve post-shock thermodynamic conditions, nitrogen is used as a tailoring gas. The stainless-steel shock tube has an internal diameter of 80 mm, with driver and driven section lengths of 2.0 m and 5.5 m respectively. Diaphragms were made of aluminium Al 6061, 1.2 mm thick, with a cross groove (0.5–0.6 mm) to enable measurements across a range of pressures (2–9 bar). Prior to each experiment, the test section and driven section were vacuumed to a pressure below 10^{-3} bar

using a turbo molecular pump to minimize the contamination effects on ignition delay measurements. Research-grade ethylene, acetylene, oxygen and nitrogen with purity ≥ 99.95% were used. When producing test gas mixtures, the fuel was first introduced into a thin-walled stainless-steel mixing tank at 8 bar using the partial pressure method. A three-test gas mixture was then prepared based on molar fractions using the partial pressure method. After filling, the mixtures were allowed to equilibrate for 30 minutes to ensure compositional homogeneity prior to experimentation. Table 1 displays the designed mixture composition for the experimental test. The shock tube facility used in this study has been extensively used in earlier investigations on ignition delay [22, 27–29], rupture dynamics [19, 30], and blast wave mitigation.

Table 1. Gas mixture compositions

Mixture	Composition	C_2H_4 [%]	C_2H_2 [%]	Φ
1	$C_2H_4/C_2H_2/O_2/N_2$	95%	5%	1
2	$C_2H_4/C_2H_2/O_2/N_2$	90%	10%	1
3	$C_2H_4/C_2H_2/O_2/N_2$	80%	20%	1

Ignition delay time was determined using two diagnostics: (1) excited CH radical (CH*) emission near 431 nm, (ii) sidewall pressure measurements. The shock tube was physically cleaned with argon to reduce the effect of contaminants on the IDT results. Following this procedure, highly repeatable IDT data were obtained. Figure 1 shows the representative pressure and CH* chemiluminescence signals for three ethylene-acetylene/air mixtures at $\phi = 1.0$ from the oscilloscope.

3. Results and discussion

3.1. Ignition delay times for 95% ethylene/5%acetylene/ air mixtures

The reflected-shock temperature (T_5) and pressure (P_5) were computed from the measured incident-shock velocity using standard one-dimensional shock equations. Ignition delay was defined as the time interval between the arrival of the reflected shock and the maximum rate of rise of CH* chemiluminescence at 431 nm, a sensitive indicator of early hydrocarbon breakdown and radical formation. The CH* signal was detected using a photomultiplier with appropriate band-pass filtering. The repeatability of tests was verified through multiple tests at selected conditions, with an estimated overall uncertainty of ±10%, primarily due to uncertainties in temperature determination. Shock strength was adjusted by tailoring the driver gas composition, specifically the helium-to-nitrogen ratio. High-enthalpy conditions were achieved by increasing the helium partial pressure to 8 bar, resulting in higher incident shock velocities.

Ignition delay times for the C_2H_4/C_2H_2 (95/5) fuel-air mixture were measured behind reflected shocks over 580–1020 K and 2.7–8.4 bar. The experimental series covered a Mach number range of 1.67 to 2.45 for the reflected shock wave. Driver pressure (P_4) was varied between 6.4 and 9.3 bar, using different concentrations of Helium to obtain the shock strength. The post-reflected shock pressures (P_5) range from 2.7 bar to 8.4 bar. The data reveal the monotonic decrease in ignition delay with increasing temperature and pressure, represented by the following pressure-dependent Arrhenius correlation:

$$\tau = 4.58 \times 10^{-4} \exp(21930/RT_5)$$

Pearson correlation analysis confirms that temperature is the dominating parameter and ln(τ) exhibits a strong negative correlation with T_5. Reflected-shock pressure also significantly influences reactivity. The ignition delay time for this mixture decreased monotonically as the reflected pressure and temperature increased (Fig. 2 and Fig. 3). The 95/5 mixture exhibited the longest ignition delay times

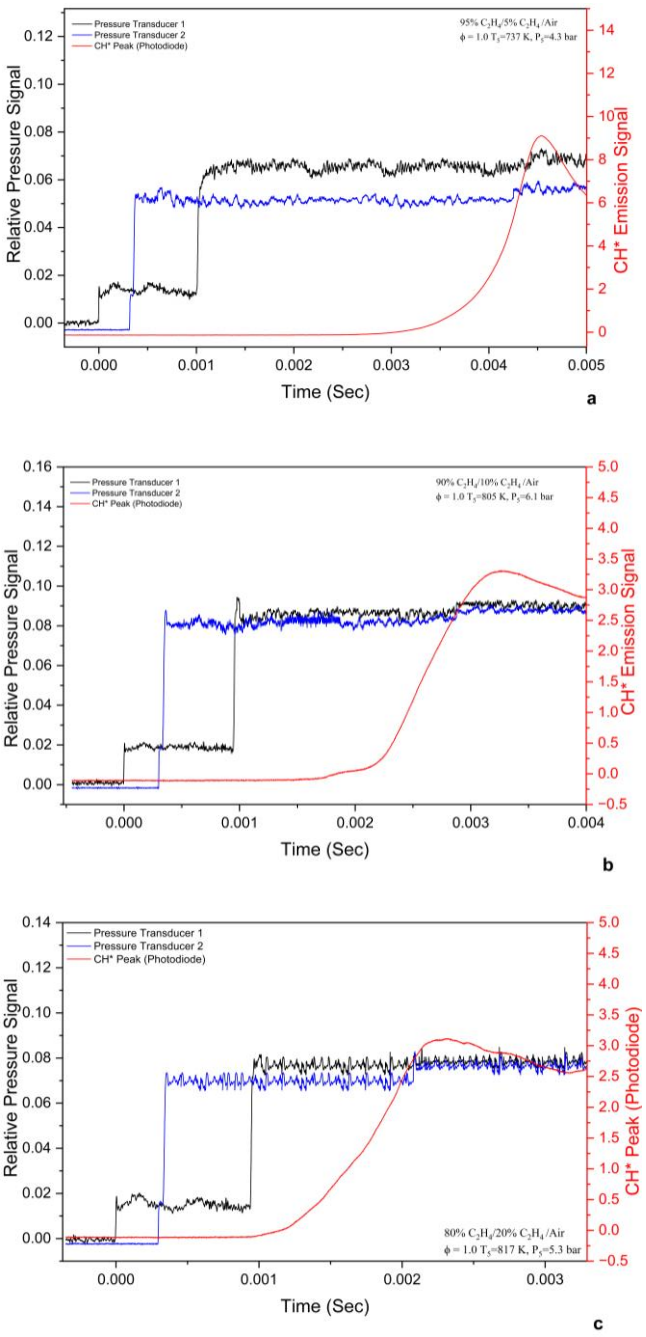

Fig. 1. Representative ignition delay time measurements for ethylene-acetylene/air mixtures at $\phi = 1.0$

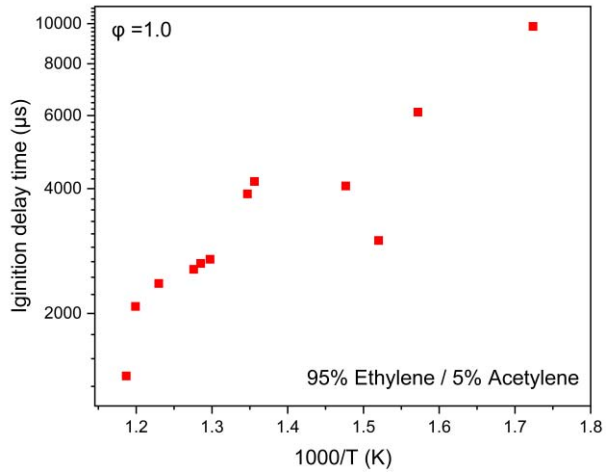

Fig. 2. Arrhenius plot for the ignition delay time of the 95% ethylene / 5% acetylene blend

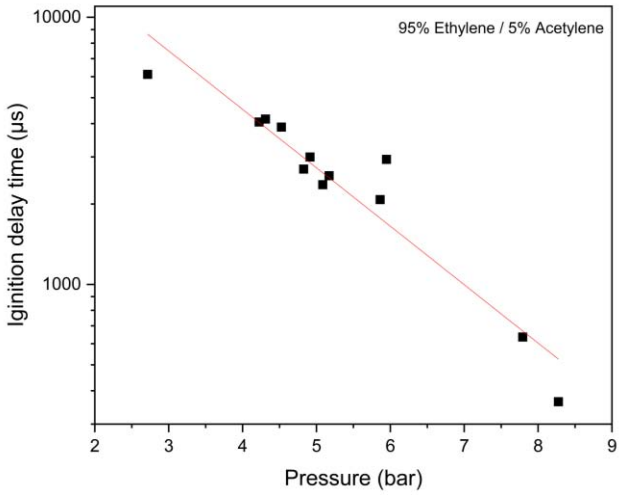

Fig. 3. Variation of ignition delay time with pressure for a 95% ethylene/ 5% acetylene mixture

among the three blends due to its lower oxidation pathways. At high pressure (7–8 bar), ignition delay time decreases, whereas at low pressure (3–4 bar) and temperature < 800 K, ignition delays exceed 6–10 ms.

3.2. Ignition delay times for 90% ethylene/ 10%acetylene/air mixtures

Ignition delay times were measured for a premixed ethylene/acetylene (90/10)-air mixture at an equivalence ratio of ϕ = 1.0 (Fig. 4 & 5) over a reflected-shock temperature range of 560 K to 1026 K. The incident shock Mach numbers range from 1.62 to 2.46, resulting in reflected shock pressures of 2.5-9.0 bar. The study exhibits strong Arrhenius behaviour, with IDT decreasing with increasing temperature. The shortest delay of 315 μs was observed at 1027 K, achieved using a helium-dominant driver gas. However, low-temperature study (560–650 K) highlights longer ignition delays exceeding 8ms, close to the limits of the shock tube's reliable test time. Strong negative statistical correlations indicate that an increase in driver helium fraction and shock strength consistently results in shorter ignition delays. The measured ignition delay times exhibited a strong inverse dependence on reflected shock temperature, consistent with Arrhenius kinetics. The experimental ignition delay times for the 90/10 ethylene-acetylene/air mixture were well represented by the following pressure-dependent Arrhenius correlation:

$$\tau = 2.54 \times 10^{-4} \exp\left(24430/RT_5\right)$$

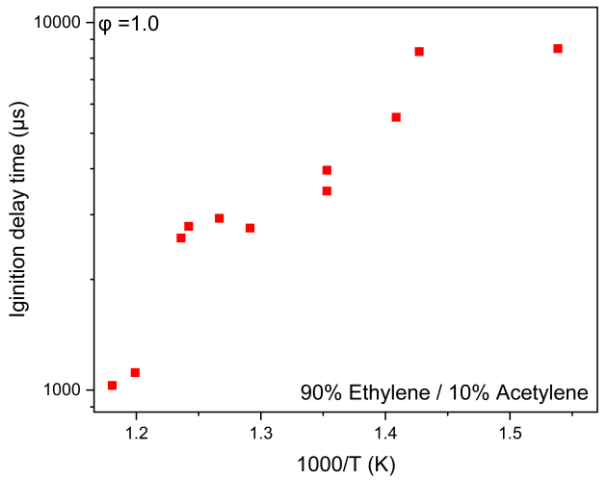

Fig. 4. Arrhenius plot for the ignition delay time of the 90% ethylene/10% acetylene blend

Influence diagnostics identify one low-temperature shot (T_5 = 560 K) as highly influential. Raw pressure and CH* traces for this data are inspected and found to be error-free. Hence, the point is retained in the global fit but noted as a possible exemplar of enhanced low-temperature variability.

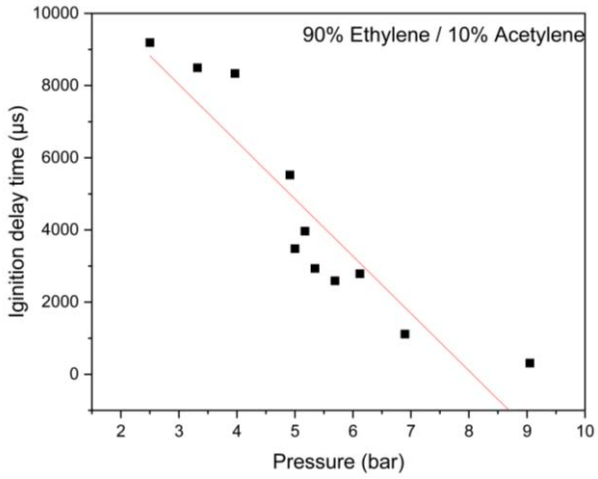

Fig. 5. Variation of ignition delay time with pressure for a 90% ethylene/ 10% acetylene mixture

The 90/10 mixture shows shorter ignition delays than the 95/5 blend, indicating the strong impact of increasing acetylene concentration. At a given pressure, ignition delays are about 40–60% shorter than in the 95/5 mixture.

3.3. Ignition delay times for 80% ethylene/ 20%acetylene/air mixtures

Ignition delay time measurements were obtained for a premixed 80% ethylene/20% acetylene-air mixture at an equivalence ratio of ϕ = 1.0 (Fig. 6 and Fig. 7). The post-

reflected-shock conditions spanned a temperature range of 650–870 K and pressures of 3.5–6.5 bar, covering the low to intermediate temperature ignition regime relevant to high-speed propulsion applications. The 80/20 mixture is the most reactive among the three blends and displays much shorter ignition delays.

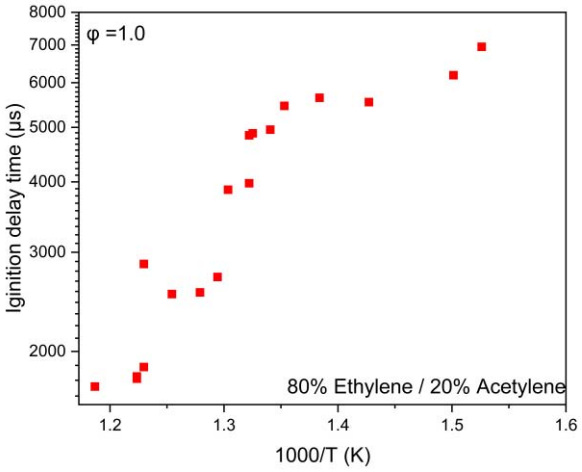

Fig. 6. Arrhenius plot for the ignition delay time of the 80% ethylene/20% acetylene blend

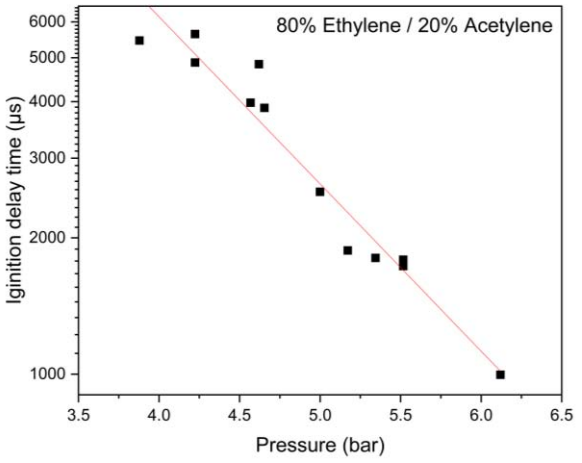

Fig. 7. Variation of ignition delay time with pressure for 80% ethylene/ 20% acetylene mixture

The measured ignition delays exhibit a strong Arrhenius-type temperature dependence. The statistical correlations demonstrate that driver composition and shock strength parameters strongly influence ignition delay. Increased helium fraction, higher shock velocity, and higher shock Mach number all correlate with progressively shorter ignition delays. These factors increase incident-shock strength and raise the reflected-shock temperature, thereby accelerating the production of H, O, and OH radicals. At low temperatures (650–700 K), longer ignition delays up to 7 ms were observed, indicating slow radical buildup dominated by peroxy and HO_2 chemistry. In the intermediate range (720–790 K), the measured data show a rapid decrease in delay time, consistent with the onset of high-temperature chain-branching reactions. At higher temperatures (> 800 K), ignition occurs rapidly (< 2 ms) due to accelerated decomposition pathways in acetylene and ethylene. Repeatability was confirmed at intermediate temperatures, specifically, three independent shocks near 815 K yielded highly consistent IDTs clustered around 1800 ±50 μs.

A mild pressure dependence was observed, with τ decreasing approximately as $P^{-0.6}$. The experimental data were fitted using a modified Arrhenius correlation of the form:

$$\tau = 7.1 \times 10^{-5} \exp(40300/RT_5)$$

The fitted correlation aligns well with the experimental ignition delay time between 650–870 K and 4–6 bar. With $R^2 = 0.808$, the model captures nearly 81% of the variance in ln(τ) based on temperature and pressure dependencies. The RMSE in ln-space was 0.219, which corresponds to a multiplicative 1σ uncertainty factor of 1.24, or roughly ±24% deviation between measured and predicted ignition delay times. This level of scatter is consistent with reflected-shock ignition measurements at low and intermediate temperatures, where small uncertainties in T_5 (±5–10 K) produce large exponential variations in ignition delay.

3.4. Comparative effect of acetylene addition on ignition delay

Comparison of ignition delay times for the three ethylene-acetylene/air blends investigated in this study (Fig. 8). IDT measurements for acetylene [27] and ethylene [15] were performed using the same facility (Table 2). Under similar temperature and pressure conditions, increasing acetylene fraction results in a monotonic reduction in ignition delay time. Approximately at 800 K and 4 bar, the 90/10 blend ignites 40–50% faster than the 95/5 mixture, while the 80/20 blend exhibits a further reduction of 20–30%.

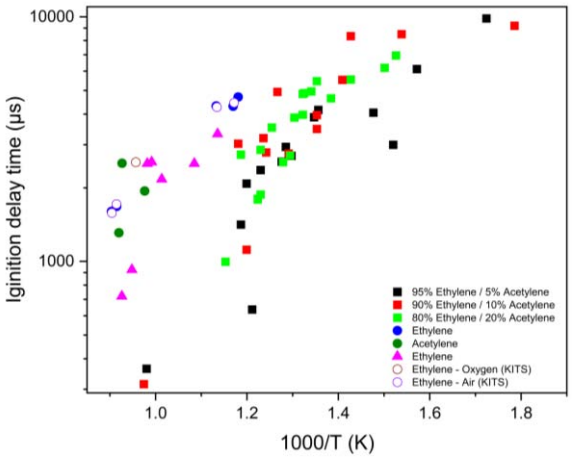

Fig. 8. Arrhenius plot comparing ignition delay times for various ethylene/ acetylene fuel blends and pure components

Table 2. Ignition delay trends for ethylene- acetylene blends

Blend	Relative IDT	Pressure sensitivity	Dominant chemistry
95/5	Longest	Strong	HO_2–H_2O_2 dominated
90/10	Intermediate	Moderate	Mixed HO_2/HCCO
80/20	Shortest	Weak	HCCO-driven OH

4. Kinetic modelling

In this work, CHEMKIN simulations were carried out using four mechanisms – NUIG [34], ARAMCO [35], LLNL [20], and SD [5] to evaluate autoignition of three mixtures. IDT is defined numerically as the maximum gradient of temperature and OH/CH radical concentration with respect to time for the shock tube simulations. All mechanisms failed to predict ignition below 750 K, indicating the absence of low-temperature peroxy and QOOH pathways that are essential for C_2 hydrocarbon oxidation. In the temperature region (900–1100 K), the NUIG and ARAMCO mechanisms produced physically reasonable ignition delay trends, with NUIG showing the closest agreement to experimental timescales and Arrhenius behaviour. In contrast, the LLNL and SD mechanisms displayed non-physical trends, including excessively long delays and increased ignition times at higher temperatures. Among the mechanisms considered, NUIG exhibits the highest computational cost, followed by Aramco, LLNL and San Diego mechanism. This is mainly due to differences in the number of species, reactions, and pressure-dependent formulations included in each mechanism. Across all four mechanisms, increasing acetylene content systematically reduces the ignition delay.

4.1. Ignition kinetics of ethylene-acetylene blends using the ARAMCO mechanism

Sensitivity analysis (Fig. 9) identifies $H_2O_2(+M) \rightleftharpoons 2OH(+M)$ as the key promoting reaction for ignition across all three blends, controlling the transition from HO_2-dominated induction phase to rapid OH-driven chain branching. The sensitivity of this reaction increases with acetylene fraction, and reaches a maximum for the 80% ethylene-20% acetylene mixture, indicating a stronger dependence of ignition on peroxide decomposition in acetylene-rich blends. Additionally, $C_2H_4 + HO_2 \rightleftharpoons C_2H_4O + OH$ and $C_2H_3 + O_2 \rightleftharpoons CH_2CHO + O$, directly contribute to OH and atomic oxygen formation, reflecting enhanced coupling between ethylene oxidation and acetylene-derived radical pathways.

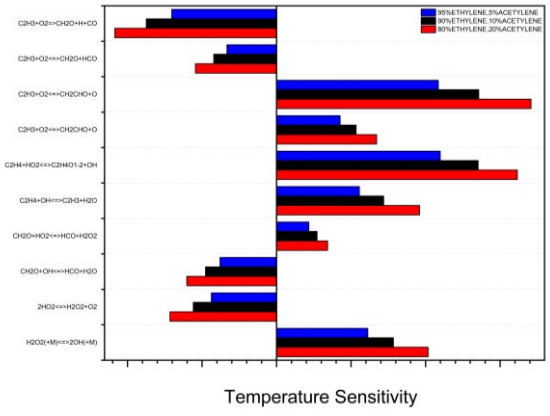

Fig. 9. Temperature sensitivity analysis (Aramco mechanism)

The dominant inhibiting reactions (Fig. 9) include $2HO_2 \rightleftharpoons H_2O_2 + O_2$, $CH_2O + OH \rightleftharpoons HCO + H_2O$, and $C_2H_3 + O_2 \rightarrow CH_2O + HCO$, which suppress ignition by recombining radicals into less reactive reservoirs. Although these inhibiting pathways remain significant for all mixtures, their influence decreases with increasing acetylene content, indicating that acetylene-derived radical chemistry compensates for radical losses. Table 3 summarises the dominant reactions for 95% C_2H_4 / 5% C_2H_2 (Aramco).

Table 3. Top sensitivity reactions – Aramco mechanism (95% C_2H_4/5% C_2H_2)

Rank	Reaction	Sensitivity	Effect
1	$C_2H_4 + HO_2 \rightleftharpoons C_2H_4O + OH$	2198	Accelerates ignition
2	$C_2H_3 + O_2 \rightleftharpoons CH_2CHO + O$	2171	Accelerates ignition
3	$H_2O_2 (+M) \rightleftharpoons 2OH (+M)$	1225	Accelerates ignition
4	$C_2H_3 + O_2 \rightleftharpoons CH_2O + HCO$	-667	Inhibits ignition
5	$CH_2O + OH \rightleftharpoons HCO + H_2O$	-760	Inhibits ignition

ROP analysis at 850 K and 2 bar (Fig. 10–12) reveals that OH formation is dominated by $O_2 + H \rightleftharpoons O + OH$, followed by $O + H_2O \rightleftharpoons 2OH$ and $HO_2 + H \rightleftharpoons 2OH$. The contribution of these reactions increases with the acetylene fraction, particularly for $O_2 + H \rightleftharpoons O + OH$, indicating greater availability of atomic hydrogen. This enhancement arises from acetylene oxidation pathways involving HCCO and CH_2CO chemistry, leading to earlier radical runaway in acetylene mixtures. The dominant OH absorption reactions include $CO + OH \rightleftharpoons CO_2 + H_2$, $CH_2O + OH \rightleftharpoons HCO + H_2O$, and $HCCO + OH \rightarrow H_2 + 2CO$, with the importance of HCCO related OH consumption increasing as acetylene fraction raises. HCCO formation is dominated by $C_2H_2 + O \rightleftharpoons HCCO + H$, with secondary contribution from $CH_2CO + H \rightleftharpoons HCCO + H_2$ and $CH_2CO + OH \rightleftharpoons HCCO + H_2O$, confirming acetylene as primary driver of C_2 radical chemistry. HCCO consumption occurs mainly through reactions with OH, O, and H, which regenerate H and O atoms, and directly reinforce OH formation pathways. The H_2O_2 ROP study confirms that peroxide chemistry acts as the primary ignition bottleneck, H_2O_2 accumulates primarily through HO_2 recombination and subsequently decomposes through

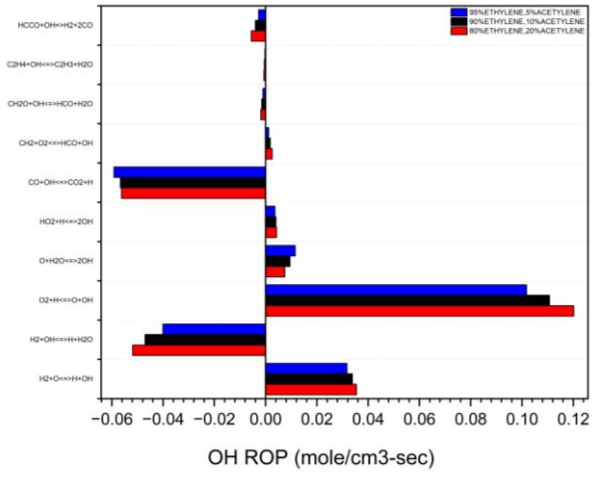

Fig. 10. Rate of production analysis of OH (Aramco mechanism)

$H_2O_2(+M) \rightleftharpoons 2OH(+M)$, triggering rapid OH release. Increasing acetylene fraction, enhances the net decomposition rate of H_2O_2, thereby accelerating the transition from HO_2 controlled chemistry to OH dominated chain branching.

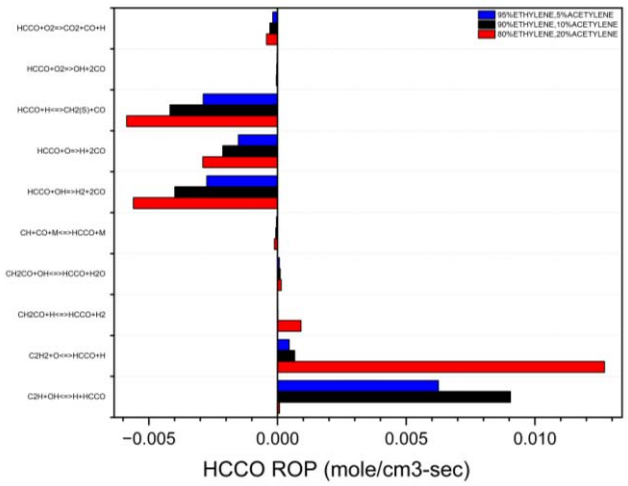

Fig. 11. Rate of production analysis of HCCO (Aramco mechanism)

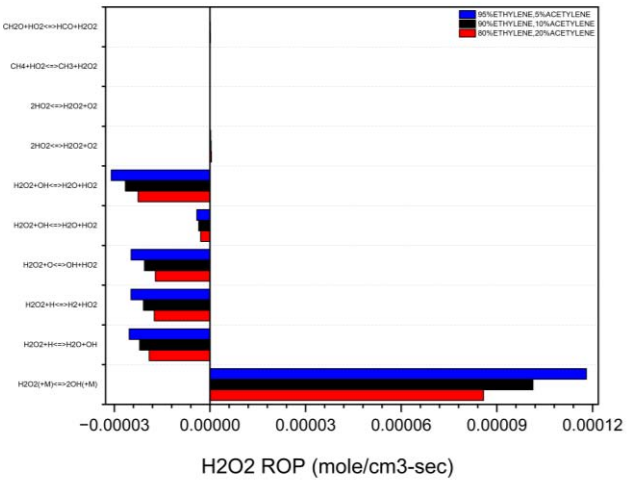

Fig. 12. Rate of production analysis of H_2O_2 (Aramco mechanism)

4.2. Ignition kinetics of ethylene–acetylene blends using the LLNL mechanism

The sensitivity study using the LLNL mechanism at 850 K and 2 bar presented (Fig. 13) reveals that ignition of ethylene-acetylene mixtures is predominantly governed by peroxide-driven radical branching. Across all three blends, the most influential ignition-promoting reaction is $2OH (+M) \rightleftharpoons H_2O_2 (+M)$, confirming that ignition onset is controlled by transition from a peroxide-dominated radical reservoir to rapid OH chain branching. In addition, acetylene oxidation exhibits strong positive sensitivity, particularly $C_2H_2 + O_2 \rightleftharpoons HCCO + OH$, demonstrating that LLNL mechanism strongly couples acetylene consumption to OH formation, partially bypassing slower HO_2 mediated pathways. The sensitivity decreases with decreasing acetylene fraction but remains significant even at 5% acetylene. Ethylene abstraction reactions such as $C_2H_4 + OH \rightleftharpoons C_2H_3 + H_2O$ also promote ignition by accelerating fuel breakdown and radical propagation. The dominant inhibiting reactions (Fig. 17), includes $C_2H_3 + O_2 \rightleftharpoons CH_2O + HCO$, $CH_2O + OH \rightleftharpoons HCO + H_2O$, and $H_2O_2 + OH \rightleftharpoons H_2O + HO_2$, suppress ignition by redirecting reactive radicals into less active reservoirs. Table 4 summarises the dominant reactions identified in sensitivity analysis for 80% C_2H_4/20% C_2H_2 (LLNL)

Table 4. Top sensitivity reactions – LLNL mechanism (80% C_2H_4/20% C_2H_2)

Rank	Reaction	Sensitivity	Effect
1	$C_2H_2 + O_2 \rightleftharpoons HCCO + OH$	7166	Accelerates ignition
2	$2OH (+M) \rightleftharpoons H_2O_2 (+M)$	5126	Accelerates ignition
3	$C_2H_3 + O_2 \rightleftharpoons CH_2HCO + O$	3813	Accelerates ignition
4	$C_2H_3 + O_2 \rightleftharpoons CH_2O + HCO$	–3723	Inhibits ignition
5	$C_2H_4 + OH \rightleftharpoons C_2H_3 + H_2O$	2256	Accelerates ignition

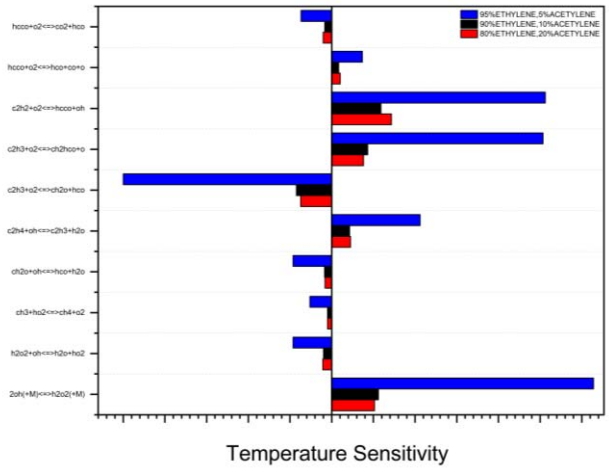

Fig. 13. Temperature sensitivity analysis (LLNL mechanism)

The OH ROP analysis (Fig. 14) indicates that OH production in the LLNL mechanism is dominated by H-O interconversion reactions once sufficient atomic oxygen is available, with $O + H_2 \rightleftharpoons OH + H$ and $O + OH \rightleftharpoons O_2 + H$. dominating during the rapid ignition phase. HO_2 chemistry indirectly serves primarily as a precursor to H2O2, which subsequently decomposes, triggering OH runaway. Increasing the acetylene fraction moderately enhances OH production by increasing the availability of H and O atoms. However, peroxide decomposition remains the principal ignition trigger across all blends.

HCCO (Fig. 15) emerges as a key intermediate in the LLNL mechanism linking to radical regeneration. HCCO formation is dominated by $C_2H_2 + O \rightleftharpoons HCCO + H$, with secondary contributions from CH_2CO based pathways. HCCO consumption occurs primarily through reactions with H, O, and OH, all of which regenerate H and O atoms, thereby yielding OH.

The H_2O_2 ROP analysis (Fig. 16) confirms that peroxide chemistry acts as the rate-limiting ignition bottleneck in the LLNL mechanism. During the induction period, H_2O_2 is

slowly formed by HO_2 recombination and decomposes rapidly near ignition, releasing OH and initiating chain branching. Although acetylene addition slightly accelerates decomposition by increasing radical availability, peroxide breakdown remains the controlling step for ignition across all mixtures.

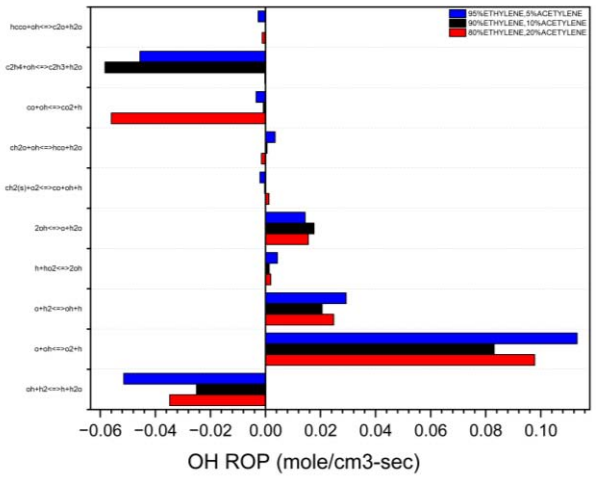

Fig. 14. Rate of production analysis of OH (LLNL mechanism)

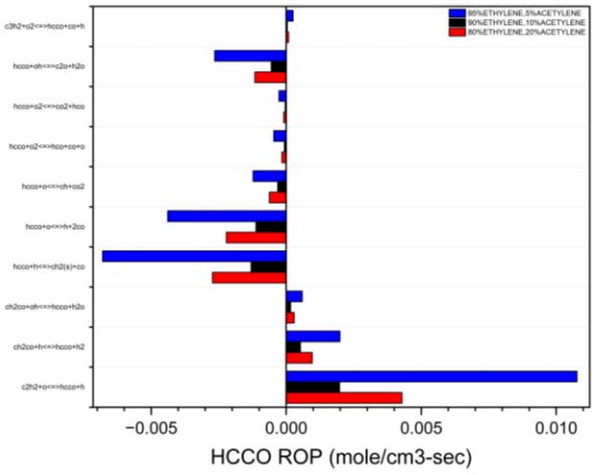

Fig. 15. Rate of production analysis of HCCO (LLNL mechanism)

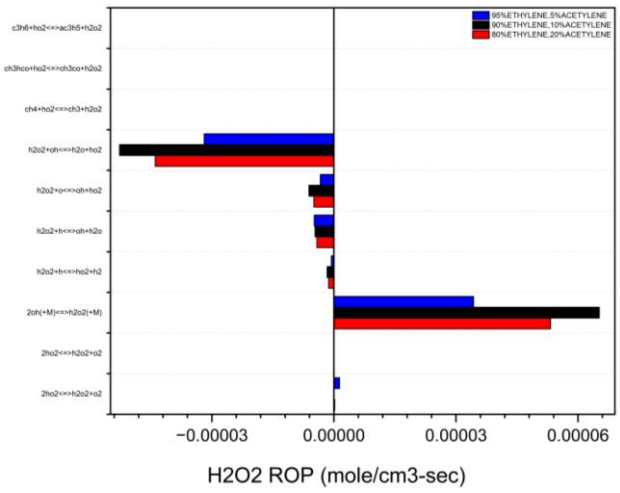

Fig. 16. Rate of production analysis of H_2O_2 (LLNL mechanism)

4.3. Ignition kinetics of ethylene–acetylene blends using SD mechanism

The sensitivity study using the SD mechanism at 850 K and 2 bar (Fig. 17) shows that the ignition of ethylene–acetylene blends is primarily governed by peroxide-controlled chemistry. The dominant reaction across all mixtures is 2OH (+M) ⇌ H_2O_2 (+M), indicating that ignition onset is dictated by the transition from HO_2/H_2O_2 dominated chemistry to rapid OH radical chain branching.

This sensitivity increases with acetylene fraction and is highest for the 90/10 and 80/20 mixtures, highlighting the significance of peroxide-controlled ignition pathways. Furthermore, promoting reactions include C_2H_4 + HO_2 ⇌ C_2H_4O + OH and C_2H_2 + OH ⇌ C_2H_3 + H_2O, highlighting the role of fuel-assisted conversion in accelerating ignition (Table 5). In contrast, reactions such as $2HO_2$ ⇌ H_2O_2 + O_2 and CH_2O + OH ⇌ HCO + H_2O retard ignition by limiting OH buildup.

Table 5. Top sensitivity reactions – SD mechanism (90% C_2H_4/10% C_2H_2)

Rank	Reaction	Sensitivity	Effect
1	C_2H_3 + O_2 ⇌ CH_2CHO + O	16695	Accelerates ignition
2	C_2H_3 + O_2 ⇌ CH_2O + HCO	–14180	Inhibits ignition
3	C_2H_4 + HO_2 ⇌ C_2H_4O + OH	9935	Accelerates ignition
4	2OH (+M) ⇌ H_2O_2 (+M)	8037	Accelerates ignition
5	CH_2O + OH ⇌ HCO + H_2O	–1900	Inhibits ignition

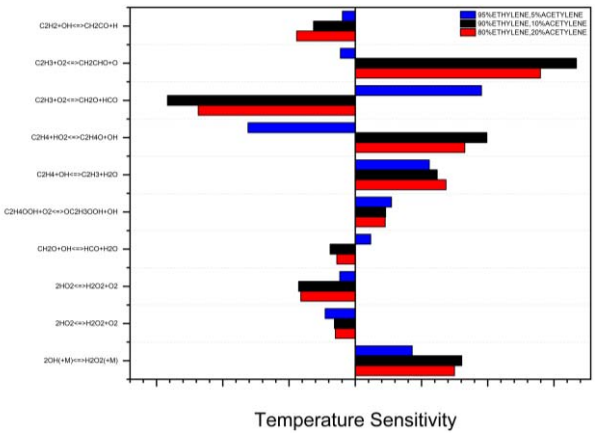

Fig. 17. Temperature sensitivity analysis (SD mechanism)

ROP analysis (Fig. 18–20), reveals that OH formation in the SD mechanism is dominated by classical H-O chain-branching reactions, with H + O_2 ⇌ OH + O as principal source of OH once ignition is initiated. Increasing acetylene fraction enhances the contribution of these reactions by increasing the availability of H and O atoms through C_2 chemistry. OH consumption pathway is dominated by CO + OH ⇌ CO_2 + H, CH_2O + OH ⇌ HCO + H_2O, and CH_3 + OH ⇌ CH_2 + H_2O, which act as strong sinks during the induction period.

The HCCO formation (Fig. 19) is dominated by C_2H_2 + O ⇌ HCCO + H, with additional contributions from ketene related pathways. The monotonic increase in HCCO for-

mation with acetylene fraction confirms that acetylene directly enhances C_2 radical chemistry. HCCO consumption occurs primarily through H, O and O_2, regenerating reactive radicals and contributing to chain branching. Despite this enhancement, the H_2O_2 ROP analysis (Fig. 20) reveals that peroxide decomposition remains the dominant ignition bottleneck in the SD mechanism, with acetylene addition moderately accelerating the transition to OH-dominated chemistry.

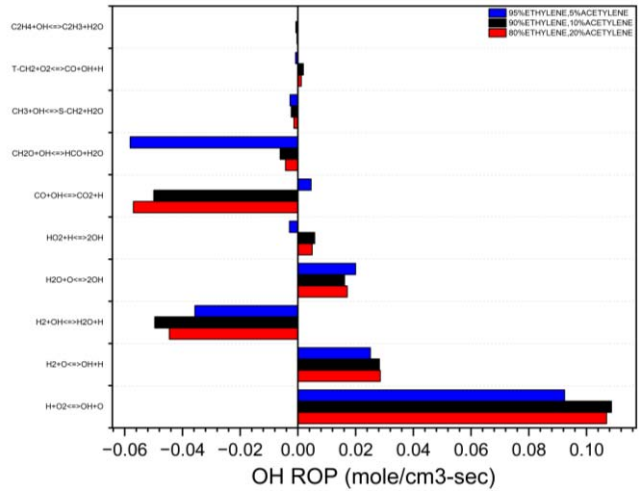

Fig. 18. Rate of production analysis of OH (SD mechanism)

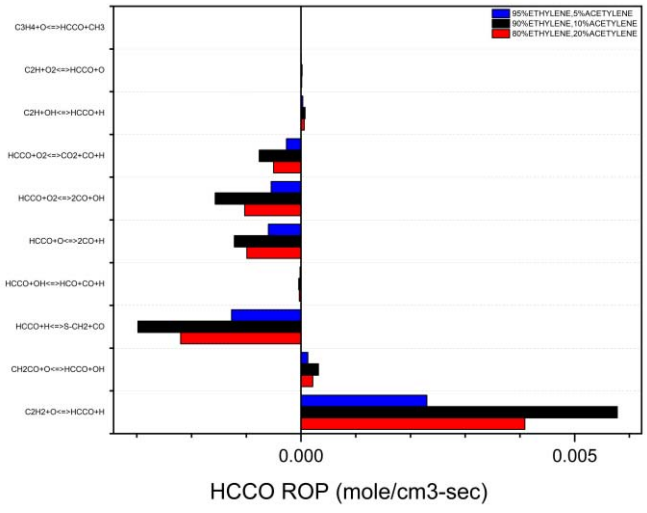

Fig. 19. Rate of production analysis of HCCO (SD mechanism)

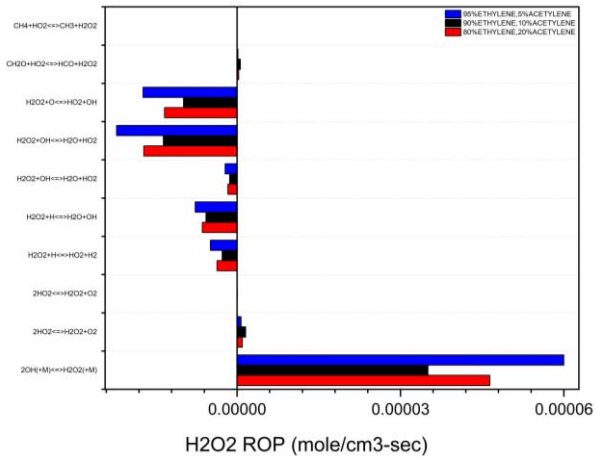

Fig. 20. Rate of production analysis of H_2O_2 (SD mechanism)

5. Conclusion

Ignition delay characteristics of binary ethylene–acetylene/air mixtures were experimentally investigated in a shock tube over 560–1030 K and 2.5–9 bar at ϕ = 1.0 for three blend ratios. The ignition delay time decreases with increasing acetylene fraction, with reductions up to ~60% for an 80% C_2H_4–20% C_2H_2 mixture relative to a 95% C_2H_4–5% C_2H_2 mixture at comparable temperature – pressure conditions. Among the tested blends, the 80% ethylene–20% acetylene mixture exhibits the shortest ignition delays and the earliest onset of OH radical emission, while the 95% ethylene 5% acetylene mixture displays the longest induction periods and the greatest pressure sensitivity. Arrhenius correlations confirm that temperature remains the dominant controlling parameter, with acetylene addition gradually shifting toward faster ignition.

The systematic underprediction of ignition reactivity by all kinetic mechanisms (NUIG, ARAMCO, LLNL, and San Diego) below 750 K highlights persistent deficiencies in low-temperature C_2 oxidation chemistry and in cross-fuel radical coupling. Across all mechanisms, ignition is controlled by HO_2–H_2O_2 chemistry, with thermal decomposition of H_2O_2 acting as the primary trigger for OH radical runaway. Acetylene enhances ignition by strengthening HCCO-mediated radical-regeneration pathways, increasing H and O atom availability, and accelerating the transition from peroxide-controlled induction to chain-branching chemistry. These findings demonstrate that acetylene addition can significantly enhance ethylene ignition under short-residence-time conditions, providing direct guidance for fuel formulation and kinetic model development for scramjet and high-speed propulsion systems.

Nomenclature

A	pre-exponential factor
C_2H_4	ethylene
C_2H_2	acetylene
CH_2O	formaldehyde
CH*	chemiluminescence of the excited CH radical
E_a	apparent activation energy
HCO	formyl radical
HO_2	hydroperoxyl radical
H_2O_2	hydrogen peroxide
HCCO	ketyl radical
OH	hydroxyl radical
IDT	ignition delay time
LLNL	Lawrence Livermore National Laboratory mechanism

NUIG	National University of Ireland, Galway mechanism	SD	San Diego mechanism
ROP	rate of production	τ	ignition delay time

Bibliography

[1] Baigmohammadi M, Patel V, Nagaraja S, Ramalingam A, Martinez S, Panigrahy S. Comprehensive experimental and simulation study of the ignition delay time characteristics of binary blended methane, ethane, and ethylene over a wide range of temperature, pressure, equivalence ratio, and dilution. Energy Fuels. 2020;34(7):8808-8823. https://doi.org/10.1021/acs.energyfuels.0c00960

[2] Baigmohammadi M, Patel V, Martinez S, Panigrahy S, Ramalingam A, Burke U. A comprehensive experimental and simulation study of ignition delay time characteristics of single fuel C1-C2 hydrocarbons over a wide range of temperatures, pressures, equivalence ratios, and dilutions. Energy Fuels. 2020;34(3):3755-3771. https://doi.org/10.1021/acs.energyfuels.9b04139

[3] Boruc ŁJ, Kapusta J, Kindracki J. Selection of the method for determination of ignition delay of hypergolic propellants. Combustion Engines. 2024;199(4):104-111. https://doi.org/10.19206/CE-192420

[4] Burcat A, Scheller K, Lifshitz A. Shock-tube investigation of comparative ignition delay times for C1-C5 alkanes. Combust Flame. 1971;16(1):29-33. https://doi.org/10.1016/S0010-2180(71)80007-X

[5] Chemical-kinetic mechanisms for combustion applications. San Diego Mechanism Web Page. University of California San Diego. Available from: http://combustion.ucsd.edu

[6] Dagaut P, Boettner JC, Cathonnet M. Ethylene pyrolysis and oxidation: A kinetic modeling study. Int J Chem Kinet. 1990;22(6):641-664. https://doi.org/10.1002/kin.550220608

[7] Dagaut P, Cathonnet M, Boettner J. Kinetics of ethane oxidation. Int J Chem Kinet. 1991;23(5):437-455. https://doi.org/10.1002/kin.550230509

[8] De Vries J, Hall JM, Simmons SL, Rickard MJA, Kalitan DM. Ethane ignition and oxidation behind reflected shock waves. Combust Flame. 2007;150:137-150. https://doi.org/10.1016/j.combustflame.2006.10.008

[9] De Vries J, Petersen EL. Autoignition of methane-based fuel blends under gas turbine conditions. Proc Combust Inst. 2007;31(2):3163-3171. https://doi.org/10.1016/j.proci.2006.07.206

[10] Gallagher SM, Curran HJ, Metcalfe WK, Healy D, Simmie JM, Bourque G. Rapid compression machine study of propane oxidation in the negative temperature coefficient regime. Combust Flame. 2008;153(1-2):316-333. https://doi.org/10.1016/j.combustflame.2007.09.004

[11] Herzler J, Jerig L, Roth P. Shock-tube study of the ignition of propane at intermediate temperatures and high pressures. Combust Sci Technol. 2004;176(10):1627-1637. https://doi.org/10.1080/00102200490487201

[12] Holton M, Gokulakrishnan P, Klassen MS, Roby RJ, Jackson GS. Autoignition delay time measurements of methane, ethane, and propane pure fuels and methane-based fuel blends. J Eng Gas Turbines Power. 2010;132(9):1-9. https://doi.org/10.1115/1.4000590

[13] Huang J, Li F, Qi Y. Comparative study on the impact of ethane/ethylene/acetylene addition on ignition of fuel-rich n-decane/air flame. Bull Ser B. 2020;82(4):185-198.

[14] Jach I, Cieślak I, Teodorczyk A. Investigation of glycerol doping on ignition delay times and laminar burning velocities of gasoline and diesel fuel. Combustion Engines. 2017;169(2):167-175. https://doi.org/10.19206/ce-2017-230

[15] Kesavan M, Sundararaj AJ, Williams M, Konda S, Kumar W. Experimental investigation of auto ignition of ethylene and propulsion grade kerosene. Russ J Phys Chem B. 2025; 19(6):1338-1352. https://doi.org/10.1134/S1990793125701076

[16] Kopp M, Donato NS, Petersen EL, Metcalfe WK, Burke SM, Curran HJ. Oxidation of ethylene-air mixtures at elevated pressures, part 1: experimental results. J Propuls Power. 2014;30(3):790-798. https://doi.org/10.2514/1.B34890

[17] Leschevich VV, Martynenko VV, Penyazkov OG, Sevrouk KL, Shabunya SI. Auto-ignitions of a methane/air mixture at high and intermediate temperatures. Shock Waves. 2016; 26(5):657-672. https://doi.org/10.1007/s00193-016-0665-9

[18] Lowry W, De Vries J, Krejci M, Petersen E, Serinyel Z, Metcalfe W. Laminar flame speed measurements and modeling of pure alkanes and alkane blends at elevated pressures. J Eng Gas Turbines Power. 2011;133(9):1-9. https://doi.org/10.1115/1.4002809

[19] Lyle JL, Guna KR, Kumar P, Sundararaj AJ. Rupture dynamics of shock-tube diaphragm. Proc Int Conf Recent Adv Aerosp Eng (ICRAAE). 2017:1-4. https://doi.org/10.1109/ICRAAE.2017.8297207

[20] Marinov NM, Pitz WJ, Westbrook CK, Vincitore AM, Castaldi MJ. Aromatic and polycyclic aromatic hydrocarbon formation in a laminar premixed n-butane flame. Combust Flame. 1998;114(1-2):192-213. https://doi.org/10.1016/S0010-2180(97)00275-7

[21] Martinez S, Patel V, Panigrahy S, Sahu A, Nagaraja B. Experimental and kinetic modeling study of ignition delay characteristics of ethane/propane and ethylene/propane blends. Combust Flame. 2021;228:401-414. https://doi.org/10.1016/j.combustflame.2021.02.009

[22] Rose MS, Sundararaj AJ, Kumar S. Investigation of ignition delay of hydrocarbon fuel using shock tube. Int J Pure Appl Math. 2018;118(20):3687-3692.

[23] Sander R, Longwic R, Tarkowski S. Analysis of the influence of the n-hexane content in the mixture with rapeseed oil on the auto-ignition delay angle of the fuel. Combustion Engines. https://doi.org/10.19206/CE-211729

[24] Saxena S, Kahandawala MSP. Shock tube study of ignition delay in the combustion of ethylene. Combust Flame. 2011;158(6):1019-1031. https://doi.org/10.1016/j.combustflame.2010.10.011

[25] Shao J, Davidson DF. Shock tube study of ignition delay times in diluted methane, ethylene, propene and their blends at elevated pressures. Fuel. 2018;225:370-380. https://doi.org/10.1016/j.fuel.2018.03.146

[26] Song C, Saggese C, Kang D, Goldsborough SS, Wagnon SW, Kukkadapu G. Autoignition and heat release of gasoline surrogates and ethanol blends at engine-relevant conditions. Combust Flame. 2021;228:57-77. https://doi.org/10.1016/j.combustflame.2021.01.033

[27] Sundararaj AJ, Pillai BC, Subash AN, Haran AP, Kumar P. Investigation of ignition delay for low molecular weight hydrocarbon fuel using shock tube in reflected shock mode. J Geol Soc India. 2019;93:218-220. https://doi.org/10.1007/s12594-019-1155-3

[28] Sundararaj AJ, Pillai BC, Guna KR. Effect of temperature on ignition behaviour of seeded refined kerosene. Thermochim Acta. 2020;683:178469. https://doi.org/10.1016/j.tca.2019.178469
[29] Sundararaj AJ, Guna KR, William M. Effect of temperature on ignition of modified kerosene. Int J Engine Res. 2022; 23(3):460-468. https://doi.org/10.1177/1468087420988191
[30] Sundararaj AJ, Jose D, Sunny A, John ST, Kumar N, Gopalsamy. Effect of blast pressure on discrete models using a shock tube. Proc Int Conf Recent Adv Aerosp Eng (ICRAAE). 2017:1-4. https://doi.org/10.1109/ICRAAE.2017.8297238
[31] Walker BC. Shock-tube investigation of ignition delay times of blends of methane and ethane with oxygen. Aerosp Eng Commons. 2007. https://stars.library.ucf.edu/etd/3399/
[32] Wan Z, Zheng Z, Wang Y, Zhang D, Li P, Zhang C. Shock tube study of ethylene/air ignition characteristics over a wide temperature range. Combust Sci Technol. 2020; 192(12):2297-2305. https://doi.org/10.1080/00102202.2019.1643333
[33] Wang H, Liu Y, Weng J, Glarborg P, Tian Z. New insights in low-temperature oxidation of acetylene. Proc Combust Inst. 2017;36(1):355-363. https://doi.org/10.1016/j.proci.2016.06.163
[34] Wang H, Dames E, Sirjean B, Sheen DA, Tango R, Violi A. High-temperature chemical kinetic model of n-alkanes and cycloalkanes oxidation (JetSurF). Available from: http://web.stanford.edu/group/haiwanglab/JetSurF/
[35] Zhou CW, Li Y, Burke U, Banyon C, Somers KP. Experimental and kinetic modeling study of 1,3-butadiene combustion: ignition delay time and laminar flame speed measurements. Combust Flame. 2018;197:423-438. https://doi.org/10.1016/j.combustflame.2018.08.006

Kesavan Marimuthu – Division of Aerospace Engineering, Karunya Institute of Technology and Sciences, India.
e-mail: *m.kesavan02@gmail.com*

Aldin Justin Sundararaj – Division of Aerospace Engineering, Karunya Institute of Technology and Sciences, India.
e-mail: *aldinjustin@karunya.edu*

Abhijith Girish Nair – Division of Aerospace Engineering, Karunya Institute of Technology and Sciences, India.
e-mail: *abhijithg.n963@gmail.com*

Thangapandi Muthumari – Division of Aerospace Engineering, Karunya Institute of Technology and Sciences, India.
e-mail: *t.muthumarikesavan@gmail.com*

Article citation info:
Bebkiewicz K, Grzelak P, Chłopek Z, Biernat K. Modeling of stochastic passenger car velocity processes for the purpose of pollutant emissions inventory. Combustion Engines. 2026;206(3):151-158. https://doi.org/10.19206/CE-218133

Katarzyna BEBKIEWICZ
Paulina GRZELAK
Zdzisław CHŁOPEK
Krzysztof BIERNAT

Combustion Engines
Polish Scientific Society of Combustion Engines

Modeling of stochastic passenger car velocity processes for the purpose of pollutant emissions inventory

ARTICLE INFO

Received: 10 May 2025
Revised: 8 February 2026
Accepted: 9 February 2026
Available online: 3 March 2026

This paper discusses the potential use of stochastic processes as road vehicle velocity models for road transport emissions inventory purposes. Empirical studies have presented stochastic passenger-car velocity models, each modeling traffic conditions: in traffic congestion, in cities outside traffic congestion, outside cities, and on highways and expressways. Zero-dimensional characteristics of the model velocity processes have been examined. The characteristics of passenger car emissions for 2020 have been determined using simulation methods. Road pollutant emissions from passenger cars under specific velocity process implementations have been determined and analyzed. The research results have been assessed, among other things, for their variability. Based on the results, the feasibility of using stochastic processes as road vehicle velocity models for road transport emissions inventory purposes has been assessed.

Key words: *road transport, inventory of pollutant emissions, vehicle velocity processes, stochastic processes*

This is an open access article under the CC BY license (http://creativecommons.org/licenses/by/4.0/)

1. Introduction

In the inventory of pollutant emissions, in accordance with the guidelines in force in the European Union [5–7], means of road transport are classified into categories based on:

– intended use
– conventional size
– combustion engine properties
– fuel
– technical level.

A category is a set of entities with specific characteristics and interconnected by relationships.

The elementary category of road vehicles is the set of vehicles that meet all the same criteria. The set of road vehicles that do not all share the same criteria is a cumulative category.

Cumulative vehicle categories based on their use are [5-7]:

– passenger cars – PC
– light commercial vehicles (light duty vehicles) – LCV
– heavy-duty trucks (heavy-duty vehicles) – HDT
– urban buses – UB
– long-distance buses (coaches) – C
– motorcycles, mopeds, quads, and microcars – L.

Fuel consumption and pollutant emissions from internal combustion engines depend on their operating states [4], including engine speed, load (most often measured by torque), and the engine's thermal state. The engine's thermal state can be described by the set of temperatures of engine parts and their operating fluids, primarily the engine oil and, in the case of indirect engine cooling, the coolant. With a stabilized engine thermal state, fuel consumption and pollutant emissions depend on engine speed and load. In static engine operating conditions, these are functional dependencies (functions with numerical values), while in dynamic conditions, they are operational dependencies (functional) [4].

For road vehicle engines, the engine operating states are determined by the vehicle velocity process. Therefore, pollutant emissions and fuel consumption can be tested under vehicle traffic conditions (light vehicles: passenger cars, light duty vehicles, minibuses, and L-category vehicles) [15] or under conditions simulating vehicle traffic, as is the case with heavy vehicles (trucks and buses), where the tests involve the engine itself, in states simulating the engine states in vehicle traffic [6, 15, 16].

There are many publications presenting results of tests on pollutant emissions and fuel consumption from road vehicles (mainly light vehicles) under various conditions, as determined by different tests, including road conditions in the RDE (Real Driving Emissions) test [1, 6, 15].

In real driving conditions, there is a degree of uncertainty in engine operating states, primarily due to the uncertainty in the vehicle velocity process. This justifies treating the vehicle process as a stochastic process [11, 12]. A model of a stochastic process can be a set of its realizations [11, 12]. For this reason, this paper addresses problems related to research on fuel consumption and pollutant emissions under stochastic vehicle velocity processes.

2. Stochastic driving tests of a passenger car

The task of determining the realization of stochastic passenger car velocity processes was undertaken as part of our own work.

Figures 1–4 present four realizations of stochastic passenger car vehicle processes in traffic conditions [5, 7]: in traffic congestion – C, in cities outside traffic congestion – U, outside cities – R, and on highways and expressways – H.

The individual realizations were determined based on empirical studies of vehicle velocity in real driving conditions [1, 4]. For each traffic model, several dozen (more than 20) realizations of the velocity process were recorded at a frequency of 1 Hz. Then, based on the analysis of the zero-dimensional statistical characteristics of the recorded waveforms, four representative realizations of the modeled stochastic vehicle velocity processes were selected.

Each realization was processed using a Savitzky-Golay filter of second order [14] to reduce high-frequency noise in the signals [9, 10, 13].

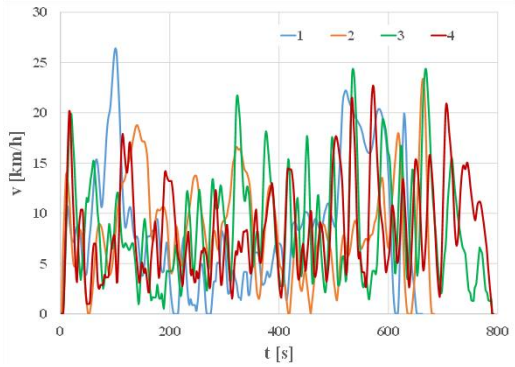

Fig. 1. Stochastic CT test: driving in cities in traffic congestion (own research)

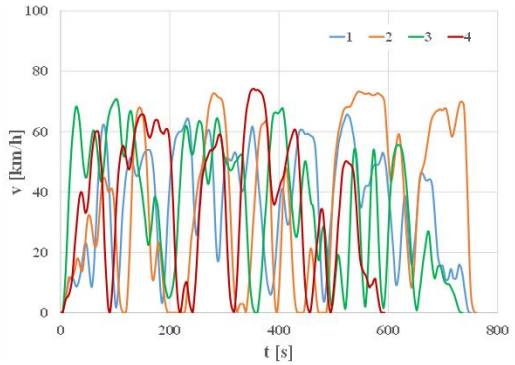

Fig. 2. Stochastic UT test: driving in cities outside traffic congestion (own research)

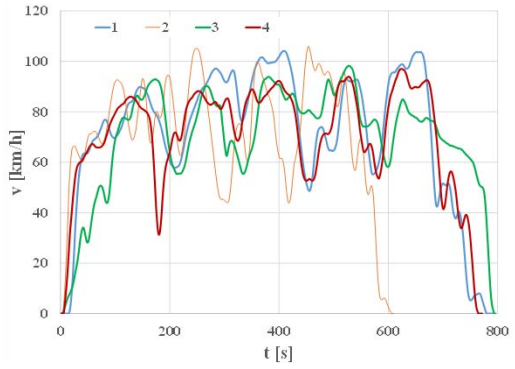

Fig. 3. Stochastic RT test: driving outside cities (own research)

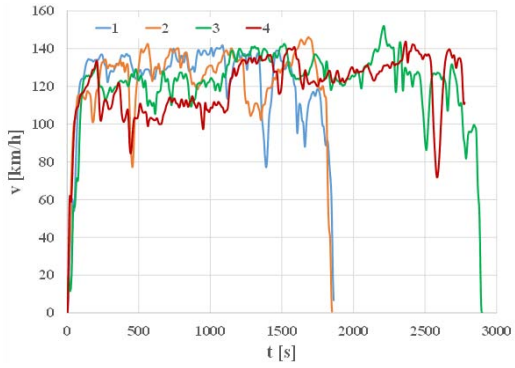

Fig. 4. Stochastic HT test: driving on highways and expressways (own research)

The individual implementations of the stochastic velocity models show many similarities, which will be quantitatively confirmed in the next chapter.

3. Driving test analysis

Table 1 presents the results of the statistical analysis of individual driving test implementations – zero-dimensional characteristics of individual implementations [9]:
Min – minimum value, Max – maximum value, Rg – range, AV – mean value, D – standard deviation, W – coefficient of variation.

Table 1. Zero-dimensional characteristics of driving tests

Test type	1	2	3	4	Min
	v_{AV} [km/h]				
CT	8.59	8.51	8.54	8.45	8.45
UT	36.04	36.00	35.98	36.02	35.98
RT	70.73	70.59	69.57	70.66	69.57
HT	122.49	122.99	121.38	117.94	117.94
Test type	Max	Rg	AV	D	W
	v_{AV} [km/h]				
CT	8.59	0.14	8.52	0.059	0.007
UT	36.04	0.06	36.01	0.025	0.001
RT	70.73	1.16	70.39	0.549	0.008
HT	122.99	5.05	121.20	2.276	0.019

Figure 5 shows the mean, minimum, and maximum values of the average velocity for individual model processes.

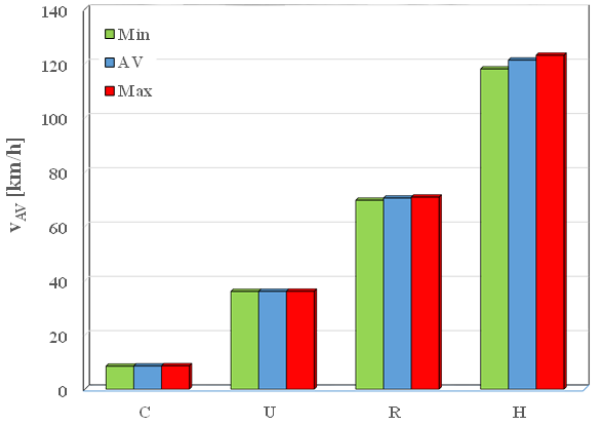

Fig. 5. Average value – AV, minimum value – Min and maximum value – Max of average velocity values – V_{AV} in model traffic conditions in stochastic tests: C – cities in traffic congestions, U – cities outside traffic congestions, R – outside cities, H – on motorways and expressways

In urban traffic conditions, there is virtually no difference between the minimum and maximum average velocity values. The largest difference occurs for driving on motorways and expressways. Figure 6 presents the coefficient of variation of the velocity process for driving under model traffic conditions in individual implementations, as well as the average value of the coefficient of variation – AV.

The coefficient of variation is highest for the traffic model in traffic congestion, which results from the low average velocity – approximately 8.5 km/h. The coefficient of variation is lowest for driving on motorways and expressways – in this case, the average velocity is greater than

120 km/h. Figure 7 presents the coefficient of variation of the average velocity in individual process implementations under the model traffic conditions.

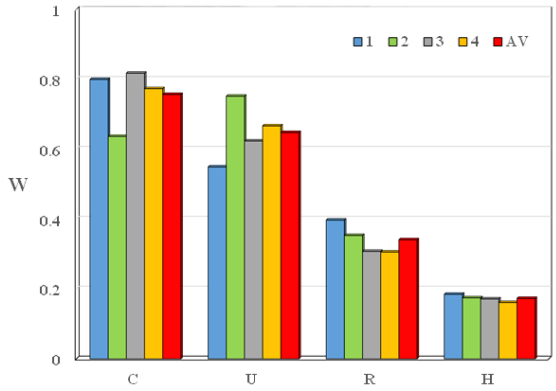

Fig. 6. Coefficient of variation of the velocity process for driving in model traffic conditions in individual realizations: in cities in traffic congestions – C, in cities outside traffic congestions – U, outside cities – R and on motorways and expressways – H and the average value of the coefficient of variation – AV

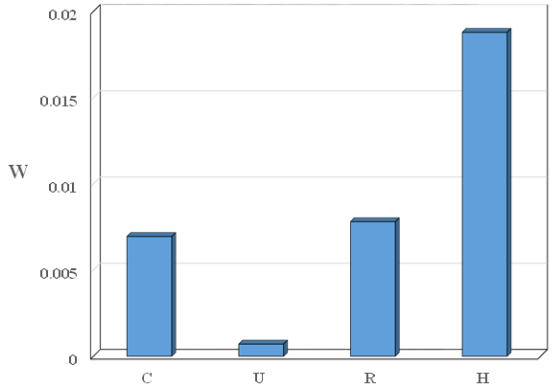

Fig. 7. Coefficient of variation of the average velocity value in individual process realizations in model traffic conditions: C – cities in traffic congestions, U – cities outside traffic congestions, R – outside cities, H – on motorways and expressways

The greatest uniformity in average velocity across individual tests is observed for traffic in cities outside congestion, and the least for traffic on highways and expressways. Overall, the numerical values of the zero-dimensional characteristics of individual implementations indicate that implementations under the same model conditions exhibit significant similarity.

4. Sensitivity of fuel consumption and pollutant emissions to engine operating states in driving tests

To assess the sensitivity of fuel consumption and pollutant emissions to engine operating states during driving tests, test results for the passenger car category were obtained for 2020. Fuel consumption and pollutant emissions characteristics were determined using INFRAS software [8] for the state of engines heated to a stable temperature for all possible driving models. Average values were determined for mass fuel consumption (q), which is the derivative of the mass of fuel consumed relative to the distance traveled by the vehicle, and for road pollutant emissions (b), which is the derivative of pollutant emissions relative to the distance traveled by the vehicle.

The pollutants considered were as follows: carbon monoxide (CO); hydrocarbons (HC); nitrogen oxides (NO_x); particulate matter (PM); and carbon dioxide (CO_2).

The sets of values of average mass road fuel consumption and road pollutant emissions as functions of average velocity were approximated by a fourth-degree polynomial function. This resulted in the characteristics shown in Fig. 8–13.

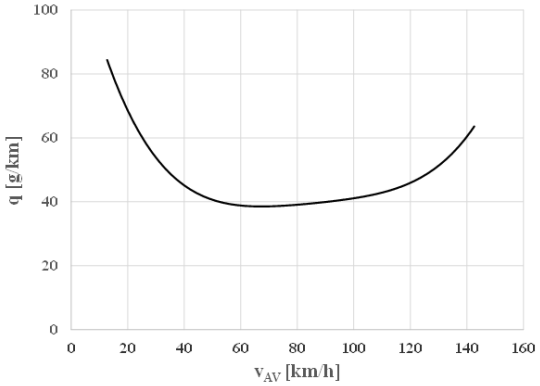

Fig. 8. Dependence of mass road fuel consumption on average velocity for the cumulative category of passenger cars in 2020

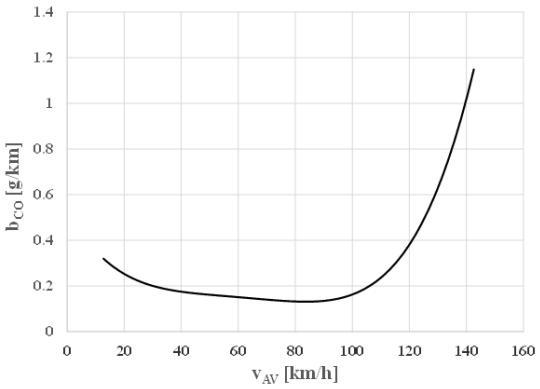

Fig. 9. Dependence of road carbon monoxide emissions on average velocity for the cumulative category of passenger cars in 2020

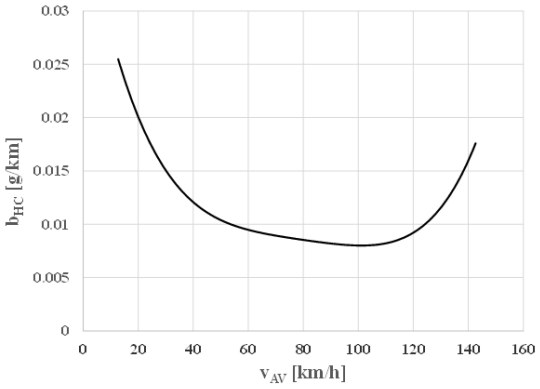

Fig. 10. Dependence of road hydrocarbon emissions on average velocity for the cumulative category of passenger cars in 2020 (own research)

The specific characteristics determined are typical for passenger car engines with respect to pollutant emissions

and fuel consumption [1, 4]. The zero-dimensional characteristics of mass road fuel consumption and road pollutant emissions are presented in Tables 2–5.

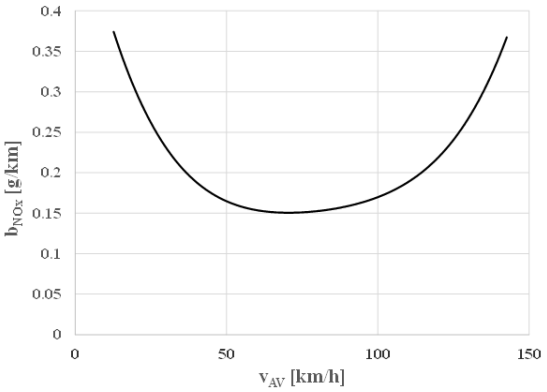

Fig. 11. Dependence of road emissions of nitrogen oxides on the average velocity for the cumulative category of passenger cars in 2020

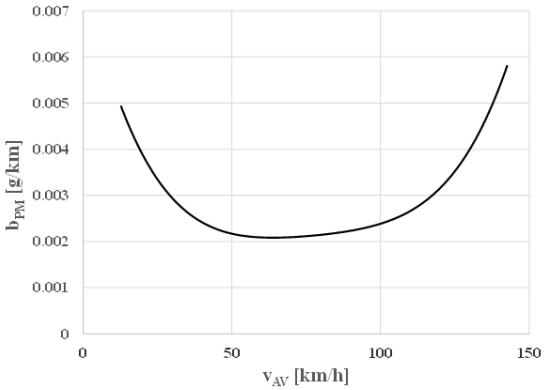

Fig. 12. Dependence of road particulate matter emissions on average velocity for the cumulative category of passenger cars in 2020

Table 2. Zero-dimensional characteristics of mass road fuel consumption and road pollutant emissions in cities in traffic congestions – C

Parameter	1	2	3	4	Min
	[g/km]				
q	95.7	95.9	95.8	96.1	95.7
b_{CO}	0.373	0.374	0.373	0.375	0.373
b_{HC}	0.029	0.029	0.029	0.030	0.029
b_{NOx}	0.426	0.427	0.427	0.428	0.426
b_{PM}	0.006	0.006	0.006	0.006	0.006
b_{CO2}	267.3	267.9	267.7	268.5	267.3
Parameter	Max	Rg	AV	D	W
	[g/km]				
q	96.1	0.4	95.9	0.176	0.002
b_{CO}	0.375	0.002	0.37	0.001	0.002
b_{HC}	0.030	0.000	0.03	0.000	0.002
b_{NOx}	0.428	0.002	0.43	0.001	0.002
b_{PM}	0.006	0.000	0.01	0.000	0.002
b_{CO2}	268.5	1.18	267.8	0.490	0.002

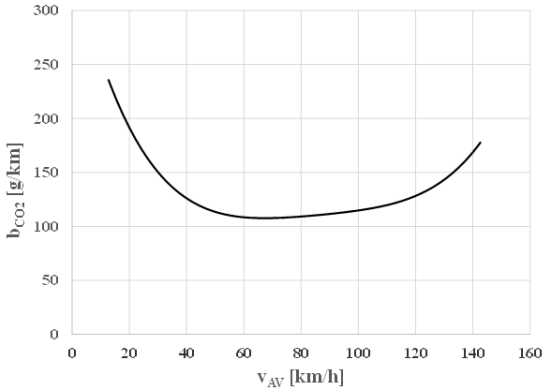

Fig. 13. Dependence of road carbon dioxide emissions on average velocity for the cumulative category of passenger cars in 2020 (own research)

Table 3. Zero-dimensional characteristics of mass road fuel consumption and road pollutant emissions in urban driving conditions outside traffic congestions – U

Parameter	1	2	3	4	Min
	[g/km]				
q	49.9	125.5	125.5	125.5	49.9
b_{CO}	0.183	0.183	0.183	0.183	0.183
b_{HC}	0.013	0.013	0.013	0.013	0.013
b_{NOx}	0.203	0.203	0.203	0.203	0.203
b_{PM}	0.003	0.003	0.003	0.003	0.003
b_{CO2}	134.0	134.1	134.1	134.0	134.0
Parameter	Max	Rg	AV	D	W
	[g/km]				
q	125.5	75.5	106.6	37.76	0.354
b_{CO}	0.183	0.000	0.18	0.000	0.000
b_{HC}	0.013	0.000	0.01	0.000	0.001
b_{NOx}	0.203	0.000	0.20	0.000	0.000
b_{PM}	0.003	0.000	0.00	0.000	0.000
b_{CO2}	134.1	0.13	134.1	0.06	0.000

Table 4. Zero-dimensional characteristics of mass road fuel consumption and road pollutant emissions in non-urban driving conditions – R

Parameter	1	2	3	4	Min
	[g/km]				
q	59.1	125.5	125.5	125.5	59.1
b_{CO}	0.140	0.140	0.141	0.140	0.140
b_{HC}	0.009	0.009	0.009	0.009	0.009
b_{NOx}	0.151	0.151	0.151	0.151	0.151
b_{PM}	0.002	0.002	0.002	0.002	0.002
b_{CO2}	107.8	107.8	107.7	107.8	107.7
Parameter	Max	Rg	AV	D	W
	[g/km]				
q	125.5	66.4	108.9	33.198	0.305
b_{CO}	0.141	0.001	0.140	0.001	0.004
b_{HC}	0.009	0.000	0.01	0.000	0.003
b_{NOx}	0.151	0.000	0.15	0.000	0.000
b_{PM}	0.002	0.000	0.00	0.000	0.001
b_{CO2}	107.8	0.08	107.7	0.04	0.000

The uniformity of average road fuel consumption values is strongest for urban driving and weakest for driving on highways and expressways. Figures 15–19 present the average road pollutant emissions under model traffic condi-

tions for the average velocity of individual implementations and the entire test.

Table 5. Zero-dimensional characteristics of mass road fuel consumption and road pollutant emissions in driving conditions on motorways and expressways – H

Parameter	1	2	3	4	Min
	[g/km]				
q	199.6	125.5	125.5	125.5	125.5
b_{CO}	0.432	0.443	0.408	0.344	0.344
b_{HC}	0.010	0.010	0.009	0.009	0.009
b_{NOx}	0.229	0.231	0.224	0.211	0.211
b_{PM}	0.003	0.003	0.003	0.003	0.003
b_{CO2}	131.3	131.9	129.9	126.1	126.1
Parameter	Max	Rg	AV	D	W
	[g/km]				
q	199.6	74.1	144.1	37.036	0.257
b_{CO}	0.443	0.099	0.41	0.044	0.109
b_{HC}	0.010	0.001	0.01	0.000	0.039
b_{NOx}	0.231	0.020	0.22	0.009	0.040
b_{PM}	0.003	0.000	0.00	0.000	0.046
b_{CO2}	131.9	5.838	129.8	2.612	0.020

Figure 14 shows the average value of mass road fuel consumption in model traffic conditions for the average velocity of individual realizations and the entire test.

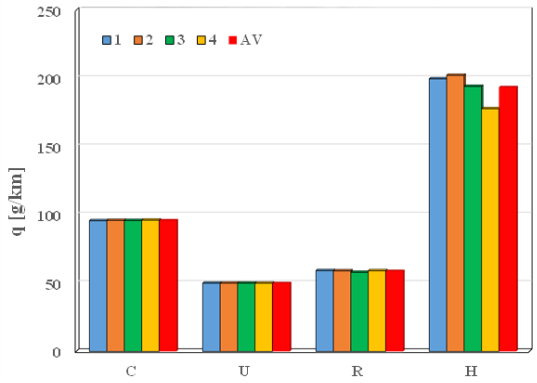

Fig. 14. Average value of mass road fuel consumption – q in model traffic conditions in stochastic tests: C – cities in traffic congestions, U – cities outside traffic congestions, R – outside cities, H – on motorways and expressways

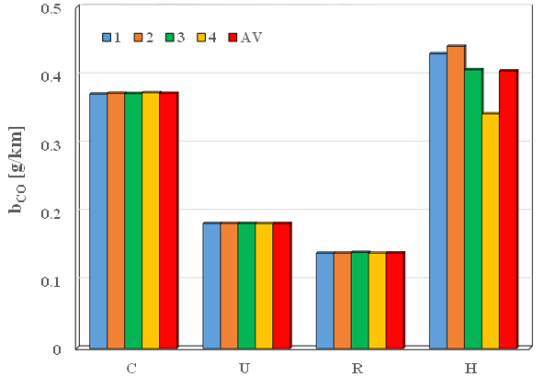

Fig. 15. Average value of road carbon monoxide emissions – b_{CO} in model traffic conditions in stochastic tests: C – cities in traffic congestions, U – cities outside traffic congestions, R – outside cities, H – on motorways and expressways

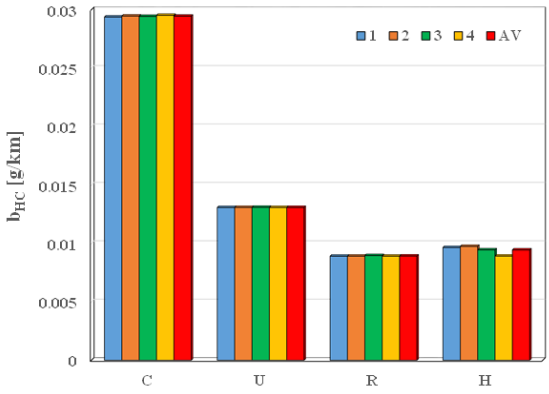

Fig. 16. Average road emissions of hydrocarbons – b_{HC} in model traffic conditions in stochastic tests: C – cities in traffic congestions, U – cities outside traffic congestions, R – outside cities, H – on motorways and expressways

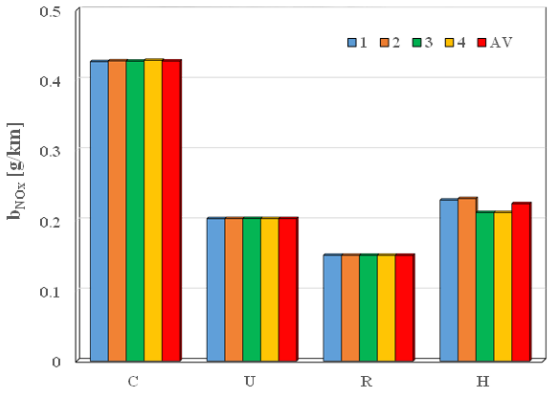

Fig. 17. Average road emissions of nitrogen oxides – b_{NOx} in model traffic conditions in stochastic tests: C – cities in traffic congestions, U – cities outside traffic congestions, R – outside cities, H – on motorways and expressways

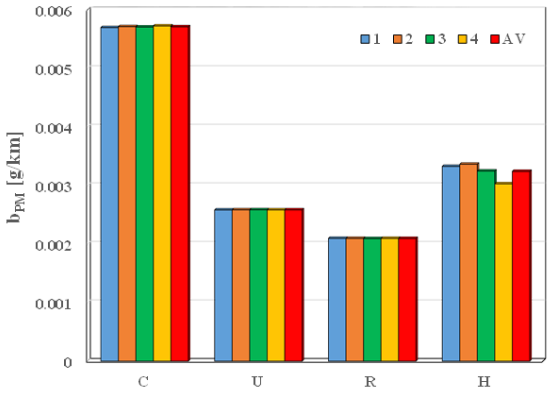

Fig. 18. Average value of road emissions of particulate matter – b_{PM} in model traffic conditions in stochastic tests: C – cities in traffic congestions, U – cities outside traffic congestions, R – outside cities, H – on motorways and expressways

Similarly, for pollutant emissions, uniformity of road emissions is strongest for vehicle traffic in cities and outside cities, and weakest for traffic on highways and expressways. This is confirmed by the coefficients of variation of the average mass road fuel consumption and road emissions of pollutants in individual process implementations under model traffic conditions – Fig. 20–25.

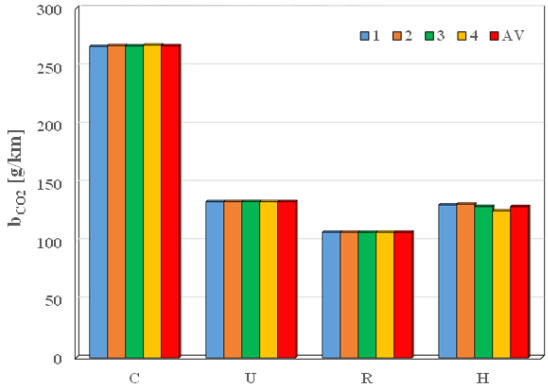

Fig. 19. Average value of road carbon dioxide emissions – b_{CO2} in model traffic conditions in stochastic tests: C – cities in traffic congestions, U – cities outside traffic congestions, R – outside cities, H – on motorways and expressways

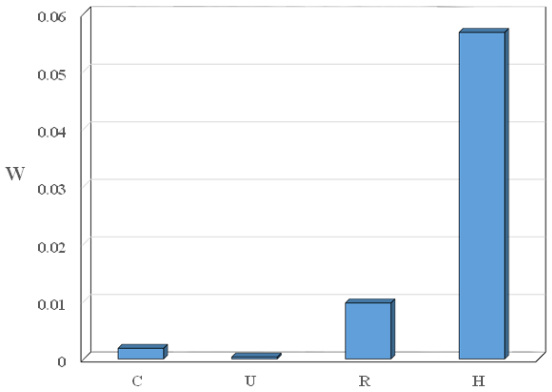

Fig. 20. Coefficient of variation of the average value of mass road fuel consumption in individual process realizations in model traffic conditions in stochastic tests: C – cities in traffic congestions, U – cities outside traffic congestions, R – outside cities, H – on motorways and expressways

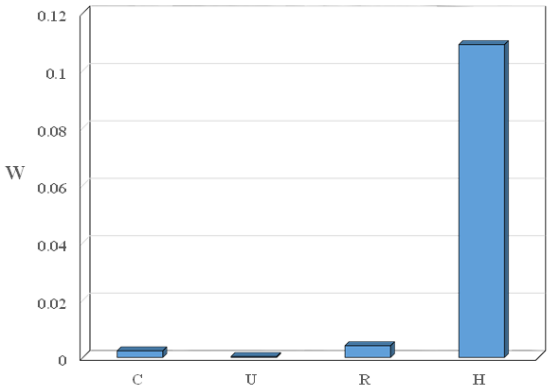

Fig. 21. Coefficient of variation of the average road carbon monoxide emission value in individual process realizations under model traffic conditions in stochastic tests: C – cities in traffic congestions, U – cities outside traffic congestions, R – outside cities, H – on motorways and expressways

Figures 26–29 present the coefficients of variation of the average mass road fuel consumption and road pollutant emissions in individual process realizations under model traffic conditions.

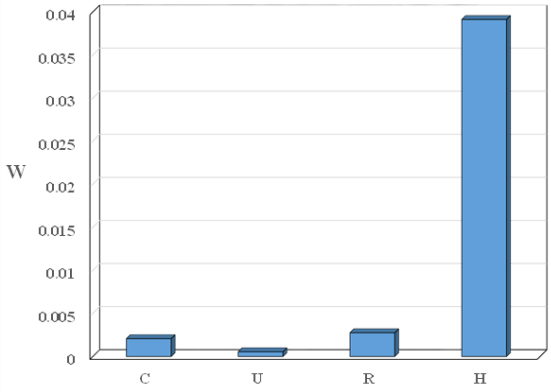

Fig. 22. Coefficient of variation of the average road hydrocarbon emission value in individual process realizations under model traffic conditions in stochastic tests: C – cities in traffic congestions, U – cities outside traffic congestions, R – outside cities, H – on motorways and expressways

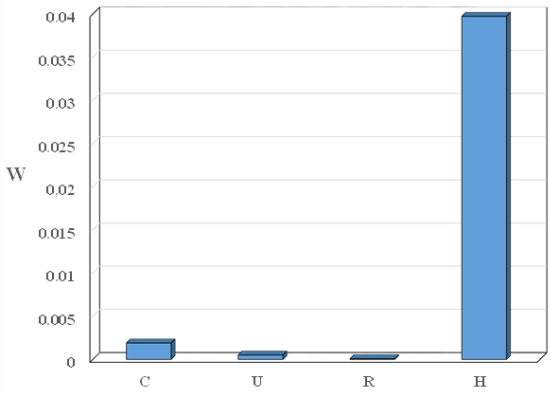

Fig. 23. Coefficient of variation of the average road emission value of nitrogen oxides in individual process realizations under model traffic conditions in stochastic tests: C – cities in traffic congestions, U – cities outside traffic congestions, R – outside cities, H – on motorways and expressways

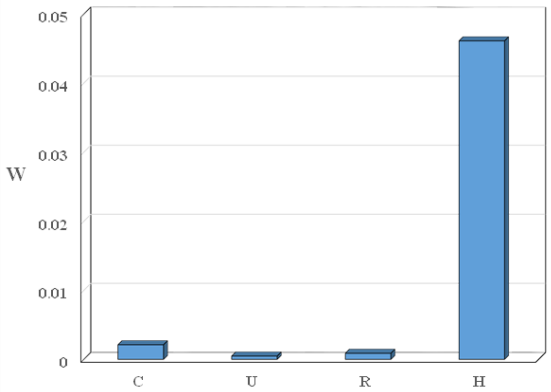

Fig. 24. Coefficient of variation of the average road particulate matter emission value in individual process realizations under model traffic conditions in stochastic tests: C – cities in traffic congestions, U – cities outside traffic congestions, R – outside cities, H – on motorways and expressways

The coefficient of variation in modeled traffic conditions and for individual pollutants and fuel consumption varies without any apparent regularity. However, the variation in average road fuel consumption and road pollutant emissions is not significant, demonstrating that fuel con-

sumption and pollutant emissions are not highly sensitive to engine operating states resulting from the modeled stochastic vehicle velocity processes.

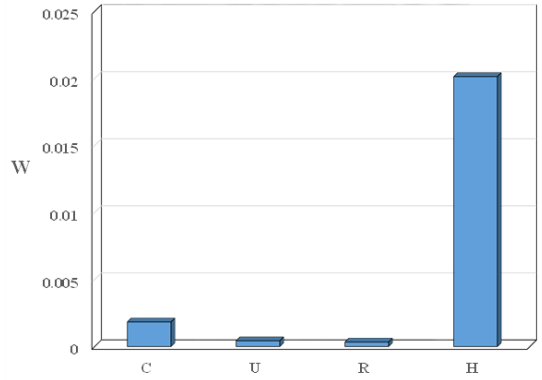

Fig. 25. Coefficient of variation of the average road carbon dioxide emission value in individual process realizations under model traffic conditions in stochastic tests: C – cities in traffic congestions, U – cities outside traffic congestions, R – outside cities, H – on motorways and expressways

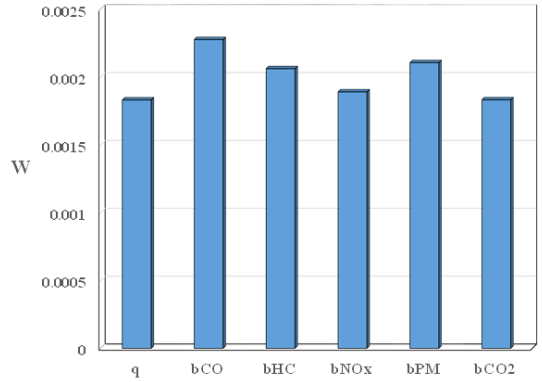

Fig. 26. Coefficient of variation of the average value of mass road fuel consumption – q and road pollutant emissions: carbon monoxide – b_{CO}, hydrocarbons – b_{HC}, nitrogen oxides – b_{NOx}, particulate matter – b_{PM} and carbon dioxide – b_{CO2} in individual process realizations in model traffic conditions in cities in traffic congestions

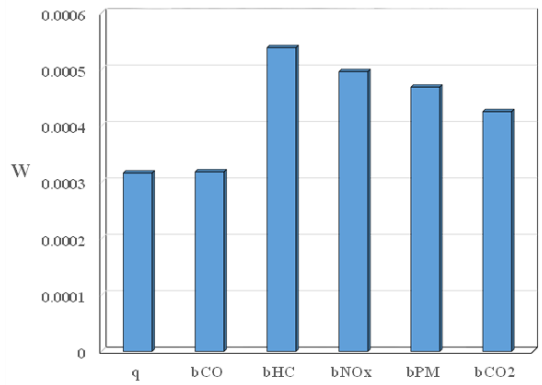

Fig. 27. Coefficient of variation of the average value of mass road fuel consumption – q and road pollutant emissions: carbon monoxide – b_{CO}, hydrocarbons – b_{HC}, nitrogen oxides – b_{NOx}, particulate matter – b_{PM} and carbon dioxide – b_{CO2} in individual process realizations in model traffic conditions in cities outside traffic congestions

The research results and considerations support the thesis that there is a real possibility of using stochastic processes as road vehicle velocity models for the purpose of road transport emissions inventory. It is clear that further work is warranted. Above all, it is necessary to establish stochastic tests for other categories of cumulative road vehicles: light duty vehicles, heavy duty vehicles, urban buses, long-distance buses (coaches), and category L vehicles (motorcycles, mopeds, quad bikes, and microcars).

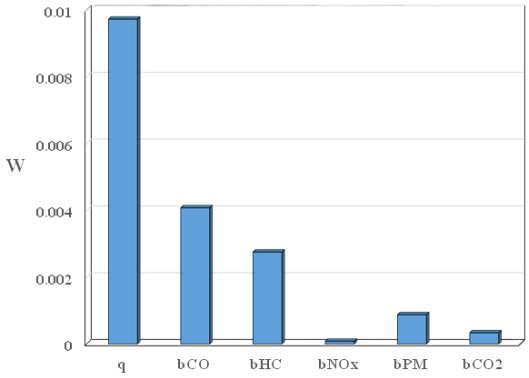

Fig. 28. Coefficient of variation of the average value of mass road fuel consumption – q and road pollutant emissions: carbon monoxide – b_{CO}, hydrocarbons – b_{HC}, nitrogen oxides – b_{NOx}, particulate matter – b_{PM} and carbon dioxide – b_{CO2} in individual process realizations in model traffic conditions outside cities

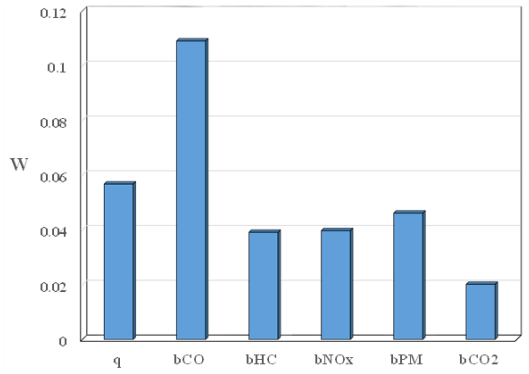

Fig. 29. Coefficient of variation of the average value of mass road fuel consumption – q and road emissions of pollutants: carbon monoxide – b_{CO}, hydrocarbons – b_{HC}, nitrogen oxides – b_{NOx}, particulate matter – b_{PM} and carbon dioxide – b_{CO2} in individual process realizations under model traffic conditions on motorways and expressways

Another research direction is to conduct tests of pollutant emissions and fuel consumption under both chassis dynamometer and real driving conditions using PEMS (Portable Emissions Measurement System) mobile equipment. RDE (Real Driving Conditions) testing could be used to create individual implementations of stochastic road vehicle velocity processes.

5. Summary

Based on the considerations presented in the article, the following conclusions can be drawn:

1. Driving tests based on accurate simulation in the time domain, treated as realizations of stochastic velocity processes of passenger cars under model driving conditions, can be used to effectively study vehicle characteristics in terms of fuel consumption and pollutant emissions. The model's driving conditions include driving in cities with

traffic congestion, in cities without traffic congestion, outside cities, and on highways and expressways. Vehicle testing under stochastic conditions allows the collection of information not only about vehicle characteristics but also about the statistical features of these characteristics.
2. It was found that tests designated as realizations of stochastic velocity processes are characterized by good repeatability of zero-dimensional characteristics for each of the model processes.
3. The results of simulation studies were used as an example to assess the sensitivity of pollutant emissions to pollutant emissions. The characteristics of pollutant emissions from passenger cars for 2020 were determined using simulation methods. The road emissions of pollutants from passenger cars were determined and analyzed under specific realizations of velocity processes under model conditions. The test results were assessed, among other things, for their variability. Good repeatability was found in sets of comparable vehicle traffic conditions.
4. Based on the results, the feasibility of using stochastic processes as road vehicle velocity models for the inventory of road transport pollutant emissions was assessed.
5. Based on the conducted research, it was determined that it would be advisable to continue the work, primarily for other categories of cumulative road vehicles.
6. Another research direction is to conduct pollutant emission and fuel consumption tests under both chassis dynamometer and real driving conditions using mobile PEMS equipment.

Nomenclature

AV	mean value
b	specific distance emission
C	cities in traffic congestions
CT	urban test in traffic congestions
D	standard deviation
H	on motorways and expressways
HC	hydrocarbons
HT	highway test
q	mass fuel consumption
R	outside cities
Rg	range
RT	rural test
U	cities outside traffic congestions
UT	urban test outside traffic congestions
W	coefficient of variation

Bibliography

[1] Andrych-Zalewska M. Research of pollutant emissions from automotive internal combustion engines in conditions corresponding to the actual use of vehicles. Combustion Engines. 2023;193(2):64-70. https://doi.org/10.19206/CE-162621

[2] Bendat JS, Piersol AG. Random data: analysis and measurement procedures. Book Series: Wiley Series in Probability and Statistics. https://doi.org/10.1002/9781118032428

[3] BUWAL (Bundesamt für Umwelt, Wald und Landschaft), INFRAS AG (Infrastruktur-, Umwelt- und Wirtschaftsberatung). Luftschadstoffemissionen des Strassenverkehrs 1950–2010, BUWAL-Bericht 1995;255.

[4] Chłopek Z, Biedrzycki J, Lasocki J, Wójcik P. Investigation of pollutant emissions from a motor vehicle engine in tests simulating real vehicle use in road traffic conditions. Combustion Engines. 2013;154(3):202-207.

[5] COPERT – Computer Programme to Calculate Emissions From Road Transport.

[6] DieselNet: Engine & Emission Technology Online. https://dieselnet.com (accessed on 2022-03-11).

[7] EEA/EMEP Emission Inventory Guidebook 2019.

[8] INFRAS AG. Handbook emission factors for road transport 3.2. Quick reference. Version 3.2. Bern, 2014.

[9] Lane DM. Introduction to statistics – Open Textbook Library. https://open.umn.edu/opentextbooks/textbooks/459

[10] Otnes RK, Enochson L. Applied time series analysis: basic techniques. John Wiley & Sons, Inc. 1978.

[11] Papoulis A, Pillai SU. Probability, random variables, and stochastic processes. Tata McGraw-Hill, 2002; 852.

[12] Parzen E. Stochastic processes. Courier Dover Publications. 2015.

[13] Ralston A, Rabinowitz P. A first course in numerical analysis: Second Edition. Dover Publications Inc. 2001.

[14] Savitzky A, Golay MJE. Smoothing and differentiation of data by simplified least squares procedures. Analytical Chemistry. 1964;36(8):1627-1639. https://doi.org/10.1021/ac60214a047

[15] Worldwide emission standards. Passenger cars and light duty vehicles. Delphi. Innovation for the real world. 2020/2021.

[16] Worldwide emissions standards. Heavy duty and off-highway vehicles. Delphi. Innovation for the real world. 2016/2017.

Katarzyna Bebkiewicz, DEng. – Institute of Environmental Protection – National Research Institute, Poland.
e-mail: *katarzyna.bebkiewicz@kobize.pl*

Paulina Grzelak, DEng. – Institute of Environmental Protection – National Research Institute, Poland.
e-mail: *paulina.grzelak@kobize.pl*

Prof. Zdzisław Chłopek, DSc., DEng. – Institute of Environmental Protection – National Research Institute, Poland.
e-mail: *zdzislaw.chlopek@kobize.pl*

Krzysztof Biernat, DEng., – Prof. PIMOT, Łukasiewicz Research Network – Automotive Industry Institute, Poland.
e-mail: *krzysztof.biernat@pimot.lukasiewicz.gov.pl*

Article citation info:
Kurzydym D. 1D model of a three-way catalyst in MATLAB/Simulink for assessing pollutant reduction in the NEDC emission test. Combustion Engines. 2026;206(3):159-169. https://doi.org/10.19206/CE-218134

Damian KURZYDYM

Combustion Engines
Polish Scientific Society of Combustion Engines

1D model of a three-way catalyst in MATLAB/Simulink for assessing pollutant reduction in the NEDC emission test

ARTICLE INFO

Received: 30 November 2025
Revised: 8 February 2026
Accepted: 14 February 2026
Available online: 20 February 2026

A one-dimensional model of a three-way catalyst (TWC) was developed in MATLAB/Simulink, consisting of a monolith pressure-drop module and a reaction block for CO/HC/NO_x. The model was validated against a reference GT-SUITE solution, with agreement in levels and trends. Kinetic parameters were tuned and verified using emission tests in the NEDC cycle. The model reproduces pressure drop, instantaneous profiles, and cumulative emissions upstream and downstream of the catalyst. Satisfactory agreement between predicted reductions and NEDC measurements confirms the model's suitability for assessing TWC effectiveness and for calibration under test conditions. The approach is computationally lightweight and ready to be extended to other driving cycles, additional physical effects, and exhaust aftertreatment systems such as a GPF.

Key words: *three-way catalyst (TWC), 1D modeling, pressure drop, reaction kinetics, emission reduction*

This is an open access article under the CC BY license (http://creativecommons.org/licenses/by/4.0/)

1. Introduction to the three-way catalyst

The development of effective three-way catalysts is crucial for mitigating harmful automotive emissions, specifically targeting nitrogen oxides, carbon monoxide, and unburnt hydrocarbons [7]. These catalysts achieve this by facilitating oxidation of carbon monoxide and hydrocarbons, alongside the reduction of nitrogen oxides. These converters are mainly used in gasoline engines that operate close to the ideal air-fuel ratio. They rely on noble metals such as platinum, palladium, and rhodium embedded in a washcoat to enable highly efficient pollutant conversion [1]. However, even with these advancements, automobiles remain significant contributors to HC, CO, and NO_x emissions, with a substantial portion occurring during cold start operations [6]. Advanced modeling techniques are required to precisely predict catalyst light-off and breakthrough across diverse driving conditions, including accelerations, decelerations, and high-speed extra-urban phases [14]. To avoid the high costs associated with extensive experimental optimization, computational simulations have become an invaluable tool in catalyst development and performance assessment [1, 16]. Consequently, a robust one-dimensional (1D) model capable of simulating the complex transient behavior of catalytic converters, offers a computationally efficient alternative for optimizing catalyst design and control strategies [13, 17].

A typical three-way catalytic converter (Fig. 1) comprises a ceramic or metallic monolith substrate with numerous parallel channels, coated with a washcoat containing precious metals (e.g., Pt, Pd, Rh) and oxygen storage materials (e.g., ceria) [1, 7]. This complex structure is vital for providing a large surface area for chemical reactions and improving catalytic efficiency by enabling easier adsorption and reaction of exhaust gases. The catalytic reactions, which convert pollutants such as carbon monoxide, hydrocarbons, and nitrogen oxides into less harmful substances such as carbon dioxide, water, and nitrogen, are governed by complex kinetic mechanisms influenced by these material properties and dynamic operating conditions [6, 9]. The interaction between the exhaust gas and the catalyst surface, particularly within the washcoat, involves complex mass transfer phenomena and detailed chemical kinetics, which significantly influence overall conversion efficiency [6, 20].

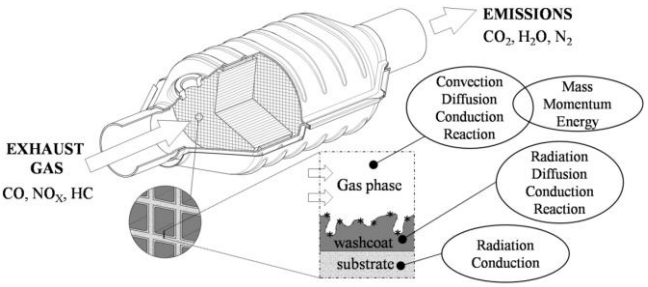

Fig. 1. Catalytic converter with physical and chemical processes [10]

To accurately capture these phenomena, various mathematical models have been developed, with one-dimensional models offering a balance between computational efficiency and predictive accuracy for simulating automotive catalytic converter performance, especially under transient conditions [4, 16]. These 1D models typically approximate the entire monolith by analyzing a single representative channel, then extrapolating the results using geometric scaling parameters like cell density, wall thickness, and monolith dimensions [13]. The development of advanced 1D models for exhaust aftertreatment systems is crucial for a comprehensive simulation of engine and catalyst setups. Studies demonstrate that integrated 1D models can effectively predict the impact of aftertreatment systems on performance, ensuring high accuracy while maintaining acceptable computational time. Such an approach enables the optimization of catalyst geometry and pollution conversion efficiency [8].

The novelty of this work is the development of an original 1D three-way catalyst model built from scratch in MATLAB/Simulink. The model integrates pressure-drop prediction with chemical reaction kinetics and is capable of

simulating both steady-state and transient operating conditions. Its applicability is demonstrated through full-cycle emission assessment under the New European Driving Cycle (NEDC), providing a lightweight, flexible analysis tool.

2. Research methodology

2.1. 1D equations describing pressure drop

Accurate prediction of this pressure drop is crucial for optimizing exhaust system design, as an uneven flow distribution can degrade conversion efficiency and accelerate catalyst aging [5]. Darcy-Weisbach or Darcy-Forchheimer equations, often employed for calculating pressure drop in pipe flows, can be adapted for monolith channels by considering factors such as friction losses and changes in momentum due to flow acceleration or deceleration [11, 13]. However, it is important to note that the pressure drop within the monolithic brick itself is a primary contributor to the overall pressure drop in the catalytic converter, with the inlet and outlet cones also playing a significant role in flow distribution. Therefore, a detailed understanding of the fluid dynamics, including turbulence and momentum transfer within the wash-coated channels, is essential for precise pressure drop modeling. Additionally, viscous and inertial effects, alongside turbulence, significantly influence the pressure drop within the monolith, which can vary considerably with temperature. This necessitates the application of porous media models to accurately represent the complex flow resistance, where the monolith is treated as a distributed resistance with empirically derived coefficients to account for inertial and viscous losses [5, 10].

The three-way catalyst (TWC) was modeled as a regular monolith, where the channel pitch p (center-to-center distance between adjacent channels) was determined based on the cell density (cpsi). The total frontal area A_{face} was set equal to the converter face area.

$$A_{face} = \pi \left(\frac{D}{2}\right)^2 \tag{1}$$

$$p = \frac{1}{\sqrt{cpsi}} \tag{2}$$

where: A_{face} – monolith frontal area, m^2, D – substrate diameter, m, p – channel pitch, m, cpsi – cell density, cells/in^2 (converted to cells/m^2).

Square-channel geometry is characterized by the open channel width derived from pitch and wall thickness, the hydraulic diameter is taken equal to this width, and from these, the monolith's open frontal area and total open flow area are obtained.

$$a = p - t = D_h \tag{3}$$

$$OFA = \left(\frac{a}{p}\right)^2 \tag{4}$$

$$A_{open} = OFA \cdot A_{face} \tag{5}$$

where: a – channel width, m, t – channel wall thickness, m, D_h – hydraulic diameter of a single channel (equals a for a square), m, OFA – open frontal area fraction, A_{open} – total open area for flow, m^2.

Density is evaluated from the ideal-gas law using the inlet pressure and temperature for air. Dynamic viscosity follows the Sutherland correlation (for air), providing a realistic temperature dependence. This air-based closure is lightweight and sufficiently accurate for the pressure-drop calculations used here.

$$\rho = \frac{p_{in}}{R_{spec} \cdot T_{in}} \tag{6}$$

$$\mu(T_{in}) = \mu_0 \left(\frac{T_{in}}{T_0}\right)^{3/2} \frac{T_0 + C}{T_{in} + C} \tag{7}$$

where: ρ – gas density, kg·m^{-3}, p_{in} – absolute inlet pressure to the substrate, Pa, T_{in} – gas temperature at catalyst inlet, K, R_{spec} – specific gas constant (287), J·kg^{-1}·K^{-1}, μ(T) – dynamic viscosity, Pa·s, Sutherland constants (air): μ_0 = $1.716 \cdot 10^{-5}$, Pa·s, T_0 = 273.15 K, C = 111 K.

The bulk velocity through the channels is obtained from mass flow and the total open area.

$$U = \frac{\dot{m}}{\rho \cdot A_{open}} \tag{8}$$

where: U – mean channel (superficial) velocity, m·s^{-1}, ṁ – total mass flow rate, kg·s^{-1}.

The pressure loss across the TWC monolith is modeled as the sum of a viscous term consistent with Darcy–Weisbach and an inertial (minor-loss) term [5]. The effective coefficients A and B are determined empirically from calibration and together account for entrance and exit penalties and washcoat effects, with different values for coated and uncoated substrates.

$$\Delta p_{TWC} = A \frac{\mu U L}{D_h} + B \frac{\rho U^2}{2} \tag{9}$$

where: Δp_{TWC} – monolith pressure drop, Pa, L – substrate length, m, A – viscous loss coefficient (calibrated), B – inertial loss coefficient (calibrated). Coated monolith: A = 32, B = 0.50. Uncoated monolith: A = 28.4, B = 0.41.

Table 1 summarizes the input data used for the 1D catalyst pressure-drop simulation and the corresponding geometric parameters.

Table 1. Input data for the 1D TWC pressure drop model

Simulation time [s]	100
Temperature [K]	300
Mass flow rate [kg/s]	linear ramp (0.01 → 0.22)
Working medium	air
Tested catalyst	
Diameter [m]	0.1057 (4.16 in)
Length [m]	0.0754 (2.97 in)
Channel density [m^{-2}]	6.2×10^5 (400 cpsi)
Wall thickness [m]	1.65×10^{-4} (0.165 mm)
Active layer (washcoat)	No

2.2. 1D equations describing the reaction kinetics

A thorough understanding of the kinetics governing the catalytic reactions is crucial for accurately modeling the performance of three-way catalysts, as these reactions are highly sensitive to temperature, gas composition, and the

presence of inhibiting species. These kinetic parameters, often determined through experimental methods, are then incorporated into the model to predict conversion efficiencies for CO, HC, and NO_x under varying operating conditions [16]. Although one-dimensional models neglect radial gradients within channels, they adequately describe thermo and fluid dynamic behavior, as validated through comparisons with two-dimensional models [19]. This simplification significantly reduces the computational complexity compared to full 3D models, which would be impractical for transient regulatory cycle simulations due to extensive effort and slow computational times [4]. Such 1D models treat all channels of the monolith identically, assuming uniform boundary conditions, which allows for efficient simulation without sacrificing significant accuracy for many engineering applications [15]. However, most of these models are 1D plug-flow models that couple separate conservation equations for the gas and solid phases using transport coefficients [7]. In an efficient three-way catalyst, the primary reactions involve oxidation of CO and hydrocarbons to CO_2 and H_2O, and reduction of NO to N_2 and CO_2 [14]. The selection of appropriate kinetic expressions, such as Langmuir-Hinshelwood type rate equations, is critical for accurately representing the reaction rates and their dependence on various species concentrations and temperatures [18].

For the purpose of developing a 1D TWC catalyst model with detailed reaction mechanisms, the gas composition at the catalyst inlet was taken from a GT-SUITE ready-made example. The total molar concentration C_t is computed from inlet pressure and temperature by the ideal-gas law [16], and the initial species concentrations follow as $C_i^{(0)}$. These values define the initial condition for the 1D plug-flow calculation.

$$C_t = \frac{p_{in}}{R_u \cdot T_{in}} \tag{10}$$

$$C_i^{(0)} = y_i \cdot C_t \tag{11}$$

where: C_t – total molar concentration of the gas mixture at reactor inlet, mol·m^{-3}, R_u – universal (molar) gas constant (8.314), J·mol^{-1}·K^{-1}, $C_i^{(0)}$ – inlet molar concentration of species i, mol·m^{-3}, y_i – inlet mole fraction of species i.

To keep the 1D model compact, chemically similar species are grouped into pseudo-components with effective properties. Hydrocarbons (HC) are treated as a C3 lump that combines propane (C_3H_8) and propylene (C_3H_6), with effective oxygen demand and effective molar mass consistent with the GT-SUITE reference setup. Nitrogen oxides are handled as an NO_x lump formed by pooling nitric oxide (NO) and nitrogen dioxide (NO_2), and the lump is expressed using nitric oxide as the reference for kinetics and mass calculations. This approach preserves the key effects on oxygen consumption and product formation (CO_2 and H_2O) while reducing computational cost and the number of calibrated parameters.

$$y_{HC} = y_{C_3H_6} + y_{C_3H_8} \tag{12}$$

$$y_{NOx} = y_{NO} + y_{NO_2} \tag{13}$$

A plug–flow, isothermal 1D catalyst channel is mapped from axial coordinate x to a residence-time coordinate using the bulk gas velocity U:

$$t = \frac{x}{U} \tag{14}$$

$$\frac{dC_i}{dt} = R_i(\mathbf{C}, T) \tag{15}$$

where: t – residence-time coordinate, s, x – axial coordinate, m, C_i – molar concentration of species i, mol·m^{-3}, $R_i(\mathbf{C}, T)$ – volumetric reaction rate for species i evaluated at the current state $(\mathbf{C}, T)$, mol·m^{-3}·s^{-1}, $\mathbf{C}$ – vector of all species concentrations, mol·m^{-3}, T – as temperature, K.

For a monolith of length L the total residence time is:

$$\tau = \frac{L}{U} \tag{16}$$

where: τ – total residence time, s.

The reactor is split into N_{seg} axial segments and the marching step in the residence-time domain is

$$\Delta t = \frac{\tau}{N_{seg}} \tag{17}$$

where: N_{seg} – no. axial segments, Δt – marching step, s.

With an explicit Euler update (i.e., a first-order forward time integration that evaluates the reaction rate at the current state and advances by Δt), each species is updated segment-by-segment as:

$$C_i^{k+1} = C_i^k + R_i\left(\mathbf{C}^k, T\right)\Delta t \tag{18}$$

where: $k = 0, \ldots, N_{seg} - 1$.

This axial "time-marching" is equivalent to an upwind discretization of the 1D plug-flow balance, neglecting axial dispersion. The explicit scheme is stable for sufficiently small Δt. In the simulations, stability is ensured by choosing N_{seg} such that Δt remains small across the temperature window.

The catalytic chemistry is represented by three global reactions for CO oxidation, NO reduction by CO, and lumped C3 hydrocarbon oxidation. Kinetics follow an Arrhenius temperature law with power-law dependencies on reactant concentrations. Reaction orders and stoichiometric oxygen demand for the HC lump are effective (lumped) parameters calibrated to GT-SUITE data.

$$CO + \frac{1}{2}O_2 \rightarrow CO_2 \tag{19}$$

$$2CO + 2NO \rightarrow 2CO_2 + N_2 \tag{20}$$

$$C_3H_x + \nu_{O2,HC}O_2 \rightarrow 3CO_2 + \frac{x}{2}H_2O \tag{21}$$

where: $\nu_{O2,HC}$ – an effective oxygen demand based on the propane/propylene mixing ratio.

An effective oxygen demand $\nu_{O2,HC}$ is defined as the mole-weighted average of the stoichiometric O_2 needs of

the two ingredients (propane and propylene) under complete oxidation:

$$C_3H_8 + 5O_2 \rightarrow 3CO_2 + 4H_2O \quad (22)$$

$$C_3H_6 + 4.5O_2 \rightarrow 3CO_2 + 3H_2O \quad (23)$$

Then, an effective oxygen demand comes from the lump composition weights:

$$\nu_{O2,HC} = \frac{5y_{C_3H_8} + 4.5y_{C_3H_6}}{y_{C_3H_8} + y_{C_3H_6}} \quad (24)$$

For any global reaction j (e.g., CO oxidation, NO reduction by CO, HC oxidation), the Arrhenius rate constant is equal [4, 9]:

$$k_{p,j}(T) = A_j \exp\left(-\frac{E_j}{RT}\right) \quad (25)$$

where: A_j – the pre-exponential factor (units consistent with orders), E_j – the activation energy, J·mol^{-1}, R – universal gas constant (8.314), J·mol^{-1}·K^{-1},

Table 2 presents the kinetic parameters used for each global reaction in the 1D catalyst model.

Table 2. Kinetic parameters for the 1D TWC model with reactions

CO oxidation	
A [1/s]	2.0×10^{14}
E [J/mol]	1.50×10^{5}
NO reduction	
A [1/s]	1.0×10^{11}
E [J/mol]	7.8×10^{4}
HC oxidation	
A [1/s]	1.5×10^{13}
E [J/mol]	1.04×10^{5}
Reaction orders	
CO	1.0
NO	1.0
HC	1.0
O_2	0.5 for CO oxidation
O_2	1.0 for HC oxidation

The kinetic constants (on a pressure basis) had to be converted ($k_p \rightarrow k_c$) into concentrations:

$$k_{c,j}(T) = k_{p,j}(T)\left(\frac{RT}{p_{unit}}\right)^{\Sigma_i \alpha_{ij}} \quad (26)$$

where: $k_{c,j}$ – is the effective volumetric kinetic constant (units depend on total reaction order), p_{unit} – is a reference pressure (10^5 Pa), (RT/p_{unit}) – the multiplier transfers the law from pressures to concentrations, maintaining the correct units, α_{ij} – empirical reaction order of species i in reaction j (can differ from stoichiometric coefficient).

A nondimensional temperature damper $f_j(T)$ was introduced to mitigate unrealistically high reaction rates predicted by global kinetics at elevated gas temperatures. Above the light-off region, effects such as oxygen-storage saturation, external or internal mass-transfer limits, and thermal aging reduce the effective activity of a TWC, which simple Arrhenius power-law models do not capture. The damper leaves kinetics unchanged in the mid-temperature regime but smoothly dampens rates in the high-temperature tail, preventing overshoot of conversion. This empirical high-T correction enables agreement with GT-SUITE references while preserving the model's simplicity and numerical robustness.

$$f_j(T) = \frac{1}{1 + \left(\frac{T}{T_{drop,j}}\right)^{n_j}} \quad (27)$$

where: $f_j(T)$ – the damper is dimensionless and limited between 0 and 1, n_j – steepness exponent (dimensionless), $T_{drop,j}$ – characteristic drop temperature, K. $T_{drop,j}$ and n_j are calibrated values for each reaction.

Table 3 presents the parameters used for the high-temperature clamps for each reaction in the 1D TWC model.

Table 3. High-temperature clamps

CO oxidation	
T_{drop}	800
n	21
NO reduction	
T_{drop}	780
n	14.5
HC oxidation	
T_{drop}	730
n	13

Power-law rate expressions (reaction rate) for each reaction j can be written as:

$$r_j = k_{c,j}(T) \cdot f_j(T) \prod_i C_i^{\alpha_{ij}} \quad (28)$$

where: r_i – volumetric reaction rate (per gas volume), mol·m^{-3}·s^{-1}, C_i – gas-phase (molar) concentration of species i, mol·m^{-3}.

Hence, for the three global reactions, their reaction rates can be explicitly written:

$$r_{CO_{ox}} = k_{CO_{ox}} \cdot f_{CO}(T) \cdot C_{CO}^{a_{CO}} \cdot C_{O_2}^{b_{O_2}} \quad (29)$$

$$r_{NO_{re}} = k_{NO_{re}} \cdot f_{NO}(T) \cdot C_{CO}^{a_{CO,r}} \cdot C_{NO}^{b_{NO}} \quad (30)$$

$$r_{HC_{ox}} = k_{HC_{ox}} \cdot f_{HC}(T) \cdot C_{HC}^{a_{HC}} \cdot C_{NO}^{b_{O_2,HC}} \quad (31)$$

With an explicit Euler scheme, species concentrations are updated segment-by-segment using the power-law reaction rates:

$$C_{CO}^{k+1} = C_{CO}^{k} - \left(r_{CO_{ox}} + 2 \cdot r_{NO_{re}}\right)\Delta t \quad (32)$$

$$C_{O_2}^{k+1} = C_{O_2}^{k} - \left(0.5 \cdot r_{CO_{ox}} + \nu_{O2,HC} \cdot r_{HC_{ox}}\right)\Delta t \quad (33)$$

$$C_{CO_2}^{k+1} = C_{CO_2}^{k} + \left(r_{CO_{ox}} + 2 \cdot r_{NO_{re}} + 3 \cdot r_{HC_{ox}}\right)\Delta t \quad (34)$$

$$C_{NO}^{k+1} = C_{NO}^{k} - 2 \cdot r_{NO_{re}} \cdot \Delta t \quad (35)$$

$$C_{HC}^{k+1} = C_{HC}^{k} - r_{HC_{ox}} \cdot \Delta t \tag{36}$$

At the reactor exit, outlet mole fractions y_i^{out} are obtained from the updated concentrations and the total molar concentration C_t:

$$y_i^{out} = \frac{C_i^{out}}{C_t} \tag{37}$$

$$C_t = \sum_i C_i^{out} \tag{38}$$

Component conversions are reported from inlet to outlet on a molar basis:

$$conv_i = 100 \frac{y_i^{in} - y_i^{out}}{y_i^{in}} [\%] \tag{39}$$

Table 4 presents the input data used for simulating chemical reactions with the 1D catalyst model, together with its geometric parameters.

Table 4. Input data for the 1D TWC model with reactions

Simulation time [s]	2000
Temperature [K]	linear ramp (350 → 900)
Mass flow rate [kg/s]	0.02
Working medium and mole fraction [-]	
CO_2	0.147
H_2O	0.1
O_2	0.005228
H_2	0.001978
CO	0.006865
C_3H_8	0.000102
C_3H_6	0.000406
NO	0.003042
NO_2	0.00001
N_2	0.735369
sum	1
Tested catalyst	
Diameter [m]	0.1057 (4.16 in)
Length [m]	0.1501 (5.91 in)
Channel density [m^{-2}]	9.3×10^5 (600 cpsi)
Wall thickness [m]	1.09×10^{-4} (0.109 mm)
Active layer (washcoat)	Yes

2.3. NEDC emission test for 1D model validation

This section describes the extension of the developed 1D model and its application to the simulation of the New European Driving Cycle emission test, a standardized procedure used to assess vehicle emissions under controlled conditions. This allows for a direct comparison of the model's predicted pollutant reductions with established emission limits, thereby validating its accuracy and utility as a design tool. The model is validated by comparing predicted conversion efficiencies and temperature profiles to experimental data from real NEDC tests on vehicles [13]. This validation builds confidence in the model's accuracy for forecasting how three-way catalysts respond to changing real-world driving conditions, which is a key factor in effective emission control. This method enables detailed analysis of catalyst performance and optimization, without the excessive computational demands of higher-dimensional models [4, 12].

As an initial step in extending the model, the volumetric exhaust flow $\dot{V}_{TP}$ was obtained at the tail-pipe over the full NEDC. To interface it with the existing 1D catalyst model, it was converted to an equivalent inlet mass flow $\dot{m}$ using the ideal-gas density of the inlet mixture.

$$\dot{m}(t) = \dot{V}_{TP}(t) \cdot \rho_{in}(t) \tag{40}$$

$$\rho_{in}(t) = \frac{p_{in}(t) \cdot M_{mix}(t)}{R T_{in}(t)} \tag{41}$$

$$M_{mix}(t) = \sum_i y_i(t) \cdot M_i \tag{42}$$

where: $\dot{V}_{TP}$ – tail-pipe volumetric flow, m^3/s, ρ_{in} – mixture density at the catalyst inlet, kg/m^3, p_{in} – inlet pressure, Pa, M_{mix} – mean molar mass, kg/mol, R – universal gas constant (8.314), $J \cdot mol^{-1} \cdot K^{-1}$, T_{in} – inlet temperature, K, y_i – inlet mole fraction of species i, M_i – molar mass of species i, kg/mol, for example $M_{CO} = 28.0101$ kg/mol.

Test data outputs from NEDC test were provided as raw exhaust composition in vol% and ppm. For use in the 1D reactor, these inputs were converted to consistent mole fractions:

$$y_i = \frac{C_i[\%]}{100} \tag{43}$$

$$y_i = \frac{C_i[ppm]}{10^6} \tag{44}$$

A dedicated muffler block was added to account for downstream backpressure at the catalyst inlet. The muffler loss was represented by a power-law fit calibrated at idle:

$$\Delta p_{muf}(\dot{m}) = \Delta p_{idle} \left(\frac{\dot{m}}{\dot{m}_{idle}} \right)^n \tag{45}$$

where: Δp_{idle} – idle backpressure, Pa, $\dot{m}_{idle}$ – idle mass flow, kg/s, n – fit exponent (set to value 2).

The absolute pressure applied at the TWC inlet was the sum of ambient pressure and both drops (from TWC and muffler):

$$p_{in,TWC} = p_{atm} + \Delta p_{muf} + \Delta p_{TWC} \tag{46}$$

At idle ($\dot{m} \approx 0.003$ kg/s), the measured total backpressure upstream of the catalyst was $p_{in,TWC} \approx 24{,}000$ Pa, and the model parameters were calibrated to reproduce this point.

The emissions post-processor was implemented as a Simulink block (TWC_emissions) that converts mole to mass fractions, forms instantaneous mass rates, integrates cumulative masses, and reports g/km (or mg/km) over NEDC. The block operated at a fixed sample time (T_s = 1 s) and used the cycle distance $L_{cyc} = 11$ km.

From outlet (and inlet) mole fractions y_i and species molar masses M_i, the mixture molar mass M_{mix}, and mass fractions w_i were computed as:

$$w_i = \frac{y_i M_i}{M_{mix}} \quad (47)$$

Instantaneous mass rates (in/out) of species i, were computed as:

$$\dot{m}_i(t) = \dot{m}(t) \cdot w_i(t) \cdot 10^3 \ [g/s] \quad (48)$$

where: $\dot{m}$ – total mass flow rate, $kg \cdot s^{-1}$.

Cumulative masses M_i in [g] of species i for pre-TWC and post-TWC were determined by the trapezoidal integration:

$$M_i[k] = M_i[k-1] + \frac{1}{2}(\dot{m}_i[k-1] + \dot{m}_i[k])T_s \quad (49)$$

where: T_s – fixed sample time (1 s).

Tailpipe (post-TWC) emission index E_i of species i at the end of the cycle was reported as:

$$E_i = \frac{M_{i,out}(t_{end})}{L_{cyc}} \cdot 10^3 \ [mg/km] \quad (50)$$

where: L_{cyc} – the cycle distance (11 km).

For the NEDC simulation, the Arrhenius parameters were updated for each global reaction. Specifically, the pre-exponential factor and activation energy were calibrated to align the model's tailpipe CO/NO_x/HC with the measured NEDC g/km totals. The temperature high-T correction introduced earlier was retained to avoid unrealistic over-conversion at very high temperatures, ensuring stable fits across the full cycle.

Table 5 presents the calibrated kinetic parameters used for each global reaction of the 1D catalyst model in the NEDC emission cycle.

Table 5. Adjusted kinetic parameters for the 1D TWC model in NEDC test

CO oxidation	
A [1/s]	3.36×10^{16}
E [J/mol]	1.42×10^{5}
NO reduction	
A [1/s]	5.8×10^{11}
E [J/mol]	7.8×10^{4}
HC oxidation	
A [1/s]	2.25×10^{14}
E [J/mol]	1.04×10^{5}

Table 6. Input data for the 1D TWC model in the NEDC cycle

Simulation time [s]	1180
Temperature [K]	up to 927
Mass flow rate [kg/s]	up to 0.042
Working medium	exhaust gases
Tested catalyst	
Diameter [m]	0.1184 (4.66 in)
Length [m]	0.0762 (3.0 in)
Channel density [m^{-2}]	6.2×10^5 (400 cpsi)
Wall thickness [m]	1.65×10^{-4} (0.165 mm)
Active layer (washcoat)	Yes

Table 6 presents the input data used for simulating the NEDC emission cycle with the 1D catalyst model, together with its geometric parameters.

Figure 2 shows the NEDC cycle profile, which was conducted on a chassis dynamometer at the BOSMAL laboratory (Fig. 5).

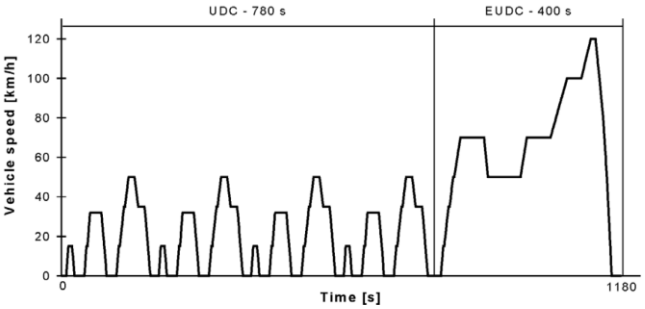

Fig. 2. Profile of the New European Driving Cycle [2]

Figure 3 shows the tested vehicle, a 2014 VW Golf VI 1.4 TSI (90 kW, Euro 5b). Figure 4 further presents the catalyst with the exhaust sampling probe and a thermocouple measuring temperature upstream of the catalytic reactor.

Fig. 3. Test vehicle evaluated under the NEDC driving cycle on a chassis dynamometer

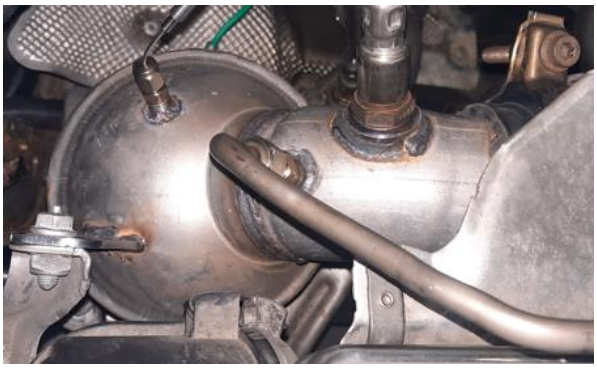

Fig. 4. Connections for raw exhaust gas sampling and temperature measurement upstream of the TWC catalyst

3. Modeling results

3.1. Pressure drop model and validation

A one-dimensional pressure-drop model of the TWC catalyst was implemented in MATLAB/Simulink. The inlet boundary conditions consisted of a ramped mass-flow rate and a fixed gas temperature, while constant geometric parameters (monolith diameter/length, cell density, wall thickness, washcoat used and absolute inlet pressure) were supplied as entrance blocks. The functional block (Fig. 6)

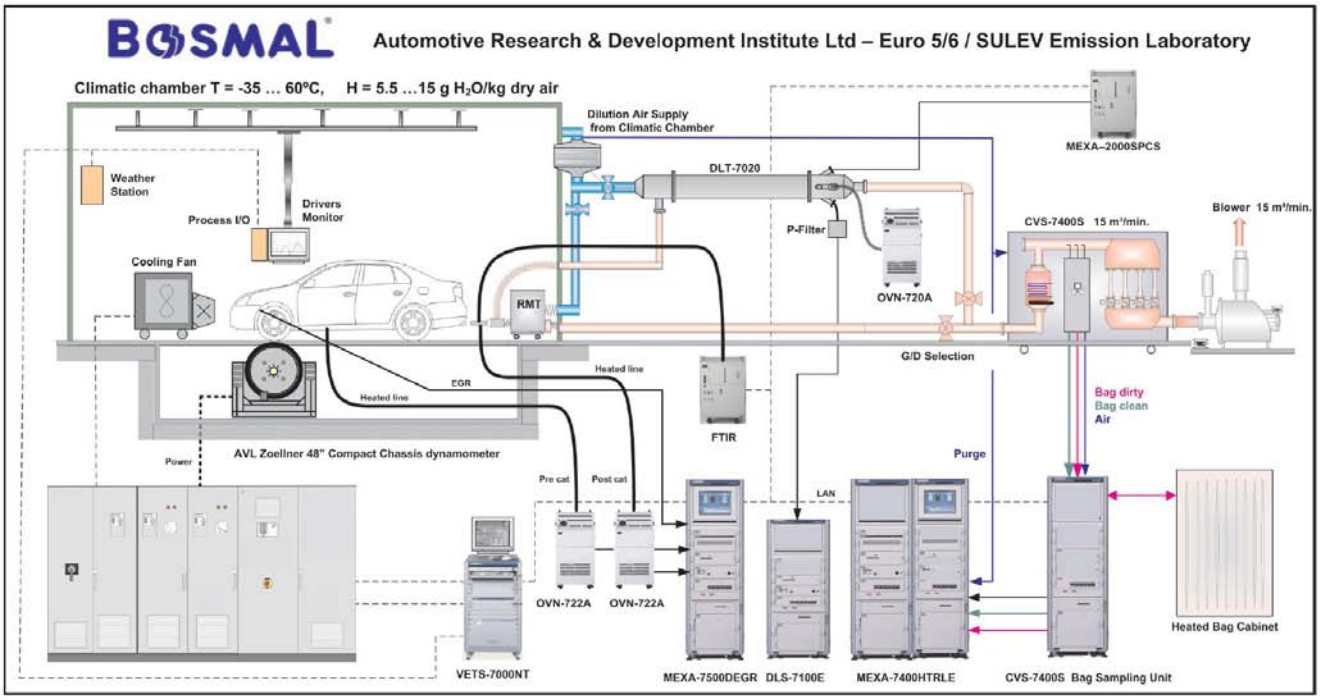

Fig. 5. Layout of the emission testing laboratory including climatic chamber, chassis dynamometer, dilution tunnel, and exhaust analysis system [3]

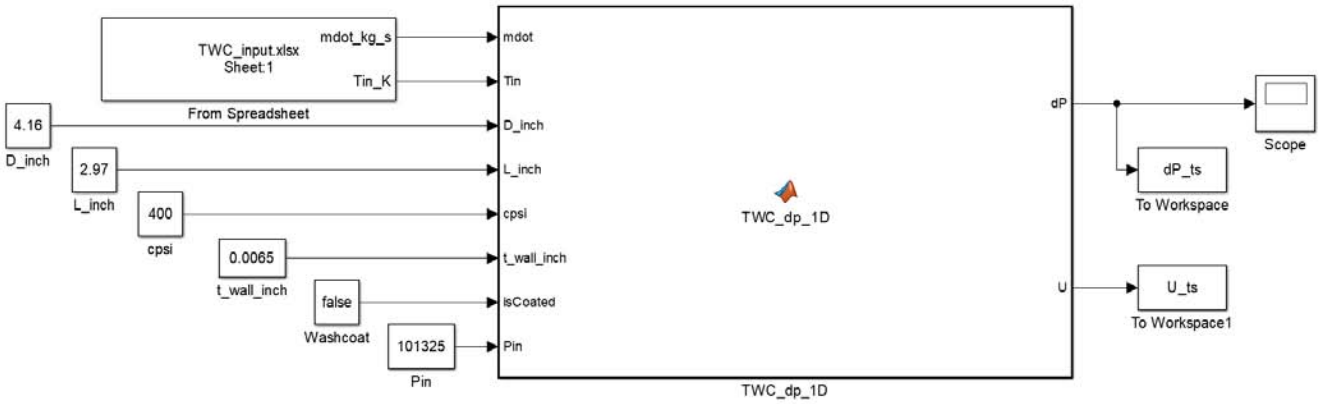

Fig. 6. One-dimensional pressure drop model for the three-way catalyst implemented in MATLAB/Simulink

was equipped with the code for the governing equations summarized in Section 2.1 (channel cross-section and OFA, ideal-gas density and viscosity model, average channel velocity, and viscous/inertial loss terms).

At the outputs, the total pressure drop across the catalyst and the corresponding mean channel velocity were computed. A post-processing script then compared the 1D model predictions with experimental measurements, reporting pressure-drop and channel-velocity agreement (Fig. 7). The model results show good agreement with literature (experimental) data reported by Ekström et al. [5], which were used for validation of the pressure-drop model.

To quantify the agreement between the 1D pressure-drop model and experimental data, the mean absolute percentage error (MAPE) was used. Lower MAPE indicates better agreement (0% is perfect).

$$\mathrm{MAPE}[\%] = \frac{100}{n}\sum_{i=1}^{n}\left|\frac{y_i^{exp} - y_i^{sim}}{y_i^{exp}}\right| \qquad (51)$$

where: y_i^{exp} – is the measured pressure drop at sample i, Pa, y_i^{sim} – is the simulated value for pressure drop at sample i, Pa, n – is the number of samples.

3.2. Reaction kinetics model and validation

An emission-chemistry model was implemented around a new 1D reaction block in MATLAB/Simulink. Exhaust-gas compositions (mole fractions, inlet temperature and flow) were first prepared in an Excel file and linked to the model via a From Spreadsheet source. The reaction block (Fig. 8) implements the power-law Arrhenius scheme summarized in Section 2.2 (global CO oxidation, NO reduction with CO, and HC oxidation), including the residence-time marching along the monolith.

For each time step the block advances species concentrations along the axial segments and computes outlet mole fractions and instantaneous conversions – these signals are logged to the MATLAB base workspace via To Workspace sinks.

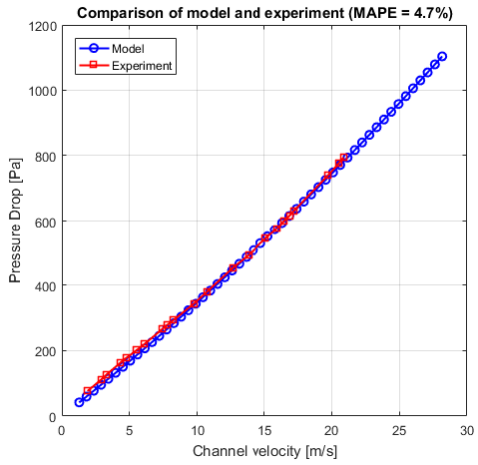

Fig. 7. Comparison of pressure drop across the TWC between the 1D model and experimental data

Validation focused on conversion versus time profiles for CO, NO, and HC. The GT-SUITE reference (from Excel file) and Simulink outputs were processed by a MATLAB script, which synchronized their time vectors and produced combined traces for all species. Across all three pollutants, the T50 (50% conversion) points from the 1D model and GT-SUITE intersected at the correct time, demonstrating strong agreement between the simulations. The initial baselines remained near zero and the final levels approached similar high conversion levels, giving satisfactory agreement at both the start and end of the transients. Figures 9–11 present representative plots, highlighting comparable rise slopes, T50 alignment, and asymptotic behavior.

The reaction kinetics model was calibrated through comparison with GT-POWER reference simulations. Arrhenius parameters and high-temperature reaction clamps were iteratively adjusted to match the transient conversion

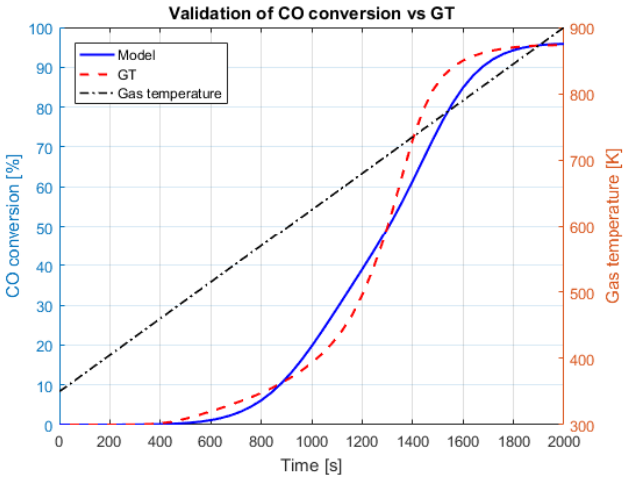

Fig. 9. Validation of CO conversion for the 1D catalyst model against GT simulation results

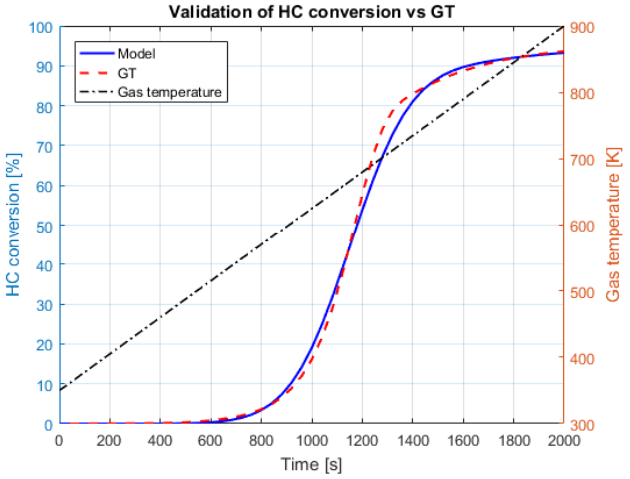

Fig. 10. Validation of HC conversion for the 1D catalyst model against GT simulation results

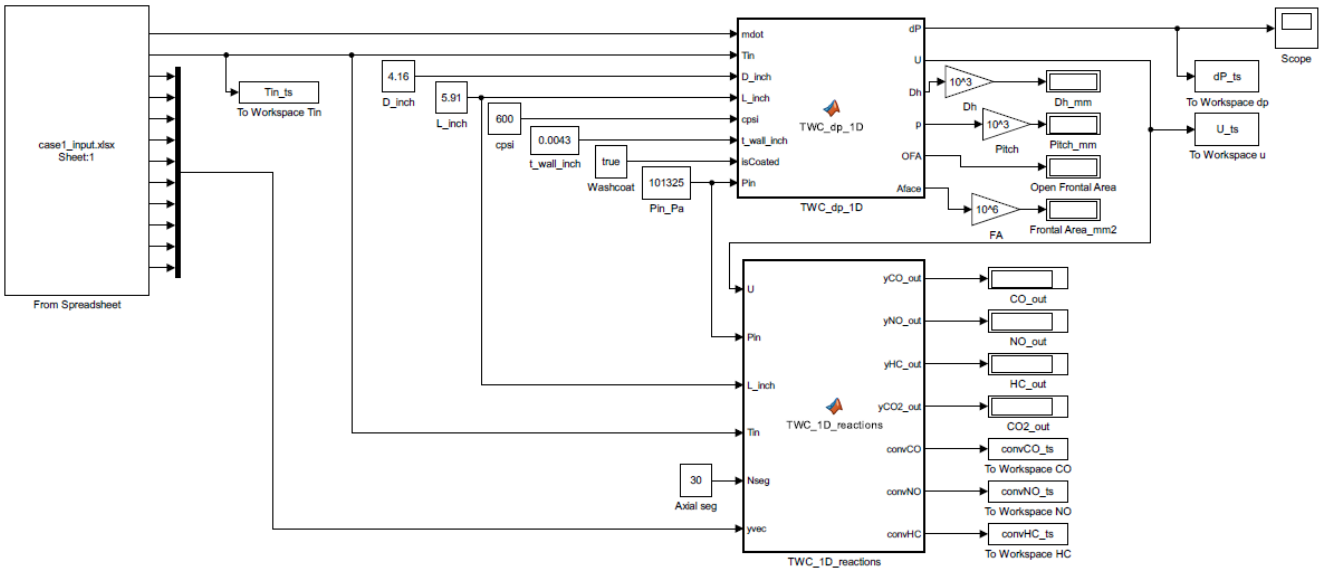

Fig. 8. One-dimensional reaction kinetics model for the three-way catalyst implemented in MATLAB/Simulink

profiles of CO, HC, and NO. Validation focused on the alignment of characteristic light-off behavior, including T10, T50, and T90 conversion points, as well as the overall shape of the conversion curves. The final parameter sets providing the best agreement are summarized in Tables 2 and 3.

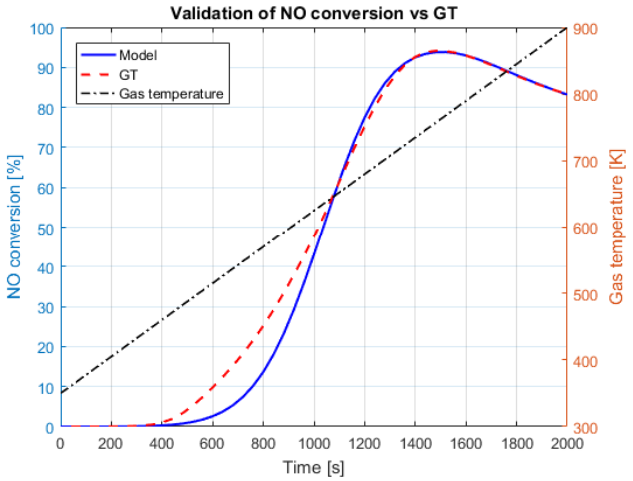

Fig. 11. Validation of NO conversion for the 1D catalyst model against GT simulation results

3.3. 1D model simulation in the NEDC test

The NEDC boundary conditions were assembled in an Excel file (time-resolved exhaust composition and temperature), then fed to the reaction block via From Spreadsheet in Simulink, analogously to the GT reference case. This provided the model with the full, second-by-second inlet vector over the ~1180 s cycle.

To reflect real exhaust system backpressure, a dedicated muffler pressure-drop block was added and calibrated to idle measurements. Its output was summed with ambient pressure to form the effective catalyst inlet pressure.

In addition, a "TWC_emissions" block (Fig. 12) was introduced to compute instantaneous tailpipe mass rates and cycle-cumulative emissions (pre- and post-TWC) for CO, NO_x, and HC, as well as final emission values (g/km) calculated for the NEDC cycle.

All computations in these functional blocks follow the formulations summarized in Section 2.3, providing a coherent assessment throughout the NEDC cycle of transient responses and cumulative emission outcomes.

A separate MATLAB script was used to generate the NEDC plots (Fig. 13–15). For each pollutant (CO, NO_x, HC) it produces two panels: instantaneous mass rate upstream and downstream of the TWC, and cumulative emissions pre- and post-TWC normalized to g/km. The cumulative panels include a black dashed line marking the corresponding EURO limit, which enables a direct visual check of compliance over the full cycle.

For the NEDC simulation, no vehicle or engine submodel was employed. Instead, the catalyst model was driven by measured, time-resolved exhaust gas composition, temperature, and mass flow obtained from the NEDC test,

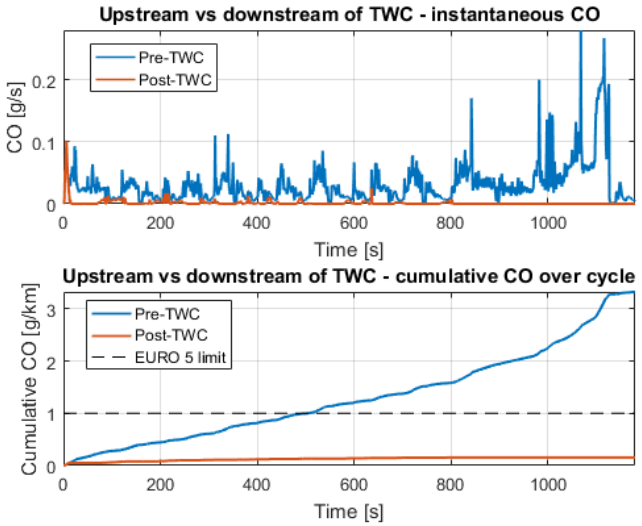

Fig. 13. Instantaneous and cumulative CO emissions upstream and downstream of the TWC from the 1D model during the NEDC cycle

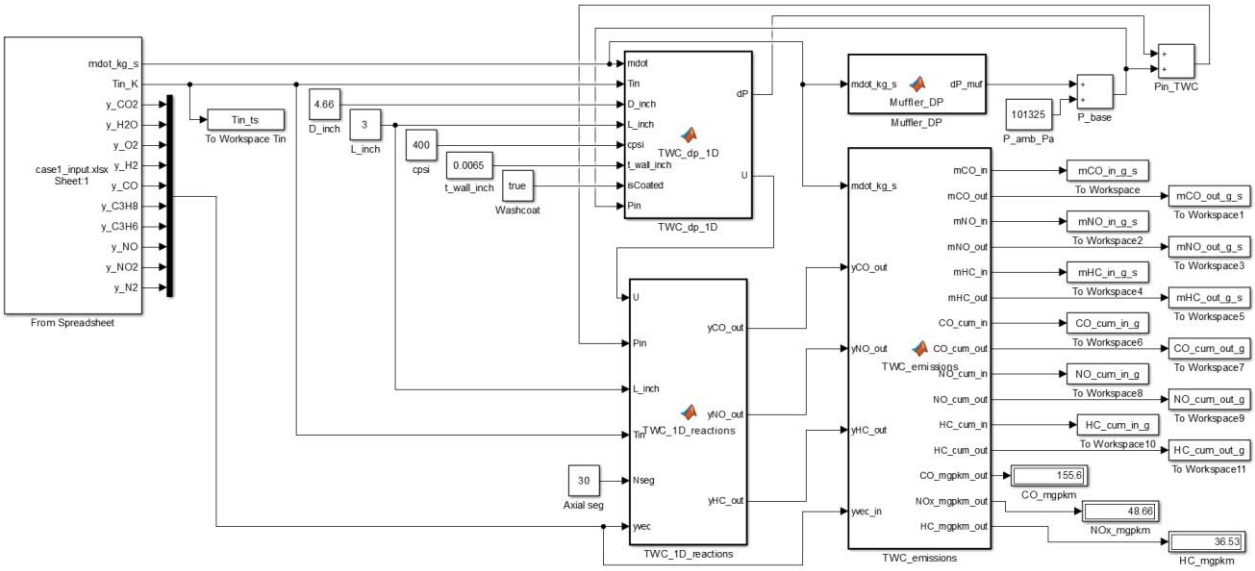

Fig. 12. One-dimensional model of the three-way catalyst under the NEDC driving cycle implemented in MATLAB/Simulink

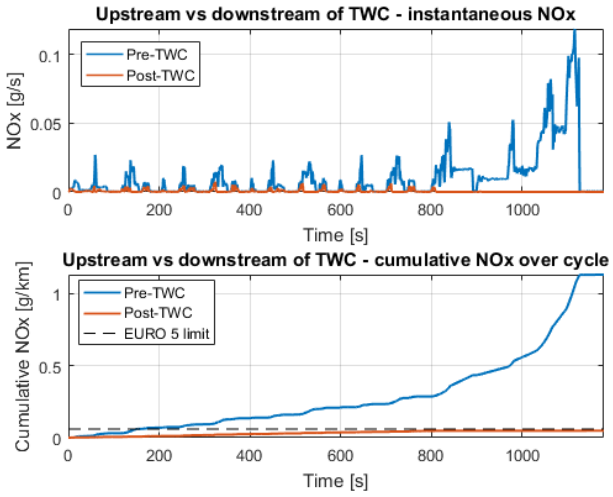

Fig. 14. Instantaneous and cumulative NO_x emissions upstream and downstream of the TWC from the 1D model during the NEDC cycle

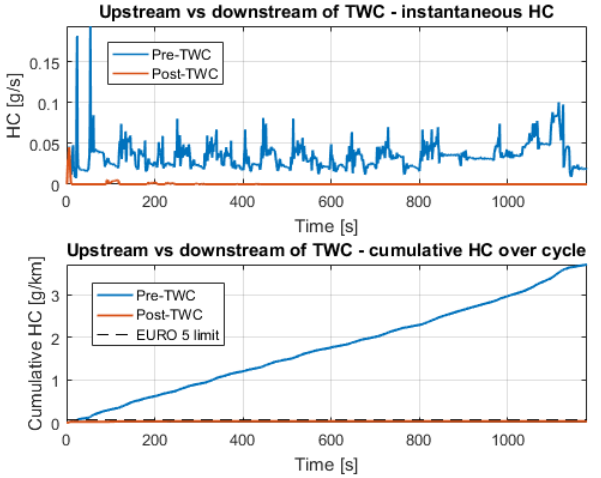

Fig. 15. Instantaneous and cumulative HC emissions upstream and downstream of the TWC from the 1D model during the NEDC cycle

which were applied directly as inlet boundary conditions. Since a different catalyst was used in the NEDC experiment, the kinetic parameters were recalibrated for this case, as summarized in Table 5.

Figures 13–15 illustrate instantaneous and cumulative emissions of CO, NO_x, and HC upstream and downstream of the TWC during the NEDC cycle. The post-TWC results show a substantial reduction of instantaneous emission peaks and cumulative tailpipe emissions compared to the pre-TWC signals. For all three pollutants, the cumulative emissions remain below the Euro 5 limits, confirming effective catalyst operation under experimentally measured NEDC conditions.

4. Summary and conclusion

This work presented a lightweight 1D plug-flow model of a three-way catalyst (TWC) in MATLAB/Simulink, expanded with a muffler backpressure block and an emissions post-processor. The model reproduces pressure-drop behavior, CO/NO_x/HC conversion trajectories, and cumulative tailpipe indices (g/km) over NEDC with satisfactory agreement against GT-SUITE and literature references, including consistent T50 light-off temperature and T10/T90 benchmarks. The model executes quickly, making it suitable for iterative calibration and sensitivity studies.

Calibration of Arrhenius parameters (A, E) proved stable and repeatable across operating profiles. Intentional simplifications, including 1D plug–flow, isothermal gas-phase, reduced chemistry (HC and NO_x lumped), and a high–temperature empirical damper, produced reliable trends and magnitudes while maintaining low model complexity. Including the muffler pressure–drop block enabled the inlet boundary pressure to capture realistic backpressure, enhancing agreement while preserving computational speed.

The present model neglects radial distributions and axial dispersion, is isothermal (no energy balance), and assumes no convective cooling, pore diffusion, or gas-film mass transfer. Kinetics follow fixed-order power-law forms without adsorption or coverage effects (no Langmuir-Hinshelwood), oxygen storage capacity (OSC), or side reactions or intermediates, while the high-T clamp is empirical. Calibrated A/E and temperature limits are case-dependent, so extending them beyond the validated range requires caution. Cold start conditions, reaction exotherms and hot-spots, as well as catalyst aging, are excluded from the model.

The integration of an energy balance, Langmuir–Hinshelwood coverage kinetics, and OSC dynamics should expand the model's scope and improve its predictive reliability, especially in light-off and high-load regimes. This approach can be applied to other aftertreatment devices (DPF/GPF, SCR) and linked with a simple engine model to enable full drive-cycle analysis. Advanced 3D CFD software, for example, ANSYS Fluent, can be used to verify geometric effects and provide input for reduced models. Overall, the proposed 1D model offers a practical balance between accuracy and speed for evaluating designs, calibrating kinetics, and assessing emission-reduction performance over regulatory cycles.

The main contribution of this work is the development of an original one-dimensional three-way catalyst model built from scratch in MATLAB/Simulink, a platform that does not provide a ready-made aftertreatment or catalyst module. The proposed model enables prediction of catalyst pressure drop, pollutant conversion efficiency, and tailpipe emissions over the NEDC cycle using a unified and computationally efficient framework. Owing to its modular structure, the model can be easily adapted to different catalyst geometries and recalibrated for various kinetic parameter sets. Furthermore, the developed approach provides a flexible foundation for future extensions toward more advanced exhaust aftertreatment configurations and integrated drive-cycle simulations.

Acknowledgements

The author of this article expresses gratitude to DRiV for funding the research. Additional appreciation is extended to the State University of Applied Sciences in Racibórz for supporting participation in the IX Young Scientists Academy conference and for funding the publication of this article.

Nomenclature

MAPE mean absolute percentage error
NEDC New European Driving Cycle
OSC oxygen-storage capacity
TWC three-way catalyst

Bibliography

[1] Aslanjan J, Klauer C, Perlman C, Günther V, Mauß F. Simulation of a three-way catalyst using transient single and multi-channel models. SAE Technical Paper 2017-01-0966. 2017. https://doi.org/10.4271/2017-01-0966

[2] Bielaczyc P, Szczotka A. The potential of current european light duty CNG-fuelled vehicles to meet Euro 6 requirements. Combustion Engines. 2012;151(4):20-33. https://doi.org/10.19206/ce-117018

[3] Bielaczyc P, Szczotka A, Pajdowski P, Woodburn J. Development of automotive emissions testing equipment and test methods in response to legislative, technical and commercial requirements. Combustion Engines. 2013;152(1):28-41. https://doi.org/10.19206/ce-117010

[4] Depcik C, Assanis D. One-dimensional automotive catalyst modeling. Prog Energy Combust Sci. 2005;31(4):308-369. https://doi.org/10.1016/j.pecs.2005.08.001

[5] Ekström F, Andersson B. Pressure drop of monolithic catalytic converters experiments and modeling. SAE Technical Paper 2002-01-1010. 2002. https://doi.org/10.4271/2002-01-1010

[6] Hayes RE, Mukadi LS, Votsmeier M, Gieshoff J. Three-way catalytic converter modelling with detailed kinetics and washcoat diffusion. Top Catal. 2004;30:411-415. https://doi.org/10.1023/b:toca.0000029783.16199.f3

[7] Holder R, Bollig M, Anderson DR, Hochmuth JK. A discussion on transport phenomena and three-way kinetics of monolithic converters. Chem Eng Sci. 2006;61(24):8010-8027. https://doi.org/10.1016/j.ces.2006.09.030

[8] Kakoee A, Hunicz J, Mikulski M. Integrated 1D simulation of aftertreatment system and chemistry-based multizone RCCI combustion for optimal performance with methane oxidation catalyst. J Mar Sci Eng. 2024;12(4):594. https://doi.org/10.3390/jmse12040594

[9] Koltsakis GC, Stamatelos AM. Modeling dynamic phenomena in 3-way catalytic converters. Chem Eng Sci. 1999; 54(20):4567-4578. https://doi.org/10.1016/s0009-2509(99)00130-x

[10] Kurzydym D, Klimanek A, Żmudka Z. Experimental and numerical analysis of flow through catalytic converters for original part and WALKER's replacement using reverse engineering and CFD. IOP Conf Ser Mater Sci Eng. 2018; 421(4):042044. https://doi.org/10.1088/1757-899x/421/4/042044

[11] Kuta K, Nadimi E, Przybyła G, Żmudka Z, Adamczyk W. Ammonia CI engine aftertreatment systems design and flow simulation. Combustion Engines. 2022;190(3):3-10. https://doi.org/10.19206/ce-143158

[12] Maio DD, Beatrice C, Fraioli V, Napolitano P, Golini S, Rutigliano FG. Modeling of three-way catalyst dynamics for a compressed natural gas engine during lean–rich transitions. Appl Sci. 2019;9(21):4610. https://doi.org/10.3390/app9214610

[13] Montenegro G, Onorati A. 1D thermo-fluid dynamic modeling of reacting flows inside three-way catalytic converters. SAE Int J Engines. 2009;2(1):14441459. https://doi.org/10.4271/2009-01-1510

[14] Papadopoulos C, Kourtelesis M, Dimaratos A, Moschovi AM, Yakoumis I, Samaras Z. Mechanistic aspects of the chemical reactions in a three-way catalytic converter containing Cu and platinum group metals. Processes. 2025; 13(3):649. https://doi.org/10.3390/pr13030649

[15] Pontikakis GN, Konstantas GS, Stamatelos AM. Three-way catalytic converter modeling as a modern engineering design tool. J Eng Gas Turbines Power. 2004;126(4):906-923. https://doi.org/10.1115/1.1787506

[16] Ramanathan K, Sharma CS. Kinetic parameters estimation for three way catalyst modeling. Ind Eng Chem Res. 2011; 50(17):9960-9979. https://doi.org/10.1021/ie200726j

[17] Real M, Hedinger R, Pla B, Onder C. Modelling three-way catalytic converter oriented to engine cold-start conditions. Int J Engine Res. 2019;22(2):640-651. https://doi.org/10.1177/1468087419853145

[18] Watling TC, Cox JP. Factors affecting three-way catalyst light-off: a simulation study. SAE Int J Engines. 2014;7(3): 1311-1325. https://doi.org/10.4271/2014-01-1564

[19] Wurzenberger JC, Peters B. Catalytic converters in a 1D cycle simulation code considering 3D behavior. SAE Technical Paper. 2003-01-1002. 2003. https://doi.org/10.4271/2003-01-1002

[20] Zhu Z, Midlam-Mohler S, Canova M. Development of physics-based three-way catalytic converter model for real-time distributed temperature prediction using proper orthogonal decomposition and collocation. Int J Engine Res. 2019; 22(3):873-889. https://doi.org/10.1177/1468087419876127

Damian Kurzydym, DEng. – Institute of Technology, University of Applied Sciences in Racibórz; Aftremarket Emission Control Engineering, DRiV Poland Sp. z o.o. (Tenneco division), Poland.
e-mail: *damian.kurzydym@akademiarac.edu.pl*

Article citation info:
Kropisz O, Skobiej K, Zandecki B. Impact of 2026 FIA technical regulations on Formula 1 power units, aerodynamics and energy management. Combustion Engines. 2026;206(3):170-178. https://doi.org/10.19206/CE-218328

Oliwia KROPISZ
Kinga SKOBIEJ
Bartłomiej ZANDECKI

Combustion Engines
Polish Scientific Society of Combustion Engines

Impact of 2026 FIA technical regulations on Formula 1 power units, aerodynamics and energy management

ARTICLE INFO

Received: 10 December 2025
Revised: 21 January 2026
Accepted: 19 February 2026
Available online: 5 March 2026

The year 2026 will bring significant changes to the regulations that will affect the technological challenges in Formula 1. The predicted impact on vehicle design and performance changes compared to the current season was evaluated. Special attention was paid to increasing the share of ecology, which affects the importance of electric power in vehicles, and is also reflected in the introduction of sustainable fuels, redesigned power units, active aerodynamic systems, and reduced body weight. These changes are analyzed for their impact on aerodynamic efficiency, vehicle dynamics, and energy management strategies. Based on technical data, information, and predictions, changes can be determined to adapt the cars to evolving restrictions in areas such as energy recovery, electric power usage, and aerodynamic balance. The analysis shows the growing role of precise design and integrated system optimization in achieving competitive results. The article highlights how the updated regulations strengthen the direction Formula 1 is heading in: greater efficiency, sustainability, and technological advancement.

Key words: *Formula 1, hybrid power units, sustainable fuels, combustion engines, energy recovery system*

This is an open access article under the CC BY license (http://creativecommons.org/licenses/by/4.0/)

1. Introduction

Formula 1 has been constantly evolving since its very first season, adapting to new technological, sporting, and environmental demands. Changes introduced to the power units have always been at the core of this evolution, effectively setting the direction for the sport's development over the decades [10]. Over the years, power units have transformed dramatically, from large, high-revving naturally aspirated engines to today's highly integrated hybrid constructions – Fig. 1.

The FIA has gradually implemented increasingly strict regulations concerning not only engine power, but also displacement and overall configuration [36]. These adjustments were driven by safety considerations and growing environmental priorities, which, in recent years, have become among the most influential factors shaping the future of motorsport. Figure 1 presents a comparison of power output and engine displacement used in Formula 1 over the past decades. A clear downward trend in engine capacity is visible, accompanied by a gradual increase or stabilization in maximum power. Early engine designs featured larger displacement but delivered relatively lower power [33]. Over time, as turbocharging technologies and later hybrid systems developed, power output increased despite reduced displacement.

The cyclical fluctuations observed in the chart reflect regulatory changes introduced by the FIA, which imposed limits on both power and engine configuration. The highest power levels were achieved during the turbo era of the 1980s, while current hybrid units, despite having the smallest displacement in F1 history, offer high efficiency and comparable performance thanks to the integration of energy recovery systems. Engineers continuously work on advanced technologies that influence the speed, reliability, and overall sophistication of Formula 1 cars. Innovations are tested and developed under extreme conditions, enabling them to reach technological maturity rapidly. Many solutions originally created for Formula 1 later find their application in road vehicles.

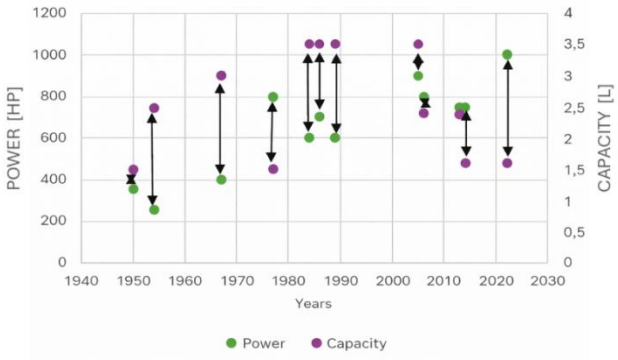

Fig. 1. A depiction of the power of racing cars over the years [32]

Moreover, F1 has a significant impact on the development of artificial intelligence and data analysis methods (Fig. 2) [30].

Fig. 2. Telemetry list [39]

The enormous amount of information collected by the cars during race weekends enables the refinement of telemetry systems and analytical tools [30]. This enables real-time monitoring of tyre condition, battery energy levels, braking forces, and other parameters essential to vehicle performance.

This article discusses the key changes that will be introduced in the 2026 season and compares them with the solutions used in current car designs [8]. The technical regulations presently in force were implemented in 2022 [9], and since then, Formula 1 cars have been continuously refined to improve both performance and reliability.

Overall, the historical evolution of power units and racing technology in Formula 1 clearly reflects the three engineering pillars highlighted in this article's title. **Speed** is increasingly shaped not only by engine performance but also by advances in aerodynamics, which determine how effectively the available power is translated into lap time. **Heat** relates to the ongoing energy transition in Formula 1, where fuels (soon fully synthetic) play a central role in meeting environmental targets. This direction is directly aligned with one of the sport's key long-term objectives: achieving **net-zero emissions** while maintaining the performance standards expected of the series. Finally, **Precision** captures the complexity of modern power units and hybrid systems, supported by advanced telemetry and data analytics that allow engineers to fine-tune every detail of the car's operation.

The following sections develop each of these themes, showing how they collectively define the engineering core of contemporary Formula 1.

2. Speed

2.1. Structural evolution of Formula 1 cars

One of the main objectives of the new regulations was to address a long-standing issue in Formula 1: the difficulty of following another car at close range. This problem significantly limited overtaking opportunities and often prevented drivers from mounting a proper attack. The root cause lay in the 2021 car design, where downforce was distributed evenly between the front, the floor, and the rear of the car approximately 33% each – Fig. 4.

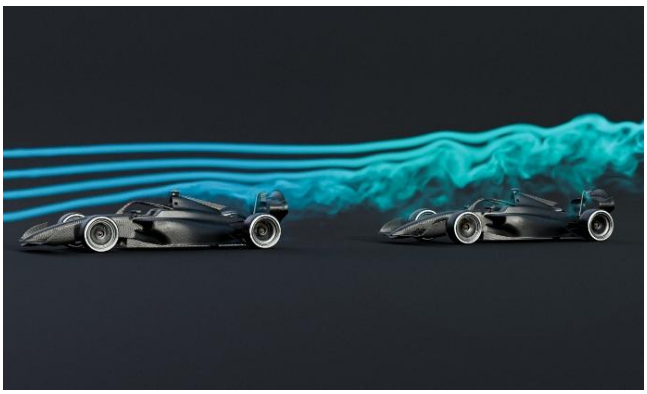

Fig. 3. Air flow representation [1]

With such a distribution, airflow disturbed by the leading car resulted in a substantial loss of front-end grip for the following driver. It is estimated that in turbulent air a car could lose up to 46% of its aerodynamic downforce [31]. This led to understeer, which, in turn, contributed to tyre overheating and accelerated tyre degradation – Fig. 3.

The turbulent wake generated by the rear of the leading car also reduced the effectiveness of the trailing car's front wing [6], further compromising stability and the ability to follow closely.

Since 2022, the role of the wings has been reduced, with greater emphasis placed on managing airflow beneath the car's floor. A simpler and more controlled aerodynamic structure was introduced, and the downforce distribution was adjusted accordingly: 25% at the front, 50% generated by the floor, and 25% at the rear – Fig. 4 [29].

The use of ground effect significantly reduced downforce loss in turbulent air, from approximately 46% in 2021 to around 10% in current designs.

Aerodynamics has always been a key factor in determining a Formula 1 car's performance. As technical regulations evolved, the approach to managing airflow around the vehicle changed repeatedly, from aggressive designs that generated extreme downforce to more regulated yet highly refined concepts used today. Each regulatory shift affected the balance between top speed, cornering stability, and the overall efficiency of using the available power.

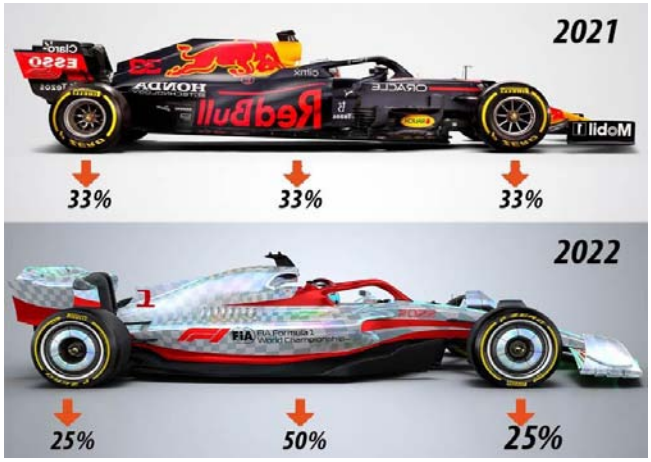

Fig. 4. Presentation of the pressure force distribution [42]

Structurally, one of the greatest challenges has been maintaining the car's minimum weight, including the driver. Modern Formula 1 cars are relatively heavy; according to regulations introduced in 2022, the car with the driver but without fuel must not exceed 798 kg [5]. For comparison, in 2005, cars were almost 200 kg lighter – Fig. 5.

The increase in weight has clear causes. Heavier and more advanced braking system components were introduced, and to a lesser extent, changes to the power unit also contributed to the weight gain. Additionally, the monocoque and impact structures had to be reinforced to meet far more stringent crash-test requirements [28].

Another challenge faced by car designers was modifying the vehicle's dimensions. Although the overall width of the car remained unchanged, the front wing was narrowed from 2000 mm to 1950 mm in accordance with the new regulations, ensuring that it no longer aligned with the outer edges of the front wheels [45].

Fig. 5. Weight of F1 cars over the years [19]

Fig. 6. Comparison of F1 car lengths over the years [7]

The new homologation procedures include more severe frontal, side, and rear impact tests, with higher collision speeds and higher energy-absorption thresholds. The chassis must maintain cockpit integrity under significantly greater loads than before, which requires additional composite layers and a strengthened structural design. As a result, driver safety has improved substantially, although at the cost of additional mass.

The car's length was also revised. Since the 2022 season, the maximum wheelbase has been limited to 3600 mm – Fig. 6. Previous regulations did not specify such a restriction, resulting in cars becoming shorter by several to over a dozen centimetres compared to earlier designs.

The 13-inch tyres used until the 2021 season were replaced with 18-inch tyres, which required the design of larger wheels and adjustments to the suspension layout. The current tyre diameter is 720 mm, making it 60 mm larger than the previous specification. The wheel widths, however, have been retained: 305 mm at the front and 405 mm at the rear – Fig. 7 [22].

The shift to larger tyres also necessitated changes to both the suspension components and the braking system. The updated regulations introduced new brake disc specifications – the number of cooling holes was reduced, and although the disc diameter was increased, its overall mass also rose. This reduced heat dissipation efficiency, making the brakes more prone to overheating during a race.

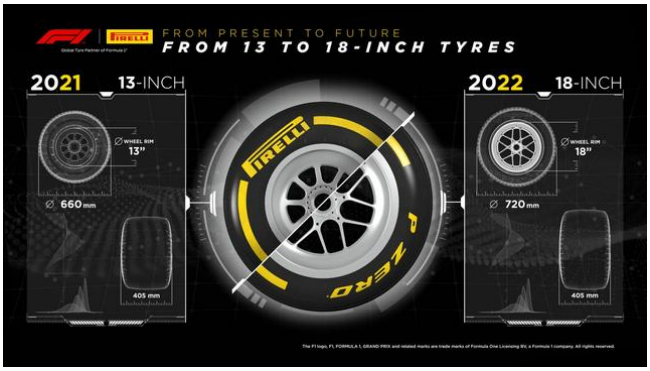

Fig. 7. Comparison of 13-inch and 18-inch tires [23]

The changes made to the tyres directly influence the evolution of the car's handling characteristics. They make the car more challenging to control at the limit and require the driver to adapt their driving style, particularly in braking behaviour and tyre temperature management [41].

The wheel covers introduced in 2022, designed to enclose the rims – Fig. 8, also serve an important aerodynamic purpose. They reduce airflow turbulence generated by the rotating wheels, which reduces the disturbed wake behind the car and improves the ability to follow another vehicle closely.

Fig. 8. The McLaren team uses hubcaps to promote their sponsor [25]

The structural changes introduced in recent years show that Formula 1 is gradually moving toward closer racing, greater safety, and more predictable on-track behaviour. The return of ground effect, simplified aerodynamics, and

the planned introduction of active aero all reshape how downforce is generated. At the same time, new requirements for weight, dimensions, and tyres affect how the car responds to loads and how it handles in corners. In practice, it is a continuous search for the right balance between performance and stability - an evolution of the car's architecture driven by the needs of modern Formula 1.

2.2. Changes in aerodynamics

Aerodynamics has undergone a similarly dynamic transformation. Since the 1970s, Formula 1 has oscillated between periods of extreme downforce generation, often followed by regulatory clampdowns introduced for safety reasons. Ground-effect cars, high-downforce sculpted bodywork, blown diffusers, and later, energy-efficient aero regulations all illustrate how the aerodynamic philosophy of F1 has repeatedly shifted in response to performance, safety, and regulatory constraints. The current technical regulations focus primarily on changes implemented in the central section of the car, where the number of aerodynamic components has been significantly reduced. This redesign enabled the reintroduction of ground effect into Formula 1 in 2022 [24]. The underbody concept is based on controlled external airflow, allowing air to move both beneath and above the vehicle and directly influencing the car's aerodynamic characteristics.

At the rear, a large diffuser has been installed, whose main function is to expand the airflow exiting the floor. This solution maximizes ground effect and enables the car to generate stable, predictable downforce.

In 2026, Formula 1 will introduce active aerodynamics [2], intended to support energy management, an essential requirement due to the characteristics of the new power units. Both the front and rear wings will feature movable elements, enabling higher cornering speeds and improved straight-line performance. The rear wing will consist of three segments – Fig. 9. At the same time, the *beam wing, the lower aero profile located beneath the main rear wing,* will be removed, and the side elements will be simplified.

Fig. 9. 2024 vs 2026 rear wing comparison [20]

The front wing, consisting of two movable flaps, will be narrowed by 100 mm. The wheel covers will also be removed and replaced with new side-section elements designed to reduce the turbulence generated by the front wheels. The car's floor will be partially flat, and the diffuser will be reduced in size and simplified [8], in order to limit ground effect and decrease the need for extremely low ride heights and very stiff suspension setups – Fig. 10.

Fig. 10. Projected car design [16]

The changes introduced in 2026 will affect the aerodynamic characteristics of the cars. Downforce is expected to decrease by around 30%, while aerodynamic drag will be reduced by 50%.

The 2026 regulations simplify key aerodynamic elements, reduce ground effect, and introduce active aero to better manage the car's performance.

2.3. Comparison of car dimensions: 2022 vs. 2026

The new technical regulations introduce changes not only to the power unit but also to the car's bodywork. The cars' dimensions will be reduced to improve agility. The maximum wheelbase will decrease from 360 cm to 340 cm, and the overall width will be reduced by 10 cm to 190 cm. Additionally, the floor width will be limited to 150 mm – Fig. 11.

These dimensional changes aim to achieve a new minimum weight of 768 kg, 30 kg lower than the current value. Calculations indicate that the car with the driver will weigh 722 kg, while the tyres will account for the remaining 46 kg. The wheels will also be narrowed while retaining their 18-inch diameter; their width will be reduced by 25 mm at the front and 30 mm at the rear [46].

Fig. 11. Comparison of the dimensions of the 2022 and 2026 cars [43]

3. Heat – sustainable fuels

One of the key factors shaping the thermal behaviour of the power unit is the type of fuel it uses. The shift toward sustainable fuels directly affects combustion characteristics, heat generation, energy efficiency, and overall engine performance. For this reason, alternative fuels naturally fall

under the *Heat* category, which defines how future Formula 1 engines will manage and convert thermal energy.

Sustainable fuels are still an emerging technology, but one with significant potential for development [17]. The new regulations give engine manufacturers considerable freedom, while simultaneously requiring them to use sustainable fuels that meet specific parameters. At present, there are two main production pathways: synthetic fuels and second-generation biofuels.

A key characteristic of sustainable fuel is its environmentally neutral lifecycle, from production to combustion. In contrast, today's fuels are derived from crude oil, and their extraction, refining, and burning all generate substantial emissions [34]. Since 2023, teams have been using fuel containing 55% bio-component content, but starting in the 2027 season, only fully synthetic, 100% sustainable fuel will be permitted – Fig. 12. Biofuels are fuels produced from biological materials such as crops, microorganisms, wood, and various types of waste. First-generation biofuels were the earliest category developed and relied mainly on food-based feedstocks such as corn, jatropha, or used cooking oils. Their use raised significant concerns, as diverting food crops for fuel production created ethical issues, affected livestock feed availability, and contributed to global food supply challenges. Second-generation biofuels, on the other hand, are produced from non-food biomass and biological waste. Formula 1 selected this type of biofuel because its production relies on materials that do not compete with food supply, including waste from the food industry, residual oils, straw, and wood. This approach is far more sustainable, making second-generation biofuels the preferred foundation for fuel development in F1 [11].

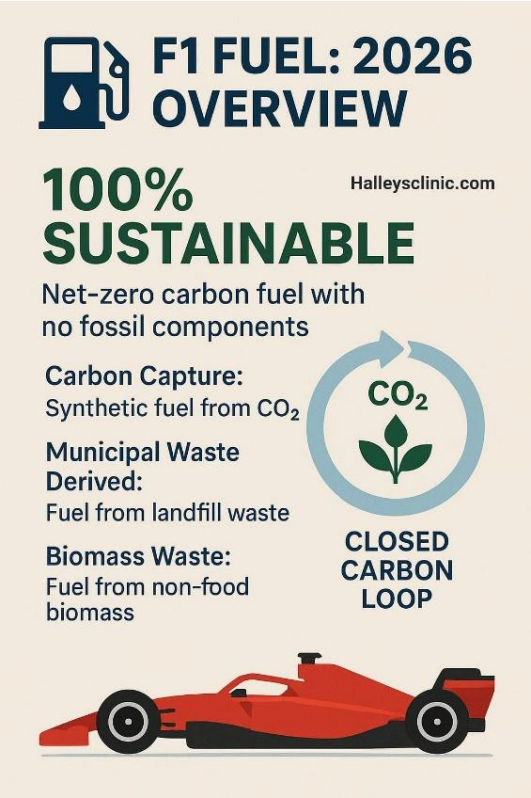

Fig. 12. Sustainable fuel in Formula 1 [14]

Synthetic fuels, also referred to as e-fuels or electrofuels, are produced by chemical processes that combine carbon dioxide captured from the atmosphere with hydrogen produced by water electrolysis [38]. The production of e-fuels requires significant electrical energy, which is why renewable energy sources are used to ensure the overall process remains environmentally neutral [4].

By capturing CO_2 directly from the atmosphere, the system forms a closed carbon loop: the amount of CO_2 released during combustion is offset by the CO_2 used to produce the fuel [18]. As a result, the use of e-fuels does not increase the total concentration of CO_2 in the atmosphere – Fig. 13.

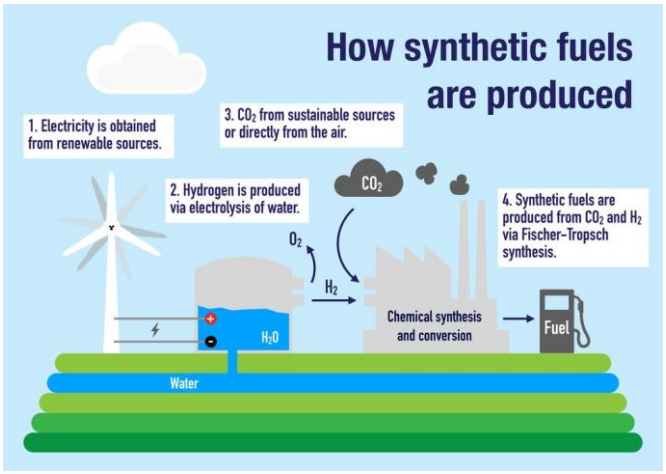

Fig. 13. Synthetic fuel production scheme [13]

Although sustainable fuels differ in their production pathways, their combustion properties share several key characteristics that influence engine behaviour. One of the most relevant parameters is energy density. Bioethanol, commonly used as a reference bio-component, has an energy density up to ~33% lower than conventional gasoline, which naturally increases fuel consumption for the same engine load [13]. Biodiesel, in contrast, remains closer to fossil diesel, with only around 8–10% lower energy content [13]. Synthetic fuels typically fall within a similar range: depending on the production method and carbon chain structure, their energy density may be comparable to advanced biofuels, although still lower than that of traditional fuels [35].

For Formula 1, this means that performance gains will not come from higher fuel energy content but rather from optimizing combustion parameters, ignition timing, and thermal management for the new fuel chemistry. The move to 100% sustainable fuels, therefore, shifts the engineering focus toward efficiency and precision in the combustion system rather than relying solely on the fuel's intrinsic energy potential.

4. Precision: engine

The power unit belongs in the *Precision* section because its performance depends on exact control of combustion, energy recovery, and thermal management. The precision required to synchronize the internal combustion engine with the electrical systems, along with the constant data-driven

adjustments made during operation, make the power unit one of the most complex and finely tuned components of the entire car.

The influence of sustainability and environmental goals has been evident in Formula 1 since 2014, when hybrid power units were introduced [37]. Starting in 2026, the FIA is taking another major step forward. Electrical energy will be required to account for 50% of the power unit's output – Fig. 14, meaning that electric and mechanical energy will be used in equal proportion [35].

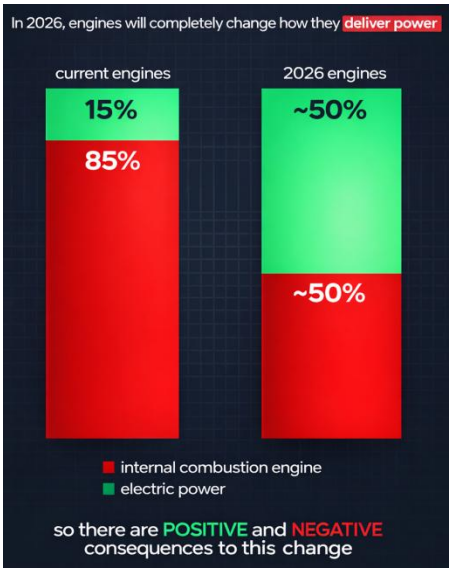

Fig. 14. The share of electricity in Formula 1 [40]

a)

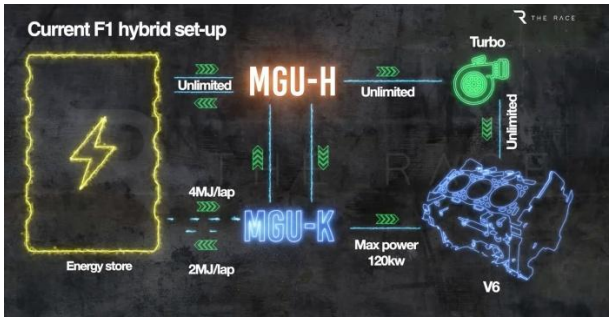

b)

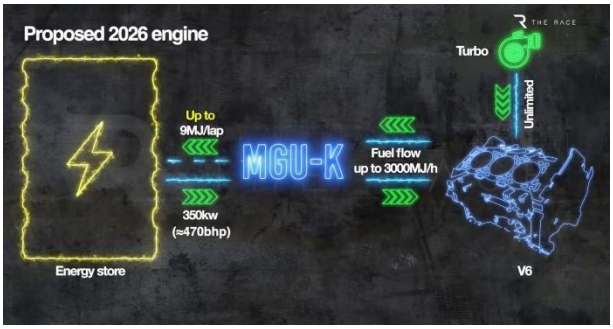

Fig. 15. Comparison of current and 2026 hybrid power unit configurations: a current F1 hybrid system layout, including the MGU-H, a) 120 kW MGU-K and unrestricted turbo operation; b) proposed 2026 power unit layout, without the MGU-H, featuring an increased 350 kW MGU-K and updated limits on energy deployment and fuel flow [21]

The 2026 Formula 1 car will debut with a newly designed power unit, in which the output of the internal combustion engine and the electric motor will be almost evenly balanced. This shift eliminates the MGU-H system and significantly increases the MGU-K's power to 350 kW, or roughly 469 HP – Fig. 15 [12].

The removal of the MGU-H is the most significant change introduced in the new power units. The way the engine generates power will change substantially, although the total output is expected to remain slightly above 1000 HP. The role of electrical energy will increase dramatically. The MGU-K is set to deliver around three times the power of 2025, from 120 kW to 350 kW [44], while the internal combustion engine will run on fully sustainable fuel. Its output will gradually decrease in proportion to the growing contribution of electrical energy [47].

However, the new power unit will be considerably heavier. The MGU-K will increase in mass from 7 kg to 20 kg, while the battery will grow from approximately 20–25 kg to a minimum of 35 kg. Despite removing the MGU-H, which saves about 4 kg, changes to other components increase the total engine weight from 151 kg to 185 kg.

Table 1. Comparison of the weight of the drive units [8, 9]

Parameter	Current engine	From 2026
Engine	~100 kg*	130 kg*
MGU-K	7 kg	20 kg**
MGU-H	4 kg	–
Battery	20–25 kg	35 kg
Total minimum weight	151 kg	185 kg
* together with the turbocharger		
** 16 kg MGU-K and 4 kg mechanical transmitter		

The updated regulations introduce two primary power unit operating modes: the standard mode mode *x* and the override mode mode *y* – Fig. 16 [3].

Fig. 16. Differences between the new engine modes [26]

In standard mode, the car may deliver the full electric output of 350 kW (476 HP) up to a speed of 290 km/h. Beyond this point, the permitted electrical energy gradually decreases, reaching 105 kW as long as the speed does not exceed 339 km/h [27]. From 340 km/h, the electric power is capped at 105 kW, and once the car surpasses 345 km/h, electrical deployment becomes unavailable. Based on the FIA's published values, the maximum speeds are expected to remain similar to those achieved today.

The override mode operates similarly but at higher speeds. Full electric power will be available up to 337 km/h, after which it will be progressively reduced until the car reaches 355 km/h. Above this threshold, electrical energy may no longer be deployed.

The 2026 power unit marks one of the biggest structural shifts in modern Formula 1. With the removal of the MGU-H, a tripled MGU-K output, and an equal 50–50 split between electric and mechanical energy, the new system relies far more on precise energy management than raw engine power. Although the total output will remain just above 1000 hp, the way this performance is generated becomes much more complex, demanding exact control of deployment, recovery, and thermal behaviour. The increased weight of key components and the introduction of two operating modes further underline how dependent future power units will be on accuracy and data-driven optimisation making precision the defining element of the 2026 engine architecture.

5. Summary

In 2022, major aerodynamic regulations were introduced to improve on-track racing and reduce the negative impact of dirty air generated by the cars. The key updates included:

- the return of ground effect – most of the downforce is generated by the floor rather than complex upper-body aero
- simplified front and rear wings – to reduce turbulence and make following another car easier
- 18-inch tyres – offering greater durability and improving race strategy.

The V6 Turbo Hybrid engines used from 2014 to 2025 produce around 1000 HP, with approximately 850 HP from the internal combustion engine and 150 HP from the MGU-K. The total weight of the power unit increased to 151 kg due to the addition of advanced electrical components and batteries.

Key technical limitations include:

- fuel-flow limit of 100 kg/h
- fuel mass limit of 110 kg per race
- engine speed capped at 15,000 rpm
- mandatory use of E10 fuel containing 10% biocomponents.

A major technological shift will take place in 2026 – Fig. 18. The most important changes include:

- removal of the MGU-H – simplifying engine architecture and reducing costs
- increasing MGU-K output to 350 kW (469 HP) – electric power will account for 50% of the total output
- introduction of fully synthetic fuels – reducing CO_2 emissions and encouraging competition between fuel suppliers
- reducing car weight to 768 kg – through updated dimensions and new materials.

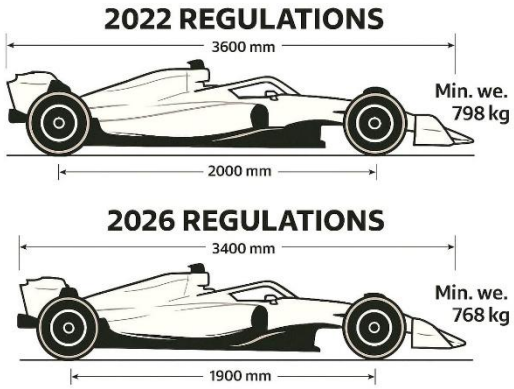

Fig. 18. Comparison of the 2022 and 2026 cars [15]

Active aerodynamics and engine operating modes: Future cars will feature active aerodynamics, with movable front and rear wings that automatically adjust based on speed and race strategy. The FIA will also introduce two operating modes for the power unit:

- standard mode X: full electric power available up to 290 km/h, gradually reduced beyond that point
- override mode Y: short bursts of increased power for overtaking, with deployment limited to speeds below 355 km/h.

Together, these updates aim to improve the racing spectacle and accelerate the transition toward more sustainable technologies. Changes Formula 1's position as a key technological testbed for future road-relevant propulsion systems, accelerating innovation in hybridisation, energy recovery and sustainable fuels.

Nomenclature

AI	artificial intelligence
E10	ethanol 10% fuel
ERS	energy recovery system
FIA	Fédération Internationale de l'Automobile
ICE	internal combustion engine
MGU-H	motor generator unit – heat
MGU-K	motor generator unit – kinetic

Bibliography

[1] Badiger R. What's the difference between slipstream and dirty air? 2025. https://www.raceteq.com/articles/2025/07/slipstream-vs-dirty-air-explained (accessed on 02.12.2025).

[2] Barretto L. FIA unveils Formula 1 regulations for 2026 and beyond. https://www.formula1.com/en/latest/article/fia-unveils-formula-1-regulations-for-2026-and-beyond-featuring-more-agile.75qJiYOHXgeJqsVQtDr2UB (accessed on 02.12.2025).

[3] Barretto L. 2026 aero regulations explained. https://www.formula1.com/en/latest/article/explained-2026-aerodynamic-regulations-fia-twitter-mode-z-mode-.26c1CtOzCmN3GfLMywrgb2 (accessed on 02.12.2025).

[4] Ekechukwu DE, Daramola GO, Kehinde OI. Advancements in catalysts for zero-carbon synthetic fuel production. GSC Adv Res Rev. 2024;19(3):215-226. https://doi.org/10.30574/gscarr.2024.19.3.0212
[5] Elshebiny Y. F1 explained: how much does a Formula 1 car weight in 2024? https://www.gpfans.com/en/f1-news/1028252/f1-car-weight-explained/ (accessed on 02.12.2025).
[6] Falkborn L, Hasselgren W. Numerical investigation of a drag-reduction system on a Formula 1 front wing. 2024. https://www.diva-portal.org/smash/record.jsf?pid=diva2:1886199 (accessed on 02.12.2025).
[7] Facebook image source. https://www.facebook.com/photo.php?fbid=5616805125079232&id=808646069228519&set=a.810005275759265&locale=ku_TR (accessed on 02.12.2025).
[8] FIA. 2026 Formula 1 Technical Regulations. https://www.fia.com/F126 (accessed on 02.12.2025).
[9] FIA. 2022 Formula 1 Technical Regulations. https://www.fia.com/sites/default/files/2022_formula_1_technical_regulations_-_iss_3_-_2021-02-19.pdf (accessed on 02.12.2025).
[10] Fry J, Brighton T, Fanzon S. Faster identification of faster Formula 1 drivers via time-rank duality. Economics Letters. 2024;111671. https://doi.org/10.1016/j.econlet.2024.111671
[11] Gautam A, Pant M, Pant G, Kumar G. Second-generation biofuels: concepts, applications, and challenges. In: Karnwal A, Mohammad Said Al-Tawaha AR (eds). Microbial applications for environmental sustainability. Springer 2024; 277-304. https://link.springer.com/chapter/10.1007/978-981-97-0676-1_16
[12] Gołowicz A. Energy recovery systems in braking. Transport Samochodowy. 2024;69(1):49-59. https://doi.org/10.5604/01.3001.0054.6268
[13] Gonzalez A. European e-fuel policy. https://www.motorfinanceonline.com/news/european-e-fuel-policy-could-save-classic-and-historic-vehicles/ (accessed on 02.12.2025).
[14] Halleys Clinic. What is the 2026 100% sustainable fuel in Formula 1? https://medium.com/@halleysclinic/what-is-the-2026-100-sustainable-fuel-in-formula-1-3aab93240ba4 (accessed on 02.12.2025).
[15] Halleys Clinic. Are F1 2026 cars lighter and smaller? 2025. https://medium.com/@halleysclinic/are-f1-2026-cars-lighter-and-smaller-new-regulation-b12e0d41da7a (accessed on 02.12.2025).
[16] Jupp E. FIA reveal 2026 F1 rules. https://www.goodwood.com/grr/f1/fia-reveal-2026-f1-rules/ (accessed on 02.12.2025).
[17] Kusz M. Formuła 1 w obliczu potrzeby zrównoważonego rozwoju (in Polish). In: W kierunku zrównoważonego rozwoju. UE. Poznań 2024;69-81. https://www.ceeol.com/search/chapter-detail?id=1307504 (accessed on 02.12.2025).
[18] Li Y, Guan B, Guo J, Chen Y, Ma Z, Zhuang Z et al. Renewable synthetic fuels: research progress and development trends. J Clean Prod. 2024;450:141849. https://doi.org/10.1016/j.jclepro.2024.141849
[19] Mazur A. Pojazdy w F1 z roku na rok rosną jak na drożdżach (in Polish). 2024. https://boop.pl/f1/pojazdy-w-f1-z-roku-na-rok-rosna-jak-na-drozdzach-jak-bardzo-ich-waga-zwiekszyla-sie-na-przestrzeni-lat#google_vignette (accessed on 02.12.2025).
[20] Mitchell-Malm S. Why F1's dropping DRS for its 2026 cars. https://www.the-race.com/formula-1/f1-dropping-drs-2026-cars-explained/ (accessed on 02.12.2025).
[21] Mitchell-Malm S. What's really going on with F1's controversial 2026 cars. https://www.the-race.com/formula-1/what-are-f1-2026-engine-chassis-rules/ (accessed on 02.12.2025).
[22] Pirelli. F1 Tires: details and technical data. https://www.pirelli.com/tires/en-us/motorsport/f1/tires (accessed on 02.12.2025).
[23] Pirelli tire comparison 2021/2022. https://www.reddit.com/r/formula1/comments/qw1pmw/pirelli_tire_comparison_between_2021_and_2022/ (accessed on 02.12.2025).
[24] Pothamsetti V. Reducing drag by optimizing the underbody with ride height in Formula 1. Am J Student Res. 2024(4): 29-33. https://doi.org/10.70251/HYJR2348.242933
[25] Prezentacja bolidu McLaren MCL38 na sezon 2024 (in Polish). https://www.cyrkf1.pl/prezentacja-bolidu-mclaren-mcl38-na-sezon-2024/ (accessed on 02.12.2025).
[26] Reddit discussion thread. https://www.google.com/url?sa=i&url=https%3A%2F%2Fwww.reddit.com%2Fr%2Fformula1%2Fcomments%2F1lj3g45%2Fask_rformula1_anything_daily_discussion_thread%2F&psig=AOvVaw0KVpHKDVJBeqzEKjYO9x-r&ust=1764706094650000&source=images&cd=vfe&opi=89978449&ved=0CBQQjhxqFwoTCKjw496YnZEDFQAAAAAdAAAAABAE (accessed on 02.12.2025).
[27] Samarins. OHV vs OHC vs SOHC vs DOHC. https://www.samarins.com/glossary/dohc.html (accessed on 02.12.2025).
[28] Savage G. Formula 1 materials engineering. In: Materials Science and Engineering. CRC Press; 2024:155-184. https://www.taylorfrancis.com/chapters/edit/10.1201/9781003580201-12/formula-1-materials-engineering-savage (accessed on 02.12.2025).
[29] Shaalan A, Assanis D, Raman A, Wijeyakulasuriya S, Senecal K. Formula 1 race car aerodynamics. SAE Technical Paper 2024-01-2078. 2024. https://doi.org/10.4271/2024-01-2078
[30] Shakila T, Baalaji K. Optimizing tyre and brake performance in Formula 1 using big data analytics: a survey on predictive models and strategies. 2025 International Conference on Emerging Trends in Industry 4.0 Technologies (ICETI4T), Navi Mumbai, India, 2025;1-6. https://doi.org/10.1109/ICETI4T63625.2025.11132168
[31] Shehadi M. Testing ground-effect aerodynamics on a scaled F1 car. 2021 ASEE Virtual Annual Conference Content Access, Virtual Conference. https://doi.org/10.18260/1-2--36524
[32] Shin A. Comparative analysis of traditional Formula 1 combustion engines and modern hybrid power units. Lens J. 2025;3(1):1-11. https://zenodo.org/records/14635481
[33] Shukurbayevich MF. Light car gas distribution mechanism structure. Web Teach Ind Res. 2025;3(2):214-216. http://webofjournals.com/index.php/1/article/view/3357
[34] Somashekarappa M, Nuchhi S. Comparative analysis of alternative fuels for internal combustion engines: biofuels, synthetic fuels and hydrogen. World J Adv Res Rev. 2022; 14(2):724-734. https://doi.org/10.30574/wjarr.2022.14.2.0383
[35] Stepien Z. The pro-ecological evolution of powertrains and fuels in Formula 1. Energies. 2025;18(22):6013. https://doi.org/10.3390/en18226013

[36] Stępień Z. A new generation of F1 race engines – hybrid power units. Combustion Engines. 2016;167(4):22-37. https://doi.org/10.19206/CE-2016-403
[37] Szumska E, Skuza A. Enhancing regenerative braking efficiency in electric vehicles through urban driving pattern analysis. Combustion Engines. 2025;203(4):191-200. https://doi.org/10.19206/CE-207871
[38] Szwajca F, Pielecha I, Mielcarzewicz D. Experimental investigation on the influence of passive/active pre-chamber injection strategy on the hydrogen knock limit. Combustion Engines. 2025;203(4):32-41. https://doi.org/10.19206/CE-207382
[39] Team Telemetry. https://www.teamtelemetry.de/team-telemetry/ (accessed on 02.12.2025).
[40] Tiktok image source. https://www.tiktok.com/@formulaworldproject/photo/7569680472750525719 (accessed on 02.12.2025).
[41] Trzesniowski M. Tyres and wheels. In: Suspension System. Springer Vieweg, Wiesbaden 2023. https://doi.org/10.1007/978-3-658-39847-7_1
[42] Trzosek K. Prostsza budowa, ale czy lepsza? (in Polish) 2022. https://f1.dziel-pasje.pl/news/34818/Prostsza-budowa-ale-czy-lepsza?-Omowienie-zmian-technicznych-na-rok-2022 (accessed on 02.12.2025).
[43] Twitter/X image source. https://www.google.com/url?sa=i&url=https%3A%2F%2Fx.com%2Fcolepearn&psig=AOvVaw2UrFkBWUzYYeJPTzIcjp-P&ust=1764699956376000&source=images&cd=vfe&opi=89978449&ved=0CBQQjhxqFwoTCKCPha2CnZEDFQAAAAAdAAAAABAE (accessed on 02.12.2025).
[44] Vasudev R. Hybrid power unit efficiency in Formula 1: thermal management, energy recovery. Strategies and performance optimization. International Journal for Multidisciplinary Research. 20257(4):1-9. https://www.ijfmr.com/papers/2025/4/53663.pdf?utm_source=chatgpt.com
[45] Winiewski J. Formuła 1 technicznie: wpływ masy na osiągi bolidu F1. https://www.redbull.com/pl-pl/f1-technika-masa-osi%C4%85gi-bolidu (accessed on 02.12.2025).
[46] Winiewski J. Formuła 1 technicznie: zmiany przed sezonem 2026. https://www.redbull.com/pl-pl/f1-zmiany-sezon-2026 (accessed on 02.12.2025).
[47] Xu J. Thermodynamic evaluation of 2026 power unit regulations. 2023. https://www.ewadirect.com/proceedings/ace/article/view/5615/pdf?utm_source=chatgpt.com (accessed on 02.12.2025).

Oliwia Kropisz, Eng. – Faculty of Civil and Transport Engineering, Poznan University of Technology, Poland.
e-mail: *oliwia.kropisz@student.put.poznan.pl*

Bartłomiej Zandecki, Eng. – Faculty of Civil and Transport Engineering, Poznan University of Technology, Poland.
e-mail: *bartlomiej.zandecki@student.put.poznan.pl*

Kinga Skobiej, DEng. – Faculty of Civil and Transport Engineering, Poznan University of Technology, Poland.
e-mail: *kinga.skobiej@put.poznan.pl*

Article citation info:
Górzyńska M, Pielecha I. Hydrogen combustion in piston engines: challenges and modeling approaches. Combustion Engines. 2026;206(3):179-198. https://doi.org/10.19206/CE-218594

Marcelina GÓRZYŃSKA
Ireneusz PIELECHA

Combustion Engines
Polish Scientific Society of Combustion Engines

Hydrogen combustion in piston engines: challenges and modeling approaches

ARTICLE INFO

Received: 8 January 2026
Revised: 20 February 2026
Accepted: 25 February 2026
Available online: 22 April 2026

This article presents a comprehensive analysis of hydrogen combustion issues in reciprocating engines and the potential for numerical modeling in the context of developing low-emission technologies. The advantages and technical and environmental challenges associated with its use are presented, with particular emphasis on nitrogen oxides emissions, ignition control, and material requirements. This article takes a closer look at how advanced numerical modeling methods – such as computational fluid dynamics, large eddy simulation, and direct numerical simulation – help better understand the hydrogen combustion process in piston engines. These methods reveal flame behavior, combustion processes, and associated emissions. The authors compare various computational programs and demonstrate how simulation can aid in combustion chamber design, ignition timing, and mixture tuning. The article summarizes the most important findings in this field and outlines the direction hydrogen technology is headed. The analysis indicates that hydrogen addition (typically 10–30% by volume) can enhance combustion stability and indicated thermal efficiency under lean conditions, although excessive hydrogen fractions do not guarantee further performance gains. At the same time, challenges related to NO_x formation, pre-ignition, and mixture control require advanced injection strategies and precise combustion calibration. The reviewed studies confirm that high-fidelity numerical modelling is essential for capturing preferential diffusion and turbulence–chemistry interactions, making it a key tool in the optimization of hydrogen-fueled piston engines.

Key words: *hydrogen combustion, internal combustion engines ICE, numerical modelling, hydrogen-enriched fuels, CFD simulation*

This is an open access article under the CC BY license (http://creativecommons.org/licenses/by/4.0/)

1. Introduction

1.1. The importance of hydrogen as a fuel in the context of energy transformation

Contemporary transformations in the energy sector are driven not only by growing energy demand but also by the urgent need to reduce the impact of human activity on the natural environment. The depletion of fossil fuel resources and the greenhouse gas emissions associated with their combustion are driving the search for alternative solutions that can ensure energy security while also promoting the decarbonization of the economy. In response to these challenges, low-emission fuels such as biofuels, natural gas, and hydrogen are increasingly being utilized [38], which could play a significant role in shaping the future of energy.

Among all emerging clean-energy options, hydrogen stands out as one of the most promising. It combines high energy content, zero-emission combustion, and flexibility of use across industry, transport, and power generation, making it a strategic part of the global energy shift [61]. In 2024, world hydrogen use reached about 100 million tons – growth fueled more by overall economic activity than by climate policy. Even with stronger policy support, low-carbon hydrogen production may hit only 6 million tons by 2030, or roughly 10 percent of what's envisioned in the NZE 2050 scenario [48]. Hydrogen's role in the energy transition is clear, but unlocking its full potential will demand both new technologies and a broader, sustainability-oriented approach to future energy planning [74].

Due to the instability of renewable sources caused by weather conditions and seasonality, they cannot ensure a continuous energy supply at the desired level [59]. Therefore, systems for hydrogen production and storage are seen as a key element in the transition to emission-free energy technologies, replacing coal-fired power plants [39]. As the transition to climate neutrality speeds up, hydrogen is gaining attention as a strategic fuel for the future. By 2030, global demand could reach 150 million tons a year, with almost half expected to come from low-carbon production. Still, most hydrogen today is produced from fossil fuels, which emit around 920 million tons of CO_2 each year. Developing cleaner ways to produce hydrogen, such as renewable-powered electrolysis or carbon-capture reforming, is now one of the top priorities for decarbonizing energy and industry [48, 66]. In 2023, hydrogen consumption rose by 2.5%, hitting a record 97 million tons (Fig. 1).

Currently, China accounts for nearly one-third of global hydrogen demand, followed by the US at roughly 14%. The increase in global hydrogen demand has been driven mainly by its broader use in oil refining, chemical processing, and ironmaking via DRI technologies that utilize hydrocarbon-based syngas. Nevertheless, fossil-derived hydrogen still dominates production, mostly without carbon capture, resulting in nearly 920 Mt of CO_2 emissions per year – exceeding those of entire nations such as France or Indonesia [48].

According to the Net Zero Emissions 2050 scenario, hydrogen consumption is forecast to reach around 150 million tonnes annually by 2030. Approximately 45% of this total will come from low-carbon production routes, while roughly 40% of the growth will originate from emerging applications such as heavy transport, industrial decarbonization, e-fuel synthesis, and renewable-based power systems [48].

1.2. Hydrogen combustion characteristics compared to conventional fuels

Hydrogen, which produces only water vapor during combustion and no CO_2, has become one of the most promising alternatives to conventional fuels. Research interest in

its use for powertrains has increased, especially in combustion and hybrid systems, where hydrogen offers a path to lower emissions without abandoning existing infrastructure. This trend is well-documented in the scientific literature, which emphasizes studies on the design, performance, and control of hydrogen-powered engines [70] and their implementation in hybrid configurations [4]. Comparative experiments involving spark-ignition engines operating on hydrogen and gasoline [56] demonstrate notable variations in efficiency, output performance, and pollutant emissions.

In addition, a growing body of work investigates hybrid engines operating on hydrogen-enriched conventional fuels [2, 3] and includes combined theoretical and experimental analyses evaluating these systems' effectiveness [62, 69].

Research consistently demonstrates that supplementing the intake charge with a hydrogen–oxygen mixture enhances energy efficiency and decreases CO and HC emissions, though it may simultaneously raise NO_x concentrations, particularly when used with low-ethanol gasoline blends [67]. At the same time, increasing research attention has been devoted to sustainable biofuels, which are now widely regarded as complementary energy carriers thanks to their advantageous combustion behaviour, often matching or even surpassing that of conventional fossil fuels [14]. Work in this area spans alcohols [7, 21], hydrogen [34], biogas [13], biofuels [28, 33], and dimethyl ether [45]. all of which display unique emission and performance profiles. Another promising line of investigation concerns nanoparticles [1], used as fuel additives, which appear to enhance flame propagation, improve thermal efficiency, and reduce pollutant concentrations.

Hydrogen's footprint in road transportation remains small but is expanding quickly. In 2023, global hydrogen demand for road transport reached approximately 60 kilotonnes, representing less than 0.1% of total consumption but marking a 55% increase from 2022. The most dynamic growth occurred in fuel-cell truck and bus fleets, particularly in China, where per-vehicle hydrogen usage is considerably higher than in passenger transport [48]. Data from 2021–2023 indicate that commercial vehicles – including trucks, delivery vans, and public buses – were the main drivers of this expansion, with hydrogen consumption nearly doubling over the course of one year. These results highlight that hydrogen currently has the greatest potential in high–energy–demand sectors of road transport, where continuous operation, practical refueling, and system efficiency best leverage its inherent advantages (Fig. 2).

Analysis of data from 2021–2023 clearly indicates that the increase in demand is primarily related to commercial vehicles. Although hydrogen consumption in the passenger car segment has been gradually increasing. In 2023, the largest share was accounted for by commercial vehicles including delivery vans and trucks, whose demand for hydrogen almost doubled compared to the previous year. The

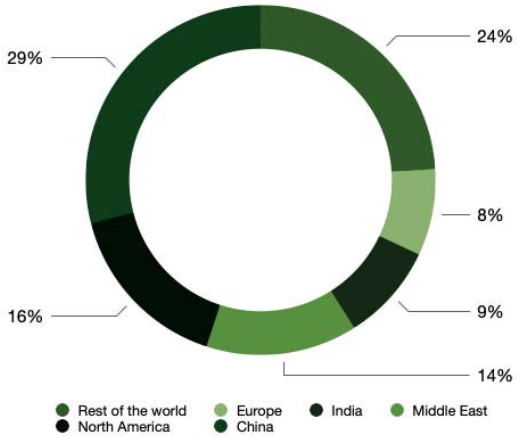

Fig. 1. Geographical differentiation of hydrogen consumption in 2023 [48]

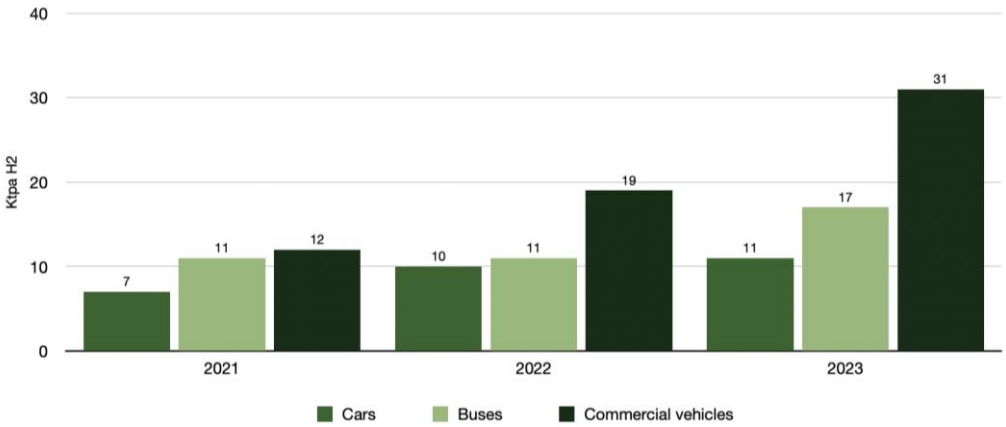

Fig. 2. Hydrogen consumption breakdown in road transport: global segment perspective [48]

bus segment also showed significant growth, reflecting the growing number of fuel cell-based urban public transport fleet projects (Fig. 2). These findings confirm that hydrogen use in road transport offers the greatest potential in sectors with high energy demands and intensive driving cycles, making buses and trucks the most natural and promising applications for this technology.

2. General overview of hydrogen as a fuel

2.1. Physicochemical properties of hydrogen affecting combustion

Hydrogen as a fuel has unique combustion properties compared to conventional fuels. Its very low ignition energy (approximately 0.02 mJ) and high combustion velocity (over 260 cm/s) make it possible to achieve ignition even with a small energy dose and in lean mixtures [19, 30, 69]. The high temperature of the hydrogen flame (approximately 2390 K) promotes efficient energy release, but can lead to increased nitrogen oxide (NO_x), emissions, requiring the use of combustion control systems such as exhaust gas recirculation or mixture cooling. [63]. Hydrogen, unlike traditional hydrocarbon fuels, does not emit carbon dioxide during combustion, making it an important contributor to efforts to reduce emissions in transport and the energy sector [30, 69].

Additionally, it is used as an admixture in alternative fuel blends, including methane (CH_4), biogas, LPG, CNG, ammonia (NH_3), and diesel fuel in dual-fuel solutions. Table 1 clearly shows that adding hydrogen, even in small to moderate amounts, has a strong positive effect on combustion. It leads to quicker ignition, greater mixture reactivity, and a faster-moving flame. When used with methane (CH_4), hydrogen allows the fuel to burn more rapidly and with less ignition energy. In ammonia-based blends, hydrogen serves to stabilize combustion by compensating for ammonia's low chemical reactivity, which results in smoother and more dependable engine operation. Likewise, in biogas-fueled setups, introducing H_2 increases the combustion rate and improves cycle-to-cycle uniformity. These effects are especially beneficial in micro-cogeneration systems, transport applications, and farm machinery. In dual-fuel systems (e.g., diesel–H_2), hydrogen as a secondary fuel not only reduces diesel consumption but also, thanks to its faster combustion, shortens ignition time. Table 1 shows that, regardless of the base fuel, H_2 admixture plays a key role in improving the efficiency and stability of combustion.

Fuel mixtures with hydrogen, so-called H_2-blends, are increasingly being analyzed as transitional solutions. Adding hydrogen to methane, biogas, LPG, or even ammonia significantly improves ignitability, increases flame speed, and combustion stability, which is particularly important in low-temperature engine operating conditions or in cogeneration technologies [47, 52]. Using hydrogen as an admixture not only reduces CO_2 and carbon monoxide emissions but also enables the combustion of more difficult fuels (e.g., ammonia) while maintaining stable engine operating conditions [52, 69]. Compared to conventional fuels, hydrogen blends demonstrate better combustion cycle repeatability, shorter ignition time, and the potential to significantly reduce harmful emissions [8].

Hydrogen also has an exceptionally high calorific value of approximately 120 MJ/kg, making it one of the most energetic fuels currently available [58]. For comparison, the calorific value of gasoline is approximately 44 MJ/kg, while that of natural gas is approximately 50 MJ/kg. Combustion of hydrogen with oxygen produces only water vapor, without the emission of carbon dioxide (CO_2), sulfur oxides (SO_x), or particulate matter [30, 31].

Due to its wide flammability range (4% to 75% by volume in air), hydrogen can be burned in very lean mixtures, making it an extremely flexible fuel across engine operating conditions [16, 30]. Moreover, hydrogen exhibits a high flame front velocity of approximately 2.65–3.25 m/s, several times higher than that of methane or gasoline. This property favors rapid and complete combustion (64), but in the absence of precise process control, it can cause undesirable phenomena such as combustion knock, flashback, or uneven reaction [69].

Storage and safety remain major limitations to the widespread use of hydrogen as a fuel. Due to its very low density under normal conditions, hydrogen must be compressed to high pressures or liquefied at low temperatures, which incurs additional energy and material costs [11, 15, 69]. Furthermore, hydrogen is colorless and odorless, and its very low ignition energy increases the risk of explosion in the event of a leak [11, 32, 67]. Despite existing limitations, hydrogen is a key element of the upcoming energy transformation. It is increasingly being treated not only as a fuel but also as an effective energy carrier and storage medium,

Table 1. Comparison of the physicochemical properties of hydrogen, methane, gasoline, and diesel [51, 57]

Property	Hydrogen	Methane	Gasoline	Diesel
Carbon content [mass%]	0	75	84	86
Density (at 1 bar & 273 K); [kg/m^3]	0.089	45.8	43.9	42.5
Molecular weight	2.016	16.043	110	170
Boiling point [K]	20	111	298–488	453–633
Auto-ignition temperature [K]	853	~813	~623	~523
Minimum ignition energy in air (at 1 bar & at stoichiometry) [mJ]	0.02	0.29	0.24	0.24
Stoichiometry air/fuel mass ratio	34.4	17.2	14.7	14.5
Quenching distance (at 1 bar & 298 K at stoichiometry) [mm]	0.64	2.1	2	–
Flammability limits in air [vol%]	4–76	5.3–115	1–7.6	0.6–5.5
Adiabatic flame temperature (at 1 bar & 298 K at stoichiometry) [K]	2480	2214	2580	2300
Octane number (R+M)/2	130+	120+	86–94	–
Cetane number [–]	–	–	13–17	40–55

capable of integrating various economic sectors: transport, energy, and industry [29]. Further progress, however, requires the development of production technologies such as electrolysis powered by renewable energy sources, the expansion of transmission and storage infrastructure, and the establishment of consistent safety standards [11, 72].

2.2. Selected technologies for the use of hydrogen in piston engines (blends)

Using hydrogen as an additive to traditional fuels in piston engines is currently considered one of the most promising solutions for reducing exhaust emissions, without requiring a complete modernization of the drive system. Hydrogen-fuel blends (H_2-blends) enable partial replacement of fossil fuels with gaseous hydrogen, reducing CO_2 and CO emissions while also affecting ignition and combustion characteristics. Due to its high reactivity, wide flammability range, and low ignition energy, hydrogen significantly alters flame front dynamics, enabling lean mixture operation and improving cycle repeatability. Depending on the base fuel used, such as methane, LPG, biogas, or diesel, various hydrogen injection strategies are used, including direct injection, sequential injection, dual-fuel systems, and premixing. To ensure stable, controlled combustion of the hydrogen-fuel mixture, it is crucial to properly develop a fuel strategy and optimize the component ratios. This helps avoid unfavorable phenomena such as combustion knock, flashback, and excessive NO_x emissions. Modern design processes increasingly use CFD numerical modeling, which enables detailed analysis of the mixture's behavior in the combustion chamber, accounting for the effects of geometry, turbulence, and gas residence time. The results of such simulations are essential for developing modern, efficient engines optimized for hydrogen fueling across diverse operating conditions.

Hydrogen as a fuel exhibits unique physicochemical properties that distinguish it from conventional hydrocarbon fuels [57]. Furthermore, its combustion rate in the engine chamber is approximately six times that of gasoline, resulting in a shorter combustion duration and reduced thermal losses. In mixtures of hydrogen with other fuels, especially gases such as methane or LPG, appropriate injection and ignition control strategies enable the exploitation of the synergistic properties of both components. Dual-fuel systems enable the adaptation of existing engines to co-combustion of hydrogen with a base fuel, but require precise control of stoichiometric ratio and ignition timing to avoid undesirable phenomena such as combustion knock, pre-ignition, or flashback [57, 74].

As shown in Table 1, hydrogen has unique physicochemical properties that significantly shape combustion in piston engines, particularly in dual-fuel systems. With its very low ignition energy (0.02 mJ) and wide flammability range (4–76% by volume), hydrogen is an exceptionally reactive fuel, capable of igniting even under conditions where traditional fuels fail. Its high flame temperature (2480 K) improves engine thermal efficiency but also increases the risk of NO_x emissions, requiring precise temperature and mixture control. Owing to its high stoichiometric air-to-fuel ratio [4, 38] and minimal flame extinction distance (≈0.64 mm), hydrogen supports very rapid combustion front movement, but also presents a higher risk of knock and flashback, notably in high-compression-ratio engines.

Its low density under normal conditions (0.089 kg/m³) limits the energy content per unit volume [MJ/m³], which is compensated for by appropriate design solutions, such as direct injection or systems operating at increased pressure [57]. Such properties require the use of advanced modeling methods, including CFD simulations, which include analysis of chemical kinetics, turbulence, and heat transfer, which allows for the prediction of the behavior of the fuel-air mixture containing hydrogen. To ensure high efficiency and low emissions with stable engine operation, precise optimization of the ignition strategy, combustion chamber shape and operating parameters is necessary depending on the type of base fuel (e.g. methane, LPG, diesel).

Controlling nitrogen oxide (NO_x) emissions remains a major challenge in operating hydrogen-fueled combustion systems. The inherently high flame temperatures of hydrogen promote NO_x formation; however, employing lean-burn mixtures, exhaust gas recirculation (EGR), and retarded ignition strategies can significantly lower emissions, keeping them within the limits of forthcoming regulatory standards. It is also worth emphasizing that hydrogen internal combustion engines (H_2-ICEs) are already close to industrial implementation, given their technological maturity and low dependence on critical raw materials, distinguishing them from fuel cell systems [4, 57].

The use of hydrogen-methane mixtures (so-called H_2–CH_4 blends) in piston engines allows for significant improvements in combustion parameters, such as flame propagation speed and shortened ignition delay time. The addition of hydrogen increases the heat release rate and shortens the time between ignition and the pressure peak, thereby improving the overall efficiency of the process. Studies show that even with H_2 contents of 10–40% by volume, flame speed can be increased by several dozen percent compared to pure methane [35]. Increasing hydrogen concentration not only accelerates the combustion reaction but also extends the mixture's ignition limits. Laboratory experiments have shown that the addition of H_2 shifts the maximum flame speed toward richer mixtures and broadens the φ range in both the lean and rich zones. For example, for a CH_4–H_2 mixture with 50% hydrogen, the ignition limit was extended from $\varphi = 0.5$ to $\varphi = 1.6$. This characteristic allows engines to operate under a wider range of load conditions [35, 62]. However, the technical aspects of combustion of such mixtures are complex and dependent on many parameters – pressure, initial temperature, gas composition, and combustion chamber geometry. Furthermore, the effect of pressure on flame velocity is not always intuitive; existing empirical relationships are subject to revision in light of the latest experimental data and CFD calculations. This demonstrates the importance of conducting further research both in laboratory conditions and in industrial-scale engines.

The introduction of hydrogen into natural gas fuel mixtures, known as HCNG (hydrogen–compressed natural gas), significantly alters their energy and combustion properties. As shown in Table 2, increasing the volumetric frac-

tion of hydrogen from 10% to 30% leads to a gradual increase in the specific calorific value of the mixture (LHV [MJ/kg]), while simultaneously reducing the volumetric calorific value (LHV_{vol} [MJ/Nm³]). Increasing the hydrogen content leads to a lower volumetric calorific value and a slight decrease in the stoichiometric energy content of the mixture. This also increases the stoichiometric air/fuel ratio (AFR_{stoich}), meaning that more air is required for complete combustion. These modifications directly impact combustion process parameters and control strategies. Table 2 presents an analysis of the impact of HCNG mixtures on pollutant emissions, energy efficiency, and engine stability.

Table 2. NG and HCNG properties [30, 38, 55]

	Natural gas	HCNG10	HCNG20	HCNG30
H_2 [% vol.]	–	10	20	30
H_2 [% energy]	–	3.2	7.0	14.4
LHV [MJ/kg]	45.3	46.2	46.7	48.5
LHV_{vol} [MJ/kg]	36.0	34.3	31.7	29.2
AFR_{stoich} [–]	15.6	15.8	16.1	16.4

HCNG mixtures are being intensively researched as fuels for internal combustion engines, particularly in the automotive sector. Numerous analyses indicate that with an appropriate blend composition, CO_2 emissions can be reduced by up to 20–30% compared to gasoline, as well as significantly reducing particulate matter and nitrogen oxide emissions [37]. Furthermore, increased energy efficiency of the drive unit is observed, making HCNG fuels an attractive transitional solution on the path to zero-emission transportation. From a technical perspective, the presence of hydrogen in HCNG increases the laminar combustion velocity, requiring an adapted ignition strategy, including an earlier ignition timing to avoid efficiency degradation during the expansion phase [37]. Figure 3 presents the dependence of the laminar burning velocity on the equivalence factor (ϕ) for fuel-air mixtures containing hydrogen, based on data from various authors (Miao, Halter, Huang, Yu) [26, 27, 40]. The graph shows that the combustion velocity increases with ϕ, reaches a maximum in the range $\phi \approx 1.1$–1.2, and then decreases. This course indicates that hydrogen significantly improves combustion rate, especially at stoichiometric and slightly rich mixture conditions, which is important for engine efficiency and for optimizing ignition timing with variable mixture composition.

The presence of methane in HCNG blends helps maintain a smooth, stable combustion process while reducing the risk of detonation and flashback. Research shows that the best results are achieved when the hydrogen content in the blend is between 10% and 30%. This range enables better engine performance and safe, predictable system operation [36]. Road tests of dual-fuel vehicles have demonstrated that HCNG fueling results in lower fuel consumption [MJ/km], which translates into more uniform and stable combustion in subsequent engine cycles. Additionally, emission tests confirmed significant reductions in CO and HC emissions and lower NO_x levels compared to systems fueled with pure methane [37], making HCNG a viable alternative for commercial vehicles and stationary cogeneration units.

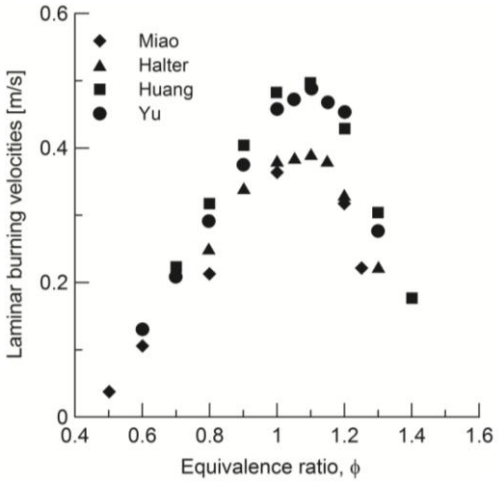

Fig. 3. Variation of unstreched laminar burning velocity with equivalence ratio (ϕ) for HCNG20 blend [37]

These results are confirmed by the analysis presented in Fig. 4, which illustrates the effect of the relative air-fuel ratio (λ) on the efficiency of an engine fueled with different fuel mixtures: pure natural gas (NG), HCNG10 (with 10% hydrogen), and HCNG20 (with 20% hydrogen). The measurement carried out at 3800 rpm, full throttle, and at MBT ignition advance showed that the addition of 10% hydrogen leads to a significant increase in engine efficiency compared to natural gas over the entire λ range [55]. At the same time, increasing the hydrogen content to 20% no longer brings additional benefits, suggesting that the efficiency improvement effect reaches a saturation point at higher hydrogen concentrations.

The influence of inert gas admixtures on hydrogen combustion in modern ignition systems is an important area of research for the development of emission-free propulsion technologies. One approach in this regard is the use of helium as a fuel mixture component, which allows for modification of the combustion process in turbulent ignition (TJI) engines. In the article [41], the influence of helium addition to hydrogen on the combustion process in a turbulent ignition (TJI) piston engine was analyzed. The studies were conducted on a single-cylinder AVL 5804 engine using H_2/He mixtures (from 100% H_2 to 60% H_2 with 40% He) at lean mixtures ($\lambda = 1.5$–3.0).

It was shown that increasing the helium content lowers the maximum combustion pressure, IMEP, and heat release rate, and also reduces the risk of combustion knock. For example, each additional 10% of helium resulted in an average 10% decrease in IMEP and up to a 75% reduction in combustion rate [41]. Further on, the authors analyzed the effects of hydrogen content, throttle opening, and excess air ratio (λ) on combustion characteristics. Figure 5 presents a three-dimensional map of these relationships, which indicates that increasing the hydrogen content in the fuel leads to the combustion of increasingly leaner mixtures (higher λ) and simultaneously increases the sensitivity of the process to changes in throttle position. Especially at H_2 content above 90%, small changes in the throttle valve caused nonlinear changes in IMEP–located in the lower part of the graph (blue).

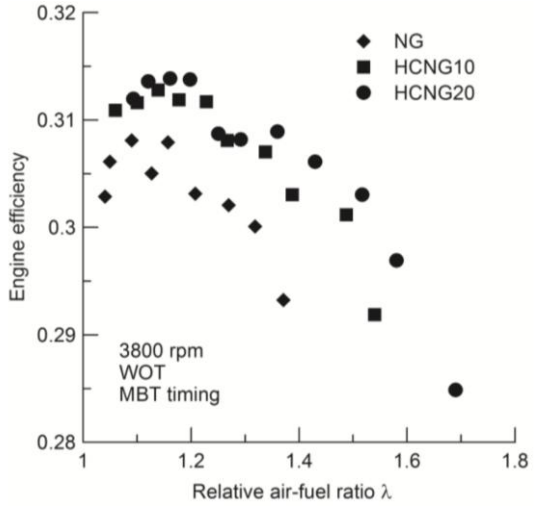

Fig. 4. Engine efficiency versus relative air-fuel ratio lambda for different fuels [55]

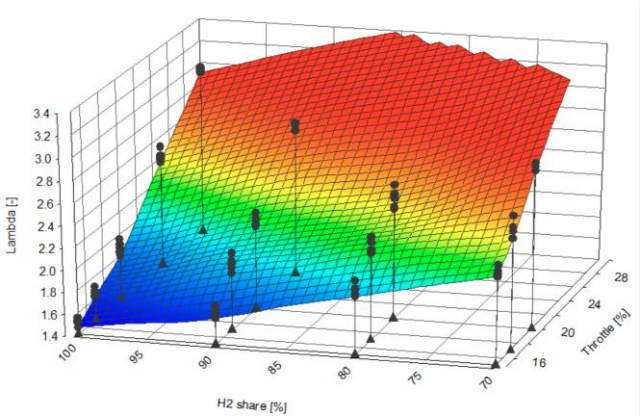

Fig. 5. Map of variations in the throttle position, hydrogen content of the mixture, and resulting excess air ratio (color-resulting excess air ratio; circles-excess air ratio values; triangles-projection onto the plane of λ-value) [41]

Research results show that both helium and hydrogen can effectively influence the combustion process. However, precise control of the mixture composition and throttle valve opening is crucial for the Turbulent Jet Ignition (TJI) engine to operate stably and efficiently when fueled with lean hydrogen mixtures.

The effect of hydrogen as a component of the fuel mixture manifests itself not only through changes in combustion dynamics but also through modification of the autoignition regime. In this article [17], a numerical analysis of autoignition was performed across various combustion systems, ranging from spark-ignition (H_2/CH_4) and compression-ignition (H_2/ON) engines to MILD technologies and detonation engines (RDE). The use of hydrogen results in a significant reduction in the mixture ignition time, but this effect is highly nonlinear and depends on thermodynamic conditions. The results of isolinear ignition delay analyses (iso-contours) showed that hydrogen can both accelerate and retard autoignition, depending on temperature and pressure, due to complex transition chemistry (e.g., the NTC effect in hydrocarbon fuels). This relationship is confirmed by the data presented in Fig. 6, which shows the effect of hydrogen in a methane (NG_2) mixture on the ignition delay time and the laminar combustion velocity under conditions typical of spontaneous ignition in a spark-ignition engine (T = 1000 K, P = 85 bar). Although pure hydrogen has a combustion velocity 6–8 times higher than methane, an increase in the hydrogen content to 50% only causes a two-fold increase in the mixture flame velocity. At the same time, a nonlinear but systematic decrease in ignition time is observed with increasing hydrogen content. The results confirm that the addition of hydrogen significantly changes the way fuel ignites. Therefore, this effect should be taken into account when developing combustion strategies and ignition calibration in engines operating on H_2/NG blends.

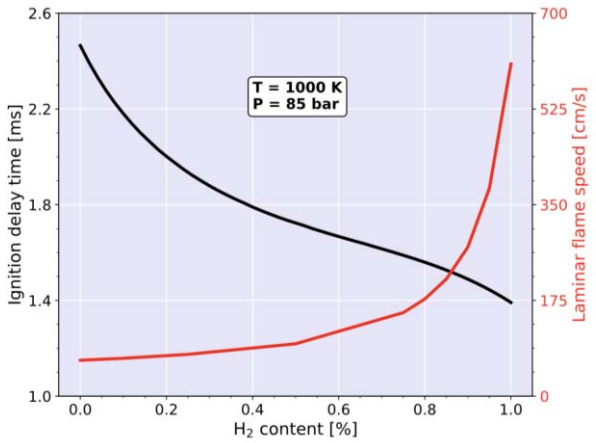

Fig. 6. Effect of hydrogen fraction in the H_2/NG_2 mixture on ignition delay time and laminar burning velocity under conditions characteristic of autoignition in a spark-ignition (SI) engine (T = 1000 K, P = 85 bar). A stoichiometric mixture (φ = 1.0) was used [17]

These conclusions are confirmed by DNS studies of hydrogen combustion under reheat combustion conditions, presented by Gruber et al. [23]. Numerical simulations in a diffusion-free system have shown that flame stabilization in the second combustion stage (e.g., in the two-stage system) can be achieved by spontaneous ignition. The key factor determining the reaction location and rate in this case is the inlet temperature of the reactants, not the mixture equivalence factor. Hydrogen reheat flames are highly sensitive to small temperature changes, which is associated with dynamic combustion instabilities and the potential occurrence of self-ignition waves in the velocity range between classical deflagration and detonation – the so-called spontaneous propagation zone.

As part of research on hydrogen co-combustion technologies in piston engines, a three-dimensional model of the Gasoline Direct Injection (GDI) engine was developed to analyze in detail the effect of hydrogen volume fraction (HVF) on combustion and emissions [18]. Simulation results showed that increasing the hydrogen content in the fuel mixture increases maximum cylinder pressure and heat release, accelerates ignition, and shortens combustion duration. It was also observed that, due to a higher OH radical content, combustion becomes more dynamic and approaches ideal isochoric combustion, which translates into an increase in the indicated efficiency (ITE). The highest efficiency increase (from 35.1% to 40.1%) was achieved with

a 10% HVF and delayed ignition. However, the authors noted that too early ignition at low HVF can intensify combustion knock (KI > 3 MPa). Importantly, because hydrogen has a higher octane number, increasing HVF mitigates the mixture's susceptibility to autoignition. Ultimately, the work indicates that appropriate selection of HVF and ignition timing can optimize efficiency and reduce emissions while maintaining safe combustion in gasoline direct injection engines. Figure 7 illustrates that increasing HVF (up to 10%) increases ITE, particularly with delayed ignition (e.g., IT = 2°CA aTDC), while a decrease in efficiency is observed with premature ignition (e.g., IT = −11°CA aTDC). This effect highlights the importance of properly calibrated ignition parameters in engines burning gasoline-hydrogen mixtures.

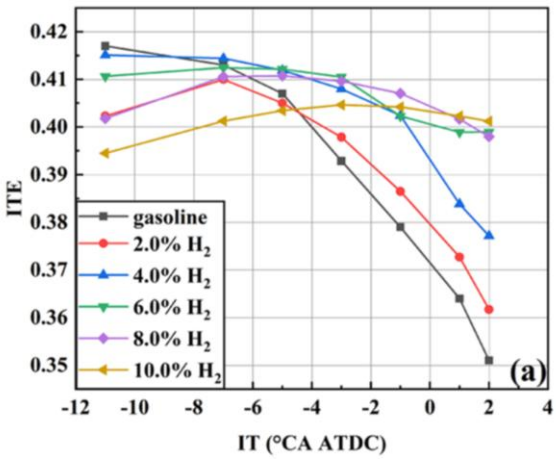

Fig. 7. Effect of hydrogen fraction in the fuel mixture (HVF) and ignition timing (IT) on the indicated thermal efficiency (ITE) of a GDI engine [18]

2.3. Technological and environmental challenges

The dynamic development of hydrogen technologies for internal combustion engines is driven by global efforts to reduce greenhouse gas emissions. Hydrogen-powered engines (H_2-ICEs) and versions powered by fuel blends, such as hydrogen with natural gas or gasoline, offer an alternative to traditional engines and fuel cells. Despite its many advantages – including the absence of CO_2 emissions in the TTW cycle, high calorific value, and rapid combustion kinetics the use of hydrogen poses numerous technical and environmental challenges. These require solutions for safety, combustion efficiency, NO_x emissions, and integration with the fuel infrastructure.

One of the main technological challenges with direct hydrogen injection remains precise control of injection timing and pressure. Late-cycle injection requires very high pressure up to 300 bar to overcome cylinder pressure and deliver fuel quickly. Injection too early leads to thermal losses and a too homogeneous mixture, while injection too late leads to incomplete fuel-air mixing, which increases NO_x emissions and reduces combustion efficiency [22]. Another limitation is that the displacement effect, the presence of hydrogen in the intake manifold, reduces the amount of air drawn into the cylinder, reducing volumetric efficiency. In conventional indirect injection (PFI) systems, additional boosting or cryogenic hydrogen injection is necessary to achieve performance similar to that of gasoline engines. Direct injection offers greater mixture control and shorter fuel preparation time, but it requires costly modifications to the fuel and control systems.

Adding hydrogen to gasoline in GDI engines improves combustion parameters by accelerating chemical reactions and increasing the proportion of active OH radicals. This shortens the ignition delay and overall combustion time. In practice, this translates into higher maximum cylinder pressure and thermal efficiency, which improve engine performance and reduce cyclic irregularities. However, increasing the hydrogen proportion in the fuel mixture can lead to early self-ignition, especially at advanced ignition angles. Additionally, despite improved knock resistance, the increase in combustion temperature with a high hydrogen content promotes NO_x generation, requiring the use of appropriate exhaust gas aftertreatment systems or lean combustion strategies [18].

In cogeneration systems, adding hydrogen to natural gas significantly alters the combustion process. At hydrogen contents up to 20% by volume, an increase in flame speed is observed, which shortens combustion time and allows for greater power with delayed ignition. However, excessive hydrogen content decreases mixture density, thereby reducing volumetric efficiency. At the same time, higher hydrogen content increases combustion temperature, leading to higher NO_x emissions. Furthermore, a shorter combustion process limits the recovery of exhaust heat energy in turbines. Therefore, it is necessary to appropriately adjust the ignition strategy and use a lean mixture to balance emissions and engine efficiency [9].

Although hydrogen is a clean fuel, its use in engines poses technological challenges, including pre-ignition, flashback, and the risk of leaks. Advanced materials resistant to operating conditions and appropriate safety systems are essential. Furthermore, producing "green" hydrogen requires significant capital expenditures, and its storage and transportation (e.g., at 700 bar) remain economically and technologically challenging. Due to hydrogen's high combustion temperature, nitrogen oxide emissions are a major environmental concern. The use of ultra-lean combustion, exhaust gas recirculation (EGR) systems, and SCR catalytic converters using hydrogen alone as a reducing agent can significantly reduce this problem, but requires precise control and matching the combustion strategy to load conditions [6].

The biggest problem with hydrogen-powered cars (H_2–ICE) is not the engine itself. Hydrogen requires special stations and tanks, which are expensive and must meet very stringent safety standards. Therefore, despite the ready-made technology, its widespread use is currently difficult. There is also the issue of safety, as hydrogen is highly flammable, so ventilation systems and leak detectors must be installed. Nevertheless, hydrogen has its advantages, H_2-ICE engines do not require rare metals and can be produced in existing factories, making them an excellent interim solution until zero-emission transport becomes the norm [70].

For engines to run on hydrogen, significant design changes are necessary. These factors impact not only the intake and exhaust systems but also the ignition method, the materials used, and the control systems. Properly selecting

injection pressure and ignition timing is particularly crucial, as hydrogen has a very low ignition energy and is prone to premature combustion, which can damage engine components. From an environmental perspective, NO_x emissions remain the biggest problem, as they increase with increasing combustion temperature. Solutions could include lean fuel mixtures, modern exhaust gas aftertreatment systems, and hydrogen as a reducing agent in SCR catalytic converters. However, the effectiveness of these methods depends on precise engine control and compatibility with existing fuel infrastructure [38]. Although hydrogen has enormous potential as a future fuel, hydrogen-powered engines are not as volumetrically efficient as conventional gasoline engines. This is because hydrogen, in its gaseous state, has a lower energy density, and in indirect injection systems it occupies part of the space intended for air. As a result, the power of such engines is usually somewhat lower, especially under heavy load. Their advantage, however, is the ability to operate on very lean mixtures, which reduces nitrogen oxide emissions. The problem is that this makes it more difficult to maintain stable combustion and avoid knocking. Therefore, increasingly advanced combustion control and modeling systems are needed to fully utilize hydrogen's potential [69].

Table 3. Summary of the main technical and environmental challenges associated with the use of hydrogen in internal combustion engines and potential directions for their mitigation [6, 9, 18, 38, 51]

Challenge	Potential solution
Pre-ignition and flame backflow	Delayed ignition, advanced injection control
High NO_x emissions in richer mixtures	Lean-burn strategy, EGR, H_2-SCR systems, and NSC catalysts
Poor hydrogen–air mixing	High-pressure direct injection and stratified mixture formation
Lack of hydrogen refueling infrastructure	Expansion of the H_2 station network, public support
High hydrogen storage pressure	Advanced Type IV composite storage tanks
Increased wear and corrosion of engine components	Protective coatings, optimization of cooling systems
Complex material requirements for injection systems	Use of resistant materials and lubricants
Secondary emissions: N_2O and NH_3	Advanced exhaust gas after-treatment systems
Lack of standardized norms and regulations	Development of harmonized international standards
Pollution from hydrogen production based on fossil fuels	Development of ICE electrolysis and green hydrogen production

Table 3 presents the main technological and environmental challenges associated with using hydrogen as a fuel in piston engines, both in single-fuel systems and in blends. It addresses typical issues related to hydrogen combustion, such as the risk of pre-ignition, difficulties in properly mixing fuel with air, and demanding material requirements for injection system components. Additionally, it summarizes possible directions for technical and system solutions. The table also considers non-engine factors, including limited availability of hydrogen refueling infrastructure, secondary emissions (N_2O, NH_3), and the impact of its production method on the actual carbon footprint. Implementing the solutions presented in the table, including direct injection, advanced cooling and exhaust gas aftertreatment systems, and the development of green hydrogen production, can significantly increase the technological maturity and environmental efficiency of H_2ICE engines. However, these actions require close cooperation among industry, research institutions, and decision-makers, particularly in regulatory harmonization, component certification, and infrastructure development.

3. The role of numerical modelling in the analysis of hydrogen combustion processes

Numerical modelling is currently a key tool in the analysis of hydrogen combustion processes in piston engines. Due to extremely short chemical reaction times, high flame propagation speeds, and the strong dependence of ignition mechanisms on local conditions, the use of experimental methods that fully capture these phenomena is often limited. Simulation tools not only allow for the reproduction of engine operating parameters under various operating conditions but also enable the analysis of temperature distributions, mixture composition, NO_x formation, and flame front propagation with very high accuracy. Models based on chemical kinetics mechanisms and CFD techniques are particularly important, as they allow for the representation of the complexity of reactions occurring in real time, including the spatial distribution of thermodynamic and flow phenomena.

Currently, numerical modelling is one of the most important tools for studying hydrogen combustion in piston engines. Due to the very rapid chemical reactions, high flame propagation speed, and the strong influence of local conditions on ignition, traditional experiments do not always fully capture these processes. Computer simulations enable the analysis of engine operating parameters under various conditions and the precise tracking of changes in temperature, mixture composition, NO_x emissions, and flame propagation. The choice of software depends on the nature of the given study or application. Each available program has its advantages but also limitations, both technological and cost-related.

AVL FIRE is one of the most accurate combustion simulation tools available. It enables the analysis of complex engine phenomena, works with GT-Power, and supports a wide range of fuels, including hydrogen and its blends. This allows for the study of emissions and combustion behaviour under various operating parameters. The program's drawbacks include high licensing costs and demanding hardware requirements. GT-Power, on the other hand, is primarily used for one-dimensional analyses. It features an intuitive interface, a large component library, and the ability to interface with 3D solvers. GT-Power's limited ability to reproduce local physicochemical phenomena poses a significant challenge when conducting detailed analyses of hydrogen combustion.

ANSYS Fluent, on the other hand, thanks to its flexibility and advanced CFD modelling capabilities, is one of the most widely used and recognized tools for hydrogen combustion simulation. It allows for the consideration of real-world geometries and complex boundary conditions, but its use requires extensive experience and significant computa-

Table 4. Comparison of selected simulation tools used in combustion modelling in hydrogen-fueled piston engines – summary of key advantages and limitations of AVL FIRE, GT-Power and ANSYS Fluent [25, 43, 64, 68, 73]

Software	Advantages	Limitations
AVL FIRE	– Advanced combustion modelling – Integration with GT-Power – High accuracy – Support for various fuels (hydrogen, ammonia) – Extensive emissions and fuel consumption analyses – Professional technical support	– High license cost – High hardware requirements – Steep learning curve for beginners – Less flexibility than open-source tools – Time-consuming simulation setup – Smaller user community
GT-Power	– Fast 1D simulations – Integration with AVL FIRE and ANSYS Fluent – Full powertrain system analysis – Rich component library – Support for various fuels – Intuitive user interface	–Limited accuracy of 1D models – High license cost – No full 3D modelling capability – Dependence on other tools for detailed analyses – Requires highly accurate input data – Limited model flexibility
ANSYS Fluent	– Advanced CFD modelling capabilities – Dedicated hydrogen combustion models – High flexibility and customization options – Integration with other ANSYS tools – Large user community and extensive documentation – Support for HPC (High-Performance Computing)	– High license cost – High hardware requirements – Steep learning curve – Time-consuming model preparation – Challenges in modelling certain physical phenomena – Strong dependence on accurate data for stratified mixture formation

tional resources. Therefore, the selection of a simulation tool should always be preceded by an analysis of the research goals, available resources, and the required accuracy. These simulation tool features are summarized in detail in Table 4, which compares the advantages and limitations of the three most commonly used programs: AVL FIRE, GT-Power, and ANSYS Fluent. This comparison provides a practical reference point when selecting software for a specific type of hydrogen combustion analysis in piston engines.

When modelling hydrogen combustion, transport phenomena arising from its characteristic properties are particularly important, especially preferential diffusion, which affects flame stability and structure. To obtain more accurate and realistic simulation results, advanced computational methods such as LES (large eddy simulation) are increasingly being used. The article [29] presents a modern approach to modelling hydrogen combustion, taking into account this phenomenon, which plays a key role in hydrogen combustion processes. Based on the results of one- and three-dimensional simulations, LES conducted for a low-vortex, lean H_2/air mixture, the authors demonstrated that the traditional FGM (Flamelet-Generated Manifold) method has limited ability to reproduce the essential properties of the combustion field. The use of an extended version of FGM-PD (taking into account preferential diffusion) not only allows for more accurate representation of temperature distributions, mixture fractions, and main chemical species but also enables the reproduction of characteristic flame structures, such as the "finger-shaped" distributions of the OH radical mass fraction, observed experimentally.

Figure 8 shows how the classic FGM method (left) differs from the extended FGM-PD method (right). As shown in Fig. 8, the classic FGM and its advanced variant, FGM-PD, reveal notably different flame behaviours. The OH radical mass fraction patterns demonstrate how FGM-PD captures a far more complex and uneven structure. From experience, this irregularity makes perfect sense, flames are rarely steady, twist, and fluctuate in reality. The root cause lies in unequal diffusion rates, especially hydrogen's, because its low Lewis number disrupts the local balance and alters how reactions evolve at the flame front [29].

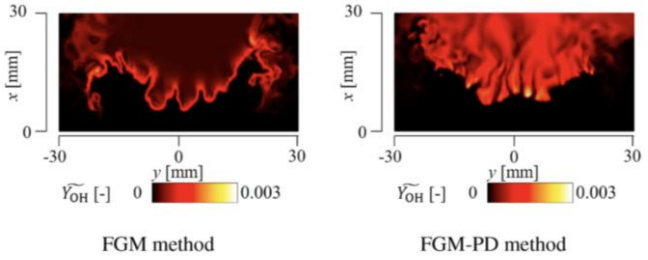

Fig. 8. Comparison of the OH radical mass fraction distribution ($\tilde{Y}_{oh}$) obtained using the classical FGM approach and the modified FGM-PD method accounting for preferential diffusion effects for an H_2/air mixture (cross-section in the plane z = 0 mm) [29]

Mixing hydrogen and air efficiently in direct-injection systems remains one of the hardest nuts to crack for engineers seeking clean, powerful combustion. The intake port's shape and airflow dynamics determine whether the mixture burns evenly. In article [71], simulations with CONVERGE were used to explore how different intake geometries affect mixture uniformity. The numerical predictions closely matched the experimental results. The authors also discovered that an optimized tumble plate increased the tumble ratio – in simple terms, it improved air swirl – leading to improved mixing before ignition. Figure 9 shows this vividly, with higher flow velocities observed in the modified design in both CFD and experiments. Such an agreement demonstrates the value of good modelling in developing efficient hydrogen engines. On top of that, the study identified how the pre-chamber couples with the main combustion chamber – insights that would be nearly impossible to pinpoint through experimental work alone.

In HCCI engines, where the mixture ignites spontaneously, the use of hydrogen as a fuel requires very careful analysis. The combustion process is exceptionally complex and strongly dependent on initial conditions. Therefore, research employs detailed chemical reaction models and three-dimensional CFD simulations, which allow for precise analysis of how the mixture composition and the reaction course change over time. Article [32] provides an example of the application of three-dimensional CFD modelling with an extended chemical kinetics mechanism to ana-

lyse hydrogen combustion in a homogeneously charged compression ignition (HCCI) engine. The main goal of this work was to investigate the influence of parameters such as swirl intensity, intake temperature and pressure, compression ratio, and equivalence factor on ignition characteristics and combustion behaviour. The model, developed using the KIVA3 code, enabled precise real-time analysis of the spatial distributions of temperature, pressure, velocity, and turbulence kinetic energy. The detailed kinetics of the hydrogen oxidation reaction enabled consideration of local phenomena, such as elevated-temperature zones that initiate ignition.

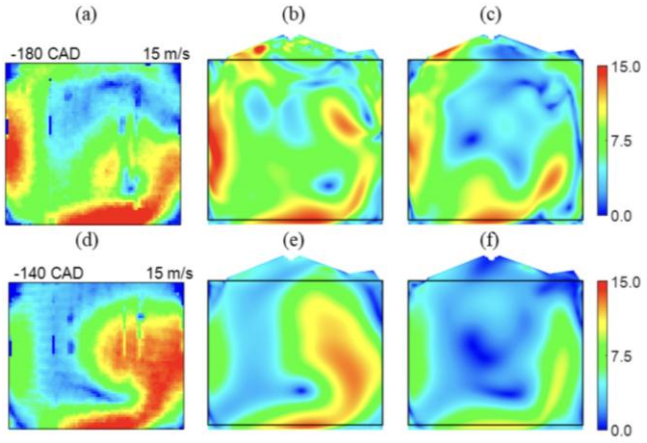

Fig. 9. Comparison of in-plane velocity magnitude (m/s) during the intake stroke under high-tumble conditions without fuel injection. The distributions are shown for two crank angle positions: −180 CAD (a–c) and −140 CAD (d–f). Experimental results are presented in (a) and (d), CFD results obtained with the modified geometry in (b) and (e), and CFD results using the baseline (original) geometry in (c) and (f). The color scale represents the velocity magnitude range from 0 to 15 m/s [71]

Studies have shown that increasing swirl intensity delays autoignition, extends combustion duration, and reduces NO_x emissions, while simultaneously lowering maximum cylinder temperatures and pressures, which may reduce the risk of combustion knock [32]. Figure 10 shows the turbulence kinetic energy (TKE) distribution in the X-Z plane of the combustion chamber of a hydrogen-fueled HCCI engine for various swirl ratio values at −1.971° crank angle (CA). The analysis showed that the intensification of swirl motion leads to a distinct differentiation of the turbulence field throughout the cylinder volume, which directly affects the rate of hydrogen-air mixing and the location of ignition initiation zones. The noticeable differences in the flow structure demonstrate that a properly selected swirl ratio can be an effective tool for controlling combustion, especially under autoignition conditions typical of HCCI engines. This figure provides a valuable complement to the numerical analysis, emphasizing the importance of three-dimensional modelling in predicting local phenomena crucial to the stability and efficiency of hydrogen combustion.

Article [60] focuses on the design and numerical validation of a modern hydrogen combustion chamber for gas microturbines. Due to limited space and extreme thermal conditions, the main goal was to develop a compact, safe, and efficient geometry enabling stable combustion of pure hydrogen. The authors presented, among other things, the concept of the Inverse Micromix injector, which operates based on axial hydrogen injection through a porous material and lateral air supply, which promotes effective mixing of the components and reduces the risk of flashback. A schematic diagram of this design is shown in Fig. 11. CFD analysis allowed for a detailed look at the hydrogen combustion process in the engine chamber. The study examined, among other things, temperature distributions, reactivity levels, and recirculation zones responsible for flame stabilization. Calculations were performed based on the EDC model and simplified chemical kinetics, allowing for optimization of the chamber geometry and verification of the effectiveness of the fuel-air mixing strategy. The obtained results demonstrate that CFD modeling is an effective tool in the design of modern hydrogen combustion systems.

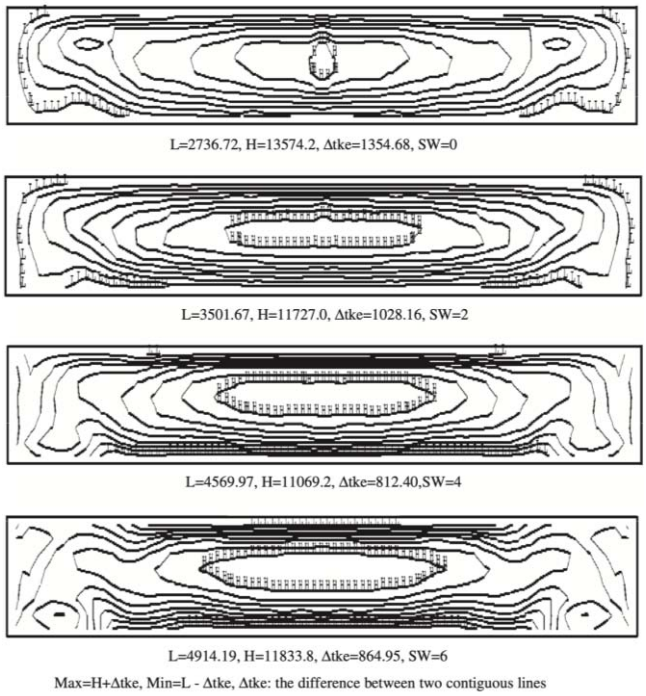

Fig. 10. Distribution of turbulent kinetic energy (TKE) in the X–Z plane of the combustion chamber of a hydrogen-fueled HCCI engine for different swirl ratio values at a crank angle of−1.971° CA [32]

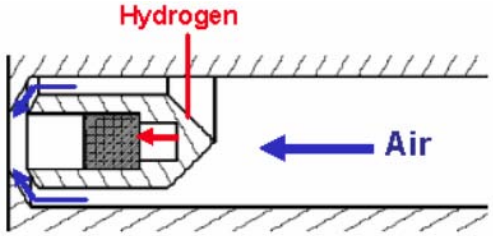

Fig. 11. "Inverse Micronix" injector: working principle [60]

Article [44] illustrates the application of numerical modeling to the analysis of hydrogen combustion processes in hypersonic conditions. The paper analyzes the influence of strut-injector geometry on the hydrogen-air mixing process and combustion characteristics in the scramjet chamber at an air velocity of 2.47 Mach and combustion at 1.5

Mach. A two-dimensional RANS model with a classical k–ε turbulence model and simplified chemical kinetics for hydrogen was used, enabling evaluation of the effectiveness of two injection configurations: a cylindrical strut end and an alternative wedge-shaped end (alternating wedge).

The calculation results showed that the use of a wedge-shaped injector leads to more intense hydrogen-air mixing and a more uniform reaction field, which directly results in an increased share of water vapor in the combustion products and higher maximum temperatures in the chamber. This setup effectively minimizes the distance needed for full reactant mixing, which is especially important in hypersonic propulsion systems, where interaction space and mixing time are severely restricted. The CFD-based study investigates how injector geometry and flow parameters influence hydrogen combustion performance under extreme flow regimes. The comparison of H_2O mass fraction contours in Fig. 12 confirms that the wedge-shaped injector enhances hydrogen conversion efficiency, demonstrating the value of computational modeling in optimizing high-speed hydrogen combustion systems [44].

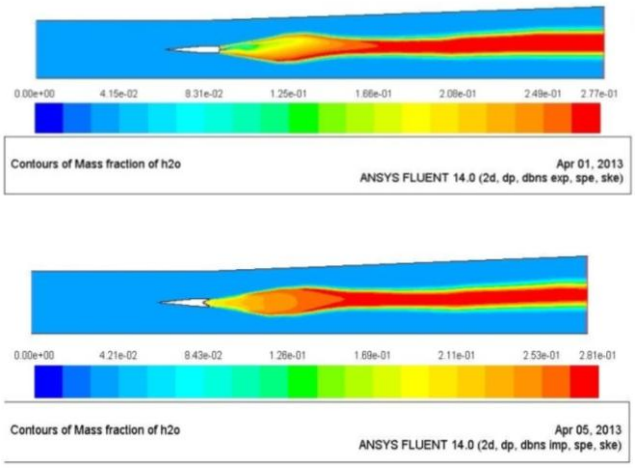

Fig. 12. Comparison of water vapor (H_2O) mass fraction contours in a hydrogen-fueled scramjet combustion chamber: top configuration with a cylindrical strut-injector; bottom configuration with an alternating wedge-shaped strut-injector [44]

The configuration used allows for a significant reduction in the path required to fully mix the reaction components, which is crucial in hypersonic systems, where the time and space for gas contact are strictly limited. CFD simulations were used to practically evaluate the impact of injection geometry and flow parameters on the stability and efficiency of hydrogen combustion under extreme conditions. Figure 12 presents the contours of the water vapor (H_2O) mass fraction for two strut geometries, visually confirming the more efficient hydrogen conversion with the wedge-shaped tip. These results demonstrate that numerical modeling can significantly support the development of modern, high-performance hydrogen-fueled hypersonic systems [44].

CFD modeling provides a powerful tool for examining how hydrogen affects combustion characteristics, even at an industrial scale in oxy-fuel systems. A study by Daurer et al. serves as a representative example, comparing hydrogen and methane combustion in a 180 kW semi-industrial furnace [12]. Their research provides a thorough investigation of hydrogen combustion under oxy-fuel conditions, where pure oxygen serves as the oxidizer. The authors concentrated on validating numerical combustion models and analyzing flame dynamics in realistic high-impulse burner operation. The simulations were performed using 3D RANS models with several turbulence and reaction schemes, covering both simplified and detailed hydrogen kinetics, including the ÓConaire mechanism.

Comparison of simulation results with experimental data for CH_4 combustion confirmed the high accuracy of the approach used. One of the key conclusions was that the turbulence modeling parameters (including modifications to the k–ε model) had the greatest impact on the quality of flame reproduction, while the influence of the combustion and radiation model selection was relatively small. Hydrogen combustion led to a significant increase in maximum flame temperatures (by approximately 400 K relative to CH_4) and a shortening of the flame length, despite the higher fuel jet velocity. This indicates greater heat transfer efficiency in the zone close to the burner and the need for precise calibration of turbulent mixing parameters [12].

Figure 13 illustrates how changes in the turbulence model parameters within the modified version of the k–ε model (P_2–H_2 variants) affect the characteristics of hydrogen combustion in a semi-industrial furnace. The visible differences in the temperature distribution and OH radical concentration intensity demonstrate that even small changes in the diffusion coefficients and turbulent energy production parameters can significantly shift the reaction zone and alter the flame length and stability. This figure provides significant support for the thesis that precise calibration of turbulence models is a key element in modeling hydrogen combustion under industrial conditions.

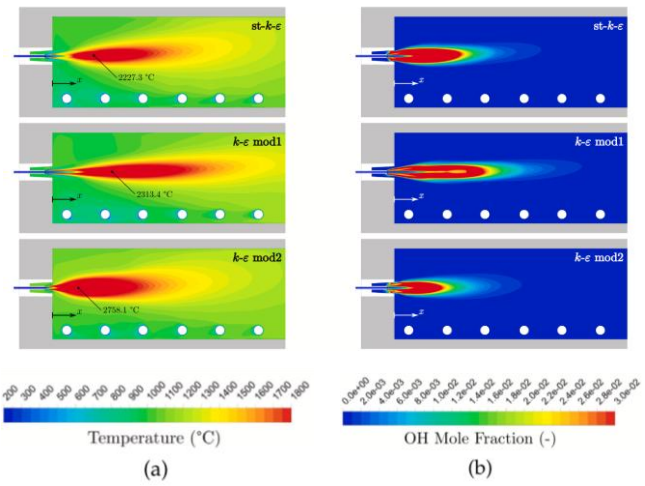

Fig. 13. Effect of parameter modification in the *k–ε* model on (a) temperature distribution and (b) molar fraction of the OH radical in the main reaction zone for the case of P_2–H_2 combustion in the oxy-fuel configuration [12]

In their work [48, 49], the authors conducted a 3D numerical analysis of premixed H_2/air combustion in a microscale chamber to examine how geometry, wall heat losses, injection design, and flow conditions affect flame

characteristics, temperature distribution, and combustion efficiency. Simulations performed in ANSYS Fluent with a detailed chemical kinetics model (9 species, 19 reactions) captured the essential thermal and reactive behavior of hydrogen combustion at small scales. The findings revealed that high wall thermal conductivity leads to significant heat losses and local flame extinction. On the other hand, introducing multi-step fuel injection effectively minimizes temperature peaks and improves temperature field uniformity. This leads to greater flame stability and improved efficiency – an important consideration for advanced hydrogen microcombustion systems.

Figure 14 shows the temperature distribution along the combustion chamber using different hydrogen injection strategies (single-, two-, and three-stage). The effect of injection staging is clearly visible, which allows not only to reduce peak temperatures in the reaction zone but also to achieve a more uniform thermal distribution throughout the volume, which translates into better operating conditions and lower thermal load on the chamber components [49].

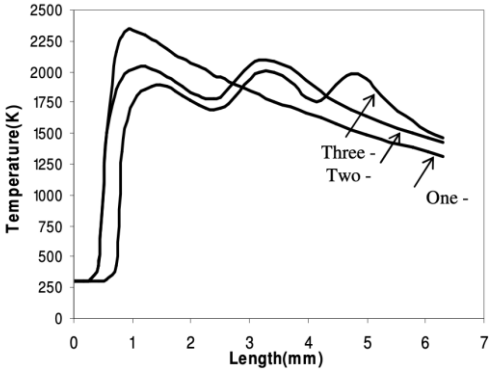

Fig. 14. Temperature distribution in a microscale hydrogen combustion chamber for different fuel supply strategies: single-, two-, and three-stage injection [49]

A significant contribution to the development of hydrogen combustion modeling is made by analyzing processes in compression ignition (CI) engines using non-standard operating atmospheres. Article [24] presents the results of numerical modeling of hydrogen combustion in a compression ignition (CI) engine in which the standard air mixture was replaced with an argon-oxygen atmosphere. The authors' primary goal was to determine the influence of parameters such as injector location, compression ratio, injection start (SOI), and initial temperature on the combustion process and emissions. The simulations were conducted using CONVERGE software and validated with experimental data from a YANMAR NF19SK engine. The findings revealed that replacing nitrogen with argon increased the combustion chamber temperature, shortened the ignition delay, and improved thermal efficiency, while simultaneously reducing NO_x emissions. Relocating the injector from the cylinder head side to its center resulted in higher in-cylinder pressure, temperature, and heat release rate (HRR), which indicates the dominance of mixture-controlled combustion. Additionally, as the compression ratio increased, both pressure and temperature rose, while the maximum HRR decreased, suggesting a more prolonged combustion process [24]. Figure 15 clearly shows how the shape and position of the hydrogen injector affect combustion. When the injector is in the center of the cylinder (G1 setup), the mixing of hydrogen with oxygen and argon becomes more efficient, leading to stronger combustion and a more balanced heat distribution.

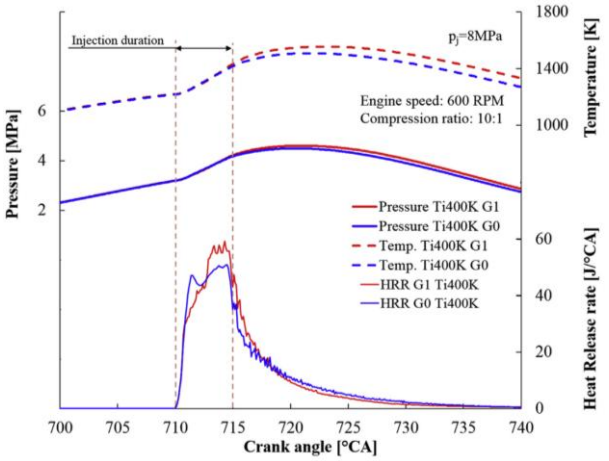

Fig. 15. Variations in pressure (p), average temperature (T_{ave}), and heat release rate (HRR) as a function of injector location [24]

In recent years, an increasing number of modeling studies have focused on local combustion phenomena, such as flame-wall contact (FWI), especially in situations involving thermal diffusion instabilities. Schneider et al. [53, 54] conducted a two-part numerical study analyzing the quenching of a hydrogen-air flame in a head-on quenching configuration, taking into account the variable parameters: equivalence factor, unburned gas temperature, and pressure. These articles provide a comprehensive analysis of the impact of thermal diffusion instabilities on the interaction of the hydrogen-air flame with the combustion chamber walls. These studies, conducted as direct numerical simulations (DNS), focus on the head-on quenching (HOQ) phenomenon – the process of flame quenching as a result of its direct contact with the wall.

In the first part of the work by Schneider et al. [53], high-resolution DNS modeling of the hydrogen–air flame interaction with a wall in a head-on quenching (HOQ) configuration was performed, taking into account thermodiffusion instabilities. The analysis revealed that local mixture fluctuations resulting from differences in hydrogen diffusion lead to a significant increase in local flame reactivity and, consequently, to higher heat fluxes to the wall and shorter quenching distances. This phenomenon is illustrated in Fig. 16, which presents profiles of the normalized heat flux Φ, the local equivalence factor φ/φ_u, the hydrogen mass fraction YH_2, and the heat release rate HRR within a single "flame finger" impinging on the wall [53].

The second part of the analysis covers a broader range of operating conditions relevant to industrial applications, including piston engines and gas turbines. The equivalence factor (φ = 0.4–1.0), pre-ignition mixture temperature (T_u = 298–700 K), and pressure were varied over 1–20 bar. The results show that the intensity of instabilities and their effect on the wall heat flux increase with decreasing φ and

Tu, and with increasing pressure, which increases local reactivity and thermal loads. Based on the obtained data, a predictive model is proposed to estimate the maximum heat flux to the wall as a function of the one-dimensional flame's characteristics. The effects of increased instability on quenching behaviour and wall thermal loads are examined. Figure 17 presents how variations in the equivalence ratio (φ), the unburned mixture temperature (T_u), and the operating pressure (p) affect selected combustion and heat transfer characteristics in the H_{OQ} configuration. The analysis covers the maximum and normalized wall heat flux (φ_q, φ_{q*}), the extinction distance (x_q), and the Péclet number (P_{eq}), indicating a clear dependence of near-wall heat transfer and flame quenching behavior on the imposed thermodynamic conditions. [54].

To improve the accuracy and efficiency of hydrogen combustion modeling under turbulent conditions, Malé, Lapeyre, and Noir ay developed a new method based on deep learning in their paper "Hydrogen reaction rate modeling based on a convolutional neural network for large eddy simulation" [36]. A deep learning model based on CNN architecture was trained with filtered high-fidelity DNS results to determine local reaction rate distributions in LES calculations. This methodology enables a more realistic representation of preferential diffusion mechanisms and turbulence–chemistry coupling, which are particularly significant in lean hydrogen combustion modeling.

The effectiveness of the method is illustrated in Fig. 18, which presents planar cross-sections of the computational domain for φ = 0.4. The actual reaction rates from the DNS simulation were compared with those from the CNN model at different LES filtering levels (σ = 4, 8, 16). The apparent consistency in the distribution and intensity of the reaction zones demonstrates that the neural network maintains high precision even at lower computational resolution, confirming its suitability for industrial applications involving hydrogen combustion [36].

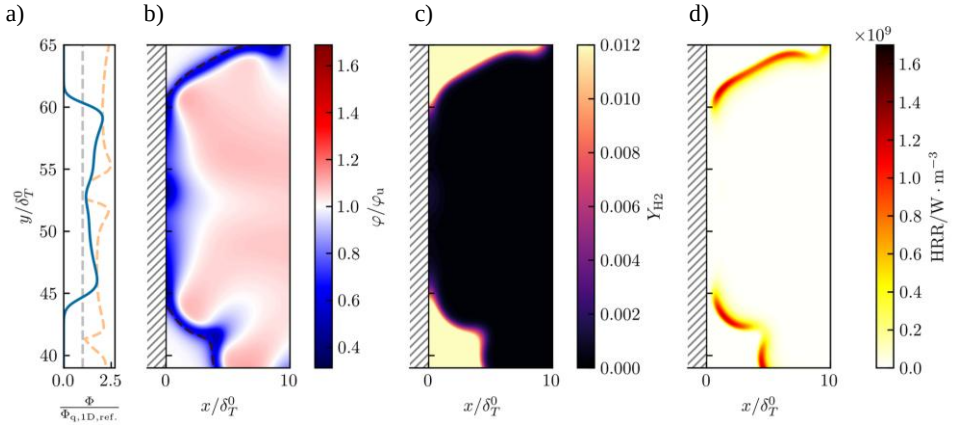

Fig. 16. Normalized heat flux ($\Phi/\Phi_{q,1D,ref}$) – a), equivalence factor (φ/φ_u) – b), hydrogen mass fraction (Y_{H2}) – c), and heat release rate (HRR) – d) along the symmetry axis of a single flame finger at the moment of its contact with the wall. Results obtained for an unstable H_2/air flame (φ = 0.4, 1 bar) in the HOQ configuration [53]

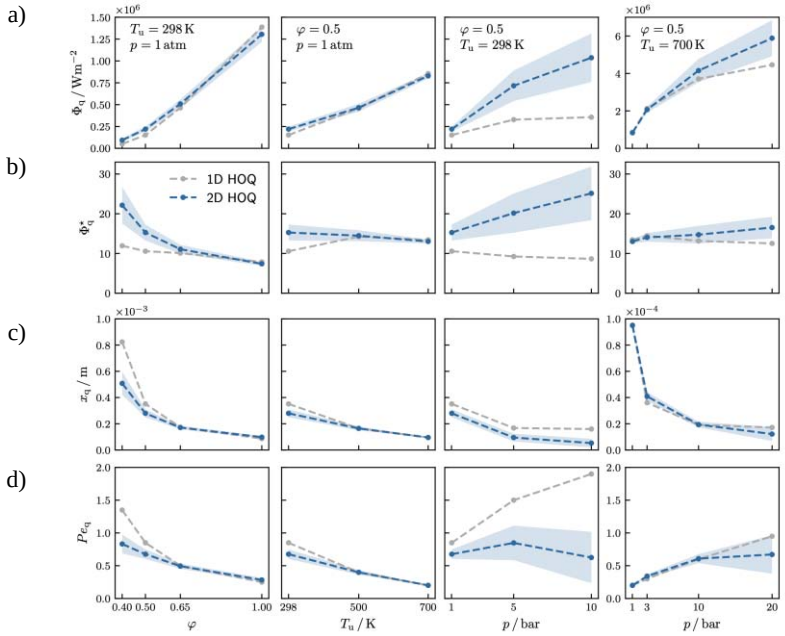

Fig. 17. Influence of changes in the equivalence factor (φ), unburned mixture temperature (T_u) and pressure (p) on: a) maximum heat flux to the wall (Φ_q); b) normalized heat flux (Φ_{*q}); c) extinction distance (x_q) and d) Péclet number (P_{eq}) in the HOQ configuration [54]

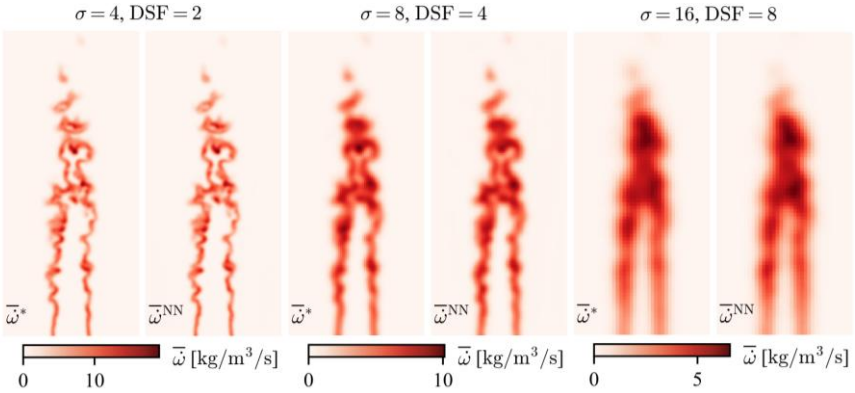

Fig. 18. Comparison of the actual (DNS) and convolutional neural network (CNN) – predicted hydrogen combustion reaction rates in a transverse cross-sectional plane for φ = 0.4 and different LES filter widths (σ = 4, 8, 16) [36]

To better understand the self-ignition and flame stabilization processes at high temperatures, Gruber et al. conducted direct numerical simulations (DNS) of hydrogen combustion in reheat mode [23]. This mode, typical of second-stage combustion in gas turbines, is characterized by the absence of classical spark ignition; ignition is initiated solely by autoignition, placing high demands on modeling reaction kinetics and turbulent phenomena. The analysis considered a wide range of inlet conditions – from laminar to highly turbulent – as well as the influence of heat losses and inlet mixture temperature. Of particular importance were observations of the cyclic appearance and extinction of ignition fronts near the so-called crossover temperature, as well as the identification of self-excited flame instabilities arising from the coupling between the reaction zone and pressure waves [23]. The results of the study are illustrated in Fig. 19, which shows the variation of the reaction front velocity (S_t) over time for different turbulence levels (u′ = 3, 6, 12, and 25 m/s). It is clearly visible that an increase in the intensity of turbulent fluctuations leads to an acceleration of the reaction front and, at the same time, to an increase in the amplitude of its oscillations. This figure provides significant evidence that strong turbulence not only affects combustion acceleration but also the dynamics and stability of the entire self-ignition process.

In the context of developing hydrogen combustion systems in non-overmixed configurations, three-dimensional CFD modeling of the combustion of a hydrogen-methane mixture in a combustion chamber with a variable number of nozzles was performed using the RNG k–ε turbulence model and a simplified non-overmixed combustion model [42]. The study examined how variations in mixture composition, injection geometry, and methane jet velocity influence thermal distribution, combustion efficiency, and possible NO_x emissions. According to the simulation results, enriching the mixture with hydrogen elevates the maximum temperature in the combustion chamber, while shortening the flame and advancing the reaction zone toward the inlet. At the same time, it was found that hydrogen content above 40% increases the risk of excessive NO_x emissions, which requires appropriate calibration of the system geometry. Among the analyzed variants, the best results in terms of combustion stability and temperature uniformity were obtained for the configuration with 16 injection nozzles [42].

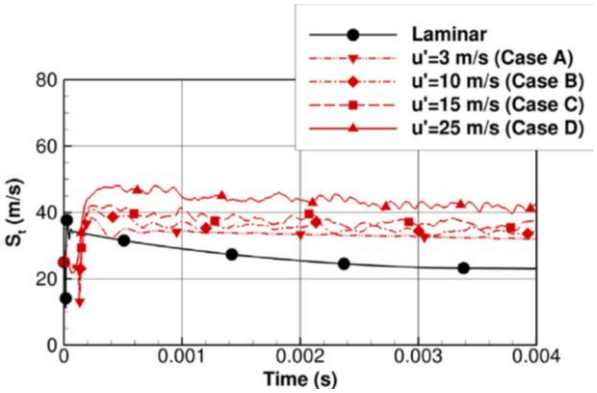

Fig. 19. Temporal evolution of the reaction front propagation speed (S_t) for turbulent hydrogen combustion under autoignition (reheat combustion) conditions, at different turbulence intensities (u′ = 3, 6, 12, 25 m/s); based on DNS data [23]

The characteristic effect of hydrogen content in the fuel on the temperature distribution is shown in Fig. 20, which compares the axial temperature cross-sections in the combustion chamber for mixtures containing 10% to 60% H_2. The noticeable changes in the flame structure and the location of high-temperature zones confirm the importance of selecting the appropriate fuel composition in the design of low-emission, highly efficient hydrogen combustion systems.

The studies described in [10] utilized direct numerical simulations (DNS) to accurately model hydrogen combustion under real-world piston engine operating conditions. The simulations were performed for a full-scale combustion chamber, making this one of the first studies to combine full-resolution flame-scale phenomena with the actual operating parameters of a spark-ignition engine (φ = 0.4237, 800 rpm). The nekCRF solver, based on the spectral-element method and optimized for GPU architecture, was used for the calculations. This approach enabled highly accurate modeling of flow, transport, and chemical reactions. Analysis of the results showed that flame development is strongly dependent on the flow structures generated by the tumble effect, which deform the ignition front and influence its velocity and direction of propagation. Particular attention was paid to flame-wall interactions – both head-on quenching and side-wall quenching – which lead to

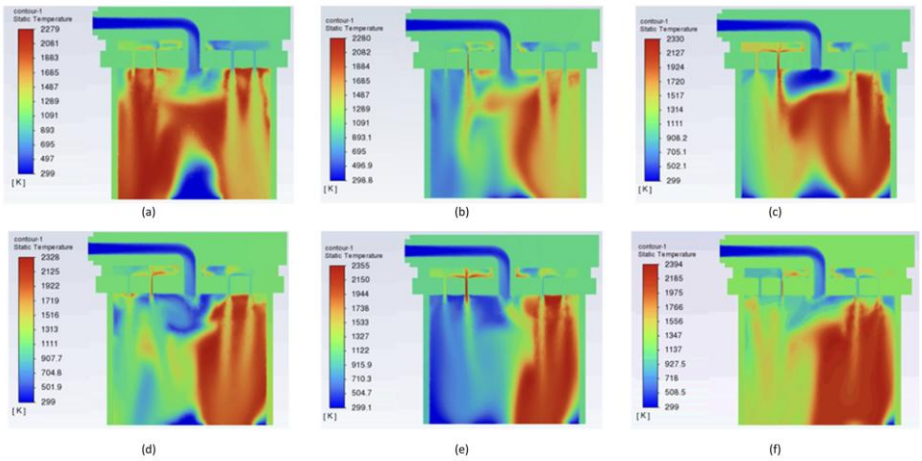

Fig. 20. Temperature distribution in the axial cross-section of the combustion chamber for different hydrogen shares in the H_2/CH_4 mixture (10%, 20%, 40%, 60%) – the influence of the fuel composition on the flame structure and the location of high-temperature zones [42]

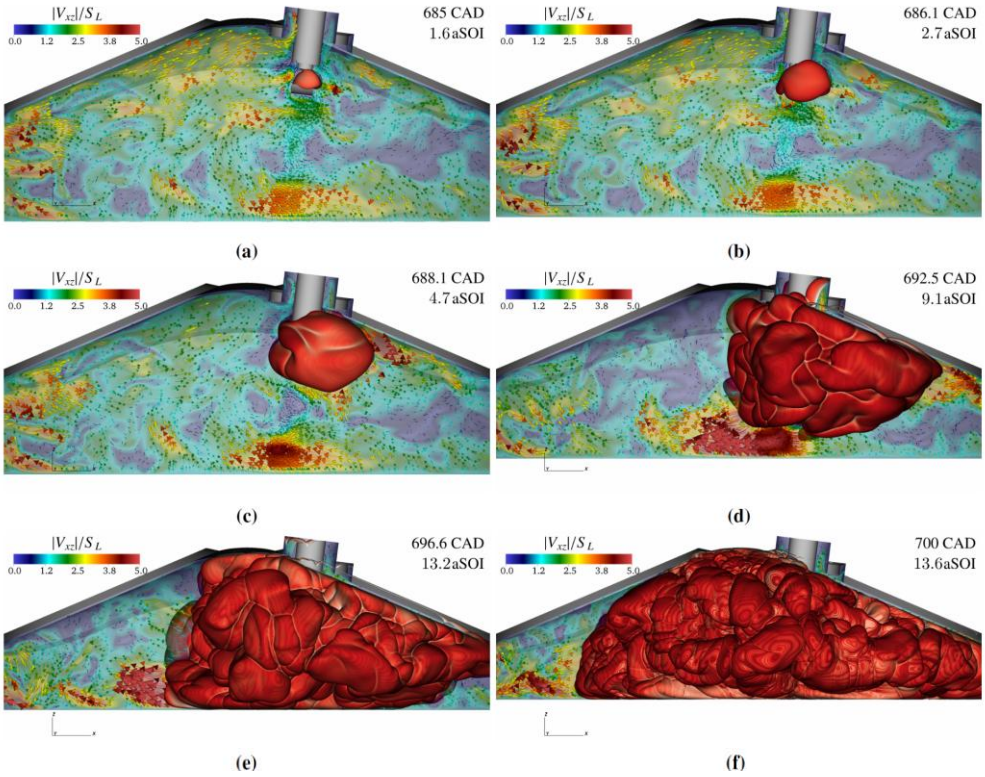

Fig. 21. Temporal development of the flame kernel identified by the $Y_{H2} = 0.0048$ iso-surface, overlaid on the velocity magnitude field in the mid-plane (y = 0), normalized by the local laminar flame speed S_L. Snapshots correspond to: a) 685 CAD; 1.6 aSOI; b) 686.1 CAD; 2.7 aSOI; c) 688.1 CAD; 4.7 aSOI; d) 692.5 CAD; 9.1 aSOI; e) 696.6 CAD; 13.2 aSOI, and f) 700 CAD; 13.6 aSOI. The flame structure is colored according to the heat release rate [10]

a local increase in heat flux, which is crucial for the durability of engine components [10]. The flame front's evolution over time is illustrated in Fig. 21, which shows successive hydrogen isosurfaces ($Y_{H_2} = 0.0048$) in the combustion chamber's symmetry plane. The sequence of images clearly shows the three-dimensional evolution of ignition and its deformation as a result of interaction with the variable flow field and chamber geometry, up to the point of collision with the piston. This figure provides an important complement to the qualitative analysis, showing the dynamics of hydrogen combustion on a real scale with full DNS resolution.

4. Critical comparison of modeling approaches and author-driven selection framework

Although a wide range of numerical techniques has been applied to hydrogen combustion in piston engines, the literature often discusses them separately, without clearly positioning them relative to one another. When these approaches are viewed side by side, certain patterns become apparent. RANS-based simulations continue to dominate engine-scale studies, mainly because they allow full-cycle calculations at an acceptable computational cost. In many practical optimization studies, this trade-off is understandable [50]. At the same time, their averaged formulation can

obscure transient flame–turbulence interactions, which are far from negligible in hydrogen-fueled engines where flame propagation is rapid and mixture inhomogeneities strongly influence combustion development.

LES offers a different perspective. Resolving the larger turbulent structures provides a more detailed description of unsteady combustion behavior and is particularly useful when abnormal combustion events or cycle-to-cycle variations are of interest [29]. The improvement in physical representation, however, comes at a substantial computational expense, which makes large parametric campaigns difficult to justify. A similar balance must be considered when selecting combustion models. Flamelet-based approaches provide an efficient compromise for premixed and partially premixed hydrogen operation, whereas detailed chemical mechanisms enhance predictive capability for ignition and NO_x formation but introduce additional numerical stiffness [65].

Taken together, these observations suggest that model selection should not be driven by convention alone. Instead, it should follow a clearly defined logic that links the research objective, the combustion regime, and the available computational resources. On this basis, the present study proposes a structured selection approach intended to make future CFD investigations of hydrogen-fueled internal combustion engines more transparent, consistent, and methodologically grounded.

5. Critical synthesis and positioning of the reviewed studies

The reviewed studies collectively demonstrate that hydrogen combustion in piston engines cannot be treated as a simple fuel substitution problem. Instead, it represents a systemic transformation of combustion physics, engine calibration strategies, and modelling requirements. Experimental studies conducted over the past years leave little doubt that introducing hydrogen into the combustion process profoundly alters flame behaviour. In practical terms, the flame front tends to travel faster, ignition occurs earlier, and engines can operate at much leaner conditions than with conventional fuels. These effects are frequently highlighted as major advantages of hydrogen-based systems. The very features that enhance reactivity and combustion speed also promote higher combustion temperatures, which in turn favor NO_x formation. Moreover, the high reactivity of hydrogen increases the likelihood of phenomena such as pre-ignition or flashback, especially if mixture preparation and ignition timing are not carefully controlled [20].

Second, studies on hydrogen blends (HCNG, H_2–gasoline, H_2–diesel) show that moderate hydrogen fractions (typically 10–30% by volume) yield the most balanced improvements in efficiency and emissions. Beyond this range, diminishing returns or increased instability are frequently observed. This suggests that transitional blend strategies may be technologically more robust in the short term than full hydrogen conversion [6, 30].

Third, numerical modelling has evolved from a supporting tool to a fundamental research driver. Classical FGM and RANS approaches often fail to fully capture preferential diffusion and thermo-diffusive instabilities characteristic of hydrogen flames. The reviewed works clearly show that advanced approaches – LES, DNS, and machine-learning-assisted reaction modelling – are required to accurately predict flame structure, quenching behavior, and turbulence–chemistry interactions.

Viewed as a whole, the body of research does not point to a single universal solution but rather outlines several key paths that appear particularly promising for the continued development of hydrogen combustion systems.

One noticeable shift concerns the way combustion is modelled. Traditional steady-state approaches, although still useful, appear insufficient for hydrogen flames. Because hydrogen combustion is highly sensitive to thermodynamic and diffusive imbalances and preferential diffusion effects, local instabilities often govern flame structure and propagation [29]. Capturing these phenomena reliably requires modelling frameworks capable of resolving fine-scale interactions rather than relying solely on equilibrium-based or averaged descriptions.

A closer reading of the available studies also challenges a fairly intuitive assumption that adding more hydrogen will automatically translate into better engine performance. In reality, the relationship is far more nuanced. Modest hydrogen additions often improve flame responsiveness and allow operation under leaner conditions, but pushing the hydrogen fraction too far does not necessarily bring proportional benefits [46]. In some cases, it can even compromise combustion stability or deliver only marginal efficiency improvements. What appears to matter most is not the absolute hydrogen content but how well the mixture composition aligns with the combustion concept, engine architecture, and control settings. In that sense, precise tuning and system-level optimization outweigh the simple strategy of maximizing hydrogen share.

At the same time, numerical studies consistently point to another critical aspect: combustion outcomes are tightly linked to physical design choices inside the cylinder. The injector location, the generation of swirl and tumble motions, and the distribution of the mixture before ignition all shape the subsequent flame evolution and emission profile [71, 72]. Ignition timing and pollutant formation cannot be understood without considering these flow structures. In other words, combustion chemistry does not operate in isolation, but it unfolds within a geometrically defined, highly dynamic environment. Effective engine development, therefore, requires simultaneous attention to both in-cylinder aerodynamics and reaction kinetics from the earliest design stages [5].

When considered collectively, the reviewed studies suggest three major directions for future hydrogen combustion research:

1. Shift from steady-state modelling to instability-focused modelling

Hydrogen combustion is dominated by thermodynamic and diffusive effects, including preferential diffusion, which require high-resolution modelling beyond classical equilibrium-based methods.

2. Optimization rather than maximization of hydrogen fraction

The literature does not support the assumption that higher hydrogen content always yields better performance.

Instead, optimal fractions depend on combustion regime, engine type, and control strategy.

3. Coupled design of combustion chamber geometry and injection strategy

Numerical studies repeatedly demonstrate that injector placement, swirl intensity, and tumble enhancement significantly alter ignition behaviour and emissions, highlighting the importance of geometry–chemistry coupling.

The body of work discussed here shows that hydrogen combustion research now occupies a space between traditional combustion theory and the rapidly evolving field of advanced numerical simulation. Earlier investigations focused on fairly direct questions about how hydrogen affects emissions, how quickly the flame propagates, and how stable combustion is under different conditions. Today, the scope has broadened. Researchers are increasingly examining interactions spanning multiple scales, from microscopic reaction pathways to large-scale flow structures, while also exploring turbulence-chemistry coupling and data-driven modelling techniques that were previously rarely considered.

At this stage, the key challenges no longer lie in proving that hydrogen can burn efficiently in piston engines. What seems to limit wider industrial adoption is something more complex: integrating hydrogen combustion into complete engine systems, ensuring stable operation across load ranges, and adapting existing infrastructure to accommodate hydrogen's specific fuel requirements. The obstacles are now largely systemic rather than purely scientific.

This review presents a descriptive compilation of existing studies by integrating findings from experimental combustion research, numerical modelling, and engine system optimization. The collected evidence demonstrates that hydrogen combustion in piston engines represents not only a fuel substitution strategy but a distinct combustion regime characterized by strong thermo–diffusive effects, high reactivity, and sensitivity to flow structures.

A key contribution of this review is the identification of three overarching trends:

- the transition from steady-state modelling approaches toward instability-resolving frameworks (LES, DNS)
- the recognition that optimal hydrogen fraction depends on engine architecture and combustion mode rather than simple maximization strategies
- the growing importance of geometry–chemistry coupling in combustion chamber and injector design.

Furthermore, several research gaps remain insufficiently addressed in the literature:

- limited long-term durability analyses under hydrogen combustion conditions
- insufficient validation of high-fidelity models under transient engine loads
- lack of standardized modelling methodologies for preferential diffusion effects
- incomplete integration of combustion modelling with full powertrain system optimization.

By synthesizing these aspects, this review provides a structured research roadmap for future development of hydrogen combustion.

6. Summary and conclusions

The use of hydrogen as an admixture to conventional fuels in piston engines is one of the most promising transitional solutions towards decarbonizing transport and energy. Simulation and experimental studies clearly confirm that even a small proportion of hydrogen in the fuel mixture can significantly improve combustion parameters, such as ignition speed, heat release intensity, and indicated efficiency.

Hydrogen, due to its high octane rating and low ignition energy, facilitates stable combustion while reducing carbon monoxide and unburned hydrocarbon emissions. However, without proper optimization of operating parameters, for instance, if ignition timing is too advanced, issues such as knocking or elevated NO_x formation may arise. Therefore, precise calibration of the ignition timing, injection method, and hydrogen quantity in the mixture is necessary.

Technologies that blend hydrogen with traditional fuels in GDI and TJI systems demonstrate that it is possible to combine high energy efficiency with engine operational safety. The final result depends on many factors, including the level of hydrogen enrichment, initial conditions, mixture characteristics, and combustion chamber geometry. The inherent complexity of hydrogen combustion phenomena highlights the need for sophisticated CFD modeling tools and systematic optimization of engine operating conditions to guide further technological advancements.

Beyond summarizing prior work, this review identifies several structural trends in hydrogen combustion research. A noticeable shift is observed from steady, globally averaged models toward approaches capable of resolving thermo-diffusive instabilities and turbulence–chemistry interactions. The literature also confirms that combustion chamber geometry, in-cylinder flow structures, and chemical kinetics form a coupled system, while the optimal hydrogen fraction depends on engine configuration and control strategy rather than simple maximization. Further progress will require tighter integration of high-fidelity CFD modelling with experimental validation, particularly under transient operating conditions relevant to automotive applications. In addition to summarizing the available literature, this review examines how current modeling approaches perform when confronted with combustion phenomena characteristic of hydrogen. These include its exceptionally high laminar flame speed, increased susceptibility to abnormal combustion events, and the strong sensitivity of NO_x formation under lean operating conditions. Rather than merely listing existing methods, the paper identifies where current modeling strategies remain insufficient or inconsistent, especially in engine-relevant configurations. On this basis, a structured approach to selecting numerical methods is proposed to support more reliable, physically consistent CFD studies of hydrogen-fueled internal combustion engines in future research.

Future research should focus on multi-scale modelling approaches that bridge detailed chemical kinetics with system-level engine simulations. Particular attention should be paid to the interactions among turbulence, preferential diffusion, and ignition control in highly diluted and ultra-lean regimes. The integration of data-driven methods with physics-based CFD models is a promising approach to reduce

computational costs while maintaining predictive accuracy. Ultimately, advancing hydrogen combustion in piston engines requires coordinated progress in combustion science, digital modelling, materials engineering, and regulatory harmonization to ensure both technical reliability and environmental effectiveness.

Acknowledgements

The authors acknowledge the financial support received from the PhD Boost programme, organized by Poznan University of Technology, which made this research possible.

Nomenclature

AVL FIRE	commercial CFD software for engine combustion modelling (brand name)
CFD	computational fluid dynamics
CJ	Chapman-Jouguet (detonation condition)
CNG	compressed natural gas
DNS	direct numerical simulation
EGR	exhaust gas recirculation
FGM	flamelet generated manifold
FGM-PV	flamelet generated manifold-progress variable
Fluent (ANSYS Fluent)	commercial CFD software by ANSYS (brand name)
GT-Power	engine system simulation software (brand name)
H_2-ICEs	hydrogen internal combustion engines
H_2/NG blend	mixture of hydrogen and natural gas
HCCI	homogeneous charge compression ignition
HCNG	hydrogen-enriched compressed natural gas
HPC	high-performance computing
ITE	indicated thermal efficiency
IMEP	indicated mean effective pressure
LES	large eddy simulation
LHV	lower heating value
LPG	liquefied petroleum gas
MBT	minimum spark advance for best torque
MCCI	mixed-controlled compression ignition
MILD	moderate or intense low-oxygen dilution combustion
MVF	mixture volume fraction
NG_2	methane-dominant composition
OH	hydroxyl radical
PDF	probability density function
RANS	Reynolds-Averaged Navier-Stokes
SCR	selective catalytic reduction
TJI	turbulent jet ignition
TKE	turbulent kinetic energy
ZND	Zeldovich-von Neumann-Döring (detonation model)

Bibliography

[1] Abubakre OK, Medupin RO, Akintunde IB, Jimoh OT, Abdulkareem AS, Muriana RA et al. Carbon nanotube-reinforced polymer nanocomposites for sustainable biomedical applications: a review. J Sci Adv Mater Devices. 2023; 8(2):100557. https://doi.org/10.1016/j.jsamd.2023.100557

[2] Arat HT. Simulation of diesel hybrid electric vehicle containing hydrogen enriched CI engine. Int J Hydrog Energy. 2019;44(20):10139-10146. https://doi.org/10.1016/j.ijhydene.2018.10.004

[3] Arat HT. Alternative fuelled hybrid electric vehicle (AF-HEV) with hydrogen enriched internal combustion engine. Int J Hydrog Energy. 2019;44(34):19005-19016. https://doi.org/10.1016/j.ijhydene.2018.12.219

[4] Beccari S. On the Use of a hydrogen-fueled engine in a hybrid electric vehicle. Appl Sci. 2022;12:12749. https://doi.org/10.3390/app122412749.

[5] Beşinci M, Arslan A, Çıkar R, Yamal MO, Selim A, Kolbakır C. Experimental study on flow visualization and aerodynamic effects of rotating cylinders on airfoils. 13th Ankara International Aerospace Conference. 17.09.2025.

[6] Cecere G. Hydrogen as fuel for ICEs: state of art and technological challenges. J Eng. 2024;2024:9930258. https://doi.org/10.1155/2024/9930258.

[7] Chen Z, Chen H, Wang L, Geng L, Zeng K. Parametric study on effects of excess air/fuel ratio, spark timing, and methanol injection timing on combustion characteristics and performance of natural gas/methanol dual-fuel engine at low loads. Energy Convers Manag. 2020;210:112742. https://doi.org/10.1016/j.enconman.2020.112742

[8] Cinieri G, Fontanarosa D, De Giorgi MG. Combustion characteristics of hydrogen/air mixtures in a plasma-assisted micro combustor. Energies. 2023;16:2272. https://doi.org/10.3390/en16052272

[9] Costa M, Piazzullo D, Dolce A. Hydrogen addition to natural gas in cogeneration engines: optimization of performances through numerical modeling. Front Mech Eng. 2021;7: 680193. https://doi.org/10.3389/fmech.2021.680193.

[10] Danciu BA, Giannakopoulos GK, Bode M, Frouzakis CE. Direct numerical simulation of hydrogen combustion in a real-size IC engine. 2025. https://doi.org/10.48550/arXiv.2502.16318

[11] Das L. Hydrogen engine: research and development (R&D) programmes in Indian Institute of Technology (IIT), Delhi. Int J Hydrog Energy. 2002;27:953-965. https://doi.org/10.1016/S0360-3199(01)00178-1.

[12] Daurer G, Schwarz S, Demuth M, Gaber C, Hochenauer C. Evaluation of numerical modeling and combustion characteristics of hydrogen oxy-fuel combustion in a semi-industrial furnace. Fuel. 2024;369:131690. https://doi.org/10.1016/j.fuel.2024.131690

[13] Deheri C, Acharya SK, Thatoi DN, Mohanty AP. A review on performance of biogas and hydrogen on diesel engine in dual fuel mode. Fuel. 2020;260:116337. https://doi.org/10.1016/j.fuel.2019.116337

[14] Dutta PP, Das A, Pandey V, Devi M. Fuel characteristics of some locally available biomass as a potential gasification feedstock for thermal application. Ind Eng Chem Res. 2014; 53:19806-19813. https://doi.org/10.1021/ie5034107

[15] Eberle U, Felderhoff M, Schüth F. Chemical and physical solutions for hydrogen storage. Angew Chem Int Ed. 2009; 48:6608-6630. https://doi.org/10.1002/anie.200806293

[16] European Communities. Hydrogen storage: state-of-the-art and future perspective. Luxembourg: Publications Office; 2003.

[17] Ferreira Gomes FA, Yang Y, Talei M. Decarbonizing combustion with hydrogen blended fuels: An exploratory study

of impact of hydrogen on hydrocarbon autoignition. Fuel. 2024;364:131028. https://doi.org/10.1016/j.fuel.2024.131028

[18] Fu Z, Li Y, Chen H, Du J, Li Y, Gao W. Effect of hydrogen blending on the combustion performance of a gasoline direct injection engine. ACS Omega. 2022;7:13022-13030. https://doi.org/10.1021/acsomega.2c00343

[19] Ghazal OH. Combustion analysis of hydrogen-diesel dual fuel engine with water injection technique. Case Stud Therm Eng. 2019;13:100380. https://doi.org/10.1016/j.csite.2018.100380

[20] Ghodbane H, Khaldi F, Derradji B. The impact of hydrogen enrichment on engine performance and exhaust emissions in LPG-hydrogen blends. J Ren Energies. 2025;28|(5):13-19. https://doi.org/10.54966/jreen.v28i5.1540

[21] Gong C, Li Z, Yi L, Liu F. Experimental investigation of equivalence ratio effects on combustion and emissions characteristics of an H2/methanol dual-injection engine under different spark timings. Fuel. 2020;262:116463. https://doi.org/10.1016/j.fuel.2019.116463

[22] Goyal H, Jones P, Bajwa A, Parsons D, Akehurst S, Davy MH et al. Design trends and challenges in hydrogen direct injection (H2DI) internal combustion engines – a review. Int J Hydrog Energy. 2024;86:1179-1194. https://doi.org/10.1016/j.ijhydene.2024.08.284

[23] Gruber A, Bothien MR, Ciani A, Aditya K, Chen JH, Williams FA. Direct numerical simulation of hydrogen combustion at auto-ignitive conditions: Ignition, stability and turbulent reaction-front velocity. Combust Flame. 2021;229: 111385. https://doi.org/10.1016/j.combustflame.2021.02.031

[24] Hafiz NM, Mansor MRA, Wan Mahmood WMF. Simulation of the combustion process for a CI hydrogen engine in an argon-oxygen atmosphere. Int J Hydrog Energy. 2018;43: 11286-11297. https://doi.org/10.1016/j.ijhydene.2018.05.022

[25] Halouane Y, Dehbi A. CFD simulations of premixed hydrogen combustion using the eddy dissipation and the turbulent flame closure models. Int J Hydrog Energy. 2017;42:21990-22004. https://doi.org/10.1016/j.ijhydene.2017.07.075

[26] Hu E, Huang Z, Liu B, Zheng J, Gu X. Experimental study on combustion characteristics of a spark-ignition engine fueled with natural gas–hydrogen blends combining with EGR. Int J Hydrog Energy. 2009;34:1035-1044. https://doi.org/10.1016/j.ijhydene.2008.11.030

[27] Huang B, Hu E, Huang Z, Zheng J, Liu B, Jiang D. Cycle-by-cycle variations in a spark ignition engine fueled with natural gas–hydrogen blends combined with EGR. Int J Hydrog Energy. 2009;34:8405-8414. https://doi.org/10.1016/j.ijhydene.2009.08.002

[28] Jin C, Pang X, Zhang X, Wu S, Ma M, Xiang Y et al. Effects of C3–C5 alcohols on solubility of alcohols/diesel blends. Fuel. 2019;236:65-74. https://doi.org/10.1016/j.fuel.2018.08.129

[29] Kai R, Tokuoka T, Nagao J, Pillai AL, Kurose R. LES flamelet modeling of hydrogen combustion considering preferential diffusion effect. Int J Hydrog Energy. 2023;48: 11086-11101. https://doi.org/10.1016/j.ijhydene.2022.12.164

[30] Karim GA. Hydrogen as a spark ignition engine fuel. Int J Hydrog Energy. 2003;28(5):569-577. https://doi.org/10.1016/S0360-3199(02)00150-7

[31] Khatri N, Khatri KK. Hydrogen enrichment on diesel engine with biogas in dual fuel mode. Int J Hydrog Energy. 2020; 45:7128-7140. https://doi.org/10.1016/j.ijhydene.2019.12.167

[32] Liu C, Karim G. A simulation of the combustion of hydrogen in HCCI engines using a 3D model with detailed chemical kinetics. Int J Hydrog Energy. 2008;33:3863-3875. https://doi.org/10.1016/j.ijhydene.2008.04.028

[33] Liu H, Wang X, Zheng Z, Gu J, Wang H, Yao M. Experimental and simulation investigation of the combustion characteristics and emissions using n -butanol/biodiesel dual-fuel injection on a diesel engine. Energy. 2014;74:741-752. https://doi.org/10.1016/j.energy.2014.07.041

[34] Liu J, Duan X, Yuan Z, Liu Q, Tang Q. Experimental study on the performance, combustion and emission characteristics of a high compression ratio heavy-duty spark-ignition engine fuelled with liquefied methane gas and hydrogen blend. Appl Therm Eng. 2017;124:585-594. https://doi.org/10.1016/j.applthermaleng.2017.06.067

[35] Makaryan IA, Sedov IV, Salgansky EA, Arutyunov AV, Arutyunov VS. A comprehensive review on the prospects of using hydrogen–methane blends: challenges and opportunities. Energies. 2022;15:2265. https://doi.org/10.3390/en15062265

[36] Malé Q, Lapeyre CJ, Noiray N. Hydrogen reaction rate modeling based on convolutional neural network for large eddy simulation. Data-Centric Eng. 2025;6:e11. https://doi.org/10.1017/dce.2025.1

[37] Mariani A, Morrone B, Unich A. A review of hydrogen-natural gas blend fuels in internal combustion engines. In: Khan S, (ed). Foss. Fuel Environ., InTech. 2012. https://doi.org/10.5772/37834

[38] Markowska K, Wittek K, Kabiesz P, Stecuła K, Aydın B, Pawlak S et al. Hydrogen-powered engines: a study on selected technological and emissions issues. Energies. 2025; 18:1675. https://doi.org/10.3390/en18071675

[39] Mekonnin AS, Wacławiak K, Humayun M, Zhang S, Ullah H. Hydrogen storage technology, and its challenges: a review. Catalysts. 2025;15:260. https://doi.org/10.3390/catal15030260

[40] Miao H, Ji M, Jiao Q, Huang Q, Huang Z. Laminar burning velocity and Markstein length of nitrogen diluted natural gas/hydrogen/air mixtures at normal, reduced and elevated pressures. Int J Hydrog Energy. 2009;34:3145-3155. https://doi.org/10.1016/j.ijhydene.2009.01.059

[41] Mielcarzewicz D, Pielecha I. The influence of helium addition on the combustion process in a hydrogen-fueled turbulent jet ignition engine. Appl Sci. 2024;14:8996. https://doi.org/10.3390/app14198996

[42] Okolo ME, Adebayo DS, Oduoza CF. Numerical modelling of non-premixed hydrogen blended combustion in a 3D-combustor with jet optimisation. React Chem Eng. 2025: 10.1039.D4RE00537F. https://doi.org/10.1039/D4RE00537F

[43] Olufisayo OE, Inambao FL, Stopforth R. GT-Power for internal combustion engine simulation: a review. J Propuls Technol. 2025;46(1):1161-1171. https://www.propulsiontechjournal.com/index.php/journal/article/view/9008

[44] Pandey KM, Nath B. Numerical simulation of a hydrogen fueled scramjet combustor at Mach 1.5 using strut injectors at Mach 2.47 air speed. Adv Aerodyn, San Diego, California. ASME. 2013;1.V001T01A046. https://doi.org/10.1115/IMECE2013-66036

[45] Park SH, Lee CS. Applicability of dimethyl ether (DME) in a compression ignition engine as an alternative fuel. Energy Convers Manag. 2014;86:848-863. https://doi.org/10.1016/j.enconman.2014.06.051

[46] Pietras PJ, Andrych-Zalewska M. Conversion of a diesel internal combustion engine to hydrogen power. Rail Veh Szyn. 2025:3-14. https://doi.org/10.53502/RAIL-214617

[47] Quadri SAP, Rentala GS, Sarap R. Performance, combustion and exhaust emissions analysis of HCNG fuelled single cylinder diesel engine at different injection opening pressures. World J Eng. 2018;15:710-718. https://doi.org/10.1108/WJE-03-2017-0054
[48] Remme U. Global Hydrogen Review 2024.
[49] Reza S, Alsairafi AA. CFD study on hydrogen-air premixed combustion in a micro scale chamber. 2010;29.
[50] Roberta Santos Righi A, Halila GLO, Azevedo JLF. Smooth transitional RANS model and applications with crossflow effects. Adv Aerodyn. 2026;8:3. https://doi.org/10.1186/s42774-025-00208-5
[51] Rueda-Vázquez JM, Serrano J, Pinzi S, Jiménez-Espadafor FJ, Dorado MP. A review of the use of hydrogen in compression ignition engines with dual-fuel technology and techniques for reducing NOx emissions. Sustainability. 2024;16:3462. https://doi.org/10.3390/su16083462
[52] Sagar SMV, Agarwal AK. Experimental investigation of varying composition of HCNG on performance and combustion characteristics of a SI engine. Int J Hydrog Energy. 2017;42:13234-13244. https://doi.org/10.1016/j.ijhydene.2017.03.063
[53] Schneider M, Nicolai H, Schuh V, Steinhausen M, Hasse C. Flame-wall interaction of thermodiffusively unstable hydrogen/air flames – part I: characterization of governing physical phenomena. 2024. https://doi.org/10.48550/arXiv.2411.17590
[54] Schneider M, Nicolai H, Schuh V, Steinhausen M, Hasse C. Flame-wall interaction of thermodiffusively unstable hydrogen/air flames – part II: parametric variations of equivalence ratio, temperature, and pressure. 2024. https://doi.org/10.48550/arXiv.2411.18106
[55] Sierens R, Rosseel E. Variable composition hydrogen/natural gas mixtures for increased engine efficiency and decreased emissions. J Eng Gas Turbines Power. 2000;122: 135-140. https://doi.org/10.1115/1.483191
[56] Sopena C, Diéguez PM, Sáinz D, Urroz JC, Guelbenzu E, Gandía LM. Conversion of a commercial spark ignition engine to run on hydrogen: performance comparison using hydrogen and gasoline. Int J Hydrog Energy. 2010;35:1420-1429. https://doi.org/10.1016/j.ijhydene.2009.11.090
[57] Stępień Z. A comprehensive overview of hydrogen-fueled internal combustion engines: achievements and future challenges. Energies. 2021;14:6504. https://doi.org/10.3390/en14206504.
[58] Sui R, Mantzaras J. Combustion stability and hetero-/homogeneous chemistry interactions for fuel-lean hydrogen/air mixtures in platinum-coated microchannels. Combust Flame. 2016;173:370-386. https://doi.org/10.1016/j.combustflame.2016.08.011.
[59] Tang D, Tan G-L, Li G-W, Liang J-G, Ahmad SM, Bahadur A et al. State-of-the-art hydrogen generation techniques and storage methods: a critical review. J Energy Storage. 2023; 64:107196. https://doi.org/10.1016/j.est.2023.107196
[60] Trilla J, Grossen J, Robinson A, Bosschaerts W, Hendrick P. Development of a hydrogen combustion chamber for an ultra micro gas turbine. Proceedings of PowerMEMS 2008+ microEMS 2008, Sendai, Japan. November 9-12;2008.
[61] Uliasz-Misiak B, Misiak J, Tarkowski R. Research trends in underground hydrogen storage: a bibliometric approach. Energies. 2025;18:1845. https://doi.org/10.3390/en18071845
[62] Verhelst S. Recent progress in the use of hydrogen as a fuel for internal combustion engines. Int J Hydrog Energy. 2014; 39:1071-1085. https://doi.org/10.1016/j.ijhydene.2013.10.102
[63] Verhelst S, Wallner T. Hydrogen-fueled internal combustion engines. Prog Energy Combust Sci. 2009;35:490-527. https://doi.org/10.1016/j.pecs.2009.08.001
[64] Visser DC, Houkema M, Siccama NB, Komen EMJ. Validation of a FLUENT CFD model for hydrogen distribution in a containment. Nucl Eng Des. 2012;245:161.171. https://doi.org/10.1016/j.nucengdes.2012.01.025
[65] Walsh SL, Zhu Y, Liu F, Sirignano WA. Performance of flamelet models with epsilon tracking for diffusion flame simulations. AIAA SCITECH 2026 Forum, Orlando, FL: American Institute of Aeronautics and Astronautics; 2026. https://doi.org/10.2514/6.2026-2908
[66] Wang B, Shao Y, Yang L, Guo K, Li X, Sun M, et al. Sustainable hydrogen production with negative carbon emission through thermochemical conversion of biogas/biomethane. Energies. 2025;18:1804. https://doi.org/10.3390/en18071804
[67] Wang L, Liu D, Yang Z, Li H, Wei L, Li Q. Effect of H2 addition on combustion and exhaust emissions in a heavy-duty diesel engine with EGR. Int J Hydrog Energy. 2018;43: 22658-22668. https://doi.org/10.1016/j.ijhydene.2018.10.104
[68] Wei S, Zhang Z, Li X, Wu C, Yang F. Simulation analysis of fuel economy of the GDI engine with a Miller cycle and EGR based on GT-Power. Processes. 2022;10:319. https://doi.org/10.3390/pr10020319
[69] White C, Steeper R, Lutz A. The hydrogen-fueled internal combustion engine: a technical review. Int J Hydrog Energy. 2006;31:1292-1305. https://doi.org/10.1016/j.ijhydene.2005.12.001
[70] Wróbel K, Wróbel J, Tokarz W, Lach J, Podsadni K, Czerwiński A. Hydrogen internal combustion engine vehicles: a review. Energies. 2022;15:8937. https://doi.org/10.3390/en15238937
[71] Wu B, Torelli R, Pei Y. Numerical modeling of hydrogen mixing in a direct-injection engine fueled with gaseous hydrogen. Fuel. 2023;341:127725. https://doi.org/10.1016/j.fuel.2023.127725
[72] Zhu W, Zhang X, Zhang M, Yin S, Wu X, Long W et al. Numerical investigation on turbulent flame jet characteristics of ultra-lean H2/air ignited by pre-chamber enrichment strategy. Energy Convers Manag X. 2025;26:100954. https://doi.org/10.1016/j.ecmx.2025.100954
[73] Zhukov VP. Verification, validation, and testing of kinetic mechanisms of hydrogen combustion in fluid-dynamic computations. ISRN Mech Eng. 2012;2012:1-11. https://doi.org/10.5402/2012/475607
[74] Zöldy M, Virt M, Lukács K, Szabados G. A comprehensive analysis of characteristics of hydrogen operation as a preparation for retrofitting a compression ignition engine to a hydrogen engine. Processes. 2025;13:718. https://doi.org/10.3390/pr13030718

Marcelina Górzyńska, MEng. – Faculty of Civil and Transport Engineering, Poznan University of Technology, Poland.
e-mail: *marcelina.gorzynska@doctorate.put.poznan.pl*

Prof. Ireneusz Pielecha, DSc., DEng. – Faculty of Civil and Transport Engineering, Poznan University of Technology, Poland.
e-mail: *ireneusz.pielecha@put.poznan.pl*

Article citation info:
Khrulev A, Dmytriev S. Study of pulse jet engine thermodynamic cycle using workflow mathematical modeling. Combustion Engines. 2026;206(3):199-209. https://doi.org/10.19206/CE-218595

Alexander KHRULEV
Serhii DMYTRIEV

Combustion Engines
Polish Scientific Society of Combustion Engines

Study of pulse jet engine thermodynamic cycle using workflow mathematical modeling

ARTICLE INFO

Received: 23 November 2025
Revised:10 February 2026
Accepted: 25 February 2026
Available online: 16 March 2026

The paper presents a theoretical analysis of possible thermodynamic cycles of a pulse jet engine. To clarify the type of thermodynamic cycle, equations for calculating the polytropic index from instantaneous gas parameters in the combustion chamber are derived. The classic Argus As 014 valved pulse-jet engine workflow, both at static conditions and at 800 km/h, has been simulated. The simulation results confirm the known data that the real operating cycle of a valved pulse jet engine during static conditions is the Lenoir cycle. However, for the engines with straight air intake and with increasing flight speed, the specific workflow nature, i.e. the presence of polytropic pre-compression before heat release, that corresponds to the Humphrey cycle rather than the Lenoir cycle, has been found. Unlike a straight intake engine, a valved pulse jet engine with a side air intake that does not have air pre-compression has also been found to exhibit increased performance with increasing flight speed. The obtained data confirm that, in general, the thermodynamic cycle of a valved pulse jet engine can be represented as the Humphrey cycle, which in specific cases, such as zero flight speed and/or a side air intake, does not experience polytropic pre-compression before heat release and corresponds to the Lenoir cycle.

Key words: *pulse jet engine, pulsejet, thermodynamic cycle, workflow, modeling*

This is an open access article under the CC BY license (http://creativecommons.org/licenses/by/4.0/)

1. Introduction

Although no production pulse jet engines have been developed since World War II, this type of engine has been periodically considered for use in unmanned aerial vehicles (UAV) for 80 years. However, until recently, the generally accepted, long-held concept of limited application of "smart," high-precision, and expensive systems virtually ruled out the need and feasibility of using pulse jet engines in unmanned aircraft. However, the rapidly changing nature of 21st-century military conflicts is forcing a reconsideration of established opinions and proven technologies.

An analysis of some open sources indicates a gradual shift away from expensive, low-production systems, which were just recently considered the only feasible ones for a wide range of operational and tactical tasks [2, 3], toward inexpensive systems for mass production and application [29]. But the first problem arises with the scaling of engine production. Thus, with the number of unmanned aerial vehicles reaching hundreds or even thousands per day, equipping them with piston engines produced in similar series is technically difficult or even economically questionable. Moreover, piston engines are currently not used on UAVs at speeds above 250 km/h [46] and, in principle, do not allow achieving the high flight speeds (700 km/h and above) typical of jet engines. At the same time, mass production of turbojet engines in a series of sizes under consideration is not only extremely difficult technically, but also practically impossible, including for economic reasons. In such a situation, the search for an alternative again naturally leads to the long-forgotten pulse jet engine [32].

However, analyzing any parameters or characteristics of pulse jet engines, with their previous position as "smart" and highly precise, but expensive and unique systems, loses its meaning from the outset. For example, most analysts, when considering a UAV with a pulse jet engine, immediately cite the pulse jet engine's specific fuel consumption [30], which is three times higher than that of a turbojet engine. Further, for added persuasiveness, they usually add the extremely high noise and thermal radiation levels, or even the short service life of the reed valves [21], as well as the "inaccuracy" and "non-selectivity" of German V-1 cruise missiles produced in 1944–45 (as if they were still around this time), after which they lose interest.

In fact, such a superficial analysis is inconsequential. For example, today's UAVs with a range of 1000–1200 km often use 2-stroke piston engines, but no one mentions their specific fuel consumption, which is almost twice that of 4-stroke engines [3]. This example demonstrates that an aircraft's mission performance is determined not by its engine's specific fuel consumption, but by its speed and range. Furthermore, the negative impact of some features of a pulse jet engine, which are important for a single application, is mitigated by mass deployment, where features such as noise and thermal radiation can even become advantages. Moreover, the main advantages of a pulse jet engine for UAV use have remained unchanged for 80 years, particularly in mass-production conditions: extreme simplicity of design, low deployment cost, and scalability without significant capital expenditures. All this makes the use of pulsejets on UAVs of various types, especially high speed, possible, and their research to justify the choice of parameters and their coordination with the characteristics of UAVs relevant.

2. Sources review and problem statement

A preliminary analysis of different sources on pulse jet engine research (Fig. 1) shows that significant progress in developing their theory has not been achieved. Since the late 1940s, there have been virtually no serious experimental studies of the pulse jet engine workflow, except for a few specific problems [1, 43]. As a result, no significant

new data on the processes, parameters, and/or characteristics of aircraft pulsejets, expanding on the known data from the first half of the 1940s from the leading German developers of the classic Argus As 014 engine [9], have been obtained during this entire period.

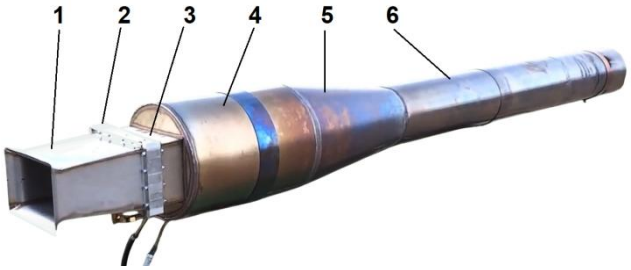

Fig. 1. Schematic diagram of a classic valved pulse jet engine with straight air intake: 1 – inlet device; 2 – valve grid; 3 – Venturi diffuser; 4 – combustion chamber; 5 – cone (nozzle); 6 – resonance tube

The situation with theoretical research is no better. Thus, the method of characteristics [37], developed in the first half of the 1940s, remained, for many decades, one of the few available methods for theoretically studying the pulse-jet engine workflow. Numerous works devoted to theoretical research and the development of methods for modeling motors [8, 44] have not led to greater clarity of the processes than was investigated by the founders of the pulsejet technology in Germany 80 years ago [36]. It is characteristic that even half a century after the creation of this project, in the subsequent decades of general computerization, not a single computer program for modeling the workflow and characteristics of a pulse jet engine has been developed that is accessible to a wide range of users, although significant efforts have been made to this end, including the use of the most modern 3-D modeling [39, 40].

The lack of a systematic approach in research naturally leads to difficulties in assessing the feasibility of various engine designs. As a result, for many decades, numerous enthusiasts, primarily amateurs, unsuccessfully attempted to make various exotic pulsejet designs work, including valveless designs [22, 45], while the experience of German developers clearly indicates the ineffectiveness of such designs in aviation [6] and the practical absence of an alternative to the valve-based pulsejet design [9].

The reasons for these failures are ambiguous. On the one hand, it is worth noting the lack of interest in this engine type in "large" aviation since the late 1940s, which led to the closure of all areas of development and application of aviation pulsejets in favor of turbojet engines. Consequently, research into pulse jet engine processes has become a proactive endeavor, where a lack of, or even complete absence of, adequate funding for this topic prevents the full implementation of all necessary research [35, 38]. On the other hand, significant research has been devoted to investigating pulse combustion [33, 44], including efforts to develop industrial installations and devices based on this phenomenon [26, 27]. Since the purpose of such work was not to obtain the characteristics of an aircraft engine, including thrust and specific fuel consumption, their results have rather limited application for aviation.

In general, it should be noted that the insufficient research into these processes leaves a wide range of possibilities for the emergence of various theories unsupported by theoretical modeling and experiments, which are the basis for numerous attempts to create inefficient [28] or completely inoperable engine designs [41]. This situation is understandable, since for many decades the main field of application of the pulse jet engine was aircraft modeling [11], where the main "scientific centers" were workshops and garages, and the main research tools were metal cutters and welding machines [23]. It is for this reason that significant gaps are observed, first and foremost, in the fundamentals of the theory of pulsejets, including in the study of their thermodynamic cycles.

An analysis of known sources on the topic of pulsejets allows us to draw the preliminary conclusion that German developers clearly justified the thermodynamic cycle of the pulse jet engine as the Lenoir cycle [36]. As is known [34], the ideal Lenoir cycle (Fig. 2a) consists of three processes. Initially, heat is released to the working fluid during isochoric combustion at constant volume, increasing the working fluid's pressure. This is followed by polytropic (adiabatic) expansion, after which heat is released to the environment at constant atmospheric pressure in isobaric cooling. In other words, the key feature of the Lenoir cycle is that pressure increases solely as a result of heat release, without the use of mechanical boosters such as compressors or superchargers. This explains the low maximum cycle pressure, p_{max}, relative to ambient pressure, p_0 – in pulsejets, the cycle pressure ratio ($\pi = p_{max}/p_0$) does not exceed 2.2–2.4.

The closed curve of the component processes forms the diagram of the ideal working cycle (Fig. 2a) of a pulse jet engine. This is not merely a theoretical diagram; on the contrary, it demonstrates that during operation, the state of the working fluid in the engine, not only in the combustion chamber but also in all other sections, undergoes continuous changes in accordance with the circular movement of the diagram at a frequency of 40–200 Hz. This feature characterizes the pulse jet engine as a periodic-flow engine [16], by analogy with an internal combustion engine [4]. But at the same time, it significantly distinguishes this engine from other air-breathing engines (turbojets and ramjets), in which the flow is stationary [42], that is, the state of the working fluid in a specific section of the engine remains constant over time.

Despite the indication of the German developers [36], and also taking into account the fact that no serious theoretical studies of the pulse jet engine cycle have been conducted for almost 80 years, in some sources [7], nevertheless, there have been claims that the engine's workflow is described by another, more efficient thermodynamic cycle – the Humphrey cycle (Fig. 2b).

The main difference between the Humphrey cycle and the Lenoir cycle lies in the preliminary polytropic (adiabatic) compression before the onset of heat release at constant volume [19]. In other words, an engine operating on the Humphrey cycle, unlike the Lenoir cycle, has an additional compression process in the chamber in addition to the combustion itself. In addition, the Humphrey cycle can be

considered a kind of modification of the Brayton cycle, typical of ramjet engines [7], but instead of heat release at constant pressure, heat is released at constant volume, and there is no gas exchange, instead there is a conditional process of heat removal from the cycle to the environment at a constant atmospheric pressure.

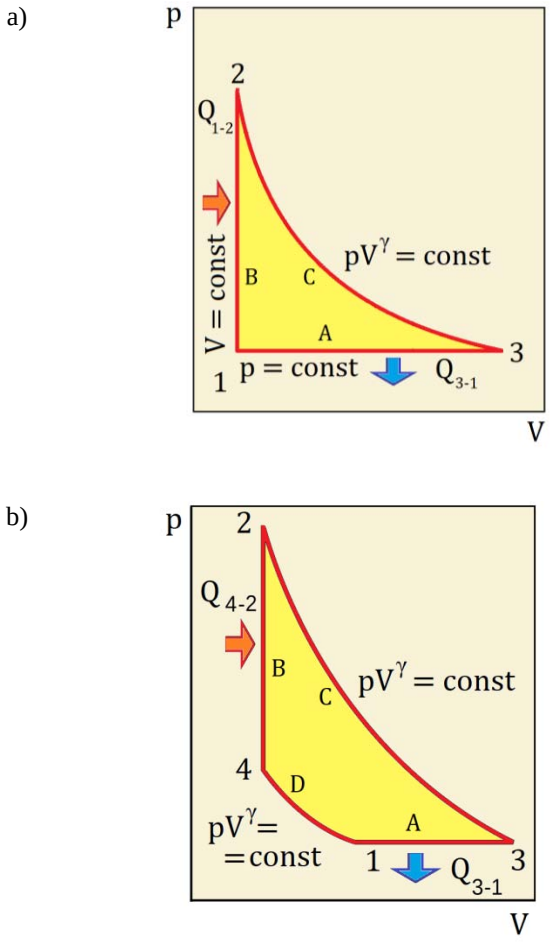

Fig. 2. Diagrams of thermodynamic cycles attributed to a pulse jet engine and their individual processes (phases): a – Lenoir cycle [5], b – Humphrey cycle [7]; A – isobaric gas exchange (intake) and heat removal; B – isochoric heat release (combustion); C – polytropic (adiabatic) expansion; D – preliminary polytropic (adiabatic) compression

According to proponents of this concept [14], preliminary compression also occurs in a pulse jet engine; however, no studies supporting this claim are presented in these works. Some sources provide an additional clarification, albeit without proper justification, stating that the thermodynamic cycle of a pulse jet engine can be represented by two variants [26]. Thus, the cycle of a valve engine when operating at a stationary speed, at zero speed, and a valveless engine remains, as previously believed, the Lenoir cycle [12, 20]. However, at a non-zero flight speed, it was proposed to treat the valve engine cycle as a Humphrey cycle [12]. This later enabled some researchers [7, 14] to completely exclude the Lenoir cycle, treating it as a special case of the Humphrey cycle at zero speed, and to consider the Humphrey cycle as the only working cycle of a pulse jet engine without additional conditions [20]. Thus, contrary to the data of the German founders, it was proposed to describe the working cycle of a pulse jet engine as a modification of a ramjet engine, with heat release at constant volume.

It means adding another process to the Lenoir cycle of a pulse jet engine can create a contradiction. A pulse jet engine, as noted above, is a periodic, not continuous, engine. It features gas exchange, as in an internal combustion engine, rather than constant-temperature heat removal at constant atmospheric pressure, as in other types of jet engines. This workflow characteristic significantly influences seemingly obvious patterns, or at least requires substantiation.

For example, all air jet engine types have an appropriate inlet device that brakes the oncoming airflow, but ramjet and turbojet engines are not engines with a periodic workflow; their operating cycle is open, closed only conditionally by the conventional process of heat removal to the environment at constant atmospheric pressure. In contrast, the pulse jet engine's operating cycle is closed, so the introduction of a new process, such as preliminary braking and air compression, must be substantiated by relevant data.

However, such data is currently unavailable. Furthermore, when describing the pulse jet engine workflow using the Humphrey cycle, well-known designs of valved pulse jet engines [24] with a side intake (Fig. 3) are often omitted. It is perfectly clear that such a design does not allow for straight air intake and pre-compression as flight speed increases. However, the most important fact is that all researchers, without exception, consider only the ideal theoretical cycle of a pulse jet engine. Such a cycle, whether the Lenoir or Humphrey cycle (Fig. 2), bears no relation to specific operating pulsejets constructed of metal. Accordingly, a purely theoretical representation of the workflow, without its connection to real objects and their processes, as well as attempts to use theoretical assumptions without verification and to link them to a specific object of study, do not allow us to identify real operating principles for subsequent practical application.

Fig. 3. McDonnell XPJ40-MD-2 valved pulse jet engine with side air entry (McDonnell TD2D Katydid air target [24])

Therefore, there is every reason to believe that insufficient research into the processes involved has led to uncertainty, or even a contradiction, regarding the actual operating thermodynamic cycle of a heat engine known for over 80 years – namely, the pulse jet engine. It is also unclear which of the known thermodynamic cycles is more efficient in a pulse jet engine, and how to practically implement either cycle in a real product. These questions are quite important, as they may be fundamental both to the correct evaluation of the efficiency of existing pulse jet engine designs and to the development of potential new designs for this type of engine.

In light of the identified contradictions and problems, this work aims to determine the actual operating cycle of a pulse jet engine. To achieve this goal, the following tasks must be resolved:

1) Perform a theoretical analysis of known thermodynamic cycles of a pulse jet engine.

2) Consider the possibility of using software tools to simulate the pulse jet engine cycle.

3) Obtain calculation equations for determining the polytropic exponent in the pulsejet thermodynamic cycle.

4) Simulate the pulse jet engine's workflow, calculate the polytropic exponent, and determine the actual thermodynamic cycle of the pulse jet engine.

5) Compare the obtained thermodynamic cycles of pulsejets of different designs and identify the general effect of flight speed on their workflow.

3. Research materials and methods

3.1. Real operating cycle of pulse jet engine: preliminary notices

At first, a valved pulse jet engine operating under static conditions, that is, at zero airspeed, has been considered. Next, analyze the operating cycle of such an engine, taking into account that, as reported in various sources [19, 31, 36], it corresponds to the Lenoir cycle. We begin with the differences between ideal and real thermodynamic cycles.

In the handbook on internal combustion engine (ICE) theory [10], the relationship between cylinder pressure and its volume in a piston engine, or equivalently, piston position, is commonly referred to as an indicator diagram. This relationship was historically determined using a special indicator device, hence the name of the diagram. Characteristically, an indicator diagram in a piston engine is a graphical representation of the real operating cycle of the internal combustion engine, used to analyze engine efficiency, as opposed to the theoretical (ideal) Otto, Diesel, Atkinson, and Miller cycles, which are typically needed primarily to understand the operating principles of internal combustion engines.

In other words, an indicator diagram is a graphical representation of the change in pressure and volume of gases inside the cylinder during internal combustion engine operation under real conditions. It captures all the features of the real operating cycle, including gas exchange processes, heat loss and combustion imperfections and incompleteness. Obviously, such diagram can be made not only experimentally, on a real engine, but also simulated using an engine computer model through numerical experiments. Thus, the ICE indicator diagram precisely corresponds to the actual operating cycle of a specific engine, from which it was measured experimentally or simulated.

Unlike the ICE, no real operating cycle of a pulse jet engine has been considered to date. Numerous studies only consider theoretical (ideal) Lenoir and/or Humphrey cycles, which are unsuitable for analyzing real engine operation. On the other hand, when analyzing the operating cycle of jet engines with a steady flow of the working fluid [42], it is customary to determine which points correspond to which cross-section of the engine's flow path. This approach to a pulse jet engine yields only the ideal thermodynamic cycle diagram (Fig. 2).

The real operating cycle diagram cannot be constructed in this way; its construction requires certain assumptions, including volumetric combustion (heat release) and a uniform distribution of instantaneous gas parameters throughout the combustion chamber. The key feature of interpreting the real operating cycle of a pulse jet engine is that it lacks a cylinder with a moving piston, and the combustion chamber volume, conventionally defined, remains constant during engine operation. This means that a complete analogy with an ICE is not possible in this case. However, consider the piston analogy or "liquid piston" method [15, 16] adopted when describing gas flow in a resonance tube, the gas volume in a pulse jet engine, limited by the “liquid” piston in the tube, also changes over the cycle time due to gas periodic expulsion. This is generally consistent with the process of an ICE with piston movement in the cylinder.

In ICE theory, it is common to represent the real operating cycle (indicator diagram) in $p - v$ coordinates, where $v = V/m$ is the specific volume of the cylinder, i.e., relative to the mass of gas in the cylinder. This value is the reciprocal of the current (instantaneous) density ρ of the gas in the cylinder, i.e.:

$$v = \frac{V}{m} = \frac{1}{\rho}$$

The same can be achieved in a pulse jet engine. Furthermore, in an ICE, the mass of the gas in the cylinder remains constant during the compression and power strokes, but changes during intake and exhaust (gas exchange). In a pulse jet engine, by contrast, with a constant combustion chamber volume, the mass changes, and the gas exchange process is generally little different from that in an ICE.

In essence, this means that the movement of a hypothetical “liquid” piston in the exhaust tube of a pulse jet engine can be represented by analogy with the movement of a metal piston in an ICE cylinder. In this case, it becomes quite acceptable and reasonable to refer to the real operating cycle diagram of a pulse jet engine as an indicator diagram, as is the case with an ICE. This is indeed important for practice, as it highlights the fundamental difference between the real operating cycle of a pulse jet engine discussed in this paper and the previously widely known ideal theoretical cycle. This name, indicator diagram, for the real operating cycle of a pulse jet engine is proposed in this paper and used below.

3.2. Theoretical analysis of possible thermodynamic cycles of a pulse jet engine

Thus, it is known that the following assumptions are typically made in studies of ideal (reversible) thermodynamic engine cycles [34]:

1) The working fluid is an ideal gas.

2) The mass of the working fluid is constant and the same throughout all processes.

3) Compression and expansion processes are assumed to be adiabatic.

4) Heat is supplied to the working fluid by heat transfer from a hot source.

5) Gas exchange processes are replaced by a reversible process of heat removal from the working fluid to a cold source.

Since such an idealized representation of the workflow is far from reality, it can yield significant errors when used to identify the characteristics of a real engine. For example, assuming a constant mass of the working fluid, an adiabatic expansion process with extremely hot walls, and neglecting the gas exchange processes that determine the filling of the combustion chamber – such crude assumptions make the results of theoretical analysis more than questionable for practical application. It follows that reliable data on the engine's workflow, especially with a periodic one, can only be obtained through the analysis of real cycles. This is confirmed by the experience of theoretical analysis of the operating process of another type of engine with a periodic workflow – internal combustion engines [24].

Indeed, the actual cycle of a pulse jet engine differs significantly from the ideal one, and one of the main differences is that instead of a constant heat removal process at constant atmospheric pressure and a constant mass of the working fluid, the actual cycle involves a process of gas exchange with a variable mass of incoming and outgoing gas. It is also known that during this period, the pressure in the combustion chamber of a pulse jet engine is not constant and does not equal atmospheric pressure, but rather drops significantly to 0.60–0.65 atmospheric [21]. Moreover, in the actual process, one should not expect ideal heat release at constant volume, nor an ideal subsequent adiabatic expansion. All this suggests that the expected indicator diagram of the real cycle (Fig. 4a) will also differ significantly from the ideal one (Fig. 2a). Under such conditions, the polytropic indices of individual processes depicted on the indicator diagram can be particularly important for understanding the operating cycle. To determine patterns of polytropic index change, all possible thermodynamic processes can be represented as functions of their direction (Fig. 4b), with a distinction made between positive (yellow) and negative (blue) polytropic exponent values. Based on these values, the limiting values of the polytropic index can be shown on the real indicator diagram (Fig. 3a).

Thus, approximately halfway through the gas exchange process, the polytropic index increases from –∞ and passes through n = 0, which corresponds to isobaric heat removal (cooling). However, it will continue to increase and, at the beginning of the heat-addition phase, reach +∞. Obviously, during heat addition, a discontinuity in the value of n will occur, since this phase of the process begins at +∞ and ends at –∞, with a transition (discontinuity) from +∞ to –∞. Thereafter, n will gradually increase to approximately the adiabatic expansion exponent γ = 1.4, from where it will gradually increase to +∞, with the new cycle beginning with a discontinuity and again at –∞.

An approximate picture of the change in the polytropic index during a circular walk through the indicator diagram of Fig. 4a is shown in Fig. 5a as a function of time. The cycle is taken to start at the time of intake (gas exchange) at point 3. For comparison, Fig. 5b shows a similar dependence, but for the ideal cycle depicted in Fig. 2a. The vertical line in the middle of the heat addition process indicates a conditional discontinuity associated with the change in sign of the polytropic index from +∞ to –∞ between the end of the isobaric heat removal process with n = 0 and the beginning of the adiabatic expansion with n = γ. The discontinuities in the polytropic index values do not always lend themselves to a precise physical explanation, but in this task, they should be considered and used as transition points between processes.

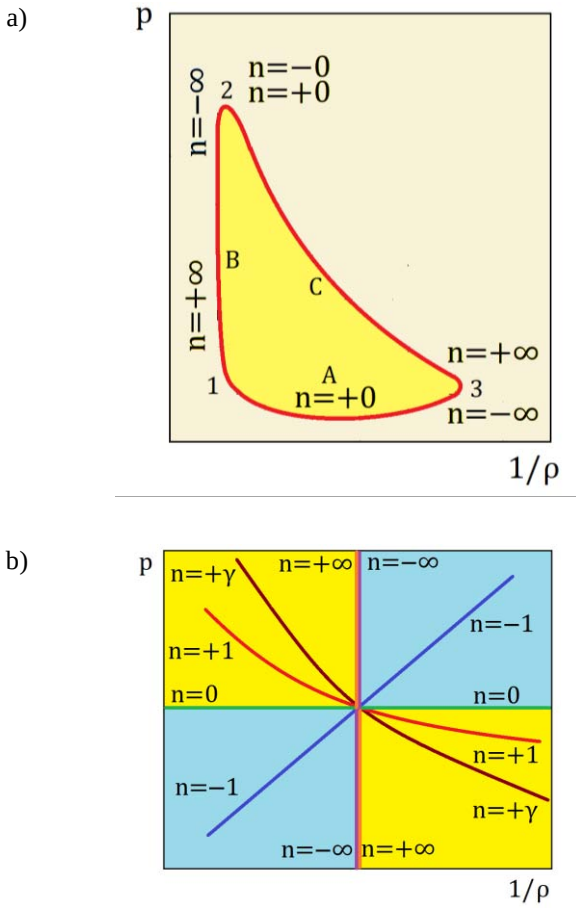

Fig. 4. Changes in the polytropic index in thermodynamic cycles: a – in a hypothetical real operating cycle of a pulse jet engine, constructed based on a theoretical logical analysis of the engine's workflow (the specific volume, the inverse of the gas density, is used instead of volume V); b – ranges of values of the polytropic index of the processes (the field of positive values is shown in yellow, the field of negative values in blue)

Overall, one can note the qualitative agreement between the diagrams of the polytropic index change for the expected real and ideal cycles – despite significant simplifications, the difference in the nature of the n dependence in the ideal cycle (Fig. 5b) and the real cycle (Fig. 5a) is not as great as one might expect.

Similar calculations could be made by assuming that the thermodynamic cycle of a pulse jet engine is a Humphrey cycle. It can then be assumed that at the beginning of the curve's rise, immediately before heat input at constant volume, a section D of polytropic air compression (Fig. 6a) may appear. In this case, a characteristic step will appear in the diagram of the change in the polytropic index (Fig. 6b), corresponding to the transition from the gas-exchange pro-

cess A (3–1) through the preliminary compression D (1–4) to the isochoric heat input B (2–3).

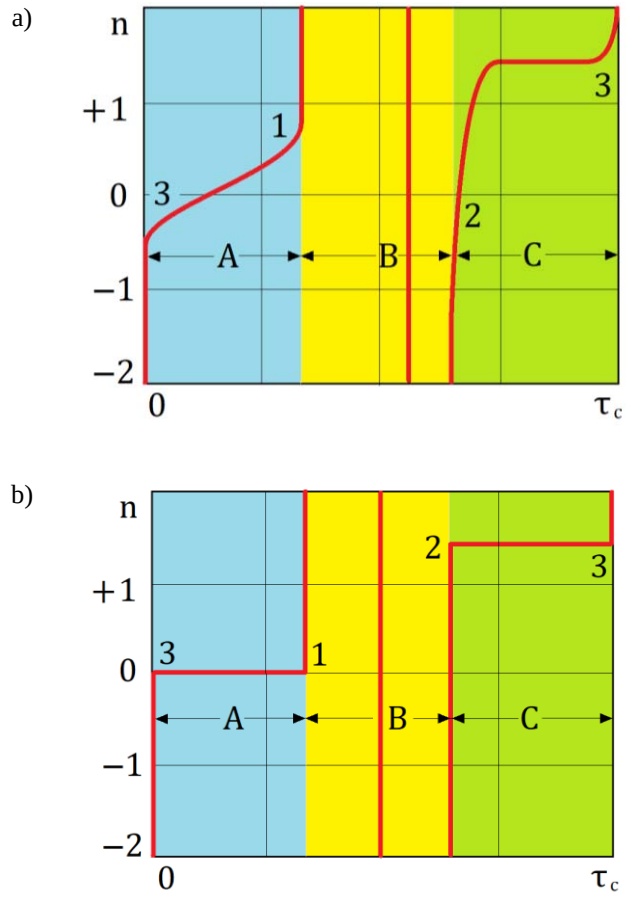

Fig. 5. Change in the polytropic index over time in the operating cycle of a pulse jet engine corresponding to the Lenoir cycle (according to Fig. 2a): a – real cycle (expected change); b – ideal cycle; A – gas exchange (air intake) at constant pressure; B – combustion at constant volume; C – polytropic expansion (exhaust)

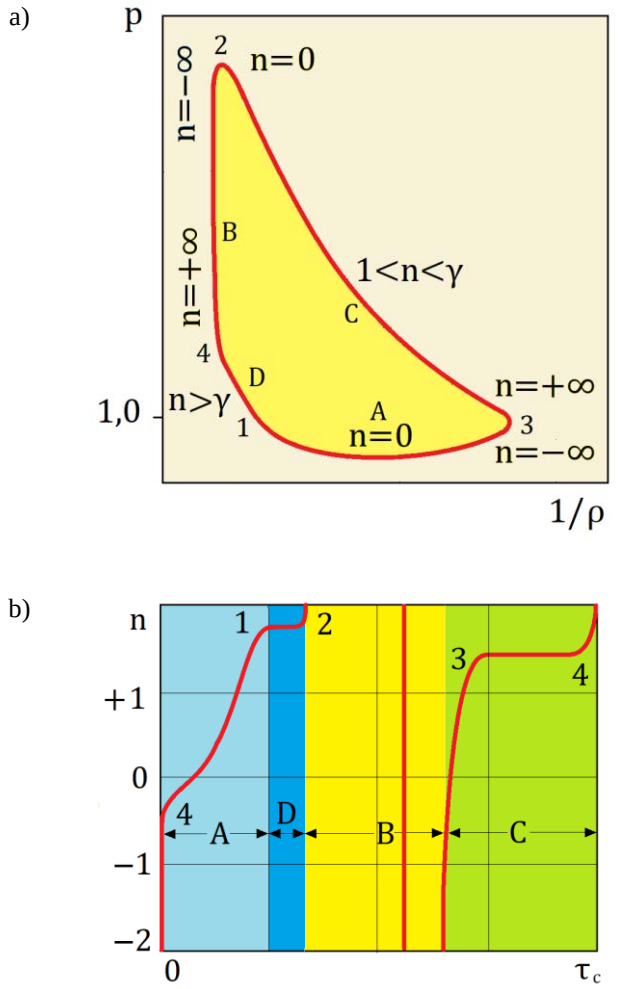

Fig. 6. Representation of the pulse jet engine operating cycle as a thermodynamic Humphrey cycle (according to Fig. 2b): a – hypothetical real cycle; b – hypothetical change in the polytropic index in the real cycle; A – gas exchange (air intake); D – preliminary polytropic compression; B – combustion; C – polytropic expansion (exhaust)

This step should be considered an indication of preliminary compression in the pulsejet working cycle, as shown by a comparison of the nature of the change in the polytropic index for both cycles (Fig. 5b and Fig. 6a). In fact, for the Lenoir cycle (Fig. 5a), there is only a smooth transition of the polytropic index during gas exchange through 0 from –∞ to +∞, while for the Humphrey cycle, after passing through 0, a step must still appear that characterizes the polytropic air compression (braking).

Despite its logical consistency, the theoretical construction of the real operating cycle (Fig. 4–6) may prove erroneous, especially when attempting to accurately depict the aforementioned air deceleration in the inlet device at high flight speeds. Therefore, it is necessary to verify and confirm preliminary assumptions about the actual nature of processes in the real operating cycle.

This can be accomplished by constructing an indicator diagram (and the dependence of the polytropic index change in the cycle) based on modeling the pulse jet engine workflow using the Pulsejet-Sim program [18, 31].

3.3. Using Pulsejet-Sim software for modeling pulse jet engine operating cycle

The Pulsejet-Sim software is based on a thermodynamic model of volumetric combustion of a fuel-air mixture in a combustion chamber and the "piston analogy" model for gas flow in a resonance tube [15]. The program specifies the engine's geometric dimensions and the UAV's flight mode, then numerically calculates changes in the instantaneous gas parameters over time for a selected number of cycles, with increments of 0.01 milliseconds (10^{-5} s).

The calculation results in diagrams of changes in instantaneous pressure and temperature in the combustion chamber, velocity in the resonance tube and intake duct, and other parameters, including an indicator diagram in "pressure-specific volume" coordinates [34]. The program also accounts for air deceleration at the inlet, taking into account total pressure losses (using the total pressure recovery coefficient σ [13]), enabling the comparison of engine operating modes at various flight speeds.

In general, the Pulsejet-Sim program replicates the methods of thermodynamic modeling of instantaneous gas parameters in the cylinder of an internal combustion engine

[17, 25], with the difference that in a pulse jet engine, the combustion chamber volume, unlike in an internal combustion engine cylinder, remains constant [31]. However, both engines share a key property: their workflow is periodic rather than steady-state, making it possible to apply research methods used in internal combustion engines to pulse jet engines.

Thus, by using the program to obtain diagrams of changes in instantaneous gas parameters in the chamber, it becomes possible to calculate the instantaneous value of the polytropic index of the process occurring in the combustion chamber at a given moment.

3.4. Derivation of calculation equations for determining the polytropic index in a pulsejet thermodynamic cycle

To derive the calculation relationships, considered the process of changing gas parameters in the pulsejet combustion chamber. According to the definition of a polytropic process for an ideal gas [34]:

$$pv^n = const \tag{1}$$

where p is the gas pressure; $v = V/m = 1/\rho$ is the gas specific volume; m, V, ρ are the gas mass, volume, and density, respectively.

Let's rewrite equation (1) as:

$$p = \rho^n const \tag{2}$$

Let's assume that the polytropic process occurs between the adjacent time points 1 and 2 in the thermodynamic cycle (the Pulsejet-Sim program calculates 1000 time points during the pulsejet working cycle [18], which yields a very short time interval between time points). Then the following relation holds:

$$\frac{p_2}{p_1} = \left(\frac{\rho_2}{\rho_1}\right)^n \tag{3}$$

Hence, the polytropic index of the process between these points is:

$$n = \frac{\ln\left(\frac{p_2}{p_1}\right)}{\ln\left(\frac{\rho_2}{\rho_1}\right)} \tag{4}$$

From the equation of state of an ideal gas, its density is related to pressure p and temperature T:

$$p = \rho RT \tag{5}$$

where R is the gas constant.

Then equation (4) can be rewritten as:

$$n = \frac{\ln\left(\frac{p_2}{p_1}\right)}{\ln\left(\frac{p_2}{p_1}\frac{T_1}{T_2}\right)} = \frac{\ln\left(\frac{p_2}{p_1}\right)}{\ln\left(\frac{p_2}{p_1}\right) - \ln\left(\frac{T_2}{T_1}\right)} \tag{6}$$

From here, the polytropic index is expressed in terms of the pressure and temperature in the combustion chamber:

$$n = \frac{1}{1 - \frac{\ln\left(\frac{T_2}{T_1}\right)}{\ln\left(\frac{p_2}{p_1}\right)}} \tag{7}$$

For ease of calculations directly from the resulting engine indicator diagram in "pressure-specific volume" coordinates, where the specific volumes are the inverse of the density, expression (4) can be transformed as follows:

$$n = \frac{\ln\left(\frac{p_2}{p_1}\right)}{\ln\left(\frac{\rho_2}{\rho_1}\right)} = \frac{\ln\left(\frac{p_2}{p_1}\right)}{\ln\left(\frac{1/v_2}{1/v_1}\right)} = \frac{\ln\left(\frac{p_2}{p_1}\right)}{\ln\left(\frac{v_1}{v_2}\right)}. \tag{8}$$

Formulas (7) and (8) have a specific points at the beginning of the engine calculation: when the pressures, temperatures, and gas densities in all engine sections are the same and equal to the initial (atmospheric) values, the result of calculations using formula (7) may be undefined and equal to 0/(1–0/0), while using formula (8) it may simply be equal to 0/0.

To eliminate uncertainty, including random uncertainty, a safeguard was introduced into the calculation. Thus, for $p_2/p_1 = 1$, a small value was added to the logarithm in the denominator of the fraction in formula (7):

$$\ln\left(\frac{p_2}{p_1}\right) + 0.00001 \tag{9}$$

A similar technique was used for the entire denominator of formulas (7) and (8).

Thus, when calculating the closed thermodynamic cycle of a pulse jet engine, as determined by its indicator diagram, it becomes possible to obtain a diagram of the change in the instantaneous value of the polytropic exponent throughout the cycle. This diagram can be used to directly determine where and when, in the pulse jet engine cycle (if it occurs at all), the preliminary compression of air during its deceleration in the inlet device occurs, and which thermodynamic process it corresponds to.

4. Research results

The well-known Argus As 014 valved pulse jet engine [9] was selected for the calculations. Even after 80 years, it remains the only fully and comprehensively studied engine of this type [6]. Furthermore, this engine is also one of the standard engines in the Pulsejet-Sim program [18, 31].

After confirming the engine dimensions, the program simulates the start-up and calculates a specified number of cycles (10 cycles were calculated), which allows us to obtain diagrams of instantaneous gas parameters (Fig.7). These parameters are displayed in dimensionless form in the diagrams: pressure p/p_0, temperature T/T_0, gas velocity in the resonance tubev_a/a_0, air velocity at the inlet$v_e/a_0$and heat release rated$Q/dt(1/(a_0Cp_0T_0))$ where parameters with the index "0" correspond to the environment; a_0, Cp_0 are the speed of sound and the heat capacity of the ambient air at constant pressure.

In addition to the diagrams of instantaneous parameters, the program also plots the pulse jet engine's indicator diagram in the "dimensionless pressure – dimensionless specific volume" coordinates for the last specified calculation cycle. To verify the assertion that, at non-zero flight speeds, the thermodynamic cycle of a valved pulse jet engine smoothly transforms from the Lenoir cycle to the Humphrey cycle, similar indicator diagram calculations were also performed for a speed of 800 km/h (Fig. 8). The indicator

diagram data then allows one to directly plot a diagram of the polytropic index change in the pulsejet operating cycle (Fig. 9), using formula (8) for different flight speeds.

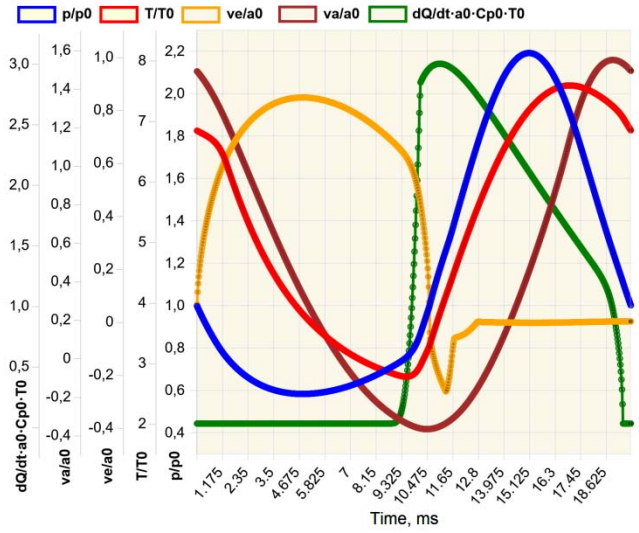

Fig. 7. Diagrams of instantaneous dimensionless parameters: pressure, temperature, inlet velocity, resonance tube velocity, and heat release rate, which were obtained using the Pulsejet-Sim program [31] for the classic Argus As 014 pulse jet engine during operation at zero flight speed $v_f = 0$

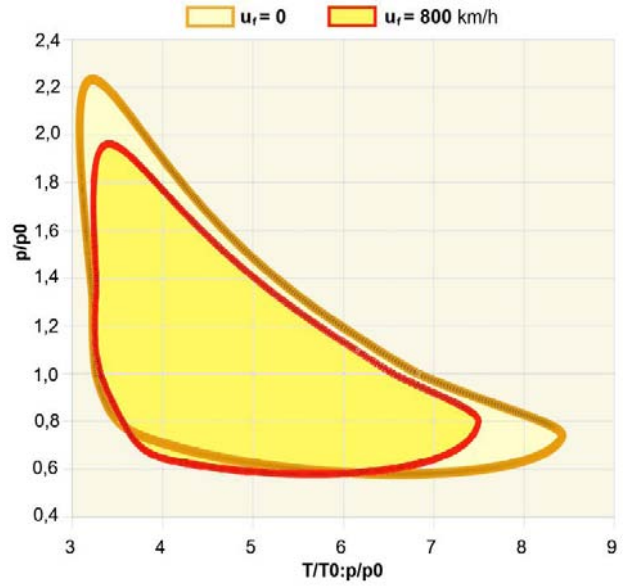

Fig. 8. Indicator diagram (the real operating cycle) of the valved pulse jet engine, obtained using the Pulsejet-Sim program [31] for the Argus As 014 engine during operation at speeds of $u_f = 0$ and $u_f = 800$ km/h

To explain and synchronize the processes, diagrams (from bottom to top) of the heat release rate, inlet air velocity, and combustion chamber temperature and pressure are shown above the diagram of the process's polytropic exponent change. The vertical lines sequentially show four characteristic moments in time (Fig. 9): 1 – the start of combustion (heat release), 2 – reaching the maximum heat release rate, 3 – the end of the intake phase (change in the pressure drop across the valves from positive to negative), and 4 – closing of the valve system petals (end of backflow from the chamber).

In addition, the obtained diagrams of the change in the polytropic index (Fig. 9) conventionally indicate the phases of the pulse jet engine operating cycle, including gas exchange (intake) shown in blue, heat supply during combustion in yellow, and expansion in green.

To ensure a complete study, a simulation of the Argus As 014 engine with a side air inlet was also performed. Fig. 10 presents the operating cycle simulation and calculation results for instantaneous parameter changes, including the indicator diagram and the polytropic index of the process for this engine design at the same flight speed of 800 km/h.

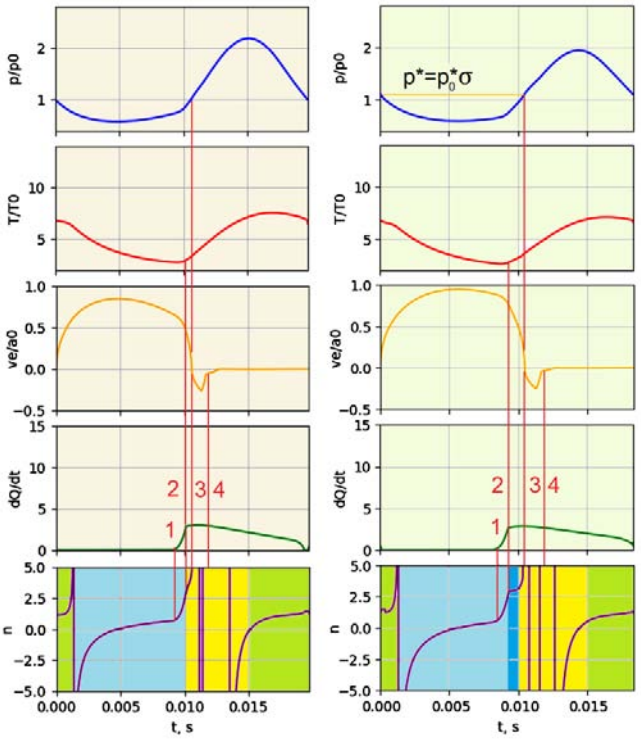

a) b)

Fig. 9. Calculated change in instantaneous parameters of the Argus As 014 pulse jet engine with parameter synchronization over time in the operating cycle shown in Fig. 7 and 8 (from top to bottom): pressure, temperature, inlet air velocity, heat release rate, polytropic index; a – at zero flight speed $u_f = 0$; b – at flight speed of $u_f = 800$ km/h

5. Discussion and results analysis

From the obtained results, it follows that the calculated indicator diagram (Fig. 8) for static conditions closely matches the diagram constructed solely based on theoretical inferences (Fig. 4a). A fairly close match is also observed between the diagram of the change in polytropic index (Fig. 9a) and the diagram shown in Fig. 4a. This confirms the fact that the thermodynamic cycle of a valved pulse jet engine during stationary operation is a Lenoir cycle. At the same time, as shown in the comparison of the diagrams for a straight intake engine at 0 and 800 km/h (Fig. 9), increasing airspeed and inlet dynamic pressure produce noticeable changes in the indicator diagram.

First, the significant increase in airflow (Fig. 9b) is understandable for a straight intake design with an open downstream resonance tube. However, this design degrades combustion chamber performance at higher airspeeds, as the amplitudes of pressure and temperature fluctuations

a)

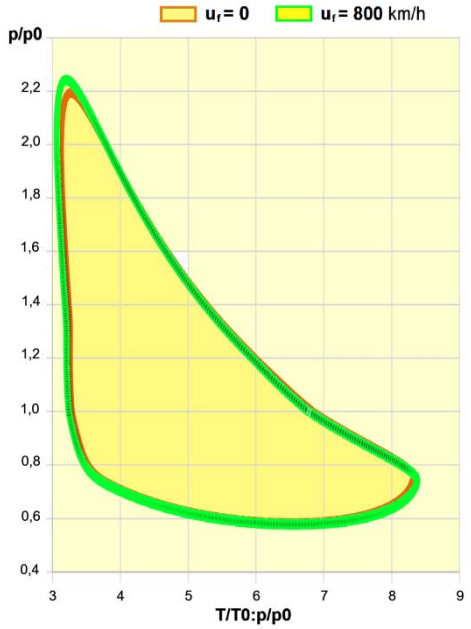

b)

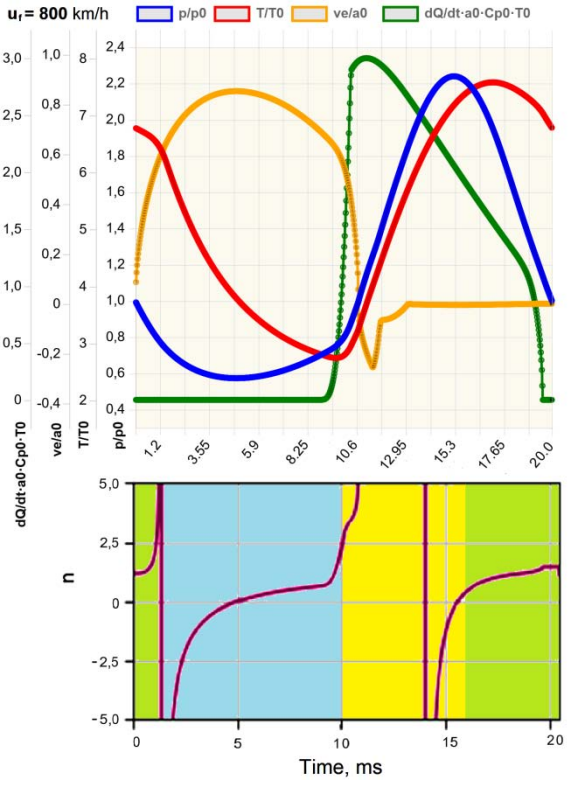

Fig. 10. Results of modeling the workflow of Argus As 014 valved pulse jet engine with a side air intake: a – indicator diagram at flight speeds of 0 and 800 km/h; b – change in instantaneous parameters (top) and polytropic index over cycle time at flight speed of 800 km/h

decrease. This is clearly visible in the indicator diagram (Fig. 8), where, as airspeed increases, a drop in maximum pressure along the vertical axis is accompanied by a proportional drop in maximum specific volume along the horizontal axis, which is proportional to temperature. It's also significant that, as flight speed increases, the air pressure at the engine inlet rises due to the dynamic head (accounting for the total pressure loss). As a result, in the upper diagram at 800 km/h (Fig. 9c), the intake phase begins and ends at a pressure above atmospheric, although below the total free-stream pressure.

The second major difference observed in the indicator diagram of the valved pulse jet engine with a straight air intake at 800 km/h (Fig. 8) is a characteristic slope in the lower-left corner, absent from the indicator diagram for engine operation at zero flight speed. This slope corresponds to a "shelf" in the polytropic index curve at the very beginning of the heat release process (Fig. 9b), which is also absent at zero speed (Fig. 9a).

Let's examine this slope in more detail. As shown in Fig. 9b, at the end of the gas exchange (intake) process, the polytropic index stabilizes for some time at $n > 2.5$, which is significantly higher than in the adiabatic process with $n = \gamma$. In other words, this is a polytropic pre-compression process, but with a significant energy loss.

Such losses are understandable. Really, in a valved engine, significant hydraulic losses should be expected as air flows through the petal valve grid. Furthermore, the Pulsejet-Sim program calculates instantaneous pressure and temperature values in the combustion chamber, accounting for heat losses from all outer engine walls, including the resonance tube [18]. Accordingly, heat losses from the combustion chamber during the air inlet process are significant, as indicated by the increased polytropic index. It follows that, as flight speed increases, the actual operating cycle of a valved pulsejet with a straight air intake corresponds to the Humphrey cycle, not the Lenoir cycle.

However, the validity of this statement for all valved pulsejets should be verified. Thus, in a valved pulse jet engine with a side air intake, as follows from the diagrams (Fig. 10), the inlet pressure does not increase with increasing flight speed. Accordingly, unlike a straight intake engine (Fig. 8 and 9), a preliminary air deceleration (compression) section does not occur in a side-entry engine. As a result, the indicator diagram changes only slightly with increasing speed (Fig. 10a). This is confirmed by the appearance of the diagram of the change in the polytropic index for the such engine workflow (Fig. 10b), as well as by its comparison with the diagram of the change in the polytropic index for an engine operating at zero flight speed (Fig. 9a) – in both cases, no air deceleration section is observed.

Therefore, a valved pulse jet engine with a side air intake, unlike a straight intake engine, continues to operate in accordance with the Lenoir thermodynamic cycle even at high flight speeds. However, the results of the study confirm that, at least within the investigated range of parameters and operating conditions, the thermodynamic cycle of a valved pulse jet engine can be represented as a Humphrey cycle, which in special cases, at zero flight speed and/or with a side air intake, does not have polytropic pre-compression before the heat supply and corresponds to the Lenoir cycle.

Significantly, a comparison of the pulsejet cycles of different designs (Fig.8 and 10a) at zero flight speed and high-speed flight indicates a clear advantage of the side-intake engine operating on the Lenoir cycle over the classic straight intake pulse jet engine operating on the Humphrey

cycle. At least, the cycle work, estimated by the area under the indicator diagram curve, at high flight speed, is significantly higher for the side-inlet engine operating on the Lenoir cycle. However, due to limitations in the parameter ranges and operating modes considered, as well as the assumptions and errors of the methods used, the results obtained are preliminary and require further study, verification, and justification (or refutation).

6. Conclusions

A preliminary theoretical analysis of possible thermodynamic cycles of a pulse jet engine revealed that two types of thermodynamic cycles – the Lenoir cycle and the Humphrey cycle can correspond to the workflow of this type of engine. At the same time, a significant difference between the theoretical ideal cycle of a pulse-jet engine and its actual operating cycle is noted. The characteristics of the real operating cycle and the similarity of its processes to those of internal combustion engines suggest that it can be called the indicator diagram of a pulse jet engine.

To clarify the type of thermodynamic cycle of a pulse jet engine, equations for calculating the polytropic index based on instantaneous values of gas parameters in the combustion chamber, were derived. The classic Argus As 014 valved pulse jet engine workflow was simulated using the Pulsejet-Sim program at both static condition and at a flight speed of 800 km/h.

The workflow simulation results show that the actual thermodynamic cycle of a valved pulse jet engine in static condition is the Lenoir cycle. However, in a straight intake engine, the shape of the indicator diagram changes with increasing flight speed, developing a characteristic slope absent at zero flight speed. At the same time, the polytropic index curve before the onset of heat release exhibits a brief stabilization at $n > 2.5$, which is significantly higher than in an adiabatic process with $n = \gamma$ and corresponds to a polytropic pre-compression process. This process pattern indicates significant hydraulic and heat losses from the combustion chamber during the air intake process, but confirms that the real thermodynamic cycle of a straight intake valved pulse jet engine at high flight speed corresponds to the Humphrey cycle, not the Lenoir cycle.

Unlike a straight intake engine, in a side-intake valved pulse jet engine, pre-compression of the air does not occur as flight speed increases, and the indicator diagram changes only slightly. As a result, the valved pulse jet engine with a side air intake operates according to the Lenoir thermodynamic cycle across the entire flight speed range.

The study results confirm that, at least within the studied range of parameters and operating conditions, the thermodynamic cycle of a valved pulse jet engine can be represented as a Humphrey cycle. However, in specific cases, such as at zero flight speed and/or with a side air intake, polytropic pre-compression before heat release is absent, and the real operating cycle corresponds to the Lenoir cycle.

Despite the apparent higher efficiency of the Humphrey cycle compared to the Lenoir cycle, due to the design features of the valved pulse jet engine, organizing the workflow at high flight speeds in accordance with the Lenoir cycle (side air intake) may offer advantages in key parameters over the Humphrey cycle (straight air intake). However, this issue requires further research and substantiation.

Bibliography

[1] Anand V, Jodele J, Zakh A, Geller A, Prisell E, Lyrsell O et al. Revisiting the Argus pulsejet engine of V-1 buzz bombs: an experimental investigation of the first mass-produced pressure gain combustion device. Exp Therm Fluid Sci. 2019;109:109910. https://doi.org/10.1016/j.expthermflusci.2019.109910

[2] Austin R. Unmanned Aircraft Systems. UAVs design, development and deployment. Chichester: John Wiley & Sons Ltd 2010.

[3] Beneigh T et. al. Introduction to unmanned aircraft systems. Barnhart RK, Hottman SB, Marshall DM, Shappee E (eds). Boca Raton: CRC Press, Taylor & Francis Group 2012.

[4] Cupiał K, Tutak W, Jamrozik A, Kociszewski A. The accuracy of modeling of the thermal cycle of a compression ignition engine. Combustion Engines. 2011;144(1):37-48.

[5] Dhananiya Lakshmi Sri M, L. Oblisamy L, Mari Prabu G. Combustion of acetylene and its performance in valveless pulse jet engine. International Journal of Engineering Research & Technology. 2016;5(06):135-141. https://doi.org/10.17577/IJERTV5IS060226

[6] Diedrich G. The aero-resonator power plant of the V-l flying bomb. Project SQUID. New Jersey: Princeton 1948. https://apps.dtic.mil/sti/pdfs/ADA800231.pdf

[7] El-Sayed AF. Fundamentals of aircraft and rocket propulsion. London: Springer-Verlag 2016.

[8] Gieras M, Trzeciak AM. New aspects of the pulse combustion process. Energies. 2024;17(6):1427. https://doi.org/10.3390/en17061427

[9] Gosslau F. Development of the V-1 pulse jet. A history of German guided missiles development. Benecke T, Quick AW (eds). First Guided Missiles Seminar. Munich Germany, April 1956. Brunswick. 1957:400-418.

[10] Heywood JB. Internal combustion engine fundamentals. 2nd ed. New York: McGraw-Hill Education 2018.

[11] Home-made Jet Forum. 2025. https://www.pulse-jets.com/phpbb3/index.php

[12] Humphrey cycle. Wikipedia. 2025. https://en.wikipedia.org/wiki/Humphrey_cycle

[13] Kazula S, Wöllner M, Grasselt D, Höschler K. Ideal geometries and potential benefit of variable pitot inlets for subsonic and supersonic business aviation. 8th European Conference for Aeronautics and Space Sciences (EUCASS). 2019: 15. https://doi.org/10.13009/EUCASS2019-314

[14] Khalatov AA, Nemchin AF, Kobzar SG, Kuzmin AV, Borisov II. Pulse detonation engines: current state and results of studies. Part 1: current state. Khalatov AA (ed.). Dnipro LIRA 2024.

[15] Khrulev A. Determination of gas parameters in resonant pipes and channels of engines with a periodic workflow using the piston analogy method. Eastern-European Journal of Enterprise Technologies. 2023;5(7(125)):50-59. https://doi.org/10.15587/1729-4061.2023.288520

[16] Khrulev A, Muntyan V. Mathematical model and computer program development for online modeling of pulse jet engine working cycle, parameters and characteristics. Drone Systems and Applications. 2025;14:1-32. https://doi.org/10.1139/dsa-2025-0027

[17] Khrulev A, Saraiev O, Saraieva I, Vorobiov O. Modeling of thermodynamic processes in internal combustion engine cylinder during cranking in compression measurement tests. Combustion Engines. 2024;198(3):98-109. https://doi.org/10.19206/CE-187380
[18] Khrulev O, Muntyan V. Development of universal mathematical model and computer program for online modeling of valved and valveless pulse jet engines. Aerospace Technic and Technology. 2024;4,2(206):6-29. https://doi.org/10.32620/aktt.2025.4sup2.01
[19] Kumar S, Prasad SS, Krishna V. Design of pulse jet engine for UAV. International Journal of Engineering Research & Technology (IJERT). 2014;3(9):670-675. https://www.ijert.org/research/design-of-pulse-jet-engine-for-uav-IJERTV3IS090544.pdf
[20] Lenoir cycle. Wikipedia. 2025. https://en.wikipedia.org/wiki/Lenoir_cycle
[21] Litke P, Schauer F, Paxson D, Bradley R, Hoke J. Assessment of the performance of a pulsejet and comparison with a pulsed-detonation engine. 43rd AIAA Aerospace Sciences Meeting and Exhibit. 10-13 January 2005, Reno, Nevada. 2005:10. https://doi.org/10.2514/6.2005-228
[22] Lockwood RM. Hiller pulse reactor lift engine. Final report. Advanced research. Report NO. ARD 308. Bureau of Naval Weapons. Propulsion Dept. Contract No. 61-0226-c. Springfield: National Technical Information Service 1963. https://apps.dtic.mil/sti/tr/pdf/AD0601715.pdf
[23] Maddoxjets. The final word in pulsejets. 2025. https://maddoxjets.com
[24] McDonnell PJ40. Wikipedia. 2025. https://en.wikipedia.org/wiki/McDonnell_PJ40
[25] Medina A, Curto-Risso PL, Hernández AC, Guzmán-Vargas L, Angulo-Brown F, Sen AK. Quasi-dimensional simulation of spark ignition engines from thermodynamic optimization to cyclic variability. London: Springer-Verlag 2014.
[26] Melo ASM. Pulsejet engine performance estimation (Versão Revista Após Discussão) Universidade da Beira Interior, Engenharia. Dissertação para obtenção do Grau de Mestre em Engenharia Aeronáutica (Ciclo de estudos integrado). Covilhã: Universidade da Beira Interior 2019.
[27] Meng X, de Jong W, Kudra T. A state-of-the-art review of pulse combustion: principles, modeling, applications and R&D issues. Renew Sustain Energy Rev. 2015;42. https://doi.org/10.1016/j.rser.2015.10.110
[28] Mittal V. The novel pulse jet engine powering the Ukrainian Trembita missile. Forbes: Jan.13;2025. https://www.forbes.com/sites/vikrammittal/2025/01/13/the-novel-pulse-jet-engine-powering-the-ukrainian-trembita-missile/
[29] Newdick T. Pulsejet drone flies, could have big impact on cost of future weapons. The War Zone. Mar 6;2024. https://www.twz.com/news-features/pulsejet-drone-flies-could-have-big-impact-on-cost-of-future-weapons
[30] O'Brien JG. The pulsejet engine – a review of its development potential national technical information service. Springfield: U.S. Department of Commerce. 1974:118. https://apps.dtic.mil/sti/tr/pdf/AD0787439.pdf
[31] Pulsejet engine workflow simulation program Pulsejet-Sim. 2025. https://pulsejet-sim.com/en/
[32] Pulsejet. Wikipedia. 2025. https://en.wikipedia.org/wiki/Pulsejet
[33] Rahmatika AM, Widiyastuti W, Winardi S, Nurtono T, Machmudah S, Kusdianto Joni IM. CFD simulation of pulse combustion's performance. AIP Conference Proceedings. 2016;1712:040006. https://doi.org/10.1063/1.4941883
[34] Rajput RK. Engineering thermodynamics (for engineering students of all Indian Universities and competitive examinations). Third Edition. New Delhi: LAXMI Publications LTD 2007.
[35] Sánchez AA. Design, construction and testing of a Pulsejet engine (versão final após defesa). Dissertação para obtenção do Grau de Mestre em Engenharia Aeronáutica (2º ciclo de estudos). Covilhã: Universidade de Beira Interior 2022.
[36] Schmidt P. On the history of the development of the Schmidtrohr. A history of German guided missiles development. Benecke T, Quick AW (eds). First Guided Missiles Seminar. Munich Germany, April, 1956. Brunswick. 1957: 375-399.
[37] Shultz-Grunow F. Gas-dynamic investigations of the pulse-jet tube. Parts I and II. National Advisory Committee for Aeronautics. Technical Memorandum No. 1131. Technical High School, Aachen, Germany. Washington: NACA 1947: 112.
[38] Szymański GM, Wyrwas B, Klekowicki M, Strugarek K, Nowak M, Ludwiczak A et al. Simulation research of the feasibility of developing a multi-fuel valved pulsejet engine. Combustion Engines. 2025;201(2):91-102. https://doi.org/10.19206/CE-203139
[39] Tao Geng T, Paxson DE, Zheng F, Kuznetsov AV, Roberts WL. Comparison between numerically simulated and experimentally measured flowfield quantities behind a pulsejet. 44th Joint Propulsion Conference and Exhibit, cosponsored by AIAA, ASME, SAE, and ASEE, Hartford: Connecticut, July 21–23. 2008:13. https://ntrs.nasa.gov/api/citations/20080045534/downloads/20080045534.pdf
[40] Tegner J. Analysis of the operation of the pulsejet engine. 33rd Congress of the International Council of the Aeronautical Sciences. Stockholm, Sweden, 4-9 September. Stockholm: 2022:24. https://www.icas.org/icas_archive/ICAS2022/data/papers/ICAS2022_0120_paper.pdf
[41] Tesla pulsejet engine. Texas Tech University. Capstone Design Projects, 2023. https://www.depts.ttu.edu/me/CapstoneDesign_Projects/4-Tesla-Pulse-Jet-Engine.pdf
[42] The jet engines. Fifth ed. Birmingham: Rolls-Royce plc. 1996.
[43] Trzeciak AM, Gieras M. Temperature estimating method for exhaust gases in valveless pulsejet engine. Combustion Engines. 2020;182(3):3-9. https://doi.org/10.19206/CE-2020-301
[44] Van Heerbeek PA. Mathematical modelling of a pulse combustor of the Helmholtz-type. Delft: Delft University of Technology. 2008:146. https://homepage.tudelft.nl/d2b4e/numanal/heerbeek_afst.pdf
[45] Wave Engine Corp. 2025. https://wave-engine.com
[46] Zhang B, Song Z, Zhao F, Liu C. Overview of propulsion systems for unmanned aerial vehicles. Energies. 2022;15: 455. https://doi.org/10.3390/en15020455

Alexander E. Khrulev, DEng. – Senior Researcher, forensic auto expert, International Motor Bureau, Ukraine.
e-mail: *info@engine-expert.com*

Prof. Serhii Oleksiyovych Dmytriev, DEng.– Aircraft Continuing Airworthiness Department, National Aviation University, Ukraine.
e-mail: *sad@nau.edu.ua*

Article citation info:
Pham VC, Ngo DN, Hoang VS, Le VV. Comprehensive review of methanol and LNG as alternative fuels for marine diesel engines. Combustion Engines. 2026;206(3):210-228. https://doi.org/10.19206/CE-218596

Van Chien PHAM
Duy Nam NGO
Van Si HOANG
Van Vang LE

Combustion Engines
Polish Scientific Society of Combustion Engines

Comprehensive review of methanol and LNG as alternative fuels for marine diesel engines

ARTICLE INFO

Received: 28 November 2025
Revised: 12 February 2026
Accepted: 25 February 2026
Available online: 7 April 2026

The maritime sector is undergoing a critical transition driven by increasingly stringent emissions regulations from the International Maritime Organization (IMO) and the European Commission (EC). Among the leading alternative fuels for marine diesel engines, methanol and liquefied natural gas (LNG) have gained significant attention. This review synthesizes recent research and industry data to compare the two fuels across physico-chemical properties, combustion performance, emission behavior, safety, and economic feasibility. Methanol, a liquid under ambient conditions, enables easier storage and refueling using existing liquid-fuel infrastructure while providing substantial reductions in sulfur oxides (SO_x), nitrogen oxides (NO_x), and particulate matter (PM) emissions. However, its low energy density and the formation of formaldehyde remain drawbacks. In contrast, LNG offers higher volumetric energy density and immediate reductions in carbon dioxide (CO_2), SO_x, and NO_x emissions but requires expensive cryogenic storage systems and faces the persistent challenge of methane slip. Economically, LNG engines entail higher capital investment yet support short-term regulatory compliance, whereas renewable methanol offers a scalable pathway toward long-term carbon neutrality. Overall, the optimal choice between methanol and LNG depends on operational profiles and strategic objectives, with LNG serving as a transitional solution and methanol representing a flexible, future-proof option for sustainable marine propulsion.

Key words: *methanol, liquefied natural gas, alternative fuels, marine diesel engines, decarbonization*

This is an open access article under the CC BY license (http://creativecommons.org/licenses/by/4.0/)

1. Introduction

The global maritime industry stands at an important juncture. As international trade volumes continue to expand, the sector faces growing scrutiny over its environmental footprint. Shipping is responsible for approximately 3% of global anthropogenic CO_2 emissions and contributes a substantial share of global NO_x (≈ 15%) and SO_x (≈ 4–9%) emissions [38, 53, 96, 141]. These pollutants are now recognized as major contributors to both climate change and regional air quality degradation, driving international policy reform. The IMO and the EC have therefore introduced increasingly stringent measures to decarbonize maritime transport, including the IMO's 2023 Greenhouse Gas (GHG) Strategy, the Carbon Intensity Indicator (CII) framework, and the extension of the European Union (EU) Emissions Trading System (ETS) to the shipping sector [4, 17, 31, 33, 136, 182]. The IMO's 2023 GHG Strategy for shipping sets an ambition for the sector to reduce carbon intensity by at least 40% by 2030 (vs 2008) and to achieve net-zero greenhouse-gas emissions by or around 2050. Meanwhile, the EU's FuelEU Maritime Regulation (Regulation (EU) 2023/1805) mandates the use of renewable and low-carbon fuels on board ships calling at EU ports from 1 January 2025 [30, 31, 33, 44, 110].

Conventional marine fuels such as heavy fuel oil (HFO) and marine diesel oil (MDO) have long dominated the sector due to their low cost and established infrastructure, but they have been increasingly criticized for their contribution to air pollution and climate change [20, 115, 159]. The combustion of these fuels releases high levels of SO_x, NO_x, CO_2, and particulate matter (PM), leading to both local air-quality degradation and global warming impacts [45, 71, 134, 150]. Consequently, identifying and adopting alternative marine fuels that can ensure energy security, regulatory compliance, and long-term sustainability has become a strategic priority across the maritime industry [20, 27, 51].

A broad spectrum of alternative energy carriers has been proposed, including hydrogen, ammonia, biofuels, LNG, and methanol, as well as emerging options such as synthetic (e-)fuels and hybrid-electric systems [20, 123, 179]. Each pathway offers unique advantages and challenges in terms of energy density, handling safety, storage requirements, infrastructure availability, and overall lifecycle emissions [94, 166]. However, among these options, LNG and methanol have emerged as the most technically mature and commercially deployable alternatives for near- and medium-term adoption in the maritime sector [121, 179].

While hydrogen and ammonia offer significant decarbonization potential, their storage complexities, toxicity risks, and limited infrastructure pose major barriers to large-scale deployment in the current decade [103, 155, 156]. Similarly, biofuels face challenges of feedstock sustainability, cost volatility, and an uncertain lifecycle emissions-reduction potential [20, 80, 107]. In contrast, LNG and methanol occupy a pragmatic middle ground – they are compatible with current engine technology and logistics, can be produced from both fossil and renewable sources, and are supported by established industrial supply chains. Their comparative readiness makes them strong candidates for transitional and early-adopter decarbonization strategies under the IMO's 2030 and 2050 frameworks [20, 94, 123, 179].

However, despite growing deployment, the two fuels embody fundamentally different decarbonization philosophies. LNG offers an incremental, bridge-fuel approach, providing immediate reductions in SO_x, NO_x, and PM, albeit con-

strained by methane slip and upstream leakage [8, 10, 56, 69, 154]. Methanol, conversely, presents a transformational long-term solution, capable of achieving near-zero life-cycle emissions when produced from renewable hydrogen and captured CO_2 ("green" methanol) [5, 20, 40, 105].

The literature contains numerous studies addressing either LNG or methanol independently. However, a unified comparative review that synthesizes the latest data on performance, lifecycle emissions, safety, infrastructure, and economics, particularly for dual-fuel (DF) marine diesel engines, remains limited. This paper addresses that gap by providing a comprehensive, integrative analysis of both fuels, combining recent findings from peer-reviewed literature, life-cycle assessments (LCAs), and industry data. It aims to clarify the relative advantages, trade-offs, and strategic implications of choosing between LNG and methanol as alternative fuels for diesel engines, and to identify key research needs for supporting the maritime sector's ongoing transition toward carbon neutrality.

2. Methodology

2.1. Search strategy and information sources

This review followed the Preferred Reporting Items for Systematic Reviews and Meta-Analyses (PRISMA 2020) guidelines. Literature searches were conducted on 15 September 2025 across three major databases: Scopus, Web of Science Core Collection, and ScienceDirect. The search covered the period from January 2010 to September 2025 and was limited to English-language, peer-reviewed journal papers.

Exact search strings:

Scopus:

TITLE-ABS-KEY(("methanol" OR "liquefied natural gas" OR LNG) AND ("marine fuel" OR "ship" OR "diesel engine" OR "dual-fuel") AND ("emission" OR "performance" OR "life cycle" OR "LCA" OR "well-to-wake"))

Web of Science:

TS=(("methanol" OR "liquefied natural gas" OR LNG) AND ("marine fuel" OR "shipping" OR "dual-fuel engine") AND ("emission" OR "LCA" OR "life-cycle" OR "efficiency"))

ScienceDirect:

"methanol" OR "LNG" AND ("marine fuel" OR "dual-fuel engine") AND ("emission" OR "LCA" OR "performance") in Title, Abstract, Keywords.

Manual searches of Energy Conversion and Management, Fuel, Journal of Marine Engineering & Technology, Journal of Marine Science and Engineering, and Applied Energy were also performed to capture in-press or early-view articles. Reference lists of key papers were hand-checked to identify additional studies.

2.2. Eligibility criteria (PICO framework)

The review used the PICO framework to identify publications. In which:

- Population (P): Marine diesel or DF engines and ship propulsion systems
- Intervention (I): Operation using methanol or liquefied natural gas (LNG) as an alternative or DF
- Comparison (C): Conventional marine diesel oil (MDO), and heavy fuel oil (HFO)
- Outcomes (O): Engine performance (BTE, power output), regulated and unregulated emissions, well-to-wake (WtW) greenhouse-gas emissions, techno-economic metrics, and safety or infrastructure aspects.

Only peer-reviewed original research and review articles providing experimental, numerical, or life-cycle-based data were included. Exclusion criteria comprised: (a) conference abstracts without full text, (b) non-English papers, (c) studies lacking clear methodology or quantitative results, (d) conceptual opinion papers, and (e) non-marine or unrelated power applications.

2.3. Screening and selection protocol

All retrieved records (n = 523) were imported into EndNote X21 for de-duplication, leaving n = 412 unique records. Two independent reviewers screened titles and abstracts. Disagreements were resolved by discussion with a third reviewer. During title and abstract screening, 288 records were excluded for the following reasons: out of scope (n = 156), non-English language (n = 42), conference abstracts without full text (n = 47), and studies lacking quantitative engine or LCA data (n = 43). After initial screening, 124 full-text papers were evaluated for eligibility. Finally, 48 studies were included in the qualitative synthesis, and 36 in the quantitative comparison. The PRISMA 2020 flow diagram summarizing identification, screening, eligibility, and inclusion is shown in Fig. 1.

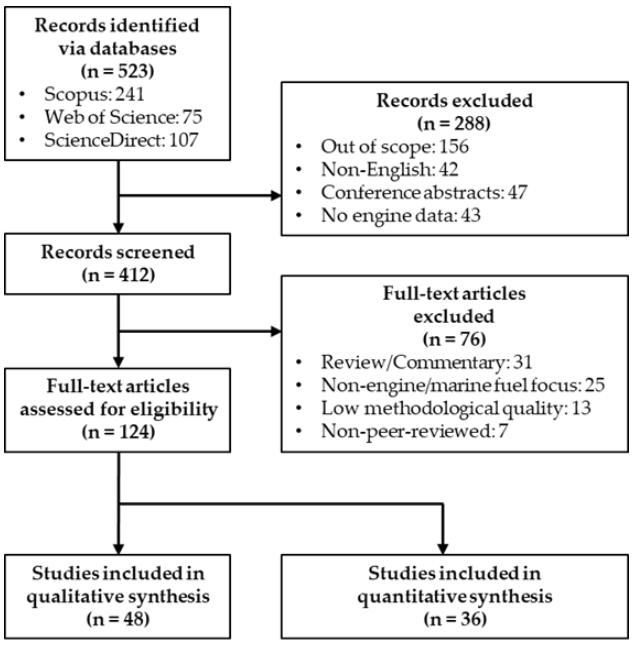

Fig. 1. PRISMA 2020 flow diagram

2.4. Quality evaluation and data extraction

Each included study underwent methodological quality assessment using the Critical Appraisal Skills Program (CASP) checklist for quantitative studies, complemented by ROBINS-I for risk-of-bias evaluation where applicable. Scores were assigned on a 10-point scale; papers scoring < 6 were excluded from quantitative synthesis but discussed qualitatively.

Key variables extracted included: fuel type and properties, engine configuration and operating conditions, emis-

sion metrics (CO_2, CH_4, NO_x, SO_x, PM, aldehydes), LCA boundary assumptions, and techno-economic indicators (CAPEX, retrofit cost, fuel price). Extraction was performed independently by two reviewers using standardized forms to ensure consistency.

3. Fuel properties and characteristics

3.1. Properties of methanol (CH_3OH)

Methanol is a colorless, volatile liquid with a faintly sweet, alcohol-like odor and is completely miscible with water [158]. One of its most notable characteristics is its low energy density. By weight, it has an energy density of approximately 22 MJ/kg, and by volume, this figure is only 15.7 MJ/L [128, 187]. This means that methanol has a significantly lower energy density than both diesel and LNG.

In terms of combustion properties, methanol has a very low cetane number (below 5) and a high octane number (109), making it unsuitable for direct use in conventional compression-ignition engines (CIEs). Another property to note is that methanol burns with a faint, nearly invisible blue flame that produces no smoke or soot [158, 187].

3.2. Properties of LNG

LNG is natural gas, primarily methane (CH_4), that has been cooled to an extremely low temperature of approximately −162°C to convert it to a liquid. This process reduces its volume to about $1/600^{th}$ of its gaseous state. In its liquid state, LNG is colorless, odorless, non-corrosive, and non-toxic [82, 130, 151].

LNG has a higher energy density than methanol, with a volumetric density of 23.4 MJ/L. By weight, it has an energy density of 53.6-55 MJ/kg [185]. A critical parameter for LNG is the Methane Number (MN). This parameter indicates a fuel's resistance to knocking in an engine; a higher MN value (above 80) indicates better fuel quality and optimized engine performance. The MN is highly dependent on the composition of the LNG. In which "heavy LNG" (with a higher content of ethane and propane) has a lower MN than "light LNG" (with a higher methane content) [84].

3.3. Synthesis of fuel characteristics

A fundamental difference between these two fuels lies in the trade-off between volumetric energy density and handling complexity. As mentioned, methanol has a lower energy density than both LNG and diesel [117, 132]. This directly results in the need for larger storage tanks to achieve the same operating range. However, methanol is a liquid at ambient temperature and pressure, allowing it to be handled and stored similarly to conventional fuels, though with safety and corrosion considerations [68].

Conversely, LNG's higher energy density is tied to its cryogenic state. This requires specialized, highly insulated storage systems that are more complex and expensive. LNG's higher energy density, an advantage, is offset by the complexity of cryogenic storage, a major disadvantage. Meanwhile, methanol's low energy density, a disadvantage, is offset by its simple physical state, a major advantage. This is not just a list of facts but a fundamental, causal trade-off that affects design, cost, and logistics [6, 52, 165]. A comparison of the physical and chemical properties of methanol and LNG is presented in Table 1.

Table 1. Comparison of methanol and LNG physical and chemical properties

Property	Methanol (CH_3OH)	LNG (Primarily CH_4)
Physical state	Liquid (at ambient temp. & pressure) [173]	Cryogenic Liquid (at approx. −162°C) [101, 130]
Energy density (MJ/L)	15.7 [158, 187]	23.4 [185]
Energy density (MJ/kg)	22 [158, 187]	53.6–55 [185]
Cetane number	< 5 [158, 187]	N/A (requires methane number) [84]
Octane number	109 [158, 187]	> 120 [13]
Flash point	12°C [108]	−188°C (volatile) [148]
Flame characteristics	Invisible, blue flame [108]	Visible when burning [133]

4. Engine technology and performance

4.1. Methanol DF engine systems

Methanol has a very low cetane number, which means it cannot self-ignite in a traditional diesel compression-ignition cycle [59, 178]. Therefore, its combustion requires a catalyst, most commonly a small amount of diesel fuel in a pilot injection system [39].

DF technologies, such as High-Pressure Direct Injection (HPDI), work by injecting a small amount of diesel to initiate combustion, which raises the temperature and pressure inside the cylinder, followed by the injection of methanol into the combusting mixture [90, 118, 137, 161-164, 175, 186]. Other injection strategies have been proposed and tested to optimize performance and reduce knocking, including injecting methanol before or after the diesel injection, or even in a split-injection mode [97].

Existing engine conversion solutions are available from major manufacturers such as Wärtsilä and Everllence (formerly MAN B&W). These conversions require the addition of new components and double-walled piping systems to ensure safety [39]. Real-world projects have demonstrated the successful conversion of small tugboats and large container vessels to run on methanol [32].

4.2. LNG DF engine systems

LNG can be used in two main types of engines: Low-Pressure Dual-Fuel (LPDF, Otto-cycle premixed combustion) engines and High-Pressure Dual-Fuel (HPDF, based on high-pressure direct injection – HPDI) [18, 79, 127, 131]. HPDF, often referred to as the Diesel-cycle engines, is becoming increasingly popular in heavy-duty applications. Similar to methanol, the HPDI system utilizes a small amount of diesel (approximately 5% of the total fuel volume) as a "liquid spark plug" to initiate combustion [18, 79, 127, 129, 131].

However, converting a diesel engine to run on LNG often requires a "complete overhaul" [13, 34, 109, 114]. This involves fundamental mechanical changes, such as modifying pistons to lower the compression ratio and installing spark plugs, modifying injection systems, adding a gas supply, and installing safety systems, particularly for Otto cycle engines [13, 18, 34, 79, 109, 114, 131]. The system also requires a high-pressure cryogenic pump to convert low-pressure liquid LNG into a high-pressure gas ready for injection [72, 79]. Table 2 summarizes the key technical

and strategic differences between methanol- and LNG-fueled marine engine systems.

Table 2. Conceptual comparison of methanol and LNG dual-fuel marine engine systems

Aspect	Methanol D) engine	LNG DF engine
Fuel Physical State	Liquid at ambient temperature and pressure	Cryogenic liquid (approx. −162°C)
Onboard Storage	Non-pressurized tanks; conventional liquid-fuel storage with material compatibility measures	Cryogenic Type C insulated tanks; vacuum insulation; boil-off management
Fuel Supply System	Low-pressure liquid fuel supply; double-walled piping; leak detection systems	Cryogenic pumps, vaporizers, high-pressure gas lines; insulated piping
Injection Strategy	Diesel pilot injection + direct methanol injection	Diesel pilot injection + high-pressure gas injection (HPDF) or low-pressure premixed injection (LPDF)
Combustion Mode	Compression-ignition (CI)-based dual-fuel operation	HPDF: Diesel-cycle stratified combustion; LPDF: Otto-cycle premixed combustion
Engine Modification Level	Incremental retrofit; addition of fuel system and safety components	Major modification or complete overhaul (especially LPDF conversions)
Brake Thermal Efficiency (Typical Range)	approx. 40–46% (optimized high-load operation may exceed diesel baseline)	HPDF: approx. 44–46% (diesel-like); LPDF: approx. 38–44% depending on load
Tank-to-Wake Emission Characteristics	SOx: approx. 99% reduction; PM: approx. 95–99% reduction; NO_x: approx. 40–80% reduction; possible increase in aldehydes (formaldehyde)	SOx: approx. 100% reduction; PM: approx. 100% reduction; NO_x: approx. 80–90% reduction; methane slip possible
Well-to-Wake Climate Performance	Grey methanol: may exceed diesel CO_2e; Green methanol: approx. 50–70% reduction	HPDF LNG: approx. 15–23% reduction; performance sensitive to methane slip
Infrastructure Requirements	Compatible with existing liquid-fuel logistics; simpler bunkering	Requires cryogenic infrastructure; complex bunkering procedures
Safety Profile	Toxicity risk; low flash point; invisible flame; requires containment and gas detection	Cryogenic hazards; vapor cloud explosion risk; methane-air flammability (5–15%)
Strategic Decarbonization Role	Long-term pathway toward carbon neutrality via green methanol	Transitional “bridge fuel”; near-term regulatory compliance advantage

4.3. Performance and efficiency

Methanol-fueled engines can achieve high brake thermal efficiency (BTE), even outperforming the original diesel engine under certain conditions, thanks to their high octane number and high heat of vaporization. Guo et al. reported that a marine DF engine with approx. 90% methanol energy fraction, with methanol injection at approx. 80°CA (crank angle) BTDC (before top dead center) and diesel pilot at approx. 12°CA BTDC, has thermal efficiencies of about 46% at high loads, approx. 45% at medium, and approx. 43% at low loads. The study highlights that thoughtful timing and injection strategies can leverage methanol’s characteristics (e.g., heat of vaporization, etc.) to approach or exceed diesel-mode efficiency in many load cases [58]. Karvounis et al. noted that methanol’s high latent heat of vaporization reduces in-cylinder temperatures, thereby reducing heat losses and, under some conditions, improving indicated or BTE [77]. Lebedevas and Milašius reported that the marine engine cycle modeling with approx. 95% methanol injected (direct injection) alongside a diesel pilot, under optimized conditions, produced an approx. 4.2% higher thermal efficiency compared to diesel in that mode [91]. Liu et al. showed that methanol, when used in high-compression-ratio engines, has the potential to achieve high indicated efficiency. Methanol’s latent heat of vaporization is approx. 2.6 times higher than that of diesel per unit mass, which cools the intake charge and lowers the in-cylinder temperatures, which reduces heat transfer losses [99]. Pu et al. mentioned that methanol engines (including turbocharged and high-compression concepts) reach very high thermal efficiencies. The review reported a peak BTE of approx. 43% in a turbocharged engine with a compression ratio (CR) of 19.5. The authors explicitly connect such high efficiencies to operation strategies that exploit methanol’s high octane and strong charge-cooling (high latent heat) to enable advanced phasing and lean/low-temperature combustion modes [132]. Treacy et al. reported in [153] that under optimized intake temperature, injection timing and higher CR, methanol direct-injection (DI) compression-ignition (CI) operation can achieve competitive indicated/thermal efficiency. The paper emphasizes the latent heat and mixing/auto-ignition roles of methanol, as well as the need for intake preheating to stabilize combustion. This explains how high heat of vaporization cools the intake/charge air, enabling favorable combustion phasing and reduced heat losses. Karvounis et al. summarized that many bench studies have shown that methanol, when used in partial- or DI strategies, increases BTE under medium-to-high loads when injection timing, CR, and intake temperature are optimized. They review and attribute efficiency gains to methanol’s higher resistance to knock (high RON/RON-like behavior in premixed strategies) and its charge-cooling effect, which reduces combustion/heat losses [77]. A single-cylinder experimental work reported a net fuel conversion efficiency of approx. 42.5% for methanol in a high-compression research engine under stoichiometric/controlled conditions. The efficiency of methanol in this study is higher than several alternative fuels tested. The study results demonstrate practical efficiency benefits traceable to methanol’s favorable knock resistance (allowing higher compression) and its cooling during vaporization, which alters heat transfer/loss profiles [49]. An experimental and parametric study on a marine engine showed that optimized methanol injection timing and injection strategy (single-point vs multi-point) produced BTE increases up to approx.4–5% relative to diesel-only operation in certain configurations. The authors explicitly link the

BTE gains to phasing changes enabled by methanol properties (cooling during vaporization that reduces heat loss and high knock resistance) [58]. However, some studies have shown a slight decrease in engine performance (power output) with methanol blends, offset by a significant reduction in emissions. Hassan et al. showed that low-to-moderate methanol blends can reduce peak power slightly while lowering carbon monoxide (CO), unburnt hydrocarbon (uHC), and soot, and improving brake-specific fuel consumption (BSFC) at many operating points [60]. Kadhim et al. reported measurable reductions in CO, uHC, and PM with increasing methanol fraction, along with small reductions in power output at some loads [74]. Vișan et al. showed that methanol/biofuel blends can cause a few percent decrease in brake effective power relative to pure diesel while substantially reducing particulate and uHC emissions [160]. Vargün et al. reported slight reductions in peak power with methanol addition in some blends, coupled with reduced PM and CO emissions and mixed NO_x response depending on operating point [157].

Regarding LNG-fueled engines, the HPDI system in HPDF engines that injects gaseous fuel at high pressure near top dead center (TDC), producing diesel-like stratified combustion but with NG as the primary fuel. This preserves the diesel combustion phasing and in-cylinder thermodynamics that give diesel its high BTE. Recent experimental and review studies report that HPDF engines achieve thermal efficiencies similar to those of diesel engines. The HPDF concept is explicitly shown to approach diesel BTE while keeping the emissions benefits of gaseous fuels [28]. Babayev et al. reported in a numerical study that HPDF preserves diesel-like thermodynamic behavior and can achieve high thermal efficiency with appropriate injection/combustion phasing [14]. Recent review of new DF combustion modes (pre-chamber-ignited HPDF, premixed stratified, etc.) concluded that PI-HPDF and related high-pressure concepts can achieve diesel-like BTE while reducing PM and SO_x [23]. Zhang et al. reported that advancing pilot diesel injection timing increases power and thermal efficiency in a pilot-ignited NG engine, but also affects NO_x and CH_4 slip [183]. Wei et al. reported that split/high-pressure injection strategies can optimize heat release and increase BTE in NG HPDF engines while reducing methane slip [170].

Meanwhile, the LPDF and port-injection DF systems, in which gas is supplied at low pressure and premixed with intake air, result in more premixed combustion and can shift heat release earlier, sometimes increasing knock/uHC or requiring pilot diesel for ignition. The efficiency depends strongly on load and gas fraction. Several reviews and field studies show LPDF engines often have somewhat lower BTE at low loads or at high gas substitution, though at medium–high loads, efficiency can be near diesel if optimized. A comparative analysis shows that LPDF and port-injection systems are simpler but often show lower BTE at part load than HPDF [22]. Overall, HPDF tends to show the best chance of matching diesel [124, 149].

The conversion of diesel engines to LNG has many differences compared to methanol. The literature consistently describes converting diesel engines to LNG-fueled engines as a "complete overhaul", involving fundamental mechanical changes such as piston modification and the addition of spark plugs. This implies a more complex and costly process [21, 50, 73, 106, 146, 152]. In contrast, methanol conversions are described as "retrofit solutions" and the "addition of components" to the existing diesel cycle [167].

Table 3. Comparative performance and thermal efficiency of methanol- and LNG-fueled engines

Fuel	Engine configuration/ operating mode	Typical BTE [%]	Performance characteristics and key observations	References
Methanol	DF marine engine (≈90% methanol, diesel pilot)	High load: 46%; Med. load: 45%; Low load: 43%	Optimized methanol injection (~80°CA BTDC) and pilot diesel (~12°CA BTDC) achieve BTE approaching or exceeding diesel at all loads. High octane and strong charge-cooling enable efficient combustion phasing.	[58]
	DI DF marine engine (≈95% methanol, pilot diesel)	Increase 4.2% vs. diesel	Modeling shows ~4.2% higher cycle efficiency vs. diesel due to optimized combustion phasing and methanol's latent heat.	[91]
	Turbocharged methanol engine (CR ≈19.5)	approx. 43%	High compression ratio and turbocharging leverage methanol's charge-cooling and knock resistance; high efficiency under lean operation.	[132]
	High-compression research engine (stoichiometric DI)	approx. 42.5%	Methanol exhibits higher efficiency than other tested fuels due to reduced heat losses and favorable autoignition control.	[49]
	General DF/DI strategies (medium–high load)	40–46%	Methanol's high latent heat reduces in-cylinder temperatures and heat transfer losses; injection timing and CR strongly influence BTE.	[58, 77, 99, 153]
	Blended operation (methanol–diesel or methanol–biofuel)	Slightly reduced power (–1–3%)	Small reduction in power output offset by improved BSFC, lower CO, uHC, and PM emissions.	[60, 74, 157, 160]
LNG (high-pressure)	HPDI (high-pressure direct injection) DF engine	44–46% (≈Diesel)	Maintains diesel-like combustion and thermodynamic cycle; high efficiency with diesel pilot ignition and late high-pressure gas injection; low PM/SOx.	[14, 23, 28, 170, 183]
	Pre-chamber or stratified HPDI concepts	43–45%	Advanced HPDI and PI-HPDI systems achieve near-diesel BTE with lower soot and improved combustion control.	[14, 23]
	HPDI with split/advanced injection	Increase 1–2% over baseline	Optimized injection strategies improve heat release, enhance BTE, and reduce CH_4 slip.	[170, 183]
LNG (low-pressure)	LPDF/port-injection DF engine	38–44%	Simpler system, lower pressure, higher substitution possible, but lower BTE at part load due to earlier heat release and incomplete combustion at high gas fractions.	[22, 124, 149]
	Complete overhaul or spark-ignited conversions	–	Requires complete mechanical overhaul (spark plugs, piston redesign). Higher complexity and cost than methanol retrofit.	[21, 50, 73, 106, 146, 152]

This suggests that an LNG conversion requires a fundamental shift in the engine's operating principle (from compression-ignition to spark-ignition), whereas a methanol conversion is an incremental modification to the existing diesel combustion process [35, 39, 83, 184]. This difference has direct implications for the capital cost, downtime, and technical complexity of a conversion project. A comparative performance and thermal efficiency of methanol- and LNG-fueled engines is presented in Table 3.

5. Environmental and emission profile

5.1. Tank-to-wake emissions

Methanol combustion is extremely clean. It significantly reduces SO_x emissions by up to 99%, NO_x by up to 60%, and PM by up to 95% compared to conventional fuels [9, 111]. Parris et al. also reported in [123] that methanol dramatically reduces SO_x (up to approx. 99%) and PM (up to approx. 95%), while NO_x is reduced by up to approx. 80% compared to HFOs. Methanol Institute reported the same tendency [66]. Aakko-Saksa et al. stated that methanol and LNG yield near-complete elimination of SO_x and large reductions in PM compared to HFO/MDO, and provide comparative ranges for NO_x benefits [2]. IMO reported in GreenVoyage2050 that methanol can achieve approx. 92–99% SO_x reduction, approx. 55% NO_x reduction (lifecycle average), and very large PM reductions when replacing HFO/MDO [64].

Multiple experimental and numerical studies reported that methanol combustion tends to produce higher levels of unregulated aldehydes (notably formaldehyde) and other partial-oxidation products than conventional hydrocarbon fuels [169, 171]. Methanol oxidation proceeds through partial-oxidation intermediates ($CH_3OH \rightarrow HCHO \rightarrow HCOOH \rightarrow CO/CO_2$). Under engine conditions, especially in quench zones, crevices, or regions with short residence time / low local temperature, oxidation can stop at formaldehyde, which is less oxidized and can be emitted. Crevice/quenching and incomplete mixing effects (and certain low-temperature or lean-combustion modes) increase the fraction of formaldehyde escaping the cylinder [102]. Williams et al. reported that formaldehyde is the dominant aldehyde emitted from methanol combustion and that HCHO emissions are substantially higher when methanol (or methanol blends) are used compared with gasoline [172]. Ma et al. reported in [102] that formaldehyde forms in crevice/quench regions and can be emitted. Chao et al. showed that adding methanol to diesel can increase formaldehyde emissions by up to 4.5 times at low engine loads [26]. A summary of the emission-reduction effectiveness of methanol and LNG compared with conventional marine fuels is presented in Tables 4 and 5, respectively.

Regarding LNG, multiple studies and real-world measurements show that LNG combustion can reduce SO_2 and PM emissions by nearly 100% relative to MDO and yield NO_x reductions of 80–90% [2, 62, 100, 116]. Aakko-Saksa et al. reported that LNG-fueled ships have demonstrated nearly complete elimination of SO_x and PM emissions and approx. 90% reduction in NO_x compared to conventional marine fuel oil engines [2]. Lebedevas et al. stated that switching from diesel to LNG fuel resulted in the reduction of SO_2 by approx. 91% and NO_x by 65%, while CO_2 decreased by about 23% [92]. Anderson et al. reported that LNG operation resulted in near elimination of sulfur and particulate emissions and an approx. 85–90% reduction in NO_x relative to HFO [10].

Table 4. Summary of methanol's emission reduction effectiveness in comparison to conventional marine fuels (HFO/MDO)

Pollutant	Max/typical reductions	References
SO_x	approx. 92–99%	[64, 66]
PM	approx. 90–99%	[48, 66]
NO_x	approx. 40–60%	[2, 64]

Table 5. Summary of LNG's emission reduction effectiveness in comparison to conventional marine fuels

Researchers	NO_x reduction	SO_x reduction	PM reduction	References
Livaniou et al.	83.7%	approx. 100%	approx. 100%	[100]
Aakko-Saksa et al.	approx. 90%	approx. 100%	approx. 100%	[2]
Lebedevas et al.	65%	91%	—	[92]
Anderson et al.	85–90%	approx. 100%	approx. 100%	[10]
Heikkilä et al.	88%	99%	97%	[62]

5.2. Well-to-wake emissions

While both methanol and LNG are cleaner than diesel, they each pose unique challenges regarding non-CO_2 emissions. For methanol, it is the increase in unregulated aldehyde emissions [26, 102, 169, 171, 172]. For LNG, it is "methane slip", the leakage of unburned methane from the engine exhaust. Of these, methane slip is the more concerning issue.

Methane is a potent GHG, with a Global Warming Potential (GWP) of up to 28–36 times that of CO_2 over a 100-year timescale (GWP_{100} = 28–36) [16, 78]. Methane slip is increasingly recognized as a major challenge for realizing the climate benefits of LNG in marine propulsion [12, 61, 70, 85-89, 139, 154, 176, 181]. Methane slip is particularly concerning for LPDF engines and at low engine loads (e.g., in port or during maneuvering). Multiple onboard studies reported that methane slip rises sharply at low engine loads. Engine load monitoring on a RoPax vessel with an LPDF engine measured a yearly average fuel-slip coefficient of approx. 1.57% [142]. The primary causes identified are incomplete combustion due to low-pressure injection or poor mixing, quenching or crevice-volume losses, and low temperatures [95]. Mitigation strategies under study include catalytic aftertreatment, design optimizations (reduced crevices, improved injection pressure), and operational measures such as minimizing low-load operation [12, 139, 176, 181]. Unregulated aldehyde and methane slip create a direct trade-off: the choice between a powerful but short-lived GHG (methane) and a pollutant with harmful health effects (formaldehyde). This decision is a choice between global environmental impact and local air pollution.

Another critical difference lies in the decarbonization pathway. Based on analysis from several sources, fossil LNG (often called “grey LNG”) provides an immediate and significant GHG emissions reduction on a WtW basis, up to 23% compared to conventional fossil fuels, especially with high-pressure engines [69, 125]. LNG is widely recognized

as a transitional marine fuel capable of delivering measurable WtW GHG reductions compared with conventional marine fuels. The magnitude of this benefit depends strongly on engine technology, operational conditions, and upstream methane management. LCAs have demonstrated that low-speed, high-pressure DF (HPDF) engines, which operate on the Diesel cycle and exhibit minimal methane slip, offer the most substantial WtW GHG reductions, typically in the range of 15–23% relative to very-low-sulfur fuel oil (VLSFO) or MDO [3, 69, 143]. In contrast, LPDF engines can offset these gains through higher unburned methane emissions [3, 125]. The comprehensive industry LCA by Sphera and SEA-LNG [143] reported up to 23% WtW reduction for LNG in HPDF configurations, a finding broadly supported by independent peer-reviewed studies [3, 69]. However, the potential advantage is sensitive to methane slip and upstream leakage, as emphasized by the International Council on Clean Transportation (ICCT) [125], underscoring that the overall climate performance of LNG as a marine fuel hinges on both engine design and methane management across the supply chain.

In contrast, fossil methanol (often called "grey" or "brown" methanol) has a worse WtW CO_2 footprint than diesel, meaning it is not a viable long-term decarbonization solution on its own. Multiple recent LCAs and reviews showed that methanol made from fossil feedstocks (NG or coal) often has higher WtW CO_2e emissions than conventional MDO, because methanol production (steam methane reforming, gas-to-methanol, or coal-to-methanol) is energy-intensive and emits CO_2s upstream; when these upstream emissions are included in a WtW accounting, "grey/brown" methanol can exceed diesel's CO_2e footprint unless low-carbon electricity, carbon capture, or renewable feedstocks are used [56, 93, 126, 140, 180]. Fossil methanol production requires conversion of carbon feedstock to synthesis gas and then to methanol; these steps consume heat and generate CO_2 (and fugitive methane in upstream stages), so that well-to-tank (WtT) emissions are high and may outweigh any modest combustion-phase benefits, producing WtW CO_2e greater than diesel for certain production routes and assumptions [93, 126, 140, 180].

However, "blue" and "green" methanol offer dramatically improved climate performance compared to fossil methanol, provided production is powered by low-carbon energy and/or paired with carbon capture. LCAs show that "green" methanol (bio- or electro-methanol) can reduce WtW GWP_{100} emissions by approximately 50-70% relative to conventional diesel under favorable conditions (e.g., imported "green" methanol offers approx. 66% reduction; local "green" methanol offers approx. 57% reduction) [7, 166]. "Blue" methanol, industrial methanol with upstream CO_2 capture (or using renewable CO_2), delivers moderate improvements over "grey" methanol and diesel, but performance depends heavily on capture rate, feedstock supply, and upstream emissions; in some cases "blue" methanol still falls short of the reductions achievable by "green" methanol [166]. Hence, while "blue" methanol can serve as a transitional pathway, only "green" methanol constitutes a viable long-term decarbonization solution for marine propulsion, assuming scale-up of renewable hydrogen or sustainable biomass use [120].

Although biomethane (bio-LNG) and synthetic methane (e-LNG) can be produced and used as low-carbon marine fuels, multiple techno-economic and life-cycle studies concluded that there is no direct "green-LNG" pathway that is as practical and scalable as "green" methanol. Green (e or bio) methanol benefits from higher synthesis efficiency, a mature synthesis industry, and more favorable economics and scaling potential (power-to-methanol), whereas power-to-methane followed by liquefaction suffers larger conversion losses, higher costs, and greater constraints on sustainable biomass availability for biomethane. Hence, e-/bio-LNG remains less favorable in most near-term decarbonization scenarios [29, 37, 46, 55, 76]. This distinction points to a strategic trade-off. The choice between the two fuels is between immediate benefits (LNG) and a long-term, deep-decarbonization potential that requires a leap of faith in the development of the green supply chain (methanol).

5.3. Emission reduction effectiveness of methanol and LNG compared to conventional marine fuels

Methanol and LNG both demonstrate substantial emission reduction potential compared to conventional marine fuels (HFO and MDO). On a tank-to-wake (TtW) basis, methanol offers nearly complete elimination of SO_x emissions (~ 99%) and significant reductions in PM (~ 95%) and NO_x (~ 55–80%), owing to its sulfur-free composition and oxygenated nature, which promote more complete combustion [2, 9, 64, 66, 111, 123]. However, methanol combustion tends to form unregulated aldehydes (particularly formaldehyde) through partial oxidation pathways ($CH_3OH \rightarrow HCHO \rightarrow HCOOH \rightarrow CO/CO_2$), especially under low-temperature or quench-zone conditions [26, 102, 169, 171, 172]. LNG, in contrast, also yields near-total elimination of SO_x and PM emissions and achieves 80–90% reductions in NO_x due to its clean-burning characteristics and high hydrogen-to-carbon ratio [2, 10, 62, 92, 100, 116].

On a WtW basis, fossil LNG ("grey" LNG) offers an immediate and measurable GHG reduction potential of up to approx. 23% relative to conventional fuels, particularly in HPDF Diesel-cycle engines with minimal methane slip [3, 69, 124, 143]. However, methane slip from LPDF engines, especially under low load conditions, can partially or completely offset these gains [12, 61, 70, 85-89, 95, 139, 142, 154, 176, 181]. Fossil methanol ("grey" or "brown" methanol) generally exhibits a higher WtW CO_2e than diesel, mainly due to the CO_2-intensive upstream reforming and synthesis processes [56, 93, 126, 140, 180]. Conversely, "blue" methanol (fossil-based methanol with carbon capture) and "green" methanol (bio- or electro-methanol from renewable sources) offer substantial WtW emission reductions—approx. 50–70% lower than diesel, depending on feedstock and energy source [7, 120, 166]. In contrast, bio-LNG and e-LNG pathways exist but remain less favorable due to higher conversion losses and costs, with limited scalability compared to methanol-based alternatives [29, 37, 46, 55, 76]. The comparative emission profile of methanol and LNG is presented in Table 6.

Table 6. Comparative emission profile of methanol and LNG

Fuel	Emission category	Reduction vs. HFO/MDO	Key characteristics	Main challenges	References
Methanol (TtW)	SO_x	approx. 99% reduction	Sulfur-free fuel	—	[2, 9, 64, 66, 111, 123]
	NO_x	approx. 55–80% reduction	Lower combustion temperature, oxygenated molecule	A slightly lower flame temperature may affect performance	
	PM	approx. 95–99% reduction	Clean, oxygenated combustion	—	
	Unregulated aldehydes	Increase (Formaldehyde dominant)	Partial oxidation intermediates (HCHO, HCOOH)	Local air toxicity, health risk	[26, 102, 169, 171, 172]
LNG (TtW)	SO_x	approx. 100% reduction	No sulfur content	—	[2, 10, 62, 92, 100, 116]
	NO_x	approx. 80–90% reduction	Lean premixed combustion	Engine-type dependent	
	PM	approx. 100% reduction	No heavy hydrocarbons	—	
LNG (WtW)	CO_2e	approx. 15–23% reduction (HPDF engines)	High efficiency, lower carbon ratio	Methane slip (up to 1–2%)	[3, 12, 61, 69, 70, 85-88, 95, 124, 139, 142, 143, 154, 176, 181]
Methanol (WtW)	CO_2e	Grey/Brown: more than Diesel (increase)	Fossil feedstock (coal/natural gas)	High upstream CO_2	[56, 93, 126, 140, 180]
	CO_2e	Blue: Moderate reduction	Fossil methanol + CO_2 capture	Capture efficiency critical	[7, 120, 166]
	CO_2e	Green: approx. 50–70% reduction	Renewable H_2 + CO_2 captured from air/biogenic	Cost and scalability	
e-/bio-LNG	CO_2e	Potential Moderate reduction, but less than “green” methanol	Renewable methane synthesis	High cost, low efficiency	[29, 37, 46, 55, 76]

5.4. Limitations and uncertainty

Despite extensive literature coverage and methodological harmonization, several limitations and uncertainties should be acknowledged when interpreting the comparative findings of methanol and LNG as alternative marine fuels.

First, LCA heterogeneity remains a key challenge. Published WtW studies differ substantially in their system boundaries, allocation methods, and upstream process emission factors. Some include full supply-chain emissions from extraction to combustion, whereas others limit the scope to WtT or TtW phases. These methodological inconsistencies introduce uncertainty of up to ±20–30% in the reported WtW GHG reduction potential.

Second, methane slip variability significantly affects the real-world climate performance of LNG-fueled engines. Reported slip rates range from below 0.2% for HPDF engines to over 3% for LPDF engines, depending on engine type, operating load, and maintenance conditions. Even small deviations in slip rates can negate much of LNG’s nominal CO_2 advantage over diesel on a GWP_{100} basis, particularly under low-load or maneuvering operation.

Third, there is considerable uncertainty surrounding the scalability and supply chain maturity of green methanol. Current global production capacity for electro- and bio-methanol is limited, and its cost remains several times higher than that of fossil methanol or LNG. The climate benefits of green methanol are strongly dependent on the carbon intensity of the hydrogen source and the capture efficiency of the CO_2 feedstock. Supply-chain emissions associated with renewable electricity generation and CO_2 transport also introduce variability across case studies.

Finally, data transparency and measurement gaps, particularly the lack of consistent onboard monitoring of methane emissions and aldehyde formation, limit the ability to validate modeled or laboratory results under operational conditions. In addition, the dynamic regulatory landscape (e.g., updates to IMO GHG strategy and FuelEU Maritime) adds uncertainty to long-term economic projections and compliance costs.

Future research should prioritize:

1. Standardized WtW methodologies for marine fuels that harmonize functional units, GWP metrics, and boundary definitions.
2. Continuous onboard monitoring of methane slip and unregulated emissions to build real-world datasets for model validation.
3. Techno-economic optimization studies evaluating the integration of carbon capture and renewable hydrogen for scalable green methanol pathways.
4. Cross-sectoral LCA databases with transparent data sharing to reduce duplication and improve comparability across studies.

Together, these actions would enhance the robustness of future assessments and support evidence-based decision-making in the maritime decarbonization transition.

6. Infrastructure, storage, and safety

6.1. Onboard storage and space requirements

Methanol has a volumetric energy density of approx. 15.7 MJ/L versus approx. 36.6 MJ/L for MDO. Therefore, on an equal-energy basis, methanol requires roughly 2.2–2.5 times of the tank volume of MDO to achieve the same range [65, 66, 104]. Because methanol is a liquid at ambient temperature and pressure, it can be stored in simple, non-pressurized tanks and handled with conventional liquid-fuel systems (with material compatibility and gas detection precautions), and several retrofit studies and pilot projects have demonstrated that existing ballast tanks can be repurposed as methanol fuel tanks (subject to coatings, cofferdams and safety segregation) when performing a conversion [36, 66, 123].

LNG fuel storage generally requires significantly more volume than MDO to achieve the same operational range.

The difference arises primarily from LNG's lower volumetric energy density (approx. 22 MJ/L) compared with MDO (approx. 36.6 MJ/L). Peer-reviewed analyses indicated that the net LNG fuel volume required to supply equivalent energy is typically about 1.6–2.0 times that of MDO [63, 122, 135]. However, when system-level factors, such as cryogenic insulation, structural supports, and safety spacing, are considered, the effective installed volume of LNG tanks can reach 2.5–4.0 times that of MDO tanks. This higher space requirement results from the need for specialized, highly insulated cylindrical or spherical Type C containment systems that minimize boil-off and maintain cryogenic conditions [122]. Consequently, LNG fuel storage imposes additional design constraints on ship layout, increases overall weight, and can reduce available cargo capacity, particularly for retrofit installations or small vessels [63, 135]. In summary, while the intrinsic physical energy properties of LNG dictate roughly double the fuel volume requirement, practical marine engineering considerations amplify this to an overall onboard space penalty of approx. 3-4 times that of MDO.

6.2. Bunkering Infrastructure

Methanol bunkering is operationally simpler and less capital-intensive than LNG bunkering. As a liquid at ambient temperature and pressure, methanol can be handled, stored, and transported using conventional chemical-industry infrastructure, allowing existing tankage and pipelines to be adapted with minor modifications [81, 123, 168]. Bunkering can be performed via truck-to-ship (TtS) or ship-to-ship (StS) operations without cryogenic or high-pressure systems, leading to shorter transfer times, typically reported as up to 50% faster than LNG operations in industry practice [66, 123]. Comparative techno-economic analyses confirmed that methanol infrastructure investment and handling costs are significantly lower than those for LNG, largely due to the absence of specialized insulation, vapor recovery systems, and safety clearances required for cryogenic fuels [123, 179]. Furthermore, methanol distribution benefits from mature global supply chains, with storage facilities already available at over 100–125 major ports worldwide according to the Methanol Institute, a figure reported and cited in peer-reviewed assessments of port readiness [81, 168]. This extensive infrastructure base, combined with simplified logistics and lower capital costs, underpins methanol's growing attractiveness as a near-term marine fuel alternative to LNG.

Unlike methanol, LNG bunkering is a complex and capital-intensive process due to its cryogenic nature and the stringent safety requirements involved. LNG must be stored at approx. −162°C, necessitating double-walled, vacuum-insulated storage systems and specialized transfer pipelines [20, 177]. The bunkering process involves multiple safety zones, inert gas purging, and boil-off gas management, all of which contribute to longer bunkering times and higher operational costs compared to conventional liquid fuels [15, 20]. Typical LNG bunkering operations take roughly twice as long as those for methanol or MDO and require extensive crew training and emergency procedures to mitigate cryogenic and flammability hazards [177]. Infrastructure availability also remains limited. As of 2024, LNG bunkering is supported at approx. 200 ports worldwide, far fewer than the more than 125 ports capable of handling methanol [15, 177]. Consequently, while LNG provides substantial emission benefits, its high infrastructure cost, operational complexity, and logistical constraints hinder rapid deployment compared to methanol, which leverages existing liquid fuel handling systems and port facilities.

In conclusion, methanol and LNG differ substantially in terms of bunkering logistics, infrastructure requirements, and operational complexity. Methanol, being a liquid at ambient temperature and pressure, can be handled using conventional fuel storage and transfer systems, allowing for easy integration into existing port infrastructure. Methanol bunkering is considered to be relatively simple, less expensive, and can typically be completed in about half the time required for LNG refueling. Moreover, methanol benefits from a well-established global logistics network, with storage and handling facilities already available at more than 125 of the world's largest ports. Its compatibility with existing liquid-fuel supply chains allows for retrofitting of conventional bunkering terminals with minimal modifications.

In contrast, LNG bunkering presents more stringent technical and safety challenges. LNG must be stored at cryogenic conditions of approx. −162°C, requiring double-walled, vacuum-insulated tanks and specialized transfer systems equipped with boil-off gas management and inert gas purging. These design and operational constraints significantly increase both the capital cost and complexity of LNG bunkering operations. Typical LNG refueling takes roughly twice as long as that for methanol or MDO and demands strict adherence to safety protocols and crew training standards. Although LNG bunkering infrastructure has expanded rapidly, reaching roughly 200 ports worldwide by 2024, it still lags behind methanol in terms of global availability and logistical flexibility. Consequently, while LNG provides substantial emission reduction potential, its deployment is limited by the higher cost, operational complexity, and infrastructure demands associated with cryogenic fuel systems, whereas methanol's ambient liquid state and compatibility with existing infrastructure position it as a more practical near-term solution for low-carbon marine fuels.

6.3. Safety and handling

The safety profiles of methanol and LNG are fundamentally different and require distinct mitigation strategies. Methanol's hazards are primarily static, stemming from its inherent chemical properties. It is highly toxic through ingestion, inhalation, or skin absorption, exposure to as little as 30 mL can cause blindness or death, and its low flash point of approx. 12°C makes it easily flammable with an almost invisible flame under sunlight, posing significant fire risks during handling and operation [1, 68, 123]. Consequently, methanol safety management emphasizes containment integrity, double-walled fuel systems, continuous gas detection, and specialized crew training [68, 123].

In contrast, LNG's hazards are dynamic, associated with its cryogenic physical state and the risks arising from phase change. In its liquid form, LNG is neither flammable nor explosive; however, when vaporized, methane–air mixtures

within 5–15% concentration become flammable and can form large vapor clouds capable of ignition or explosion [24, 57]. Additionally, contact with cryogenic LNG can cause severe cold burns and structural embrittlement, while the rapid vaporization of a small spill may displace oxygen, leading to asphyxiation hazards. Therefore, LNG risk mitigation primarily focuses on preventing and controlling vapor releases, maintaining cryogenic containment integrity, and ensuring safe venting and insulation practices [24, 57, 119].

7. Economic viability and total cost of ownership

7.1. Capital and operating costs

The capital cost implications of adopting alternative marine fuels vary considerably between methanol and LNG. Industry and peer-reviewed studies consistently indicate that LNG-fueled new buildings require substantially higher capital expenditure (CAPEX) than conventional MDO designs, typically approx. 22–40% higher, due to the need for cryogenic tanks, double-wall piping, and complex fuel-gas handling systems. In contrast, methanol-fueled newbuilds show smaller CAPEX premiums, commonly in the range of 10–25%, because methanol can be stored at ambient temperature and pressure using simpler fuel-delivery equipment [19, 144].

For existing tonnage, retrofit costs for methanol engines are estimated at roughly €250–€650 per kW, encompassing engine conversion, fuel-supply system, and safety upgrades, with lower values expected for subsequent retrofits as experience grows [67, 174]. Comparable LNG retrofits generally demand higher investment because of cryogenic storage and gas-handling complexity. Collectively, these data illustrate that methanol offers a less capital-intensive pathway to compliance and early decarbonization than LNG, albeit with smaller immediate GHG benefits.

7.2. Fuel costs and regulatory impact

Economic and techno-environmental analyses indicate that the total cost of ownership (TCO) and lifetime fuel costs of LNG and methanol pathways depend strongly on engine technology, regulatory context, and fuel price assumptions. Peer-reviewed LCAs and cost studies show that while both fuels entail higher capital expenditure than conventional designs, their operational and compliance costs vary substantially across scenarios [54, 75, 93, 174, 179]. Kanchiralla et al. [75] and Gore et al. [54] demonstrated that the economic competitiveness of LNG and methanol is highly sensitive to carbon pricing and upstream energy intensity. Similarly, Lee et al. [93] and Zamboni et al. [179] reported that methanol's viability improves markedly under decarbonization policies such as FuelEU Maritime, while LNG remains favorable in low-carbon-price contexts due to lower near-term compliance costs. Wu et al. [174] performed a full TCO analysis and concluded that methanol DF vessels exhibit only a modest cost premium compared with conventional diesel ships when lifetime operating costs and potential carbon charges are included. Industry analyses corroborate these findings: the SEA-LNG consortium reported that the lifetime fuel cost of the LNG pathway can be approx. half that of methanol when regulatory compliance costs are considered [42], reflecting the fact that grey LNG already meets short- to mid-term GHG compliance thresholds, whereas grey methanol requires immediate blending with costly green fuels. Conversely, a DNV commercial case study found that the TCO for a methanol-fueled 5,500 TEU container vessel was only 0.4% higher than a conventional counterpart over a 25-year life cycle, emphasizing that the increased fuel-flexibility capability comes at little to no extra cost [41]. Overall, these results suggest that the modest CAPEX premium for methanol-capable designs represents a strategic investment in long-term fuel optionality, while LNG offers short-term economic advantages under current compliance regimes. The comparative economic indicators for Methanol and LNG as marine fuels are presented in Table 7.

Table 7. Comparative economic indicators for methanol and LNG as marine fuels

Parameter	Methanol	LNG	References
Newbuilding CAPEX	Increase 10% over conventional diesel vessels (typical range: increase 8–12%) due to minor engine and tank modifications.	Increase 22% over conventional diesel vessels (typical range: increase 20–25%) due to cryogenic storage systems, double-walled piping, and safety equipment.	[41, 75, 174, 179]
Retrofit Cost	Estimated €250–650 per kW depending on engine type and tank design. Retrofit usually involves add-on components (fuel system, tanks, control upgrades).	Requires near complete overhaul of fuel system and engine; cost can exceed €800–1,200 per kW.	[41, 174, 179]
Fuel Price (2024 average)	Fossil methanol approx. $500–650 / t; "green" methanol approx. $1,200–1,800 / t (price volatility high; limited supply).	Fossil LNG approx. $350–450 / t; Bio-LNG/e-LNG approx. $1,000–1,500 / t.	[42, 54, 75, 93]
Cost of Compliance (FuelEU Maritime, 2025–2040)	Requires immediate blending with "green" methanol to meet GHG targets; high short-term compliance cost but low long-term penalty once green supply scales.	Fossil LNG provides sufficient GHG reduction for compliance until approx. 2040 under FuelEU Maritime; blending not required initially.	[41, 42, 93]
Total Cost of Ownership (TCO)	approx. +0.4% higher than diesel over 25 years; flexible transition pathway to "green" methanol.	Lifetime fuel cost approx. 50% lower than methanol pathway due to lower compliance costs and established infrastructure.	[41, 42, 174]
Strategic Outlook	"Future-proof" long-term decarbonization option with seamless transition to "green" methanol.	"Bridge fuel" offering immediate compliance and cost advantages but challenged by methane slip and long-term GHG limits.	[41, 42, 54, 75, 93, 174, 179]

8. Real-world applications and market outlook

8.1. Case studies and pilot projects

Methanol adoption in shipping has accelerated in recent years, driven by both commercial orders and demonstration projects that signal market confidence in the fuel pathway. Recent review and comparative studies document growing interest in methanol as a near-term low-carbon fuel and summarize the expanding project pipeline [123, 179]. A.P. Moller-Maersk's strategic decision to order multiple methanol-capable vessels in mid-2023 represents a major market signal, demonstrating that leading container operators view methanol as a credible primary decarbonization route [113]. Real-world demonstrations further underline progress: the Port of Antwerp–Bruges-supported "Methatug" project delivered the world's first methanol-powered tug, and industry announcements describe the retrofit of the containership Maersk Halifax to DF methanol operation, both milestones that illustrate technical and operational feasibility at different vessel scales [11, 112, 147]. By contrast, LNG has a much longer maritime history (the first seaborne LNG operations date to the Methane Pioneer era in the late 1950s) and today there are substantially more LNG DF vessels in service and on order than methanol ships; industry fleet databases and independent analyses report hundreds of LNG-fueled vessels and a continuing orderbook, with major operators such as CMA CGM committing to large-scale LNG deployment alongside other fuel strategies [20, 25, 43, 98, 145]. The major milestones in the adoption of Methanol and LNG as marine fuels are presented in Table 8.

8.2. Strategic outlook

LNG's longer history in commercial shipping has produced a clear first-mover advantage, an established installed base of DF vessels, bunkering infrastructure and supply chains, which generates positive feedbacks that lower unit costs and further entrench LNG as a pragmatic near-term option [47, 140]. However, recent strategic commitments by major shipowners, most notably A.P. Møller-Maersk's large methanol orders and upstream supply agreements, signal a competing industry vision that prioritizes a fuel pathway with a clearer long-term route to deep decarbonization, even if that choice requires a more active role in developing green supply chains and policy frameworks [123, 138]. The academic literature frames this divergence as two legitimate strategic approaches to the maritime energy transition: an incremental/bridge strategy (LNG) that reduces near-term emissions and leverages existing infrastructure, and a transformational strategy (methanol/e-methanol/bio-methanol) that seeks long-term carbon neutrality but depends on the emergence of scalable green feedstocks and supportive regulation [93, 138, 179]. Empirical studies and techno-economic modelling demonstrate that the economic attractiveness of each path is highly scenario-dependent, sensitive to carbon pricing, methane-slip performance, and the pace and cost of green fuel deployment, so fleet decisions increasingly reflect corporate risk profiles and regulatory expectations as much as current fuel price differentials [93, 179].

9. Conclusions and strategic recommendations

9.1. Conclusions

This review provides a structured, PRISMA-based comparative synthesis of methanol and LNG as alternative fuels for marine diesel engines, integrating engine thermodynamics, TtW emissions, WtW LCAs, infrastructure constraints, safety considerations, and techno-economic performance into a unified decision-oriented framework.

Key scientific contributions of this review

1. Integrated multi-dimensional comparison

Unlike prior fuel-specific reviews, this study consolidates performance, lifecycle emissions, safety, infrastructure, and cost data into a single comparative structure, enabling cross-domain evaluation rather than parallel narrative discussion.

Table 8. Major milestones in the adoption of Methanol and LNG as marine fuels

Year	Fuel	Milestone/Project	Description and Significance	References
1959	LNG	Methane Pioneer voyage	First-ever seaborne LNG cargo; marked the start of LNG marine transportation and development of cryogenic fuel systems.	[20]
2014–2019	LNG	Early commercial DF vessels	Widespread adoption of LNG DF engines (MAN ME-GI, Wärtsilä DF) for ferries, container ships, and tankers; proven operational safety and reliability.	[20, 145]
2022	LNG	CMA CGM fleet expansion	CMA CGM confirms large-scale LNG strategy, planning > 150 DF vessels by 2029, combining LNG and biomethane options.	[25, 98]
2023	Methanol	Maersk methanol vessel order	Maersk orders six methanol-powered container ships—first global top-tier liner commitment to methanol as a decarbonization pathway.	[113]
2024	Methanol	Methatug project (Port of Antwerp–Bruges)	Delivery of the world's first methanol-fueled tugboat, a milestone for port operations and small-vessel decarbonization.	[11]
2024	Methanol	Maersk Halifax retrofit	World's first large container ship converted to DF methanol operation, proving retrofit feasibility at commercial scale.	[112, 147]
2025	LNG	Record LNG-fueled orderbook	DNV reports "unprecedented year" for LNG-fueled ship orders; LNG remains dominant among alternative-fuel designs.	[43, 145]

2. Technology-dependent climate differentiation

The analysis demonstrates that LNG's climate benefit is not fuel-intrinsic but engine-configuration-dependent. HPDF engines can achieve approx. 15–23% WtW GHG reduction, whereas low-pressure systems may negate this advantage due to methane slip variability (0.2–3%). Thus, LNG's decarbonization effectiveness is conditional rather than universal.

3. Pathway-dependent methanol performance

Fossil ("grey") methanol does not offer WtW climate advantages over diesel, while "green" methanol can reduce WtW emissions by approx. 50–70%, making feedstock origin the decisive factor in its long-term viability.

4. Strategic trade-off clarification

The LNG–methanol choice is fundamentally a trade-off between:

- Immediate regulatory compliance with moderate GHG reduction (LNG), and
- Long-term carbon neutrality potential with supply-chain uncertainty (green methanol).

Decision-oriented strategic synthesis

Based on the integrated findings:

- For short-term (2025–2040) compliance under FuelEU Maritime or IMO CII frameworks, LNG – particularly in HPDF configuration – offers lower compliance risk and stronger near-term economic competitiveness.
- For long-term net-zero alignment (post-2040 scenarios), methanol provides a clearer decarbonization trajectory due to its compatibility with scalable renewable hydrogen pathways.
- For retrofit feasibility and infrastructure simplicity, methanol presents lower CAPEX premiums (≈10–25% vs 22–40% for LNG newbuilds) and reduced bunkering complexity.
- For vessels sensitive to cargo-space penalties, LNG imposes higher volumetric installation penalties (up to 3–4× effective tank volume vs MDO when system factors are included).

Overall strategic conclusion

LNG should be regarded as a bridge fuel whose climate credibility depends on methane-slip control, while methanol should be considered a platform fuel whose ultimate success depends on green production scale-up.

Therefore, the optimal fuel pathway is not universal but scenario-dependent, shaped by:

- Carbon pricing trajectories
- Methane regulation intensity
- Renewable hydrogen deployment speed
- Vessel lifetime and retrofit horizon.

Future research must prioritize standardized WtW methodologies, real-world methane monitoring, and techno-economic optimization of green methanol production to reduce decision uncertainty.

Table 9 synthesizes the integrative strategic comparison between methanol and LNG under different regulatory and technological scenarios.

Table 9. Decision-oriented strategic comparison of Methanol and LNG as marine fuels

Decision dimension	Methanol pathway	LNG pathway	Strategic implication
Near-Term Regulatory Compliance (2025–2040)	Requires blending with green methanol to meet stringent GHG targets	HPDF LNG provides immediate approx. 15–23% WtW GHG reduction	LNG favored for short-term compliance under moderate carbon pricing
Long-Term Net-Zero Alignment (Post-2040)	Green methanol enables approx. 50–70% WtW reduction; scalable with renewable H_2	Fossil LNG limited by methane slip; e-/bio-LNG less scalable	Methanol favored for long-term deep decarbonization
Engine Technology Maturity	Retrofit-friendly; incremental modification of CI engines	HPDF mature; LPDF sensitive to methane slip	Both technically viable; LNG performance more configuration-dependent
Methane / Aldehyde Risk	Formaldehyde formation (local toxicity concern)	Methane slip (high GWP climate concern)	LNG risk more critical for global climate metrics
Onboard Space Requirement	approx. 2.2–2.5× MDO tank volume	Effective 3–4× MDO volume (system-level)	Methanol more favorable for space-constrained retrofits
Infrastructure Complexity	Compatible with existing liquid-fuel logistics	Requires cryogenic bunkering and safety zones	Methanol easier for rapid infrastructure scaling
Capital Expenditure (Newbuild)	approx. +10–25% vs diesel	approx. +22–40% vs diesel	Methanol lower upfront premium
Strategic Role	Platform fuel for green transition	Transitional bridge fuel	Choice depends on corporate risk horizon

9.2. Strategic recommendations

- Shipowners: Adopt methanol-ready or DF designs to ensure compliance flexibility under progressively stringent carbon-intensity and fuel life-cycle regulations (e.g., IMO CII, FuelEU Maritime)
- Engine manufacturers: Prioritize R&D on methanol combustion optimization and high-pressure LNG systems that minimize methane slip and maximize thermal efficiency
- Policy-makers: Implement targeted incentives for renewable methanol and bio-LNG infrastructure, including carbon credits, green corridor support, and certification frameworks to accelerate scale-up
- Researchers: Harmonize WtW LCA methodologies and expand real-world measurement campaigns on unregulated aldehyde emissions (methanol) and methane slip (LNG)
- Port authorities and regulators: Establish a coordinated international framework to standardize methanol bunkering safety protocols and mandate transparent monitoring and reporting of methane slip from LNG-fueled vessels. These measures will ensure safe fuel handling, enhance inter-port data consistency, and underpin glob-

ally harmonized compliance systems aligned with the IMO's 2023 GHG Strategy.

Collectively, these actions will enable a balanced transition – leveraging LNG's readiness for near-term compliance while building the foundation for a methanol-based, carbon-neutral maritime sector in the coming decades.

Acknowledgements

This work was supported by University of Transport HO CHI MINH CITY, grant number KHTĐ2316.

Nomenclature

bio-LNG	biomethane
BSFC	brake-specific fuel consumption
BTDC	before top dead center
BTE	brake thermal êfficiency
CA	crank angle
CAPEX	capital expenditure
CH_3OH	methanol
CH_4	methane
CIEs	compression-ignition engines
CII	carbon intensity indicator
CO	carbon monoxide
CO_2	carbon dioxide
CR	compression ratio
DF	dual-fuel
DI	direct-injection
EC	European Commission
e-LNG	synthetic methane
ETS	emissions trading system
EU	European Union
GHG	greenhouse gas
GWP	global warming potential
HFO	heavy fuel oil
HPDI	high-pressure direct injection
ICCT	International Council on Clean Transportation
IMO	International Maritime Organization
LCAs	life-cycle assessments
LNG	liquefied natural gas
MDO	marine diesel oil
MN	methane number
NO_x	nitrogen oxides
PM	particulate matter
R&D	research and development
SOx	sulfur oxides
StS	ship-to-ship
TCO	total cost of ownership
TDC	top dead center
TtS	truck-to-ship
TtW	tank-to-wake
uHC	unburnt hydrocarbon
VLSFO	very-low-sulfur fuel oil
WtW	well-to-wake

Bibliography

[1] (ABS), American Bureau of Shipping. Methanol bunkering: technical and operational advisory; international institute of marine surveying (IIMS). 2024. https://ww2.eagle.org/content/dam/eagle/advisories-and-debriefs/methanol-bunkering-advisory.pdf

[2] Aakko-Saksa P, Lehtoranta K. Ship emissions in the future. 2019. https://publications.vtt.fi/julkaisut/muut/2019/VTT-R-00335-19.pdf

[3] Aakko-Saksa PT, Lehtoranta K, Kuittinen N, Järvinen A, Jalkanen J-P, Johnson K et al. Reduction in greenhouse gas and other emissions from ship engines: current trends and future options. Prog Energy Combust Sci. 2023;94:101055. https://doi.org/10.1016/j.pecs.2022.101055

[4] Abrahams LS, Samaras C, Griffin WM, Matthews HS. Life cycle greenhouse gas emissions from U.S. liquefied natural gas exports: implications for end uses. Environ Sci Technol. 2015;49(5):3237-3245. https://doi.org/10.1021/es505617p

[5] Adnan MA, Kibria MG. Comparative techno-economic and life-cycle assessment of power-to-methanol synthesis pathways. Appl Energy. 2020;278:115614. https://doi.org/10.1016/j.apenergy.2020.115614

[6] Al-Breiki M, Bicer Y. Overall comparison of energy carriers. in sustainable energy carriers for energy storage and transport. Springer Nature Switzerland. Cham. 2025: 139-226. https://link.springer.com/chapter/10.1007/978-3-031-91615-1_8

[7] Alamoudi AS. Decarbonizing heavy-duty transportation in Saudi Arabia: a life cycle assessment of renewable methanol. Kaust 2025. https://repository.kaust.edu.sa/items/d319725b-2357-40fe-aabe-177d0a6973be

[8] Alanen J, Isotalo M, Kuittinen N, Simonen P, Martikainen S, Kuuluvainen H et al. Physical characteristics of particle emissions from a medium speed ship engine fueled with natural gas and low-sulfur liquid fuels. Environ Sci Technol. 2020;54(9):5376-5384. https://doi.org/10.1021/acs.est.9b06460.

[9] Ammar NR. An environmental and economic analysis of methanol fuel for a cellular container ship. Transp Res D Trans Environ. 2019;69:66-76. https://doi.org/10.1016/j.trd.2019.02.001

[10] Anderson M, Salo K, Fridell E. Particle- and gaseous emissions from an LNG powered ship. Environ Sci Technol. 2015;49(20):12568-12575. https://doi.org/10.1021/acs.est.5b02678.

[11] Antwerp-Bruges P. Methatug: the first methanol-powered tugboat. https://www.portofantwerpbruges.com/en/methatug-first-methanol-powered-tugboat (October 19th 2025).

[12] Ao X, Gan H, Xin M, Cong Y, Lu, D.; Guo, A et al. Numerical investigation on the effects of pilot fuel and natural gas injection pressures on methane slip in a large marine dual-fuel engine. Energy. 2024;312:133675. https://doi.org/10.1016/j.energy.2024.133675

[13] Arefin MA, Nabi MN, Akram MW, Islam MT, Chowdhury MW. A review on liquefied natural gas as fuels for dual fuel engines: opportunities, challenges and responses. Energies. 2020;13(22):6127. https://doi.org/10.3390/en13226127

[14] Babayev R, Moren M, Johansson B. Comparative computational study of hydrogen and natural gas in high-pressure direct-injection (HPDI) compression-ignition engines: Com-

bustion characteristics, thermal efficiency, and local pollutant and greenhouse gas emissions. Fuel. 2025;395:135126. https://doi.org/10.1016/j.fuel.2025.135126
[15] Balcombe P, Brierley J, Lewis C, Skatvedt L, Speirs J, Hawkes A et al. How to decarbonise international shipping: Options for fuels, technologies and policies. Energy Convers Manag. 2019;182:72-88. https://doi.org/10.1016/j.enconman.2018.12.080
[16] Balcombe P, Speirs JF, Brandon NP, Hawkes AD. Methane emissions: choosing the right climate metric and time horizon. Environ Sci Process Impacts. 2018;20(10):1323-1339. https://doi.org/10.1039/c8em00414e
[17] Bilgili L, Ölçer AI. IMO 2023 strategy – where are we and what's next? Marine Policy. 2024;160:105953. https://doi.org/10.1016/j.marpol.2023.105953
[18] Boretti A. Numerical analysis of high-pressure direct injection dual-fuel diesel-liquefied natural gas (LNG) engines. Processes. 2020;8(3):261. https://doi.org/10.3390/pr8030261
[19] Boyland J. From pilots to practice: mmethanol and ammonia as shipping fuels. Global Maritime Forum. Copenhagen 2025. https://globalmaritimeforum.org/report/from-pilots-to-practice-methanol-and-ammonia-as-shipping-fuels/
[20] Brynolf S, Fridell E, Andersson K. Environmental assessment of marine fuels: liquefied natural gas, liquefied biogas, methanol and bio-methanol. J Clean Prod. 2014;74:86-95. https://doi.org/10.1016/j.jclepro.2014.03.052
[21] Burkhart JH. Method of converting diesel engine to natural gas engine. Google Patents 2005.
[22] Campora U, Coppola T, Micoli L, Mocerino L, Ruggiero V. Techno-economic comparison of dual-fuel marine engine waste energy recovery systems. J Mar Sci Appl. 2023;22(4): 809-822. https://link.springer.com/article/10.1007/s11804-023-00368-0
[23] Cao J, Liu Z, Shi H, Dong D, Kang S, Bu L. A review of marine dual-fuel engine new combustion technology: turbulent jet-controlled premixed-diffusion multi-mode combustion. Energies. 2025;18(15):3903. https://doi.org/10.3390/en18153903
[24] Čapalija E, Vidmar P, Perkovič M. Safety of LNG-fuelled cruise ships in comparative risk assessment. Journal of Marine Science and Engineering. 2025;13(10):1896. https://doi.org/10.3390/jmse13101896
[25] CGM C. Company announcements on LNG newbuild programme and fleet strategy. https://www.cma-cgm.com/ (October 19th 2025).
[26] Chao HR, Lin TC, Chao MR, Chang FH, Huang CI, Chen CB. Effect of methanol-containing additive on the emission of carbonyl compounds from a heavy-duty diesel engine. J Hazard Mater. 2000;73(1):39-54. https://doi.org/10.1016/s0304-3894(99)00162-4
[27] Chen C, Saikawa E, Comer B, Mao X, Rutherford D. Ship emission impacts on air quality and human health in the Pearl River Delta (PRD) region, China, in 2015, with projections to 2030. Geohealth. 2019;3(9):284-306. https://doi.org/10.1029/2019GH000183
[28] Chen G, Kong W, Xu Y, Shen Y, Wei F. Thermal efficiency and emissions improvement of the lean burn high compression ratio HPDI NG engine at different combustion modes. Appl Therm Eng. 2024;247:123061. https://doi.org/10.1016/j.applthermaleng.2024.123061
[29] Cho HH, Strezov V, Evans TJ. Life cycle assessment of power-to-methane and renewable methane production technologies. Renew Sustain Energy Rev. 2024;206:114856. https://doi.org/10.1016/j.rser.2024.114856
[30] Commission European. Decarbonising maritime transport – FuelEU Maritime (Regulation (EU) 2023/1805) – overview. Brussels 2023. https://transport.ec.europa.eu/transport-modes/maritime/decarbonising-maritime-transport-fueleu-maritime_en
[31] Commission European. Fit for 55 Package – Maritime Transport Regulation. https://www.consilium.europa.eu/en/policies/fit-for-55/ (October 23rd 2025).
[32] Commission European. The world's first methanol-powered tugboat highlights a greener future for shipping. https://projects.research-and-innovation.ec.europa.eu/en/projects/success-stories/all/worlds-first-methanol-powered-tugboat-highlights-greener-future-shipping (October 10th 2025).
[33] Czermański E, Cirella GT. Energy transition in maritime transport: solutions and costs. Human Settlements: Urbanization, Smart Sector Development, and Future Outlook. Springer 2021;79-88. https://link.springer.com/chapter/10.1007/978-981-16-4031-5_5
[34] de Luna FET, Jaguaribe EF, Rumão AS, Henríquez JR. A turbocharged diesel engine adapted to operate in dual diesel/natural gas mode. Arab J Sci Eng. 2024:1-14. https://link.springer.com/article/10.1007/s13369-024-09651-w
[35] Dejaegere Q, Ballerini A, Demiddeleer S, Vanderbeken T, Bracke K, Gyselinck B et al. Assessment of a heavy-duty diesel engine retrofitted to dual-fuel and neat methanol SI operation. SAE Technical Paper. 2025-01-8440. 2025. https://doi.org/10.4271/2025-01-8440
[36] Delft T. Public final report – methanol as an alternative fuel for vessels. 2018. https://sustainableworldports.org/wp-content/uploads/MKC-TNO-and-TU-Delft_2018_Methanol-as-an-alternative-fuel-for-vessels-report.pdf
[37] Dell'Aversano S, Villante C, Gallucci K, Vanga G, Di Giuliano A. E-fuels: a comprehensive review of the most promising technological alternatives towards an energy transition. Energies. 2024;17(16):3995. https://doi.org/10.3390/en17163995
[38] Deng S, Mi Z. A review on carbon emissions of global shipping. Mar Dev. 2023:1(4). https://link.springer.com/article/10.1007/s44312-023-00001-2
[39] Dierickx J, Verbiest J, Janvier T, Peeters J, Sileghem L, Verhelst S. Retrofitting a high-speed marine engine to dual-fuel methanol-diesel operation: a comparison of multiple and single point methanol port injection. Fuel Commun. 2021;7:100010. https://doi.org/10.1016/j.jfueco.2021.100010
[40] Dieterich V, Buttler A, Hanel A, Spliethoff H, Fendt S. Power-to-liquid via synthesis of methanol, DME or Fischer–Tropsch-fuels: a review. Energy Environ Sci. 2020;13(10): 3207-3252. https://doi.org/10.1039/D0EE01187H
[41] DNV-GL Commercial case study: methanol-fuelled 5,500 TEU containership — TCO analysis; 2024.
[42] DNV-GL Comparison of Alternative Marine Fuels; 2019-0567; Rev. 4. 2019. https://sea-lng.org/wp-content/uploads/2020/04/Alternative-Marine-Fuels-Study_final_report_25.09.19.pdf
[43] DNV LNG powers unprecedented year for orders of alternative-fuelled vessels. 2025. https://www.dnv.com/news/lng-powers-unprecedented-year-for-orders-of-alternative-fuelled-vessels-257832
[44] DNV Maritime Forecast to 2050: Pathways to Net Zero; Oslo, Norway. 2025. https://www.dnv.com/maritime/maritime-forecast/
[45] Eyring V, Köhler H, van Aardenne J, Lauer A. Emissions from international shipping: 1. The last 50 years. J Geophys Res Atmos. 2005;110(D17). https://doi.org/10.1029/2004JD005619

[46] Fasihi M, Breyer C. Global production potential of green methanol based on variable renewable electricity. Energy Environ Sci. 2024;17(10):3503-3522. https://doi.org/10.1039/D3EE02951D
[47] Foretich A, Zaimes GG, Hawkins TR, Newes E. Challenges and opportunities for alternative fuels in the maritime sector. Marit Transport Res. 2021;2:100033. https://doi.org/10.1016/j.martra.2021.100033
[48] Fridell E, Salberg H, Salo K. Measurements of emissions to air from a marine engine fueled by methanol. J Mar Sci Appl. 2021;20(1):138-143. https://doi.org/10.1007/s11804-020-00150-6
[49] Gandolfo J, Lawler B, Gainey B. An experimental comparison of methanol combustion strategies: spark ignition versus compression ignition. J Eng Gas Turbines Power. 2025; 147(9):091007. https://doi.org/10.1115/1.4067404
[50] Garcia P. Experimental investigations on natural gas-diesel dual fuel combustion. Lund University 2018. https://lup.lub.lu.se/search/publication/ff5abaa0-209f-4c69-b78e-5d63ef0f0273
[51] Geels C, Winther M, Andersson C, Jalkanen J-P, Brandt J, Frohn L et al. Projections of shipping emissions and the related impact on air pollution and human health in the Nordic region. Atmos Chem Phys. 2021;21(16):12495-12519. https://doi.org/10.5194/acp-21-12495-2021
[52] Ghorbani B, Zendehboudi S, Saady NMC. Advancing hybrid cryogenic natural gas systems: a comprehensive review of processes and performance optimization. Energies. 2025; 18(6):1443. https://doi.org/10.3390/en18061443
[53] Golbazi M, Archer C. Impacts of maritime shipping on air pollution along the US East Coast. Atmos Chem Phys. 2023; 23(23):15057-15075. https://doi.org/10.5194/acp-23-15057-2023
[54] Gore K, Rigot-Müller P, Coughlan J. Cost assessment of alternative fuels for maritime transportation in Ireland. Transp Res D Trans Environ. 2022;110:103416. https://doi.org/10.1016/j.trd.2022.103416
[55] Gray N, O'Shea R, Smyth B, Lens PN, Murphy JD. What is the energy balance of electrofuels produced through power-to-fuel integration with biogas facilities? Renew Sustain Energy Rev. 2022;155:111886. https://doi.org/10.1016/j.rser.2021.111886
[56] Gronholm T, Makela T, Hatakka J, Jalkanen J-P, Kuula J et al. Evaluation of methane emissions originating from LNG ships based on the measurements at a remote marine station. Environ Sci Technol. 2021;55(20):13677-13686. https://doi.org/10.1021/acs.est.1c03293
[57] Gu Y, Zeng Y, Loh HS. Quantitative risk assessment of liquefied natural gas bunkering hoses in maritime operations: a case of Shenzhen Port. J Mar Sci Eng. 2025;13(8): 1494. https://doi.org/10.3390/jmse13081494
[58] Guo H, Başhan V, Yu C, Bolat F, Demirel H, Tian X. Effect of methanol injection timing on performance of marine diesel engines and emission reduction. J Mar Sci Eng. 2025; 13(5):949. https://doi.org/10.3390/jmse13050949
[59] Hassan QH, Al-Abboodi H. Experimental investigation of the impact of methanol-diesel blends on diesel engine emissions and performance. Combustion Engines. 2025;201(2): 150-157. https://doi.org/10.19206/CE-204494
[60] Hassan QH, Ridha GSA, Hafedh KAH, Alalwan HA. The impact of methanol-diesel compound on the performance of a four-stroke CI engine. Mater Today Proc. 2021;42:1993-1999. https://doi.org/10.1016/j.matpr.2020.12.247
[61] Heikkilä M, Jalkanen J-P, Aakko-Saksa P, Lehtoranta K. Methane slip emissions from LNG vessels-review. 2023. https://www.researchgate.net/publication/372829648_Methane_slip_emissions_from_LNG_vessels_-review#fullTextFileContent
[62] Heikkilä M, Kuittinen N, Grönholm T. Comparing modelled and measured exhaust gas components from two LNG-powered ships. Atmos Environ X. 2024;23:100275. https://doi.org/10.1016/j.aeaoa.2024.100275
[63] Hwang S, Jeong B, Jung K, Kim M, Zhou P. Life cycle assessment of LNG fueled vessel in domestic services. J Mar Sci Eng. 2019;7(10):359. https://doi.org/10.3390/jmse7100359
[64] IMO Methanol as a marine fuel – environmental benefits, technology readiness and economic feasibility. 2016. https://greenvoyage2050.imo.org/wp-content/uploads/2021/01/methanol-as-marine-fuel-environmental-benefits-technology-readiness-and-economic-feasiblity.pdf
[65] Institute Methanol. Innovation Outlook: Renewable Methanol; International Renewable Energy Agency, Abu Dhabi 2021. https://www.irena.org/-/media/Files/IRENA/Agency/Publication/2021/Jan/IRENA_Innovation_Renewable_Methanol_2021.pdf
[66] Institute Methanol. Marine methanol – future-proof shipping fuel. 2023. https://methanol.org/wp-content/uploads/2023/05/Marine_Methanol_Report_Methanol_Institute_May_2023.pdf
[67] Institute Methanol. Methanol as a marine fuel: technical and economic assessment. 2023. https://methanol.org/wp-content/uploads/2018/08/FCBI-Marine-Fuel-Report-REVISED.pdf
[68] Ismail AM, Metwalli MMA, Alamoush AS. Towards safe maritime decarbonization: safety barriers of methanol fuel. Sustainability. 2025;17(11):4896. https://doi.org/10.3390/su17114896
[69] Jang H, Jeong B, Zhou P, Ha S, Nam D. Demystifying the lifecycle environmental benefits and harms of LNG as marine fuel. Appl Energy. 2021;292:116869. https://doi.org/10.1016/j.apenergy.2021.116869
[70] Jensen MV, Cordtz RF, Schramm J. Numerical analysis of methane slip source distribution in a four-stroke dual-fuel marine engine. J Mar Sci Technol. 2021;26(2):606-617. https://link.springer.com/article/10.1007/s00773-020-00760-3
[71] Corbett JJ. Updated emissions from ocean shipping. J Geophys Res. 2003;108(20);1-13. https://doi.org/10.1029/2003JD003751
[72] Juliussen L. ME-GI and ME-LGI gas technologies–development status and results. Dieselfacts: 2016. http://www.marinemethanol.com/download/dieselfacts_2016-02-me-giandme-lgi.pdf
[73] Kabeyi MJB, Olanrewaju OA. In Feasibility of conversion from diesel engine to natural gas power plants, IECON 2022 – 48th Annual Conference of the IEEE Industrial Electronics Society. 2022;1-7. https://doi.org/10.1109/IECON49645.2022.9968428
[74] Kadhim MQ, Oshchepkov PP. Experimental investigation of emissions from a single-cylinder diesel engine using methanol–diesel blends. Front Energy Res. 2024;12:1449652. https://doi.org/10.3389/fenrg.2024.1449652
[75] Kanchiralla FM, Brynolf S, Malmgren E, Hansson J, Grahn M. Life-cycle assessment and costing of fuels and propulsion systems in future fossil-free shipping. Environ Sci Technol. 2022;56(17):12517-12531. https://doi.org/10.1021/acs.est.2c03016
[76] Kanchiralla FM, Brynolf S, Mjelde A. Role of biofuels, electro-fuels, and blue fuels for shipping: environmental and

economic life cycle considerations. Energy Environ Sci. 2024;17(17):6393-6418. https://doi.org/10.1039/D4EE01641F

[77] Karvounis P, Theotokatos G, Vlaskos I, Hatziapostolou A. Methanol combustion characteristics in compression ignition engines: a critical review. Energies. 2023;16(24):8069. https://doi.org/10.3390/en16248069

[78] Kholod N, Evans M, Pilcher RC, Roshchanka V, Ruiz F, Cote M, Collings R. Global methane emissions from coal mining to continue growing even with declining coal production. J Clean Prod. 2020;256:120489. https://doi.org/10.1016/j.jclepro.2020.120489

[79] Kim J-S, Lee W-J, Pham VC, Choi J-H. A numerical study on fuel injection optimization for a ME-GI dual-fuel marine engine based on CFD analysis. Appl Sci. 2022;12(7):3614. https://doi.org/10.3390/app12073614

[80] Kinchin C, Tan ECD, Harris K, Tifft SM, Steward D, Adoption of biofuels for marine shipping decarbonization: a long-term price and scalability assessment. Biofpr. 2022;16(4): 942-961. https://doi.org/10.1002/bbb.2350

[81] Klopott M, Popek M, Urbanyi-Popiołek I. Seaports' role in ensuring the availability of alternative marine fuels a multifaceted analysis. Energies. 2023;16(7):3055. https://doi.org/10.3390/en16073055

[82] Korlak PK. Comparative analysis of the heat balance results of the selected Tier III-compliant gas-fuelled two-stroke main engines. Combustion Engines. 2023;193(2):24-28. https://doi.org/10.19206/CE-158545

[83] Kryshtopa S, Górski K, Longwic R, Smigins R, Kryshtopa L. Increasing parameters of diesel engines by their transformation for methanol conversion products. Energies. 2021; 14(6):1710. https://doi.org/10.3390/en14061710

[84] Kuczyński S, Łaciak M, Szurlej A, Włodek T. Impact of liquefied natural gas composition changes on methane number as a fuel quality requirement. Energies. 2020;13(19): 5060. https://doi.org/10.3390/en13195060

[85] Kuittinen N, Heikkilä M, Jalkanen J-P, Aakko-Saksa P, Lehtoranta K. Methane slip emissions from LNG vessels, 30th CIMAC Congress 2023. 2023:629. https://cris.vtt.fi/ws/portalfiles/portal/85067970/CIMAC_paper_629.pdf

[86] Kuittinen N, Heikkilä M, Lehtoranta K. Review of methane slip from LNG engines. GREEN RAY Project. Deliverable: 2023. https://tuhat.helsinki.fi/ws/portalfiles/portal/282364163/D1.1_Review_of_methane_slip_from_LNG_engines.pdf

[87] Kuittinen N, Heikkilä M, Vesala H, Karppanen M, Koponen P, Piimäkorpi P et al. Methane slip from LNG engines – review and on-board study. Joint TAP and S&E Conference 2023. https://cris.vtt.fi/ws/portalfiles/portal/101232316/Kuittinen_et_al_TAPSE2023_ExtendedAbstract.pdf

[88] Kuittinen N, Heikkilä MA, Lehtoranta K, Consortium GR. Review of methane slip from LNG marine engines. 2023.

[89] Kuittinen N, Koponen P, Vesala H, Lehtoranta K. Methane slip and other emissions from newbuild LNG engine under real-world operation of a state-of-the art cruise ship. Atmos Environ X. 2024;23:100285. https://doi.org/10.1016/j.aeaoa.2024.100285

[90] Kumar D, Valera H, Agarwal AK. Numerical predictions of in-cylinder phenomenon in methanol fueled locomotive engine using high pressure direct injection technique. SAE Technical Paper. 2021. 2021-01-0492. https://doi.org/10.4271/2021-01-0492

[91] Lebedevas S, Milašius E. Comparative assessment of the thermal load of a marine engine operating on alternative fuels. J Mar Sci Eng. 2025;13(4):748. https://doi.org/10.3390/jmse13040748

[92] Lebedevas S, Norkevičius L, Zhou P. Investigation of effect on environmental performance of using LNG as fuel for engines in seaport tugboats. J Mar Sci Eng. 2021;9(2):123. https://doi.org/10.3390/jmse9020123

[93] Lee H, Lee J, Roh G, Lee S, Choung C, Kang H. Comparative life cycle assessments and economic analyses of alternative marine fuels: Insights for practical strategies. Sustainability. 2024;16(5):2114. https://doi.org/10.3390/su16052114

[94] Lehtoranta K, Aakko-Saksa P, Murtonen T, Vesala H, Ntziachristos L, Ronkko T et al. Particulate mass and nonvolatile particle number emissions from marine engines using low-sulfur fuels, natural gas, or scrubbers. Environ Sci Technol. 2019;53(6):3315-3322. https://doi.org/10.1021/acs.est.8b05555

[95] Lehtoranta K, Kuittinen N, Vesala H, Koponen P. Methane emissions from a state-of-the-art LNG-powered vessel. Atmosphere. 2023;14(5):825. https://doi.org/10.3390/atmos14050825

[96] Li Y, Jia P, Jiang S, Li H, Kuang H, Hong Y et al. The climate impact of high seas shipping. Natl Sci Rev. 2023; 10(3). https://doi.org/10.1093/nsr/nwac279

[97] Li Z, Wang Y, Yin Z, Geng H, Zhu R, Zhen X. Effect of injection strategy on a diesel/methanol dual-fuel direct-injection engine. Appl Therm Eng. 2021;189:116691. https://doi.org/10.1016/j.applthermaleng.2021.116691

[98] List L. Number of ships using LNG up significantly; orderbook expands. 2025. https://www.lloydslist.com/

[99] Liu H, Ma J, Tong L, Ma G, Zheng Z, Yao M. Investigation on the potential of high efficiency for internal combustion engines. Energies. 2018;11(3):513. https://doi.org/10.3390/en11030513

[100] Livaniou S, Chatzistelios G, Lyridis DV, Bellos E. LNG vs. MDO in marine fuel emissions tracking. Sustainability. 2022;14(7):3860. https://doi.org/10.3390/su14073860

[101] Livaniou S, Papadopoulos GA. Liquefied natural gas (LNG) as a transitional choice replacing marine conventional fuels (heavy fuel oil/marine diesel oil), towards the era of decarbonisation. Sustainability. 2022;4(24):16364. https://doi.org/10.3390/su142416364

[102] Ma B, Yao A, Yao C, Chen C, Gao J, Qu G. Numerical study on methanol and formaldehyde emissions of diesel methanol dual fuel engine with different valve overlaps. International Conference on Applied Energy 2020. https://www.energy-proceedings.org/wp-content/uploads/enerarxiv/1607519944.pdf

[103] Machaj K, Kupecki J, Malecha Z, Morawski A, Skrzypkiewicz M, Stanclik M et al. Ammonia as a potential marine fuel: A review. Energy Strategy Reviews. 2022;44:100926. https://doi.org/10.1016/j.esr.2022.100926

[104] Maluck L. Green methanol for MTU marine engines. https://www.mtu-solutions.com/na/en/stories/marine/green-methanol-will-power-innovative-mtu-marine-engines.html (October, 17th 2025).

[105] Martin JA, Tan ECD, Ruddy DA, King J, To AT. Temperature-pressure swing process for reactive carbon capture and conversion to methanol: techno-economic analysis and life cycle assessment. Environ Sci Technol. 2024; 58(31):13737-13747. https://doi.org/10.1021/acs.est.4c02589

[106] Martz J. The basics of converting diesels to dual-fuel operation. 2012. https://www.mshs.com/wp-content/uploads/2022/05/Dual_Fuel_CTech-1.pdf

[107] Masum FH, Zaimes GG, Tan ECD, Li S, Dutta A, Ramasamy KK et al. Comparing life-cycle emissions of biofuels

for marine applications: hydrothermal liquefaction of wet wastes, pyrolysis of wood, Fischer-Tropsch synthesis of landfill gas, and solvolysis of wood. Environ Sci Technol. 2023;57(34):12701-12712. https://doi.org/10.1021/acs.est.3c00388

[108] Medicine NL. Methanol. https://pubchem.ncbi.nlm.nih.gov/compound/Methanol (October 9th 2025).

[109] Meng C, Si JP, Liang GX, Niu JH. The technical modification and performance analysis of diesel/LNG dual fuel engines. Adv Mater Res. 2013;724:1383-1388. https://doi.org/10.4028/www.scientific.net/AMR.724-725.1383

[110] MEPC R. 2023 IMO strategy on reduction of GHG emissions from ships. 2023.

[111] Mohammadpour J, Salehi F. A review of alternative liquid fuels in marine engines. Appl Energy Combust Sci. 2025; 100394. https://doi.org/10.1016/j.jaecs.2025.100394

[112] Moller-Maersk AP. Maersk completes first large container vessel conversion to dual-fuel methanol engine. https://www.maersk.com/news/articles/2024/11/18/maersk-completes-first-large-container-vessel-conversion-to-dual-fuel-methanol-engine (October 19th 2025).

[113] Moller-Maersk AP. Maersk orders six methanol powered vessels. https://www.maersk.com/news/articles/2023/06/26/maersk-orders-six-methanol-powered-vessels (October 19th 2025).

[114] Muratov A, Lyashenko V. Design features of switching diesel engines to the gas-diesel operation using natural gas as a fuel. International Conference on Industrial Engineering. Springer 2022:60-67. https://link.springer.com/chapter/10.1007/978-3-031-14125-6_7

[115] Murcia Gonzalez JC. Analysis and measurement of SOx, CO(2), PM and NOx emissions in port auxiliary vessels. Environ Monit Assess. 2021;193(6):374. https://doi.org/10.1007/s10661-021-09145-4

[116] Nari HP. Comparative study of exhaust emissions diesel fueled ships and liquefied natural gas (LNG). Jurnal Maritim Malahayati. 2023;4(2):102-105.

[117] Nasser MA, Elgohary MM, Abdelnaby M, Shouman MR. Environmental and economic performance investigation of natural gas and methanol as a marine alternative fuel. Res Sq. 2022. https://doi.org/10.21203/rs.3.rs-1947354/v1

[118] Negri C, Coppo M, Malin M. Tailor-made solutions for high-pressure direct injection of methanol and ammonia. 31st CIMAC World Congress. 2025. https://papers2025.cimaccongress.com/pdf/CIMAC_paper_257.pdf

[119] Nubli H, Sohn JM, Kim S. Determination of cryogenic temperature loads for finite-element model of LNG bunkering ship under LNG release accident. Curved Layer Struct. 2023;10(1):20220205. https://doi.org//10.1515/cls-2022-0205

[120] Nunes LJ, Renewable methanol as an agent for the decarbonization of maritime logistic systems: a review. Future Transp. 2025;5(2):54. https://doi.org/10.3390/futuretransp5020054

[121] Orysiak E, Zielski H, Gawle M. LNG logistics model to meet demand for bunker fuel. Energies. 2024;17(7):1758. https://doi.org/10.3390/en17071758

[122] Park Y-I, Cho J-S, Kim J-H. Structural integrity assessment of independent type-C cylindrical tanks using finite element analysis: comparative study using stainless steel and aluminum alloy. Metals. 2021;11(10):1632. https://doi.org/10.3390/met11101632

[123] Parris D, Spinthiropoulos K, Ragazou K, Giovou A, Tsanaktsidis C. Methanol, a plugin marine fuel for green house gas reduction – a review. Energies. 2024;17(3):605. https://doi.org/10.3390/en17030605

[124] Pavlenko N, Comer B, Zhou Y, Clark N, Rutherford D. The climate implications of using LNG as a marine fuel. 2020. https://theicct.org/sites/default/files/publications/LNG%20as%20marine%20fuel,%20working%20paper-02_FINAL_20200416.pdf

[125] Pavlenko N, Comer B, Zhou Y, Clark N, Rutherford D. The climate implications of using LNG as a marine fuel. Swedish Environmental Protection Agency: Stockholm, Sweden 2020.

[126] Perčić M, Vladimir N, Fan A. Life-cycle cost assessment of alternative marine fuels to reduce the carbon footprint in short-sea shipping: a case study of Croatia. Appl Energy. 2020;279:115848. https://doi.org/10.1016/j.apenergy.2020.115848

[127] Pham VC, Choi J-H, Rho B-S, Kim J-S, Park K, Park S-K et al. A numerical study on the combustion process and emission characteristics of a natural gas-diesel dual-fuel marine engine at full load. Energies. 2021;14(5);1342.

[128] Pham VC, Le VV, Choi J-H, Lee W-J. CFD analysis of equivalence ratio effects on combustion and emissions in a methanol–diesel dual-fuel marine engine. Energies. 2026; 19(3):626. https://doi.org/10.3390/en19030626

[129] Pham VC, Le VV, Yeo S, Choi J-H, Lee W-J. Effects of the injector spray angle on combustion and emissions of a 4-stroke natural gas-diesel DF marine engine. Appl Sci. 2022;12(23):11886. https://doi.org/10.3390/app122311886

[130] Pham VC, Rho B-S, Kim J-S, Lee W-J, Choi J-H. Effects of various fuels on combustion and emission characteristics of a four-stroke dual-fuel marine engine. J Mar Sci Eng. 2021;9(10):1072. https://doi.org/10.3390/jmse9101072

[131] Printz P, Topaloglou S, Cartalemi C, Goranov S. WinGD 12X92DF, the most powerful Otto-cycle Engine. MTZ Worldwide. 2022;83(5):40-47. https://doi.org/10.1007/s38313-022-0776-x

[132] Pu Y-H, Dejaegere Q, Svensson M, Verhelst S. Renewable methanol as a fuel for heavy-duty engines: A review of technologies enabling single-fuel solutions. Energies. 2024;17(7):1719. https://doi.org/10.3390/en17071719

[133] Raj PK. LNG fires: a review of experimental results, models and hazard prediction challenges. J Hazard Mater. 2007;140(3):444-64. https://doi.org/10.1016/j.jhazmat.2006.10.029

[134] Ramacher MO, Tang L, Moldanová J, Matthias V, Karl M, Fridell E et al. The impact of ship emissions on air quality and human health in the Gothenburg area–Part II: Scenarios for 2040. Atmos Chem Phys. 2020;20(17): 10667-10686. https://doi.org/10.5194/acp-20-10667-2020

[135] Ramsay W, Fridell E, Michan M. Maritime energy transition: future fuels and future emissions. J Mar Sci Appl. 2023;22(4):681-692. https://doi.org/0.1007/s11804-023-00369-z

[136] Rauca L, Batrinca G. Impact of carbon intensity indicator on the vessels' operation and analysis of onboard operational measures. Sustainability. 2023;15(14):11387. https://doi.org/10.3390/su151411387

[137] Rektorik P, Schmid F, Wloka J, Buchholz B. Optical spray investigations and 3D-CFD numerical analysis of the nozzle flow of a methanol HPDI injector for maritime applications. Automot Engine Technol. 2023;8(3):193-209.

[138] Reuters Maersk to buy bio-methanol shipping fuel from China's LONGi.

https://www.reuters.com/markets/commodities/maersk-buy-bio-methanol-shipping-fuel-chinas-longi-2024-10-30/
[139] Rochussen J, Jaeger NS, Penner H, Khan A, Kirchen P. Development and demonstration of strategies for GHG and methane slip reduction from dual-fuel natural gas coastal vessels. Fuel. 2023;349:128433. https://doi.org/10.1016/j.fuel.2023.128433
[140] Roux M, Lodato C, Laurent A, Astrup T. A review of life cycle assessment studies of maritime fuels: critical insights, gaps, and recommendations. Sustainable Production and Consumption. 2024;50:69-86. https://doi.org/10.1016/j.spc.2024.07.016
[141] Roy A, Chakraborty M. A review of ship emissions impacts on environmental, health, societal impacts and IMO's mitigation policies. Reg Stud Mar Sci. 2025;81: 103964. https://doi.org/10.1016/j.rsma.2024.103964
[142] Sagot B, Defossez R, Mahi R, Villot A, Joubert A. An engine load monitoring approach for quantifying yearly methane slip emissions from an LNG-powered RoPax vessel. J Mar Sci Eng. 2025;13(7):1379. https://doi.org/10.3390/jmse13071379
[143] Schuller O, Kupferschmid S, Hengstler J, Whitehouse S. 2nd life cycle GHG emission study on the use of LNG as marine fuel. Technical Report. Sphera 2021.
[144] SEA-LNG LNG as a marine fuel – the investment opportunity; 2020. https://sea-lng.org/wp-content/uploads/2020/04/SEA-LNGStudyVLCC4_compressed.pdf
[145] SEA-LNG SEA-LNG fleet and infrastructure statistics/ reports. 2025. https://sea-lng.org/
[146] Solutions ME. Retrofits for two-stroke marine engines. https://www.man-es.com/services/industries/marine/retrofit-upgrade/two-stroke-engines? (October 10th 2025).
[147] Solutions ME. World's first VCLV methanol retrofit represents blueprint for future projects. https://www.man-es.com/ (October 19th 2025).
[148] Stabilis safety data sheet of liquefied natural gas (LNG). 2025. https://stabilis-solutions.com/wp-content/uploads/2020/08/Stabilis-SDS-LNG-Rev-4.pdf
[149] Sütheö G, Háry A. Comparison of Carbon-Dioxide Emissions of Diesel and LNG heavy-duty trucks in test track environment. Clean Technol. 2024;6(4):1465-1479. https://doi.org/10.3390/cleantechnol6040070
[150] Tang L, Ramacher MOP, Moldanová J, Matthias V, Karl M, Johansson L et al. The impact of ship emissions on air quality and human health in the Gothenburg area – Part 1: 2012 emissions. Atmos Chem Phys. 2020;20(12):7509-7530. https://doi.org/10.5194/acp-20-7509-2020
[151] Thomson H, Corbett JJ, Winebrake JJ. Natural gas as a marine fuel. Energy Policy. 2015;87;153-167. https://doi.org/10.1016/j.enpol.2015.08.027
[152] Tiwari A. Converting a diesel engine to dual-fuel engine using natural gas. Int J Energy Sci Eng. 2015;1(5):163-169.
[153] Treacy M, Xu L, Fatehi H, Kaario O, Bai X-S. Performance of a methanol-fueled direct-injection compression-ignition heavy-duty engine under low-temperature combustion conditions. Energies. 2024;17(17):4307. https://doi.org/10.3390/en17174307
[154] Ushakov S, Stenersen D, Einang PM. Methane slip from gas fuelled ships: a comprehensive summary based on measurement data. J Mar Sci Technol. 2019;24(4):1308-1325. https://doi.org/10.1007/s00773-018-00622-z
[155] Valera-Medina A, Xiao H, Owen-Jones M, David WI, Bowen PJ. Ammonia for power. Prog Energy Combust Sci. 2018;69:63-102. https://doi.org/10.1016/j.pecs.2018.07.001
[156] Van Biert L, Godjevac M, Visser K, Aravind PV. A review of fuel cell systems for maritime applications. J Power Sources. 2016;327:345-364. https://doi.org/10.1016/j.jpowsour.2016.07.007
[157] Vargün M, Yılmaz IT, Sayın C. Investigation of performance, combustion and emission characteristics in a diesel engine fueled with methanol/ethanol/nHeptane/diesel blends. Energy. 2022;257:124740. https://doi.org/10.1016/j.energy.2022.124740
[158] Verhelst S, Turner JW, Sileghem L, Vancoillie J. Methanol as a fuel for internal combustion engines. Prog Energy Combust Sci. 2019;70:43-88. https://doi.org/10.1016/j.pecs.2018.10.001
[159] Viana M, Rizza V, Tobias A, Carr E, Corbett J, Sofiev M et al. Estimated health impacts from maritime transport in the Mediterranean region and benefits from the use of cleaner fuels. Environ Int. 2020;138:105670. https://doi.org/10.1016/j.envint.2020.105670
[160] Visan NA, Niculescu DC, Ionescu R, Dahlin E, Eriksson M, Chiriac R. Study of effects on performances and emissions of a large marine diesel engine partially fuelled with biodiesel B20 and methanol. J Mar Sci Eng. 2024;12(6): 952. https://doi.org/10.3390/jmse12060952
[161] Wang P, Long W, Pang B, Xu X, Liu S, Wang J et al. Investigation on ignition chamber performance in a methanol-fueled TJI-HPDI engine: synergy of nozzle structure, swirl ratio, and spray angle. Energy. 2025;136957. https://doi.org/10.1016/j.energy.2025.136957
[162] Wang P, Long W, Zhao W, Dong P, Lu M, Wang Y et al. Combustion characteristics of methanol engine applying TJI-HPDI with optimized pre-chamber nozzle structure under different injection and spark strategy. Energy. 2024; 312:133503. https://doi.org/10.1016/j.energy.2024.133503
[163] Wang P, Long W, Zhao W, Lu M, Dong P, Tian H et al. Effects of jets interaction and injection strategy on the combustion characteristics in TJI-HPDI methanol engine. Fuel. 2025;393:135058. https://doi.org/10.1016/j.fuel.2025.135058
[164] Wang X, Chang X, Liu J, Gao J, Wu J, He H. Experimental investigation of high-pressure methanol spray characteristics for engines. Appl Therm Eng. 2025;271: 126388. https://doi.org/10.1016/j.applthermaleng.2025.126388
[165] Wang Y, Wright LA. A comparative review of alternative fuels for the maritime sector: economic, technology, and policy challenges for clean energy implementation. World. 2021;2(4):456-481. https://doi.org/10.3390/world2040029
[166] Wang Y, Xiao X, Ji Y. A review of LCA studies on marine alternative fuels: fuels, methodology, case studies, and recommendations. J Mar Sci Eng. 2025;13(2):196. https://doi.org/10.3390/jmse13020196
[167] Wärtsilä Marine Methanol Conversion. https://www.wartsila.com/services-catalogue/engine-services-4-stroke/marine-methanol-conversion (October 10th 2025).
[168] Wei H, Müller-Casseres E, Belchior CR, Szklo A. Evaluating the readiness of ships and ports to bunker and use alternative fuels: a case study from Brazil. J Mar Sci Eng. 2023;11(10):1856. https://doi.org/10.3390/jmse11101856
[169] Wei H, Zhang Z, Zhang X, Dong F, Yuan W, Chen H. Overview for methanol and formaldehyde unregulated emissions of methanol fueled engines. J Energy Inst. 2025; 102089. https://doi.org/10.1016/j.joei.2025.102089

[170] Wei L, Lu X, Huang W, Song Q. Effects of split injection on combustion, emissions, and intermediate species of natural gas high-pressure direct injection engine. J Mar Sci Appl. 2025;24(1):210-223. https://doi.org/10.1007/s11804-024-00456-9
[171] Wei Y, Liu S, Liu F, Liu J, Zhu Z, Li G. Formaldehyde and methanol emissions from a methanol/gasoline-fueled spark-ignition (SI) engine. Energy Fuels. 2009;23(6): 3313-3318. https://doi.org/10.1021/ef900175h
[172] Williams RL, Lipari F, Potter RA. Formaldehyde, melhanol and hydrocarbon emissions from methanol-fueled cars. Journal of the Air & Waste Management Association. 1990;40(5):747-756. https://doi.org/10.1080/10473289.1990.10466720
[173] Wissner N, Healy S, Cames M, Sutter J. Methanol as a marine fuel. Naturschutzbund Deutschland: Stuttgart 2023.
[174] Wu P-C, Lin C-Y. Feasibility and cost-benefit analysis of methanol as a sustainable alternative fuel for ships. J Mar Sci Eng. 2025;13(5):973. https://doi.org/10.3390/jmse13050973
[175] Xiahou M, Lu T, Feng Y, Zhang D, Yan P, Sun K et al. Experimental study on the performance and optimization of pilot diesel-ignited high-pressure direct-injection methanol combustion at low loads. Energy. 2025;136326. https://doi.org/10.1016/j.energy.2025.136326
[176] Xin M, Gan H, Cong Y, Wang H. Numerical simulation of methane slip from marine dual-fuel engine based on hydrogen-blended natural gas strategy. Fuel. 2024;358: 130132. https://doi.org/10.1016/j.fuel.2023.130132
[177] Xing H, Spence S, Chen H. A comprehensive review on countermeasures for CO_2 emissions from ships. Renew Sustain Energy Rev. 2020;134:110222. https://doi.org/10.1016/j.rser.2020.110222
[178] Yao A, Yao C. Study of diesel/methanol dual fuel combustion in CI engines and its practice in China. International Journal of Automotive Manufacturing and Materials. 2023;2-2. https://doi.org/10.53941/ijamm0201002
[179] Zamboni G, Scamardella F, Gualeni P, Canepa E. Comparative analysis among different alternative fuels for ship propulsion in a well-to-wake perspective. Heliyon. 2024; 10(4). https://doi.org/10.1016/j.heliyon.2024.e26016
[180] Zamboni G, Scamardella F, Gualeni P, Canepa E. Comparative analysis among different alternative fuels for ship propulsion in a well-to-wake perspective. Heliyon. 2024; 10:e26016. https://doi.org/10.1016/j.heliyon.2024.e26016
[181] Zarrinkolah MT, Hosseini V. Methane slip reduction of conventional dual-fuel natural gas diesel engine using direct fuel injection management and alternative combustion modes. Fuel. 2023;331:125775. https://doi.org/10.1016/j.fuel.2022.125775
[182] Zhang C, Zhu J, Guo H, Xue S, Wang X, Wang Z et al. Technical requirements for 2023 IMO GHG strategy. Sustainability. 2024;16(7):2766. https://doi.org/10.3390/su16072766
[183] Zhang X, Gao J, Fan D, Yang Q, Han F, Yu H. Impact of pilot diesel injection timing on performance and emission characteristics of marine natural gas/diesel dual-fuel engine. Sci Rep. 2024;14(1):10713. https://doi.org/10.1038/s41598-024-61672-5
[184] Zhao Y, Liu X, Kook S. Combustion mode evaluation of a methanol–diesel dual direct injection engine with a control of injection timing and energy substitution ratio. SAE Int J Engines. 2025;18(1):3-17. https://doi.org/10.4271/03-18-01-0002
[185] Zhu H, Zhou L, He D, Chen Z, Liu J. LNG density measurement by gravimetric method. Cryogenics. 2024;142: 103925. https://doi.org/10.1016/j.cryogenics.2024.103925
[186] Zhu Y, Fan L. Fuel delivery system for alternative fuel engines: a review. Potential and challenges of low carbon fuels for sustainable transport. 2022;67-95. https://doi.org/10.1007/978-981-16-8414-2_4
[187] Zincir B, Deniz C. Methanol as a fuel for marine diesel engines. Alcohol as an alternative fuel for internal combustion engines. Springer 2021:45-85.

Van Chien Pham, DEng. – AIT Research Group, University of Transport Ho Chi Minh City, Vietnam.
e-mail: *chien.pham@ut.edu.vn*

Van Si Hoang, DEng. – Maritime Academy, University of Transport Ho Chi Minh City, Vietnam.
e-mail: *si.hoang@ut.edu.vn*

Duy Nam Ngo, DEng.– AIT Research Group, University of Transport Ho Chi Minh City, Vietnam.
e-mail: *nam.ngo@ut.edu.vn*

Van Vang Le, DEng.– AIT Research Group, University of Transport Ho Chi Minh City, Vietnam.
e-mail: *levanvang@ut.edu.vn*

Article citation info:
Nowak M, Flis B. Engines used in modern unmanned aerial vehicles. Combustion Engines. 2026;206(3):229-236. https://doi.org/10.19206/CE-219239

Mateusz NOWAK
Bartłomiej FLIS

Combustion Engines
Polish Scientific Society of Combustion Engines

Engines used in modern unmanned aerial vehicles

ARTICLE INFO

Received: 23 June 2025
Revised: 25 January 2026
Accepted: 12 March 2026
Available online: 28 March 2026

For several years, a rapid growth in interest in unmanned aerial vehicles (UAVs) in many applications has been observed. The UAVs are seen as both entertaining equipment for kids and sophisticated tools for agriculture, archaeology, and terrain scanning. There are also military applications for these flying objects across various missions. This allows multiple UAV configurations to be observed, thereby addressing specific requirements. The wide variety of UAV applications requires a wide range of propulsion systems. In the present paper, the authors sought to present and evaluate specific engine parameters used in modern UAVs. There are described electric motors, piston engines, and turbine engines that produce from about 18 W to 900 kW of power. That is a very wide power range, so the presented engines cannot be compared directly. However, after obtaining the power-to-weight ratio, it can be seen that, in most cases, it stays between 0.1 and 0.15 kW/kg. In some specific cases, this ratio has different values.

Key words: *UAV, fixed-wing, multirotor, VTOL, UAV engines*

This is an open access article under the CC BY license (http://creativecommons.org/licenses/by/4.0/)

1. Introduction

Unmanned aerial vehicles are often presented as a synonym of modernity, yet their history dates back about 100 years, to 3rd September 1924, when the first successful flight of a radio-controlled aircraft without a safety pilot was performed. In 1933, the UAF was first used as a target drone, and in 1944, both Germany and the USA first used UAVs in combat missions [7].

Recently, the unmanned aerial vehicle market has been growing rapidly. The forecast for 2022-2028 predicts an average annual increase in the value of unmanned aerial vehicle sales worldwide of 21.6% [52]. This is because unmanned aerial vehicles are increasingly used, both in civil and military applications [41, 42]. The variety of requirements placed on UAVs results in a range of structures differing in configuration and size. This entails different requirements placed on the propulsion units. In this paper, the units used to propel civil and military unmanned aerial vehicles will be analyzed from multiple perspectives.

Apart from the recreational use of unmanned aerial vehicles, in utility applications, such objects have numerous advantages over the use of manned aircraft, such as [44, 51]:

- Mass – no need to carry the pilot (or crew) and their equipment (seats, operational instruments and installations); this is a very important parameter in agricultural aviation or military applications
- Shape – no need to integrate the crew cabin, so the design could be focused on aerodynamic or useful properties
- Safety – the UAVs can enter areas, which could be dangerous for humans, like biological research, polar or volcanic research, disaster areas with high risk (flood, fire areas) of an accident or areas with radiation, military reconnaissance
- Efficiency – Some of the UAVs can perform autonomous or predefined missions, including the collection of specific data
- Higher maneuverability because the pilot's resistance to overloads during flight does not have to be taken into account, which is especially important in military applications.

There are applications where UAVs are the only possible solution. Such an area is training on air defense systems, where the target is to destroy the target [43].

An important factor in the use of military unmanned aerial vehicles is the lack of fear of losing the pilot, which, aside from the humanitarian factor, represents a loss of money spent on the pilot's training. According to U.S. Air Force data, for military pilots, costs can range from 1.1 million USD to about 11 million USD [49].

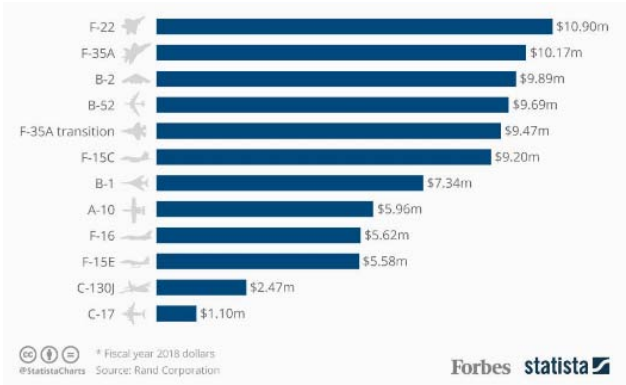

Fig. 1. The cost of training U.S. Air Force Pilots for different types of aircraft [49]

The aim of the paper is to present and evaluate specific parameters of engines used in modern UAVs. In the following chapters, the authors will describe the classification of UAVs and then the types of engines used to propel different types of UAVs. In that chapter, the data of engines used to propel the selected UAVs will also be presented. The next chapter will present an evaluation of parameters characterizing the analyzed engines and the flight parameters of the UAVs powered by them.

2. Unmanned aerial vehicles classification

Due to the variety of available UAVs, there are many criteria for categorizing them. In the literature, you can find classifications based on parameters such as weight, flight range, flight duration, wing loading, maximum ceiling, and engine type [16]. Among the most popular classifications are those based on takeoff mass and range. According to the literature, 5 takeoff mass classes are listed (Table 1) [7]. Classification by UAV range comprises three classes that also depend on flight endurance (Table 2) [7].

Table 1. UAV classification according to takeoff mass [6, 7, 31, 45, 46]

Class	UAV mass [kg]	Example
Super heavy	Over 2000	RQ-4B Global Haewk
Heavy	200–2000	Bayraktar TB2
Medium	50–200	HESA Shahed 136
Light	5–50	Albatros
Micro	Less than 5	Hee Wing Ranger T1

Table 2. UAV classification according to UAV range and endurance [7, 13, 25]

Class	UAV range [km]	UAV endurance [hr]	Example
High	Over 1500	Over 24	MQ-9 Reaper
Medium	100–400	5–24	Camcopter S-100
Low	Less than 100	Less than 5	AeroVironment FQM-151 Pointer

The most popular and easily noticeable UAV classification is according to its configuration, following types of UAVs can be distinguished (Fig. 2) [1, 48, 55]:

– Fixed-wing
– Multirotor (Rotary-wing)
– VTOL (Hybrid).

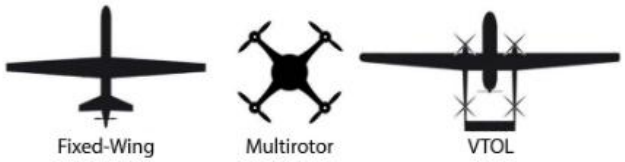

Fig. 2. Example of UAV classification [1]

In some classifications, different types are also listed, such as helicopters (which can be considered a type of rotary-wing configuration), blimps, and flapping-wing aircraft [55].

Due to the widespread use of UAVs, categories are sometimes created that incorporate multiple classification criteria. This is how the MALE (Medium-Altitude Long-Endurance) and HALE (High-Altitude Long-Endurance) classes were created. These classes refer mainly to drones in fixed-wing configuration, which are used both for military and civil purposes [36, 50]

Fixed-wing aircraft are designed to monitor large areas. This type of platform often resembles a typical aircraft (Fig. 3). It is particularly suitable for mapping terrain, monitoring high-voltage lines, or performing reconnaissance missions. This type of platform is characterized by higher cruising speeds and lower energy consumption than multi-rotors, which makes them well-suited for flights over longer distances. This type of UAV platform is less popular than multi-rotors due to the requirement of a more experienced pilot, more space for take-off and landing, and legal restrictions on flights beyond visual line of sight (BVLOS) [47].

Fig. 3. Example of UAV in fixed-wing configuration [54]

Multi-rotor platforms, in addition to standard flight, are characterized by their ability to hover and move at low speeds. The hovering feature, similar to helicopters, is particularly useful during monitoring point infrastructure and work requiring precision or time to collect the appropriate amount of data (Fig. 4). Another advantage of this type of platform is the possibility of vertical take-off and landing, which allows the mission to start and end on a small piece of flat terrain. This feature allows to work in difficult environments, such as urban or forested areas. These platforms are typically equipped with electric motors that drive propellers (main rotors), mounted symmetrically on the arms. The most common configurations of multi-rotor aircraft use 4 to 8 rotors [47].

Fig. 4. Example of UAV in multirotor configuration [34]

The solution that combines the advantages of both presented technical solutions is a hybrid VTOL platform (Fig. 5). It is most often built as a fixed-wing aircraft with a push or pull propeller and additional rotors, enabling vertical take-off and landing. Of course, this type of solution slightly disrupts aerodynamic properties during flight or reduces the payload, but these are small compromises compared to the wide range of flight properties. This type of construction is used in the unmanned transport of blood samples on the Warsaw-Sochaczew and Warsaw-Pułtusk lines.

Fig. 5. Example of VTOL UAV platform [23]

In a fixed-wing configuration, most objects use only one engine to maintain the thrust to fly. Unmanned aircraft base their flight characteristics mainly on the strong lift generated by the wing. The engine, engine-gearbox-propeller assembly, or combination provides the necessary thrust to maintain flight conditions. Models with this solution take off in a conventional way, via a runway run, or with a launcher (pneumatic or mechanical), or manually (from "hand"). This group also includes unmanned helicopter models.

Fixed-wing aircraft can also use two engines. They use the same flight mechanics principle as the machines in the above-mentioned category with one engine. Two engines can be used, for example, to distribute thrust, allowing us to use cheaper engines that often generate less thrust as a single drive. The methods of getting into the air are also duplicated from the second paragraph of this subsection, but with some exceptions. Some concept models can take off vertically – these are the so-called "Tailsitters". They take off from a parking position, resting on their tail. Remote-controlled helicopters can also fall into this category.

Devices using three or more drive units are the largest group, including popular multi-rotor, fixed-wing, and tiltrotor aircraft. Remotely controlled multi-engine fixed-wing aircraft, however, are mainly found in hobby designs, e.g., models reproducing aircraft from the events of the last century.

Multirotor platforms typically use an even number of engines, such as four, six or eight (higher numbers are less common), but designs with three engines also exist.

3. Engines in unmanned aerial vehicles

Most commonly used propulsion systems are electric motors and combustion engines, which drive a propeller directly or via a gearbox. Additionally, in UAVs, turbine engines are used, which generate thrust via a propeller. The smallest group is the turbojet engines, which generate thrust directly by the exhaust gases leaving the engine.

Electric drives consist of an electric motor assembly directly connected to a propeller, with various parameters such as diameter, pitch, and number of blades, depending on the needs of the structure.

Electric motors themselves can be divided into three categories:

1. Due to the shaft arrangement:
   - with an internal shaft (so-called Inrunner): the housing is stationary, the shaft is inside, and it transmits the power
   - with an external shaft (so-called Outrunner): the movable housing transmits the torque, the shaft is embedded in it.
2. Due to the power supply method:
   - single phase or DC power supply – only two wires required
   - three phase power supply – minimum three wires required.
3. Electric motors may or may not contain brushes.

Internal shaft motors are also most often brush motors. This design is being replaced in many applications by brushless phase motors, but is still used in cheaper designs due to its low cost and simple operation and production. Such motors have different shapes and sizes. Such units are powered by direct current.

Brushless electric outrunner motors are the most popular type of this drive. They are characterized by high torque and high efficiency. They are powered by one or three phases. This motor, thanks to the shaft attached directly to the housing, which contains a certain (even) number of magnets, does not require the use of brushes, because the winding creating the magnetic field is located on the stator placed inside the housing.

The control system is usually implemented as a power amplifier based on switching transistors, the number of which depends on the number of stator windings. It performs basic functions such as changing the rotational speed, regulating acceleration, and analyzing rotor position information from feedback.

Table 1. Specifications of selected UAV equipped with electric motors [2–6, 11, 12, 19, 20, 29, 30, 38]

UAV name	UAV mass [kg]	Range [km]	Flight time [hh:mm]	Max ceiling [m]	Power of one engine [W]
DJI Mini 3[1]	0.25	18	00:38	4000	22.3
Helion 10[1]	0.95	10	00:30	7000	2143.8
BETA FPV Cetus X[1]	0.055	0.1	00:05	100	18.5
DJI Agras T25[1]	32	2	04:00	120	1305
Altura Zenith ATX 8[1]	9.65	1	00:40	1000	400
Albatros[2]	10	280	04:00	10000	260
Hee Wing Ranger T1 VTOL[2]	0.75	30	01:05	1000	206
1 – Multirotor, 2 – Fixed-wing					

An example of UAVs powered by electric motors is shown in Fig. 6 and 7. The first object is a typical recreational UAV, and the second is more professional in a fixed-wing configuration. Electric-motor UAVs are the most popular, especially in civil applications (recreational and professional). In fixed-wing applications, a single engine is often sufficient (Fig. 7). In contrast, multirotor platforms require multiple engines (Fig. 6).

Piston engines in the described designs are most often four-stroke units, with an even number of pistons (usually four). The cylinder arrangement is most often a boxer, though there are units with a linear or "V" arrangement. The ignition method in UAV engines is dominated by spark ignition (SI) with a carburetor, but compression ignition (CI) has been implemented, e.g., in the MQ-1C Gray Eagle,

Table 2. Specifications of selected UAVs equipped with piston combustion engines [9, 13–16, 22, 24, 25, 31, 33, 35, 37, 39, 53]

UAV name	Engine name	UAV mass [kg]	Range [km]	Flight time [hh:mm]	Max ceiling [m]	Power of one engine [kW]
Bayraktar TB2[1]	Rotax 914	700	300	27:00	5486	75
Elbit Hermes 900[1]	Rotax 916	1270	1000	36:00	9100	160
HESA Shahed 136[1]	Mado MD-550	200	2500	--:--	4000	37.3
MQ 1 Predator[1]	Rotax 914	1020	1250	24:00	7600	86
MQ 1C[1]	Thielert Centurion 1.7	1633	400	27:00	7600	123
IAI Heron[1]	Rotax 914	1150	1000	45:00	10500	160
Mohajer 6[1]	Rotax 914	670	200	12:00	5500	84.6
Wing Loong I[1]	Rotax 914	1100	4000	20:00	5000	75
Kronsztadt Skorpion[1]	Itłan APD-115T	1150	1440	24:00	7500	86
Forpost[1]	APD-85	454	350	16:00	5797	58.85
Falco Xplorer[1]	Rotax 914	1300	300	24:00	9144	86
Camcopter S-100[2]	AE-50R	200	100	06:00	5900	40.4
1 – Fixed-wing, 2 – Helicopter						

which uses the Thielert Centurion 1.7 HFE (Heavy Fuel Engine). It can be seen that many unmanned aerial vehicles use engines used in small aviation, such as the Rotax 914, which is used not only in UAVs but also in many small manned aircraft.

Fig. 6. DJI Mini 3 [19]

Fig. 7. UAV Albatros [6]

Combustion engines used in UAVs are divided into piston engines and turbine engines: turboshaft, turboprop, or turbojet. Each of them is connected to the propeller via an appropriate gearbox, except for turbojet engines, which generate thrust directly (they do not drive propellers). It should be emphasized at this stage that the use of a combustion engine by civilian unmanned aerial vehicles is legally prohibited (except for model and specialist models) - such designs are not classified in the open category. Therefore, we can expect these engines to be used in specialist and military designs.

Piston engines are mostly used in fixed-wing UAVs, but this type of powerplant also propels other UAV configurations, such as helicopters (Fig. 8 and Fig. 9). This type of propulsion system is used more in military than in civil applications.

Fig. 8. UAV Bayraktar TB 2 [10]

Fig. 9. Unmanned helicopter Camcopter S-100 [17]

Turbine engines in UAV systems are of three types: turboshaft, turboprop, and turbojet. Two of the three types predominate in implementation. Turboshaft and turboprop engines allow for a significant increase in power while slightly increasing weight. They also enable flights at much higher altitudes, resulting in increased flight time and range.

Jet engines are used in the heaviest unmanned aerial vehicles and are mainly used in structures intended for mili-

tary purposes. Currently, only two such machines are used – the RQ-4B Global Hawk and the Guizhou WZ 7 Soaring Dragon (it should be mentioned that other producers work on that type of UAVs). Both designs are specialized machines, though their tasks differ slightly. The Global Hawk is a machine with an almost global range, which acts as a machine for collecting radio-electronic and radar information about the battlefield (e.g. SIGINT – Signal Intelligence). The mission specification of the WZ 7 is not fully known, though it is assumed to be a heavy-strike drone.

Table 3. Specifications of selected UAVs equipped with turbine engines [8, 13, 26, 27, 32, 40, 45]

UAV name	Engine name	UAV mass [kg]	Range [km]	Flight time [hh:mm]	Max ceiling [m]	Power of one engine [kW*]
MQ-8[1]	RR 250	1430	203.7	08:00	6100	313
IAI Eitan[2]	PT6-67A	5400	7400	30:00	14000	900
Bayraktar AKINCI[2]	–	6000	7500	24:00	13750	560
MQ-9 Reaper[2]	TPE331-10	2223	1900	27:00	15420	671
RQ-4B[2]	F137-RR-100	14628	22800	34:00	18000	34 kN
UZGA AL-TIUS[2]	WK-800S	7500	3600	48:00	12000	589
Guizhou WZ 7[2]	Guizhou WP-13	7500	7000	10:00	18000	43.1 kN

1 – Helicopter, 2 – Fixed-wing
* – beyond another unit in the cell

The turbine engines are used mostly in military drones, like RQ-4B Global Hawk (Fig. 10). In most civil applications sufficient power is delivered by electric motors or piston engines.

Fig. 10. RQ-4B Global Hawk in flight [28]

4. Comparison of UAV engines

Small UAVs powered by electric motors have different applications, which implies different efficiencies across the criteria shown in the above graphs. The Helion 10 UAV is a system designed to fly in FPV (First Person View) mode, allowing real-time observation of the drone's flight from the camera's perspective. Such systems are characterized not necessarily by a large range but by a very high engine power-to-weight ratio, which ensures high maneuverability and speed of the remotely controlled multi-rotor.

It should be noted that for legal reasons, civilian UAVs do not use combustion engines, except for strictly model-oriented designs (the author of the article noted the dominance of single-cylinder two-stroke piston engines in this area of use) or special-purpose designs (however, these designs/systems require certification, e.g., from the domestic Civil Aviation Authority). The list included in this article includes all designs, therefore, as military, special-purpose, and/or experimental. Such a decision is also driven by the desire to achieve, for example, greater UAV performance, such as flight endurance. Of course, today the army also uses UAVs powered by electric motors (e.g. the Polish Warmate system from the WB Electronics Group), but it is not limited only to them, as is the case with civilian customers.

The range of UAVs produced for different applications is very broad. The mass of those objects ranges from about 100 g to 8000 kg. Also, drones are produced for different uses, which is why engine power ranges from about 18 W to 900 kW (Fig. 11). As shown in the figure, electric drones are very close to zero at the left edge of the graph. Also, the piston-engine drones differ by only a very narrow range, which is why there are additional graphs for electric UAVs (Fig. 12) and piston-engine UAVs (Fig. 13). Of course, the most powerful are the turbine-engine UAVs. Of course, the turbine drones are the heaviest too – up to 7500 kg for the analyzed objects. However, the turbine engine-propelled drones, in case of their application, operate at higher speeds and altitudes than other UAVs.

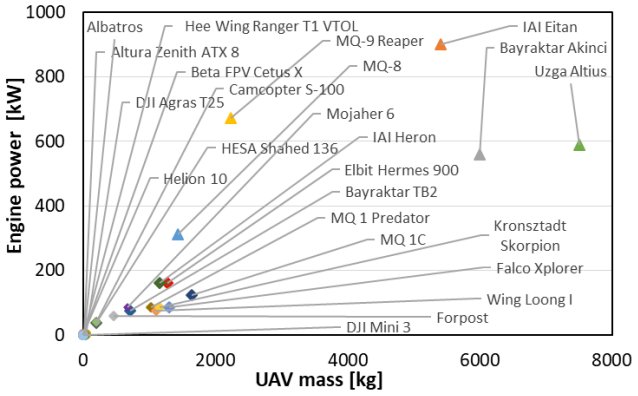

Fig. 11. Engine power as a function of UAV mass in all categories of analyzed UAVs

In the presented UAVs which use an electric motor, there are only civil drones. Despite it the motor power and UAV mass vary respectively from about 2 W to 2.1 kW and from 100 g to 32 kg (Fig. 12). These values range, because also in that class of UAVs, there can be several applications listed, like: recreational use with camera (DJI Mini), very fast flying (Helion 10) and agricultural application, where payload is also important (DJI Agras).

The power and weight parameters of UAVs with piston engines vary between 40 kW to 160 kW and 200 kg to 1600 kg (Fig. 13).

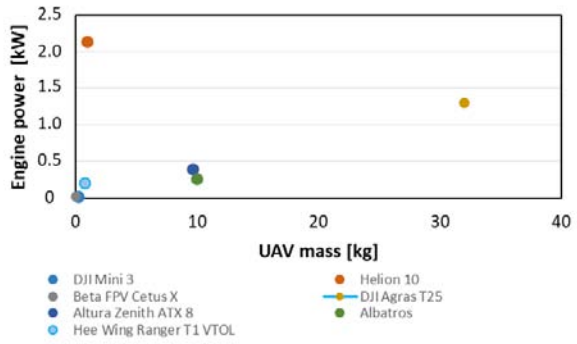

Fig. 12. Electric motor power as a function of UAV mass in electric motor-propelled UAVs

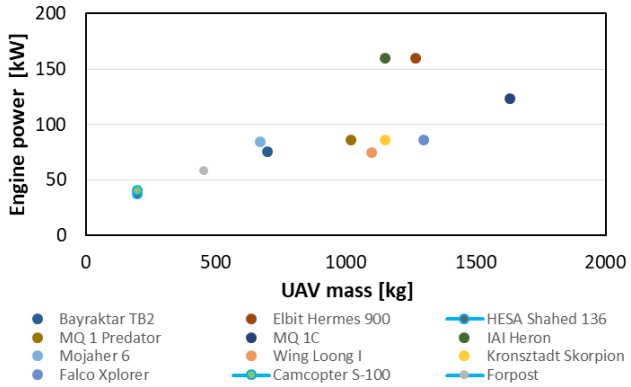

Fig. 13. Piston engine power in function of UAV mass in piston engine-powered UAVs

An interesting comparison is the power-to-mass ratio in kW of engine power per 1 kg of UAV mass (Fig. 14). Most drones have values around 0.1 kW/kg. That value is especially relevant for a fixed-wing configuration. There are higher values of that parameter in some multirotor or helicopter configurations, like Camcopter (0.2 kW/kg) or BETA FPV Cetus X (0.34 kW/kg). Higher values are observed for special-purpose objects, such as the MQ-9 Reaper (0.3 kW/kg).

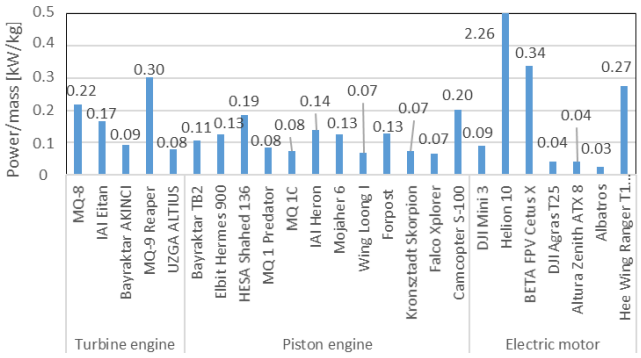

Fig. 14. Power-to-mass ratio for analyzed UAVs

Similar observations could be formulated in the case of the presented UAVs range (Fig. 15). Most of these objects can fly up to a few hundred kilometers. Some fixed-wing aircraft can fly around 1000 km, and some specialized applications can reach up to 7500 km (Bayraktar AKINCI and IAI Eitan).

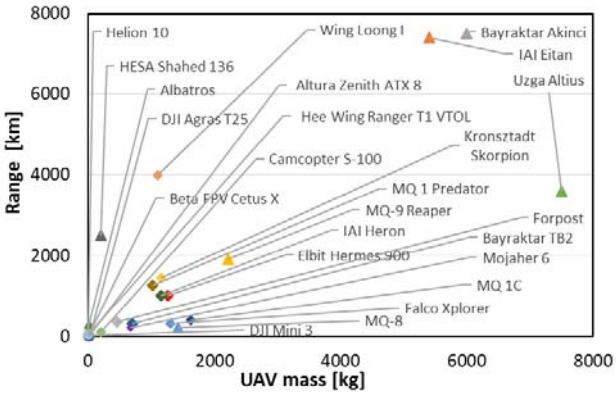

Fig. 15. Range for analyzed UAVs

It should be noted that at this point, UAVs with jet engines have been omitted due to the difference in the method of generating thrust. The graphs include unmanned systems powered by internal combustion turbine engines of the turboshaft or turboprop type.

The use of an internal combustion turbine engine is associated with higher costs of purchasing and maintaining the drive unit than the previously mentioned types of engines. However, it should be noted that these are also the most powerful engines of the types described in this article, allowing one to reach nearly any place in the world and to reach the highest altitudes.

Summary

Work on UAVa began shortly after the first flight of an aircraft – the first launch of an unmanned aircraft took place in 1922. That was a RAE 1921 Target for training purposes. After the mentioned date, the development of military drones accelerated, culminating in the first combat mission in 1944 [7]. However, last years make the UAVs more popular in civil applications, which can be used for transport of goods, archaeology, agriculture, or even a drone can be a play for kids. Very often in some applications, the UAVs have to carry some specific equipment, like cameras, lidar or ground penetrating radar. Agricultural drones have to carry the spraying equipment, along with fertilizers or plant protection agents. Even more sophisticated requirements are sometimes set for military drones, because the agricultural drone, even if it has to carry some load, does not have to fly to another continent; it can just turn around to charge or change the battery, whereas the military drone often has to fly longer distances and/or stay in the air for a long time.

Above listed requirements resulted in a very wide range of UAVs on the market. If we assume the drone's mass as a criterion, we can find a drone weighing about 100 g, while on the other end of the scale, a drone weighing about 8000 kg. The different masses of objects that should be propelled result in the power of a single engine, which varies from about 18 W for Beta FPV Cetus X to 900 kW in IAI Eitan.

Only the engine's power isn't everything. The characteristics of every drone can vary depending on the type of engine used, which can also affect the power-to-weight ratio. For recreational use, only electric motors are used. This type of propulsion is also used in military drones,

where the electric motor provides silent operation. Another type is the piston engine, which is used in heavier UAVs. Also, this type of engine is used when a longer range is needed, because liquid fuels have a higher energy density than electric batteries. The largest UAVs with the highest ceiling use turbine engines.

Interesting results are observed regarding the power-to-mass ratio. In that case, most of the analyzed UAVs represent values at around 0.1 kW/kg. It can be observed that this value is specific to the aircraft (fixed-wing configuration). The multirotor and helicopter configurations are more likely to exhibit higher power-to-weight ratios. Also, some specialized application drones exhibit higher values of the mentioned ratio, such as the MQ-9 Reaper (0.3 kW/kg).

The presented material shows the variety of UAVs and their engines. According to the analysis in this paper, drones used for civil applications are propelled by smaller, less powerful engines. The reasons are the operational parameters, which, compared to military drones, are: mostly lower mass (less than 50 kg), lower flight speed, and lower ceiling. It should also be noted that turbojet engines are not considered in this paper. Turbojet engines are characterized by thrust rather than power, so it will be problematic to compare all the powerplants together. Nevertheless, it can be very valuable to include that type of engine in the comparison in the future, thereby making the study more complex. This type of drive will become increasingly popular as new UAVs are developed (e.g., Bayraktar Kizilelma).

Bibliography

[1] Alghamdi Y, Munir A, Manh La H. Architecture, classification, and applications of contemporary unmanned aerial vehicles. IEEE Consumer Electronics Magazine. 2021;10(6). https://doi.org/10.1109/MCE.2021.3063945

[2] Altura Zenith ATX 8. https://www.aerialtronics.com/downloads/EN-Specsheet_aerialtronics-AlturaZenith_ATX8_16.06.2017.pdf (accessed on 16.09.2024).

[3] Altura Zenith ATX 8. https://southerncrossdrones.com/download/aerilatronics-sxd-.pdf (accessed on 16.09.2024).

[4] Applied Aeronautics Albatross. https://www.appliedaeronautics.com/albatross-uav (accessed on 16.09.2024).

[5] Applied Aeronautics Albatross. https://www.appliedaeronautics.com/far (accessed on 16.09.2024).

[6] Applied Aeronautics – Albatross UAV. https://www.unmannedsystemstechnology.com/wp-content/uploads/2015/03/Applied-Aeronautics-Albatross-UAV.jpg (accessed on 16.09.2024).

[7] Arjomandi M. Classification of unmanned aerial vehicles. Mech Eng. 3016. University of Adelaide, Australia.

[8] Bayraktar Akinci. https://baykartech.com/en/uav/bayraktar-akinci/ (accessed on 16.09.2024).

[9] Bayraktar TB2. https://en.wikipedia.org/wiki/Bayraktar_TB2#Specifications_(TB2) (accessed on: 16.09.2024).

[10] Bayraktar TB-2 https://kresy.pl/wp-content/uploads/2020/05/Bayraktar-TB-2-na-Ukrainie.-Fot.-ArmijaInform.jpg (accessed on 16.09.2024).

[11] Beta FPV Cetus X. https://avifly.pl/pl/fpv/00313290 (accessed on 12.09.2024).

[12] Beta FPV Cetus X. https://megadron.pl/pl/products/dron-betafpv-cetus-x-kit-elrs-27424.html (accessed on 16.09.2024).

[13] Butowski P. Russian UAV systems. Long-endurance unmanned aircraft (2). Lotnictwo. Aviation International (in Polish). 2024;6.

[14] Butowski P. Russian UAV systems. Tactical unmanned aerial vehicles and their armament (3). Lotnictwo. Aviation International (in Polish). 2024;7.

[15] Camcopter S-100. https://pl.wikipedia.org/wiki/Camcopter_S-100 (accessed on 16.09.2024).

[16] Camcopter S-100. https://schiebel.net/products/camcopter-s-100/ (accessed on 16.09.2024).

[17] Camcopters 100. https://cdn.defence24.pl/2021/04/21/1920xpx/qrx8n7-camcopters100estonia2.jpeg (accessed on 16.09.2024).

[18] Çoban S, Oktay T. Unmanned Aerial Vehicles (UAVs) according to engine type. Journal of Aviation. 2018;2(2): 177-184. https://doi.org/10.30518/jav.461116

[19] DJI e2000. https://www-v1.dji.com/e2000/spec.html (accessed on 16.09.2024).

[20] DJI Mini 3. https://www.dji.com/pl/mini-3/specs (accessed on 12.09.2024).

[21] DJI Mini 3 Fly More Combo. https://ispot.pl/img/imagecache/87001-88000/680x383/product-media/87001-88000/DJI-Mini-3-Fly-More-Combo-drone-32622-680x383-nobckgr.webp (accessed on 16.09.2024).

[22] Elbit Hermes 900. https://en.wikipedia.org/wiki/Elbit_Hermes_900 (accessed on 16.09.2024).

[23] Farada G1. https://faradagroup.com/farada-g1/ (accessed on 25.10.2024).

[24] General Atomics MQ_1C. https://en.wikipedia.org/wiki/General_Atomics_MQ-1C_Gray_Eagle#Specifications (accessed on 16.09.2024).

[25] General Atomics MQ-1 Predator. https://en.wikipedia.org/wiki/General_Atomics_MQ-1_Predator#Specifications (accessed on 16.09.2024).

[26] General Atomics MQ-9 Reaper. https://en.wikipedia.org/wiki/General_Atomics_MQ-9_Reaper#Specifications (accessed on 16.09.2024).

[27] Giuzhou WZ-7 Soaring Dragon. https://en.wikipedia.org/wiki/Guizhou_WZ-7_Soaring_Dragon (accessed on 16.09.2024).

[28] Global Hawk. https://pl.wikipedia.org/wiki/Plik:Global_Hawk_1.jpg (accessed on 16.09.2024).

[29] Heewing Ranger VTOL. https://www.heewing.com/products/t-1-ranger-vtol-pnp (accessed on 16.09.2024).

[30] Helion 10. https://megadron.pl/pl/products/dron-helion-10-hd-o3-air-unit-6s-bnf-6s-dji-29272.html (accessed on 12.09.2024).

[31] Hesa Shahed 136. https://en.wikipedia.org/wiki/HESA_Shahed_136 (accessed on 16.09.2024).

[32] IAI Eitan. https://en.wikipedia.org/wiki/IAI_Eitan#Specifications (accessed on 16.09.2024).
[33] IAI Heron. https://www.iai.co.il/p/heron (accessed on 16.09. 2024).
[34] Indian Railways to deploy drones for project monitoring. https://www.geospatialworld.net/news/indian-railways-deploy-drones-project-monitoring/ (accessed on 25.10. 2024).
[35] Leonardo Falco Xplorer. https://milmag.pl/siae2019-leonardo-falco-xplorer/ (accessed on 16.09.2024).
[36] MALE and HALE drone developments: Evolving existing systems and introducing new aircraft https://euro-sd.com/2025/06/articles/44958/male-and-hale-drone-developments-evolving-existing-systems-and-introducing-new-aircraft/ (accessed on 04.09.2025)
[37] Mohajer 6. Lotnictwo. Aviation International (in Polish). 2024;7.
[38] Motors specs, weight and KV. https://forum.dji.com/thread-271146-1-1.html (accessed on 16.09.2024).
[39] MQ-1C Gray Eagle. https://odin.tradoc.army.mil/WEG/Asset/MQ-1C_Gray_Eagle_American_Medium-Altitude (accessed on 16.09.2024).
[40] MQ-8 Fire Scout. https://en.wikipedia.org/wiki/Northrop_Grumman_MQ-8_Fire_Scout (accessed on 16.09.2024).
[41] Nowak M, Flis B, Andrzejewski M. Overview of the use of Light Detection and Ranging and Ground Penetrating Radar implemented on an Unmanned Aerial Vehicle. J Civ Eng Transp. 2024;6(4):27-37. https://doi.org/10.24136/tren.2024.015
[42] Nowak M, Flis B, Sikora W. Environmental benefits of agricultural aviation development. Combustion Engines 2025;200(1):136-144. https://doi.org/10.19206/CE-202210
[43] Nowakowski M. Issues related to the development of unmanned aerial vehicles at the Air Force Institute of Technology (in Polish). Logistyka. 2011;6:3129-3139.
[44] Pros and cons of UAV. https://equinoxsdrones.com/10-major-pros-cons-of-unmanned-aerial-vehicleuav-drones/ (accessed on 15.06. 2025).
[45] RQ-4 Global Hawk. https://en.wikipedia.org/wiki/Northrop_Grumman_RQ-4_Global_Hawk#Specifications_(RQ-4B_Block_30/40) (accessed on 16.09.2024).
[46] Samolot Long Rage FPV HeeWing T1 Ranger KIT. https://avifly.pl/pl/drony-fpv-long-range/heewing-t1-ranger-kit?srsltid=AfmBOoqwBOT-0bxmgzgiI2KmxKbaBFBsaDXvDP69wSlbd0raJ5bfGuWj (accessed on 04.09.2025)
[47] Sherrock E, Neubecker K. Unmanned Aircraft system applications in international railroads. U.S. Department of Transportation. Federal Railroad Administration; Office of Research, Development and Technology Washington, DC 20590 DOT/FRA/ORD-18/04, Final Report February 2018.
[48] Stewart MP, Martin ST. Unmanned aerial vehicles: Fundamentals, components, mechanics and regulations. Unmanned Aerial Vehicles, Chapter 1. Nova Science Publishers, Inc. 2021.
[49] The cost of training U.S. Air Force fighter pilots. https://www.forbes.com/sites/niallmccarthy/2019/04/09/the-cost-of-training-u-s-air-force-fighter-pilots-infographic/ (accessed on 12.06.2025).
[50] Tsach S, Yaniv A, Avni H, Penn D. High altitude long endurance (HALE) UAV for intelligence missions. 20th Congress of the International Council of the Aeronautical Sciences – ICAS 1996. Napoli 1996;1:368-379.
[51] UAS Uses and Benefits. https://www.commerce.nd.gov/economic-development-finance/autonomous-systems/uas-uses-and-benefits (accessed on 15.06.2025).
[52] Unmanned Aerial Vehicle (UAV) Market Share Worth US$ 73.91 Bn, Globally, by 2028 at 21.6% CAGR – Exclusive Report by The Insight Partners. https://www.globenewswire.com/en/news-release (access date 04/09/2025).
[53] Wing Loong I. https://en.wikipedia.org/wiki/CAIG_Wing_Loong#Specifications_(Wing_Loong_I) (accessed on 16.09.2024).
[54] Your mission is our mission. https://www.appliedaeronautics.com/ (accessed on 25.10. 2024).
[55] Zhang B, Song Z, Zhao F, Liu C. Overview of propulsion systems for unmanned aerial vehicles. Energies. 2022;15: 455. https://doi.org/10.3390/en15020455

Mateusz Nowak, DEng. – Faculty of Civil and Transport Engineering. Poznan University of Technology, Poland.
e-mail: *mateusz.s.nowak@put.poznan.pl*

Bartłomiej Flis, Eng. – Faculty of Civil and Transport Engineering. Poznan University of Technology, Poland.
e-mail: *bartlomiej.flis@student.put.poznan.pl*

Article citation info:
Cebulska W, Hadryś D, Rajca A. Comparison of magnetic induction emissions in electric, hybrid and conventional cars. Combustion Engines. 2026;206(3):237-243. https://doi.org/10.19206/CE-217945

Wioletta CEBULSKA
Damian HADRYŚ
Adam RAJCA

Combustion Engines
Polish Scientific Society of Combustion Engines

Comparison of magnetic induction emissions in electric, hybrid and conventional cars

ARTICLE INFO

Received: 10 May 2025
Revised: 8 February 2026
Accepted: 9 February 2026
Available online: 17 February 2026

The article analyses magnetic induction levels in vehicles with three different drive types: electric, hybrid, and conventional. The aim of the research was to determine the intensity of low-frequency magnetic fields generated by the drive systems and their effect on the driver and passengers of the vehicle. The paper describes methods for measuring magnetic induction at various locations within the vehicle, including the engine compartment and the power supply system. Measurements of magnetic induction were also performed during the charging of an electric car. The research results indicate that the highest magnetic induction occurs in electric cars and in the charging area during charging. In conventional drive cars, magnetic induction is mainly limited to the operation of the alternator. The power of the drive system significantly affects magnetic induction. In the case of measurements of magnetic flux density emitted by the power supply system and drive systems of fully electric and hybrid cars, the studies also showed that the location of elements such as the DC/AC converter and the cables connecting the converter to the electric motor and their distance from the driver's and passenger seats significantly affect their exposure level.

Key words: *electromobility, magnetic flux density, electric drive, hybrid drive, conventional drive*

This is an open access article under the CC BY license (http://creativecommons.org/licenses/by/4.0/)

1. Introduction

The electromagnetic field (also called electromagnetic radiation), abbreviated as EMF, is the effect of electric and magnetic fields. The magnetic field is a manifestation of the electromagnetic field with frequencies in the range from 0 Hz (constant fields) to 300 GHz (microwave radiation). Above the upper limit of the indicated range, the following radiations are distinguished: infrared, visible, ultraviolet, X-ray, gamma and cosmic radiation. Electromagnetic fields are divided into natural and artificially generated. Natural magnetic fields are associated with phenomena occurring in the atmosphere (e.g. lightning during a storm), while artificially generated fields are a manifestation of human activity. They may differ in wavelength and frequency. An alternative quantity to the magnetic field intensity – magnetic induction – is often used to characterize low-frequency magnetic fields. Magnetic induction (B) is a component of the magnetic field, which is measured in teslas (T) or gauss (G). This is a quantity related mainly to the magnetic field, regardless of whether it is constant (e.g. the field of a magnet) or variable (e.g. around a conductor with alternating current). Magnetic induction is presented by formula (1) [7, 12]:

$$B = \mu H \tag{1}$$

where: B – magnetic induction, T, μ – magnetic permeability, T·m/A, H – magnetic field intensity, A/m.

The main difference between electromagnetic field measurement and magnetic flux density measurement is that magnetic flux density measurement deals only with the magnetic component of the field, whereas electromagnetic field measurement includes both electric and magnetic components, often in the context of electromagnetic waves.

It should be emphasized that measuring the electromagnetic field differs significantly from measuring magnetic flux density. EMF measurement encompasses both the electric and magnetic components of the field and is typically used to analyze electromagnetic waves, especially in the high-frequency range. Magnetic induction measurement, on the other hand, concerns only the magnetic component and is primarily used to analyze low-frequency fields, such as those in the immediate vicinity of electrical devices and test vehicles [5–7].

2. Electromagnetic field in motor vehicles

Electric car engines and the AC power supply system emit frequencies from 20 Hz to 600 Hz, depending on the driving mode. Battery charging stations emit EMF with frequencies from 20 kHz to 100 kHz. The vehicle structure is largely made of metal elements, which at operating frequencies of 0.8–150 kHz constitute a barrier against electromagnetic field emissions. The electromagnetic field in electric vehicles ranges from low-frequency fields to microwave radiation. The engines and the inverter with wires in electric cars, as well as the alternator in combustion cars, emit low-frequency magnetic fields, i.e. magnetic induction [6–9, 13, 15].

Main sources of magnetic induction in electric cars:

- Electric motor – in the motor, the flow of current through the stator windings generates a magnetic field that affects the rotor. Since the rotor is often made of magnetic materials (e.g. permanent magnets or ferromagnetic cores), this field creates magnetic induction, which creates torque and drives the wheels.
- High-voltage cables – electrical cables and connections, e.g. between the battery and the inverter, also generate a magnetic field.
- Inverter – controls the flow of current to the motor, converting direct current (DC) from the battery to alter-

nating current (AC). The alternating current in the motor windings creates an alternating magnetic field.
- Batteries and charging systems – although the batteries themselves do not generate an alternating magnetic field (DC), alternating currents can occur during charging (e.g. in chargers).

In a conventional car, the sources of magnetic induction (B) differ from those in an electric car, but they still occur. The main sources are:
- Alternator – the main source of the magnetic field. Inside the alternator, the rotor with the winding generates a variable magnetic field.
- Ignition coil and high-voltage wires – change the voltage from 12V to several thousand volts to generate a spark in the spark plug. The flow of current through the coil creates a strong magnetic field, which then disappears, inducing high voltage.
- Starter motor – generates a magnetic field in the windings. Although it works only for a moment, it generates strong magnetic field pulses [1, 2, 15,16, 19–22].

In hybrid vehicles, the classic alternator and starter are replaced by one or more electric motor–generator units, which can function as both a drive motor and a generator to charge the traction battery. These components, such as electric motors, inverters, DC/DC converters, and high-voltage cables, generate magnetic fields due to the flow of current [1, 3].

The scientific literature contains numerous studies on magnetic field emissions from vehicles with different drive types. Tell et al. measured magnetic field intensity in electric and combustion cars, showing that electric vehicles generate significantly higher magnetic fields, especially in the drive systems and passenger compartment. The greatest exposure was in the area around the driver's and front passenger's legs [17].

He et al. studied the effects of static magnetic fields generated by electric vehicles on drivers' cognitive functions. Their results suggest that even fields with intensity consistent with applicable standards may affect the nervous system and reaction time during long-term exposure [6].

In Poland, studies by Gryz et al. found higher magnetic induction levels in hybrid and electric vehicles than in conventional vehicles. It was indicated that the main sources of emissions are inverters, high-voltage cables, and electric motors, and that field values in the area of the driver's feet can reach 10–15 μT [7].

In turn, Wang et al. [20] conducted long-term monitoring of low-frequency magnetic fields in electric vehicles and observed significant variations in emission levels depending on driving mode, load and arrangement of drive system components. The highest values were recorded during acceleration and battery charging [21].

The conclusions from the cited studies clearly indicate that electric and hybrid vehicles exhibit higher levels of magnetic field emissions, and user exposure is significantly influenced by the power of the drive system, component arrangement, and distance from the field sources [6, 22].

3. The effects of electromagnetic fields on humans

An electromagnetic field can stimulate excitable tissue by inducing electric currents in the body. This phenomenon is most significant at frequencies lower than several hundred kHz. In addition, tissue heating occurs due to the absorption of field energy (the so-called thermal effect), and the most important aspect is its occurrence at frequencies above 1 MHz. Moving in an electromagnetic field can also cause, among other things, dizziness, nausea, and impaired eye-hand coordination. They stop after moving away from the source. An electromagnetic field can cause undesirable changes in the body's functioning. The results of scientific research indicate that possible effects of electromagnetic fields include disorders of the nervous, cardiovascular, and immune systems, neoplastic processes, and subjective complaints such as headaches, fatigue, and memory disturbances. A large number of diseases are reported in people living near transmission lines, electricity generators and similar interfering devices. A 1979 study by physicist Ed Leeper showed that children exposed to just 0.3 μT had twice the incidence of leukemia. In 1998, the New York State Department of Health repeated the study and confirmed the previous study's results. Studies show that the protective threshold for direct exposure to an AC electric field should not exceed 5 V/m at ground potential and 1.5 V/m without ground potential. The AC magnetic field emission should not exceed 0.1 μT. [6–11, 13, 14, 22, 23].

4. Apparatus and subject of research

The measurements were carried out using two electromagnetic field meters, TM-191 and TM-196. The TM-191 meter operates in the range of 30–300 Hz, while the TM-196 meter operates in the range from 10 MHz to 8 GHz.

Fig. 1. Electromagnetic field meter TM-191 [17]

Table 1. Technical parameters of the TM-191 electromagnetic meter [17]

Feature	Value
Measured field	Very low frequency (LF) magnetic field 30–300 Hz
Measurement method	Single-axis sensor
Measurements	For frequencies 30–300 Hz
H (magnetic field)	200.0/2000 mG; 20.00/200.0 μT
Accuracy	±2.5% for frequencies 50/60 Hz
X, Y, Z measurement	none

Bench measurements were performed, as were magnetic induction measurements during charging of an electric

vehicle at a charging station. To avoid interference with the measurements, the radio and other electronic devices were turned off for the duration of the measurement.

Fig. 2. Electromagnetic field meter TM-196 [17]

Table 2. Technical parameters of the TM-196 electromagnetic meter [17]

Feature	Value
Measured field	Radio frequency electromagnetic field 10 MHz–8 GHz
Measurement method	Digital measurement 3-axis
Directional characteristic	Isotropic, triaxial
CAL coefficient	Settable in the range 0.10–9.99 (default 1)
Measurements	CW signal (f > 50 MHz)
E (electric field)	38.0 mV/m; 11.0 V/m
H (magnetic field)	53.0 µA/m.; 28.64 mA/m
S (power density)	0.1000 µW/m^2; 309.3 mW/m^2
Dynamic ranges	0.1000 µW/cm^2; 30.93 µW/cm^2
Accuracy	75 dBm
Isotropic deviation	Absolute error ±0.1 dBm at 1 mV/m and 2.45 GHz
X, Y, Z measurement	Selection: all axes, X-axis, Y-axis or Z-axis

The research object is three passenger cars. A conventional drivetrain car of the Dacia Sandero III brand with a 1.0 Tce petrol engine with a turbocharger with an output of 67 kW. An electric car of the Dacia Spring brand with a synchronous motor with a permanent magnet with an output of 33 kW [4, 5]. A hybrid drive car of the Toyota C-HR brand with a 1.8 internal combustion engine with an output of 72 kW and an electric motor with an output of 53 kW. The total power of the hybrid system is 90 kW [18]. All vehicles were manufactured in 2021 and had Crossover bodies. However, this brand does not offer a hybrid car, which is why a Toyota hybrid drive [3] was selected for comparison.

a) Conventional drive vehicle

Fig. 3. Conventional drive car Dacia Sandero

Table 3. Technical data of the Dacia Sandero [5]

Model	Dacia Sandero III Hatchback; 2021
Drivetrain type	ICE
Engine	1.0 Tce petrol turbocharged
Displacement	999 cm^3
Engine power	67 kW, 90 HP for 4600 rpm
Torque	160 Nm for 2100–3750 rpm
Drive	Front axle
Range	962 km
Current weight	1152 kg

b) Battery electric vehicle

Fig. 4. Electric drive car Dacia Spring

Table 4. Technical data of the Dacia Spring [4]

Model	Dacia Spring Crossover Electric; 2021
Drivetrain type	Electric
Engine	Permanent magnet synchronous
Engine power	33 kW, 45 HP for 3000–8200 rpm
Torque	125 Nm for 500–2500 rpm
Drive	Front axle
Battery	lithium-ion
Gross battery capacity	27 kWh
Charging time socket/fast	13 h/1h
Range	230 km
Own weight	920 kg

c) Hybrid electric vehicle

Fig. 5. Toyota C-HR hybrid car – view under the engine cover

Table 5. Technical data of the Toyota C-HR [18]

Model	Toyota C-HR Crossover SUV; 2021
Drivetrain type	Hybrid (HEV)
Engine	1.8 Hybrid
Engine system power	Power 90 kW, 122 HP at 5200 rpm
Petrol engine power	72 kW, 98 HP at 3600 rpm
Petrol engine torque	142 Nm at 3600 rpm
Electric engine power	53 kW, 72 HP
Electric engine torque	163 Nm
Battery	lithium-ion
Gross battery capacity	1 kWh
Gearbox type	Automatic e-CVT
Range	895 km
Current weight	1380 kg

5. Research

5.1. Stationary measurements

a) Conventional drive vehicle

In a conventional drive car, magnetic induction measurements were taken in the vicinity of the alternator. Each time, 20 measurements were taken directly at the device and at distances of 0.2 m and 0.5 m. During the measurements, the temperature was about 15°C.

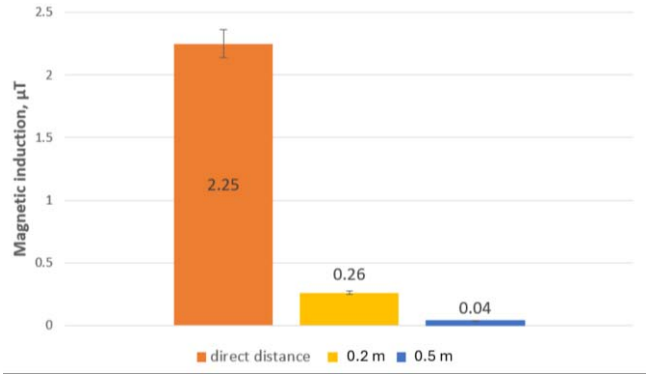

Fig. 6. Magnetic induction in the vicinity of the alternator – conventional vehicle

During bench tests, the magnetic induction in a conventional car with an ICE near the alternator was recorded at a level of 2.25 µT, which at a distance of 20 cm was already below 1 µT.

b) Battery electric vehicle

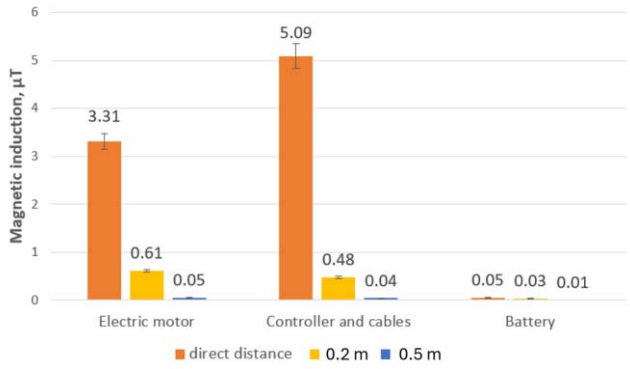

Fig. 7. Magnetic induction – electric vehicle

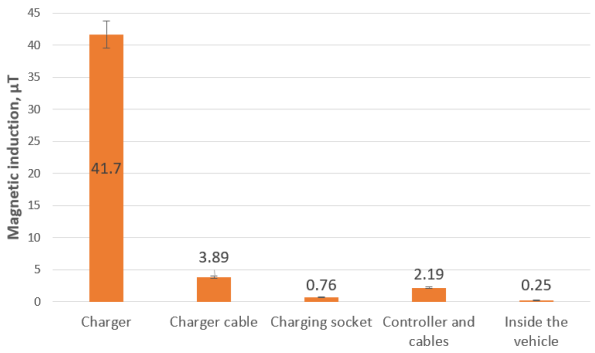

Fig. 8. Magnetic induction in the area of the charger during charging of an electric vehicle

In the electric car, during the bench test, magnetic induction occurred in the vicinity of the inverter and cables (5 µT) and near the engine (3.3 µT), while in the case of the alternator in a combustion engine vehicle, after moving away from the source by 20 cm, it was only from 0.4 µT to 0.6 µT. The highest magnetic induction was recorded during charging of the electric car in the vicinity of the charger and high-voltage cables. It amounted to 41.7 µT. At the charger cable, it was 3.9 µT, and in the vicinity of the inverter and vehicle cables, 2.2 µT.

c) Hybrid electric vehicle

In the hybrid car, magnetic induction measurements were taken in the vicinity of the generator, electric motor, inverter, and high-voltage cables. Each time, 20 measurements were taken directly at the device and at distances of 0.2 m and 0.5 m. During the measurements, the temperature was around 15°C.

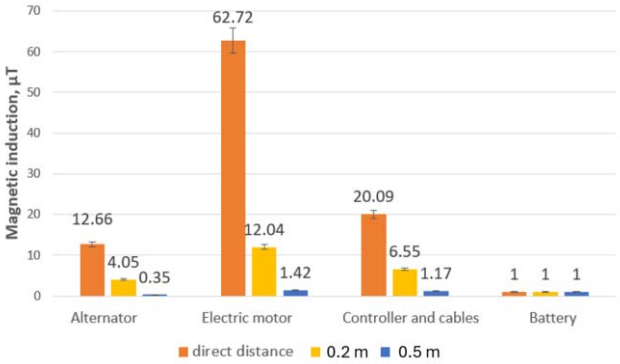

Fig. 9. Magnetic induction – hybrid vehicle

During tests in a hybrid car, magnetic induction of 62.7 µT was recorded near the electric motor, 20 µT near the inverter and cables, and 12.6 µT near the generator. At a distance of 20 cm from the sources, it was: 12.4 µT for the engine, 6.5 µT for the inverter, and 4 µT for the generator.

5.2. Measurements while driving

The magnetic field intensity measurements were conducted inside each of the three vehicles across four driving conditions. The measurements were taken with a TM-196 three-axis electromagnetic field meter operating in the high-frequency range. The first measurements were taken in city traffic at 30 km/h and 50 km/h, then in motorway traffic at 100 km/h and 140 km/h. During measurements at 30 km/h, only the electric motor was running in the hybrid car; at other speeds, the combustion engine was running. Each time, 20 measurements were taken. The measurements were taken in the afternoon and evening, with temperatures around 15°C. There was no wind and no precipitation. There was no snow cover. The meter was mounted near the driver's seat. To avoid interference with the measurements, the radio and other electronic devices were turned off for the duration of the measurement. The results presented are the result of the X, Y, and Z axes (geometric sum). Measurements are presented as an arithmetic mean of the collected results, excluding the lowest and highest values. Error bars are marked on the graphs.

a) 30 km/h

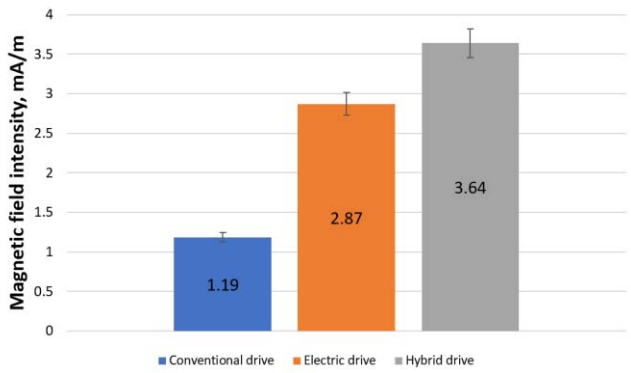

Fig. 10. Summary results of magnetic field intensity measurements at vehicle speeds of 30 km/h

b) 50 km/h

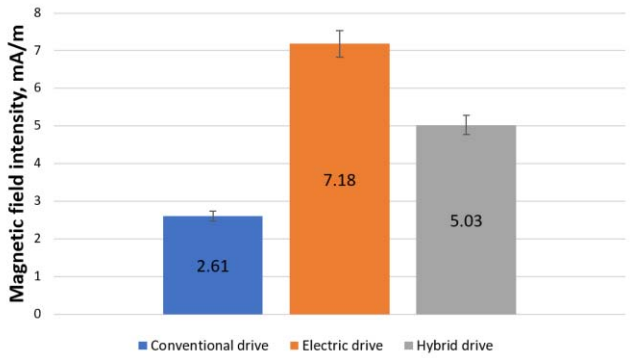

Fig. 11. Summary results of magnetic field intensity measurements at vehicle speeds of 50 km/h

During city driving, the magnetic field strength was highest for the hybrid vehicle (3.6 mA/m), slightly lower for the electric vehicle (2.8 mA/m), and lowest for the conventional vehicle (1.2 mA/m) at 30 km/h. At 50 km/h, the values were highest for the electric vehicle (7.2 mA/m), followed by the hybrid vehicle (5 mA/m), and lowest for the conventional vehicle (2.6 mA/m). The hybrid vehicle emitted lower values when the conventional rather than the electric system operated at higher speeds.

c) 100 km/h

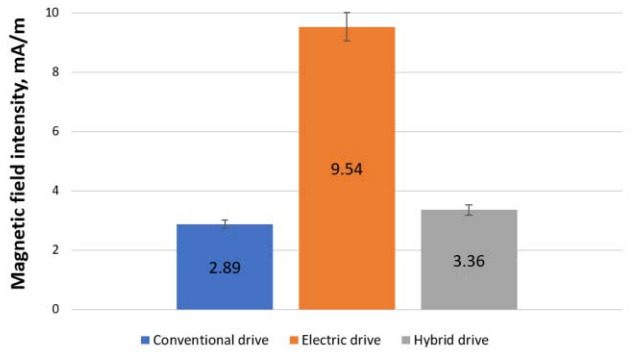

Fig. 12. Summary results of magnetic field intensity measurements at vehicle speeds of 100 km/h

d) 140 km/h

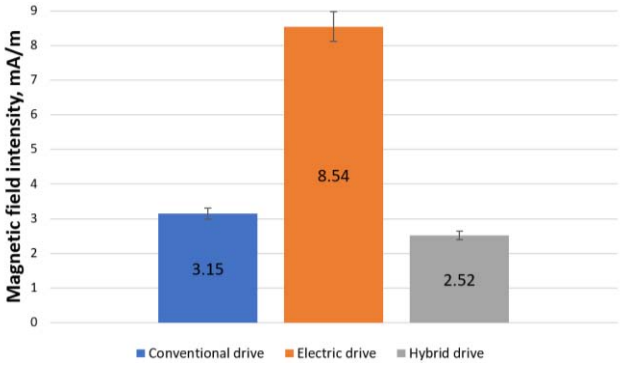

Fig. 13. Summary results of magnetic field intensity measurements at vehicle speeds of 140 km/h

During motorway driving at 100 km/h, the magnetic field strength was highest for the electric vehicle (9.7 mA/m), lower for the hybrid (3.4 mA/m) and lowest for the conventional vehicle (2.9 mA/m). At 140 km/h, it was the highest for the electric vehicle (8.5 mA/m), lower for the conventional vehicle (3.1 mA/m) and lowest for the hybrid (2.5 mA/m).

6. Conclusions

The conducted tests allowed obtaining different values of magnetic flux density depending on the type of vehicle, the measurement location, and the distance from the source of field emission. In a car with a conventional drive (Dacia Sandero), the highest value of the magnetic field was recorded in the immediate vicinity of the alternator and amounted to 2.25 μT. This value decreased rapidly with increasing distance–already at a distance of 20 cm the magnetic field dropped below 1 μT, which indicates a limited range of this source and low exposure of the driver and passengers to magnetic flux density.

In the electric vehicle (Dacia Spring), the field values were much higher. During operation of the drive system, the maximum magnetic flux density was 5.0 μT in the vicinity of the inverter and high-voltage cables, and 3.3 μT at the engine. After moving away by 20 cm, these values dropped to 0.4–0.6 μT, confirming the strong dependence of the field intensity on distance from the source. However, the highest magnetic field emission was recorded during vehicle charging, when the field reached 41.7 μT in the immediate vicinity of the charger, 3.9 μT at the charging cable, and 2.2 μT in the inverter area inside the vehicle. The measured value of 41.7 μT indicates a potential health risk from prolonged exposure in the immediate vicinity of the charger. The highest magnetic field values were recorded in the hybrid vehicle (Toyota C-HR). The field strength in the area of the electric motor was 62.7 μT. Values of around 20 μT were measured near the inverter and high-voltage cables, and 12.6 μT near the generator. Even at a distance of 20 cm from the source, the values were significant: 12.4 μT, 6.5 μT and 4.0 μT respectively. Such high values in a hybrid vehicle may be due to the drive system's higher power and the more complex electrical system configuration compared to a lower-power electric vehicle. Summarizing the results of measurements during driving, the high-

est magnetic field strengths occur in electric vehicles, especially at higher speeds, due to the continuous, intensive operation of the electrical system, including the inverter, engine, and high-voltage cables. In hybrid vehicles, the magnetic field is higher at lower speeds because the electric motor is used more often in urban conditions. At higher speeds, the hybrid drive system primarily runs on the combustion engine, reducing field emissions. Conventional vehicles generate the lowest values, because their field sources–such as the alternator or ignition system – work less intensively and have a smaller share in generating the magnetic field compared to electric vehicles. The comparative analysis showed that electric and hybrid cars generate significantly higher magnetic fields than conventional-drive vehicles. The value of the magnetic flux density is significantly influenced by the power of the drive system and the location of components, such as the electric motor, inverter, or high-voltage cables, relative to the vehicle users. In addition, the measurements confirmed that the field intensity decreases exponentially with distance from the source, which is crucial for protecting the driver's and passengers' health. The field values measured in the immediate vicinity of the devices, especially during charging of the electric vehicle or operation of the electric motor in a hybrid vehicle, approach the limits permitted by international standards. Therefore, the choice of the drive system components' locations and the design of their shields should aim to minimize the user's exposure to the magnetic field. All observed values are below the permissible levels specified by the International Commission on Non-Ionizing Radiation Protection (ICNIRP), which sets a limit of 100 μT (for magnetic flux density) or about 80 mA/m (for field intensity) for magnetic fields at vehicle frequencies (approximately 50–60 Hz). This means that despite clear differences between vehicles, the level of exposure of drivers and passengers remains within safe limits. However, long-term exposure in the immediate vicinity of some sources (e.g. a charger when charging an electric vehicle) may require further monitoring, especially in the context of possible effects on particularly sensitive individuals.

Nomenclature

AC	alternating current
DC	direct current
EMF	electromagnetic field
ICE	internal combustion engine

Bibliography

[1] Bazhynov AV, Kravtsov MM. Electromagnetic danger of electric and hybrid vehicles. J Mech Eng Transp. 2023; 18(2):3-9. https://doi:10.31649/2413-4503-2023-18-2-3-9

[2] Berisha SH, Karady GG, Ahmad R, Hobbs R, Karner D. Magnetic field generated from different electric vehicles. SAE Technical Paper 951934. 1995. https://doi.org/10.4271/951934

[3] Cebulska W, Hadrys D. Comparison of vibration emissions in electric and conventional cars. Combustion Engines. 2025;202(3):74-80. https://doi.org/10.19206/CE-204690

[4] Dacia Poland. New electric city car Spring – Dacia. https://www.dacia.pl/samochody/nowy-spring.html (accessed on 2024 Sep 12).

[5] Dacia Poland. Sandero. https://www.dacia.pl/samochody/sandero.html (accessed on 2024 Sep 12).

[6] Dong X, Gao Y, Lu M. The electromagnetic exposure level of a pure electric vehicle inverter based on a real human body. Appl Sci. 2024;14(1):32. https://doi.org/10.3390/app14010032

[7] Gryz K, Karpowicz J, Zradziński P, Tokarski T, Kapcia Ł. Ekspozycja na pole elektromagnetyczne podczas użytkowania pojazdów samochodowych z napędem elektrycznym lub hybrydowym (in Polish). Bezpieczeństwo Pracy: Nauka i Praktyka. 2020;(12):18-21. https://doi.org/10.5604/01.3001.0014.5756

[8] He Y, Sun W, Leung PS-W, Chow Y-T. Effect of static magnetic field of electric vehicles on driving performance and on neuro-psychological cognitive functions. Int J Environ Res Public Health. 2019;16(18):3382. https://doi.org/10.3390/ijerph16183382

[9] Hristov R, Stefanov S, Kostov P. Investigation of the electromagnetic field in electric and hybrid cars. IOP Conf Ser Mater Sci Eng. 2020;1031:012027. https://doi.org/10.1088/1757-899X/977/1/012022

[10] ICNIRP – International Commission on Non-Ionizing Radiation Protection. https://www.icnirp.org (accessed on 2024 Dec 19).

[11] Marková I, Oravec M, Osvaldová LM, Sventeková E, Jurč D. Magnetic fields of devices during electric vehicle charging: a Slovak case study. Symmetry. 2021;13(11):1979. https://doi.org/10.3390/sym13111979

[12] Mercola J. Electromagnetic Fields (EMF). Białystok: Vital Publishing 2020.

[13] Ministry of Health (Poland). Regulation of the Minister of Health of 17 December 2019 on permissible levels of electromagnetic fields in the environment. Journal of Laws 2019, item 2448 (in Polish).

[14] Olabi AG, Abdelkareem MA, Wilberforce T, Alkhalidi A, Salameh T, Abo-Khalil A et al. Battery electric vehicles: progress, power electronic converters, strength (S), weakness (W), opportunity (O), and threats (T). Int J Thermofluids. 2022;16:100212. https://doi.org/10.1016/j.ijft.2022.100212

[15] Priya A, Kumar S. Review on converters used in electric drive system. Int J Mod Trends Sci Technol. 2023;9(1):1-9. https://doi.org/10.46501/IJMTST0901001

[16] Tell RA, Kavet R, Bailey WH, Halliwell J, Swanson J, Lotz WG. ELF magnetic fields in electric and gasoline-powered vehicles. Bioelectromagnetics. 2012;33(2):109-115. https://doi.org/10.1002/bem.21730

[17] TM-191 Magnetic Field Meter. Unitor s.c. https://unitor.com.pl/mierniki-pola-elektromagnetycznego/198-miernik-pola-elektromagnetycznego-tm-191.html (accessed on 2024 Mar 30).

[18] Toyota Poland. Toyota C-HR Configurator. https://www.toyota.pl/nowe-samochody/nowa-toyota-c-hr/konfigurator (accessed on 2024 Sep 12).

[19] Trentadue F, Cavagnaro M, Pisa S, Feliziani M. Assessment of low-frequency magnetic fields emitted by DC fast charging columns. Bioelectromagnetics. 2020;41(5):308-317. https://doi.org/10.1002/bem.22254
[20] Wang Y, Zhang Y, Li Z, Liu J, Wang X, Liu Y et al. Long-term monitoring of extremely low frequency magnetic fields in electric vehicles. Int J Environ Res Public Health. 2019; 16(19):3765. https://doi.org/10.3390/ijerph16193765
[21] Zachariasz M, Dybkowski M. Analiza układu napędowego pojazdu hybrydowego z silnikiem indukcyjnym (in Polish). Prace Naukowe Instytutu Maszyn, Napędów i Pomiarów Elektrycznych Politechniki Wrocławskiej. 2021;70:55-64. https://bibliotekanauki.pl/articles/1813994
[22] Zhao L, Liu X, Wang C, Yan K, Lin X, Li S et al. Magnetic fields exposure and childhood leukemia risk: a meta-analysis based on 11,699 cases and 13,194 controls. Leuk Res. 2014;38(3):269-274. https://doi:10.1016/j.leukres.2013.12.008
[23] Zimakowska-Laskowska M, Laskowski P. Comparison of pollutant emissions from various types of vehicles. Combustion Engines. 2024;197(2):139-145 https://doi.org/10.19206/CE-181193

Wioletta Cebulska, DEng. – Faculty of Transport and Aviation Engineering, Silesian University of Technology, Poland.
e-mail: *wioletta.cebulska@polsl.pl*

Adam Rajca – Faculty of Transport and Aviation Engineering, Silesian University of Technology, Poland.
e-mail: *ar305843@student.polsl.pl*

Prof. Damian Hadrys, DSc., DEng. – Faculty of Transport and Aviation Engineering, Silesian University of Technology, Poland.
e-mail: *damian.hadrys@polsl.pl*

Czołowy producent agregatów prądotwórczych w Polsce

Fogo®

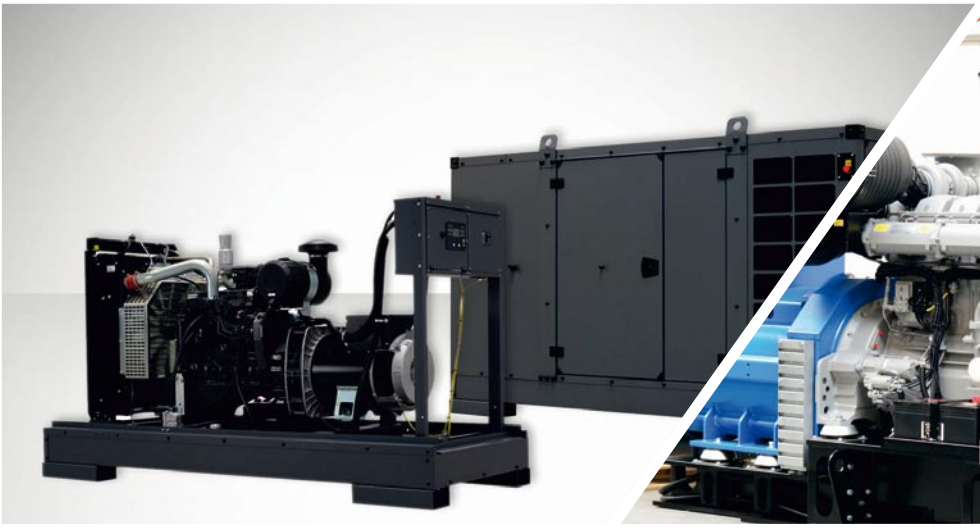

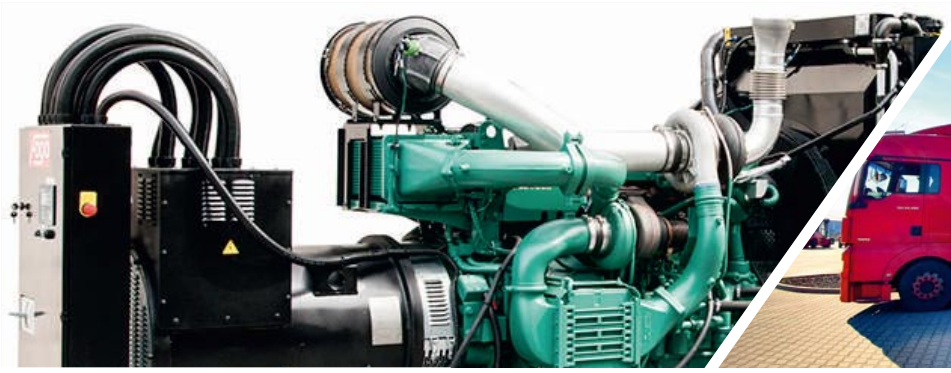

pewna **ENERGIA**

www.fogo.pl

Publisher:

Polish Scientific Society of Combustion Engines

Combustion Engines

Polskie Towarzystwo Naukowe Silników Spalinowych

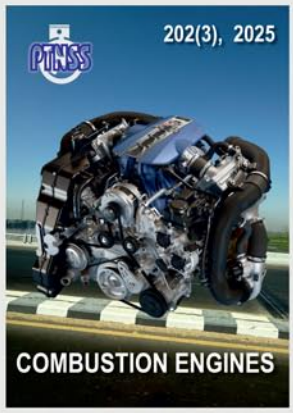

ISSN: 2300-9896
eISSN: 2658-1442

www.combustion-engines.eu